PB85-161909

Symposium on the Transfer and Utilization of Particulate Control Technology (4th). Volume 2 Electrostatic Precipitation

Denver Research Inst., CO

Prepared for

Environmental Protection Agency
Research Triangle Park, NC

Nov 84

U.S. Department of Commerce
National Technical Information Service
NTIS

United States
Environmental Protection
Agency

Industrial Environmental Research
Laboratory
Research Triangle Park NC 27711

EPA-600/9-84-025b
November 1984

PB85-161909

Research and Development

EPA

Fourth Symposium on the Transfer and Utilization of Particulate Control Technology:

Volume II. Electrostatic Precipitation

REPRODUCED BY
NATIONAL TECHNICAL
INFORMATION SERVICE
U.S. DEPARTMENT OF COMMERCE
SPRINGFIELD, VA. 22161

TECHNICAL REPORT DATA

(Please read Instructions on the reverse before completing)

1. REPORT NO.
EPA/600/9-84/025b

2\.

3. RECIPIENT'S ACCESSION NO.
PB85 161909 /AS

4. TITLE AND SUBTITLE
Fourth Symposium on the Transfer and Utilization of Particulate Control Technology; Volume II. Electrostatic Precipitation

5. REPORT DATE
November 1984

6. PERFORMING ORGANIZATION CODE

7. AUTHOR(S)
F.P. Venditti, J.A. Armstrong, and M.D. Durham (Compilers)

8. PERFORMING ORGANIZATION REPORT NO.

9. PERFORMING ORGANIZATION NAME AND ADDRESS
Denver Research Institute
P.O. Box 10127
Denver, Colorado 80210

10. PROGRAM ELEMENT NO.

11. CONTRACT/GRANT NO.
Cooperative Agreement CR809301

12. SPONSORING AGENCY NAME AND ADDRESS
Air and Energy Engineering Research Laboratory
Office of Research and Development
U.S. Environmental Protection Agency
Research Triangle Park, NC 27711

13. TYPE OF REPORT AND PERIOD COVERED
Proceedings; 1/82-10/84

14. SPONSORING AGENCY CODE
EPA/600/13

15. SUPPLEMENTARY NOTES
IERL-RTP project officer is Dale L. Harmon, Mail Drop 61, 919/541-2429.

16. ABSTRACT

The papers in the three volumes (of which this is one) were presented at the Fourth Symposium on the Transfer and Utilization of Particulate Control Technology in Houston, TX, October 11-14, 1982. Volume I relates to fabric filtration; Volume II, to electrostatic precipitation; and Volume III, to mechanical collectors, coal characteristics, inhalable particulates, and advanced energy and novel control devices. The symposium brought together researchers, manufacturers, users, government representatives, educators, and students to discuss new technology. It provided an effective way to transfer this technology out of the laboratory and into the user's hands. The various technologies were discussed from the perspectives of economics, new technical advances in science and engineering, and applications. Several papers dealt with combinations of devices and technologies, leading to a concept of using a systems (rather than a device) approach to particulate control. Other topic areas were high temperature/high pressure applications, fugitive emissions, measurement techniques, and cost analysis.

17. KEY WORDS AND DOCUMENT ANALYSIS

a. DESCRIPTORS		b. IDENTIFIERS/OPEN ENDED TERMS	c. COSATI Field/Group	
Pollution	Fabrics	Pollution Control	13B	11E
Particles	Electrostatics	Stationary Sources	14G	20C
Electrostatic Precipitators	Measurement	Particulate Control		14B
Scrubbers	Cost Analysis	Fabric Filters	13I	14A
Filters	Processing	Fugitive Emissions	07A	13H
	Leakage			

18. DISTRIBUTION STATEMENT
Release to Public

19. SECURITY CLASS *(This Report)*
Unclassified

20. SECURITY CLASS *(This page)*
Unclassified

21. NO. OF PAGES
560

22. PRICE

EPA Form 2220-1 (9-73)

EPA-600/9-84-025b
November 1984

FOURTH SYMPOSIUM ON THE TRANSFER AND UTILIZATION OF PARTICULATE CONTROL TECHNOLOGY
VOLUME II. ELECTROSTATIC PRECIPITATION

Compiled by:

F. P. Venditti, J. A. Armstrong, and Michael D. Durham

Denver Research Institute
P. O. Box 10127
Denver, Colorado 80210

Grant Number: CR 809301

Project Officer

Dale L. Harmon
Office of Environmental Engineering and Technology
Industrial Environmental Research Laboratory
Research Triangle Park, North Carolina 27711

INDUSTRIAL ENVIRONMENTAL RESEARCH LABORATORY
OFFICE OF RESEARCH AND DEVELOPMENT
U. S. ENVIRONMENTAL PROTECTION AGENCY
RESEARCH TRIANGLE PARK, NORTH CAROLINA 27711

i.a

DISCLAIMER

This document has been reviewed in accordance with U.S. Environmental Protection Agency policy and approved for publication. Mention of trade names or commercial products does not constitute endorsement or recommendation for use.

ABSTRACT

The papers in these three volumes of Proceedings were presented at the Fourth Symposium on the Transfer and Utilization of Paticulate Control Technology held in Houston, Texas during 11 October through 14 October 1982, sponsored by the Particulate Technology Branch of the Industrial Environmental Research Laboratory of the Environmental Protection Agency and coordinated by the Denver Research Institute of the University of Denver.

The purpose of the symposium was to bring together researchers, manufacturers, users, government agencies, educators and students to discuss new technology and to provide an effective means for the transfer of this technology out of the laboratories and into the hands of the users.

The three major categories of control technologies - electrostatic precipitators, scrubbers, and fabric filters - were the major concern of the symposium. These technologies were discussed from the perspectives of economics; new technical advancements in science and engineering; and applications. Several papers dealt with combinations of devices and technologies, leading to a concept of using a systems approach to particulate control rather than device control. Additional topic areas included novel control devices, high temperature/high pressure applications, fugitive emissions, measurement techniques, and economics and cost analysis.

Each volume of these proceedings contains a set of related session topics to provide easy access to a unified technology area.

Since the spirit and style of the panel discussion are not reproducible in print, the initial remarks presented by the panelists have been included in the volume to which their input to the panel pertained, in the interest of providing unified technological organization.

CONTENTS

Page

VOLUME II - CONTENTS v
VOLUME I - CONTENTS ix
VOLUME III - CONTENTS xii

Section A - Industrial Applications

MODELING OF WET BOTTOM AGITATOR SYSTEMS FOR ELECTROSTATIC PRECIPITATORS ON RECOVERY BOILERS 1
M.A. Sandell, R.R. Crynack

DESIGN AND PERFORMANCE OF ELECTROSTATIC PRECIPITATORS UTILIZING A NEW RIGID DISCHARGE ELECTRODE DESIGN 17
G.R. Gawreluk, R.L. Bump

DEVELOPMENT AND EVALUATION OF NEW PRECIPITATOR EMITTER ELECTRODE 35
R.L. Adams, P. Gelfand,

INDUSTRIAL APPLICATIONS OF TWO-STAGE TUBULAR ELECTROSTATIC PRECIPITATORS 51
H. Surati, M.R. Beltran

Section B - Advanced Technology

PILOT DEMONSTRATION TWO STAGE ESP TEST RESULTS 65
P. Vann Bush, D.H. Pontius

EVALUATION OF PRECHARGERS FOR TWO-STAGE ELECTROSTATIC PRECIPITATORS 84
G. Rinard, D. Rugg, M. Durham

INITIAL EXPERIMENTS WITH AN ELECTRON BEAM PRECIPITATOR TEST SYSTEM 96
W.C. Finney, R.H. Davis, J.S. Clements, E.C. Trexler, J.S. Halow, O. Tokunaga

EXPERIMENTS WITH WIDE DUCTS IN ELECTROSTATIC PRECIPITATORS . . . 111
E. Weber

A RECONCILIATION: WIDE VERSUS NARROW SPACED COLLECTING PLATES FOR PRECIPITATORS 126
D.G. Puttick

PULSE CORONA AS ION SOURCE AND ITS BEHAVIORS IN MONOPOLAR CURRENT EMISSION 139
S. Masuda, Y. Shishikui

Preceding page blank

Section C - Fundamentals

A NEW CORRECTION METHOD OF MIGRATION VELOCITY IN DEUTSCH EFFICIENCY EQUATION FOR CONVERSION OF ELECTROSTATIC PRECIPITATOR SIZING FROM A PILOT-SCALE TO FULL-SCALE 154
F. Isahaya

DISTORTION OF PULSE VOLTAGE WAVE FORM ON CORONA WIRES DUE TO CORONA DISCHARGE 169
S. Masuda, H. Nakatani

ELECTROSTATIC PRECIPITATOR ANALYSIS AND SYNTHESIS 184
T. Chiang, T.W. Lugar

COMPUTER MODEL USE FOR PRECIPITATOR SIZING 194
G.W. Driggers, A.A. Arstikaitis, L.A. Hawkins

IMPROVEMENTS IN THE EPA/SRI ESP PERFORMANCE MODEL 204
M.G. Faulkner, R.B.Mosley, J.R. McDonald, L.E. Sparks

NUMERICAL SIMULATION OF THE EFFECTS OF VELOCITY FLUCTUATIONS ON THE ELECTROSTATIC PRECIPITATOR PERFORMANCE 218
E.A. Samuel

CORONA - INDUCED TURBULENCE 230
M. Mitchner, G.L. Leonard, S.A. Self

VELOCITY AND TURBULENCE FIELDS IN NEGATIVE CORONA WIRE-PLATE PRECIPITATOR 243
H.P. Thomsen, P.S. Larsen, E.M. Christensen, J.V. Christiansen

THE EFFECT OF TURBULENCE ON ELECTROSTATIC PRECIPITATOR PERFORMANCE 261
D.E. Stock

FACTORS LEADING TO ELECTRICAL BREAKDOWN OF RESISTIVE DUST LAYERS AND SUSTAINED BACK CORONA 271
P.A. Lawless, L.E. Sparks

ELECTRICAL BREAKDOWN OF PARTICULATE LAYERS 288
G.B. Moslehi, S.A. Self

ELECTROMECHANICS OF PARTICULATE LAYERS 306
G.B. Moslehi, S.A. Self

LATERAL PROPAGATION OF BACK CORONA IN TWIN-ELECTRODE TYPE PRECIPITATORS 322
S. Masuda, T. Itagaki

FIRST MEASUREMENTS OF AEROSOL PARTICLE CHARGING BY FREE ELECTRONS 337
J.L. DuBard, M.G. Faulkner, L.E. Sparks

Section D - Operation & Maintenance

GAS FLOW DISTRIBUTION MODEL TESTING 349
D.R. Cook, J.M. Ebrey, D. Novogoratz

AIR FLOW MODEL STUDIES 369
L.H. Bradley

COLLECTING ELECTRODE RAPPING DESIGNED FOR HIGH EFFICIENCY ELECTRIC UTILITY BOILER ELECTROSTATIC PRECIPITATORS 384
A. Russell-Jones, A.P. Baylis

ELECTROSTATIC PRECIPITATOR AND FABRIC FILTER OPERATING AND MAINTENANCE EXPERIENCE 401
P.R. Goldbrunner, W. Piulle

Section E - Conditioning

ECONOMICAL FLY ASH COLLECTION BY FLUE GAS CONDITIONING 416
E.L. Coe, Jr.

EXPERIENCES AT DETROIT EDISON COMPANY WITH DECLINING PERFORMANCE OF SULFUR TRIOXIDE FLUE GAS CONDITIONING EQUIPMENT 430
L.A. Kasik, W.A. Rugenstein, J.L. Gibbs

ESP CONDITIONING WITH AMMONIA AT THE MONROE POWER PLANT OF DETROIT EDISON COMPANY 444
E.B. Dismukes, J.P. Gooch, G.H. Marchant, Jr.

FLY ASH CHEMISTRY INDICES FOR RESISTIVITY AND EFFECTS ON ELECTROSTATIC PRECIPITATOR DESIGN AND PERFORMANCE 459
H.J. Hall

Section F - Control Systems

A NEW ENERGIZATION METHOD FOR ELECTROSTATIC PRECIPITATORS MITSUBISHI INTERMITTENT ENERGIZATION SYSTEM 474
T. Ando, N. Tachibana, Y. Matsumoto

SOME MEASURED CHARACTERISTICS OF AN ELECTROSTATIC PRECIPITATOR OBTAINED USING A MICROCOMPUTER CONTROLLER 489
M.J. Duffy, T.S. Ng, Z. Herceg, K.L. McLean

ELECTROSTATIC PRECIPITATOR ENERGIZATION AND CONTROL SYSTEMS . . 499
K.M. Bradburn, K. Darby

APPLYING MODULAR MICROCOMPUTER CONTROL ELEMENTS IN A PRECIPITATOR CONTROL SYSTEM 521
I.M. Wexler

Section G - Plenary Session

THE CURRENT STATUS, FUTURE DIRECTIONS, AND ECONOMIC CONDITIONS IN THE APPLICATION OF ESP'S 534
S. Oglesby

AUTHOR INDEX 539

VOLUME I

FABRIC FILTRATION

Section A - Fabric Filters: Fundamentals

THEORY OF THE TEMPORAL DEVELOPMENT OF PRESSURE DROP ACROSS A FABRIC FILTER DURING CAKE INITIATION 1
E.A. Samuel

PULSE JET FILTRATION THEORY - A STATE-OF-THE-ART ASSESSMENT. . . 22
R. Dennis, L.S. Hovis

LABORATORY TECHNIQUES FOR DEVELOPING PULSE JET COLLECTORS. . . . 37
R.R. Banks, J.T. Foster

OFF-LINE PULSE-JET CLEANING SYSTEM 48
T.C. Sunter

Section B - Fabric Filters: Measurement Techniques

FIELD EVALUATION OF THE DRAG OF INDIVIDUAL FILTER BAGS 62
W.T. Grubb, R.R. Banks

A DUAL-DETECTOR BETA-PARTICLE BACKSCATTER GAUGE FOR MEASURING DUST CAKE THICKNESS ON OPERATING BAG FILTER AND ESP UNITS. . . . 77
R.P. Gardner, R.P. Donovan, L.S. Hovis

MIT FLEX ENDURANCE TESTS AT ELEVATED TEMPERATURE 91
J.T. Foster, W.T. Grubb

THE ONE-POINT IN-SITU CALIBRATION METHOD FOR USING A BETA-PARTICLE BACKSCATTER GAUGE FOR CONTINUOUSLY MEASURING DUST CAKE THICKNESS ON OPERATING BAG FILTER AND ESP UNITS 107
R.P. Gardner, R.P. Donovan, L.S. Hovis

Section C - Fabric Filters: Coal Fired Boilers

PULSE-JET FABRIC FILTER EXPERIENCE USING NON-GLASS MEDIA AT AIR TO CLOTH RATIOS OF 5 TO 1 ON A PULVERIZED COAL FIRED BOILER 121
G. Pearson, D.D. Capps

START-UP AND OPERATION OF A FABRIC FILTER CONTROLLING PARTICULATE EMISSIONS FROM A 250 MW PULVERIZED COAL-FIRED BOILER 132
C.B. Barranger, N. Spence, J. Saibini

VOLUME I CONTENTS (Cont.)

PERFORMANCE OF A 10 MW FABRIC FILTER PILOT PLANT AND COMPARISON TO FULL-SCALE UNITS 148
W.B. Smith, K.M. Cushing, R.C. Carr

THE DESIGN, INSTALLATION, AND INITIAL OPERATION OF THE W.H. SAMMIS PLANT, UNIT 3 FABRIC FILTER 164
D.R. Ross, J.R. Howard, R.M. Golightley

RESULTS FROM THE FABRIC FILTER EVALUATION PROGRAM AT COYOTE UNIT #1 179
H.J. Peters, A.A. Reisinger, W.T. Grubb, M. Lewis

BAGHOUSE PERFORMANCE AND ASH CHARACTERIZATION AT THE ARAPAHOE POWER STATION 192
R.S. Dahlin, D.R. Sears, G.P. Green

AN EVALUATION OF FULL-SCALE FABRIC FILTERS ON UTILITY BOILERS. 210
J.W. Richardson, J.D. McKenna, J.C. Mycock

STATUS OF SPS INVESTIGATION OF HARRINGTON STATION UNIT 2 FABRIC FILTER SYSTEM 226
R. Chambers, D. Harmon

UPDATE OF SPS PILOT BAGHOUSE OPERATION 239
R. Chambers, S. Kunka, D. Harmon

THE USE OF SONIC AIR HORNS AS AN ASSIST TO REVERSE AIR CLEANING OF A FABRIC FILTER DUST COLLECTOR 255
A. Menard, R.M. Richards

Section D - Fabric Filters: Electrostatic Enhancement

ELECTROSTATIC STIMULATION OF REVERSE-AIR-CLEANED FABRIC FILTERS 287
D.A. Furlong, G.P. Greiner, D.W. VanOsdell, L.S. Hovis

ELECTRICAL STIMULATION OF FABRIC FILTRATION: ENHANCEMENT BY PARTICLE PRECHARGING 303
G.E.R. Lamb, R. Jones, W. Lee

ESFF AS A FIELD EFFECT 316
L.S. Hovis, G.H. Ramsey, R.P. Donovan

ELECTRICAL ENHANCEMENT OF FABRIC FILTRATION: PRECHARGING VS. BAG ELECTRODES 327
R.P. Donovan, L.S. Hovis, G.H. Ramsey

PERMEABILITY OF DUST CAKES COLLECTED UNDER THE INFLUENCE OF AN ELECTRIC FIELD 342
D.W. VanOsdell, R.P. Donovan, D.A. Furlong, L.S. Hovis

VOLUME I CONTENTS (Cont.)

Section E - Fabric Filters: Practical Considerations

HIGH VELOCITY FABRIC FILTRATION FOR INDUSTRIAL COAL-FIRED BOILERS 357
G.P. Greiner, S. Delaney, L.S. Hovis

OPTIMIZING THE LOCATION OF ANTI-COLLAPSE RINGS IN FABRIC BAGS 382
J. Musgrove

PULSE JET ON-LINE CLEANING FILTER FOR FLY ASH 420
W.G. Wellan

TOP INLET VERSUS BOTTOM INLET BAGHOUSE DESIGN 431
R.M. Jensen

UPGRADE OF FLY ASH COLLECTION CAPABILITY AT THE CROMBY STATION 446
T.J. Ingram, R.J. Biese, R.O. Jacob

HIGH SULFUR FUEL, FABRIC FILTER STARTUP EXPERIENCE 460
P. Hanson, L. Adair, R.N. Roop, R.B. Moyer

FUNDAMENTAL STRATEGIES FOR CLEANING REVERSE AIR BAGHOUSES. . . . 482
M. Ketchuck, M.A. Walsh, O.F. Fortune,
M.L. Miller, M. Whittlesey,

Section F - Dry Scrubbers

DESIGN CONSIDERATIONS FOR BAGHOUSE - DRY SO_2 SCRUBBER SYSTEMS 494
O.F. Fortune, R.L. Miller

RESULTS OF BAGHOUSE AND FABRIC TESTING AT RIVERSIDE 506
H.W. Spencer III, Y.J. Chen, M.T. Quach

REACTIVITY OF FLY ASHES IN A SPRAY DRYER/FABRIC FILTER FGD PILOT PLANT 521
W.T. Davis, R.E. Pudelek, G.D. Reed

Section G - Plenary Session

FABRIC FILTRATION - AS IT WAS, HAS BEEN, IS NOW AND SHALL BE 536
E.R. Frederick

AUTHOR INDEX 551

VOLUME III

CONTENTS

Keynote Address

PARTICULATE CONTROL TECHNOLOGY AND WHERE IT IS GOING xv
K.E. Yeager

Section A - Economic Comparisons

A COMPARISON OF A BAGHOUSE VS. ESP'S WITH AND WITHOUT GAS CONDITIONING FOR LOW SULFUR COAL APPLICATIONS 1
W.H. Cole

APPLICATION OF THE BUBBLE CONCEPT TO FUEL BURNING SOURCES AT A NAVAL INDUSTRIAL COMPLEX 12
C.S Thompson

Section B - Mechanical Collectors

CYCLONE PERFORMANCE: A COMPARISON OF THEORY WITH EXPERIMENTS 26
J.A. Dirgo, D. Leith

HIGH FLOW CYCLONE DEVELOPMENT 41
W.B. Giles

CYCLONE SCALING EXPERIMENTS 53
W.B. Giles

TEST METHODS AND EVALUATION OF MIST ELIMINATOR CARRYOVER 66
V. Boscak, A. Demian

Section C - Coal Characterization

FILTRATION CHARACTERISTICS OF FLY ASHES FROM VARIOUS COAL PRODUCING REGIONS 81
J.A. Dirgo, M.A. Grant, R. Dennis, L.S. Hovis

FLY ASH FROM TEXAS LIGNITE AND WESTERN SUBBITUMINOUS COAL: A COMPARATIVE CHARACTERIZATION 97
D.R. Sears, S.A. Benson, D.P. McCollor, S.J. Miller

USE OF FUEL DATABANKS FOR THE EFFECTIVE DESIGN OF STEAM GENERATORS AND AQC EQUIPMENT 114
N.W. Frisch, T.P. Dorchak

VOLUME III CONTENTS (Cont.)

Section D - Inhalable Particulate Matter

DEVELOPMENT OF INHALABLE PARTICULATE (IP) EMISSION FACTORS . . . 131
D.L. Harmon

INHALABLE PARTICULATE MATTER RESEARCH COMPLETED BY GCA/TECHNOLOGY DIVISION 141
S. Gronberg

RESULTS OF TESTING FOR INHALABLE PARTICULATE MATTER AT MIDWEST RESEARCH INSTITUTE 154
K. Wilcox, F. Bergman, J. Kinsey, T. Cuscino

INHALABLE PARTICULATE EMISSION FACTORS TEST PROGRAMS 166
J.W. Davison,

CHARACTERIZATION OF PARTICULATE EMISSION FACTORS FOR INDUSTRIAL PAVED AND UNPAVED ROADS 183
C. Cowherd, Jr., J.P. Reider, P.J. Englehart

CONDENSIBLE EMISSIONS MEASUREMENTS IN THE INHALABLE PARTICULATE PROGRAM 198
A.D. Williamson, J.D. McCain

Section E - Advanced Energy Applications

GAS CLEANING AND ENERGY RECOVERY FOR PRESSURIZED FLUIDIZED BED COMBUSTION 211
A. Brinkmann, P.M. Kutemeyer

DEMONSTRATION OF THE FEASIBILITY OF A MAGNETICALLY STABILIZED BED FOR THE REMOVAL OF PARTICULATE AND ALKALI 226
L.P. Golan, J.L. Goodwin, E.S. Matulevicius

TEST RESULTS OF A HIGH TEMPERATURE, HIGH PRESSURE ELECTROSTATIC PRECIPITATOR 241
D. Rugg, G. Rinard, J. Armstrong, T. Yamamoto, M. Durham

COAL-ASH DEPOSITION IN A HIGH TEMPERATURE CYCLONE 256
K.C. Tsao, A. Rehmat, D.M. Mason

DUST FILTRATION USING CERAMIC FIBER FILTER MEDIA — A STATE-OF-THE-ART SUMMARY — 271
R. Chang, J. Sawyer, W. Kuby, M. Shackleton,
O.J. Tassicker, S. Drenker

HIGH TEMPERATURE AND PRESSURE PARTICULATE FILTERS FOR FLUID BED COMBUSTION 282
D.F. Ciliberti, T.E. Lippert, O.J. Tassicker, S. Drenker

VOLUME III CONTENTS (Cont.)

MOVING BED-CERAMIC FILTER FOR HIGH EFFICIENCY PARTICULATE AND ALKALI VAPOR REMOVAL AT HIGH TEMPERATURE AND PRESSURE . . . 300
D. Stelman, A.L. Kohl, C.A. Trilling

TESTING AND VERIFICATION OF GRANULAR BED FILTERS FOR REMOVAL OF PARTICULATES AND ALKALIS 318
T.E. Lippert, D.F. Ciliberti, R. O'Rourke

BAGHOUSE OPERATION IN GEORGETOWN UNIVERSITY COAL-FIRED, FLUIDIZED-BED BOILER PLANT, WASHINGTON, D.C. 335
V. Buck, D. Suhre

Section F - Novel Devices

PARTICLE CAPTURE MECHANISMS ON SINGLE FIBERS IN THE PRESENCE OF ELECTROSTATIC FIELDS 347
M.A. Ranade, F.L. Chen, D.S. Ensor, L.S. Hovis

PILOT DEMONSTRATION OF PARTICULATE REMOVAL USING A CHARGED FILTER BED 362
P.H. Sorenson

PILOT DEMONSTRATION OF MAGNETIC FILTRATION WITH CONTINUOUS MEDIA REGENERATION 370
C.E. Ball, D.W. Coy

Section G - Plenary Session

NOVEL PARTICULATE CONTROL TECHNOLOGY 386
S. Masuda

AUTHOR INDEX 406

MODELING OF WET BOTTOM AGITATOR SYSTEMS FOR ELECTROSTATIC PRECIPITATORS ON RECOVERY BOILERS

by: Michael A. Sandell
Robert R. Crynack
Air Pollution Control Division
Wheelabrator-Frye Inc.
5100 Casteel Drive
Coraopolis, Pennsylvania 15108

ABSTRACT

Wet bottom precipitator designs are becoming more common on black liquor recovery boiler applications. A black liquor-filled pan under the precipitator mixes the collected salt cake as it is circulated with rotating agitators. Undesirable buildup can result due to improper mixing and poor flow patterns. In order to verify that the design of a complex wet bottom agitator system is adequate, three dimensional scale modeling should be employed. The paper presents the results of several such model studies. The results discussed include a) visualization of flow and mixing patterns, b) identification of poor mixing areas, c) specification of location and size of baffles to improve areas of poor mixing, d) determination of agitator speed and direction of rotation, e) evaluation of paddle design and orientation, and f) location of feed and drain pipes. The theory of modeling, which considers the temperature and viscosity of the black liquor and which establishes the scaling factors and model fluid parameters, is also discussed. This modeling technique provides a valuable tool for users, consultants, and manufacturers to minimize on-line problems.

BACKGROUND

Precipitators have been used in the pulp and paper industry on recovery boiler applications since the late 1930's. Initially dust removal was accomplished with pyramidal hoppers. Because of the hydroscopic nature of salt cake, extensive heat tracing and insulation were necessary for satisfactory dust removal. To overcome this, drag conveyor dust removal systems were developed. With drag conveyors, the salt cake is collected in a dry pan beneath the precipitator collection zone and then removed from the pan by a scraping mechanism. This type of system had high maintenance requirements because of the many moving mechanical components. To overcome some of the problems with drag conveyors, the wet bottom design evolved and came into use on direct contact evaporator (DCE) recovery boiler precipitators around 1948. (1)

During the '60's and early '70's when environmental considerations increased, the recovery process was scrutinized for ways of reducing malodorous emissions. The principal source of these emissions was the contact of the black liquor and flue gas in the DCE. One technology response was the non-contact evaporator (NCE) and dry bottom precipitator (ESP). The NCE boiler and dry bottom ESP began commercial operation in the USA in 1969. Many of the first NCE recovery units and their dry bottom precipitators had problems requiring rebuilding and had long down times because of the precipitator.

Because of these early dry bottom problems, the first NCE recovery wet bottom precipitator came on line in 1972. In 1974 the second NCE wet bottom unit came on line. Limited testing has indicated that odorous emissions from these wet bottoms are negligible. By 1978 an industry survey showed that wet bottom ESP's comprised 25% of new NCE's installed.

The design of a wet bottom generally calls for a pan filled with black liquor under the entire collecting surface of the ESP. The pan, with rotary agitators, mixes the collected dust and the black liquor. This wet bottom concept is easily integrated into the black liquor recovery process. (2) The black liquor which has been circulated through the pan is fired in the recovery boiler. The salt cake collected by the ESP which has been mixed with the liquor in the wet bottom is eventually returned to the boiler.

The high solids concentration of the black liquor and inadequate mixing of the salt cake and black liquor have caused salt cake build-ups in several wet bottom agitator pans. These buildups can reach to the collecting area of the precipitator and short out the electrical fields. The shorting of several fields causes emission levels to increase. This can create a maintenance headache for the operating company who has to enter the precipitator and remove the salt cake buildup. The purpose of this paper is to discuss model studies performed to increase the degree of confidence that the full-scale agitator systems will operate satisfactorily with little or no build-up problems.

THEORY

For complete similarity between a model and the full-scale system to exist, it is necessary to have geometric, kinematic and dynamic similarity. Geometric similarity exists when the ratios of all corresponding dimensions of the model and the full-scale system are equal. Kinematic similarity exists when the streamlines are geometrically similar. Dynamic similarity exists when the ratios of all forces are the same. There are five dimensionless parameters which define the fluid dynamics of a system. These are the Reynolds, Froude, Weber, Euler and Mach numbers. For dynamic similitude to be maintained, these five dimensionless parameters for the model must equal the five dimensionless parameters of the full scale system. In actuality, it is not practical to maintain the equality of all five parameters. Therefore, the model must at least consider those dimensionless parameters which are most important to the system being modeled.

For modeling an agitator type system, the most important parameters are those associated with the Reynolds number and the Froude number. The Reynolds number is important because it defines the relationship between size, viscosity and velocity. The Froude number defines the relationship between velocity and gravitational acceleration. The Mach number which defines compressibility, the Weber number which defines surface tension and the Euler number which defines pressure were all judged to be of minor significance in these model studies.

The Reynolds number is the ratio of the inertial forces to the frictional forces usually in terms of convenient flow and geometrical parameters. It is given by the equation

$$Re = \frac{\rho LV}{\mu} = \frac{LV}{\nu}$$

where ρ = density, L = length, V = velocity, μ = absolute viscosity and ν = Kinematic viscosity. The Froude number is the ratio of the inertial forces to the force of gravity. Given a free surface, the form of the waves will be directly affected by the force of gravity and so the Froude number is significant. It is given by the equation

$$F = \frac{V^2}{LG}$$

where V = velocity, L = length, and G = gravitational acceleration. By equating the Reynolds and Froude numbers of the model and the full scale system, scaling factors between the two systems can be determined. The length scaling factor and velocity scaling factor is determined to be

$$\frac{L_1}{L_2} = \left(\frac{\nu_1}{\nu_2}\right)^{2/3} \qquad \frac{V_1}{V_2} = \left(\frac{\nu_1}{\nu_2}\right)^{1/3}$$

As can be seen both the length and velocity scaling factors are dependent upon the ratio of the kinematic viscosities of the fluids used in the model and full scale systems.

MODEL DESIGN

The objective in modeling a wet bottom ESP is to provide information which can be used to increase the degree of confidence that the agitator system for the low odor recovery boiler will function satisfactorily with little or no particulate buildups. The parameters of the full scale system which are important in the model program are dependent upon the black liquor properties and the physical design of the wet-bottom. Those black liquor properties which are important are 1) viscosity of the black liquor, 2) solids concentration of the black liquor, 3) liquor temperature, 4) liquor feed rate. The elements of the wet bottom design which are important are 1) pan size, 2) number of agitators and 3) agitator size. The black liquor characteristics should be given both for normal operating conditions and worst-case conditions.

The parameters of the full scale system set the limits and variables for the wet bottom model. The length scaling factor should be restricted to the range of 6:1 to 12:1. It is felt that any model scaled outside this range would either be too small or too large to be easily constructed or modified after construction. The exact length scaling factor is dependent upon the ratio of the kinematic viscosity of the black liquor in the full scale system to the kinematic viscosity of the fluid used in the model. The kinematic viscosity of black liquor is dependent upon many factors, with temperature and concentration of dissolved solids being two of the most important. (Figure 1) (3)

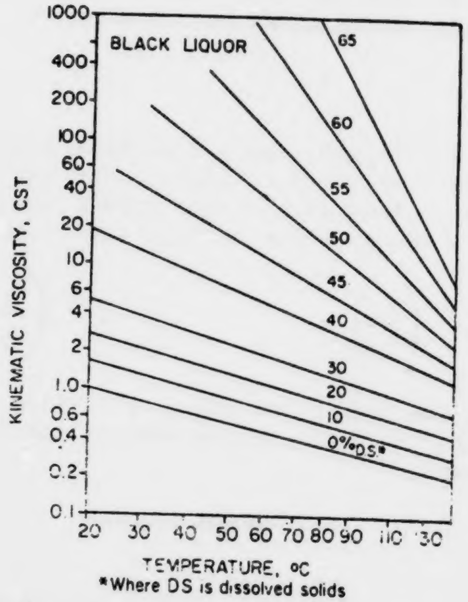

*Where DS is dissolved solids

FIGURE 1 KINEMATIC VISCOSITY OF BLACK LIQUOR

It has been our experience that the slow flow areas in the full scale system have the greatest effect on the operation of the wet bottom system. Slow flow areas allow the salt cake collected from the precipitator to drop out of suspension and buildups to occur. These salt cake buildups can occur to the extent the precipitator fields are shorted and efficiency of the precipitator reduced. While it is not practical to simulate the actual operation of the precipitator above the model, the relative motion of the fluid can be observed. Thus, the thrust of the model study is to minimize the fluid residence time in the slow flow areas.

The variables of the model which can be examined are 1) direction of agitator rotation, 2) agitator rotational speed, 3) paddle porosity, 4) paddle angle from agitator arm, 5) synchronized vs non-synchronized agitator rotation, 6) slow dispersion area baffling, 7) fluid viscosity, 8) liquor feed locations, 9) liquor feed rates, 10) normal and emergency overflow locations and 11) liquor level. For each variable specific items were noted. These included 1) identification of slow flow areas, 2) overall flow patterns, 3) fluid swirling and eddying, and 4) fluid splashing.

MODEL EQUIPMENT AND PROCEDURES

The results of three different model studies are presented in this paper. The models varied in the number of agitator arms and black liquor viscosities. The systems examined had 2, 3, and 6 agitators The viscosities examined ranged from 20 centistokes to 2,000 centistokes. This corresponds to a dissolved solids concentration in the black liquor of 55% to 70% respectively.

The agitator arms have been generally made from carbon steel rods on which the metal paddles were attached. The metal paddles were attached to the agitator arms using screws and nuts. This allowed the paddle angle to be adjusted quickly and easily.

The agitators were driven from above the liquid rather than below as in the full scale system. This eliminates the need for sealed bearings and allowed maximum flexibility in the model. The speed of agitator rotation was adjustable from 1 RPM to the maximum. The direction of rotation could be reversed either by the drive mechanism or by a loop in the drive chains. Synchronized vs non-synchronized rotation was examined using both duplicate drive mechanisms and by offsetting the agitator arms 90° from one another.

Several fluids were used in the models examined. These included water, ethylene glycol, and a glycerin and water mixture. The selection of the fluid was based upon its physical properties. The kinematic viscosity of the modeling fluid is the critical factor in the scale factor determination. Other factors which were considered were availability, ease of cleaning, low odor and low toxicity. The added advantage to the selection of the glycerin and water mixture was the ability to change the proportion of glycerin to water and thus, change the kinematic viscosity.

Because it was not practical to simulate the actual operation of a precipitator above the model, only the relative motion of the fluid could be observed. This was accomplished by dropping a given amount of dye into the model fluid and observing the relative motion and speed with which it dispersed. In order to compare the dispersion rate of the dye in one area with respect to another, the rate of dispersion was timed. The sides of the model pan were labeled A, B, C, and D with the respective corners being identified a corner AB, corner BC, etc. (Figure 2) Dispersion was defined as 100% of the dye being removed from the immediate area. Slow flow areas and overall flow patterns were examined in the greatest detail.

RESULTS

DIRECTION OF AGITATOR ROTATION

The direction of agitator rotation is dependent upon the design of the full scale system. System complexity varies with the number of agitator arms, the size of the arms, the size of the pan, and the viscosity of the fluid. Because of this variation in complexity, each system must be evaluated individually. When all the agitators of a given wet bottom rotate in the same direction, a fluid flow which rotates around the perimeter of the tank develops. The fluid flow in the center of the pan, however, lacks the force of the main flow. The result of this lack of force produces stagnant areas of swirling liquor between any two agitators. (Figure 2)

When two adjacent agitators rotate in different directions, the liquor is moved through the center of the two agitators. However, a stagnant area now develops where the two agitators rotate toward each other. (Figure 3) The direction of the rotation for each system must be selected on the basis of the location of slow flow areas and the overall flow pattern of the black liquor for that system.

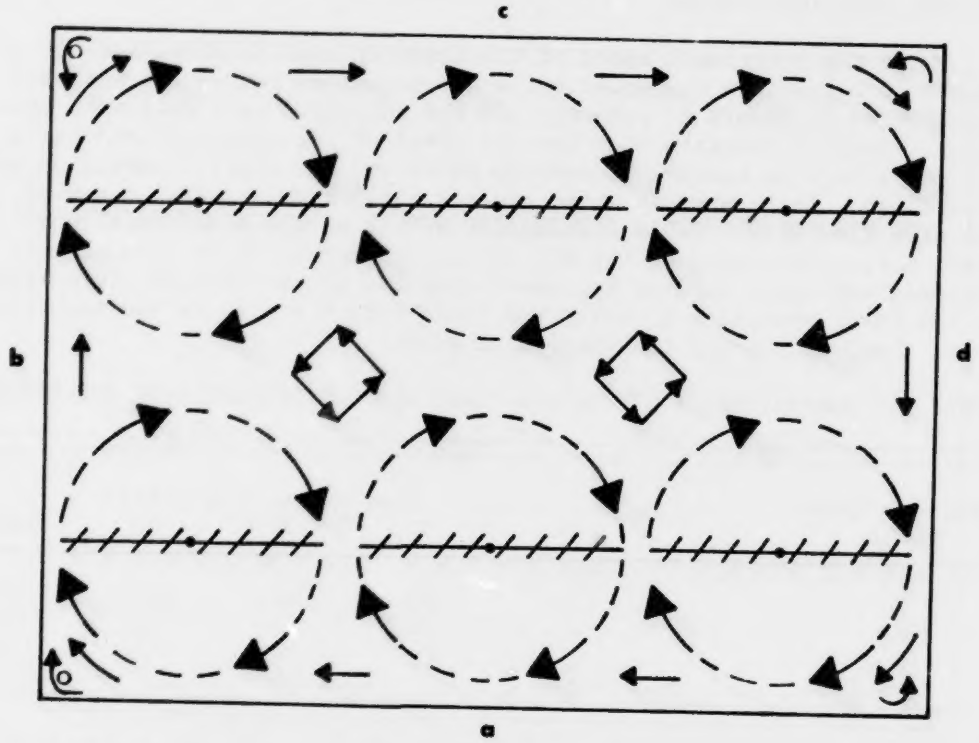

FIGURE 2. AGITATORS ROTATING IN THE SAME DIRECTION

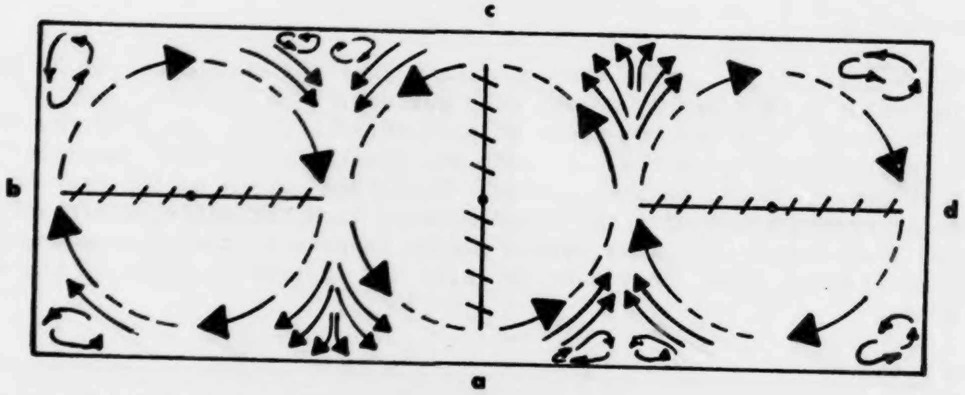

FIGURE 3. AGITATORS ROTATING IN OPPOSITE DIRECTIONS

AGITATOR ROTATIONAL SPEED

While the rotational speed of the agitator arms is discussed, it is, in reality, the agitator tip speed not the revolutions per minute which is the major factor necessary to properly mix the collected salt cake with the black liquor. Results indicate that the tip speed of the agitator arms has a significant effect on the dye dispersion rates and the overall mixing of the model fluid. Increased tip speed reduces the dispersion time measured in each slow flow area. Table 1 shows the effect of increased rotational speed, i.e., tip speed, on the dye dispersion rates. It is assumed that the increased arm speed imparts increased momentum to the viscous fluid, providing the force necessary to drive the fluid into the corners and slow flow areas, thus, decreasing the dispersion times.

TABLE 1. COMPARISON OF DISPERSION TIMES FOR VARIOUS AGITATOR ARM SPEEDS

Agitator Speed (RPM)	Dispersion time (sec)				
	AB	BC	CD	AD	Center
7	180+	180+	180+	180+	75
9	40	50	60	60	70
11	30	35	50	50	40

It was also demonstrated in the model studies that the agitator tip speed has an optimum speed. At tip speeds greater than this optimum speed, the agitator arm can cause excessive wave action and splashing. This higher speed may cause a salt cake buildup on the pan walls above the fluid level or on the anti-sneakage baffles in the precipitator. Proper sizing of the agitator drive systems can considerably reduce equipment costs as well as energy consumption.

PADDLE POROSITY

The results of the model study indicate that the outermost paddle is the most important with respect to salt cake buildup. The interior paddles should be porous to allow the fluid to pass through them. This allows for a more complete mixing of the salt cake and black liquor. The outermost paddle, however, should be less porous. This less porous paddle has the beneficial effect of driving the fluid outward from the agitator arm into the slow flow areas. The less porous paddle imparts a greater momentum to the fluid flow and thus, decreases the size and dispersion times of the slow flow areas.

PADDLE ANGLE

Four different paddle angles were examined, 0°, 15°, 30°, 45° from the center of the agitator arm, angled such that the liquor is pushed outward as the agitator rotates. The 30° angle of the paddle on the agitator arm generally provided lower dispersion rates in the corners than did a 0°, 15°, or

45° paddle angle. Table 2 illustrates these results.

TABLE 2. COMPARISON OF DISPERSION TIMES FOR VARIOUS PADDLE ANGLES

Agitator Speed (RPM)	Corner	Dispersion Time (sec) 0°	15°	30°	45°
9	AB	60+	60+	40	55
9	BC	60+	60+	50	60+
9	CD	60+	60+	60	60
9	AD	55	60+	60	180
9	Center	*	36	75	30
11	AB	60+	56	30	180
11	BC	60+	60+	35	180
11	CD	60+	60+	50	180
11	AD	55	60+	50	180
11	Center	35	47	40	20

* No measurement taken

Also examined was the effect of a paddle angled such that the liquor was drawn inward toward the center of the agitator as it rotates. Paddles angled in this manner had higher residence times in the slow dispersion areas than paddles angled outward.

SYNCHRONIZED VS NON SYNCHRONIZED AGITATOR ROTATION

Investigations performed in the model studies indicated that the differences found between the synchronized and non-synchronized operations were small. The non-synchronized rotation, however, generally produced slightly less dispersion times. Normally in full scale systems the agitators are operated independently of one another. It is difficult, therefore, to synchronize or non-synchronize the agitator operation at all times. In fact, the agitators generally are non-synchronized because of their independent operation. It was apparent, however that the optimum configuration in either mode of operation (synchronized or non-synchronized) provides sufficient fluid movement and mixing patterns.

SLOW DISPERSION AREA BAFFLING

In all the model studies performed, with no baffles in position, areas of slow flow and circular motion develop in all the pan corners. (Figure 4) The dispersion times measured with no baffles in position were exceedingly high in all cases. It was clearly indicated that stationary baffles are necessary in all corners and other areas of slow dye dispersion. The effect of stationary baffles on dispersion times is presented in Table 3. A graphic presentation of the effect of stationary baffles is presented in Figure 5.

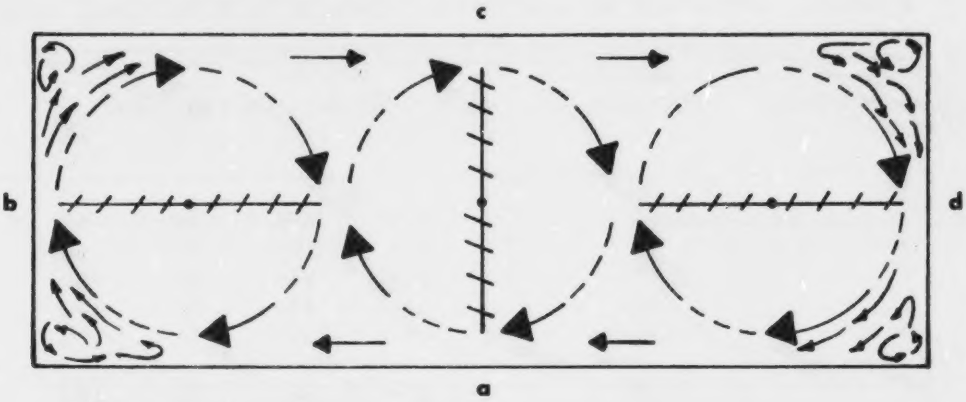

FIGURE 4. FLOW PATTERNS WITH NO BAFFLES

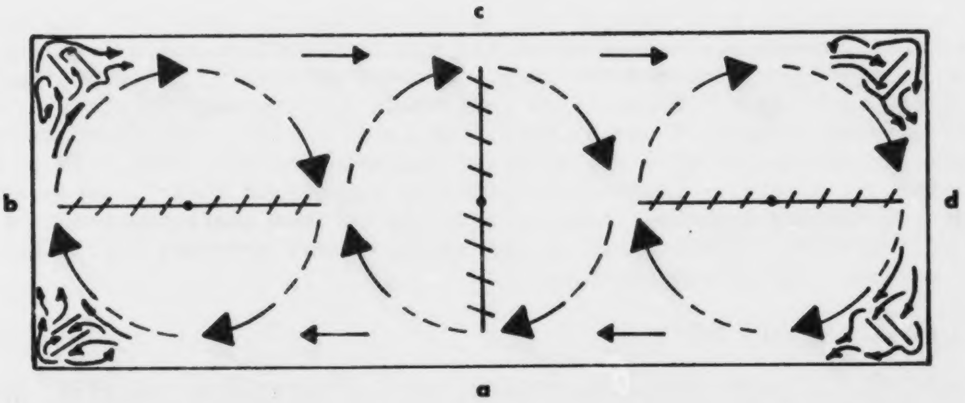

FIGURE 5. FLOW PATTERNS WITH BAFFLES

TABLE 3. COMPARISON OF DISPERSION TIMES WITH AND WITHOUT BAFFLES

Corner Baffles	Agitator Speed (RPM)	Dispersion Time (sec) AB	BC	CD	AD
No	7	120	120	180+	180+
No	9	120	120	180+	180+
No	11	120	120	150	150
Yes	7	50	60	45	45
Yes	9	30	35	25	25
Yes	11	25	45	20	20

Examination of the location of stationary baffles indicates that baffles should be placed so that no additional corners are created. The high viscosity of the black liquor prevents the fluid from sweeping into and out of the corners without the help of baffles to direct the fluid direction. Therefore, baffles should be placed away from the pan walls and positioned in such a way as to direct the black liquor to the slow flow area.

LIQUOR FEED LOCATIONS

The placement of the inlet feed was investigated. Three locations were examined. A feed located in the center of one of the short sides and a feed in either corner of the short side were investigated. (Figure 6) In one corner the feed entered from either the bottom of the pan or through the side wall. The feeds were positioned such that the inlet feed flow enhanced the mixing and flow pattern of the fluid.

At the lower viscosities, at each corner location, the mixing and flow enhancement caused by the inlet feed flow eliminated the need in that corner for baffling. At the higher viscosities (1,000 cs) a backflow area developed upstream of the inlet feed. A baffle was positioned in this corner to reduce this backflow area and enhance the fluid pattern into and out of the corner. In all feed placements the inlet feed flow had no effect on the overall flow and mixing patterns except in the location where the inlet jet stream occurred.

The inlet feed should be located under the inlet field of the precipitator and positioned so that the liquor flows across the inlet field. This placement allows the fresh black liquor to contact the greatest amount of collected salt cake and allows a longer mixing time prior to firing.

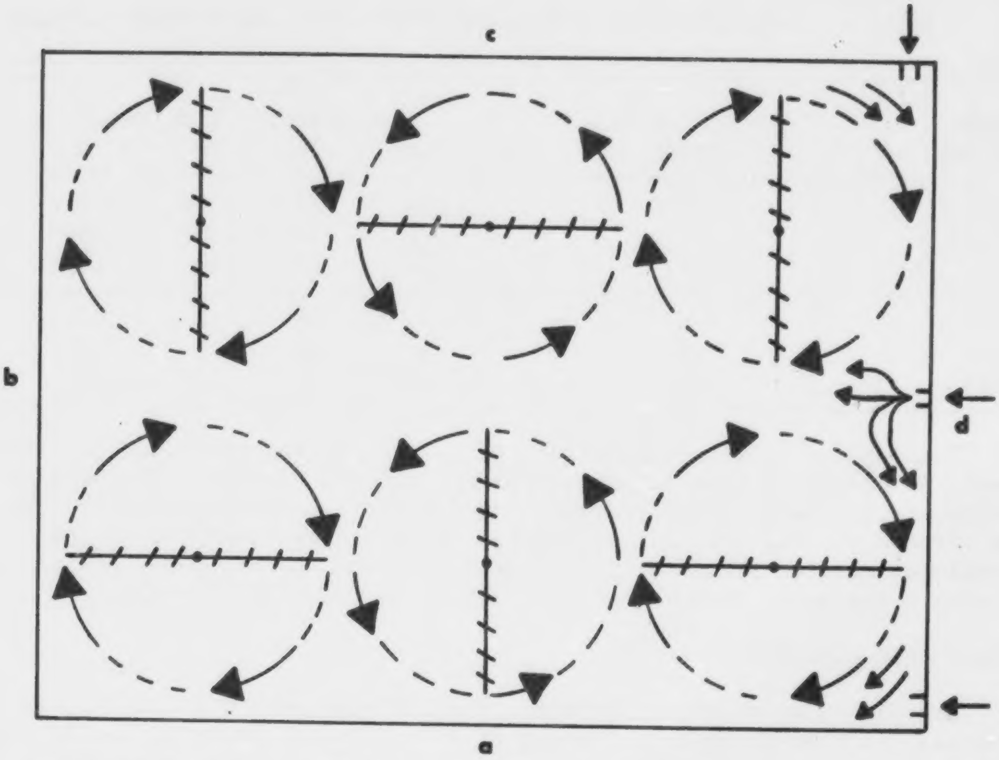

FIGURE 6. INLET FEED LOCATIONS

INLET FEED RATES

Examination of varying liquor feed rates indicates that as the feed rate increases, the possibility of a slow flow area developing at that location lessens. The critical factor in feed rates is the lowest probable black liquor flow. The lowest feed rate expected may not provide the fluid flow enhancement necessary to eliminate baffling in that location.

NORMAL AND EMERGENCY OVERFLOW LOCATIONS

The location of the normal and emergency overflow pipes was examined to determine whether they should be centered in the corner or offset either upstream or downstream of the corner. The overflow pipe was placed in various positions to determine the optimum location. Due to the close proximity of the agitator arms, the overflow pipe with its required baffling could not be positioned upstream of the corner without interfering with the agitator arm. Table 4 presents a comparison of the dispersion times measured between the centered and the offset overflow pipes. As can be seen, the offset and centered pipes had approximately the same dispersion times with no baffles in position. Once the baffles were positioned, however, the offset overflow pipe dispersion times were approximately 5 seconds less than the centered pipe.

TABLE 4. COMPARISON OF DISPERSION TIMES (SEC)
FOR CENTERED VS OFFSET OVERFLOWS

Position	Baffles	Dispersion Times (sec.)
Centered	No	27
Offset Downstream	No	28
Centered	Yes	24
Offset Downstream	Yes	19

The normal and emergency overflow pipes should also be positioned under the outlet fields of the precipitator. This placement along with the location of the liquor feed under the inlet fields permits the maximum cross-circulation and mixing time between the black liquor and the collected salt cake.

FLUID VISCOSITY

Different model fluid viscosities were used in the model studies. These viscosities ranged from 20 cs to 2,000 cs in the full scale system. The flow patterns which developed with the more viscous fluid was the same pattern as was present with the less viscous fluid. The difference between two viscosities is that there is less fluid eddying as the arm rotates with the higher viscosity fluid. It is also more difficult for the viscous fluid to change direction. This causes waves slapping against the side of the pan rather than flowing into and out of a corner. Because of the high viscosity the fluid also did not mix as readily. The higher viscosity fluid for the above reasons produced longer dispersion times in the corners and other slow flow areas even with baffling in place.

FLUID LEVEL

The optimum fluid level appears to be at the top of the agitator arm. If the fluid level is above the top of the arm, surface material is not moved and dissolved. If the fluid level is too low, there are no deleterious effects other than less than full utilization of the agitator system.

The fluid level must also be considered with respect to controlling gas sneakage around the active collecting area of the precipitator. Anti-sneakage baffles have generally been installed in full scale systems such that they extend down into the black liquor. This gives an excellent gas seal to eliminate sneakage below the precipitator. However, this procedure creates serious agitation problems. When the fluid level is above the agitator arms and paddles, effective mixing of the salt cake which falls to the surface of the black liquor is not achieved. By extending the baffles into the liquid, the surface is divided into individual segments. The salt cake falling onto the surface between any two baffles remains in that area until it is dissolved and mixed with the fluid below the baffle level. For this reason it is recommended that the anti-sneakage baffles remain above the liquor level. The sneakage area should be kept to a minimum. This generates a trade-off between the amount of gas sneakage with its corresponding loss of efficiency and the improvement in agitation.

CONCLUSIONS

In order to examine the flow patterns of a wet-bottom ESP, consideration was given to the performance of a model study. At the time there was concern that a laboratory scale model might not adequately simulate a full scale system especially the use of a model fluid other than black liquor. Investigation of the philosophy and theory of fluid flow modeling provided confidence that such a model study could be performed and adequately simulate the full scale system. The models studied and their full-scale counterparts have verified this confidence.

Although it was not practical to reproduce particulate buildup conditions in the model, an adequate simulation of the flow patterns was obtained. Flow patterns were observed in the model under a number of prototype parameters and model variables. Many of the flow patterns and dispersion times were as expected, but several flow patterns were surprisingly different than would be intuitively expected.

The conclusions which can be reached upon examination of the model studies performed are 1) the agitator arm tip speed rather a specific RPM is of critical importance. The optimum tip speed for each installation is dependent upon a combination of factors such as liquor viscosity, pan size and agitator size. A tip speed in excess of the optimum tip speed can significantly affect the component costs of the full scale system. This excessive tip speed can also cause undesirable wave action and splashing. 2) The outermost paddles on each agitator arm should be less porous than the inner paddles. The less porous paddle is necessary to impart the momentum necessary to force the fluid into the corners of the mixing chamber. 3) The inner paddles should be porous to allow greater mixing as the arm rotates and lesser torque requirements. 4) The paddles should be angled approximately 30° from the agitator arm such that the liquor is pushed outward as the agitator rotates. 5) Stationary baffles are necessary to direct the fluid flow into corners and other slow flow areas. Baffles should not be positioned to create additional corners in the mixing chamber. 6) The black liquor feed should be located in a corner of the wet bottom. The feed may enter from either beneath the wet bottom or through the end wall of the casing. The feed, however, should be directed in such a way as to enhance the black liquor fluid flow. The feed should also be located under the inlet fields of the precipitator. 7) The overflow pipes should be offset in a corner of the wet bottom rather than centered in the corner. The overflow pipes should be located under the outlet fields of the precipitator. This combined with the placement of the feed under the inlet fields provides the maximum cross-circulation of the black liquor. 8) The liquor level should not extend above the top of the agitator arms nor should anti-sneakage baffles extend down into the black liquor.

Wet bottom agitator systems cannot be perfectly modeled in the laboratory. Therefore, several basic assumptions must be made in order to practically model the system. Parameters such as black liquor viscosity were approximated but in reality can vary significantly. It should be noted that the investigation and subsequent recommendations of a model study may not eliminate mixing or buildup problems which can occur in the wet bottom. It is our opinion, however, that the model studies discussed in this paper adequately simulate their full-scale counterparts and conclusions can be drawn with a high degree of confidence. With the possibility that larger evaporators and recovery boilers will be employed by the pulp and paper industry, it is our belief that complex wet bottom agitator systems should be modeled.

The work described in this paper was not funded by the U.S. Environmental Protection Agency and therefore the contents do not necessarily reflect the views of the Agency and no official endorsement should be inferred.

REFERENCES

1. Freyaldenhoven, Ray J., Peacos, Michale M., and Henderson, J. S. The recovery boiler precipitator (A Special TAPPI Task Force Report) The NCE recovery precipitator wet bottom design and operating experience. Paper presented at the 1981 TAPPI Engineering Conference, Atlanta, Georgia.

2. Balasic, Paul J. and Peacos, Michael M. A closer look at electrostatic precipitator wet bottoms. TAPPI Vol. 63, No. 6. June 1980

3. Environmental Pollution Control - Pulp and Paper Industry, Part 1 - Air. EPA-625/7-76-001. U.S. Environmental Protection Agency, October 1980, Pg. 10-47.

DESIGN AND PERFORMANCE OF ELECTROSTATIC PRECIPITATORS UTILIZING A NEW RIGID DISCHARGE ELECTRODE DESIGN

by: Gary R. Gawreluk
Robert L. Bump
Research-Cottrell, Inc.
Somerville, New Jersey 08876

ABSTRACT

A survey of recent electrostatic precipitator buying practices indicates that rigid electrodes, as compared to weighted wires and rigid frames, are becoming more and more the electrode of choice for new equipment purchases. This paper presents some of the reasons behind this trend and discusses the rigid electrode design of one manufacturer. Additionally, the design and performance of three installations that are utilizing this rigid electrode are examined.

INTRODUCTION

Most people in our industry are familiar with the trend that emerged in the United States in the early 1970's towards more reliable discharge electrode systems for electrostatic precipitators. The trend towards heavier and mechanically stronger discharge electrodes was triggered in part by the increased use of lower sulfur fuels and in part by increased regulatory pressures which dictated the need for more reliable equipment.

During this period, the Europeans were able to penetrate the U.S. market with a relatively well-established product that was perceived as offering an improved measure of reliability. The product they offered was the rigid frame electrode and the product displaced was the weighted wire.

What most may not realize is that now, in the early 1980's, a new trend is evident with regard to discharge electrodes that promises to tip the scale back once again in favor of American technology. This development is the rigid electrode.

BACKGROUND

Generically, and briefly, most precipitator discharge electrodes may be classified in three categories (Figure 1):

- Weighted Wires consist of thin elements approximately 0.1" in diameter which hang the full length of the collecting electrode, stabilized and plumbed with a heavy weight at the bottom. Wire lengths generally do not exceed 36 feet.
- Rigid Frames also contain thin emitting elements, but limit the vertical span to roughly 6 feet and are tensioned in a structural framework. The two most common rigid frame designs are the bedspring type and the mast type.
- Rigid Electrodes, on the other hand, combine mechanical integrity and stability with corona generating properties in the same member. This results in an electrode that is easily fabricated, installed, and virtually impervious to electrical arc erosion or mechanical abuse.

The ongoing trend that was previously mentioned is illustrated in Figure 2. This graph illustrates the percentage of power industry contract awards by electrode type over the past 5 years. What is readily apparent from this graph is that while the percentage of weighted wire contracts has continually diminished since 1978, the rigid electrode has emerged as a major factor in the marketplace. From a paltry 8% share of the contracts in 1978 the rigid electrodes have succeeded in capturing 50% of all contracts for the past two years running.

A study of precipitator buying practices in other market segments further supports this trend. Figure 3 depicts the trend towards rigid electrodes that has been observed in the pulp and paper industry, which represents the second largest market for precipitators, while Figure 4 shows the trend for all miscellaneous industries combined, including pulp and paper, petrochemical, cement and metallurgical.

Why is that rigid electrodes have been so successful in such a short period of time? The answer lies not only in the inherent features of the electrode but in the design of the precipitator systems of which they are a part. As a designer and supplier of rigid electrode precipitators, Research-Cottrell has observed that the following design features and performance benefits have contributed in large part to its dramatic success in the marketplace:

- No More Electrode Breakage - Rigid electrodes, fabricated in many cases of heavier gauge steel than the collecting surfaces, have put an end to grounded out bus sections due to electrode burn-off.

- High Electrical Sectionalization Capability - The benefits of a high degree of electrical sectionalization in direction of gas flow has been well documented. Rigid electrodes permit this to be done more easily and economically than with most rigid frames. Some currently operating units, for example have up to a dozen electrical fields, each less than five feet in length.

- Rappers Out of Gas Stream - Since all rappers are roof mounted, they are not exposed to the corrosive and erosive effects of flue gas and particulate like the tumbling hammer, mechanical-type systems. Additionally, this location permits them to be inspected, and serviced if need be, while the precipitator is on line.

- Adjustable Rapping Intensity Capability - Magnetic impulse, gravity impact type rappers permit the adjustment of rapping intensity, either individually or by group, from a central control panel. This permits on-line rapping optimization for both low and high resistivity cases, providing full range adjustment of collecting surface accelerations from 0 to well over 100 g's at the least responsive points.

- Ease of Installation - Many rigid electrode precipitator designs incorporate a high degree of shop fabrication which minimizes field erection cost and duration. Among the items shop fabricated are the rigid electrodes, collecting plates, upper and lower electrode support/alignment frames and rappers. Additionally, in the Research-Cottrell design, electrode alignment is simplified since each electrode automatically hangs plumb from a single bolt connection. Moreover, an entire bus section can be assembled outside the precipitator and lifted into place.

RIGID DISCHARGE ELECTRODE DEVELOPMENT

Before considering a few case histories, it might be appropriate to take a look at the basic precipitator design as well as some of the history behind its development.

Research-Cottrell commercialized the Hi-R^{TM} rigid electrode precipitator in 1978. This culminated 6 years of research and development on this design which included not only the development of a new rigid discharge electrode, trade-named the Dura-Trode^{TM}, but also a much improved collecting plate.

The main objectives of the Dura-Trode development program were to develop an electrode that was inherently rigid, unbreakable, easy to fabricate and handle, and would distribute corona evenly along its entire length. The basic elements of the program designed to meet these objectives included:

- Corona field studies in both a laboratory precipitator as well as in a large electrolytic tank capable of reproducing typical precipitator operating voltages.

- Tooling and production studies at our electrode fabricating facility.

- Construction feasibility studies performed by individuals responsible for erecting scores of precipitators.

- Mechanical strength, electrical stability, and accelerated life testing performed in a full scale test tower.

The last phase of study before going commercial involved investigation of the actual electrode in service. This was accomplished in both pilot precipitator work as well as through backfitting hundreds of the electrodes in full scale operating units.

The final result is a roll-formed, structural member fabricated from heavy gauge steel (Figure 5). Corona sets up at discrete points on the tips of the scallops, while the flat portion of the electrode body serves to enhance the field strength at the collecting surface. Actual measurements of field strength show that this additional mass provides approximately double the field strength of wire type electrodes at equivalent distances from the electrode with equivalent gas passage spacing and energization levels (Figure 6).

As expensive and time consuming as it is, a well-developed, successful R&D effort is a necessary pre-requisite for introducing a new product into the marketplace, particularly one as traditionally conservative as the power generating industry. Successful demonstration of that product in full-scale commercial installations, however, is a necessity for continued participation in that market. The previous discussion illustrates how this first objective was met. The following case histories serve to support the second.

CASE HISTORIES

CASE HISTORY #1: COMBINATION BOILER

The first commercial Hi-R rigid electrode precipitator went on line in late 1980 at a major pulp and paper complex in the Southeast. The application required the collection of fly ash from a 500,000 lb/hr power boiler designed to fire pulverized coal from Virginia, West Virginia, and Eastern Kentucky, or a combination of bark and coal (Figure 7). Design sulfur was 0.8%. This application presented the potential for both high and very low resistivity operation; high with the coal-only case and low with the combination bark firing. Our previous experience with more than a half dozen similar combination boiler applications dictated a precipitator incorporating a low treatment velocity and variable intensity rapping in order to maximize collection and minimize rapping re-entrainment losses.

Guaranteed removal efficiency was 99.5% for the coal-only case and 99.0% for the bark/coal combination. Design gas volume, at 380°F, was 257,000 ACFM for coal, but approximately 20% higher for the combination.

Performance tests run by an independent testing laboratory at full load conditions with the unit burning coal only yielded collection efficiencies from 99.75% to 99.82%. The clear stack was indicative of an opacity level well below the 20% guarantee level. At present this unit continues to perform with no visible emissions.

CASE HISTORY #2: RECOVERY BOILER

Another southeast paper mill was the site of a second Hi-R rigid electrode precipitator which also went on line in 1980. That unit was designed to collect salt cake (sodium sulfate) from a 158,000 lb/hr low odor recovery boiler (Figure 8). Salt cake is a relatively moderate resistivity ash but, because of its sticky,tenacious nature, requires a high level of rapping acceleration to dislodge it from both discharge and collecting electrodes. The rapping system supplied can deliver in excess of 50 G's to all points in the collecting surfaces.

The precipitator designed for this application incorporated a heat jacket around the entire casing in order to minimize corrosion potential, and a wet bottom ash collection system with floors and sides fabricated of type 316 stainless steel.

This unit, which was started up only 6 months after the beginning of erection, was designed for an outlet loading of 0.0255 gr/scfd. Design gas volume was 450,000 ACFM at 420°F. Performance tests, showed that the Hi-R precipitator limited emissions to 0.01 gr/scfd which was significantly better than the guarantee level. This was equivalent to a collection efficiency of roughly 99.7%. The precipitator also produced a visibly clear stack.

CASE HISTORY #3: UTILITY BOILER

Introduction of Research-Cottrell's Dura-Trode rigid electrode into the power industry came in 1979 with an award for four Hi-R precipitators to serve 1150 MW of generating capacity at New England Electric's Brayton Point Station. These precipitators are a part of the largest single coal conversion project in the U.S. to date.

The application involved collection of fly ash from three pulverized coal-fired boilers burning Eastern bituminous coal with sulfur content ranging from 0.8 to 1.5%

(Figure 9). Design gas volumes from these two 250MW units and a 650MW unit ranged from 856,000 ACFM for each of the smaller units to 2,210,000 ACFM for the larger unit. The new precipitators were located in series behind existing precipitators built in the early 1960's that had treatment velocities of 6 to 8 feet per second.

Research-Cottrell's scope of supply on this project included not only the precipitators but also the flues from air heater to stack, heat insulation, field wiring, control houses, access facilities, and model study, as well as installation of all material supplied.

The first unit was brought on line in March, 1981, the second in June, and the third in January, 1982. Although outlet emissions for state compliance were 0.08 lb/10^6 BTU, contract levels were set at 0.019 gr/acf, approximately equal to 0.06 lb/10^6 BTU, and had to be met with one entire field across the precipitator de-energized.

Performance testing on the first two units has proven that the precipitators are operating well within guarantee with average emissions less than 0.02 lb/10^6 BTU and test opacities at 0%. Although test results on Unit #3 are not yet available, the clear stack gives every indication that compliance on that unit will also be achieved.

CONCLUSION

The previous case histories illustrate only a few of the many diverse applications for which contracts have thus far been received for Dura-Trode rigid electrodes (Figure 10). Other applications include cyclone fired as well as pulverized coal fired power boilers, burning coal with sulfur contents ranging from 0.5 to 4%, as well as applications in the petroleum, cement and other miscellaneous industries. All told more than 32 precipitators with Dura-Trodes have been sold to date. In the power industry alone, this represented by more than 3500 megawatts of generating capacity.

More than a decade ago, United States industry was offered what was perceived to be a more reliable alternative to the weighted wire design. The ensuing years found rigid frame type precipitators being more and more widely accepted. But the advent of the American design rigid electrodes has ended their corner on the market. If recent successes in both sales and demonstrated performance are any indication, these rigid electrodes will more and more become the design of choice in future precipitator purchases.

The work described in this paper was not funded by the U.S. Environmental Protection Agency and therefore the contents do not necessarily reflect the views of the Agency and no official endorsement should be inferred.

Figure 1

Discharge Electrode Types

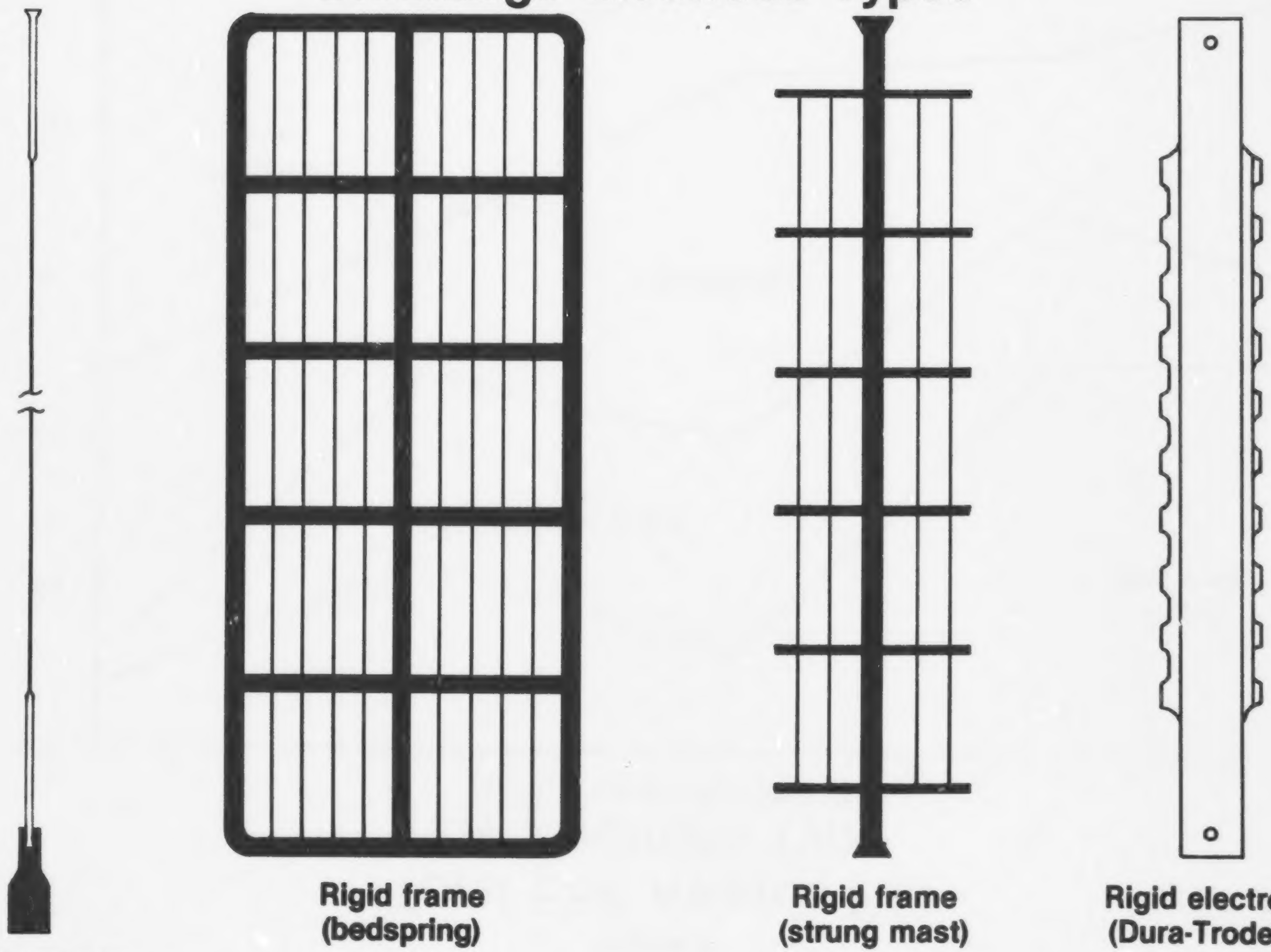

Weighted wire (shrouded)

Rigid frame (bedspring)

Rigid frame (strung mast)

Rigid electrode (Dura-Trode™)

Figure 2

Total ESP Awards (%)
By Electrode Type
(U.S. Power Industry)

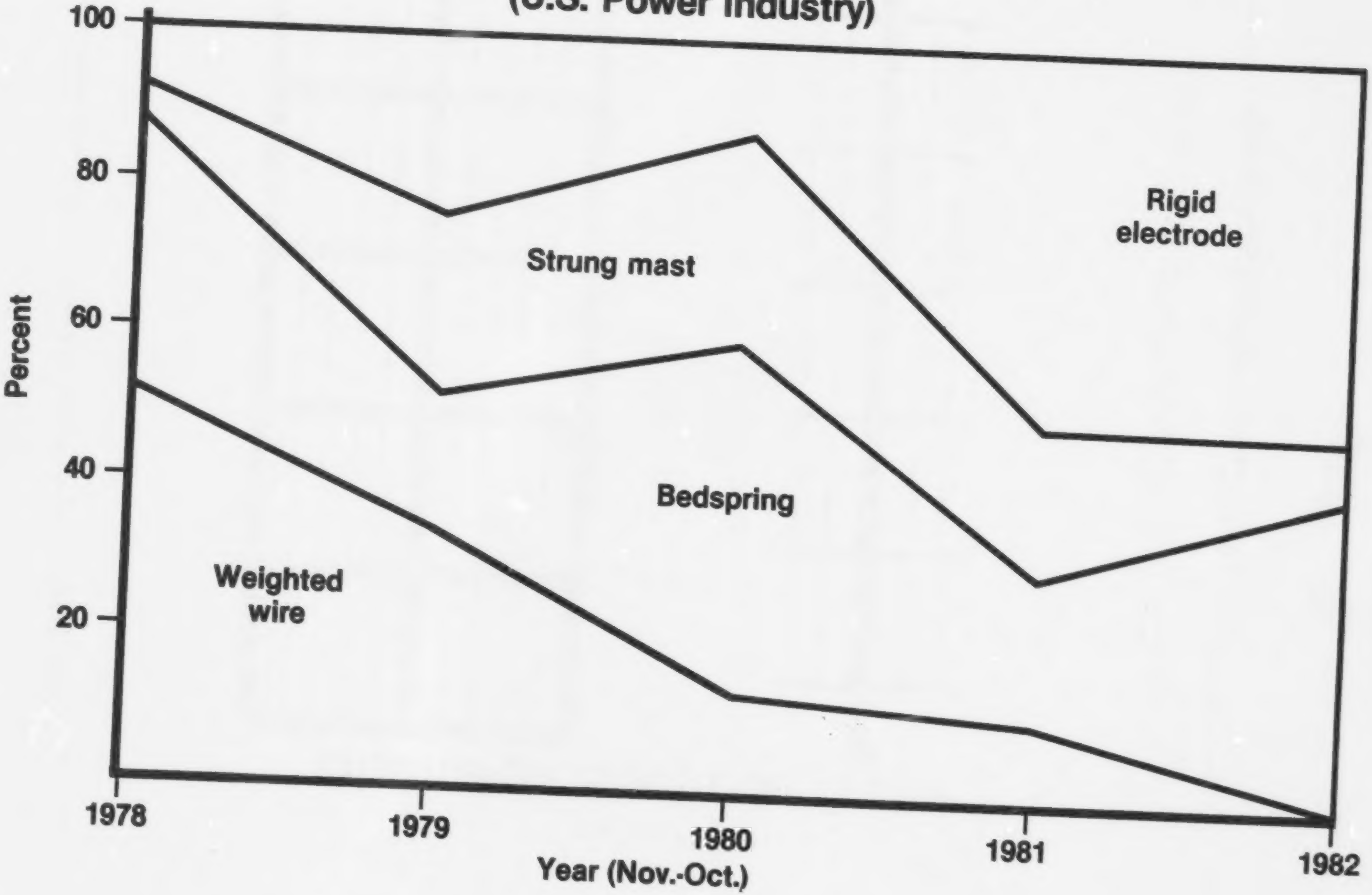

Figure 3

Major ESP Awards (%)

By Electrode Type

(U.S. Pulp & Paper)

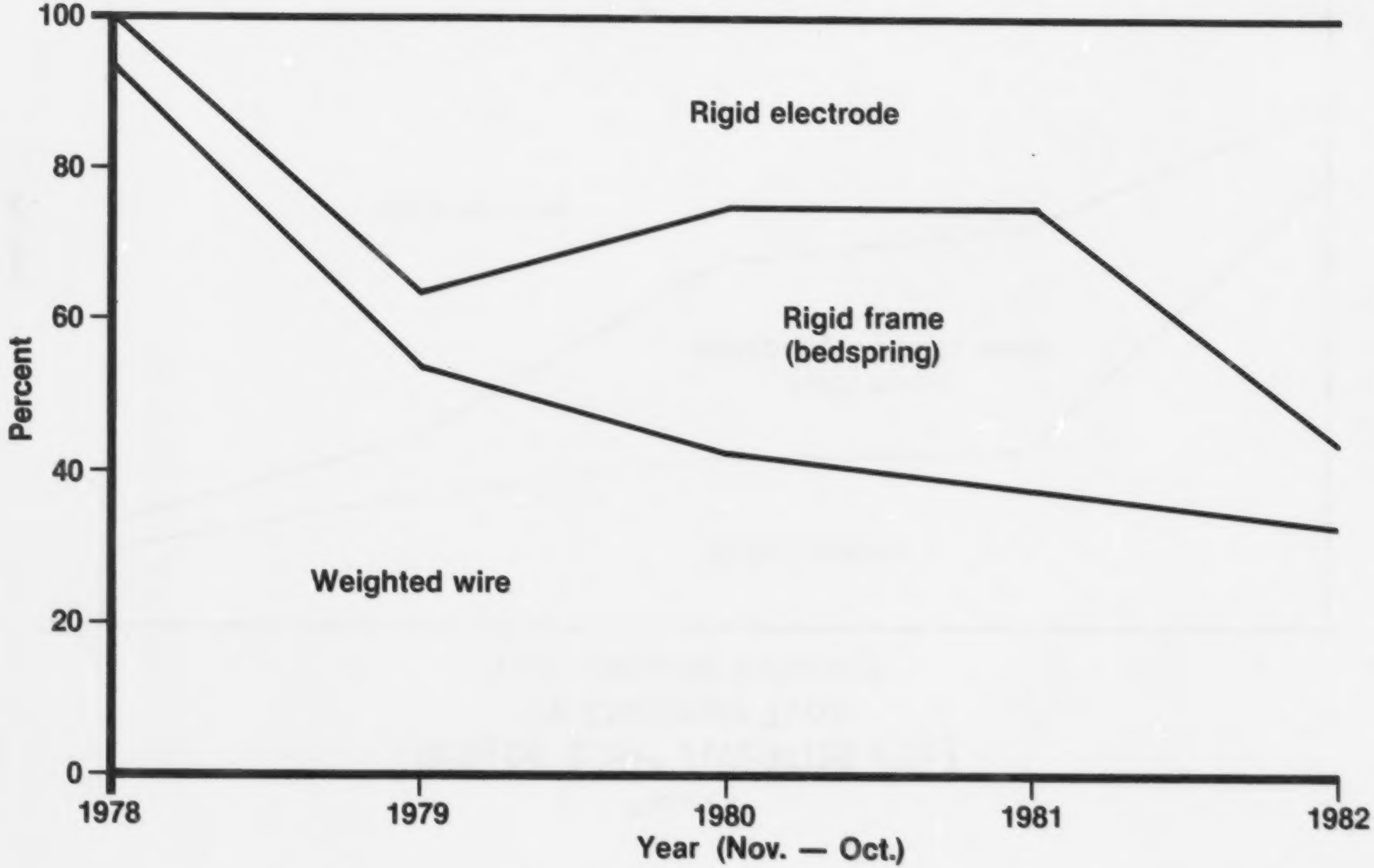

Figure 4

Major ESP Awards (%)

By Electrode Type

(U.S. General Industry)

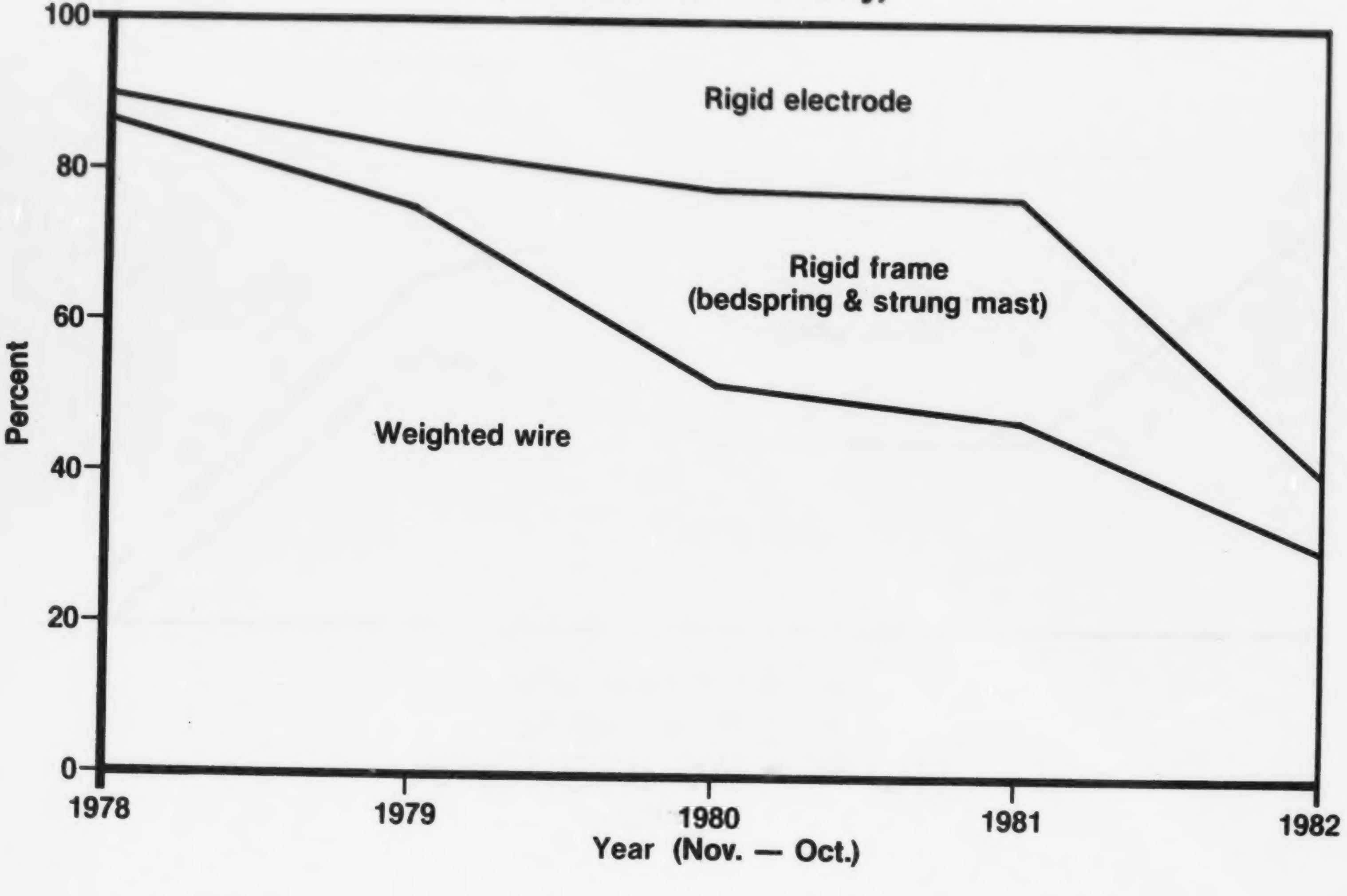

Figure 5

Rigid Discharge Electrode

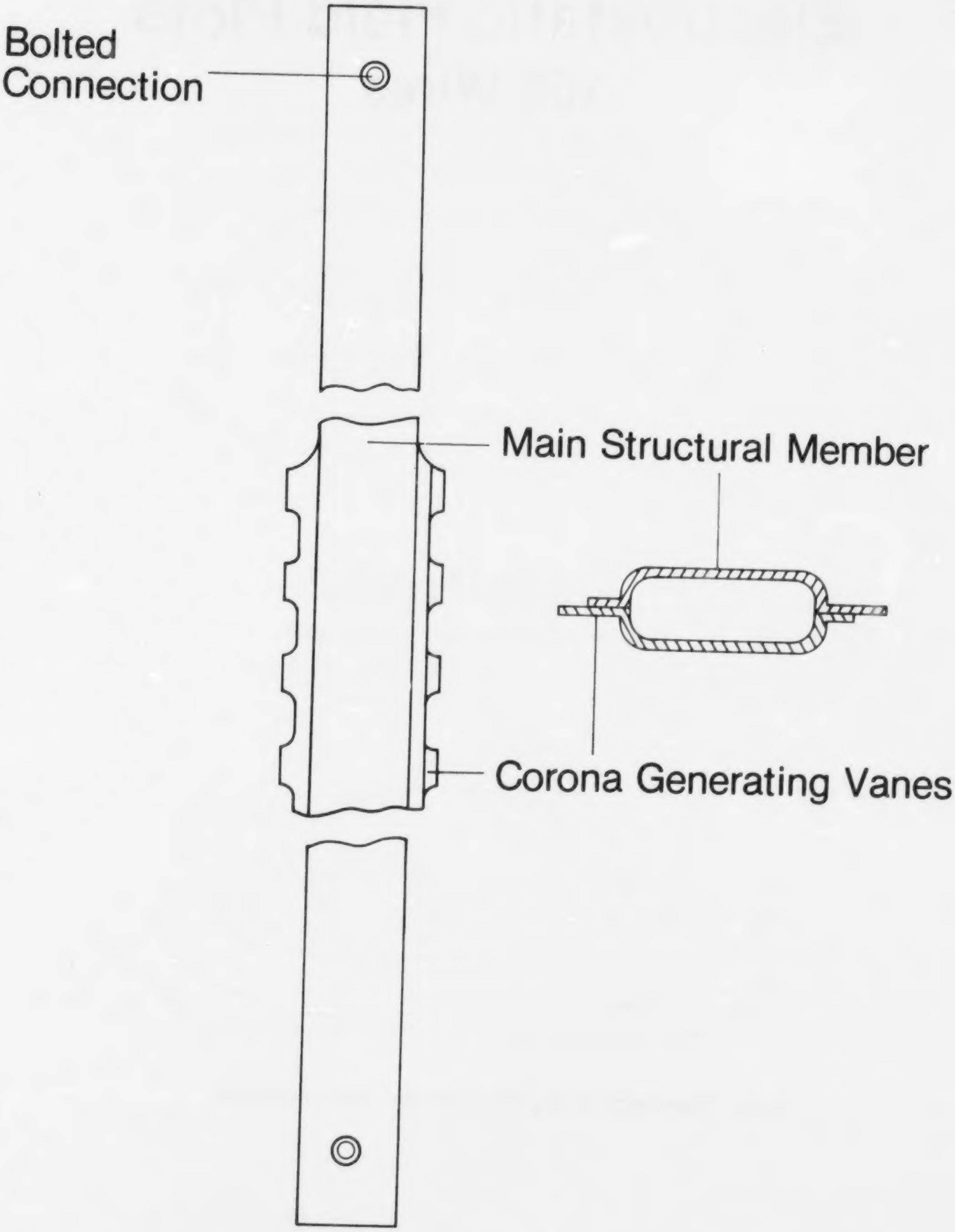
Bolted Connection
Main Structural Member
Corona Generating Vanes

Figure 6

Electrostatic Field Plots

.109 Wires

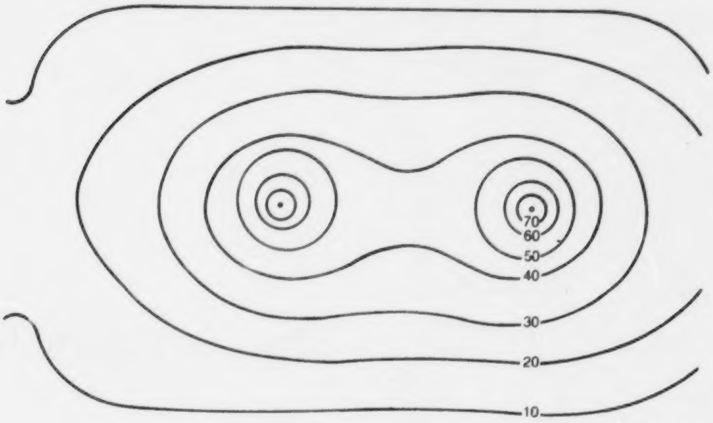

Dura-Trode

Rigid Discharge Electrode

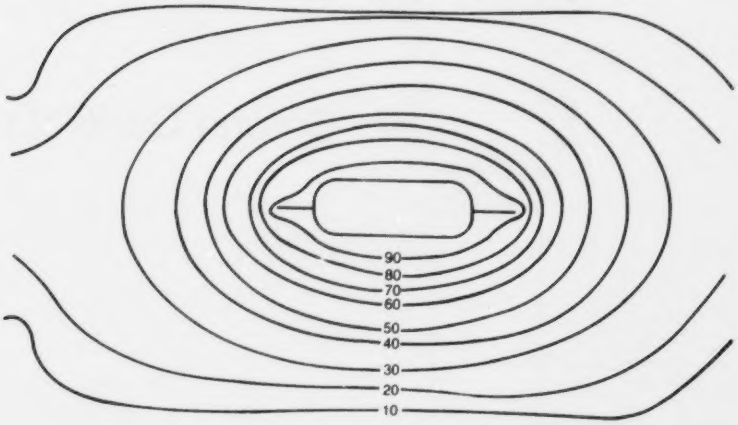

Note: Numbers designate percent field strength.

Figure 7

Case History #1
Combination Boiler

APPLICATION: P-C fired boiler burning
E. bituminous coal (0.8 % sulfur)
or coal/bark combination

	DESIGN*	ACTUAL*
Gas volume (ACFM)	257,000	295,455
Gas temperature (°F)	380	405
Inlet loading (Gr/ACF)	2.0	2.7
Outlet loading (Gr/ACF)	0.01	0.006
Efficiency (%)	99.5	99.78

*Coal only

Figure 8

Case History #2
Recovery Boiler

APPLICATION: Salt cake collection from a low odor, black liquor recovery boiler

	DESIGN	ACTUAL
Gas volume (ACFM)	450,000	423,885
Gas temperature (°F)	420	380
Inlet loading (Gr/SCFD)	7.5	2.7
Outlet loading (Gr/SCFD)	0.0255	0.01

Figure 9

Case History #3
Power Boilers

APPLICATION: Two 250 MW and one 650 MW
P-C fired boilers burning
E. bituminous coal (0.8 — 1.5% S)

	DESIGN	ACTUAL
Gas volume (ACFM)		
Unit #1	856,000	1,031,000
Unit #2	856,000	1,007,000
Gas temperature (°F)		
Unit #1	260	295
Unit #2	260	275
Outlet loading (lb./10^6 BTU)		
Unit #1	0.06	0.019
Unit #2	0.06	0.017
Opacity (%)		
Unit #1	20	0
Unit #2	20	0

Figure 10

Hi-R™ Precipitators with Dura-Trode™ Rigid Electrodes

APPLICATIONS:

- Pulverized coal fired boiler
- Cyclone fired boiler
- Oil fired boiler
- Combination coal/bark/oil fired boiler
- Low odor recovery boiler
- Conventional recovery boiler
- Fluidized catalytic cracking unit
- Cement kiln
- Alumina calciner
- Lead glass furnace

Total precipitators — 32

Total megawatt capacity — 3,790

DEVELOPMENT AND EVALUATION OF A NEW PRECIPITATOR EMITTER ELECTRODE

by: R. Adams and P. Gelfand
Air Correction Divison, UOP Inc.
Norwalk, Connecticut 06856

ABSTRACT

This paper reviews the laboratory and field development, and evaluation associated with the development, of a new rigid emitter. The paper discusses the experimental procedures and establishes the comparative criteria for the evaluation of different electrodes. Laboratory studies were conducted to measure the current density patterns formed by various electrode designs. Final laboratory data are presented comparing three different types of emitters, two rigid and one wire. The data result in a comparison of emitter performance on a theoretical basis. Final field data on a full-scale precipitator are presented which verify the laboratory results.

INTRODUCTION

As part of the development of a new electrostatic precipitator, "ADVANCOR," the Air Correction Division of UOP embarked on a program of intensive investigation of precipitator electrodes. The goals of the "ADVANCOR" design were to provide an increased performance, highly reliable precipitator. It was recognized that a key element necessary to achieve this goal was the development of a new electrode that had superior electrical corona characteristics and could be made virtually unbreakable. The development program involved both laboratory and field tests and retrofitting of a full-scale precipitator with new emitting electrode design. These efforts and the results obtained will be discussed.

HISTORY OF PRECIPITATOR ELECTRODES

There are fundamentally three generic types of precipitator electrodes (Figure 1). A brief description of each follows.

Weighted Wire

The weighted wire electrode is a free-hanging electrode suspended from the top of a precipitator and tensioned with sufficiently heavy weights at the bottom of each electrode to prevent vibration caused by the electrical field or the gas flow. Usually these weights are guided by a grid framework held by insulators to the hopper or shell to prevent swaying. In general, the geometry of the electrode can take a variety of shapes--round, square, strip-like, star, barbed wire.

Rigid Frame

The rigid frame electrode consists of a structural frame usually made with pipes containing rows of emitting electrodes similar to those used with weighted wire. Usually, the structural frame takes on the form of a box that is cross-braced for stability on all sides. To prevent electrical or mechanical vibration of the electrodes, they are made in short lengths (two to three meters) stretched, or tensioned, and mounted between pipe cross members that are installed parallel to gas flow.

Rigid Electrode

The rigid electrode is a free-hanging, mechanically rigid assembly consisting of flat or rolled plates, pipes, or masts, with discharge points or projections mounted thereon. Rigid electrodes are suspended from the top of the precipitator and guided at the bottom with a structural framework. Depending on the design, stabilizing bracing insulators may not be required.

ELECTRODE REQUIREMENTS

The essential requirements of a precipitator discharge electrode are:

- Effective corona generation: high electric fields for charging and collecting, and uniform current density at the collecting electrode with low expenditures of energy
- Cleanability: a mechanical shape that permits efficient use of rapping energy to keep the electrode free of dust build-up that could reduce corona generation
- Good gas mixing characteristics to help move the dust toward the collecting plates
- Relatively low-cost fabrication
- Ease of installation and maintenance
- High reliability: should be virtually unbreakable

There are many claims as to advantages and disadvantages of the great variety of discharge electrodes in present use.

The weighted-wire system, while offering good corona discharge, is prone to wire breakage due to electrical erosion (sparking) and hopper overfilling.

The rigid frame system, while it prevents the shortcomings of the weighted-wire, is frequently subject to misalignment due to thermal distortion of the structural frame.

The rigid electrodes are free to expand and resist breakage while at the same time providing good corona discharge and lower power consumption.

Air Correction, therefore, concentrated its design of a new electrode on the rigid type.

LABORATORY TESTING

Over a several year period, virtually all electrode shapes and designs were tested and evaluated in our laboratory. Special apparatus was built to measure the current distribution produced by an emitter (Figures 2 and 3). This equipment permitted mapping of the current density over the full surface of the plate (Figure 4).

In addition to the current density tests, air load tests were conducted to obtain corona discharge curves for each emitter. Discharge curves were measured with a simulated high-resistivity dust layer. Finally, the candidate electrodes were tested in our laboratory under a simulated hot gas and dust condition (Figure 5). This was done using heated air and re-entrained flyash.

The dust deposition pattern obtained for the mast electrode is shown in Figure 6.

The deposition pattern resembles those reported by S. Self, et al, Ref. Electromechanics & Re-entrainment of Precipitated Ash. Dust densities appeared to vary over the surface. Coarse particles were near the point discharges; fine particles were opposite the central mast. The fundamental criteria used in evaluating these tests were average electrical field, specific current density, and good unformity of current distribution on plate surface. Two "ADVANCOR" electrode candidates were selected, a barbed plate design and a mast electrode (Figure 7).

The large diameter central mast (pipe) has the advantage from a gas flow perspective of creating a turbulent wake just downstream of the mast and in the center of the gas passage. Wake helps drive dust particles toward the collecting electrodes, thus adding collection of fines particulate. The central mast construction also serves as a conduit for mechanical energy helping to keep the emitting points clean and free of build-ups.

Laboratory tests with air or hot gas and re-entrained flyash are excellent to preliminarily select or evaluate emitting electrodes but must always be followed by field tests, in situ, to confirm the effectiveness of an electrode design under real operating conditions.

Criteria for Electrode Evaluation during Field Tests

The next step in this development program was to test the candidate electrodes in a full-scale operating precipitator. The plan was to install a limited number of test electrodes and compare electrical operation. An evaluation criterion has to be developed that would permit comparisons to be made with only electrical data available at the electrode terminals. To develop this criterion, the following fundamental considerations were employed.

FUNDAMENTAL CONSIDERATIONS

Force on a charged particle (F):

$$F = qE \tag{1}$$

where: q = charge
E = electrical field strength

But from field charging theory:

$$q_{stat} = 4\pi\varepsilon_0 E_0 a^2 \left(1 + 2\frac{k-1}{k-2} \right) \tag{2}$$

where: k = relative dielectric constant
a = radius of particle
E_o = charging electric field
ε_o = 8.84×10^{-12} permitivity of free space
E = E_p the precipitating electric field

From Stokes law and Electric Force Balance:

$$W = q\frac{E_p}{6\pi a n} \tag{3}$$

where: n = viscosity of the field

$$q = q_{stat} \left(\frac{1}{1+\frac{\tau}{t}} \right) \tag{4}$$

where: t = time of exposure
τ = time constant of charging

$$\tau = 4\varepsilon_o E_o / j \quad \text{(sec)} \tag{5}$$

j = current density

Let $t \to \infty$ (6)

Then

$$\underset{t \to \infty}{W_{2a}} = q_{stat} \times \frac{E_p}{6\pi a \eta} \tag{7}$$

and

$$q_{stat} = 4\pi\varepsilon_o E_o \; a^2 \left(1 + 2\frac{k-1}{k+2}\right) \tag{8}$$

so that

$$W_{2a} \propto = \frac{E_o E_p}{\eta} \tag{9}$$

so that the precipitation rate W_{2a} for a particle size is a function of $E_o E_p$.

But, on an electrode terminal basis:

$$E \quad \propto \quad \text{Voltage applied/distrance between emitter and ground}$$

but E_p is related to current density by:

$$E = \surd \frac{2(I'/L)}{4\pi\varepsilon_o k} \left(1 - \left(\frac{a}{r}\right)^2 \right) + \left(\frac{V_o}{r \ln \frac{b}{a}} \right)^2 \qquad (10)$$

in cylindrical geometry and similarly in parallel ducts for similar duct geometries.

$$E_p \propto \surd j \qquad (11)$$

or

$$W_{2a} = c_1 \surd j \, E_o \qquad (12)$$

This relationship becomes the basis for a first order evaluation of emitter performance, so that by measuring the terminal voltages and currents, comparison on the basis of theoretical improvement can be made.

FIELD TESTING

Site Selection Criteria

To ensure that the candidate electrodes would be tested under representative conditions, the following criteria were used:

- Existing ACD Precipitators
- Cooperative Client
- Convenient Location
- Flexible Operation
- Pulverized Coal Fired Boiler
- High Resistivity Flyash Application

Mead Paper Corporation, one of Air Correction's customers, had a fire occur in one of the three weighted-wire precipitators built by Air Correction in Lynchburg, Virginia. Mead asked Air Correction to rebuild this unit. Air Correction embarked on a two-phase program. Phase I - place as much of the damaged precipitator in service as was possible, then install, at full-scale, the Air Correction test electrode stations inside a portion of the precipitator, run the tests, verify the results, select the electrode, and then enter Phase II - rebuild the complete unit with the final electrode selection for full characterization and testing (Figure 8).

Description of Mead Installation Boilers

- Three B&W "Sterling" p.c. fired boilers
- Boiler rating 90,000 lbs. st./hr.
- Fuel: Eastern bituminous coal, 12,500 Btu/lb, 0.8% sulfur

Mead Precipitators

- Three Design 24(666)26-1-3 (22,464 ft^2 of plates)
- 90,000 acfm at 450°F (each) SCA 249.6
- 94.43% collection efficiency
- Follow existing cyclone collectors (98% to 99% overall efficiency)
- 3.5 lbs/MM Btu dust loading
- 0.16 lbs/MM Btu emission limit

EVALUATION TEST PROGRAM

Phase I

The two candidate electrodes and a weighted-wire control were installed at Mead. Figure 7 shows these emitters.

- Mast
- Barbed Plate
- Weighted-Wire (Control Electrode)

Figure 9 shows the precipitator modifications and locations of our test stations. Measurements were taken with these three stations and comparisons made in accordance with the performance evaluation criteria. Results are shown in Figure 10. An analysis of these data indicate that the barbed emitter failed to perform over a period of time and that it demonstrated a sensitivity to the dust characteristics at full-scale but that the mast emitter demonstrated operation well into the acceptable region of performance. Therefore, the mast electrode was selected for Phase II in the retrofitting of the precipitator.

Phase II

Air Correction replaced all damaged collecting electrodes and retrofitted with the new mast-type emitters. Also installed was a new emitter and collecting plate rapper system with electronic controls. Then tests were conducted to fully characterize the performance of the rebuilt precipitator. These measurements were made to determine: mass emissions versus power, resistivity, particle size dependent efficiencies, and mass performance of the rebuilt precipitator, as well as an identical adjacent weighted-wire precipitator (Unit #2).

PHASE II RESULTS

Operating Conditions

Resistivity of the ash was 10^{11} ohm cm at a gas temperature of 460°F. A typical laboratory resistivity is shown in Figure 11. A good agreement with in-situ resistivity measurement was obtained. The particle inlet loading from the mechanical collector was approximately 0.4 gr/acf with a mean micron diameter of 6 and a geometric standard diameter of 4. SO_3 measurement taken using ASTM Method D 3226-73T averaged 3.56 ppm of SO_3; typically, 1.15% sulfur coal was being burned during the testing. Boiler operation was held at full load during most tests, except for one group that was conducted at a low load. The results of the mass emissions versus electrical power density are shown in Figure 12. Mass performance tests were on Unit #1 with the mast ("ADVANCOR") electrode and Unit #2 with weighted wire. The results shown the performance enhancement that was obtained with the "ADVANCOR" design. An enhancement of 21% based on the increased W_k (modified Deutsch omega) was obtained when comparing Unit #1 with Unit #2. Similarly, terminal electrical conditions for Unit #1 and Unit #2 as measured during the test, theoretically predicted an enhancement of 22% based on the evaluation criteria discussed earlier.

Interestingly, independent of the field test, Mead flyash was introduced into the hot gas laboratory apparatus equipped with the Mast electrode. The improvement was measured at 27%. All these tests strongly suggest that the "ADVANCOR" electrode will provide increased collection efficiency. More data on other installations will be needed to absolutely confirm this.

SUMMARY

The objectives for ACD's new emitter have been achieved.

1. Effective corona generation: high electric fields for charging and collecting and uniform current density at the collecting electrode with low expenditures of energy.
2. Cleanability: a mechanical shape that permits efficient use of rapping energy to keep the electrode free of dust build-up that could reduce corona generation.
3. Good gas mixing characteristics to help move the dust toward the collecting plates.
4. Relatively low-cost fabrication.
5. Ease of installation and maintenance.
6. High reliability: should be virtually unbreakable.

The work described in this paper was not funded by the U. S. Environmental Protection Agency and therefore the contents do not necessarily reflect the views of the Agency and no official endorsement should be inferred.

CLASSIFICATION OF ESP'S BY DISCHARGE ELECTRODE DESIGN

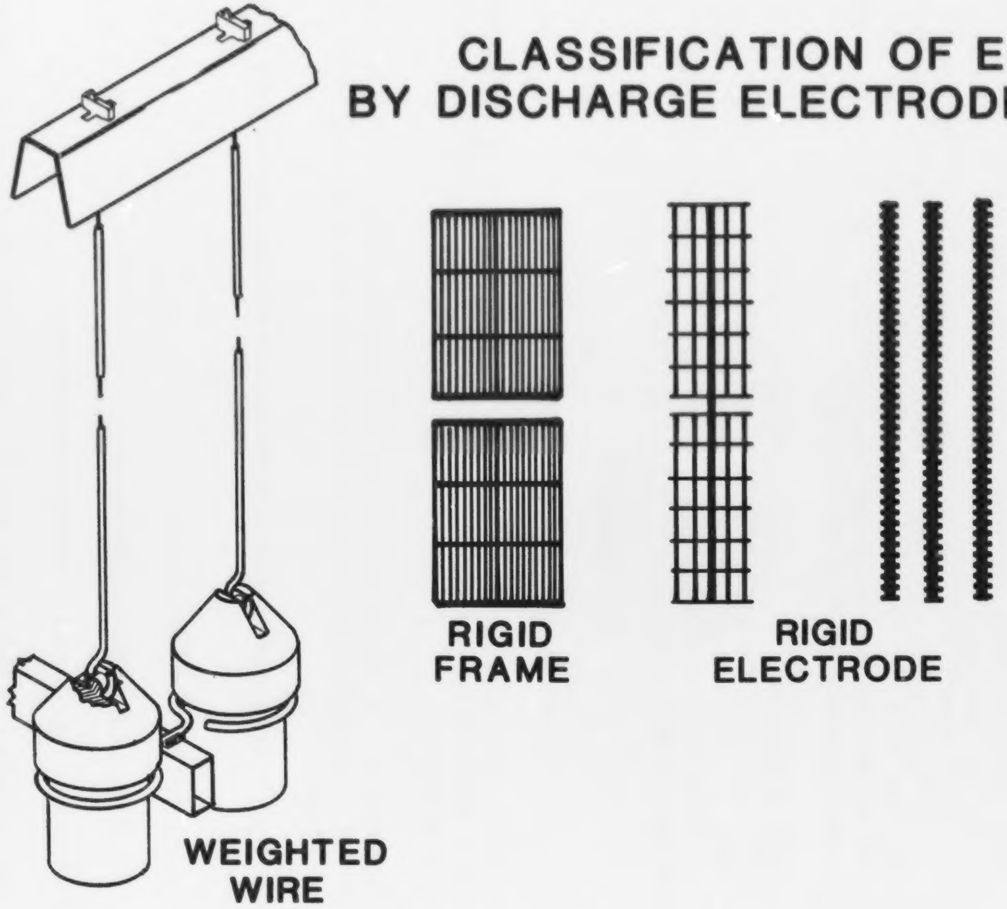
RIGID
FRAME
RIGID
ELECTRODE
WEIGHTED
WIRE

FIGURE 1

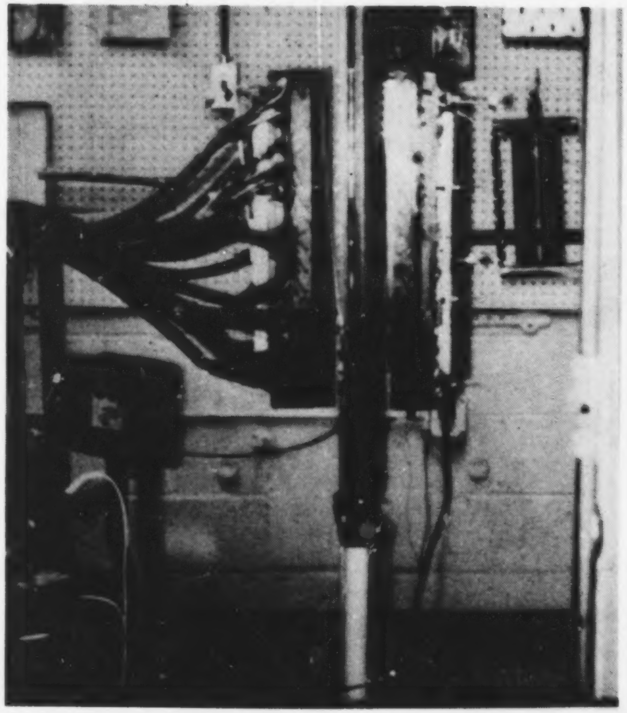

LABORATORY APPARATUS FOR
MEASUREMENT OF CURRENT DENSITY

FIGURE 2

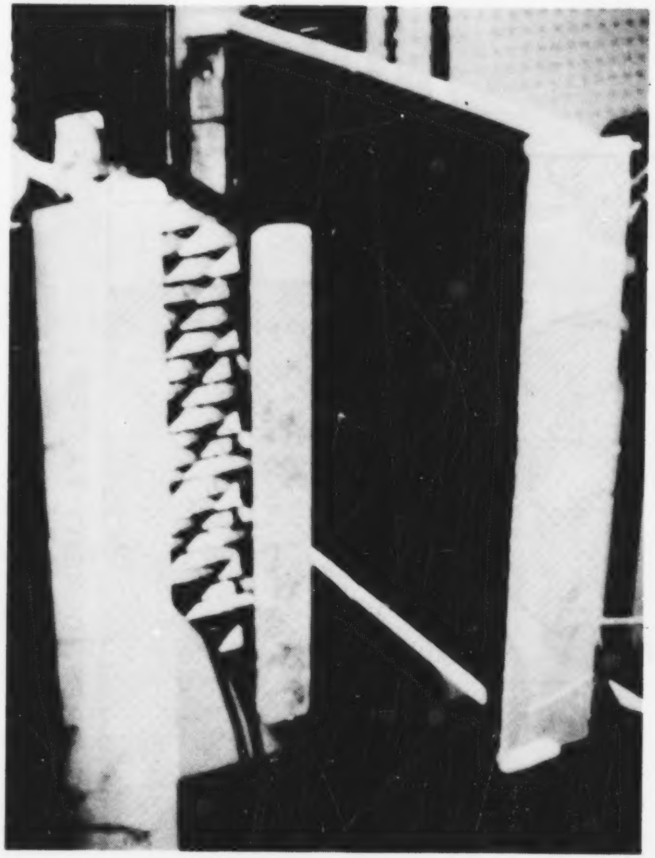

LABORATORY APPARATUS WITH TEST ELECTRODE

FIGURE 3

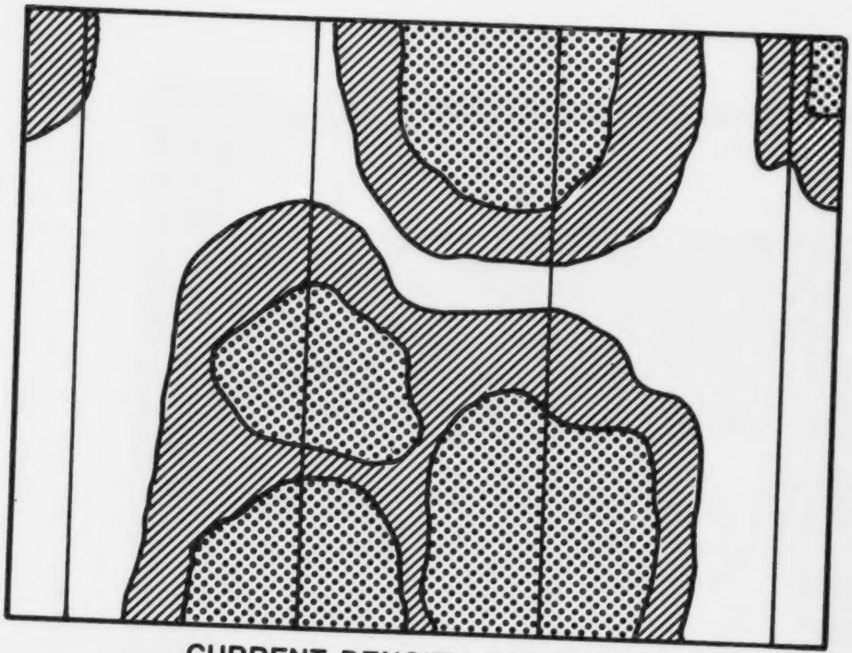

CURRENT DENSITY PATTERN
WEIGHTED WIRE DESIGN
FIGURE 4

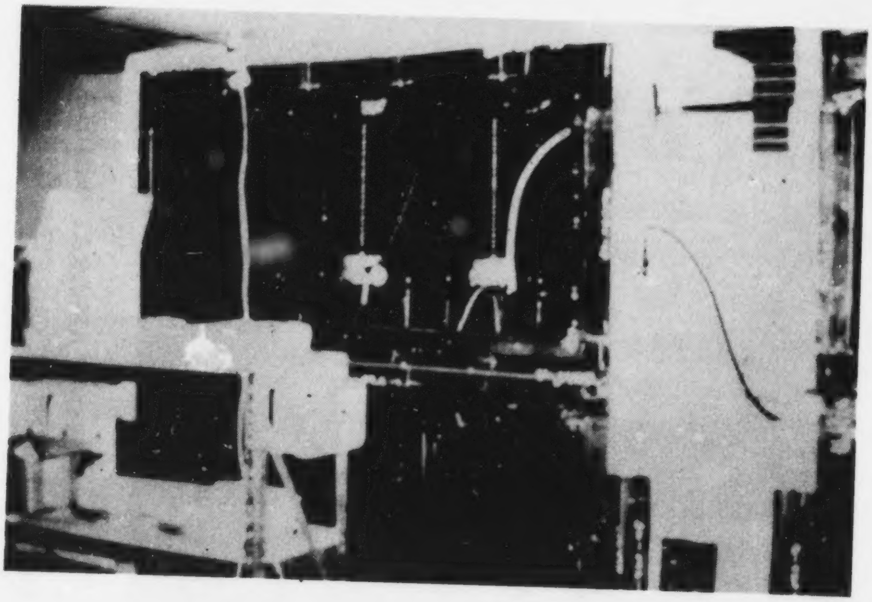

ELECTRODE TEST APPARATUS

FIGURE 5

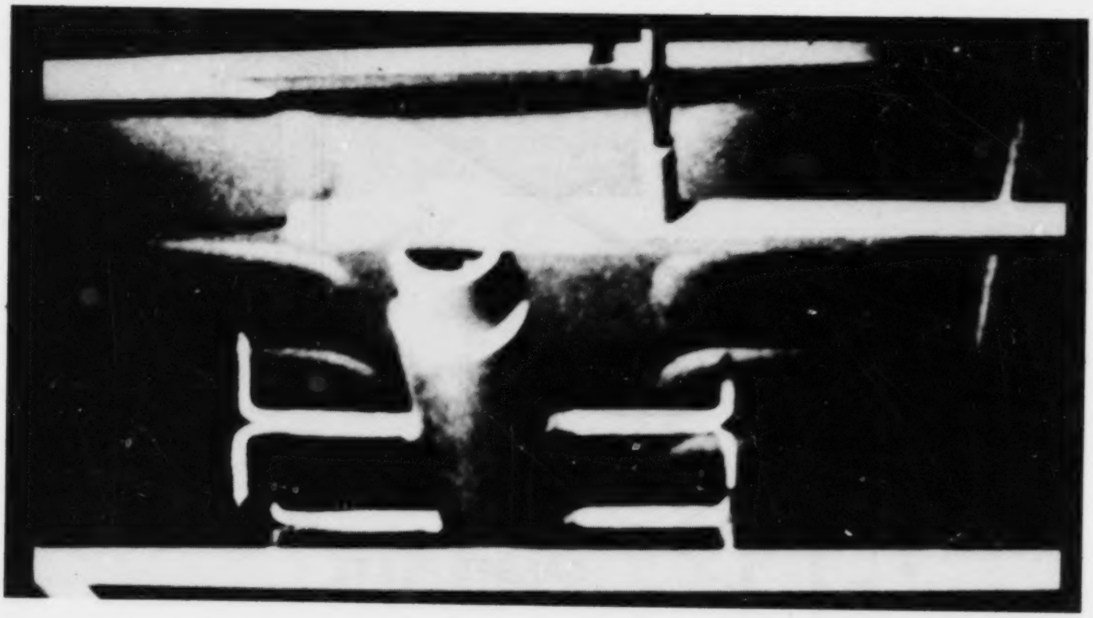

DUST DEPOSITION PATTERN MAST ELECTRODE

FIGURE 6

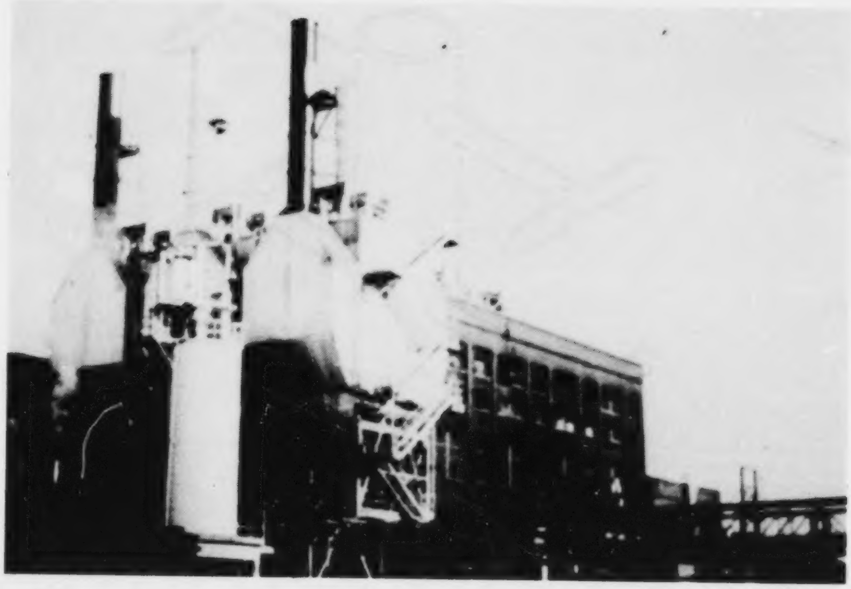

FULL SCALE TEST PRECIPITATORS

FIGURE 8

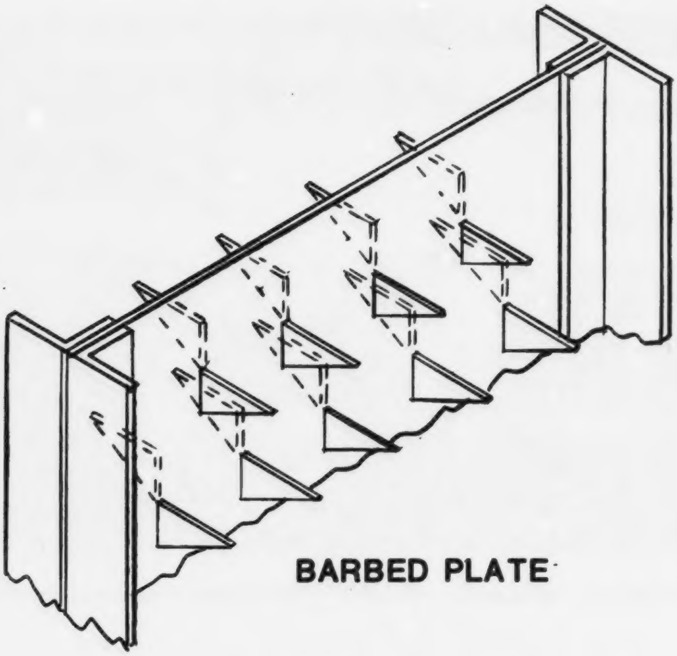

BARBED PLATE

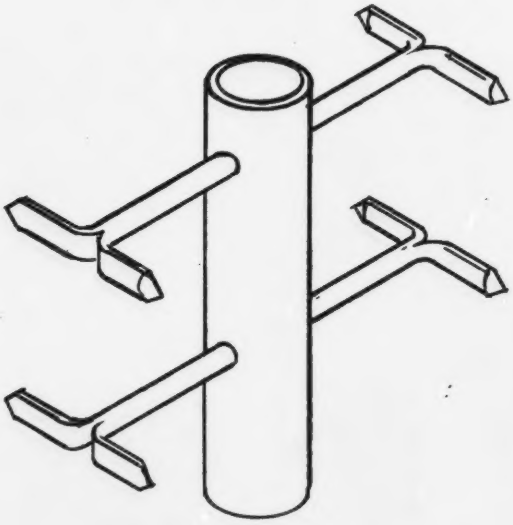

MAST

TWO PROTOTYPE EMITTERS THAT MET PRELIMINARY OBJECTIVES

FIGURE 7

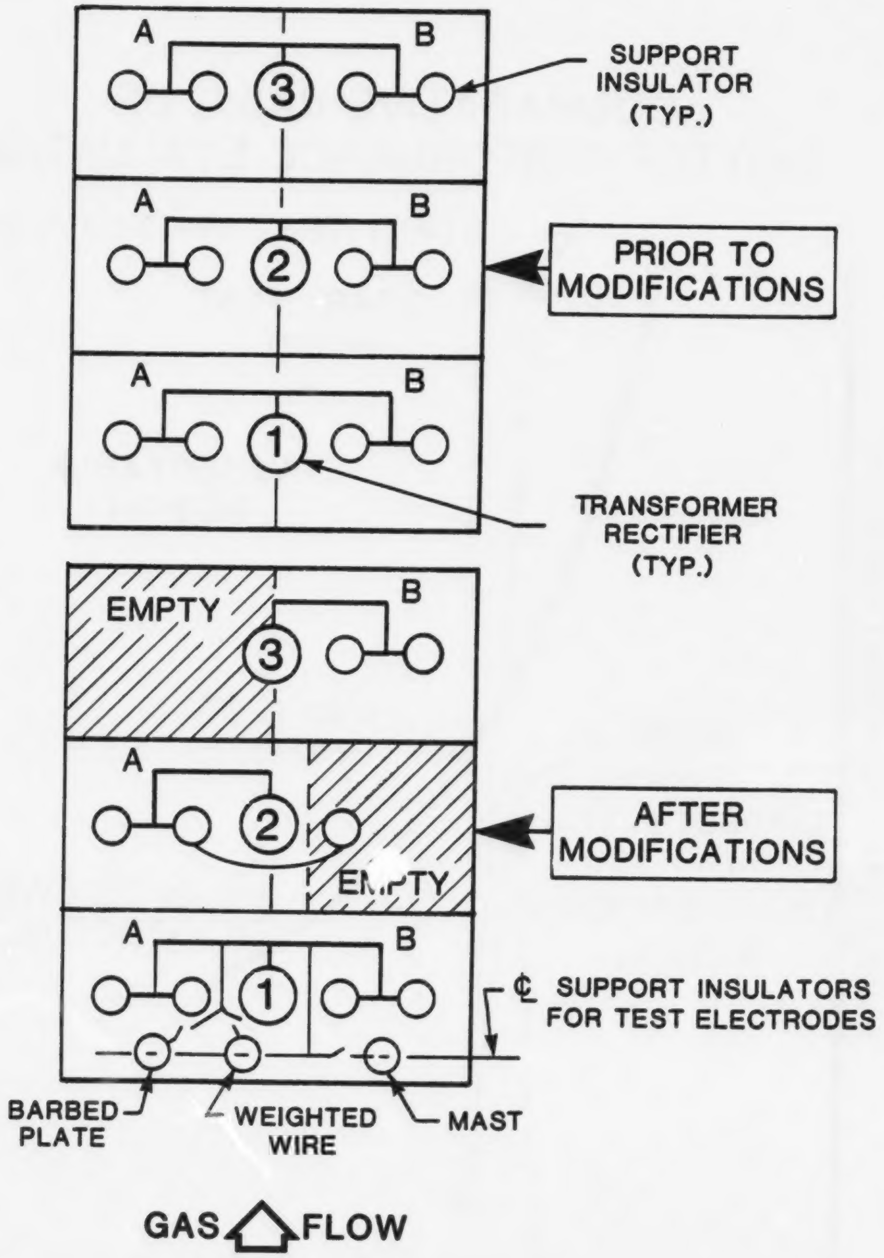
A
B
3
SUPPORT INSULATOR (TYP.)
A
B
2
PRIOR TO MODIFICATIONS
A
B
1
TRANSFORMER RECTIFIER (TYP.)
EMPTY
B
3
A
2
EMPTY
AFTER MODIFICATIONS
A
B
1
℄ SUPPORT INSULATORS FOR TEST ELECTRODES
BARBED PLATE
WEIGHTED WIRE
MAST
GAS FLOW

PHASE I - EMITTER EVALUATION
TEST SET-UP AT MEAD

FIGURE 9

COMPARATIVE BASIS OF EMITTER PERFORMANCE EVALUATION

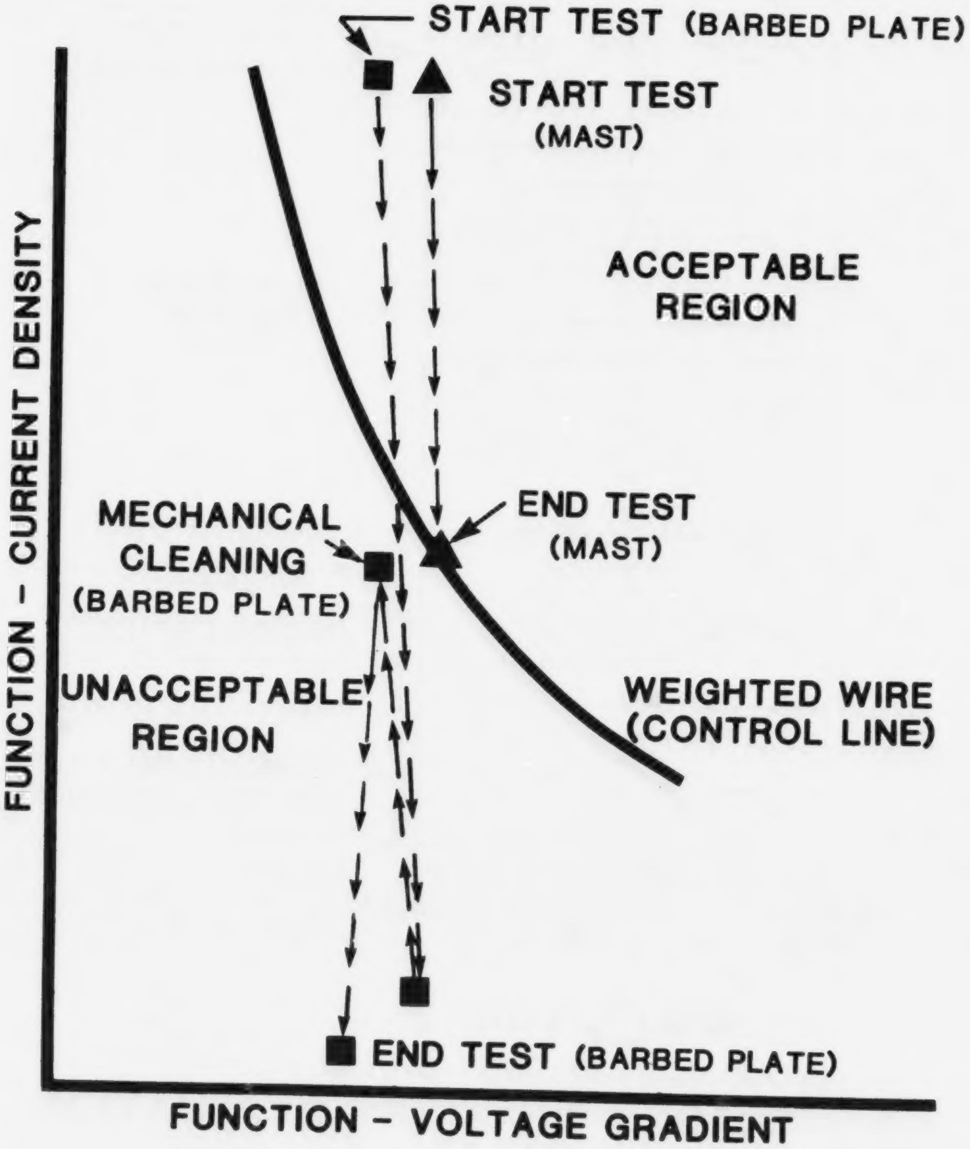
START TEST (BARBED PLATE)
START TEST (MAST)
ACCEPTABLE REGION
MECHANICAL CLEANING (BARBED PLATE)
END TEST (MAST)
UNACCEPTABLE REGION
WEIGHTED WIRE (CONTROL LINE)
END TEST (BARBED PLATE)
FUNCTION - CURRENT DENSITY
FUNCTION - VOLTAGE GRADIENT

FIGURE 10

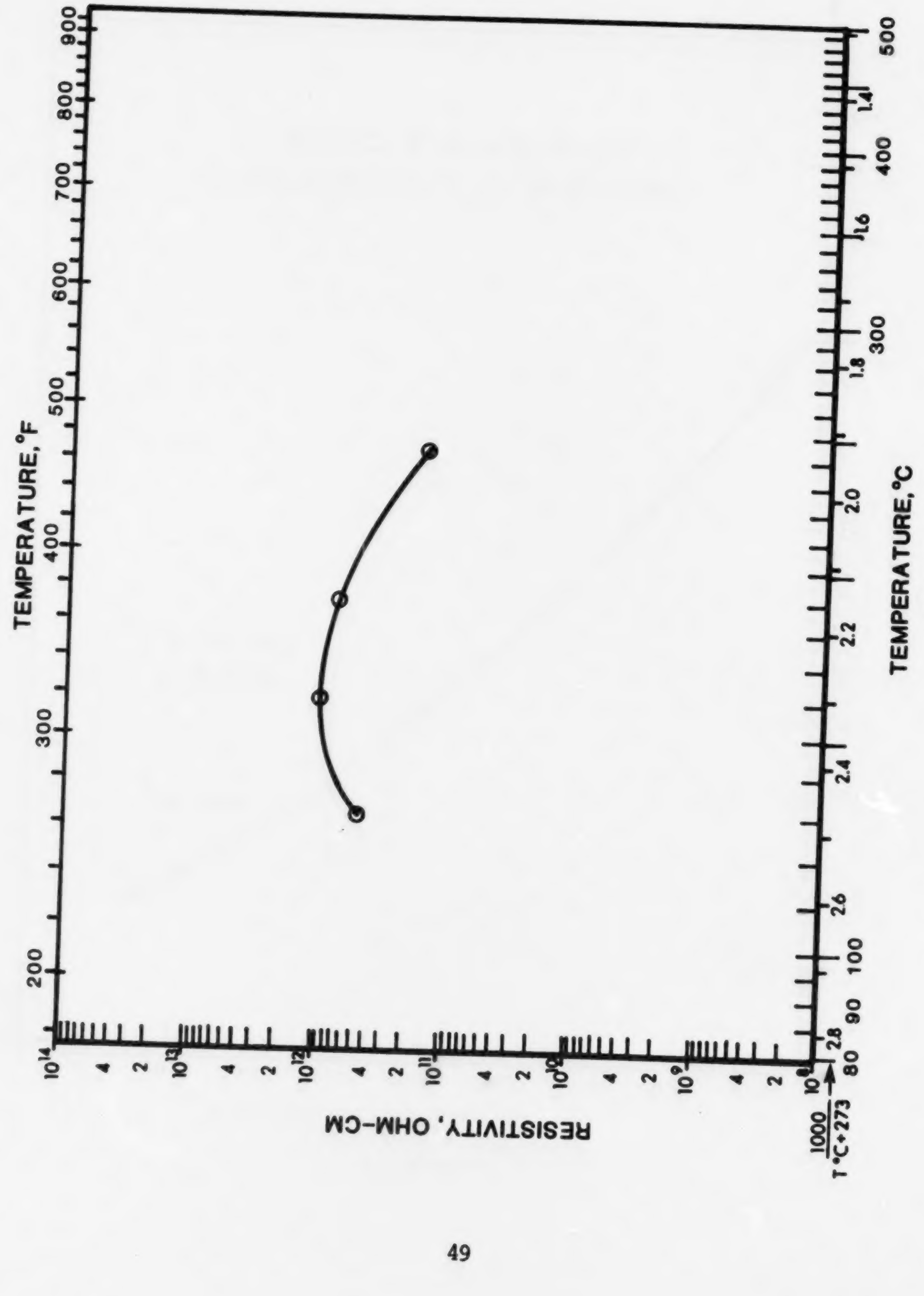
TEMPERATURE, °F
200
300
400
500
600
700
800
900
RESISTIVITY, OHM-CM
10^{14}
4
2
10^{13}
4
2
10^{12}
4
2
10^{11}
4
2
10^{10}
4
2
10^{9}
4
2
10^{8}
$\frac{1000}{T\ °C+273}$
2.8
2.6
2.4
2.2
2.0
1.8
1.6
1.4
80
90
100
300
400
500
TEMPERATURE, °C

FIGURE 11

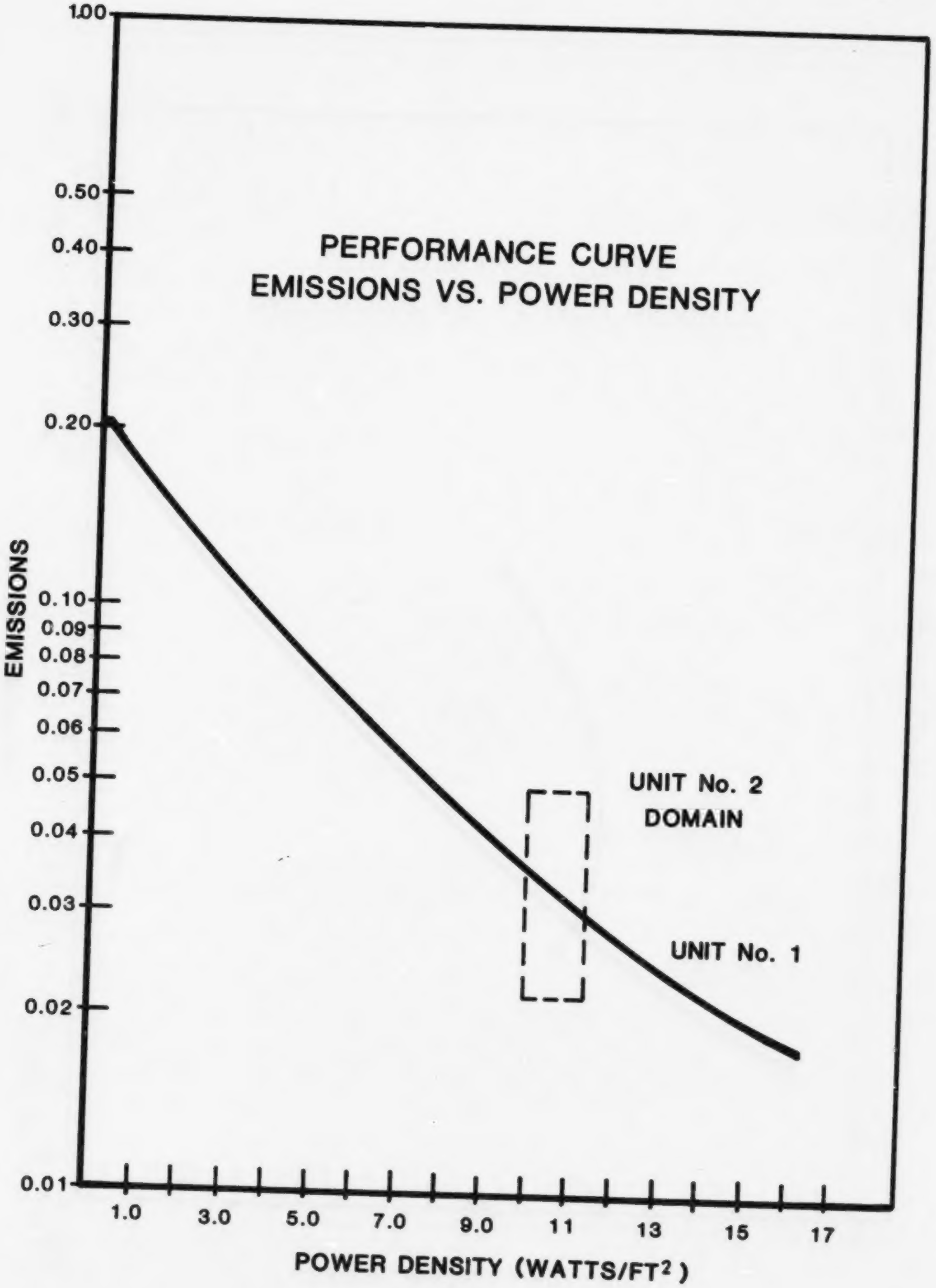
PERFORMANCE CURVE
EMISSIONS VS. POWER DENSITY
EMISSIONS
1.00
0.50
0.40
0.30
0.20
0.10
0.09
0.08
0.07
0.06
0.05
0.04
0.03
0.02
0.01
UNIT No. 2
DOMAIN
UNIT No. 1
1.0
3.0
5.0
7.0
9.0
11
13
15
17
POWER DENSITY (WATTS/FT2)

FIGURE 12

INDUSTRIAL APPLICATIONS
OF TWO STAGE
TUBULAR ELECTROSTATIC PRECIPITATORS

by: Harish S. Surati and Michael R. Beltran
Beltran Associates, Inc.
Syosset, NY 11791

ABSTRACT

Two stage Tubular precipitators incorporate best features of both the single stage and two stage type designs. Extremely high collection efficiency in sub-micron region makes these precipitators ideal choice for processes having a very high concentration of sub-micron organic mist like Retort Oil Shale or Coal/Wood gasification. Design parameters, field test data and operating data from installations on these processes are discussed in the paper.

Tubular precipitators have also found wide acceptance in ferrous and non-ferrous metallurgical applications involving sub-micron emissions, most notably from smelting, sintering, and scarfing operations. Installations on Electric Arc and Rotary Hearth Furnace exhausts are described.

Several installation details from chemical processes like Sulfuric Acid Manufacturing, Sulfonic Acid Production, Ammonia Scrubbing of SO_2, etc. are covered in the paper. Comparisons with single stage type precipitators are made wherever applicable.

INTRODUCTION

Although the two stage electrostatic precipitator was first conceived and patented in 1910, until recently most of its use was confined to in-plant air cleaning. During the last two decades, plate type designs have been modified and made suitable for industrial applications involving organic emissions, most notably in asphalt saturating, plastic curing, food processing, printing, textile finishing, and heat treating industries. A detailed discussion of plate type two stage precipitators in various industrial applications can be found in authors' other publications (1-3). However, plate type designs are inadequate where very high particulate loadings and/or extremely corrosive components are present in the exhaust stream. Two stage Tubular precipitators were developed for such applications.

Two stage Tubular precipitators incorporate best features of both the single stage and two stage type designs. Unlike single stage precipitators, two stage Tubular precipitators have a passive electric field (no corona discharge) in the collecting section. Thus, very high electric field strengths can be maintained and very high collection efficiencies can be achieved even in the submicron range. Unlike conventional plate type two stage designs, Tubular precipitators have wider spacings between discharge and collecting electrodes, thus allowing their use in applications involving very high particulate loadings.

Two stage Tubular precipitators consist of a short ionizing section followed by a comparatively very long collection section. The discharge electrode is in the form of a rod or tube with a series of sharp discharge points at the end, and is centered in the collecting tube. Various collecting tube geometries have been utilized over the years, the most common being the round and hexagonal. The square configuration shown in Figure 1 is a slight variation of the hexagonal shape and was chosen because of ease in manufacturing. The square tube geometry is much more space efficient than the round shape. Comprehensive treatment of theoretical and design parameters affecting two stage Tubular precipitators can be found in authors' other publication (4).

INDUSTRIAL APPLICATIONS

Two stage Tubular precipitators have been installed on a variety of industrial emissions. These can be broadly divided into five catagories.

(1) Alternate Energy Sources
(2) SO_2 Scrubbing Processes
(3) Primary and Secondary Non-Ferrous Metals Industry
(4) Steel Industry
(5) Chemical Industry

All of these applications involve heavy concentration of submicron particles. Submicron particles are formed by condensation phenomena or by gas phase reaction, where the product of reaction has very low vapor pressure at the reaction temperatures.

Generally particles larger than 1 micron in diameter scatter light by true reflection. Thus the loss of light is proportional to the projected surface area. For submicron particles, the relationship is more complex, since the particle diameter is comparable to or less than the wavelength of visible light spectrum (.4 to .7 micron range). Total number of particles increases inversely as the cube of the diameter. The total projected surface area increases as the reciprocal of diameter. Thus for the same concentration of particulates, viewed through the same linear distance, plume density increases with decreasing particle size.

In many applications described in this paper, serious corona quenching (current suppression) situations are encountered. When particle density approaches ion density, corona quenching occurs. When the particle concentration is mainly in the submicron range, such conditions arise even with particulate loading of a few tenths of a grain/CF. The particles are charged to the same polarity as the unipolar corona ions. Thus, the electric field gradient near the discharge electrode decreases, reducing the flow and mobility of ions. Since for submicron particles, diffusion charging is the principal means of particle charging, reduction in ion mobility affects particle charging. In two stage precipitators, higher ion densities are obtained than is possible in conventional single stage units. Corona current is a measurement of rate of deposition of corona ions on the grounded electrode. Since the charged particle mobility is order of magnitude lower than the corona ions, contribution of the charged particles depositing on grounded electrode to the corona current is minimum. This explains, in part, why even in heavy current suppression situations where current is suppressed by a factor of 40 or more, very high precipitator efficiencies are possible. To combat corona suppression type situations, high intensity ionizers, positive corona, and several electrical fields in series are generally required.

The electrostatic force exerted on the particle depend on the electrostatic field, particle diameter, and dielectric constant. The residence time and the vertical distance needed for the particle to migrate from the discharge electrode to the grounded electrodes increases with decrease in particle diameter and with lower dielectric constant (good electric insulators). For these reasons condensed hydrocarbons (dielectric constant of 2-5 and submicron size) have very low migration velocities. Water droplets (dielectric constant of 78) are thus very easy to collect compared to organic mist.

In summary, heavy concentration of submicron particles 1. create corona suppression, 2. decrease migration velocity, and 3. create higher plume densities.

ALTERNATE ENERGY SOURCES

Retort Oil Shale

Oil shale is a fine grained, compact, sedimentary rock containing an organic material called kerogen. Heating the oil shale to about 900°F decomposes this material to produce oil shale. Commercially, in situ combustion and surface retorting methods have been tried. Exhaust gases from oil shale retort contain a considerable amount of water (40 to 50 grain), and hydrocarbons (3-4 grain/SCF). Some dust as shale fines, and carbon is also present. The carrier gas is combustible and has high heating value. Very high tar mist removal efficiencies are required. Since hydrocarbon mist is formed by condensation, the majority of particles are below one micron in size. Low dielectric constant combined with very high loading of submicron particles create very tough conditions for efficient precipitation. Two Tubular precipitators in series operating 250 fpm throughput velocity have 99% plus collection efficiency. Since the carrier gas is combustible, every flange connection is sealed tightly to prevent inleakage of oxygen. The method of insulator purging is of paramount importance with inert gas and cleaned process gas being used successfully. Advanced designs incorporate insulating oil type seal to eliminate purging requirement altogether.

Coal/Wood Gasification

Coal gasification has received much attention in recent years. Similar processes have also been developed for wood gasification and municipal refuse gasification. Precipitators used in these processes are for gas clean up rather than for pollution control. Coal tar, fine unburned carbon, char ash, and voltalized heavy hydrocarbons are present in the gasifier exhaust. The gas cleaning train generally consists of a cyclone or some mechanical pre-filter after the gasifier, then a heat exchanger to recover heat, a medium or low energy scrubber to cool the gas and remove heavy tar particles, and a wet Tubular ESP to remove fine hydrocarbons. The particulate loading after the gasifier can be as high as 9-10 grain/CF of char (in case of wood gasification) and almost as much of hydrocarbons. The particle size distribution is generally bimodal with the char and carbon particles in 2 to 15 micron range and the condensed hydrocarbons in the submicron range. Outlet loading from the precipitator of 0.003 grain/CF or less are required. Presence of H_2S, ammonia and water creates fairly active corrosive conditions. Generally 304 stainless steel construction is used.

SO_2 SCRUBBING PROCESSES

Many processes generate SO_2 in concentrations that are too low to be handled effectively in acid plants but are high enough to violate air quality regulations. Scrubbing of SO_2 gases is generally accomplished using one of the following processes.

1. Lime/Limestone Slurry Systems
2. Soda Ash/Caustic Scrubbing
3. Double Alkli Processes
4. Ammonia Scrubbing

Major industrial sources where these desulfurization techniques have been utilized are:

a) Utility plants
b) Recovery boiler off gases in pulp and paper industry
c) Cogeneration using petroleum coke
d) Tail gases from some metal smelting operations
e) Tail gases from single absorption type acid plants.

FGD systems for utility plants is a topic for a seperate paper by itself. We will cover remaining four processes in this paper.

Paper Industry

In paper making, large quantities of steam are required at three stages. First for cooking the wood chips, then to seperate the individual cellulose fibers from the binding material lignin, and finally for evaporation of water in which cellulose fibers are dispersed for paper making. Economic considerations have led to development of some special type of boilers using pulp mill by products. These include sand impregnated salt water borne bark and hogged wood fired boilers and recovery boilers using black kraft liquor and spent sulfite liquor.

In ammonia based acid sulfite pulping processes, recovery boiler off gases are passed through an ammonia absorber. In the absorber, Ammonium sulfite and Ammonium bisulfite are produced by the following reactions.

$2NH_3 + H_2O + SO_2 \rightleftharpoons (NH_4)_2SO_3$ Ammonium Sulfite

$NH_3 + H_2O + SO_2 \rightleftharpoons NH_4\ HSO_3$ Ammonium Bisulfite

These reactions take place in the liquid phase and the ratio of the sulfite to bisulfite produced depends on the pH of the solution. To maximize absorption of SO_2 and to minimize ammonia partial pressures, the absorber is operated at minimum practical temperatures. Figure 2 and Figure 3 (5) show the number size distribution and the mass size distribution of the particulates in the Ammonia absorber off gases. Very dense plume is observed at the absorber stack. The particle size is extremely fine, between 0.1 and 0.5 microns in diameter. The particles are not completely soluble in water. In the past, FRP construction Brink type fiber bed filters have been used to control these emissions. However, pluggage and gradually increasing pressure drop through the fiber bed plague these systems. Moreover, when pH control is not very accurate, free ammonia is generated, causing corrosion of the glass fiber.

Tubular precipitators used on these applications are constructed of fiberglass. A specially conductive fiberglass resin was developed for this application. This eliminates the need for, and also the problems associated with, maintaining water film on the collecting electrode. The high voltage discharge electrode is made of graphite and high moly stainless steel. Carpenter-20 discharge discs have also been used. The particulate concentration is generally in 0.4 to 0.6 grain/CF range for properly operated units. Increase in absorber temperature or in pH of the scrubbing liquor can significantly increase particulate concentration. Two pass Tubular precipitators have collection efficiencies in excess of 99 percent under entire range of process conditions. The collection efficiencies were measured using modified EPA method 5 and a forward light scattering photometer. Excellent agreement was found between these two measurements. Heavy current suppression was encountered. This is believed to have been caused by heavy concentration of extremely fine particles and enormous moisture loading (saturated stream at 160^oF).

Cogeneration

Cogeneration using petroleum coke feedstock has been investigated. The exhaust from tagentially fired pulverized coke boiler is first cleaned by a Dry ESP. Ammonia scrubbing or Double alkali processes are used for SO_2 scrubbing. The presence of heavy metal impurities in the fuel act as a catalyst to promote further oxidation of SO_2 to SO_3. Tubular precipitators are used to collect fine acid mist and fine sulfite-bisulfite emissions. The SO_2

concentration has to be reduced to 5-10 ppm level to comply with opacity regulations.

Metal Smelting

Primary and secondary metal production usually involves smelting of the ore in a reduction furnace. Sulfur oxides generated during this operation are generally cleaned and taken to the acid plant if the concentration is above 5 percent. Weak gases are generally scrubbed using lime/limestone slurry processes and emissions are collected using a baghouse. However, in some applications where caustic/soda ash or Ammonia scrubbing is used and/or where appreciable quantity of acid mist is present, Tubular precipitators are used to control emissions. These precipitators are operated wet. Particulate loadings of about 0.3 to 0.4 grain/CF are common and heavy moisture load is usually present. Corrosive conditions dictate use of plastic or special alloy construction.

Acid Plants

In older acid plants and in single absorption plants, 98% SO_2 conversion efficiency can be achieved. Tail gases from these plants require SO_2 scrubbing systems to comply with Federal regulations on allowable SO_2 emissions. Ammonia scrubbing is widely used. Tubular precipitators are used to control acid mist and sulfite-bisulfite emissions.

NON-FERROUS METALS INDUSTRY

Two stage Tubular precipitators have been used in following Non-Ferrous Metal operations.

1. Zirconium Calcining
2. Silver/Gold Refining
3. Molybdenum Roasting
4. Nickle Recovery using Electric Arc Furnace

Zirconium Calcining

Zirconium and Hafnium are used in the nuclear industry for the fuel rod casings. These metals are immune to corrosion attack from most of the chemicals and can withstand very high temperatures. Neutrons pass through Zirconium, whereas they are absorbed in Hafnium. Thus the nuclear reaction can be controlled by use of Zirconium and Hafnium tubes. Zirconium and Hafnium are mined as Zircon sand. The ore is chlorinated, selectively precipitated, passed through seperation operation, chlorinated again, and then reduced. The exhaust from the calciner contains Zirconium oxide, Hafnium oxide, a trace amount of elemental sulfur, some chlorides and sulfuric acid mist and sulfur dioxide. The exhaust is first treated in a caustic packed bed scrubber. The two pass Tubular precipitator made of FRP is used to remove fine particulates and acid mist. High moisture loading and high concentration (.4 to .5 grain/CF) of submicron particulates cause severe current suppression. Two pass in series are effective in combating the suppression effects. Collection efficiencies in 97 to 99 percent range are observed.

Silver/Gold Refining

In the bisulfate slime fusion process, filtered slime obtained from the tank house electrolytic refining operations is fused in two rotary batch kilns. The typical charge for the rotary kiln consists of about 46% by weight slime, 41% by weight sulfuric acid and remaining sodium sulfate. The slime consists of appreciable quantities of Copper, Silver, and Selenium. Silica, Lead, Tellurium, Arsenic, Gold, and other organic materials are also present. The fusion of slime in the rotary kiln is a batch process and requires approximately six hours. The fume laden gases pass through a primary spray quench type scrubber followed by a venturi scrubber and finally through a Tubular wet ESP. The size of particles entering precipitator is thus in submicron range. Selenium in the crystalline form sticks tenaciously to solid surfaces, so collecting tubes are continuously flushed. Mild current suppression conditions are present. Generally the particulate loading is in 0.1 to .2 grain/CF but at times can go as high as .4 to .5 grain/CF. Since the exhaust volumes are small from these processes, a low throughput velocity (high SCA) single pass unit is used for this application. Collection efficiencies of 98-99% are obtained on this application.

Tubular precipitators have also been used on photographic film incinerator exhausts for recovering silver halides. Carbon and other finely divided impurities are also present in the exhaust gases. The gases are first passed through a quencher/scrubber and then through the Tubular precipitator. FRP construction is used to prevent chloride corrosion attack. Two passes are used to obtain extremely high collection efficiency.

Molybdenum Roaster

Molybdenum disulfide is oxidized in the multilevel hearth furnace to Molybdenum trioxide and sulfur dioxide. The exhaust is first passed through a baghouse and then through a lead lined quench scrubber. The exhaust stream entering the precipitator contains organic compounds and sulfuric acid mist with some oxides of Molybdenum, Selenium, Rhenium, and Mercury. Chlorides and trace amounts of fluorides are also present in the air stream. Fiberglass reinforced plastic with synthetic veil on the inside surface is used as a material of construction. Particulate and acid mist loadings of .6 to .7 grain/CF have been measured. High SCA, two pass Tubular precipitator system has collection efficiency in excess of 99 percent. The cleaned gases are then taken to an acid plant.

Nickle Recovery

Variety of wastes are generated during steel making process. These wastes are generally contaminated with slag, oil, and water. Wastes from specialty steel making processes contain appreciable amounts of Nickle and Chromium. Baghouse dust, mill scale, and grinding swarf are blended with crushed coal, powdered limestone, and high alloy grit. The mixture is pelletized, dried, and then reduced in a rotary hearth furnace. Nickle and Iron oxides are completely reduced. The hot reduced pellets are mixed with additional fluxes and coarse metallics for adjustment of slag and metal chemistry. This is then fed into electric arc furnace where Chromium oxide is reduced. The exhaust from electric arc furnace is taken to a high pressure drop (45" w.c.) venturi scrubber. The submicron particulate emission from Venturi was still very high (0.1 to 0.2 grain/CF). Apart from causing opacity problems, the particulate carryover was causing maintenance problems for the high pressure fan. Two pass Tubular precipitators installed on this process completely eliminated this problem and plume opacity is reduced to almost zero. The unit is operated continuously wet to prevent accumulation of lead and zinc on the collector plates. Throughput velocity of 7 fps was used for this application. Current suppression was of order of two to threefold.

STEEL INDUSTRY

Typical applications where Tubular precipitators are used in the steel industry are:

1. Scarfing
2. Sintering
3. Coke Oven Exhaust

Scarfing

Very fine Iron oxide particulates are created during scarfing operations. Particulate loadings of 1 grain/CF and over are commonly encountered. The particle size is mainly in submicron to 2 micron range. The exhaust stream coming from scarfer is generally completely saturated. Wet Tubular precipitators are used in this application. Collection efficiency of 99% and higher are required to meet with opacity regulations. ASTM 304 L stainless steel construction is used. The collected particulates are very easy to wash off. Tubular precipitators used on this application have very high collection efficiencies even at high throughput velocity, as can be seen from Figure 4.

Sintering

Sintering is generally used to beneficiate ores by a high temperature agglomeration process. Sintering process transforms raw ore into a product which is uniform in size, has not many fines, is convenient to handle, and has better chemistry. Particulate loading from these processes range in 0.1 to 0.5 grain/CF. Very high amount of condensable organic matter is also present (0.05 to 0.3 grain/CF). Sintering machines using recycle draft and strand cooling have lower emissions and lower exhaust volumes. Tubular units using stainless steel construction have been used in this application.

Coke Oven Exhaust

Exhausts from coke oven batteries are cooled in a quencher and then cleaned in a Tar mist type Tubular precipitator. The exhaust contains Tar, fine unburned carbon, ash, etc. The coke oven gas after being cleaned can be used as a fuel source. Part of the cleaned gas is further cleaned in a Fuel gas precipitator to be used to fire coke oven batteries. Since the carrier gas is combustible, all the precautions required for oil shale precipitators are also applicable here. Insulator purging is done using cleaned gas from the Fuel gas precipitator.

CHEMICAL INDUSTRY

The Tubular precipitators are used as acid mist precipitators in:

1. Sulfuric Acid Plants
2. Sulfonation Plants

Sulfuric Acid Plants

Tubular precipitators have been used in metallurgical type acid plants to clean up smelter gases before they can be taken to the acid plant. Tubular precipitators are also used in sulfuric acid plants using H_2S or spent sulfuric acid as a feed material. Lead and FRP construction have been used in this service. In some applications Hastealloy has been used. Conductive FRP construction, square tube two stage Tubular precipitators have several advantages over conventional lead tube type units. Both sides of the tubes are used for collection so height of the unit is reduced by a factor of two. The FRP housing covers entire unit, thus this type of precipitator can be designed for more than 20 inches w.c. negative pressure (lead tubes are generally not designed for more than -20 inches w.c.). The units are shop assembled, thus significantly reducing installation costs. Two stage, two pass Tubular precipitators used on Copper smelter off gases and on Gold and Arsenic roaster off gases have achieved 99.5% plus efficiency. The normal criteria used in the acid industry, to check the precipitator efficiency, is to have have a 10 meter run of ductwork after the precipitator. This length of duct should be optically clear if the precipitator is performing satisfactorily.

Sulfonation Plants

Surfactants are organic compounds that have both a water soluble (hydrophilic) and a water insoluble (hydrophobic) group. The hydrophilic group for the most commercially available anionic surfactants is either a sulfonate or a sulfate. The hydrophobic portion is generally a hydrocarbon (C_8-C_{18}) in a straight or slightly branched chain. Oleum is most frequently used for sulfonation reaction. The reaction can be given by:

$$RH + H_2SO_4 \rightleftharpoons RSO_2OH + H_2O$$

Very dense white plum is generated during transfer of oleum to the storage tank. Fiber bed filters with absorption spray type devices are used for control of these emissions. The emissions from the sulfonation reactor have also been handled using filters. However, pluggage problems are encountered during manufacture of some detergents. Two stage wet type Tubular precipitators have been used in this application quite successfully. The acid mist loadings are generally 0.25 to 0.3 grain/CF. Very fine size distribution (0.1 to 0.3 micron) is encountered. Low throughput velocities are required to achieve high collection efficiencies (99.5% plus).

Tubular precipitators have also been used on the detergent spray tower emissions. Detergent slurry is sprayed from the top of the detergent spray tower. Hot gases are drawn countercurrently upwards. The organic oils are evaporated creating dense plume. The exhaust also contains carryover detergent fines and a high moisture load. Wet two stage Tubular precipitators are used to control opacity of the exhaust stream.

CONCLUSION

Two stage Tubular precipitators are ideally suited in applications involving high concentrations of fine particulates or for control of organic and acid mist. Increased use of these units in difficult and corrosive applications in envisaged.

REFERENCES

1. Surati, H.S., "Two Stage Precipitator for Hydrocarbon Emission Control," IEEE-IAS Annual Meeting, Chicago 1976, pp 340-345.
2. Surati, H.S., and Beltran, M.R., "Heat Recovery on Organic Electrostatic Precipitators," Annual Industrial Air Pollution Control Seminar, 1976 pp 5-1 - 5-10.
3. Beltran, M.R., "Smoke Abatement for the Carpet Industry," Carpet and Rug Industry, May 1973, pp 30-34.
4. Surati, H.S., Beltran, M.R., and Raigorodsky, I., "Tubular Electrostatic Precipitators of Two Stage Design," Iron and Steel Engineer, December 1980, pp 32-36.
5. Environmental Protection Technology Series, "Ammonia Absorption/Ammonium Bisulfate Regeneration Pilot Plant for Flue Gas Desulfurization" EPA-600/2-77-149, August 1977, pp 27-28.

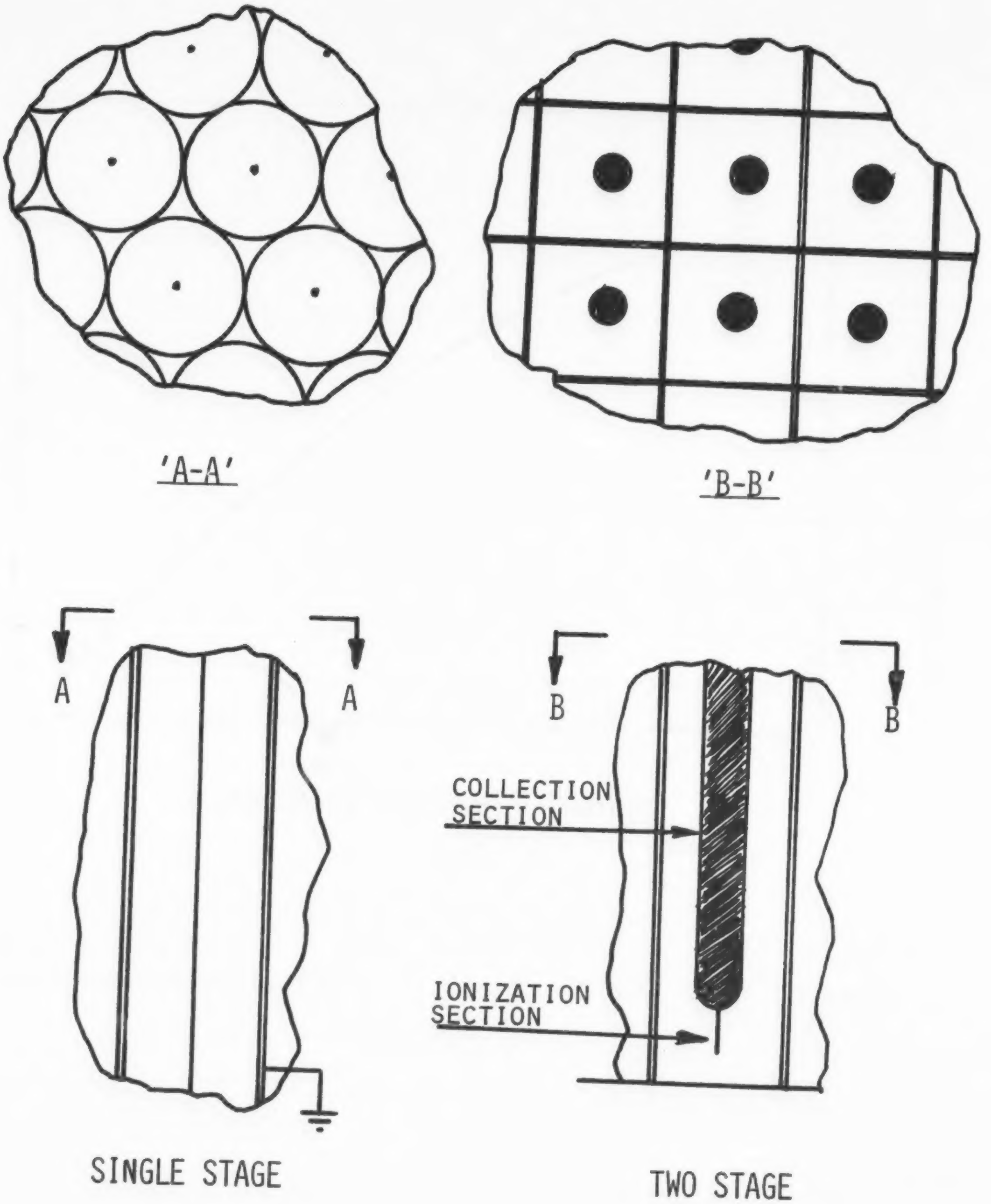
'A-A'
'B-B'
A
A
B
B
COLLECTION SECTION
IONIZATION SECTION
SINGLE STAGE
TWO STAGE

Figure 1. Round and Square Electrode Geometry

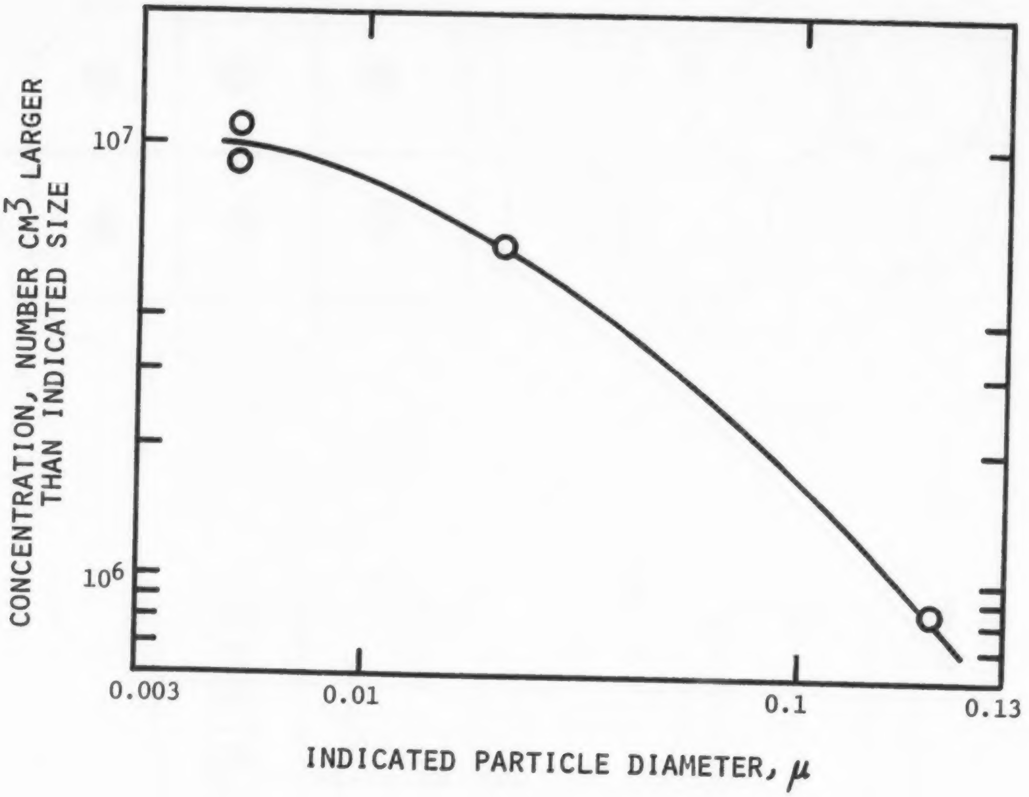

Figure 2. Number-size distribution of particulate in absorber plume.

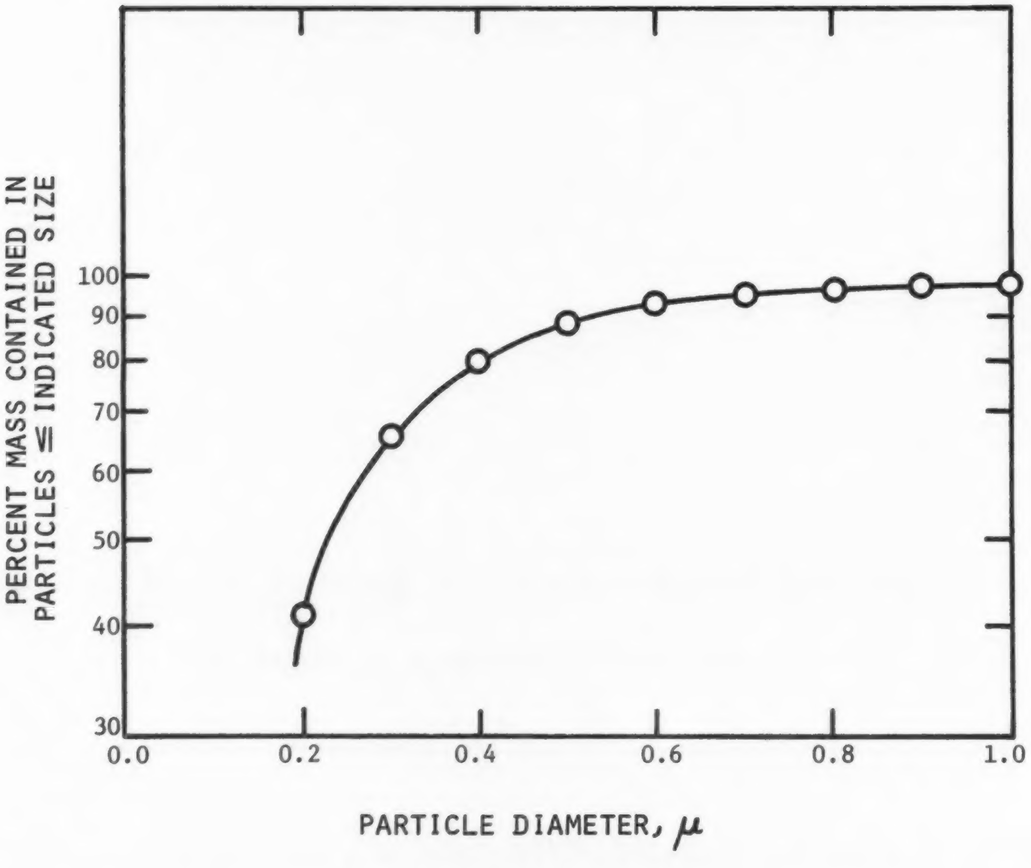

Figure 3. Mass-size distribution of particulate in absorber plume.

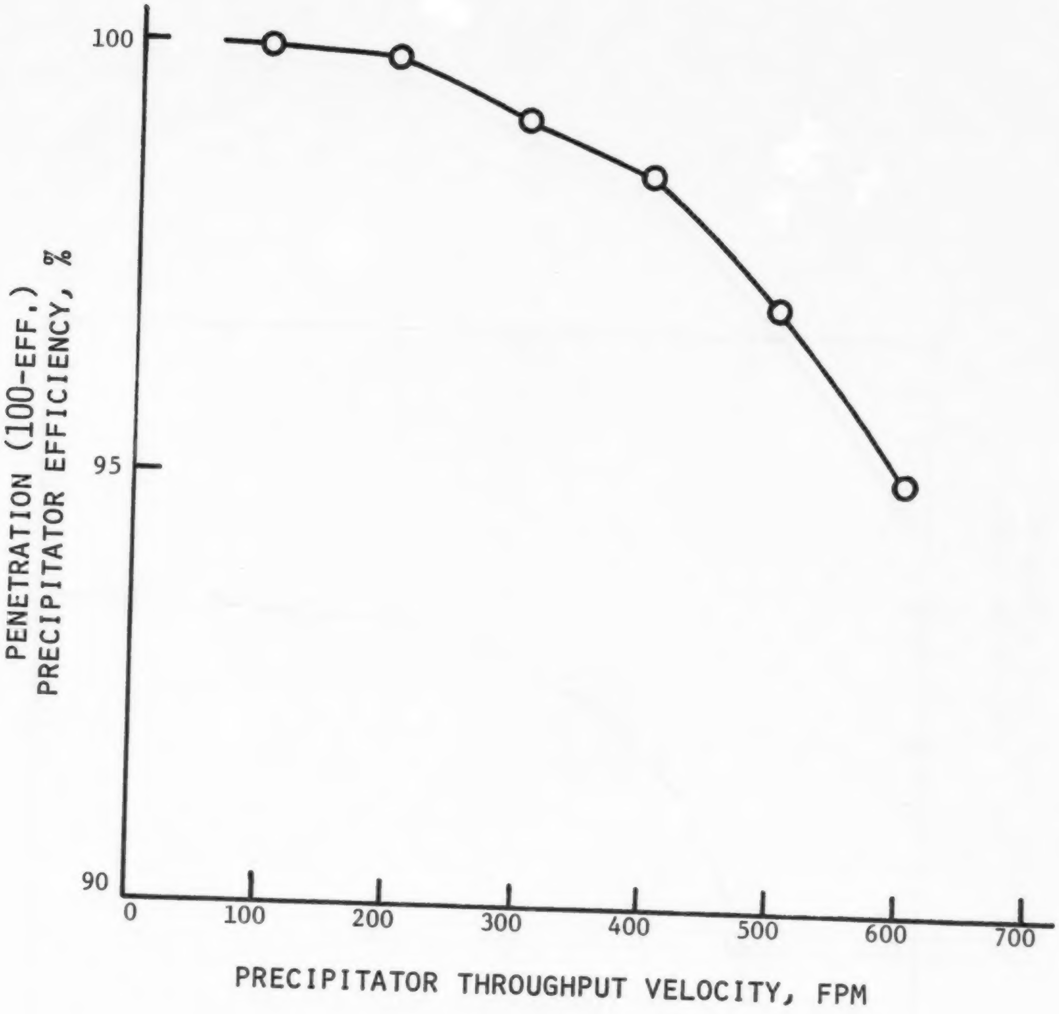

Figure 4. Precipitator Efficiency as a function of Throughput Velocity for Scarfing fume

PILOT DEMONSTRATION TWO-STAGE ESP TEST RESULTS

by: P. Vann Bush and Duane H. Pontius
Southern Research Institute
Birmingham, AL 35255-5305

ABSTRACT

Results of the evaluation of the performance of a large pilot scale two-stage ESP under a range of opeating conditions are presented in this paper. A three electrode precharger, followed by four collector sections with a total SCA of 286 ft^2/kacfm (56 $m^2/m^3/s$) and a gas flow capacity of 30,000 acfm (850 m^3/min), was tested under two ash resistivity conditions. Background information on system operation since start-up in early 1981 as well as results from recent tests are presented.

DISCLAIMER

The research described in this article has been funded wholly or in part by the U.S. EPA under Contract 68-02-2683 to Southern Research Institute, and it has been subject to the Agency's required peer review and policy review.

INTRODUCTION

The two-stage concept for electrostatic precipitation of high resistivity dust has been under investigation at Southern Research Institute since 1974 with the funding and general guidance of the Particulate Technology Branch of EPA's Industrial Environmental Research Laboratory (Research Triangle Park, NC). The majority of effort has been expended to develop and demonstrate a charging stage. The three-electrode charger has been the principal focus of development since early 1977 (1,2). Less attention has been given to the design of the collector stage of the two-stage system.

Tests of a large-pilot demonstration scale system incorporating a three-electrode charger and a four-section collector stage have been underway since early 1981. The system has a gas volume capacity of 30,000 acfm and an average, as-tested specific collection area (SCA) of 286 ft^2/kacfm. It is installed at the TVA Bull Run Steam Plant. Figure 1 is a photograph of the pilot demonstration facility.

The test program has three objectives: 1) to demonstrate reliable, high collection efficiency in the two-stage system; 2) to demonstrate the charging effectiveness of the precharger stage; and 3) to evaluate the feasibility of retrofitting a conventional ESP with a precharger stage. All of the objectives are to be achieved with high resistivity dust. The first two objectives have been addressed. Most of the remainder of the test program will address the third objective and will be completed by March 1983.

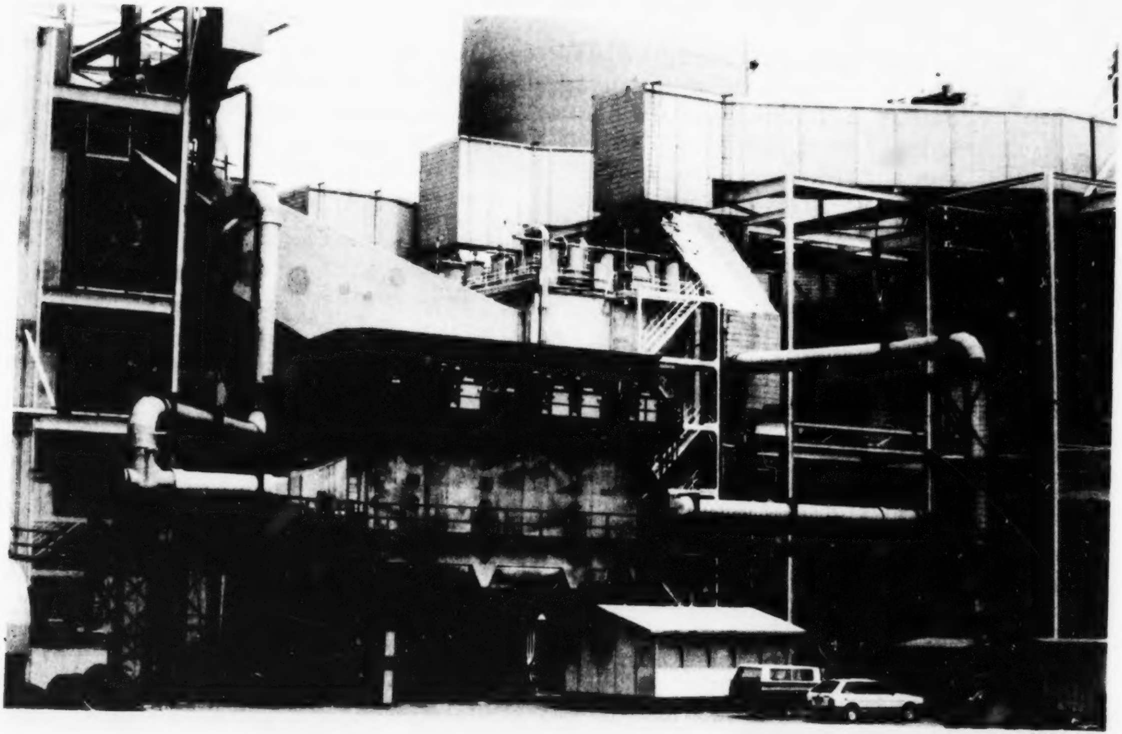
4100-232

Figure 1. Photograph of the pilot demonstration facility.

BACKGROUND

The design and installation of the two-stage system has been described previously (3). Without repeating the details, Figure 2 shows the internal arrangement of electrodes in the system. The four collector-stage electrical sections are fitted with 3/8-in. diameter rods for discharge electrodes. This design was selected in order to achieve the high electric fields at low current densities which are desirable for collector performance in two-stage systems. The design has proven to be a good choice for the two-stage system.

There were only minor problems associated with the start-up of the pilot demonstration system. A wiring problem in the precharger power supply and modification of the ash disposal system caused some delay in achieving steady operation. After 1 month of operation it was determined that additonal reactance was needed in the precharger power supplies in order to achieve optimum performance. The power sets for the precharger stage were of special design not really adequate for field service. Nevertheless, the addition of linear reactors in the precharger stage power sets allowed operation over a broader range of voltages.

INITIAL PERFORMANCE TEST

The first thorough characterization of the performance of the two-stage system was conducted in June and July 1981. The fly ash resistivity was measured to be 1-3 x 10^{11} ohm cm at the flue gas temperature of 250-260°F (120-127°C). Throughout the test period the collector stages were operated at peak voltage levels corresponding to 10-15 nA/cm^2 current densities and 4 kV/cm electric fields (50 kV applied voltage). This voltage-current operating level is evidence of the success of the 3/8-in. diameter rods in meeting the design criteria for the collector stage. The precharger was operated with 30-40 nA/cm^2 current density and 3.0-3.5 kV/cm electric field. The inlet mass loading for the test was a high 6.12 gr/scf (14 g/m^3). Both Method 17 mass loading measurements and cascade impactor measurements indicated an overall system collection efficiency of 99.7%. This is equivalent to 0.35 lb/10^6 Btu particulate emissions.

There was no apparent performance benefit due to the precharger during these tests. This was in spite of particle charging effectiveness, as determined by charge/mass (Q/m) measurements, at levels expected from theoretical predictions for the given particle size distribution and electrical conditions. The mathematical model of ESP performance (4) was used to determine what the two-stage system efficiency should be under the operating circumstances with precharger off and precharger on. Using the typical values for the contribution to the emissions due to nonideal effects (gas velocity standard deviation = 0.25 and gas sneakage = 10%), the model predicts a collection efficiency of 99.656% without the precharger, and an efficiency of 99.731% with the precharger using an SCA of 266 ft^2/kacfm. This difference of 22% in penetration, though substantial, was less than the scatter in the data.

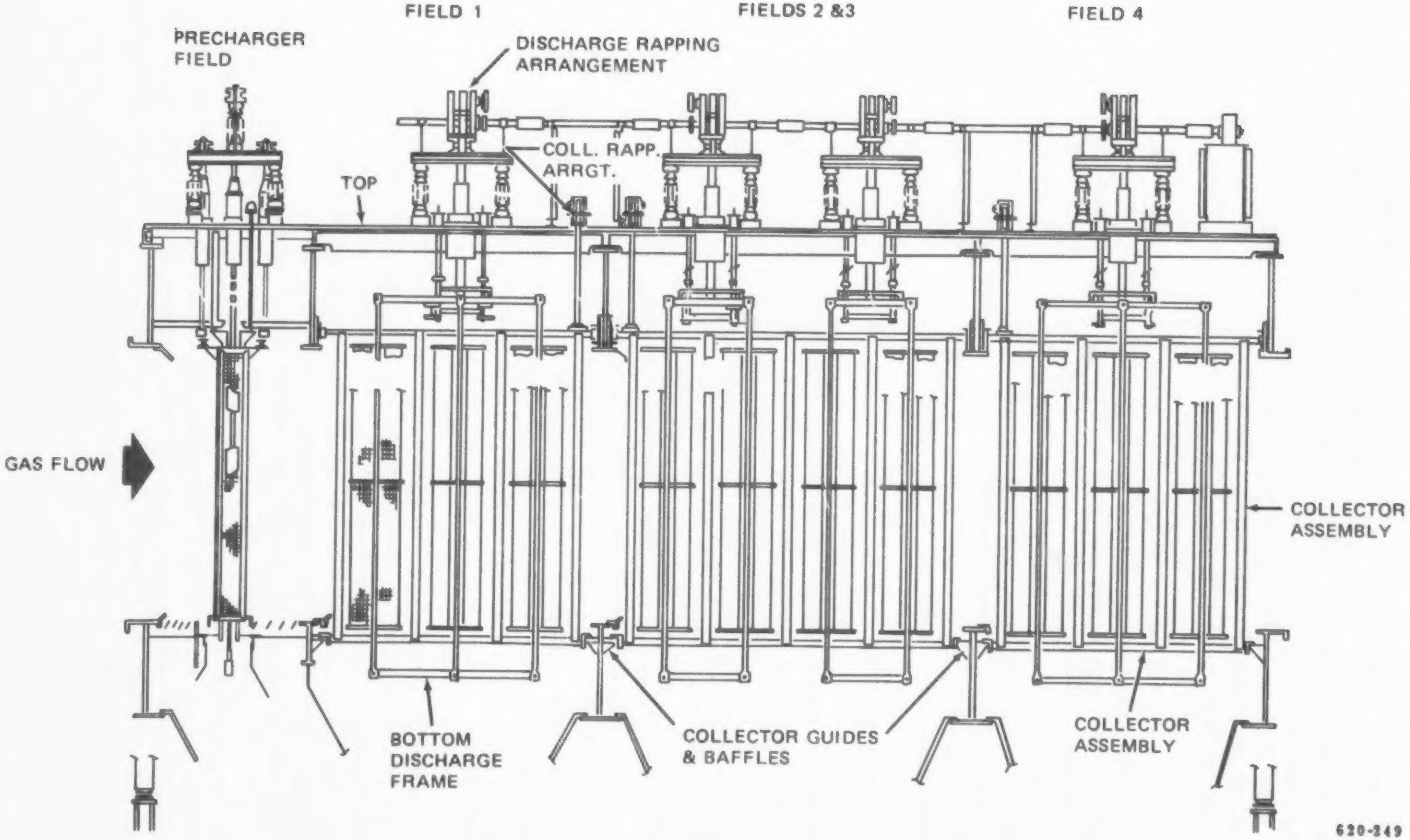
FIELD 1
FIELDS 2 &3
FIELD 4
PRECHARGER FIELD
DISCHARGE RAPPING ARRANGEMENT
COLL. RAPP. ARRGT.
TOP
GAS FLOW
COLLECTOR ASSEMBLY
BOTTOM DISCHARGE FRAME
COLLECTOR GUIDES & BAFFLES
COLLECTOR ASSEMBLY
620-249

Figure 2. Internal arrangement of the two-stage system.

The high efficiency that was measured, 99.7% for 2×10^{11} ohm cm resistivity ash with an SCA of 286 ft^2/kacfm, indicates excellent performance on the part of the downstream collector. The benefit of using large diameter discharge wires in high resistivity ash collection needs further study.

Information on particle size distribution and system electrical characteristics derived from the test data and electrical data from conventional ESP tests was used in the mathematical model to predict the efficiencies for the precharger-collector system and a conventional ESP at four values of SCA. The pilot system dimensions were used for all the conditions, and gas volume flowrate was varied to change the SCA. The two-stage system model and the conventional ESP model are plotted in Figure 3. The data points for the measured efficiencies for the pilot demonstration ESP system and the full-scale Bull Run Steam Plant ESP are shown. The data points indicate the model predictions may be used to approximate the difference in penetration between the two-stage system and conventional ESP's at a given SCA or to estimate the difference in SCA required to achieve a given emission level.

SYSTEM AND OPERATING MODIFICATIONS

Measurements made during the initial test indicated that 50% of the outlet emissions were due to rapping reentrainment losses. The rapping cycle in the outlet field was decreased from 12 raps per hour to 1 rap per hour. Optical particle counter measurements showed that a substantial reduction in outlet emissions was achieved as a result of this change. These data are summarized in Table 1.

TABLE 1. RAPPING CONTRIBUTIONS TO EMISSIONS

Particle Diameter Range (μm)	Percent Due to Rapping	
	12 raps/hr	1 rap/hr
0.464 - 1.285	1.778	21.86
1.285 - 2.631	2.773	22.38
2.631 - 4.990	32.98	31.15
4.990 - 10.009	72.69	56.29
10.009 - 17.003	82.34	67.97
>17.003	92.66	20.39

After the July 1981 test period the pilot demonstration system was operated continuously through October with no performance degradation. During November a problem in the Bull Run Steam plant heat exchangers caused an approximately 50°F drop in the flue gas temperature and concomitant reduction in resistivity. At this condition the outlet emission level was reduced to 2.4×10^{-3} gr/scf (5.5×10^{-3} g/m^3), less than half the level measured at 260°F. The

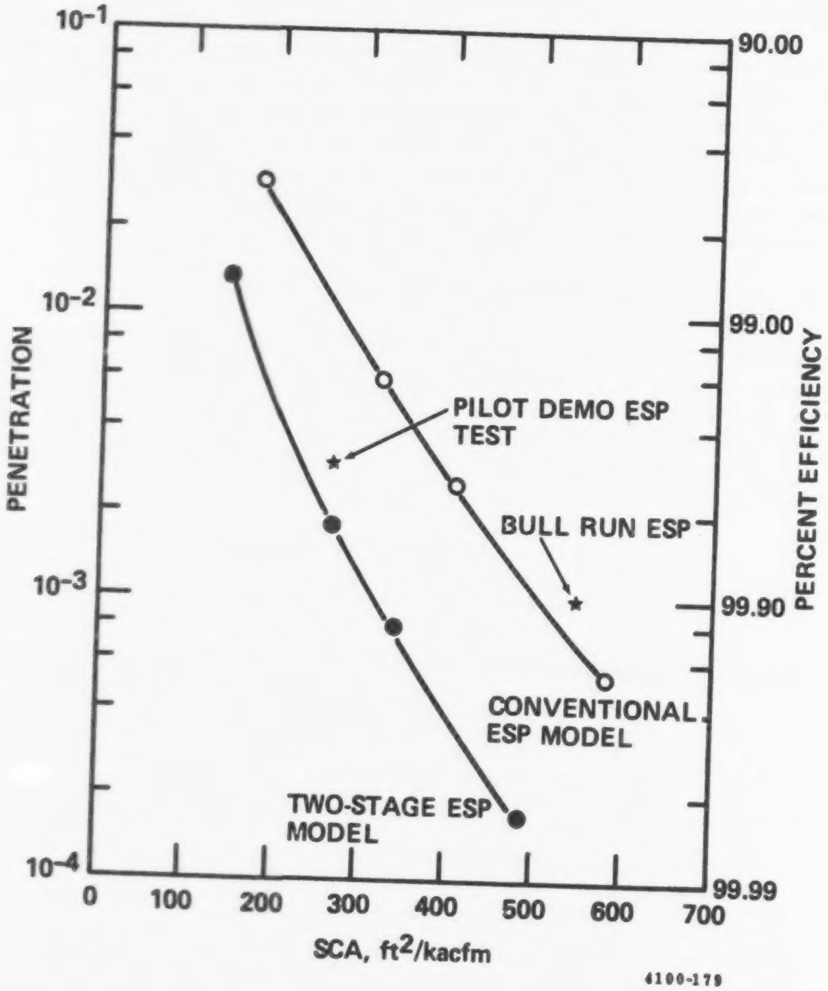

Figure 3. Model predictions for penetration as a function of specific collection area. The stars represent actual field data.

plant remained in this condition until March 1982 at which time a major maintenance outage occurred.

The ESP mathematical model confirms the desirability of another system modification. Figure 4 shows a theoretical prediction of the precharger benefit to system performance as a function of fly ash resistivity. Three curves are shown, corresponding to ideal collection and two degrees of nonidealities. Variations in ash resistivity are reflected in the model input data as variations in operating voltages and currents (based on experimental data). In order to more clearly demonstrate the precharger effect on system performance it is desirable to operate at higher ash resistivity than is available at 260°F. The resistivity of the ash at Bull Run Steam Plant is shown as a function of temperature in Figure 5. The peak resistivity occurs at about 325°F (163°C). In order to boost the flue gas temperature in the pilot demonstration system, some ductwork was added to the system during the plant outage which permits mixing hot gas from upstream of the plant's heat exchangers with the main slipstream from the cold-side duct. This addition provides an operating range of 250 to 350°F. The measured peak in resistivity is 4 x 10^{12} ohm cm at 325°F.

One other modification was made to the pilot ESP system during the plant outage. The power supply system for the precharger stage was replaced with commercial-grade transformer/rectifier sets and controllers. This was the last component in the system to be developed to the industrial standard.

RECENT TESTS

After completing the system modifications and allowing a period of stabilization it was decided to repeat the tests at 260°F before testing at the maximum resistivity condition. A new measurement tool was used to set up operating conditions for these tests. A continuous charge probe derived from the design used by EPA personnel in in-house experiments was used to determine the optimum charging condition for the precharger with 260°F flue gas. The current due to charged particles impacting the probe sensor (shown in Figure 6) was measured with an electrometer. A maximum reading was measured when the precharger was in the following operating condition: corona voltage = 17-20 kV, corona current = 20-25 mA, grid voltage = 2-4 kV, and grid current = 40 mA. At this condition, there was steady sparking in the precharger. Reducing the grid voltage until sparking diminished produced the next highest probe reading. Essentially, the only change in V-I conditions was a change in grid current to 0 mA and less than 1 kV measurable decrease in grid voltage. Q/m measurements were made at these two conditions. The average Q/m measured for the first condition was -1.45 μC/g with a maximum of -2.01 μC/g. The average Q/m value at the latter condition was -1.05 μC/g with a maximum of -1.06 μC/g. The charge probe does indicate charging performance in this application and is therefore a valuable aid in optimizing the precharger.

EVALUATION OF THE PILOT DEMONSTRATION SYSTEM AT 260°F

The test program to characterize the pilot demonstration precharger-collector system was conducted in July 1982. The objectives of the test were to

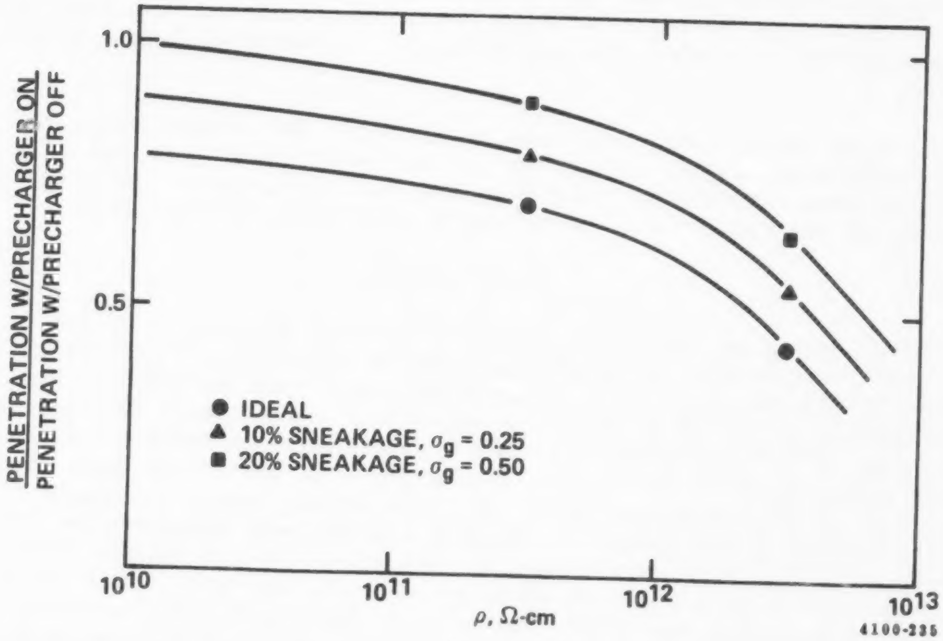

Figure 4. Theoretical predictions of precharger benefit as a function of fly ash resistivity.

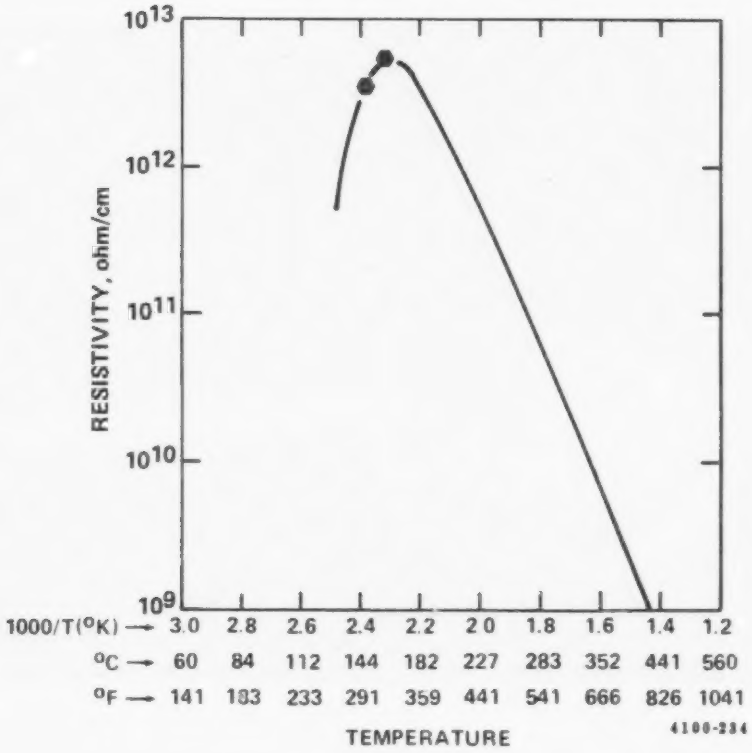

Figure 5. Ash resistivity versus temperature at Bull Run Steam Plant.

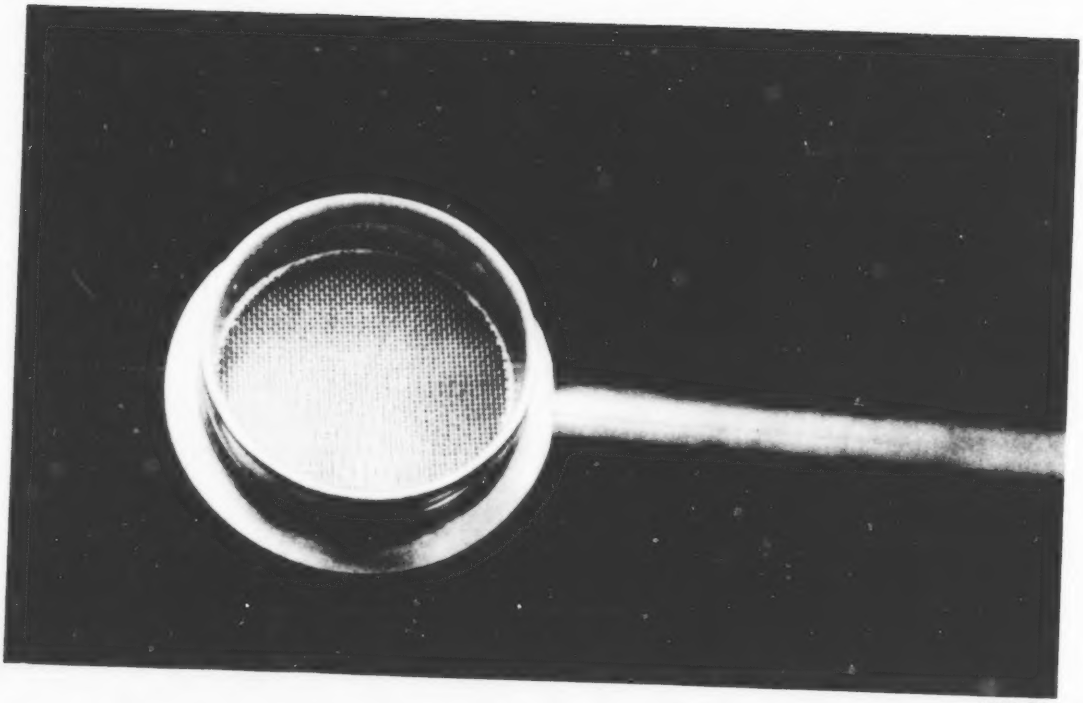

4100-201

Figure 6. Continuous charge probe sensor.

1) determine the system collection efficiency and 2) determine the percent of penetration decrease attributable to the precharger stage.

The precharger stage was optimized for the test using the continuous charge probe. An example trace of the probe reading is shown in Figure 7. As shown, the action of the grid is very important in achieving high charging effectiveness with these test conditions. The average values of voltages and currents for the precharger stage are shown in Table 2. The average Q/m ratio measured at these settings was -1.75 μC/g. This compares to a theoretical prediction of -1.81 μC/g for the given charging conditions and particle size distribution, and thus indicates essentially no degradation in charging with the optimum precharger operating condition.

TABLE 2. PRECHARGER OPERATING CONDITIONS

Corona discharge electrode voltage = 15 - 17 kV
Corona discharge electrode current = 25 - 30 mA
Charging current density = 100 - 120 μA/ft^2
Charging electric field strength = 2 kV/cm
Grid electrode voltage = 2 - 3 kV
Grid electrode current = 45 - 50 mA

The collector stage was operated at maximum stable applied voltage in each section. These operating values and the corresponding currents and current densities are shown in Table 3.

TABLE 3. COLLECTOR OPERATING CONDITIONS

Section	Voltage(kV)	Electric Field(kV/cm)	Current(mA)	Current Density(μA/ft^2)
1	45.5-46.5	3.6	14.5	6
2	45	3.5	25	16
3	50-51	4	14-16	9
4	50-51	4	26	11

Mass loading measurements which were made during the July test show a "precharger on" penetration of 0.0033 (99.67% collection efficiency) and a "precharger off" penetration of 0.0052 (99.48% collection efficiency). This 36.5% difference in penetration due to the precharger is a substantial enhancement in performance for this fly ash resistivity (measured to be 2-5 x 10^{11} ohm cm at this test condition).

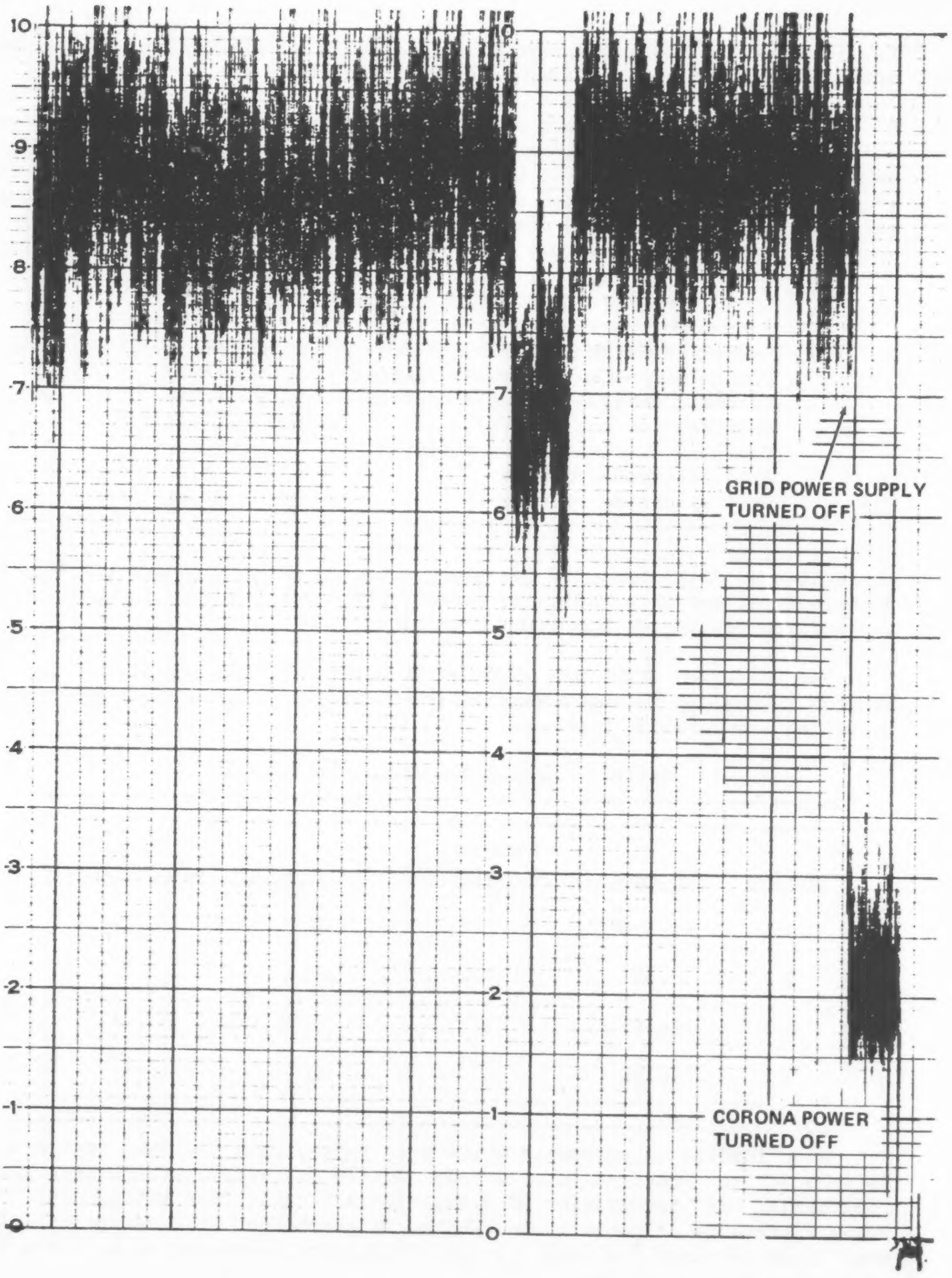

Figure 7. Example trace of the continuous charge probe output.

The particle size distribution and fractional efficiencies for particles with diameters in the range 0.5 to 10.0 μm were measured with University of Washington Mark V cascade impactors. The precharger on and precharger off penetration-efficiency curves obtained from the inlet vs. outlet comparisons are shown in Figure 8. The overall mass collection efficiencies as measured by the impactors are 99.52% with precharger on and 99.36% with precharger off. This is a 25% reduction in penetration due to the precharger stage.

Electrical aerosol analyzer (EAA) and optical particle counter systems were also used to determine the percent of collection efficiency due to the precharger for particles in the diameter range of 0.04 to 1.7 μm. These data showed a consistent difference in particle concentration throughout the measured size range of approximately 20%.

The test data all point up an enhancement in performance attributable to the precharger varying from 20 to 36% depending on the measurement technique. The major difference between this test and the test of July 1981 was the precharger operating voltages and currents. A fourfold increase in current density was achieved for the recent test. Several factors may be contributing to this difference, including the newly installed commercial-grade power supplies for the precharger, and a reduced inlet mass loading (measured to be 4.3 gr/scf (9.8 g/m^3) instead of 6.1 gr/scf as in the 1981 test).

Another difference between the 1982 and 1981 tests was the decrease in precharger off collection efficiency. The possible explanation for this difference is a reduction in inlet MMD from 32 to 13 μm. This reduction correlates with the lower inlet loading. It is not certain what factors produced this reduction.

TEST AT MAXIMUM RESISTIVITY

A test program was developed to characterize the performance of the pilot demonstration precharger-collector system when subjected to the maximum fly ash resistivity available. In order to achieve this condition, a sample flue gas stream from the boiler exhaust upstream of the heat exchangers was mixed with the cold-side slipstream. This produced a maximum ash resistivity of approximately 4 x 10^{12} ohm cm at 325°F.

The configuration of the precharger-collector system was unchanged from the test at 260°F gas temperature. The 3/8-in. diameter rods were left in the collector stage for discharge electrodes. The voltage-current relationships for the four collector sections at the high resistivity ash loading condition are shown in Figure 9. The voltage before sparkover (and concurrent sharp change in the curve slope) was less by an average of 8 kV than when the ash resistivity was 2-5 x 10^{11} ohm cm in previous tests. This V-I behavior is a typical result of back corona. The collector sections were operated at the maximum applied voltage point on the V-I curve. Typical operating values for llector section voltages and currents are shown in Table 4.

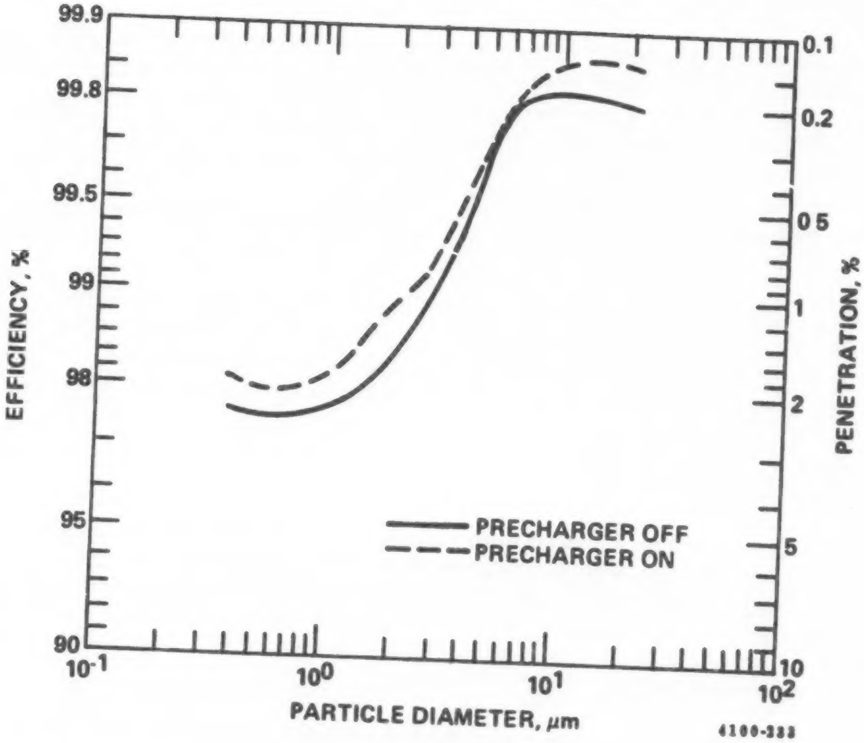

Figure 8. Precharger on and precharger off efficiency curves from tests at 260° F.

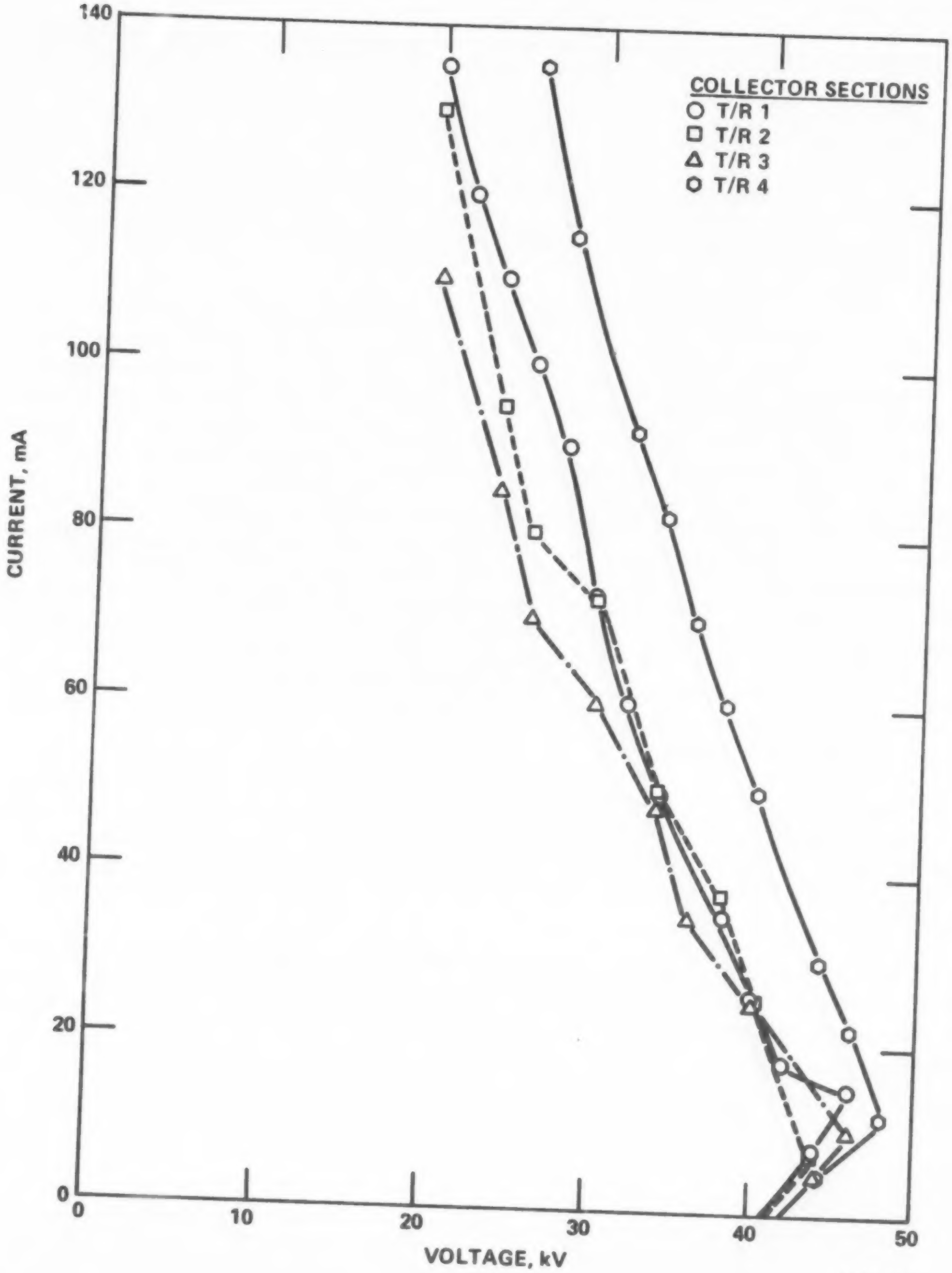

Figure 9. V-I behavior of collector sections at 325°F.

TABLE 4. COLLECTOR STAGE OPERATING DATA

Section	Voltage(kV)	Electric Field(kV/cm)	Current(mA)	Current Density(nA/cm^2)
1	40-42	3.2	5-10	2-4
2	40-42	3.2	5-10	3-7
3	42-44	3.4	8-12	5-8
4	42-44	3.4	10-20	4-9

During the early portion of the test program the precharger stage was operated at voltages and currents comparable to those maintained during the test at 260°F. After determining that the operating range of the precharger was limited by sparking on the grid electrode, several days of testing were completed with the precharger off. The system was then taken off-line, and the precharger stage was inspected to determine the cause of the spark-limit. Three grid electrodes were found to have suffered severe physical damage. It was concluded that operation of the pilot demonstration system for prolonged periods at temperatures near and below the acid dewpoint had resulted in deterioration of the grid material and had produced irregular surface edges from which corona and electrical breakdown could occur. The industrial power supply for the precharger stage allowed system operation to be maintained under heavy sparking conditions. During these heavy sparking episodes the grid suffered the damage.

Two of the three damaged grids were replaced with available spare grids. The third damaged grid was replaced with a grid from the lane nearest the casing wall, leaving that 1 lane out of 18 with a grid electrode on one side only. Though this left the precharger stage in a nonideal condition, testing resumed.

The effects of replacing the damaged electrodes in the precharger stage were slightly altered voltage operating levels and more restricted operation so as to avoid heavy sparking. The precharger voltages and currents are summarized in Table 5.

TABLE 5. PRECHARGER STAGE OPERATING DATA

	Corona Voltage (kV)	Grid Voltage (kV)	Charging Field (kV/cm)	Charging Current (mA)	Current Density (nA/cm^2)
Before repair -	17-20	2-4	~2.0	20-25	87-109
After repair -	15-17	4-6	~1.5	15-20	65- 87

The mass loading measurements taken since the damage to the precharger has been known show no statistically significant difference in system collection efficiency with or without the precharger. The precharger-collector system efficiency has been 98.87%. The collector alone has had an efficiency of 98.75%. At this level of efficiency an SCA of 370 ft^2/kacfm (72.8 m^2/m^3/s) would be required for 99.7% collection efficiency.

The charging effectiveness of the precharger was measured with Q/m samples. The average of these measurements is -1.4 μC/g. This is compared to a theoretical Q/m value under these electrical and ash size distribution conditions of -2.4 μC/g. This indicates some performance deterioration.

A strip chart record of continuous mass monitor readings indicated an increase in rapping reentrainment emissions at the 325°F gas temperature. This change in nonideal conditions, along with the precharger mechanical problems, would cause a decrease in the performance benefit of the precharger. This is evident in Figure 4. Any increase in nonideal effects would cause a decrease in expected precharger performance benefit.

The mechanical problem in the precharger stage may be seriously altering its electrical behavior and charging efficiency. The lane with damaged and missing grid electrodes constitutes 5.5% of the active area of the precharger. That much gas sneakage would be detrimental to performance by itself. However, if that lane is in severe back corona (and it most probably is), a large fraction of the precharger current may be confined to that lane. This would drastically vitiate the charging effectiveness of the precharger.

FUTURE PLANS

The first test planned for the remainder of the pilot demonstration program is a repeat of the test at maximum ash resistivity. This will occur as soon as damaged precharger components can be replaced. An effort to reduce, or quantify, the contribution other nonidealities present in the system are making to the emissions will be made prior to this test.

The final test program will be an evaluation of the precharger applicability as a retrofit to conventional ESP's. For this test the discharge electrodes downstream collector sections will be replaced with 1/8-in. diameter wires to conform to standard ESP practice. From these results of this test a cost analysis for precharger retrofit versus alternate techniques to achieve emission limits will be produced.

SUMMARY AND CONCLUSIONS

The evaluation of the pilot demonstration system has been underway for 20 months. Only minor modifications have been required to achieve a rugged commercial-grade two-stage system.

The performance of the two-stage ESP system has been evaluated under two ash resistivity conditions: 2-5 x 10^{11} ohm cm and 4 x 10^{12} ohm cm. One obvious conclusion from the tests is the excellent performance of the downstream collector stage. The 3/8-in. diameter rods used for discharge electrodes have proven very effective in providing high electric field strengths. The collector efficiency was ~99.5% for the 2-5 x 10^{11} ohm cm ash resistivity. Even at 4 x 10^{12} ohm cm ash resistivity the collector achieved 98.75% efficiency in spite of increased rapping reentrainment emissions. This is very good given the SCA of 286 ft^2/kacfm. (The full scale precipitator at Bull Run has an SCA of 570 ft^2/kacfm (112 m^2/m^3/s).) Questions remain unanswered relating to larger diameter discharge wires.

The precharger-collector system was demonstrated to operate at high efficiency, ~99.7%, in collecting 2-5 x 10^{11} ohm cm resistivity ash. The precharger reduced mass emissions by more than 20% under these conditions. Theory would predict an even greater benefit at higher ash resistivity.

The ash resistivity in the pilot system was raised by increasing the flue gas temperature. The precharger-collector system was tested at 325°F where the resistivity was measured to be 4 x 10^{12} ohm cm. Some mechanical problems developed in the precharger due to extended operation below acid dewpoint. These problems, together with increased rapping reentrainment, cloud test results at the high resistivity condition. The precharger has not been shown to contribute to enhanced collection efficiency. Tests with the precharger restored to good mechanical condition will be made as soon as possible.

REFERENCES

1. Pontius, D. H., and L. E. Sparks. A Novel Device for Charging High Resistivity Dust. APCA Journal, 27(7):698-700, 1978.

2. Pontius, D. H., P. V. Bush, and L. E. Sparks. Field Evaluation of a Two-Stage ESP for High Resistivity Dusts. Staub, 40(11): 473-477, 1980.

3. Bush, P. V., and D. H. Pontius. Pilot Demonstration of the Precharger-Collector System. In: Third Symposium on the Transfer and Utilization of Particulate Control Technology: Volume I. Control of Emissions from Coal Fired Boilers, EPA-600/9-82-005a, July 1982.

4. Mosley, R. B., M. H. Anderson, and J. R. McDonald. A Mathematical Model of Electrostatic Precipitation (Revision 2). EPA-600/7-80-034 (NTIS No. PB80-190994), February 1980.

ACKNOWLEDGEMENTS

The authors express special thanks to Todd Snyder of Southern Research Institute for his management and organization of all on-site activities at the pilot demonstration facilities.

We also express our gratitude to Leslie E. Sparks of EPA for his guidance, insight, and general supervision as Project Officer of the pilot demonstration program.

EVALUATION OF PRECHARGERS
FOR
TWO-STAGE ELECTROSTATIC PRECIPITATORS

by

George Rinard
Donald Rugg
Michael Durham
Denver Research Institute
Denver, Colorado 80208

ABSTRACT

Two-stage precipitators are being considered for high resistivity dust collection. Indications are that the size of a two-stage precipitator for this application may be considerably smaller than a conventional wire plate design. DRI is presently evaluating two-stage designs using a 7.08 m^3/s (15000 ACFM) pilot plant and slipstream of the Valmont Power Plant in Boulder, Colorado. Results of the evaluation of two precharger designs are given.

> This paper has been reviewed in accordance with the U.S. Environmental Protection Agency's peer and administrative review policies and approved for presentation and publication.

INTRODUCTION

The Valmont Test Facility, designed and constructed by the Denver Research Institute and sponsored by EPA is presently operational. This facility was constructed to provide a versatile tool for evaluating novel electrostatic precipitator concepts on an operational source of high resistivity dust. Evaluation has begun on the tri-electrode precharger developed by Southern Research Institute (SoRI). Preliminary results of this work are presented. In addition, voltage-current characteristics of the cooled-pipe charger/collector have been determined, and the results are given and compared with those obtained in the laboratory.

VALMONT TEST FACILITY

The experimental facility is set up on the grounds of the Valmont Station of Public Service of Colorado (PSCo) in Boulder, Colorado. The facility is shown in Figure 1. The test arrangement consists of the ESP, a gas delivery and return system, particulate sampling station, the instrumentation and sampling trailers, storage facilities, and support equipment made accessible by a road.

Because of a conditioning system located just downstream of the air preheater on the No. 5 unit, the slipstream is taken just upstream on the hot side of the preheater. The gas is returned to the main duct downstream of the air preheater and just upstream of the I.D. fans. A bypass duct is installed between the supply and return duct complete with a 240 kW electric heater to preheat the system. Preheating is important to avoid sudden changes in temperature and to prevent condensation. The supply and return ducts are preheated by opening a valve located in a second by-pass loop. This valve allows circulation of flue gas due to the pressure differential between the two legs of the system.

An electric-motor-driven gas circulating fan is provided. The fan is complete with an opposed-blade outlet control damper to ensure constant flow through the ESP. A venturi flow meter located downstream of the ESP is used to monitor the flow through the system. For cold-side operation a Luhr-Interel design gas/air heat exchanger is used to cool the gas. The heat exchanger is equipped with a self-cleaning mechanism to keep the outside (gas-side) surface of the tubes clean.

The particulate sampling station is located between the supply and return ducts. It consists of a prefabricated building, 3.0 x 5.5 m (10 x 18 ft) in size and is installed at an elevation of approximately 3.7 m (12 ft) above ground.

The two trailers are for instrumentation and gas sampling. The trailers are 2.4 m (8 ft) wide and 12.2 m (40 ft) long and contain a computer, controls, and gas sampling and analysis equipment. They are equipped with heaters, air conditioners, water storage, and waste disposal holding tanks.

The test facility has presently been operated for approximately 1100 hours during which 200 hours of testing has been completed. The description of the plant, its operating conditions,and the average values of the measured flue gas conditions are shown in Table 1.

It is extremely important in pilot scale work to have good flow conditions and eliminate sneakage as much as possible. The flow distribution for the test precipitator was modeled in the laboratory to ensure good quality flow. Baffles were installed at the top and bottom of each collector section, in the hoppers, and along the side of each outside plate.

During system shakedown the flow distribution was measured by taking gas velocity traverses at the inlet, center, and outlet sections of the precipitator. Figure 2 shows a histogram of the flow characteristics at the inlet. This is characteristic of the flow throughout the precipitator. The measurements indicate that the design goal to meet or exceed the Industrial Gas Cleaning Institute (IGCI) standards was accomplished.

TABLE 1

OPERATING DATA FOR VALMONT STATION OF PUBLIC SERVICE OF COLORADO

PLANT DESCRIPTION

UNIT:	No. 5
RATING:	180 MW
BOILER:	Combustion Engineering Tangential Fired
COAL:	50% Energy Coal - Colorado (0.6 - 0.8% S) 50% Colorado-Wyoming Coal Co.
ON LINE:	1963

OPERATING CONDITIONS

TIME	BOILER LOAD
2400 to 0700	70- 90 MW
0700 to 1700	100-160 MW
1700 to 2400	80-150 MW

At Peak Conditions	MAX	MIN	AVG
Boiler Load	162 MW	92 MW	126 MW
Hot-Side Temp	390°C (735°F)	310°C (590°F)	343°C (649°F)

FLUE GAS CONDITIONS

GAS CONSTITUENTS:

H_2O (Method 4)	8%
SO_3 (Controlled Condensation System)	< 0.1 ppm
SO_2 (Pulsed Fluorescence)	200 ppm
CO_2 (Gas Chromotography)	12%
O_2 (Gas Chromotography)	8%

FLY ASH:

Mass Loading	4.95 g/SCM (2.16 gr/SCF)	2.7 g/SCM (1.18 gr/ACF)
Size Distribution	14 micrometers Mass Median Diameter 4.5 Geometric Standard Deviation	
Resistivity (In Situ)	@ 150°C (300°F) @ 120°C (250°F)	2.0×10^{12} ohm-cm 7.5×10^{11} ohm-cm

TEST PROGRAM

Besides the overall performance of the ESP, the performance and characteristics of the individual charging and collecting components are to be analyzed to further the understanding of the precipitation process. Cumulative charge/mass, charge on single particles, mass loading, and particle size distribution can be measured at ports located just downstream of each precharging section. Load cells mounted on each collector section will be used to determine: the rate at which the dust is collected in each section, dust thickness prior to rapping, the effectiveness of the rapping for removing the dust, and the effectiveness of downstream charging and collecting sections in precipitating reentrained dust from upstream sections.

The parametric tests have been designed to characterize the precharger sections, the collector sections, and various combinations of precharger/collector configurations. The initial stages of each parametric evaluation of a novel concept will involve an optimization of the rapping frequency and intensity. The collector load cell readings, voltage-current characteristics, and outlet opacity will also be used to optimize the rapping. In addition, the location of upper and lower ash level detectors can be changed so that it will be possible to optimize the amount of ash in a hopper to reduce boilup.

Besides operating the prechargers and collectors at the highest voltages possible, tests will be run to determine the effects of reducing the operating levels. Tests will also be run in which one or more of the prechargers will be deenergized to determine the proper ratio of precharger to collector sections. This can be determined by analysis of the overall performance and by running charge/mass tests after each collector. If the particles exiting a collector section are not charged, then another precharger section is be required.

After the parametric tests are run to determine the operating characteristics of the novel ESP devices, the unit will be operated under optimum conditions at two different flow rates to determine operating performance as a function of precipitator size. This information will then be used in an economic evaluation of the device.

The first phase of the test program involves an evaluation to determine the optimum two-stage precipitator system. This involves testing two different prechargers interfaced with flat-plate high-voltage electrodes in the collector sections. The first precharger that is being tested is the tri-electrode precharger developed by SoRI. Preliminary results for this device are given below.

The first phase of the planned test program will be directed toward new precipitator designs the second phase will be directed toward improving existing precipitators operating on high resistivity dust. The plates in all four collector sections will be replaced with standard wire-plate configurations. Potential improvements will be in the form of advanced controllers, pulsed excitation, addition of a precharger, and lowering the operating temperature of the precipitator. The third phase of the test program will involve operating the ESP at hot side-conditions.

PRELIMINARY RESULTS FOR TRI-ELECTRODE PRECHARGER

Provisions are made in the test precipitator for as many as five precharger sections. In the testing of the tri-electrode precharger, three prechargers are being used. Each precharger is separated by two collector sections with 11.3 sec/m (57.6 ft^2/kacfm) of collector area. The final precharger is for testing of McLean's (1982) findings that the precharger should be a good collector.

The experimental set up for measuring V-I characteristics of the tri-electrode precharger is shown in Figure 3. The resistor R_b was added to increase the range of operation of the grid voltage. Without R_b the grid floats up to sparking potential with very low corona current.

Figure 4 gives the measured clean V-I characteristics for the tri-electrode precharger. It should be pointed out that these curves are plotted on voltage vs current (the reverse of standard practice for VI curve). The reason for this is that by varying R_b the voltage of the grid or corona to grid voltage is a function of the corona current. As can be seen from these curves, the operating grid voltage is reduced for increased R_b. From this figure it can be seen that the corona current vs gas gap voltage (Vc-Vg) is not a function of grid voltage. Since this is the case, the remaining V-I data will be plotted as Ic vs (Vc-Vg).

Figure 5 gives a comparison of the V-I data obtained at Valmont with that measured by DRI and McLean in the pilot precipitator in EPA/IERL-RTP's Particulate Technology Branch laboratory. The current is normalized by plotting corona current in microamps per meter length of corona wire. This allows comparison of the data for the different sized precipitators. This curve shows good argument for these cases.

Figure 6 shows V-I data after stable operating conditions had been obtained under flue gas conditions. From this figure it can be seen that the corona onset voltage is considerably higher than for the clean case. Also as attempts are made to increase the gas gap voltage above 18 kV, back corona is initiated.

A charge probe consisting of a fine mesh screen approximately 15 x 30 cm (6 x 12 in.) was used to measure negative charging vs corona current. The probe current was measured with a Keighly 616 picoammeter. The results are given in Figure 7. As can be seen from this figure charging does not vary with grid voltage.

The second fact evident from Figure 7 is that, as the corona current is increased above about 3 mA, charging decreases because of the initiation of back corona.

Figure 8 presents the same data as Figure 7 except this time the corona current is held constant and corona voltage varied. As can be seen from this figure, charging is not a function of grid voltage.

The next phase of testing of the tri-electrode precharger will involve charge-to-mass measurements at electrical operating conditions that produce optimum charging. That will be followed by mass efficiency tests.

V-I RESULTS FOR COOLED-PIPE CHARGER/COLLECTOR

The second charging device to be tested by DRI is the cooled pipe charger/collector (CPCC) (Rinard et al., 1982). CPCC's are presently installed in the second and fourth charger section of the precipitator at Valmont. This was done to allow clean and dirty V-I data to be collected.

Figure 9 shows the clean and dirty V-I characteristics for the CPCC that was obtained in the laboratory (Rinard et al., 1982). This figure shows that the back corona that is present when the pipes are not cooled vanishes for sufficiently cooled pipe surfaces. In this case the dirty V-I curves for the cooled pipes are essentially the same as the clean characteristics.

Clean and dirty curves for the CPCC installed at Valmont are given in Figure 10. These results are very similar to those obtained in the laboratory. The dirty curves with cooled pipes are shifted to the right of the clean characteristics. This is most likely due to space charge effects and the fact that the dirty curves were obtained with actual flue gas. The clean curves were for air-load conditions.

A final comment is in order for the corona onset voltage of Figure 10 when compared to Figure 6. As can be seen the corona onset voltage did not increase for the CPCC for dirty conditions as it did for the tri-electrode precharger. This is most likely due to the difference in corona electrode design (wires for the CPCC and barbs for the tri-electrode) and the higher corona current density obtained for the CPCC.

REFERENCES

McLean, Kenneth J. Analysis of the Electrical and Charging Characteristics of a Three-Electrode Precharger. In: Third Symposium on the Transfer and Utilization of Particulate Control Technology, Volume II, EPA-600/9-82-005b (NTIS PB83-149591), pp. 304-313, July 1982.

Rinard, G., M. Durham, and D. Rugg. Development of a Charging Device for High-Resistivity Dust Using Heated and Cooled Electrodes. In: Third Symposium on the Transfer and Utilization of Particulate Control Technology, Volume II, EPA-600/9-82-005b (NTIS PB 83-149591), pp. 283-294, July 1982.

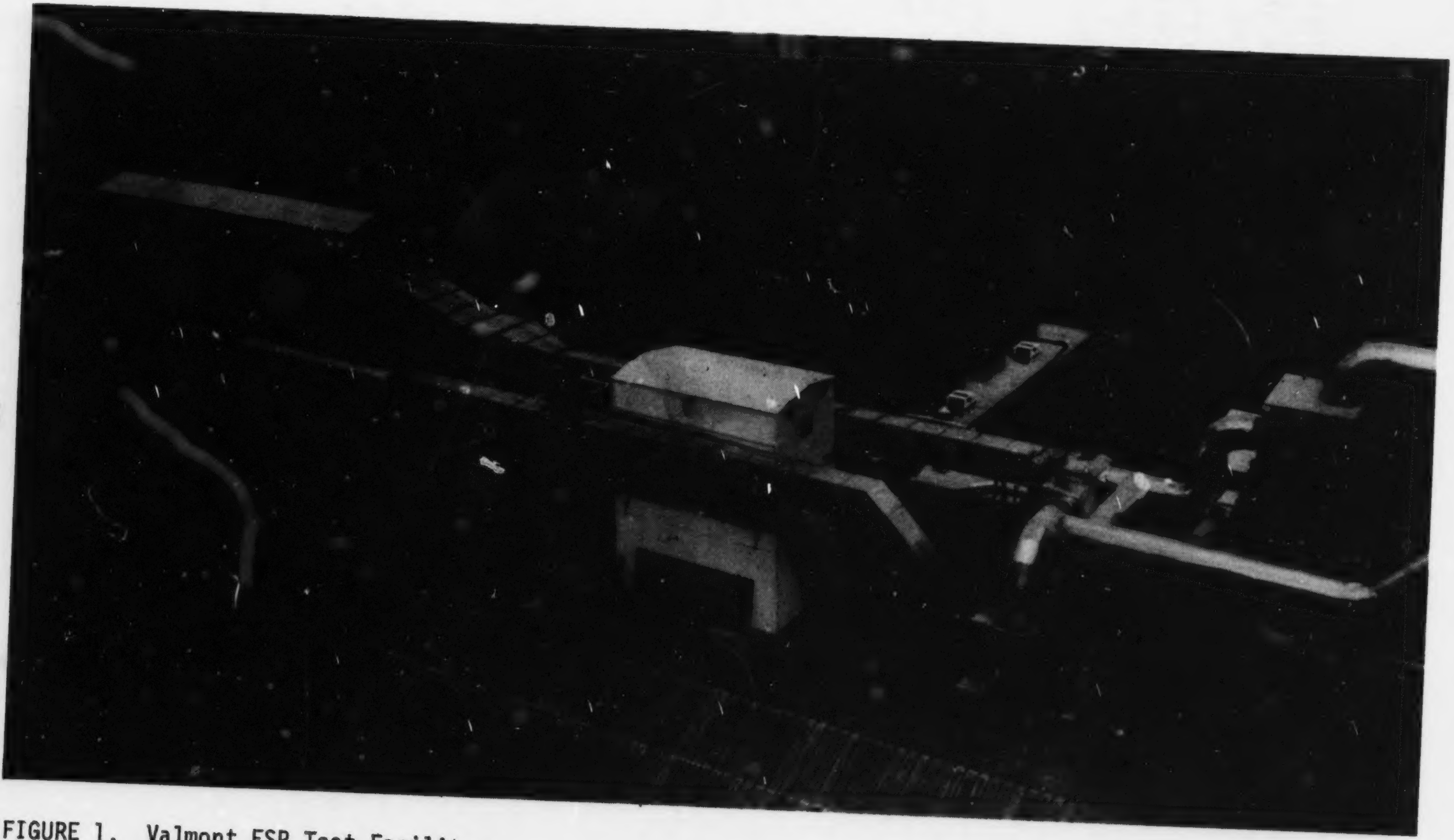

FIGURE 1. Valmont ESP Test Facility.

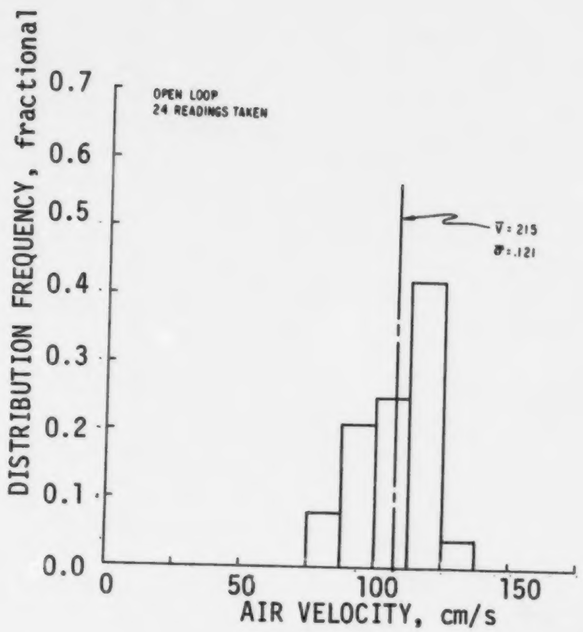

FIGURE 2. Velocity distribution histogram from the Valmont TEP No. 1 charger section

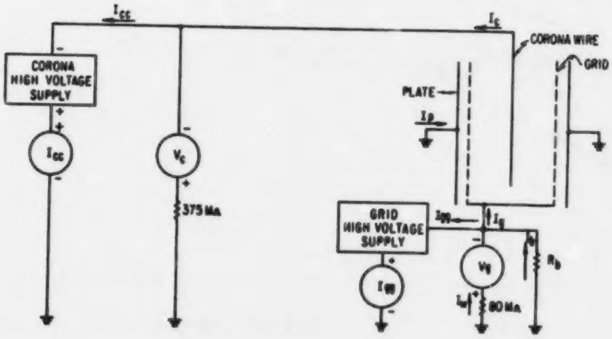
I_{cc}
I_c
CORONA WIRE
GRID
PLATE
I_p
CORONA HIGH VOLTAGE SUPPLY
I_{cc}
V_c
375 MΩ
GRID HIGH VOLTAGE SUPPLY
I_{gg}
I_g
V_g
R_b
I_{gg}
I_M
80 MΩ

FIGURE 3. Experimental setup for measuring V-I characteristics of the tri-electrode precharger.

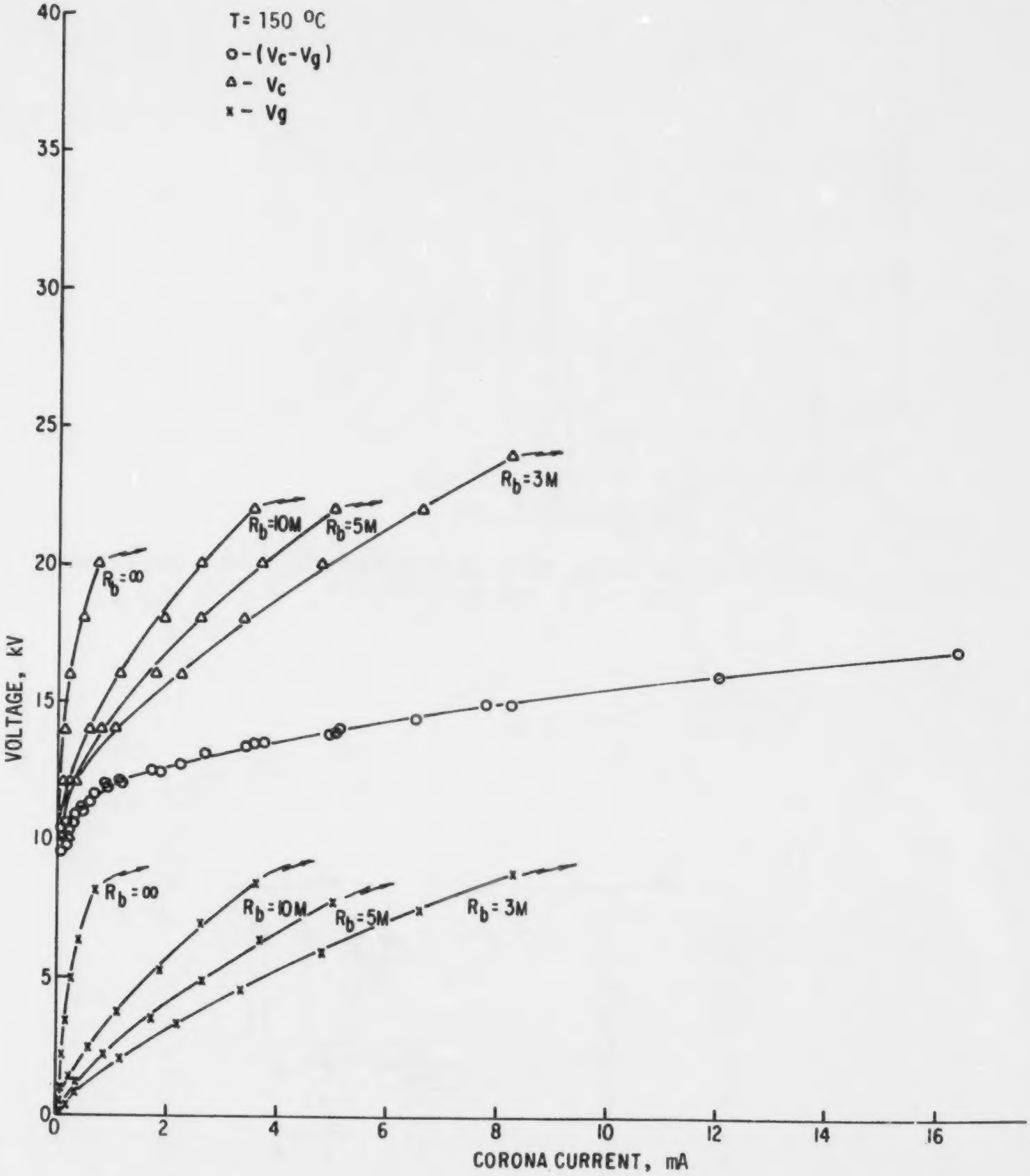

FIGURE 4. VI characteristics of tri-electrode precharger No. 1 at clean conditions.

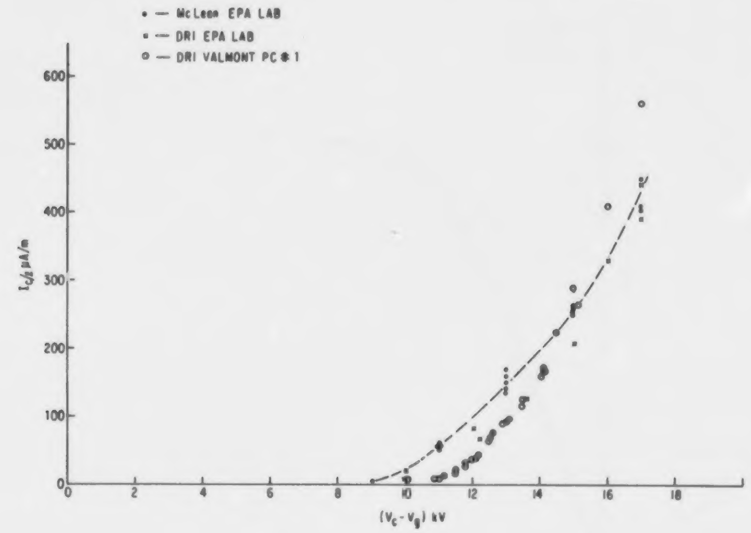

FIGURE 5. Comparison of DRI and McLean data for clean tri-electrode prechargers at (150°C).

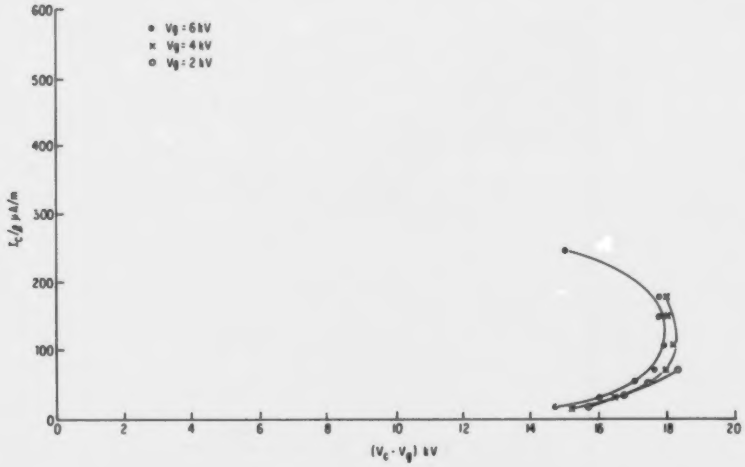

FIGURE 6. Dirty VI curves for tri-electrode precharger No. 1 at 150°C (300°F).

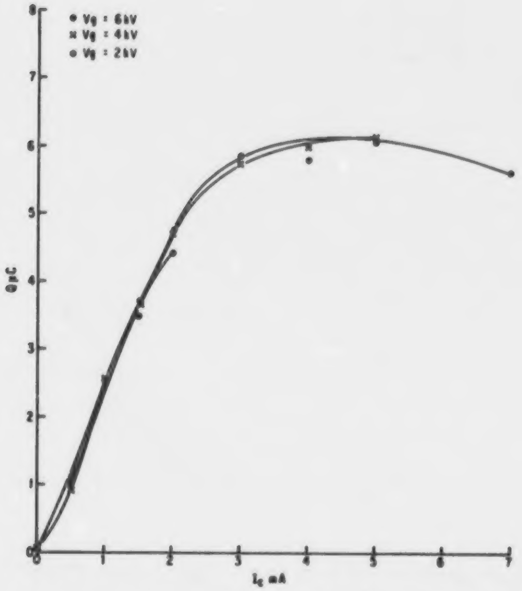

FIGURE 7. Charge probe measurements at 150^{o}C(300^{o}F) as a function of corona current.

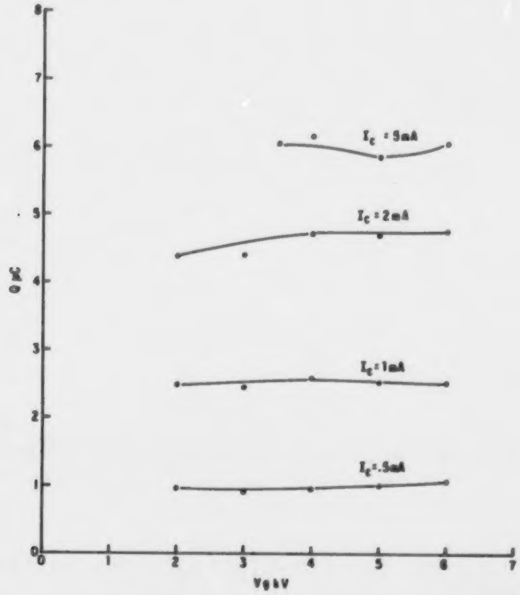

FIGURE 8. Charge probe measurements at 150^{o}C(300^{o}F) as a function of grid voltage.

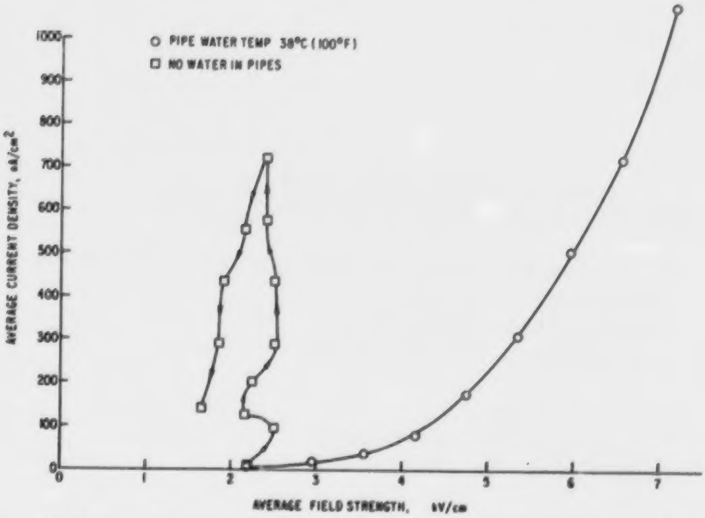

FIGURE 9. Voltage-current characteristics of 6.0 cm (2.375 in.) cooled pipes with 3.2 mm (1/8 in.) electrodes.

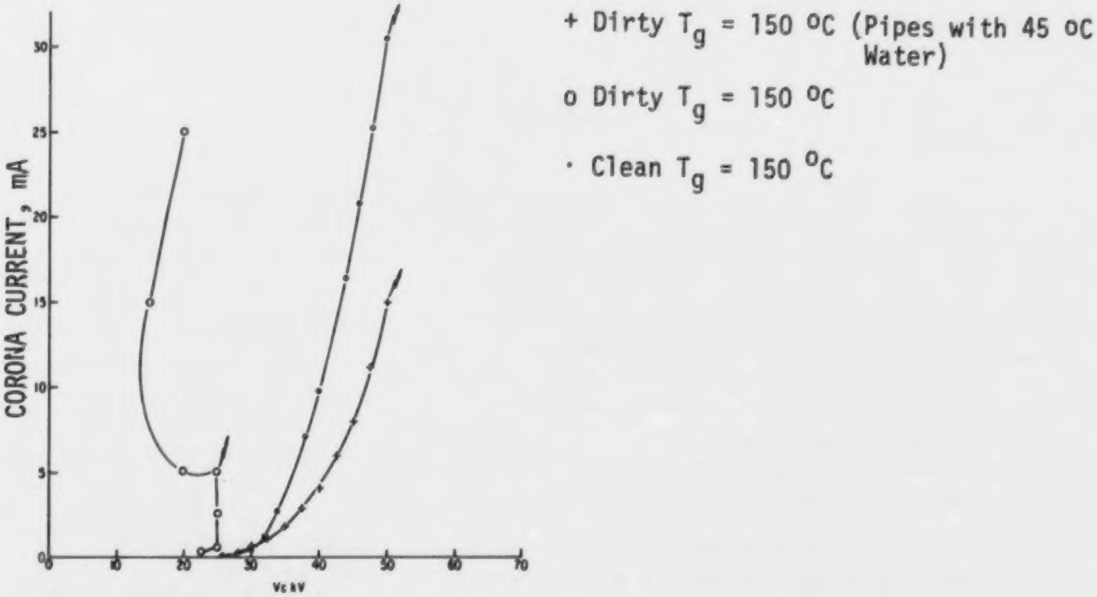

FIGURE 10. Clean and dirty V-I curves of the cooled electrode precharger at Valmont.

INITIAL EXPERIMENTS WITH AN ELECTRON BEAM PRECIPITATOR TEST SYSTEM

by: W. C. Finney, R. H. Davis, and J. S. Clements
Department of Physics
Florida State University
Tallahassee, Florida 32306

E. C. Trexler
U.S. Department of Energy
Germantown, MD 20545

J. S. Halow
Morgantown Energy Technology Center
Morgantown, WV 26505

O. Z. Tokunaga
Japan Atomic Energy Research Institute
Takasaki 370-12
JAPAN

ABSTRACT

As part of the Department of Energy's Advanced Environmental Control Technology Program, a laboratory-scale Electron Beam Precipitator test system (EBP) has been designed and constructed at the Florida State University to investigate particle charging and collection under a wide variety of experimental conditions. The system consists of a rectangular, closed-circuit wind tunnel composed of a number of interchangeable modules including an electron beam (e-beam) precharger followed by a collecting section. A model aerosol enters the e-beam precharger, is charged in an ionization zone, and then passes downstream to the collector. At a gas velocity of 10 ft/sec through the precharger the velocity in the collector is 2.5 ft/sec, giving the collector an SCA of 200.

Experimental results are presented of a preliminary investigation of e-beam precharger ionization for a wide range of electron beam currents and precharger electric fields. Experiments planned with the EBP include the determination of the charging and collection efficiency of the system using resuspended particles with properties similar to high resistivity fly ash.

INTRODUCTION

The Department of Energy (DOE) in pursuit of its mission to assist in meeting the nation's energy needs is concerned that the use of the large U.S. coal resource is neither economically nor environmentally inhibited. Approximately 70% of our domestic coal, however, is characterized by fly ash having high resistivity which causes problems with existing electrostatic precipitators (ESP's) when they are employed to meet the existing new source performance standards. Future emphasis on controlling the small size respirable particles may find existing ESP systems inadequate. The research and development target to meet future particle control needs should be to develop systems which in addition to being small, economical, and reliable, will effectively remove high resistivity ash ($> 2 \times 10^{10}\ \Omega$ -cm) and small respirable particles (0.01 - 2 μm).

Progress has been made recently in several methods for enhancing the performance and reducing the cost of ESP's. Some of the interesting evaluations of novel control devices which were sponsored by other groups include the EPRI/APS High Intensity Ionizer (1), the EPA/SRI Tri-electrode Precharger (2), the EPA/DRI Temperature Controlled Electrode ESP (3), and the University of Tokyo, Japan, Boxer Charger (4). The Electron Beam Precipitator project at the Florida State University (F.S.U.) is being sponsored by DOE because there is the potential for significant improvement over existing control devices and because this work is a companion effort to several DOE funded SO_x/NO_x removal projects. There is the possibility that there might evolve from this work an integrated SO_x/NO_x/Particle removal system which would offer many functional and economic advantages over separate systems.

Electron beam ionization (EBI) for particle charging in electrostatic precipitators has been the subject of a number of studies at F.S.U. (5,6,7). EBI in air was examined in depth using a parallel electrode apparatus within which the ion species produced by the beam could be separated by an electric field. This work characterized three ionization regimes (primary, saturation, and secondary ionization) and provided the foundation crucial to understanding the behavior of an electron beam in an actual precipitator. Enhancement of the total ionization by a high electric field (secondary ionization) has been shown to be a beneficial although inefficient means of increasing the ion current available for particle charging (8).

The experimental program examining the factors influencing EBI resulted in parameters for the design of a laboratory-scale electron beam-energized electrostatic precipitator. The Electron Beam Precipitator (EBP) test system at F.S.U. is unique in this country. It is singularly capable of treating particles with an electron beam-energized ESP under a wide variety of experimental conditions. A realistic comparison with other pilot ESP's was one goal of this program; therefore, the EBP is relatively large for a laboratory scale system. A thorough investigation of the process of electron beam precipitation is planned including the measurement of particle charging and collection efficiencies using resuspended test aerosols having properties similar to high resistivity fly ash.

A description of the basic electron beam ionization process will precede a review of the recently commissioned EBP, which was detailed in a recent paper (9). An explanation of the designed operation of the electron beam precharger and the results of some initial ionization experiments using the new precharger will be presented.

ELECTRON BEAM IONIZATION

An electron beam is a concentrated, focused stream of accelerated electrons produced by a continuously emitting electron beam source. At the Florida State University the e-beam source is a Van de Graaff electron accelerator which is rated at a maximum beam energy of 3 million volts (MeV) and a maximum current of 1 mA. A wide choice of electron beam energy and current is one advantage of this machine, which is continuously variable in these parameters. Beam geometry or positioning can be altered to suit particular experimental conditions as can the scanning frequency of the beam, which is usually set to zero.

The F.S.U. 3 MeV accelerator resides in an underground vault and is permanently installed and therefore non-transportable. The electron beam energy, current, and current distribution are remotely adjusted and measured at the accelerator control console which is separated from the target room vault. Small, industrially reliable electron beams are presently in use in such processes as plastics treatment, paint curing, and electron beam welding. Electron beam ionization has retrofit possibilities on existing precipitator installations, and field testing of electron beam ionization will require such a portable commercial electron beam.

Electrons created in the accelerator are passed down a flight tube at high vacuum and out into air through a thin foil "window" (Figure 1). The high energy, narrow beam spreads and scatters upon colliding with air molecules, creating a bipolar plasma of positive and negative ions and additional electrons. Positive ions are formed by electron stripping while negative ions result from electron attachment. In air, the energy of ionization is 32 eV per ion pair, so a 1 MeV energy beam produces about 30,000 ion pairs per electron. The total number of ions produced depends upon the beam current. When an electric field is applied to the electron beam-produced plasma, a separation of the ion species and electrons occurs; positive ions are attracted to the cathode and negative ions and electrons migrate to the anode. With no electric field the ions recombine or diffuse out of the plasma. Either positive or negative ions can be selected to charge particles, but the nonworking monopolar ion species must be removed from the ionization zone.

Corona wire ionization and electron beam ionization differ in several respects. Corona emission-producing ionization has a finite onset voltage while EBI begins as the beam voltage is raised from zero. Monopolar ions of either sign are created by a corona but EBI produces a bipolar plasma. EBI has many orders of magnitude more working ions than corona; therefore copious ionization is available for particle charging.

ELECTRON BEAM PRECIPITATOR AND SUBSYSTEMS

The Electron Beam Precipitator is basically an instrumented wind tunnel composed of a number of specialized modules separated by ductwork sections (Figure 2). A "racetrack" or closed-circuit arrangement is used to maximize energy conservation and to control humidity. Different ductwork configurations can be assembled as desired including various e-beam entry locations or a single pass arrangement. To resist corrosion and for mechanical strength the wind tunnel is entirely constructed of stainless steel. Room temperature operation is planned initially but high temperature operation is not precluded by the design of the racetrack.

The specifications of the wind tunnel ductwork are as follows: Outside Dimensions = 20 ft long by 8 ft wide; Single Pass Length = 45 ft; Ductwork Size = 12 in by 12 in (1 ft^2); Construction = #304 12 gauge stainless steel; Gas Velocity Range = 3 to 30 ft/sec; Maximum Gas Volume = 2000 ACFM; System Pressure Drop = 5 in water gauge. Specialized modules of the racetrack include the fan, an aerosol entrainment module, two monitoring modules, the precharger and collector composing the precipitator, and an absolute filter. The monitoring, aerosol entrainment, and precipitator modules each have removable plexiglass tops and opening ports on three sides for observing precipitator conditions and mounting of monitoring systems or aerosol injectors. Perforated, removable baffles of 50% open area smooth gas distribution at several locations in the wind tunnel. EBP subsystems which are associated with the wind tunnel are several high voltage power supplies for the precipitator, gas condition, particle, and charge monitors, a microcomputer with a data conditioning system, three aerosol generators, a closed-circuit TV system, and the humidity control device.

Circulating the gas and test aerosol through the wind tunnel is a stainless steel centrifugal fan rated at 2000 ACFM at 7" water gauge pressure drop. A variable opening outlet damper downstream from the blower controls the air velocity. To ensure a particle free gas flow for proper experimental control, a H.E.P.A.-type absolute filter is positioned upstream of the fan intake. Aerosols larger than 0.3 μm are collected with a 99.97% efficiency by the high volume stainless steel frame filter. For experiments with monodisperse aerosols, the filter can be removed. On the back or return leg of the wind tunnel are two long ductwork sections with removable plexiglass tops. One section just downstream from the fan outlet damper houses a humidity control device composed of a set of refrigerated coils and a compressor/condenser unit. The relative humidity within the racetrack can be reduced from ambient (50-80%) to 10% or less and can be controlled within these limits.

Aerosol entrainment into the gas stream is accomplished in the module just upstream from the 90° elbow turn preceding the first monitoring module. Particle injection is through a stainless steel tube inserted into the duct. The gas stream is smoothed by perforated baffles up- and downstream from the sampling tube, which can be aimed against or with the flow. Aerosols of two basic types are resuspended in the electron beam precipitator. The basic properties of electron beam precipitation (charging and collection efficiency, maximum field and current) should be investigated using a monodisperse aerosol at low to medium loadings. High loadings of mono- or polydisperse bulk powders are needed to test the EBP under more realistic conditions. Polystyrene latex beads (PSL) in 1.0 and 3.0 μm diameter sizes and aluminum hydroxide (Hydral), which is a cheap bulk powder of nominally 1.0 μm diameter, serve as monodisperse, basic study test aerosols at low and medium loadings, respectively. Polydisperse fly ash at high loadings will also be tested after the EBP is completely characterized with PSL and Hydral. A Collision nebulizer-based fluid atomization aerosol generator entrains PSL and a BGI Wright Dust Feeder, a rotating drum air injection bulk powder feeder, resuspends Hydral or fly ash. For high loading applications using bulk powders, a fluidized bed with a screw feeder will be employed.

Characterizing the operating conditions of the EBP requires a comprehensive group of monitoring systems. These monitors must have remote controls and readouts located in the e-beam control room since the EBP is in the accelerator target vault. Monitoring modules are located upstream and downstream from the precipitator for the purpose of before and after measurement of a number of parameters. The determination of the operating characteristics of the gas stream and the particle collection efficiency of the precipitator is the primary function of the two monitoring stations. Extraction tubes and monitor sensors within the duct are mounted in 3" sampling ports and on the plexiglass module tops.

Several monitor systems measure gas stream conditions in the wind tunnel. A hot wire-type anemometer including a solid state temperature sensor is fastened to a side port of each of the monitoring modules. Velocity and temperature signals are wired to digital readouts in the control room. Electronic ion exchange relative humidity/solid state platinum thermometer probes are fastened to plexiglass tops at two points: on the return leg of the EBP downstream from the humidity control device and on the monitoring module adjacent to the collector. Signals are sent to a multichannel analyzer which provides a display and hard copy of the data.

Two types of particle samplers monitor the EBP: real-time and time-integrated. Optical particle counters give a real time indication of the number and size of particles present in a continuously sampled gas stream. Remote sensing units located upstream and downstream from the precipitator send signals to a multichannel analyzer which can then be compared. A multistage cascade impactor and an absolute filter holder sample the gas flow downstream from the collector in a time integrated fashion. Particle size and mass measurements are obtained for discrete intervals of time depending upon the aerosol concentration in the duct.

A microprocessor-based data acquisition and analysis system was developed to coordinate most of the data outputs of the electron beam precipitator (Figure 3). It will be used to accumulate, condition, process, and store all signals from the energized sections of the precharger and collector and from the EBP electronic monitors. The computer is composed of a Z80 microprocessor, two 8" floppy disc drives, a CRT terminal with keyboard, and a printer/plotter. Interfaced to the computer are voltage and ion current signals from the precipitator through a μMac data conditioning system, the velocity and temperature sensors, and the optical particle counters and humidity/temperature probes through the multichannel analyzer. Data analysis subsequent to acquisition is performed using Basic and Fortran languages.

A closed-circuit TV system is necessary to remotely determine precharger and collector ion currents on the high voltage side of the circuit. It can also be used to monitor various precipitator conditions visually. The camera, lens, pan-tilt head, and tripod are in the accelerator target room while the video monitor, remote control panel, and video cassette recorder are contained in a rack in the control room.

The precharging configuration that is being tested initially in the EBP is the "separated" precharger (Figure 4). It operates at duct velocity and is upstream from the collector. The cross-shaped precharging module is the point of electron beam entry into the EBP. A central 1 ft^3 precharging region through which all of the system gas passes is designed to accept several precharger electrode configurations. Particle charging occurs within the e-beam ionized interelectrode volume. To insulate the interior of the stainless steel precharging module, thin plastic sheets cover the walls, floor, and any exposed metal framing. A plexiglass cupola is fitted to the plexiglass module top for insulation of the high voltage connections. Electron beam current is measured immediately after the beam enters air by a movable probe located in the precharging module. Scattering foils and a collimation baffle respectively diffuse or restrict the electron flux which enters the precharging region as needed. A thick beam dump prevents the e-beam from exiting the precharging module. The precharging of particles is discussed in another section of this paper.

Since the precharging region is 1 ft^2 cross-sectional area and the collector is 4 ft^2 area, a 1:4 expansion section connects the two modules. A removable 35% open area perforated baffle is mounted just upstream from the collector for gas distribution. Charge-to-mass (Q/M) monitors are inserted in a port downstream from the precharger within the 1 ft^2 section of the transition. Q/M measurement devices are used to quantify the effectiveness of the e-beam precharger prior to particle collection. A total Q/M sampler based on a Faraday Cage encased absolute filter (10) will measure total sample mass and total particle charge. It is a time integrated instrument and uses a cascade impactor extraction sampling train. Several types of single particle Q/M systems exist including a modified Millikan oil drop apparatus (11) and a crossed laser beam device (12) which measure the charge and mass of individual particles. After assessing the applicability of these systems one or more will be chosen to obtain single particle Q/M data.

Gas entering the collector is split into two channels each of which has three sections for a total of six typical wire-plate precipitator fields (Figure 2). The collector module frame is constructed of T and L angle stainless steel to which exterior walls with long opening access ports are welded. Plexiglass top and bottom covers seal the module. Twelve stainless steel collector plates are mounted to standoff insulation and then to the collector frame. The six corona wire assembles are each composed of six stainless steel corona wires suspended between aluminum buss rods which are insulated from the collector frame by standoff supports. A set of centrally located plates can replace the corona wire assemblies for investigation of a plate-plate collector, and a single 12" wide channel can replace the two 6" wide channels.

The specifications of the collection module and its internal components are as follows:

- Collector Module Dimensions = 7 ft 6 in long by 4 ft 3 in high by 1 ft 3 in wide.
- Corona Wire Height = 48 in (122 cm).
- Corona Wire Diameter = 0.109 in (2.8 mm).
- Wire-to-Wire Spacing = 4.5 in (11.4 cm).
- Wire-to-Plate Spacing = 3 in (7.72 cm).
- Plate-Plate Spacing = 6 in (15.2 cm).
- Plate Dimensions = 4 ft high by 2 ft 6 in wide.
- Single Plate Area = 10 ft^2.
- Total Plate Area = 120 ft^2.
- Collector Sparkover Voltage = 55-65 kV.

For: Precharger Velocity = 10 ft/sec, Collector Velocity = 2.5 ft/sec, Gas Flow = 600 ACFM:

- Collector SCA (ft^2) per 1000 ACFM Gas Flow = 200.

Three high voltage, high current DC power supplies are used to energize the precharger and collector. Two 130 kV, 30 mA units provide voltage to the precharger while a 100 kV 100 mA supply powers the collector wires. The collector fields can be sectionalized if necessary. Manual regulation of the precipitator voltages is accomplished remotely from the accelerator control room. Power supply voltages and currents are monitored at the control racks; the T-R sets are adjacent to the EBP in the vault.

ELECTRON BEAM PRECHARGING

Single stage precipitators operate by charging and collecting particles in the same location in the unit. Separating the two functions into a two stage system can offer advantages over a conventional configuration. The overall removal rate can be improved by optimizing precharging and collection in individual sections of the precipitator since the electrical and physical requirements of each are different. Much of the recent work on ESP's has focused on precharging as a more efficient means of driving up the charge on particles to the highest attainable limit. Electron beam precharging makes use of high ion current densities and electric fields to accomplish this goal.

The electron beam precharger is an ion current separation and collection device for charging particles passing through the precharging module of the EBP. It provides a high electric field for particle charging but allows an unimpeded flow of particle-laden gas. High ion current density is necessary for maximum charging rate and space charge enhancement of the electric field. An electrode configuration which approximates the electrical properties of a plane without restricting flow was the desired goal.

The precharger electrode apparatus is composed of two racks of parallel rod electrodes at the upstream and downstream boundary of the electron beam ionization region in the precharger module (Figure 3). Precharger rack rods are suspended between pairs of buss rod/holder combinations and the two racks are fastened together and to the precharging module sides. The electrode array is positioned in the precharging module through which the test aerosol flows at duct velocity. E-beam delivery is perpendicular to the gas flow direction and to the rack electric field. Rod-to-rod and rack-to-rack spacing is variable, but the design being tested initially has the following specifications:

- Two Identical Racks of 9 Rods Each.
- Rod Height = 11 in (27.9 cm).
- Rod Diameter = 0.125 in (0.32 cm).
- Rod-to-Rod Spacing = 1.25 in (3.2 cm).
- Rack-to-Rack Spacing = 6 in (15.2 cm).
- Rods 1, 2, 8, 9 (Cathode and Anode) = Non-metered (guard).
- Rods 3, 4, 5, 6, 7 (Cathode and Anode) = Metered.
- Metered Rack Plane Area = 67.2 in^2 (433.5 cm^2) for Each Rack.
- Ionization Volume = 645 in^3 (10,570 cm^3).

The electron beam is delivered into a region bounded by the two parallel racks of rod electrodes. Electron beam ionization forms a plasma of positive and negative ions and free electrons between the racks. The charge density is separated by an electric field which is imposed by the precharger electrodes. The upstream cathode rack (-) attracts positive ions while the downstream anode rack (+) attracts negative ions and electrons. As each electrode is approached from the center, the average charge becomes increasingly monopolar. Particles in the gas stream traversing the charging zone are first charged positively near the cathode, pass through the central "grounded" plasma, and then charged negatively near the anode boundary region. Charged particles pass through the anode rack because their mobility is at least several orders of magnitude lower than that of ions and electrons, which migrate rapidly to electrodes of opposite polarity. Ions and electrons not attached to particles ("waste" ions) are attracted to the racks and removed from the flow going to the collector.

One effect of electron beam precharging which may occur is that of particle impaction on the anode leading edge, causing a highly resistive buildup or cake which may reduce the maximum electric field within the charging region. Solutions are envisioned which include mechanical electrode cleaning, addition of guard electrodes, and resistivity modification of the dust cake. Since energetic electrons ionize solid particles as well as the gas in which they are entrained (13), the anode leading edge caking problem may be solved by the direct irradiation of the dust layer, leading to increased conductivity and electric field. Electron beam irradiation may also reduce the resistivity of entrained particles flowing through the precharger, but this effect must be investigated further to determine its magnitude.

Another possible problem in successful precharging is that of space charge expansion of the charged aerosol after it leaves the precharger and before it reaches the collector. Several solutions are being studied should the effect be large. A configuration where an e-beam precharger could be placed just upstream from the collector with little or no transition section would minimize space charge problems.

EXPERIMENTAL RESULTS

Experiments have determined the maximum electric field and ion current density achievable in the two rack precharger described earlier. The electrode system was positioned in the precharging module along the electron beam axis in an arrangement similar to that for the parallel plate electrode geometry used in the earlier characterization of ion current density regimes. Experimental conditions for the preliminary investigation of the rack precharger are summarized as follows: Two Rack Precharger specifications as described above; Electron Beam Energy = 1.2 MeV; Beam Current = 10 to 10,000 nA; E-Beam Tube End to Precharger Rack Distance = 50 cm. Ion currents vs. average electric field (total voltage/rack separation distance) curves were obtained for five electron beam currents and the results are shown in Table 1.

TABLE 1. MAXIMUM ION CURRENT DENSITY AND SPARKOVER VOLTAGE FOR FIVE ELECTRON BEAM CURRENTS USING THE PARALLEL RACK ELECTRODE SYSTEM

Beam Current (nA)	Maximum Electric Field (kV/cm)	Sparkover Voltage (kV±)	Maximum Ion Current (μA)	Maximum Ion Current Density* (mA/m^2)
0	6.3	48	0	0
10	6.2	47	24	0.54
100	6.0	46	98	2.26
1,000	5.5	42	565	13.05
10,000	5.2	40	2350	54.27

*43.3 μA ion current = 1 mA/m^2 ion current density.

The experimental results show that as electron beam current was increased, the maximum electric field and sparkover voltage decreased gradually. Higher beam current caused more ionization so the interelectrode volume became more conductive, resulting in a lower sparkover voltage. Sparking was between cathode and anode rods at a variety of locations. The maximum average electric field obtained was above 6 kV/cm which is high, but it is not the highest attainable. Electric fields for particle charging of 8-10 kV/cm are anticipated with improved precharger design and construction techniques. Collected ion current increased with beam current because more ions were formed by the intensified beam. At the maximum achievable electric field for each beam current, very high ion current densities were obtained. For the described rack geometry the ion current density of 54 mA/m^2 at 10,000 nA (10 μA) beam current is at least 250 times as high as that found in a conventional corona wire electrostatic precipitator with similar dimensions (14). Measured ion current densities using the two rack configuration compare favorably with results achieved using a parallel plate electrode system.

Two plots of ion current and ion current density vs. precharger electric field strength are shown in Figures 5 and 6. At an electron beam current of 10 nA, the shape of the curve is similar to that found in previous experiments using the parallel plate electrode system. The primary ionization section begins at the origin and the effect of saturation is observed at an electric field of 0.5 kV/cm. Secondary ionization effects begin to obscure the saturation plateau at approximately 2.5 kV/cm, and the curve is terminated by a slight upturn at 6.0 kV/cm.

In contrast, the curve for 10 μA beam current is rather linear (Figure 6). No separate regimes of primary, saturation, or secondary ionization can be discerned when the beam current is increased three orders of magnitude. At this current level the copious primary ionization cannot be completely separated so no saturation plateau appears. Secondary ionization effects contribute to the total measured ion current at higher electric field.

SUMMARY AND CONCLUSIONS

Full utilization of domestic coal resources is one of the top priorities of the U.S. Department of Energy, but much of the nation's coal has an ash which is high in resistivity making it difficult to collect at high efficiency for most existing electrostatic precipitators. Programs for improvement of stationary source control devices will concentrate on the removal of small, respirable particulate matter as well as high resistivity fly ash. Enhancing the collection efficiency while reducing the cost of ESP's has motivated researchers to develop novel devices to charge particles upstream from new or existing collectors. DOE is currently supporting a program at the Florida State University which concerns the development of the new control concept of electron beam ionization for electrostatic precipitators. While primarily aimed at particle charging, electron beam precipitation is a companion effort to DOE sponsored work on SO_x and NO_x removal by e-beam treatment.

Electron beam ionization investigated in a series of earlier studies characterized three ionization regimes in a parallel electrode system. From these studies emerged the design for an electron beam energized precharger within a large laboratory-scale electrostatic precipitator. The Electron Beam Precipitator test system is capable of treating model aerosols under a wide range of experimental conditions. Specialized modules separated by ductwork are arranged into a closed-circuit or "racetrack" configuration. Aerosols of several types which resemble high resistivity fly ash are resuspended at the aerosol injection module by three particle generation devices. Two monitoring modules upstream and downstream from the precipitator accept a host of gas stream, particle detection, and charge measurement sensing units to quantify EBP conditions. These are integrated with a microprocessor-based data acquisition and analysis system which allows a wide variety of signal information to be processed efficiently. Particle removal occurs in a typical corona wire-plate collector with SCA of 200 separated from a precharging module by a short transition section.

The particle charging function is handled by the electron beam precharger in the two-stage system. An electron accelerator delivers an e-beam into the precharging module through which the test aerosol flows. A double rack electrode precharger provides an electric field which separates the ionized plasma for the purpose of charging particles with a net negative charge. Unused ions and electrons are removed from the flow because of their high mobilities. Ionization experiments using the double rack precharger show that high electric fields (6 kV/cm) and ion current densities (54 mA/m^2) for particle charging can be achieved. Plots of precharger ion current vs. electric field show that as e-beam current is increased, saturation of ion current is not achieved because of the large secondary ionization effects.

The measurement of the charging and collection efficiency of resuspended test aerosols similar to and including high resistivity fly ash will be the focus of a comprehensive experimental program. The operation of the EBP and especially the e-beam precharger will be optimized to a configuration capable of being applied to a new or existing ESP installation. Modifications to the EBP for the investigation of high temperature conditions as well as for combined SO_x/NO_x/Particle treatment are feasible. Field testing of electron beam precipitation on the pilot scale will follow a thorough investigation of the concept under laboratory conditions. Electron beam precharging might be most appropriate when applied to coal fly ash boilers with high resistivity dust problems as a retrofit installation in a duct adjacent to an existing collector.

The work described in this paper was not funded by the U.S. Environmental Protection Agency and therefore the contents do not necessarily reflect the views of the Agency and no official endorsement should be inferred.

ACKNOWLEDGEMENTS

The Electron Beam Precipitator program is supported in part by U.S. Department of Energy Contract #DE-AC21-81MC16229. The authors would like to acknowledge the assistance of Kenneth J. Schafer, Stephen J. Stout, and Robert H. Hart in the design, construction, and operation of the F.S.U. Electron Beam Precipitator. We also thank J. Walter Phillips for running the 3 MeV electron accelerator.

REFERENCES

1. M. H. Anderson, J. R. McDonald, J. P. Gooch, and D. V. Giovanni. High Intensity Ionizer Development. In: Proc. 3rd Symp. Transfer and Utilization of Particulate Control Technology, Vol. II, (EPA-600/9-82-005b), pp. 334-348, 1982.

2. D. H. Pontius and L. E. Sparks. A Novel Device for Charging High Resistivity Dust. APCA Journal 28(7), pp. 698-700, July 1978.

3. G. Rinard, M. Durham, D. Rugg, and L. E. Sparks. Development of a Charging Device for High-Resistivity Dust Using Heated and Cooled Electrodes. In: Proc. 3rd Symp. Transfer and Utilization of Particulate Control Technology, Vol. II, (EPA-600/0-82-005b), pp. 283-294, 1982.

4. S. Masuda, H. Nakatani, and A. Mizuno. Boxer-Charger Mark III and Its Application in ESP's. In: Proc. 3rd Symp. Transfer and Utilization of Particulate Control Technology, Vol. II, (EPA-600/9-82-005B), pp. 380-389, 1982.

5. R. H. Davis, W. C. Finney, and L. C. Thanh. Electron Beam Ionization for Coal Fly Ash Precipitators. In: Proc. of the American Nuclear Society Topical Conference on Atomic and Nuclear Methods in Fossil Energy Research, Mayaguez, Puerto Rico, pp. 481-494, December, 1980.

6. W. C. Finney, J. S. Clements, and R. H. Davis. Primary and Secondary Ionization in an Electron Beam Precipitator System. In: Proc. 3rd Symp. Transfer and Utilization of Particulate Control Technology, Vol. II, (EPA-600-9-82-005b), pp. 358-369, 1982.

7. J. S. Clements, W. C. Finney, O. Tokunaga, and R. H. Davis. Stable Secondary Ionization in a Test Geometry for Electron Beam Precipitators. In: Conf. Record of the IEEE-Industry Applications Society Annual Meeting, Philadelphia, PA, pp. 1136-1141, October, 1981.

8. R. H. Davis, W. C. Finney, J. S. Clements, and O. Tokunaga. Secondary Ionization as Enhanced Radiation Dose. In: Conf. Record of the IEEE-

Industry Applications Society Annual Meeting, San Francisco, CA, 1981.

9. W. C. Finney, J. S. Clements, O. Z. Tokunaga, and R. H. Davis. Application of Electron Beam Technology to Particulate Matter Control. Paper 82-27.4, 75th Annual Meeting of the Air Pollution Control Association, New Orleans, LA, June 20-25, 1982.

10. M. D. Durham, G. A. Rinard, D. E. Rugg, and L. E. Sparks. Measurement and Interpretation of Current Density Distribution and Charge/Mass Data. In: Proc. 3rd Symp. Transfer and Utilization of Particulate Control Technology, Vol. II, (EPA-600/9-82-005b), pp. 54-65, 1982.

11. J. R. McDonald, M. H. Anderson, R. B. Mosely, and L. E. Sparks. Charge Measurements on Individual Particles Exiting Laboratory Precipitators. In: Proc. 2nd Symp. Transfer and Utilization of Particulate Control Technology, Vol. II, (EPA-600/9-80-0396), pp. 93-113, 1980.

12. M. K. Mazumder, R. G. Renninger, T. H. Chang, R. W. Raible, W. G. Hood, R. E. Ware, and R. A. Sims. Simultaneous Measurements of Aerodynamic Size and Electric Charge of Aerosol Particles in Real Time on a Single Particle Basis. In: Proc. 3rd Symp. Transfer and Utilization of Particulate Control Technology, Vol. II, (EPA-600/9-82-005b), pp. 160-168, 1982.

13. P. J. Heerden. The Crystal Counter, A New Instrument in Nuclear Physics. In: N. V. Noord Hollandsche Uitgevers Maatschappij, Amsterdam, 1945.

14. H. J. White, Industrial Electrostatic Precipitation. Addison-Wesley, Reading, Massachusetts, 1963.

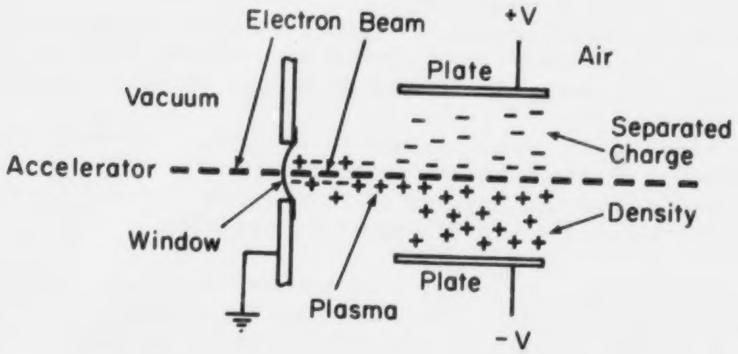

Figure 1. Electron beam ionization in air. An accelerated electron beam passes from vacuum into air through a thin foil window and ionizes air molecules. The plasma can be separated using an electric field.

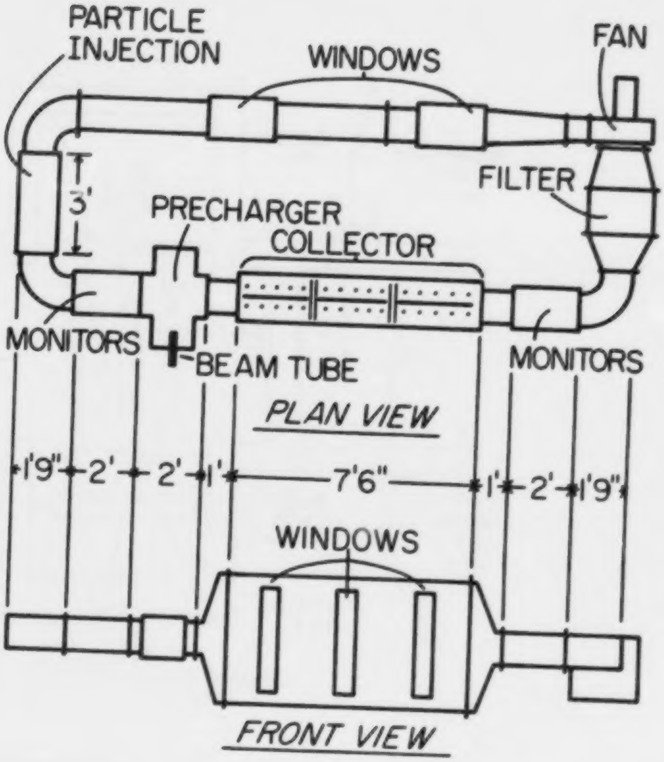
PARTICLE INJECTION
WINDOWS
FAN
FILTER
3'
PRECHARGER
COLLECTOR
MONITORS
BEAM TUBE
MONITORS
PLAN VIEW
1'9"
2'
2'
1'
7'6"
1'
2'
1'9"
WINDOWS
FRONT VIEW

Figure 2.

Plan and front views of the Electron Beam Precipitator, showing the e-beam precharger, the collector, and other specialized modules.

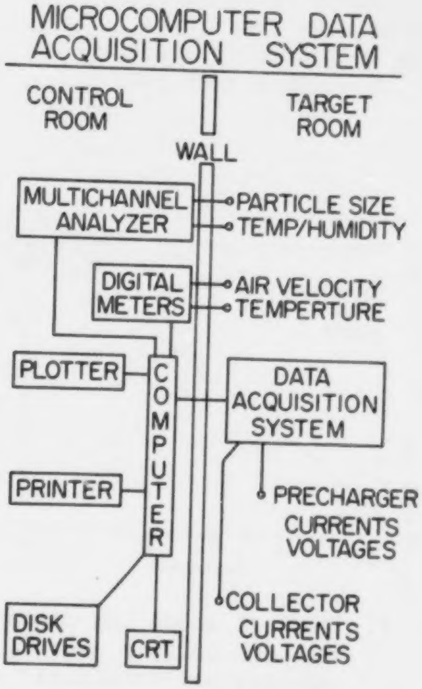
MICROCOMPUTER DATA ACQUISITION SYSTEM
CONTROL ROOM
TARGET ROOM
WALL
MULTICHANNEL ANALYZER
PARTICLE SIZE
TEMP/HUMIDITY
DIGITAL METERS
AIR VELOCITY
TEMPERTURE
PLOTTER
COMPUTER
DATA ACQUISITION SYSTEM
PRINTER
PRECHARGER CURRENTS VOLTAGES
DISK DRIVES
CRT
COLLECTOR CURRENTS VOLTAGES

Figure 3.

Layout of the microprocessor-based data acquisition and analysis system including all electrical inputs from the EBP monitoring systems.

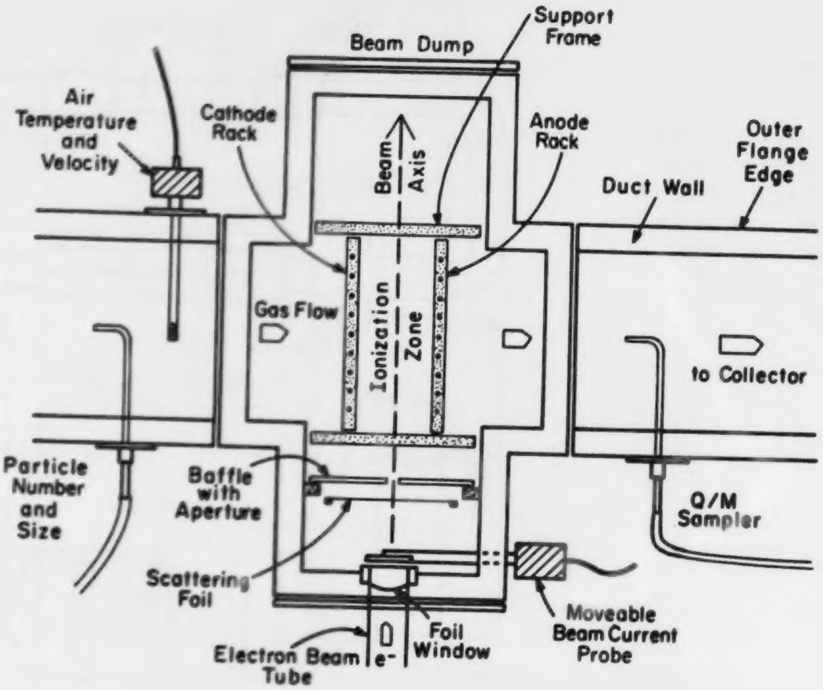
Support Frame
Beam Dump
Air Temperature and Velocity
Cathode Rack
Beam Axis
Anode Rack
Outer Flange Edge
Duct Wall
Gas Flow
Ionization Zone
to Collector
Particle Number and Size
Baffle with Aperture
Q/M Sampler
Scattering Foil
Moveable Beam Current Probe
Foil Window
Electron Beam Tube
e-

Figure 4. Top view of the precharging module showing the major functional components. Particles are charged in the e-beam energized ionization zone which is bounded by the double rack precharger.

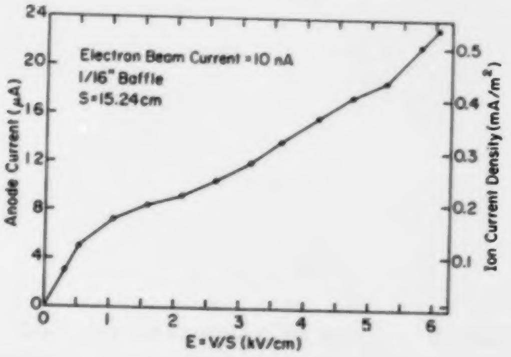

Figure 5. Plot of anode ion current and ion current density vs. applied electric field for 10 nA electron beam current.

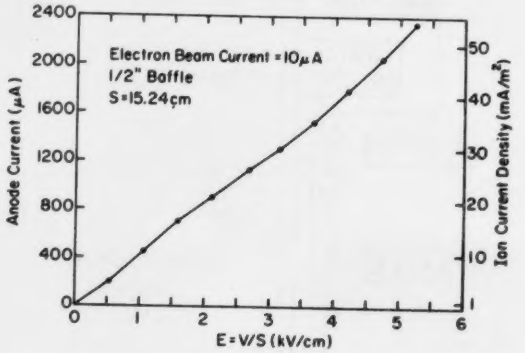

Figure 6. Plot of anode ion current and ion current density vs. applied electric field for 10 μA electron beam current.

EXPERIMENTS WITH WIDE DUCTS IN ELECTROSTATIC PRECIPITATORS

by : Ekkehard Weber
Helmut Wiggers

University of Essen
D 4300 Essen 1, West Germany

ABSTRACT

The repeatedly observed enhancement of the effective migration velocity with increasing duct width holds out the prospect of less expensive electrostatic precipitators. Vagueness still exists regarding the optimum of the width and the influencing factors on it. Based on laboratory experiments indicating almost a proportionality between migration velocity and duct width up to 715 mm a pilot precipitator with a maximum flow rate of 36,000 m^3/h was constructed. Parallel to large scale conventional electrostatic precipitators for a coal-fired power station and the romm dedustion of a sinter plant duct widths up to 1,000 mm were tested. Besides a far reaching conformity with the laboratory results an optimum width was ascertained, which is influenced for instance by the gas velocity. Moreover, with a theoretical precipitator model it succeeded to explain the corresponding influences on the migration velocity.

INTRODUCTION

With increasing requirements regarding the invironmental protection the interest grows to optimize the electrostatic precipitators, which are frequently used to dedust industrial exhaust gases. The operation of an electrostatic precipitator is often described on the basis of Deutsch's equation (1)

$$c = c_o \cdot \exp (- w\, A/\dot{V})$$

that represents the relationship between the dust concentrations of the crude and the clean gas, c_o respectively c, the total collecting area A, the volume flow rate $\dot{V}$ and the migration velocity w. According to the Deutsch theorie the migration velocity can be considered as the effective velocity of the dust particles towards the precipitation electrodes. Up to now it is not possible to calculate the migration velocity from theory. Therefore it represents a process coefficient defined by the Deutsch equation.

The nowadays used electrostatic precipitators are mostly of the plate typ, where the precipitation plates form numerous ducts appropriate to their parallel grouping. The gas to be cleaned flows in proportion through the equal wide ducts. Sparking electrodes are arranged along the centre line of each duct. As well for the precipitation electrodes as for the sparking electrodes rapper mechanisms are installed to remove in periodic time intervals the precipitated dust from the electrodes.

As a measure for the size and for the costs of an electrostatic precipitator the precipitation area of the plate electrodes can be referred to. Therefore, a substantial improvement of the electrostatic precipitators in regard to their costs implies to minimize the necessary precipitation area without producing overproportional additional costs at other parts of the precipitators. According to the Deutsch equation a reduction of the precipitation area can be obtained only by a simultaneous increase of the migration velocity, for in each application of an electrostatic precipitator the volume flow rate and the dust concentrations of crude and clean gas are defined.

To design an electrostatic precipitator one has to use extensively the experiences with already existing installations. Because fundamental changes of the construction involve an enormous risk the influences of several design parameters on the migration velocity yet need to be investigated. This is valid for instance for the duct width, that in conventional electrostatic precipitators has presently a value between 250 and 300 mm. Several investigations some years ago already indicated that wider ducts can effect higher migration velocities

(2,3,4). However the results of the corresponding works often received scepticism since they could not be explained with the common idea about the motion of the particles in an electrostatic precipitator. The same happened to the repeatedly observed increase of the migration velocity with increasing gas velocity. Considering especially the possible decrease in costs of the precipitator construction it seemed therefore necessary to clarify the interrelationship between the precipitation efficiency, the duct width and the migration velocity.

LABORATORY EXPERIMENTS

To clarify the above mentioned questions first of all extensive laboratory investigations were performed. Figure 1 shows the outline and the most significant data of the used laboratory electrostatic precipitator. It contained one duct with a height of 0.7 m and a length of 3 m. The flat precipitation electrodes without any profil were fixed in a frame permitting to vary continuously the distance of the precipitation electrodes, that is the duct width, up to 715 mm. The duct was covered above and below with plates of plexiglass, which were used simultaneously as electrical isolating mountings for the sparking electrodes. These electrodes were punched from 1.5 mm sheet-steel and had rounded emission spikes arranged mutually in a distance of 25 mm. The distance of the sparking electrodes from each other was biased by the actual duct width. Usually the corresponding relation of the distances was 0.96, which from experience is in the optimum range.

The laboratory electrostatic precipitator operated with negative corona. For that a 200 kV high-tension equipment could be used. The voltage was adjustable by hand and by automatic. To smooth the high-tension a 25 nF capacitor was wired parallel to the precipitator. A high voltage-stable resistor of 1 kΩ was in series with the capacitor to allow only an aperiodic discharge of the capacitor in case of spark over in the precipitator.

As the gas to be cleaned the air of the laboratory with a temperature of 21 °C was used, in which before quartz powder was injected. The particles of the quartz-powder had a mass median diameter of 9 µm. 10 % of its mass fraction were larger than 23 µm and 10 % were smaller than 1.8 µm. The value of the specific dust resistance was between 10^9 and 10^{10} Ωcm depending on the relative humidity of the gas, which was between 43 and 64 %. Hence normally no back corona was observed.

The electrostatic precipitator was on the suction side of a fan that could effect a volume flow rate up to 2,900 m^3/h. A fabric filter between the electrostatic precipitator and the fan permitted to operate the electrostatic precipitator also

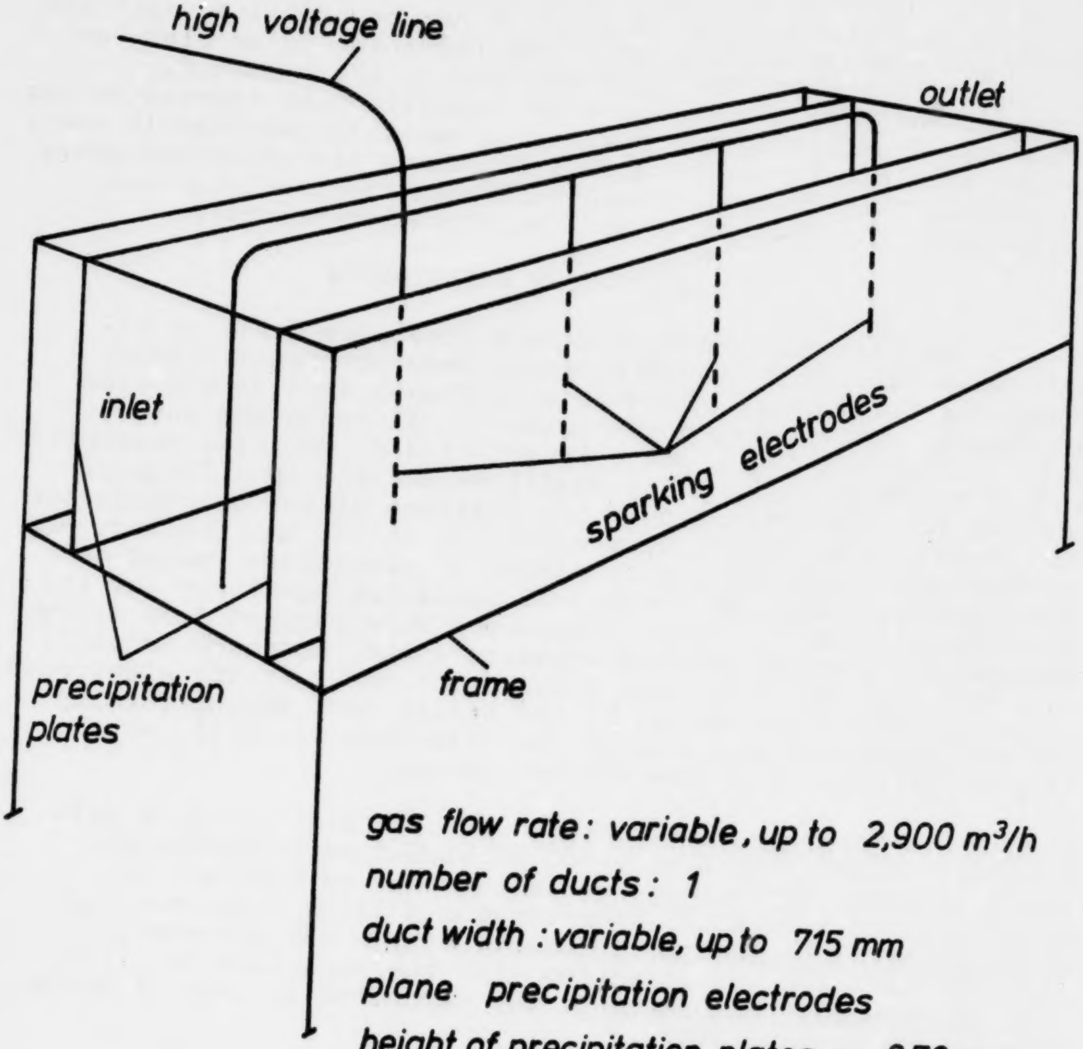
high voltage line
outlet
inlet
sparking electrodes
precipitation plates
frame

gas flow rate: variable, up to 2,900 m^3/h

number of ducts: 1

duct width: variable, up to 715 mm

plane precipitation electrodes

height of precipitation plates: 0.70 m

length of precipitation plates: 3.00 m

total collection area: 4.2 m^2

voltage: negative corona, up to 200 kV

Figure 1. Fundamental Structure and Data of the Laboratory Electrostatic Precipitator

with reduced efficiency or even without voltage. As precipitator inlet a 2.5 m long quieting duct without things build in was mounted, and before the inlet a mass force separator retained the larger particles of the gas-dust mixture. The laboratory air was sucked through a broad slit into the separator. Hence the pressure in the electrostatic precipitator was nearly that of the atmosphere. Because the laboratory electrostatic precipitator contained neither a rapper system nor hoppers, after each experimental setting it was cleaned by hand for the next measurements.

The results of the precipitation measurements are represented in the two following drawings. Figure 2 shows the migration velocity at 1.0 and 2.0 m/s gas velocity, plotted as a function of the duct width. With regard to the exactness of the single measuring points the influence can be described as a proportionality between migration velocity and duct width. That is equivalent to a constant efficiency with varying duct width. Moreover it has to be noticed that by doubling the gas velocity from 1.0 to 2.0 m/s the migration velocity becomes also nearly doubled.

In figure 3 the migration velocity at gas velocities of 1.5 and 3.0 m/s are outlined, again calculated with the defining Deutsch equation from the precipitation results. Once more the influence of the duct width on the migration velocity can be described as proportionality. By doubling the gas velocity the migration velocity increases anew, but now less than before (5).

The discovered proportionalities between duct width and migration velocity as well as the influence of the gas velocity in the precipitator on the migration velocity could not be explained with the hitherto existing theories. Besides to the economic interesting question whether or to what extend these laboratory results are valid for large scale precipitators under industrial conditions, acordinly the demand arose to explain the found dependences.

THEORY

The inability of the Deutsch theory to explain the observed influences made it necessary to introduce decisive modifications. Measurements of dust concentration profiles in the laboratory precipitator indicated that the swirling of the dust particles in the duct is not so complete as assumed before but exists nevertheless in a certain grade. The thereby produced incidental-like motion of the particles, which is superimposed to their drift to the precipitation electrodes, was described with the model of turbulent diffusion. On simplifying assumptions, for instance a constant drift velocity of the particles to the

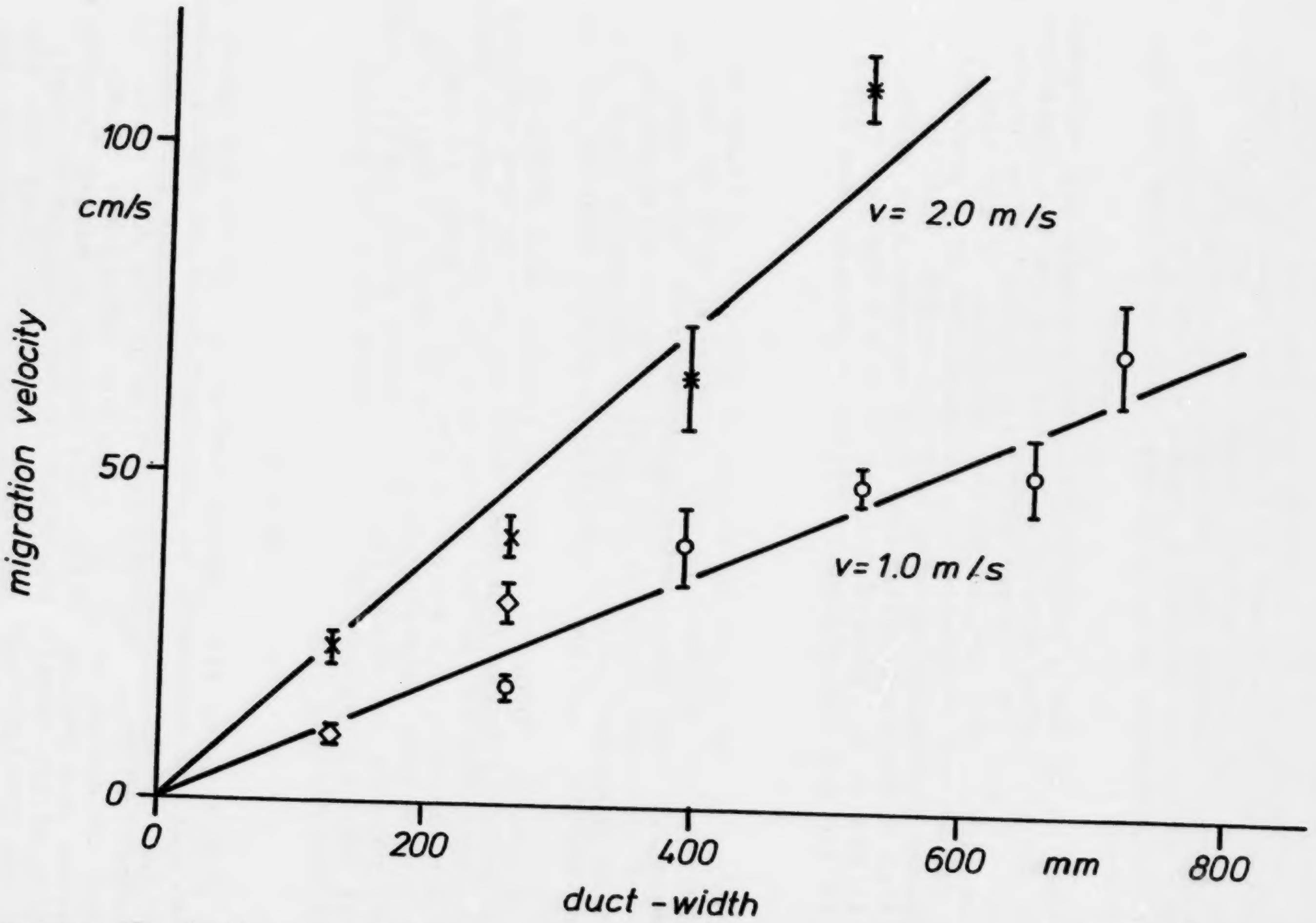

Figure 2. Influence of the Duct-Width on the Migration Velocity at Gas Velocities of 1.0 and 2.0 m/s

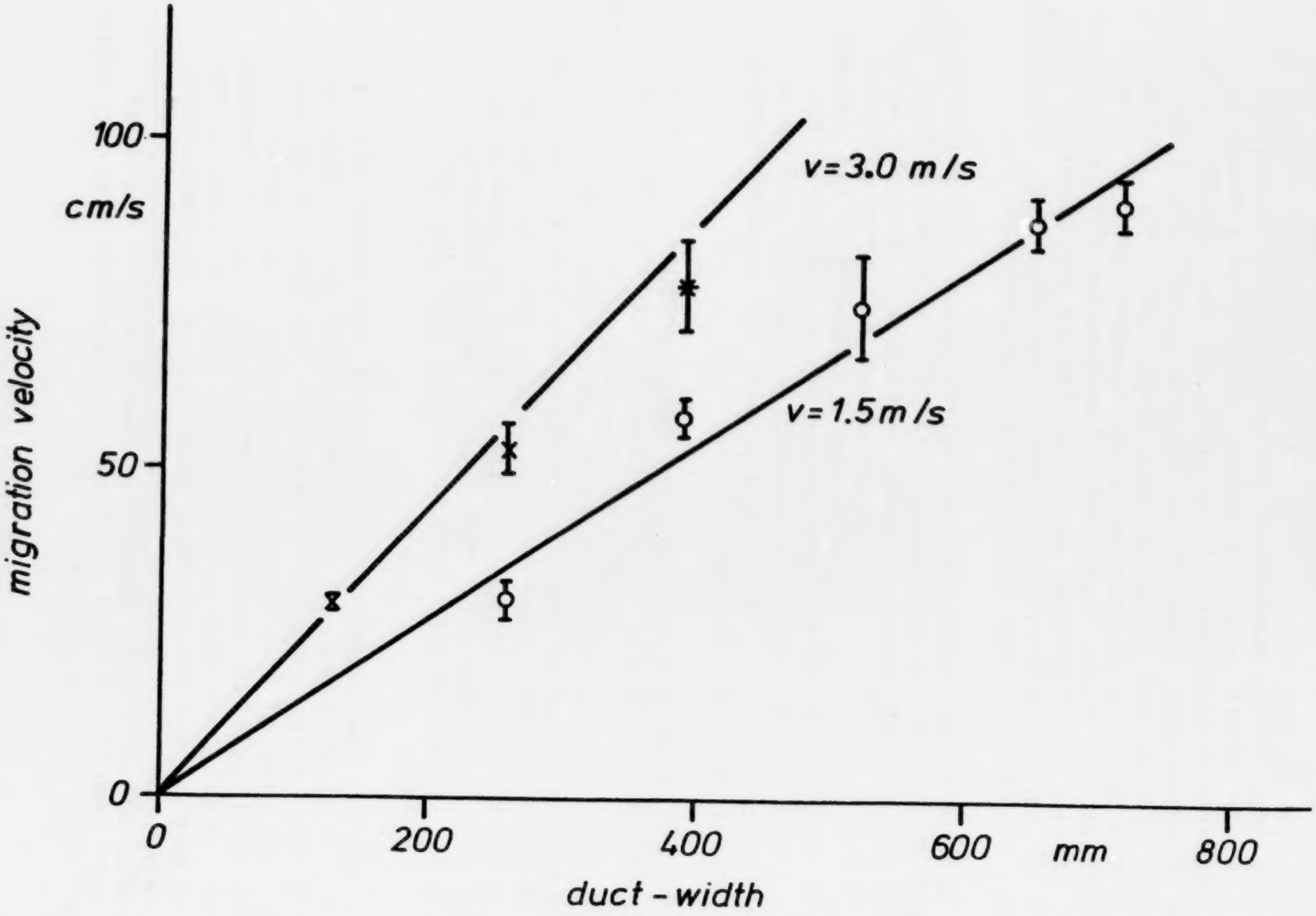

Figure 3. Influence of the Duct-Width on the Migration Velocity at Gas Velocities of 1.5 and 3.0 m/s

precipitation electrodes and a constant diffusion coefficient, a mass balance for a volume element led to a linear differential equation of the second order, that is reproduced in figure 4. The boundary conditions necessary to solve the differential equation are specified below. Boundary condition I means a constant dust concentration at the inlet of the precipitator. Condition II expresses, that there exists no effective mass flow through the center plane of the duct. Boundary condition III is a novel one. It originated from observations of precipitated dust at the plate electrodes leading to the assumption that part of the precipitated dust reentrains permanently into the gas flow. This was described with a constant dust concentration at the surface of the precipitation electrodes (6).

The differential equation was solved numerically and with the Deutsch equation the migration velocity was calculated. With acceptable values for the diffusion coefficent, for the drift velocity and for the dust concentration at the precipitation electrode it succeeded in reproducing the observed influences of the duct width and of the gas velocity on the migration velocity. According to that the measuring results are in a near relation to the partial reentrainment of already precipitated dust particles into the gas flow.

The capacity of the theoretical model turned out to be even much larger. Besides the reproduction of the influences of duct width and gas velocity on the migration velocity it offered an explanation for the often observed improvement of the precipitation with increased dust concentration in the crude gas. Concerning the specific dust precipitation observed deviations from the usually logarithmic behaviour could be theoretically reproduced too. Moreover the theoretical model offered an explaination for various dust concentration profiles publicated in the literature.

Considering the power of the theoretical model also its predictions were of interest. With regard to the influence of the duct width on the migration velocity the following was to see : The increase of the migration velocity with increasing duct width is initially nearly proportional, then it becomes weaker and finally a maximum is reached. This maximum occurs all the sooner as higher the gas velocity is. A restriction of the fundamental influences to small electrostatic precipitators could not be seen, therefore the hitherto obtained experimental results should be valid at least in their tendency for large scale precipitators.

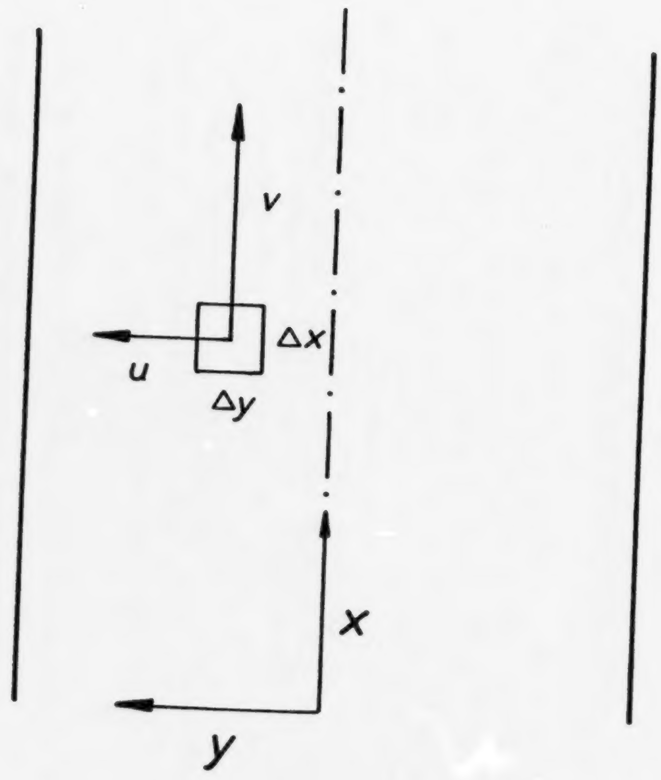

$$D\frac{\partial^2 c}{\partial y^2} - u\frac{\partial c}{\partial y} - v\frac{\partial c}{\partial x} = 0$$

$$c(x,y)\Big|_{x=0} = c_0 \qquad (I)$$

$$uc\Big|_{y=0} = D\frac{\partial c}{\partial y}\Big|_{y=0} \qquad (II)$$

$$c(x,y)\Big|_{y=a} = c_a \qquad (III)$$

a = half - width of duct
c = particle concentration
D = eddy diffusivity
u = drift velocity
v = gas velocity
x = distance from inlet
y = distance from sparking plane

Figure 4. Theoretical Model of Electrostatic Precipitation

PILOT PRECIPITATOR EXPERIMENTS

To test the laboratory results with regard to their validity under industrial conditions and their transferability to larger precipitators a large pilot electrostatic precipitator was constructed. Figure 5 presents a view of the precipitator and the most important data. The pilot precipitator consisted of two sections each having two ducts. The duct width was variable up to 1,000 mm. The effective hight of the precipitation electrodes came to 2.5 m, the length in each section was 3.0 m. This results in an effective precipitation area of 60 m^2. The volume flow rate through the electrostatic precipitator was adjustable up to 36,000 m^3/h. As power supply a 280 kV transformer was installed, its negative voltage being adjusted automatically to the highest value actually possible. Both sections of the pilot electrostatic precipitator were provided with rapper systems working independently and automatically, and the dust in the hoppers was removed automatically too. So the pilot precipitator could be operated continuously.

The first application of the pilot electrostatic precipitator was in a coal-fired power station. It operated in parallel to a large scale electrostatic precipitator that had to dedust the flue gases of a steam boiler plant of 150 MW fired with pulverized coal. During the tests the gas in the pilot precipitator had a temperature of about 120 °C. Under these conditions the specific resistance of the dust was at $4 \cdot 10^{12}$ Ωcm. Duct widths from 250 up to 1,000 mm were tested. The gas velocity in the pilot precipitator was varied between 0.5 and 2.0 m/s. Figure 6 shows the influence of the duct width on the migration velocity as it results from a regression analysis that considered also the influence of the crude gas dust concentration on the precipitation. To elucidate the nature of the law the curves are extrapolated beyond the measured duct width interval. Therewith it can be seen that initially the migration velocity increases almost proportionally to the duct width. Then the increase weakens and following a maximum the migration velocity decreases with further increasing duct width. The duct width, at which the maximum of the migration velocity occurs, depends from the gas velocity. The maximum is reached as sooner as higher the gas velocity is. Also an increase of the migration velocity with increasing gas velocity can be noticed, though at wider ducts a decrease too. In other respects, if the migration velocity of the large scale precipitator is checked with the comparable one of the pilot precipitator, correspondence can be stated.

As the second application for the pilot precipitator the room dedustion of an iron ore sintering plant was choosed. From the crude gas flow of the again already existing large scale precipitator a part was separated and after dedustion

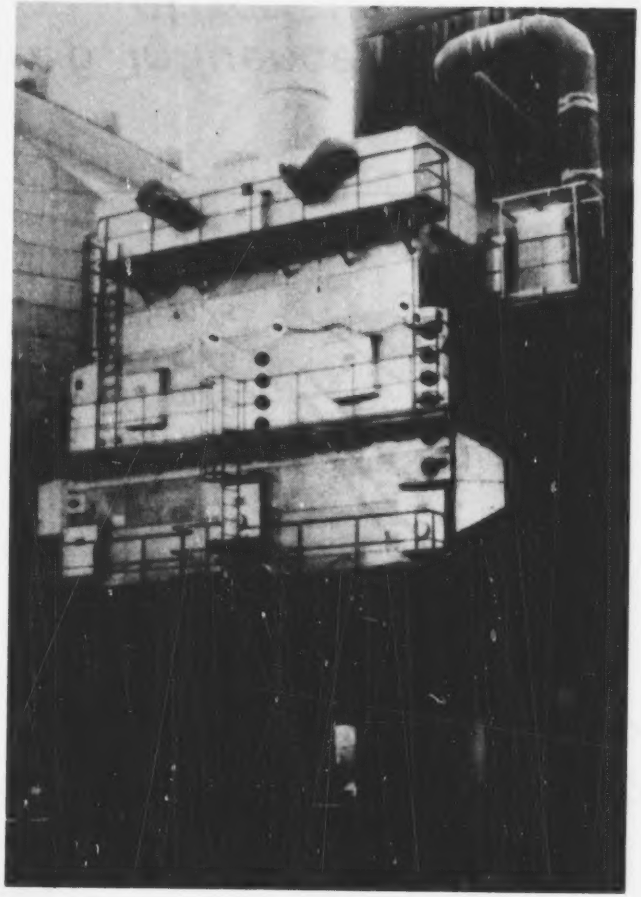

gas flow rate :

variable, up to 36,000 m^3/h

number of ducts: 2

duct-width: variable, up to 1,000mm

height of duct: 2.5 m

number of sections : 2

total length of ducts 2x3m = 6 m

total collecting area : 60 m^2

voltage :

negative corona, up to 280 kV_p

Figure 5: View and Fundamental Data of the Pilot Electrostatic Precipitator

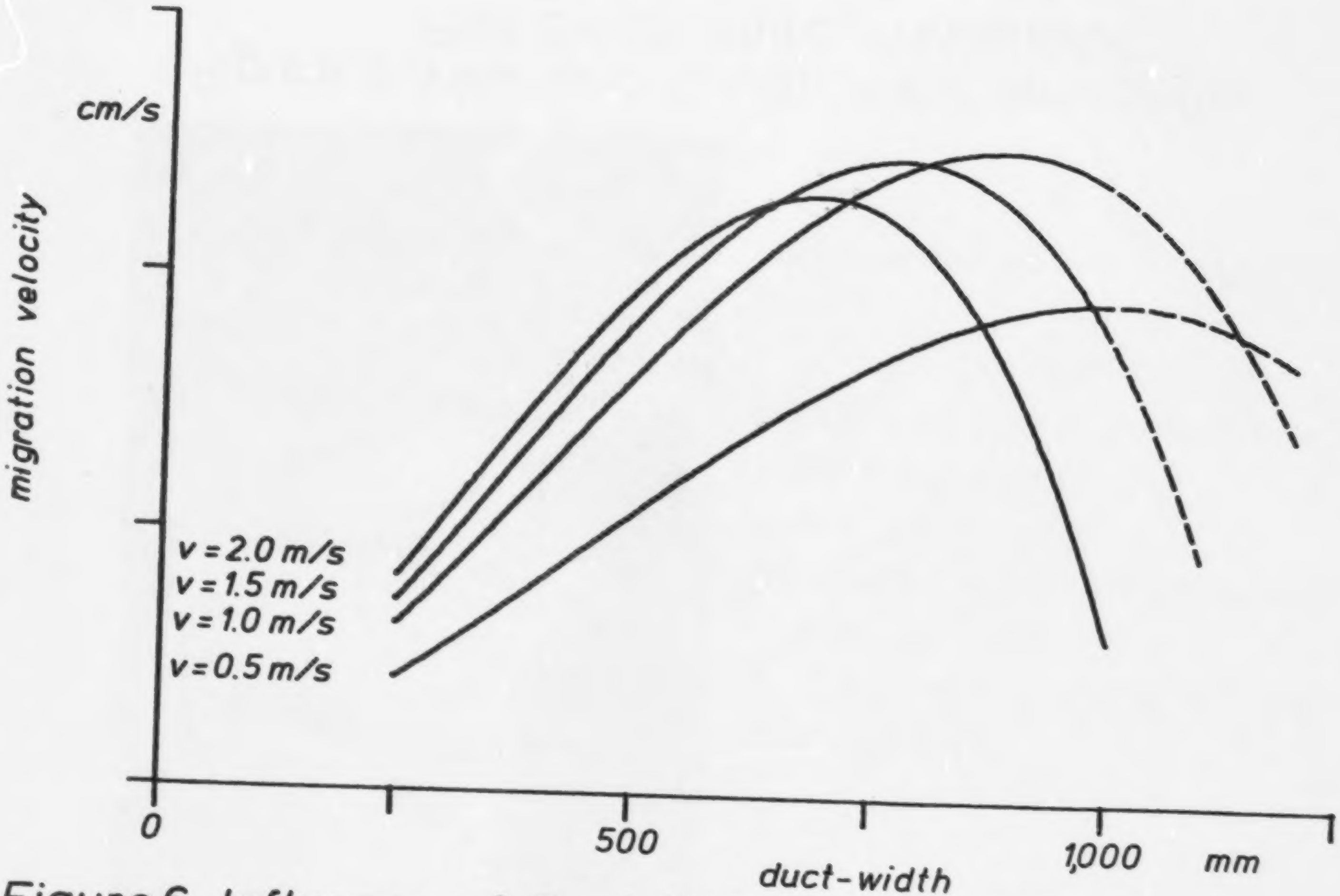

Figure 6. Influence of Duct-Width on the Migration Velocity at Various Gas Velocities (Fly Ash Collection)

was led back to the inlet of the large precipitator. The same duct widths and gas velocities as before were tested. The gas temperature in the pilot precipitator was now about 90 °C. The numerous measured values of the penetration were again analysed with a multi regression method. The result is represented in figure 7. The approximate proportionality between duct width and migration velocity at smaller duct widths can be seen clearly. The influence of the gas velocity on the position of the migration velocity maximum is in this case less evident. But also the increase of the migration velocity with increasing gas velocity is again very clear. A comparison of the migration velocity of the large electrostatic precipitator with that of the pilot precipitator shows again correspondence.

CONCLUSIONS

On the basis of experiments with a laboratory electrostatic precipitator the duct width of a larger pilot electrostatic precipitator was varied up to 1,000 mm. The tests were performed under several industrial conditions. As a result it can be noticed that at narrow duct widths like today in use the migration velocity is nearly proportional to the duct width. A maximum was found only at wider ducts and dependent from the gas velocity. To summarize theoretical and experimental investigations they confirmed the following : By increasing the usual duct width the necessary precipitation area can be reduced while the efficiency remains constant. That is aquivalent to a reduction of the costintensive things built in of an electrostatic precipitator. With this compared the costs for voltage increase of the high tension equipment can be neglected. It is imaginable that the position of the maximum is influenced by the duct length too. But this has yet to be investigated. Summarizing it can be stated that electrostatic precipitators with wide ducts of more than 500 mm are applicable and interesting for industrial use. Without reducing their efficiency they can be constructed and operated with essential less expenditure as that of the nowadays used precipitators.

ACKNOWLEDGEMENT

The necessary financal aids to perform the extensive experiments of the all together two research projects were granted by the Home Secretary of the Federal Republic of Germany, Umweltbundesamt.

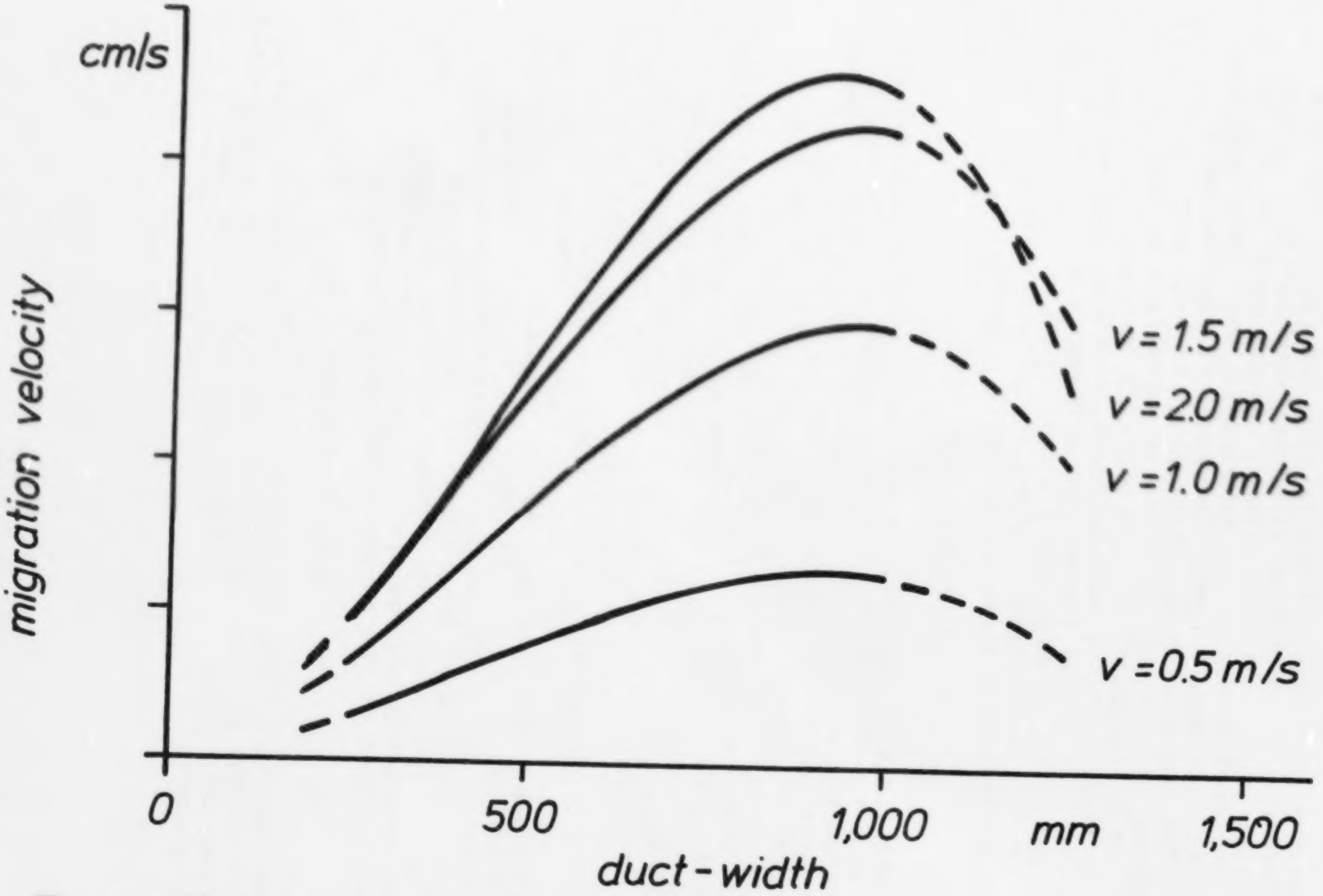

Figure 7. Influence of Duct-Width on the Migration Velocity at Various Gas Velocities (Room Dedustion)

REFERENCES

1.	Deutsch, W.	Bewegung und Ladung der Elektrizitätsträger im Zylinderkondensator. Annalen der Physik, IV. Folge, 68, pp. 335-344
2.	Aureille, R.; Blanchot,P.	Experimentelle Untersuchung verschiedener Parameter auf den Wirkungsgrad eines Elektrofilters. Staub - Reinhalt. Luft 31 (1971) Nr. 9, pp. 371 - 375
3.	Gübner, O.	Einflüsse auf die Wanderungsgeschwindigkeit, nachgewiesen mit einem Versuchselektrofilter. Dissertation, Universität Essen, 1976
4.	Heinrich, D.O.	Der große Gassenabstand im Elektrofilterbau. Staub - Reinhalt. Luft 38 (1978) Nr. 11, pp. 446 - 451
5.	Weber, E.; Wiggers, H.	Untersuchungen an einem Laborelektrofilter über die Einflüsse der Gassenbreite und der Gasgeschwindigkeit auf das Abscheideverhalten und die Staubkonzentrationsverteilung. Staub - Reinhalt. Luft 40 (1980) Nr. 11, pp. 469 - 473
6.	Wiggers, H.	Untersuchungen an einem Laborelektrofilter, insbesondere über den Einfluß der Gasgeschwindigkeit und der Gassenbreite auf das Abscheideverhalten. Dissertation, Universität Essen, 1982

A RECONCILIATION: WIDE VERSUS NARROW SPACED COLLECTING PLATES FOR PRECIPITATORS

by: Dennis G. Puttick
Peabody Sturtevant Ltd.
London, N.14.

ABSTRACT

Misaka of Hitachi, amongst others, has presented evidence for the improvement in electrostatic precipitator performance, using much wider gas passage spacing than normal (typically 20 in.). Such designs are now in general use.

This appeared to be directly contrary to the experience of Peabody Sturtevant who, on very large utility ESP plants treating highly resistive particulates, produce remarkable efficiencies with narrower spacing than normal (typically 8 in. - 9 in.) using a design first developed during the mid-1960's.

In developing his reconciliation, the author uses observations of the actual internal construction of different designs of precipitators and the effect that increasing variance from perfect electrode geometry has upon total power input and field intensity at various plate spacings.

This return to basic precipitation electrostatic theory demonstrates not only that Peabody Sturtevant is right to pursue its narrow spacing design but other companies, with their own particular standard of construction, may be equally right in developing wider spacer techniques.

It is becoming established in the electrostatic precipitator field that increasing the duct spacing, i.e. the distance between adjacent collecting plates, can result in a higher achieved efficiency. There has therefore been a tendency by many companies in the field to put forward wider plate spacing to achieve economy in total collecting plate area and more particularly as an answer to problems that have been encountered with higher resistivity dusts.

These notes propose the reasons why many plant designs have achieved better results with wider spacing and make a comparison between the Sturtevant narrow spacing system with wider spaced systems.

For many years, the norm for precipitator collector spacing (including the Sturtevant spacing) was between 10" and 12". In the early 60's, Sturtevant produced their first 8" narrow spaced precipitator. Various companies also produced narrow spaced precipitators down to 6" duct size using the package principle and with only 3 to 4M plate heights. These have generally worked well.

However, in the last 20 years or so for reasons both of economy and ground space limitations, precipitators have got taller. Plate heights have increased from typically about 30 ft. (9 metres) to 40 to 50 ft. high (12 to 15 metres).

It is also during this period that the vogue for wider duct spacings has occurred. Anybody familiar with the internal design of precipitators particularly with their final practical embodiment will be aware of the rapidly increasing divergencies from ideal in internal electrical clearances with increasing plate height.

Most plate designs are composed of vertical strips fixed to a support beam at the top and a fixing beam at the bottom with either top or bottom supports being the point of rapping.

Most of these plate designs utilise cold rolled sections. Although one in 500 is a typical straightness tolerance for most purposes, for precipitator applications this is improved to a tolerance of about one in 1,000. This tolerance means a possible inbuilt bow of up to 15mm in a 15M high plate at the production stage irrespective of any other distortions that may be produced during shipping and erection. Precipitator suppliers always attempt to improve on this but obviously the inherent problems easily result in the acceptance of plate straightness very far from the perfect plate alignment situation.

Until the 1970's, the precipitator world was divided equally between wire and weight designs and wire in frame designs. Currently, the vogue is fairly equally divided between frames and "rigid" masts; the latter frequently and often hopefully using some means of promoting a better corona than round or square wires. Wire and weight electrode systems have suffered in reputation because of poor wire designs used by some manufacturers resulting in excessive operational failures. However, Peabody Sturtevant are still using this design with considerable success and a minimal failure rate along with both frame and mast designs. The simplicity of a mast design should lend itself to inherently better clearances than the more complex frame. Our experience is that this is so.

In an attempt to overcome clearance problems for high plates, frames are frequently made in two sections with separate rapping for each section. However, this system requires further increased complexity of support steelwork and when dealing with many hundreds of lanes in a large installation, the chance of at least one mis-aligned frame occurring (thus effecting the whole stage) is considerable.

For a strip plate frame system, a reasonably "thin" plate strip will be about 35mm. The outside dimensions of the frame tubing will be similar and often a little greater. This means that with a 250mm duct spacing, the actual electrical clearances with perfect alignment will be 90mm, i.e. a clearance reduction of 35mm. This will obviously occur at many points over the plate where the horizontal tubing of the frame passes the thickest parts of each plate strip. Typical plate sections are as shown in Fig. 1.

Various Types Of Collecting Electrodes

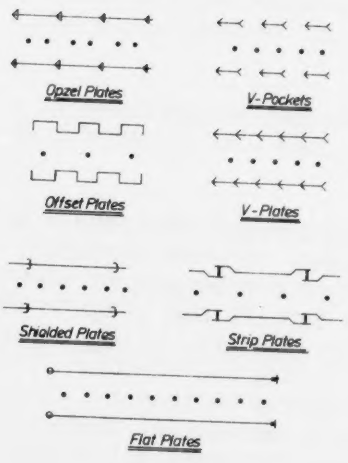

FIG. 1

Voltage/Current Parameters

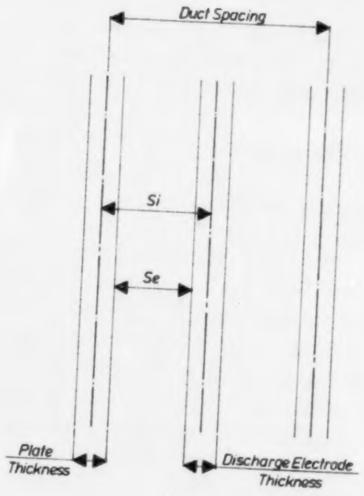

FIG. 2

With the Sturtevant flat plate/wire and weight system, a series of individual wires pass from a top grid suspension through and below the plates to bottom grid tensioning. The minimum clearance is at the top and bottom of the plates where horizontal stiffening tubes 38mm O.D. occur. This gives a perfect alignment clearance reduction of 20.5mm.

Between top and bottom stiffening tubes on this flat collecting plate, horizontal joggles give a minimum protrusion into the gas stream from the centre line of the plate. In the worst case, there is only a 10mm clearance reduction.

At the top and bottom of a Sturtevant flat plate, a practical on-site variation between wire and plate will be not more than plus or minus 3-4mm (say worse case situation of 6mm). This gives a total clearance reduction of 26.5mm at these points. With say a 13M high plate, it will be jig spaced at top, bottom and two intermediate points. This will effectively, within 2 or 3mm, ensure the verticality of the plate at all points. The clearance reduction at the joggles between top and bottom stiffening tube will, therefore, be well within 26.5mm. This means, therefore, that for a precipitator equipped with Sturtevant flat plates and wires, the clearance reduction for a practical operating embodiment of this design should not be more than this 26.5mm.

With a frame design as stated above, the clearance reduction with perfect alignment will be about 35mm. However, of more significance than this is the much poorer final site clearances that will be achieved compared to Sturtevant's flat plate/wire systems. With the best efforts, practical out of alignment figures with a frame of 10, 15, or even 20mm compared to the Sturtevant flat plate/wire, 6mm are possible when the manufacturing and assembling difficulties are considered.

In fact, these notes came about as the result of much time spent observing the internal alignment of many competitive makes of precipitator and the idea was formed that the pressure towards wide spacing was possibly due to the increasing clearance reduction observed in tall strip plate/framed type precipitators.

It was thought worthwhile to look at standard published formulae relating corona emissions to corona discharge distances and also voltage flashover distances. These distances are illustrated diagrammatically in Fig. 2.

The corona current flow for a particular operating kV will be dependent upon the distance from the point of emission discharge to the mean centre line of the plate. In practical terms, half the duct width; i.e. Si on Fig. 2. The voltage actually achievable will be dependent upon the spark gap distance, i.e. Se on Fig. 2.

Three standard formulae are relevant all of which for example appear in somewhat similar form in White - Electrostatic Precipitation; quoting earlier sources.

These formulae are as follows:-

$$E = K1.Se \qquad \text{..... (1)}$$

Where K1 = constant
E = spark over voltage
Se = spark over distance H.T. to earth.

The second formula is:

$$I = \frac{K2}{Si^2} \times \frac{E\ (E - Eo)}{\text{Log}\ \frac{4Si}{\pi R}} \qquad \ldots\ldots (2)$$

Where I = corona emission per unit length of wire
K2 = constant
Eo = corona onset voltage
Si = half duct width
R = radius (or equivalent radius) of emitter.

The final formula is:

$$Eo = K3.R.\text{Log}.\ \frac{\pi R}{2Si} \qquad \ldots\ldots (3)$$

Where K3 = constant.

K1, K2 and K3 are constants dependent upon the particular precipitator operating characteristics.

From these established formulae, we can proceed as follows:-

Combine the square of (1) with (2):

$$EI_W = K1^2.K2.\frac{Se^2}{Si^2}\ .\ \frac{(E - Eo)}{\text{Log}\ \frac{4Si}{\pi R}} \qquad \ldots\ldots (4)$$

Inserting both (1) and (3) in (4), we have:

$$EI_W = K1^2.K2.\frac{Se^2}{Si^2}\ .\ \frac{(K1.Se - K3\ \text{Log}\ \frac{\pi R}{2Si})}{\text{Log}\ \frac{4Si}{\pi R}} \qquad \ldots\ldots (5)$$

This formula is for the power discharge for one discharge electrode per unit height of this electrode. To convert this to power per unit area, we must know the discharge electrode spacing inlet to outlet of the plant. The formula (2) is in fact based on an electrode spacing which is equivalent to duct spacing.

Therefore, total power per unit height of all discharge electrodes $= EI_W \times n$.

The effective plate length $= 2 \times Si \times n$.

n = number of wires in plate length under consideration.

Therefore, power per unit area of collecting plate

$$= \frac{EI_W}{2Si} \qquad \text{..... (6)}$$

This gives a final equation for total power as follows:-

$$EI \text{ (total power)} = \frac{K1^2.K2.Se^2}{2.Se^3} . \frac{(K1.Se - K3.\text{Log}\,\frac{\pi R}{2Si})}{\text{Log}\,\frac{4Si}{\pi R}} \qquad \text{..... (7)}$$

For comparison between Si and Se with all other things being equal, it is necessary to assume a typical plant and a radius of a round collecting wire (or an equivalent radius if a round wire is not used) and also to determine K1 and K3. Since we are considering only a ratio of power with similar conditions, $K1^2.K2$. can be ignored.

For particular operating conditions, we can obtain K1 from formula (1) and K3 from formula (3); that is, by inserting E, Eo, Se, Si and R obtained from a plant operating under reasonably constant conditions.

Typical plant operating conditions have been obtained as follows:-

Operating on pf dust at 200 spacing with a total clearance reduction of 26mm and with corona onset voltage at 17kV and flashover voltage at 33kV with 1.5 equivalent radius electrode.

A second condition is under the same operating conditions with 200 duct spacing and 13kV corona onset voltage with 30kV flashover voltage, 31mm total clearance reduction and an equivalent discharge electrode radius of 1.05mm.

A further practical example under not too dissimilar operating conditions is with a framed system with 250mm duct spacing and 19kV onset voltage with 45kV flashover voltage and a total clearance reduction of 41mm with 1.4 equivalent discharge electrode radius.

For these particular cases, K1 and K3 can be calculated. Ratios of power input can then be obtained for differing total clearance reductions and increasing plate spacing. In all three cases, the results were very similar and the form of the curves produced was the same. Fig. 3 shows the resulting curves.

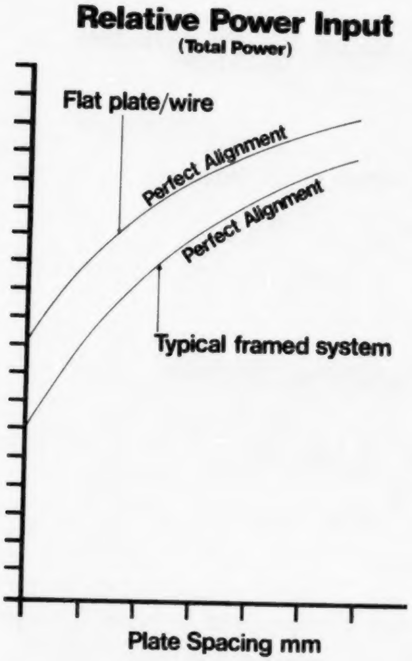

FIG. 3

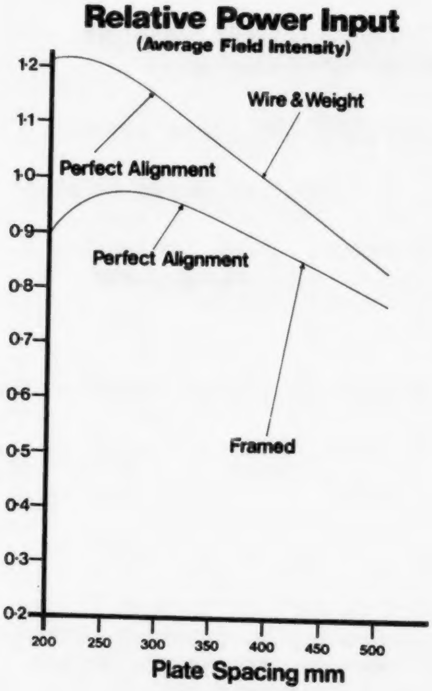

FIG. 4

As can be seen from Fig. 3, there is an increase in total power with increase in plate spacing, under perfect alignment conditions comparing a flat plate/wire plant with a typical framed system. This also illustrates the difference in total power between the two systems. The Sturtevant 200mm spacing is equivalent to a 250mm frame system in terms of total power.

Also, from this, one might conclude that there is no limit to the improvement that can be obtained by increasing plate spacing.

However, this is not necessarily correct. For practical purposes, an empirical factor "w", the effective migration velocity is used to determine achievable efficiency for a particular plant inlet volume and collecting area. In its absolute sense "w" is the velocity of the average typical particle towards the plate at right angles to the plate. Obviously, the motive power determining this absolute velocity is the immediate electrical environment of the particle. That is, the average field intensity, i.e. the power per centimetre of space gap per square metre of plate area.

Any increase in this average field intensity should produce a higher actual "w" and therefore a higher efficiency. To obtain this value, it is necessary to divide Equation (7) by 2Si. This gives us a field intensity equation as follows:-

$$\text{EI (field intensity)} = \frac{K1^2.K2.Se^2}{4.Se^4}.\frac{(K1.Se-K3.\text{Log}\frac{\pi R}{2Si})}{\text{Log}\frac{4Si}{\pi R}} \quad ..... (8)$$

Using similar plant factors as before, this gives ratios of field intensities as shown on Fig. 4.

It is seen that under perfect alignment conditions, there is considerable difference in field intensity between a framed and a wire and weight system. Although there is shown an increase in field intensity with plate spacing, a point is soon reached when increasing the plate spacing causes a fall in field intensity. This occurs earlier with a wire and weight system than with a framed system.

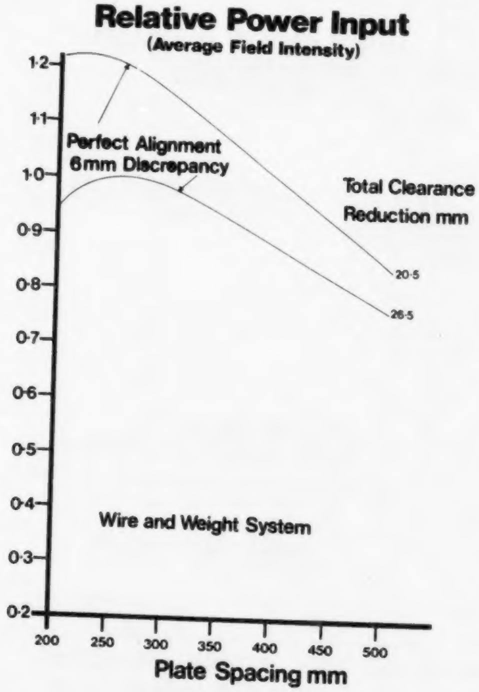

FIG. 5

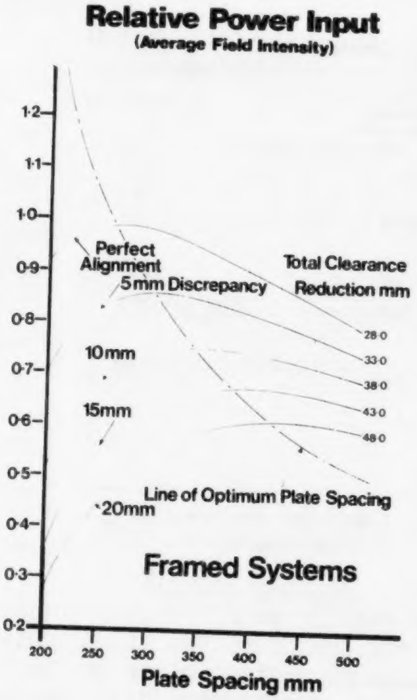

FIG. 6

Fig. 5 shows the effect on a Sturtevant flat plate/wire system of taking into account discrepancies from perfect alignment. The average field intensity falls quite sharply with this misalignment. The 6mm discrepancy is the maximum misalignment to be expected from this plant. However, it does show that the optimum field intensity is to be found at about 250mm. However, between 200 and 350mm, the field intensity varies comparatively slightly between plus and minus 3%. The pointlessness of increasing the spacing of such a plant beyond about 250mm is clearly illustrated.

In Fig. 6 is shown the perfect alignment situation for a framed system along with a series of curves showing the effect of increasing misalignment.

This shows the devastating effect on field intensity with discrepancies which are not uncommon in framed precipitators.

The other important point is that increasing discrepancies demand increasing plate spacing for optimum field intensity and therefore for maximum efficiency for the collecting plate area utilised.

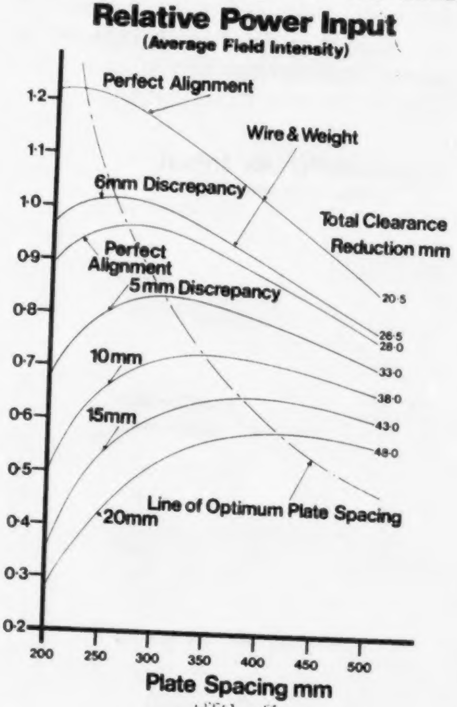

FIG. 7

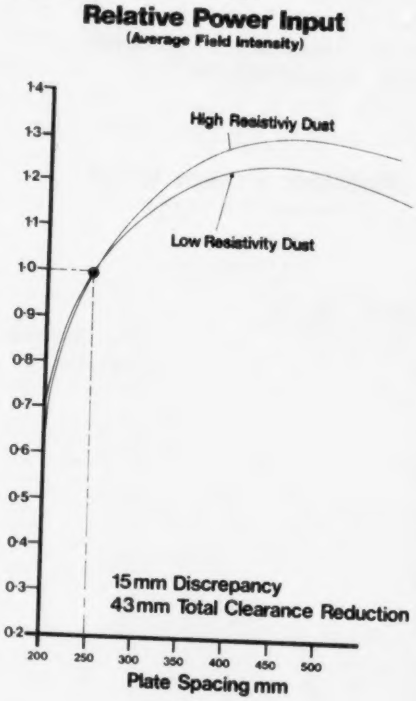

FIG. 8

In Fig. 7, we effectively combine the field intensity/plate spacing curves for the Sturtevant flat plate/wire precipitators and framed precipitators. It is clear how much penalty a framed system with 15mm or 20mm out-of-alignment discrepancy has compared to a flat plate/wire system. Despite the optimisation of the flat plate/wire systems at about 250mm, the field intensity at 200mm is still better than even the widest spaced frame system.

Thus, we arrive at a reconciliation between the anomaly of the excellence in performance of Sturtevant very narrow spaced precipitators and the need by many manufacturers particularly with tall plates to build wider duct spaced precipitators to achieve required efficiencies.

One other useful way to use Equation (8) is to compare field intensity ratios on the same precipitator operating under differing conditions. On a pf precipitator where widely differing coals were burnt, figures for corona onset voltage and maximum operating voltage were taken under low resistivity dust conditions. These parameters were also taken at a later time when the resistivity of the ash was very much higher. The net effect in this second case was a higher corona onset voltage and a lower operating voltage. With these inserted in Equation (8), curves were produced as Fig. 8.

It must be emphasised that these curves are not a comparison of the actual field intensity achieved in each case but only the difference in field intensity with increasing plate spacing for the typical out-of-alignment indicated.

This illustrates that a greater percentage improvement can be expected in field intensity with increasing plate spacing when a more highly resistive dust is being dealt with. It also illustrates that the higher resistive dust requires wider plate spacing for optimum performance.

This conclusion will probably not come as a surprize to those working in the field of wide spacing.

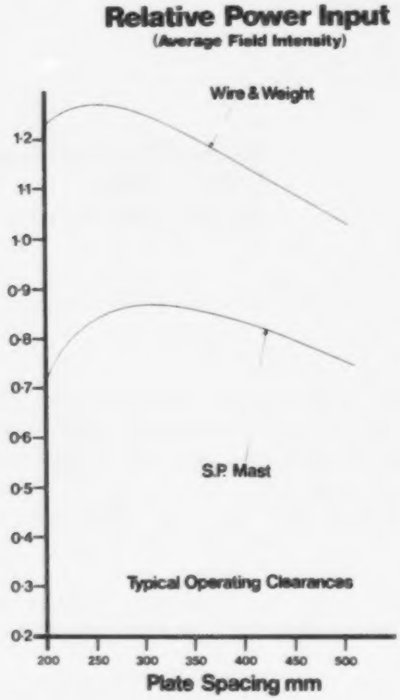

FIG. 9

So far, we have discussed comparisons between wire weight systems and framed systems. However, as already stated, there is an increasing vogue towards mast systems. These certainly have bigger problems in initial clearances and final alignments compared to a wire system. However, typically one can expect a mast system to have far less alignment problems than a framed system. In Fig. 9, we compare a wire system with a Sturtevant S.P. mast electrode system with typical operating clearances and assuming the same emitting radius in both cases.

This shows a marked reduction in field intensity using a mast system although not as great as with a typical framed system. For any manufacturer of masted systems (such as ourselves), it is extremely important that the emission characteristics of their mast system be very much better than a wire system to even achieve wire performance let alone surpass it.

In Fig. 10, we show the difference in operational characteristics of a Sturtevant S.P. mast electrode compared with a wire system.

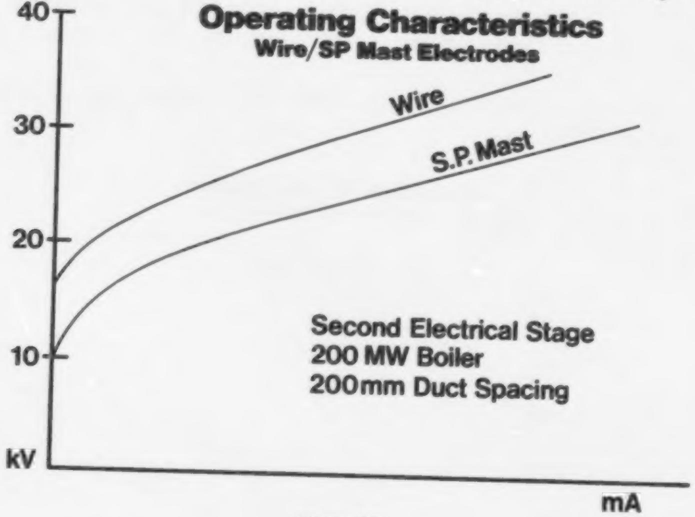

FIG IO

As can be seen at 30kV operating voltage, the S.P. mast achieves 90% more corona emission than the wire. However, for the reasons illustrated in Fig. 9, the actual overall net operational improvement in the field intensity for the S.P. mast has been found to be not more than about 10 to 20%. Manufacturers who are moving over from wire electrode systems to mast systems must bear this carefully in mind. If their mast system characteristics compared with their original wire system are not similar to Fig. 10, then they are likely to find an overall fall-off in performance compared to their original wire systems.

With regard to the various clearances chosen, some manufacturers may argue that the total clearance reduction used for perfect alignment does not apply to their own framed system particularly perhaps because of the geometry of the frames and collecting plates. There is, of course, some merit in this but it is difficult to achieve perfection in geometry for all the closest clearance points in a precipitator when dealing with the extremely large number of such points involved. However, to take some account of this factor, the perfect alignment situation for frames has been reduced from a typical figure of 35mm clearance reduction to an arbitrary 28mm.

It may also be added that in preparing this paper, a considerable number of different k factors were obtained from both wire, mast and frame systems and used in the computation of alternative curves. Although there were differences in the results, these were of comparatively low degree and the general form of the curves produced did not change.

It was not expected when resorting to established formula in order to relate duct spacing with flashover clearances that so many interesting things would emerge which explains to some extent contemporary vogues.

The reason for example why very narrow ducted Sturtevant precipitators have been operating so excellently in the last 20 years on highly resistive dusts and with plate heights up to about 13 metres. Similarly, pressure from some manufacturers to increase duct spacing particularly when dealing with highly resistive dusts is explained. The particular usefulness of mast electrodes in relation to framed systems and the particular importance of the emission characteristics of mast electrodes when comparing them to wire systems has also been indicated.

However, whilst this paper may explain the excellence of the Sturtevant wire weight flat plate performance compared to framed systems, it does not explain the apparent better reputation of European framed systems used in the U.S. compared to the generality of U.S. designed wire/weight systems.

All the Sturtevant plants referred to in addition to being flat plate specifically designed for perfection in alignment, also use the multi-rap principle. That is, rapping at more than one position up the side of each collecting plate. With this system, the rapping energy per square metre of plate area is not only well in excess of all other designs currently marketed, but the rapping occurs at optimised positions.

Local U.S. wire and weight designs are almost invariably top rapped and, as a general rule, the rapping is inferior to European bottom rapped designs and infinitely inferior to multi-rap.

All of which illustrates that no single aspect of precipitation technology can ever be considered in isolation.

The work described in this paper was not funded by the U.S. Environmental Protection Agency and therefore the contents do not necessarily reflect the views of the Agency and no official endorsement should be inferred.

REFERENCES

1. Harry J. White. Industrial Electrostatic Precipitation. Pergamon Press, 1963.

PULSE CORONA AS ION SOURCE AND ITS BEHAVIORS IN MONOPOLAR CURRENT EMISSION

by: Senichi Masuda and Yoshiaki Shishikui
Department of Electrical Engineering,
University of Tokyo
7-3-1, Hongo, Bunkyo-ku, Tokyo, JAPAN 113

ABSTRACT

The pulse voltage applied to a discharge electrode produces a weakly ionized plasma with about 5 x 10^9 ions/cm^3 in ion concentration in a very short time of about 10 - 100 nano-seconds. The monopolar ions are extracted by an externally applied dc field towards the charging area from this plasma, and the current pulse lasts for a substantially longer time of about 1 - 3 milli-seconds. This is due to a long life time of the plasma which disappears by recombination and charge separation. The expansion of the monopolar ion cloud during its migration across the charging area also contributes to the increase in the duration time of the current pulse measured at the counter electrode. The theory explaining the wave form of the ionic current by the recombination, separation and expansion of ions agree very well with the experimental results.

INTRODUCTION

The specific advantages of using an extremely short pulse high voltage with several tens to several hundreds nano-seconds duration time have been recognized in the pulse-energization of electrostatic precipitators of both twin-electrode type (1,2) and tri-electrode type (3), and also in the production of ions in a precharger called Boxer Charger (4) currently being developed by the auther.

The pulse voltage proceeds on a transmission line with a speed of ca. 28 cm per 1 nano-second, so that the geometrical length of this pulse voltage becomes comparable to the total length of the corona wires. As a result, it behaves as a travelling voltage wave to produce a very special type of streamer coronas (5,6) along the entire length of the transmission line consisting of the corona and counter electrodes or two parallel corona wires.

These streamers, although belonging to a weakly ionized plasma, possess a sufficiently high ion concentration for most of the practical charging purposes, so that they serve as a good plasma ion source emitting monopolar ions with the aid of an externally impressed extracting dc field.

The advantage of using such an extremely short pulse high voltage is two-fold. One is the ease in construction of its pulse power supply with its low initial cost. Another is its low running cost resulted by a very high power efficiency. This is due to the fact that the energy on the corona transmission line is highly localized in time and space on a travelling wave packet to be effectively converted into corona energy, and that this conversion is enhanced by the reflection of the pulse wave at the open terminal of the line, and further that the residual energy of pulse after losing its ability of producing streamers to become a loss remains quite low. It must be also emphasized that, in the presence of the extracting dc field externally applied, the travelling wave voltage primarily acts as a trigger and a substantial part of corona energy can be supplied from the dc field.

In the cource of investigations of the coronas induced by such an extremely short pulse voltage, several important phenomena are discovered. In the case when two parallel wires are used, the streamers are launched at first from the negative wire (negative streamer), and, then, the positive streamers occur from the positive wire when the pulse voltage is sufficiently high, exceeding a certain threshold (5). There seemed to be no difference in ion emission ability between the negative and positive streamers, whereas the latters consume a substantially greater energy than the formers (5,6). Although the streamers are formed in a very short time of say 10 nano-seconds or less, the ionic pulse current produced indicates a very long duration time of about 1 - 3 milli-seconds.

In consideration of the importance of better understanding of the plasma structures of these streamer coronas, investigations are made on the time-dependent ion concentration of these plasma and mechanism of producing such a long current duration time. Based on the experimental data a mathematical model is proposed on the ion separation and migration processes, and the numerical results obtained by computer simulation using this model are compared with the experimental results.

The present paper reports on the results of these experimental and theoretical investigations.

EXPERIMENTAL METHODS

The experimental apparatus used in the first series of experiments is shown in Fig. 1 (a). The upper corona electrode consists of parallel wires having a square cross-section (5 mm x 5 mm), spaced at 23 mm (face to face) and insulated from each other of two adjacent wires to form the mother and daughter wires. The lower grounded plate is an ion collecting electrode consisting of two concentric disks, insulated from each other, where the inner disk (diameter:70 mm) serves as a current measuring electrode. The distance between the upper and lower electrodes is 60 mm. An extremely short pulse high voltage with a half duration time of ca. τ_h=70 nano-seconds is applied between the mother and daughter wires in such a polarity that the latters are negative in reference to the formers throughout this paper. This produces corona discharge as a plasma ion source. The corona starts from the negative daughter wires in a form of uniformly distributed streamers (negative streamers) extending towards the positive mother wires. Then, provided pulse volttage is sufficiently high, the positive mother wires launch much brighter streamers (positive streamers) towards the negative wires (5,6). The voltage difference between the daughter and mother wires disappears very quickly through the leakage resistance R. At a certain delay time, τ_d, after the formation of the streamers a dc voltage is applied in a form of a step-function between the mother wires and ion collecting electrode so as to extract from the plasma of streamers the monopolar ions of a desired polarity. This delay time allows at the start of the ion extraction the variation of the ion concentration of the plasma undergoing recombination, and thereby the estimation of the initial plasma ion concentration.

The monopolar ions, thus extracted, travel across the inter-electrode gap, inducing a displacement current on the measuring electrode M. In order to detect the convection current of ions, which enables the estimation of local ion concentration of the moving ion cloud, a grid electrode is located close to the ion collecting electrode to screen the disturbance in a form of displacement current. A bias voltage applied to the grid makes its potential undistorted in the application of dc voltage.

With this experimental setup the first series of experiments is performed, detecting the current wave form from the measuring electrode which indicates the variation of number concentration of oncoming ions.

Then, the second series of experiments is made to measure accurately the total quantity of charge carried by the extracted monopolar ions. For this purpose the experimental apparatus is modified as shown in Fig. 1 (b) where the grid is removed to avoid its charge collection. The potential across the capacitor inserted between the measuring electrode and the ground gives the total charge. This quantity measured with variation of the delay time, τ_d, provides the information on the decay of ion concentration in the plasma with time.

Finally, the distribution of the plasma density in the transverse direction is estimated by measuring the distribution on the total charge collected on the ion collecting electrode. The ion collecting electrode is modified for this purpose as shown in Fig. 1 (c) where a series of parallel strip-like probe electrodes with 5 mm width is attached on the disk.

EXPERIMENTAL RESULTS

WAVE FORM OF IONIC CURRENT

At first the negative dc voltage is applied to the mother wires to extract negative ions, and the effects of the magnitude of the extracting dc field, E_{dc}, and delay time, τ_d, on the current wave form are observed. The wave form shown in Fig. 2 (a) and (b) represent those observed at different levels of E_{dc} with zero delay time, τ_d, and a constant pulse voltage V_p = -37 kV. A short initial pulse, induced by the dc voltage applied to the wires, serves as the time origin. It is followed by a larger pulse of convection current by the oncoming ion cloud. It can be seen that the increase in E_{dc} produces the decrease in the interval between the two peaks as a measure of ion transit time, reduction in width of the ion cloud pulse, the increase in its pulse height, and finally the increase in number of total oncoming ions given by time integration of the pulse wave form. All these effects are produced by the increase in both the separation speed of the monopolar ions in the plasma region and the migration speed of the separated ions in the gap.

Next, the effect of the delay time, τ_d, on the wave form is observed with the magnitudes of V_p and E_{dc} unaltered (Fig. 3). The first spike is induced by the pulse voltage applied across the wires, and the second small pulse by the step-wise application of the dc voltage. The interval between the second and third pulses as a measure of the ion transit time remains almost unchanged with increasing τ_d when E_{dc} is kept constant. The time integration of the third pulse as the total arriving ions, on the other hand, decreases with τ_d.

Then,the effect of the polarity of the dc extracting field is investigated. First, the positive ions are extracted in the case when a sufficiently high pulse voltage $V_p = -47$ kV is applied so as to produce both negative and positive streamers, and the dc high voltage is applied at zero delay time. The wave form in this case is shown in Fig. 4 (a). For comparison, Fig. 4 (b) shows the wave form when the negative ions are extracted under otherwise the same condition. It can be seen that the wave forms of positive and negative ionic current agree quite well, although the charge carried by positive ions is slightly less than that by negative ions. Second, the same comparison is made with a lower dc voltage possible to produce only negative streamers. The results obtained are shown in Fig. 5. In this case, the amount of positive ions extracted becomes much less than that of negative ions. Its difference becomes larger in the case when the pulse voltage V_p is in the lower level to produce only negative streamers.

AMOUNT OF EXTRACTED IONS

Changing τ_d with keeping V_p and E_{dc} constant, the total charge of the negative ions arriving at the measuring electrode M in Fig. 1 (b) is measured. The measurements are made for $V_p = -55$ kV and $V_p = -37$ kV. In the former case both positive and negative streamers occur, as shown in Fig. 6 (a). Whereas, in the latter case, only negative streamers with much less luminosity appear, as indicated in Fig. 6 (b).

The measured charge Q_i for these cases are plotted against the delay time, τ_d, in Figs. 7 and 8, respectively.

Then, the same experiment is made for the positive ions extracted. The results obtained at a lower pulse voltage $V_p = -35$ kV (only negative streamers) and $E_{dc} = 4$kV/cm are plotted against τ_d in Fig. 9. The results for the negative ions extracted are also indicated in this figure. Again in this figure, it is clearly shown that the number of negative ions extracted is larger than that of positive ions, but the rate of its decay with τ_d is almost the same.

It can be seen from these figures that
(i) the number of negative ions possible to extract from the plasma drops rapidly with increasing delay time, τ_d, probably because of a continued ion recombination process, (ii) this number of ions is also dependent upon the magnitude of the extracting dc field, E_{dc}, especially at its lower level, (iii) in spite of a great difference in luminosity between the plasma produced by both negative and positive streamers (Fig. 7) and that by negative streamers only (Fig. 8), the number of negative ions possible to extract does not indicates much difference: the former providing only twice the negative

ions by the latter, and (iv) as for the polarity of ions, the negative ions can be extracted in a greater amount than positive ions, but the dependence of the ion number possible to extract is almost the same.

DISTRIBUTION OF IONIC CHARGE ON THE ION COLLECTING ELECTRODE

The streamers produced by the extremely short pulse voltage between the wires do not represent a uniform plane-like plasma ion source with a constant ion density. Its irregularity will produce non-uniformity in the charge on the ion collecting electrode in the transverse direction perpendicular to the wires. Fig. 10 indicates the measured distribution of the ionic charge collected. Fig. 10 (a) and (b) show the results obtained at a high voltage V_p=-45 kV (both positive and negative streamers) for the negative and positive ions extracted, respectively. The pattern of the distribution does not change dependent on the polarity of the ions. In both cases, the charge becomes minimum at the points just below the wires. Fig. 10 (c) and (d) are the results obtained at a low pulse voltage V_p = -35 kV (only negative streamers) for the negative and positive ions extracted, respectively. Again in this case, the distribution is not much dependent on the polarity of ions, but the total charge of negative ions becomes about twice the charge of positive ions. It can also be seen that the distribution is not much dependent on whether both negative and positive streamers are produced, or negative streamers only.

SIMULATION OF ION SEPARATION PROCESS

The following mathematical model of ion separation process is proposed to perform its computer simulation, and its results compared with the experimental data. The model is two-dimensional, taking two infinitely large parallel plane electrodes, A and B, respectively a series of corona wires and an ion collecting electrode. The ion separation proceeds in the sequence as shown in Fig. 11 (a) - (d).

(i) Stage I (Fig. 11 (a)): At an instant of streamer formation, a uniform sheet of plasma with a thickness L_0 and ion density n_0 is produced over the entire surface of A. In the later process of ion separation, no free electrons are considered as this proceeds slowly so that all the free electrons are attached to electronegative gas molecules to form negative ions. In the subsequent period of delay time, τ_d, the bipolar ions in the plasma are allowed to recombine according to:

$$\frac{dn}{dt} = - \alpha n_p n_n \tag{1}$$

where α = recombination coefficient, n_p, n_n = number densities of positive and negative ions, and n represents either n_p or n_n.

(ii) Stage II (Fig. 11 (b)): Then, the extracting dc field is applied, and the ions of both polarities start to separate by migration driven by the time-varying local field, E(x,t). The velocity of ions is taken as μE where μ represents ion mobility. The ions of one polarity are collected by the electrode A, whereas those of another polarity migrate towards the electrode B. In this stage there are three different regions of ions; the regions of positive ions only, bipolar ions, and negative ions only. The number density of ions of each polarity is assumed to be uniform in each region. The solution of Poisson's Equation differs dependent on the region, and is given by the following equations.

a) Region of positive ions ($0 \leqq x < L_3$):

$$E(x) = -\frac{en_p}{\varepsilon_0}x + \left[\frac{1}{L}\left\{V_0 - \frac{e}{2\varepsilon_0}\left(-n_nL_1{}^2 + n_nL_2{}^2 + n_pL_3{}^2\right)\right\}\right] - \frac{en_n}{\varepsilon_0}L_1 + \frac{en_n}{\varepsilon_0}L_2 + \frac{en_p}{\varepsilon_0}L_3 \qquad (2)$$

b) Region of bipolar ions ($L_3 \leqq x < L_2$):

$$E(x) = \frac{1}{L}\left\{V_0 - \frac{e}{2\varepsilon_0}\left(-n_nL_1{}^2 + n_nL_2{}^2 + n_pL_3{}^2\right)\right\} - \frac{en_n}{\varepsilon_0}(L_1 - L_2) \qquad (3)$$

c) Region of negative ions ($L_2 \leqq x < L_1$):

$$E(x) = \frac{en_n}{\varepsilon_0}x + \left[\frac{1}{L}\left\{V_0 - \frac{e}{2\varepsilon_0}\left(-n_nL_1{}^2 + n_nL_2{}^2 + n_pL_3{}^2\right)\right\} - \frac{en_n}{\varepsilon_0}L_1\right] \qquad (4)$$

d) Ion-free region ($L_1 \leqq X < L$):

$$E(x) = \frac{1}{L}\left\{V_0 - \frac{e}{2\varepsilon_0}\left(-n_nL_1{}^2 + n_nL_2{}^2 + n_pL_3{}^2\right)\right\} \qquad (5)$$

where V_0 = dc voltage applied between A and B, e = elementary charge, ε_0 = electrical permitivity of free space, and L, L_0, L_1, L_2, L_3 are indicated in Fig. 11. In the region of bipolar ions, the recombination continues to occur according to Eq. (1) to decrease each ion concentration. The fractions of monopolar ions separated from the bipolar region in each time step of computer simulation are added, respectively to the regions of positive and negative ions in the next time step, and the averaging is repeated of ion concentration in each region. The cloud of separated negative ions migrating towards B undergoes an electrostatically induced expansion with increasing cloud thickness. This contributes to the increase in the duration time of the current pulse measured at the electrode B. In such a way, ions arrive at the electrode B one after another.

(iii) Stages III and IV (Fig. 11 (c) and (d)): These are the stages of ion migration after the bipolar region has disappeared. In the case when the electrode gap, L, is small, the stage II is followed by the stage III'. The field intensity in each region is given by Eqs. (2) - (5).

Using the model described above, computer simulations of the entire ion separation process is made for the assumed initial values of n_0 and L_0.

The curves in Fig. 12 show the results of the simulation using $n_0 = 6 \times 10^9$ /cm^3, $L_0 = 1.6$ cm. The measured values in Fig. 7 taken at a high pulse voltage to produce both positive and negative streamers are also plotted. The agreement between the simulation and the measured values is very good.

Fig. 13 gives the same results using initial values, $n_0 = 5 \times 10^9$ /cm^3, $L_0 = 1.0$ cm. These again agree quite well with the experimental plots transfered from Fig. 8 measured at a low pulse voltage to produce only negative streamers.

Next, the ionic current wave forms are derived by the simulation and compared with those measured with a grid in Fig. 14 (a) and (b). Fig. 14 (c) shows a similar comparison between simulation and measured for the case when the grid is removed so that displacement current is being observed. Again in Fig. 14 a good agreement can be seen between the simulation and measured.

The results of curve fitting in Fig. 12, 13 and 14 are likely to support the validity of the mathematical model of ion separation process produced above. Hence, the initial plasma density is assumed to be about 5 - 6 x 10^9 /cm^3 independent of the magnitude of pulse voltage V_p, i.e. whether both positive and negative streamers are produced, or only negative streamers are formed.

It should be noted in this place that the simulation produces no appreciable difference between the positive and negative ions. In reference to Fig. 9, however, the measured results obtained at a low pulse voltage indicate a substantial difference far beyond the estimation by simulation. This may be explained by a large segregation of positive and negative ions of plasma specific to the negative streamers. It is considered in this case that negative ions are localized in a region close to the mother wires, and may be subjected to a strong local extracting field to produce detachment of electrons with a very high mobility. In the case when both negative and positive streamers are produced, this strong local field will be screened by the abandant positive ions existing around the mother wires.

CONCLUSIONS

The investigations are made on the initial plasma density of streamers produced by an extremely short pulse high voltage with ca. 70 nano-seconds half duration time, and also on the process of ion separation induced by the dc extracting field. The results obtained by experiments and simulations lead to the following conclusions:

1) The initial number density of plasma estimated from the comparison between measured and simulation curves of ionic charge collected as a function of delay time provides (5 - 6) x 10^9 /cm^3 independent of whether both negative and positive streamers or only negative streamers are produced.

2) The number of ions possible to extract by dc field from the plasma is about two times higher for negative ions than for positive ions in the case when only negative streamers are produced.

3) Although the streamers as plasma ion source are produced in a very short time of about 10 nano-seconds, the current pulse by ions extracted and arriving at the ion collecting electrode indicates a much longer duration time amounting to 2 - 3 milliseconds. This is due to a fairly long recombination-dependent plasma life time and a slow ion separation process. This duration time and the ion transit time decrease with increasing extracting field intensity, while the pulse height and total charge of separated ions rise concurrently. The increase in the delay time of application of the dc extracting field causes the lowering of the pulse height and total charge as a result of ion recombination occuring in the plasma. The plasma density after recombination of 2 - 3 milli-seconds becomes one order of magnitude lower than its initial value.

4) In the mathematical model used for the simulation of ion separation process the time-dependent local value of field intensity is derived by solving Poisson's Equation in different regions of monopolar and bipolar ions, and the local velocity of ions are calculated from this field intensity using ion mobility. The recombination of ions is considered in the bipolar region. The electrostatically induced expansion of monopolar ionic cloud appears in the collective motion of the ionic cloud.

5) The computer-simulated curves of the ionic charge vs. time delay assuming suitable value of n_0 and L_0 allow a very good fitting with the measured values, and this enables the estimation of n_0 as above. The validity of the simulation is confirmed also by comparison of the computer simulated ionic current wave forms with the measured ones.

6) The transverse distribution of ionic current on the ion collecting electrode is fairly irregular with a large dip in the positions below the wires.

REFERENCES

1. Milde, H.I. and Feldman, P.L. Conf. Rec. of IEEE/IAS 1978 Annual Meet., 66.
2. Masuda, S. and Hosokawa, S. Performance of Two-Stage Electrostatic Precipitators, Conf. Rec. IEEE/IAS Annual Meet. 1982 (to be published.)
3. Masuda, S. and Nakatani, H. Distortion of Pulse Voltage Wave Form on Corona Wires Due to Corona Discharges. 1982 EPA-Symposium on Transfer and Utilization of Particulate Control Technology (Oct. 1982 to be published)
4. Masuda, S., Nakatani, H., Yamada, K., Arikawa, M. and Mizuno, A. Production of Monopolar Ions by Travelling Wave Corona Discharge, Conf. Rec. IEEE/IAS Annual Meet. 1981
5. Masuda, S. Mizuno, A., Nakatani, H. and Kawahara, H. Application of Boxer-Charger in Pulsed Electrostatic Precipitator, Conf. Rec. IEEE/IAS pp.904-911, 1980
6. Masuda, S., Nakatani, H., Kawahara, H. and Mizuno, A. Particle Charging with Travelling Wave Corona Discharge, Journal of Electrostatics, pp.171-176, 1981

The work described in this paper was not funded by U.S.Environmental Protection Agency and therefore the contents do not necessary reflect the views of the Agency and no official endorsement should be inferred.

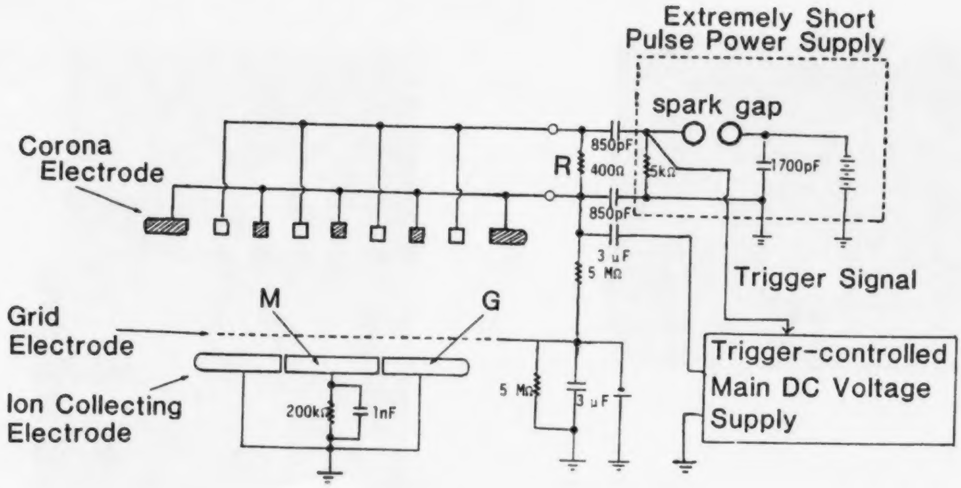
Extremely Short
Pulse Power Supply
spark gap
Corona
Electrode
850pF
R
400Ω
5kΩ
1700pF
850pF
3 μF
5 MΩ
Trigger Signal
M
G
Grid
Electrode
Ion Collecting
Electrode
200kΩ
1nF
5 MΩ
3 μF
Trigger-controlled
Main DC Voltage
Supply

(a) Current Wave Form Measurement

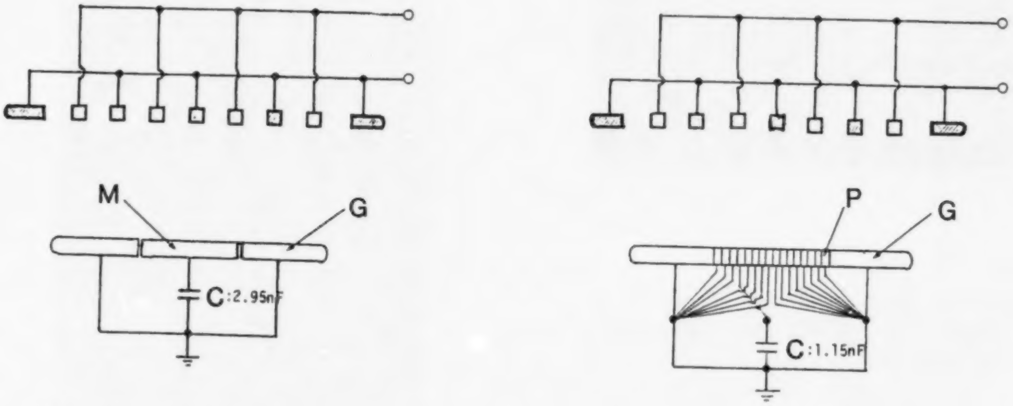
M
G
C:2.95nF
P
G
C:1.15nF

(b) Total Ionic Charge Measurement

(c) Plasma Density Distribution Measurement

▨----mother wires
☐----daughter wires
G--- guard electrode
M---measuring electrode

C----condenser for charge measurement
P----strip-like electrode

Fig. 1 Experimental Appatatus

Reproduced from
best available copy.

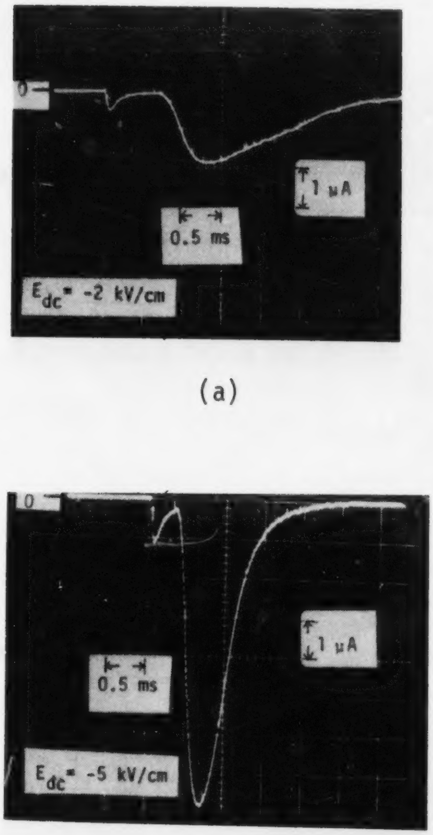

(a)

(b)

Fig. 2 Effectof DC Extracting Field, E_{dc}, on Wave Form of Negative Ionic Current
(τ_d = 0, V_p = -37 kV)

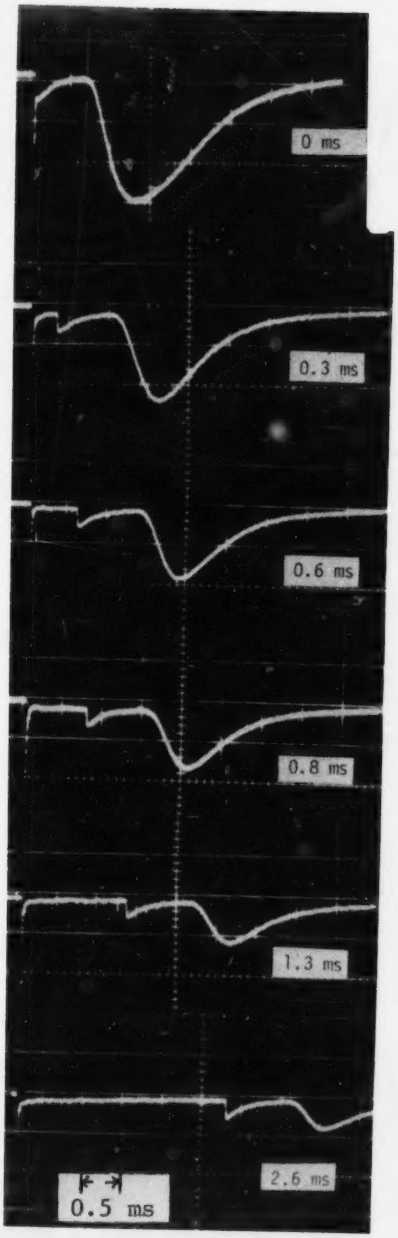

Fig. 3 Effect of Delay Time, τ_d, on Wave Form of Negative Ionic Current
(V_p = -37 kV, E_{dc} = -3 kV/cm)

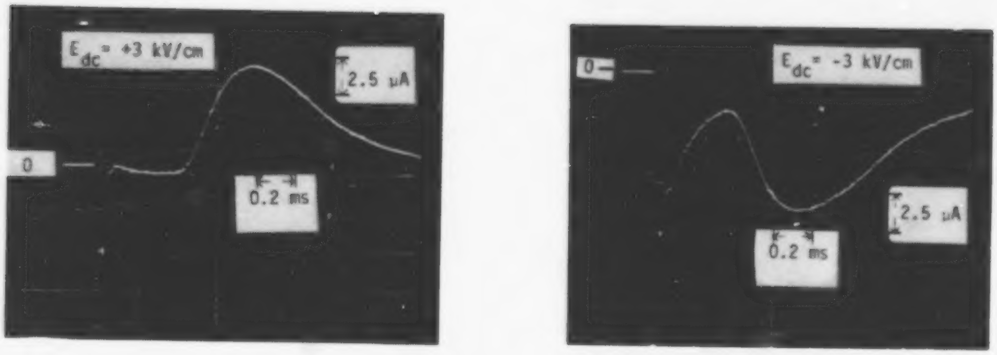

(a) positive ionic current (b) negative ionic current

Fig. 4 Comparison of Wave Form between Positive and Negative Ionic Currents
(V_p= -47 kV, E_{dc}= 3 kV/cm, τ_d= 0; both negative and positive streamers)

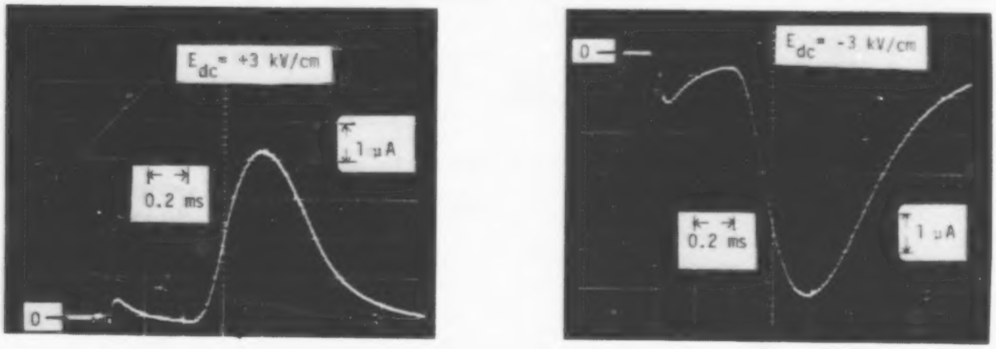

(a) positive ionic current (b) negative ionic current

Fig. 5 Comparison of Wave Form between Positive and Negative Ionic Currents
(V_p= -35 kV, E_{dc}= 3 kV/cm, τ_d= 0; only negative streamers)

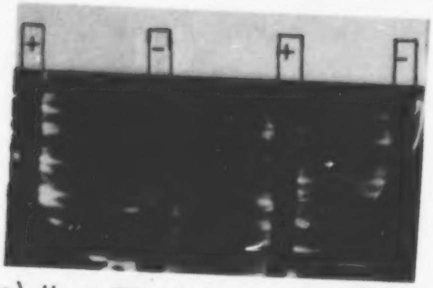

(a) V_p= -55 kV (both negative and positive streamers)

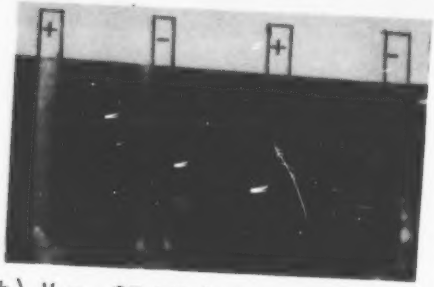

(b) V_p= -37 kV (only negative streamers)

Fig. 6 Photograph of Streamers Observed with Image Intensifier (pulse duration time τ_h= 70 ns; EMI Type 9912)

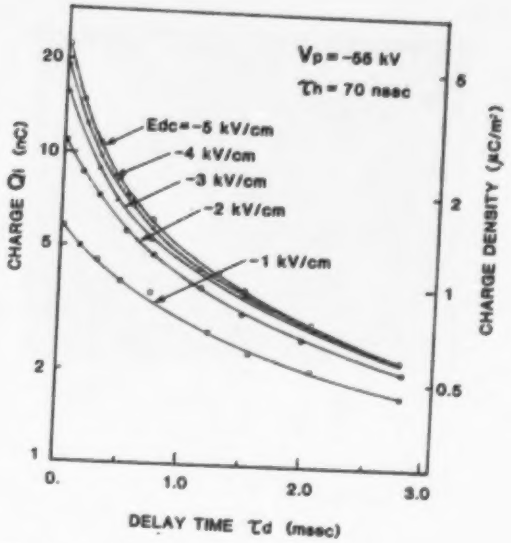

Fig. 7 Charge of Negative Ions Collected vs. Delay Time (both negative and positive streamers produced)

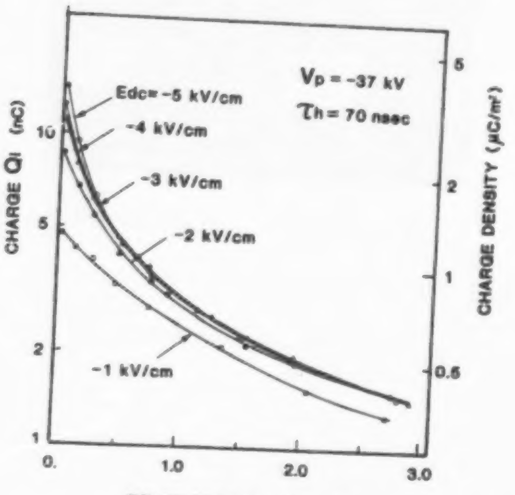

Fig. 8 Charge of Negative Ions Collected vs. Delay Time (only negative streamers produced)

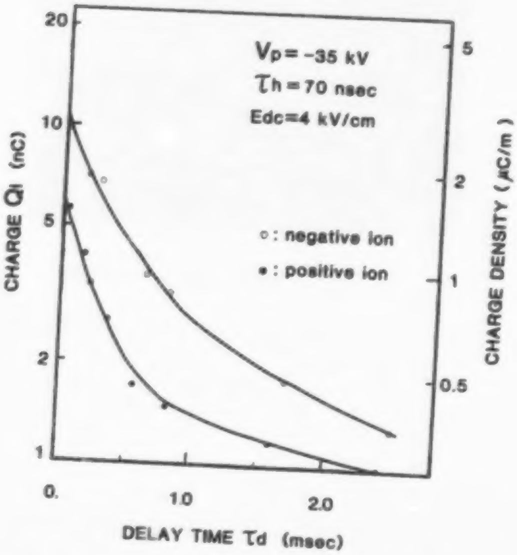

Fig. 9 Comparison of Charge Collected as a Function of Delay Time between Negative and Positive Ions

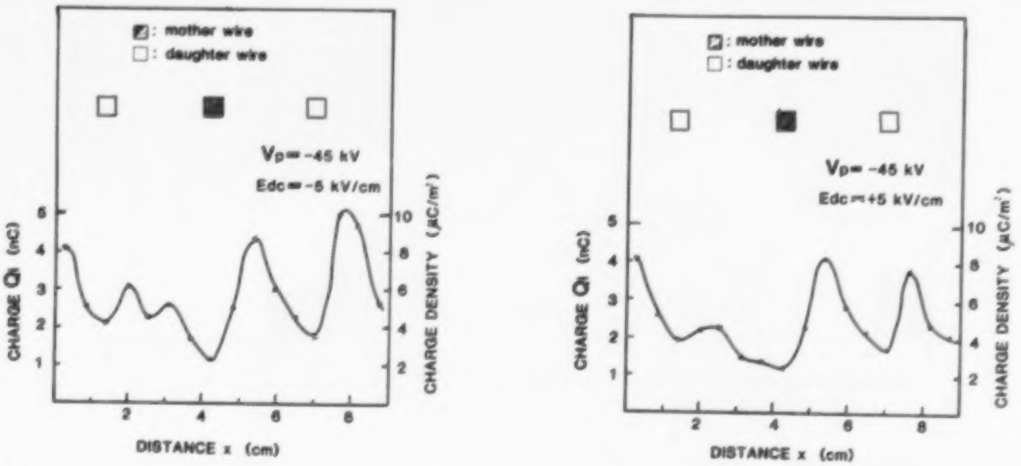

(a) negative ionic charge
(negative and positive streamers)

(b) positive ionic charge
(negative and positive
streamers)

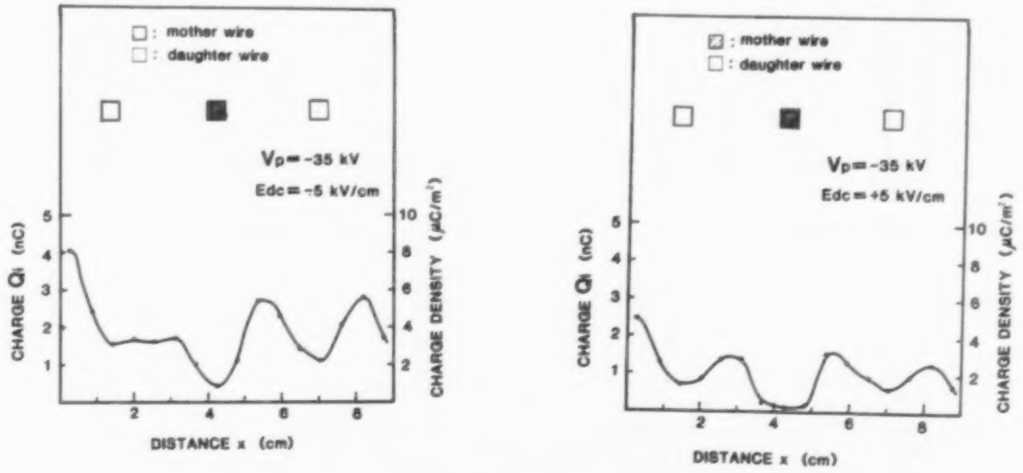

(c) negative ionic charge
(negative streamers only)

(d) positive ionic charge
(negative streamers only)

Fig. 10 Transverse Distribution of Collected Ionic Charge

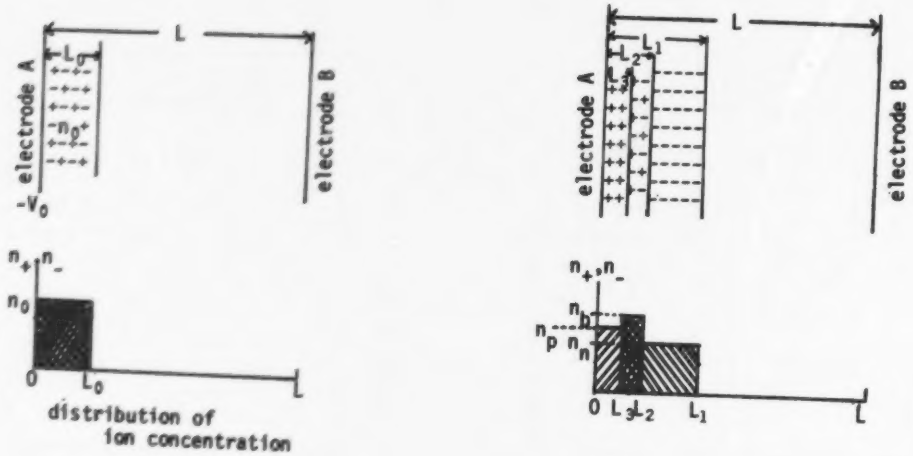
L
L0
electrode A
electrode B
-n0+
-V0
n+,n-
n0
0
L0
L
distribution of ion concentration
L
L2
L1
L3
electrode A
electrode B
n+,n-
nh
np
nn
0
L3
L2
L1
L

(a) Stage I

(b) Stage II

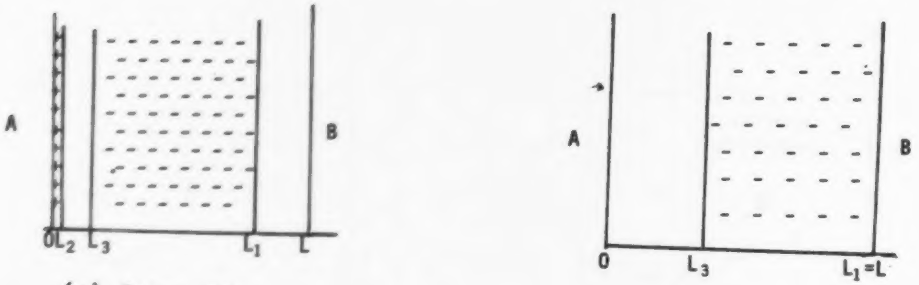
A
B
0
L2
L3
L1
L
A
B
0
L3
L1=L

(c) Stage III

(d) Stage IV

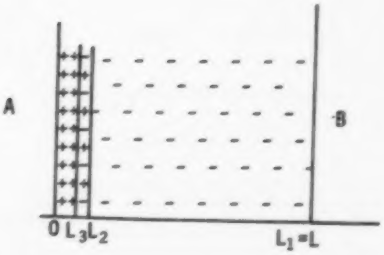
A
B
0
L3
L2
L1=L

(e) Stage III'

Fig. 11 Model of Ion Separation Process

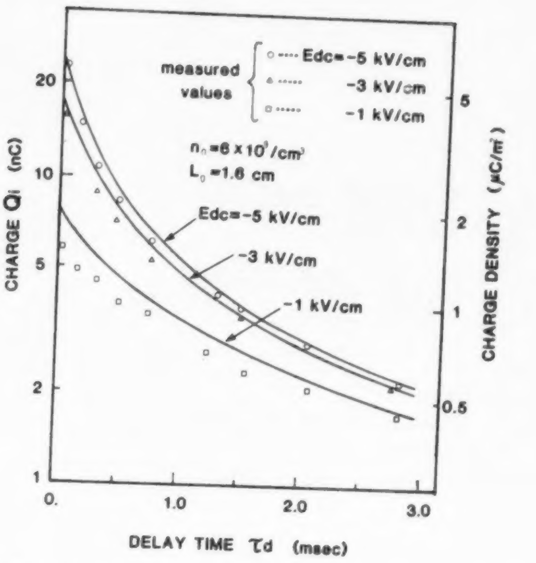

Fig. 12 Comparison between Computer-Simulated Curves and Measured Values of Charge of Negative Ions Collected vs. Delay Time
(V_p= -55 kV: negative and positive streamers)

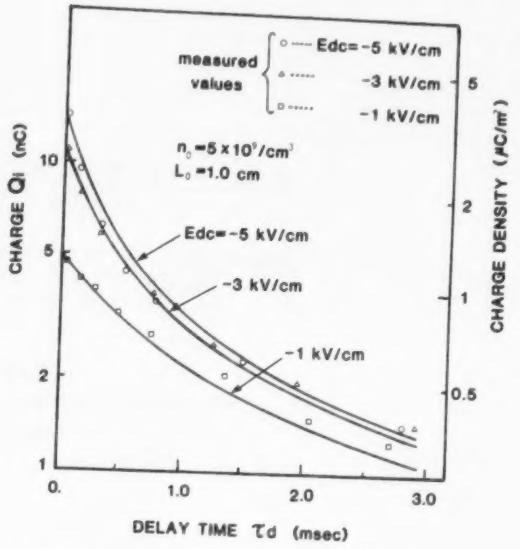

Fig. 13 Comparison between Computer-Simulated Curves and Measured Values of Charge of Negative Ions Collected Vs. Delay Time
(V_p= -37 kV: negative streamers only)

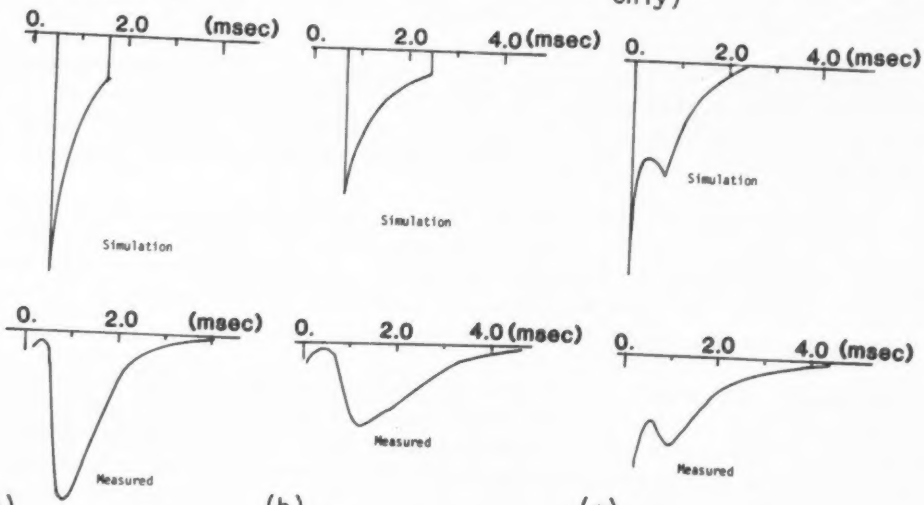

(a)
V_p= -55 kV, τ_d= 0,
E_{dc}= -4 kV/cm,
n_0= 6 x 10^9 /cm^3,
L_0= 1.6 cm
(with grid)

(b)
V_p= -55 kV, τ_d= 0,
E_{dc}= -2 kV/cm,
n_0= 6 x 10^9 /cm^3;
L_0= 1.6 cm
(with grid)

(c)
V_p= -55 kV, τ_d= 0,
E_{dc}= -2 kV/cm,
n_0= 6 x 10^9 /cm^3
L_0= 1.6 cm
(grid removed)

Fig. 14 Comparison between Simulated and Measured Wave Forms of Ionic Current

A NEW CORRECTION METHOD OF MIGRATION VELOCITY IN DEUTSCH EFFICIENCY EQUATION FOR CONVERSION OF ELECTROSTATIC PRECIPITATOR SIZING FROM A PILOT-SCALE TO A FULL-SCALE

BY:
FUMIO ISAHAYA
Hitachi Plant Engineering & Construction Co.,Ltd.
Research laboratory
1-1-14 Uchikanda, Chiyoda-ku, Tokyo 101, Japan

ABSTRACT

In order to confirm the validity of the Deutsch efficiency equation, the deposition rate distribution on the collecting electrode wall of a small size cylindrical type precipitator having a diameter of 30 mm and length of 400 mm was measured by utilizing a radioactive aerosol tracer technique.

The Thorium B solid particles as testing radioactive aerosols having a relatively uniform particle size of approximate 0.1 microns were used. As a result, the concept of the Deutsch efficiency equation was held tolerably good in the range of the gas velocity of 0.35 - 1.0 m/s, S.C.A. of 35 - 106 s/m and corona current density of 2.5 -13 μA/cm.

Accordingly, in order to put the Deutsch migration velocity to practical use in industry and to predict the required sizing and S.C.A. for a full-scale precipitator on the basis of the test results in pilot-scale one, such a new correction formula for the migration velocity in the Deutsch efficiency equation which can be corrected as a function of the aspect ratio of collecting electrode, spacing of electrode, treating gas velocity, S.C.A., corona current density, particle size distribution, a wide spacing effect and re-entrainment effect, was proposed. Furthermore, according to this formula the performance characteristics curves of collection efficiency versus S.C.A. for a pilot-scale and full-scale precipitator were given in comparison with the both in the range of the industrial use such as a coal-fired boiler plant.

INTRODUCTION

At the present state, the most reliable source of data for the prediction , evaluation and correction of the Deutsch migration velocity for the precipitator sizing for the new duty can be obtained on the basis of an actual test result in a pilot-scale electrostatic precipitator. However, the Deutsch migration velocity in a pilot-scale precipitator represents usually several times too high, compared with one of a full-scale precipitator. It has been living yet as one of the important problem awaiting solution that the reason why such a difference in the Deutsch migration velocity arises from.

The purpose of this paper is to make clear the reason for this distinct difference, furthermore to propose a new correction method of the migration velocity in the Deutsch efficiency equation for the conversion of precipitator sizing from a pilot-scale to full-scale. For instance, a usual pilot-scale precipitator has been designed with the collecting electrode height of approximate 1 - 3 m, its length on the direction of gas flow of approximate 1 - 5 m and S.C.A of approximate 15 - 100 s/m, in such case, the Deutsch migration velocity will usually represent several times too high, compared with one of a full-scale precipitator, in spite of the same testing and operating conditions between the both, such as the electrode configuration, rapping method, electrode spacing, corona current density, treating gas velocity, gas temperature, gas composition, dust particle properties and even S.C.A..

As the first step of this investigation, in order to confirm the validity of the Deutsch efficiency equation, the deposition rate distribution on the collecting wall of a small model precipitator was measured by utilizing a radioactive aerosol tracer technique using the Thorium B solid particles. Then the next step one, depending on the basis of the Deutsch migration velocity obtained from the test results in a pilot-scale precipitator, a new correction formula for the Deutsch migration velocity and S.C.A. satisfied the requirement of collection efficiency of a full-scale precipitator was proposed . Furthermore, according to this formula the performance characteristics curves of collection efficiency versus S.C.A. for a pilot-scale and full-scale precipitator were given in comparison with the both in the range of the industrial use such as a coal-fired boiler plant.

On a realistic precipitator design, it has been found widely acceptance with an international field of an electrostatic precipitation technology that the Deutsch migration velocity can be utilized as a mental image design parameter. It is widely accepted with the practical design of the electrostatic precipitator that the fundamental characteristics of collection efficiency under the influence of turbulent flow was given by the following classical Deutsch efficiency equation[1], later refined by White[2],

$$\eta = 1 - \exp - (\omega \cdot \text{S.C.A.}) \tag{1}$$

where, η is the collection efficiency, ω the Deutsch migration velocity, S.C.A.= A/Q the specific collecting area, A the effective area of collecting electrode, Q the volumetric flow rate of treating gas.

Hereupon, it is a noticeable matter that the so-called Deutsch migration velocity cannot be measured directly by some instrumentation means, it should be derived from the equation (1), giving the S.C.A. as a design parameter and the collection efficiency on the basis of the actual test results in an operating precipitator. Also simultaneously, the physical meaning of such Deutsch migration velocity is macroscopically defined as an average value based on a time and space- dependence for the charged particles cloud passing through a precipitator under the influence of the corona electric field in a turbulent flow in which some uncertain phenomena for the charged particles aerodynamic behaviour such as a turbulent diffusion, mutual coagulation, re-entrainment of the dust layer on collecting electrode and flow disturbance due to ionic wind are included. Therefore, a thoretical migration velocity for a single charged particle in a laminar flow under the influence of the static electric field and which can be derived from a force balance between the Coulomb's force and the Stokes's force becomes several times higher than the Deutsch migration velocity. Furthermore, currently the migration velocity measured by a laser Doppler velocimeter for a horizontal duct type model precipitator has been reported[3] and it shows a much higher experimental value by a factor of several ten times in comparison with the Deutsch migration velocity in industrialprecipitator. This experimental results suggest that an instantaneous velocity due to a specified time and space-dependence in the precipitation zone is measured with this method. Thus, the migration velocity based on the thoretical calculation or the experimental measurement as mentioned before is not meaningful as a means of predicting or evaluating the precipitator sizing and S.C.A. to a realistic designing for an industrial precipitator.

On the other hand, depending on the equation (1), the mathematical simulation model considered the influence of particle size distribution and electric field pattern has been investigated and the collection efficiency was computed numerically[4]. However, in this mathematical model analysis, since the influence of uncertain factors in precipitation phenomena such as a particle coagulation, re-entrainment of dust layer on collecting electrode, flow disturbance due to ionic wind, aspect ratio and configuration of collecting electrode are un-accounted, it has never been reached completion to be utilized as a simulation model, particularly the conversion of precipitator sizing from a pilot-scale to full-scale.

In other words, from a stand point of a realistic idea on a precipitator designing, the Deutsch migration velocity means a mental image design parameter in which the whole of capturing processes in dust particles from an electro-hydro-dynamics separation in turbulent gas flows until an effective gravity settling motion toward the hoppers should be included.

CONFIRMING THE VALIDITY OF DEUTSCH EFFICIENCY EQUATION BY UTILIZING A RADIOACTIVE TRACER TECHNIQUE USING THE THORIUM B AEROSOL PARTICLES[5,6]

EXPERIMENTAL PROCEDURE

The radioactive Thorium B aerosol particles were generated by an atomic disintegration of the Thoron (Rn) gas which were diffused from the Thorium oxide powders of approximate 2.5 kg piled on the bottom in the vessel having an inlet and outlet air valve. This radioactive gas with the decay half-life of approximate 54.6 sec. is disintegrated into the Thorium B of a fine solid particles, the following one another the Thorium B with the decay half-life of approximate 10.6 hours is disintegrated into the Thorium D (Pb) and finally becomes stable. The radioactive aerosol particles of Thorium B generated by such procedure were introduced into a small size cylindrical type model precipitator having a diameter of 30 mm, its length of 400 mm and a diameter of corona discharge wire of 0.4 mm, and then they were electrostatically collected on a stainless steel foil sticked closely on the inside wall of the cylindrical collecting electrode. The corona current density and treating air velocity as the experimental parameters were varied and for each experimental conditions the radioactivity of deposition rate distribution of Thorium B particles versus the down stream location of collecting electrode were measured by a radioactivity detecting instrument.

As the first step of this experiment, in order to confirm whether Thorium B would be or not, its decay half-life of the radioactivity, beta-ray and gamma-ray energy spectrum was measured. As a result, it was clearly shown that it must be Thorium B because of a decay half-life of 10.6 hours, maximum beta-ray energy of approximate 2.3 MeV and peak gamma-ray spectrum of 0.23 MeV . Furthermore, Fig.1 shows the photograph of an electron-microscope for the Thorium B particles having a relatively uniform size of approximate 0.1 μm.

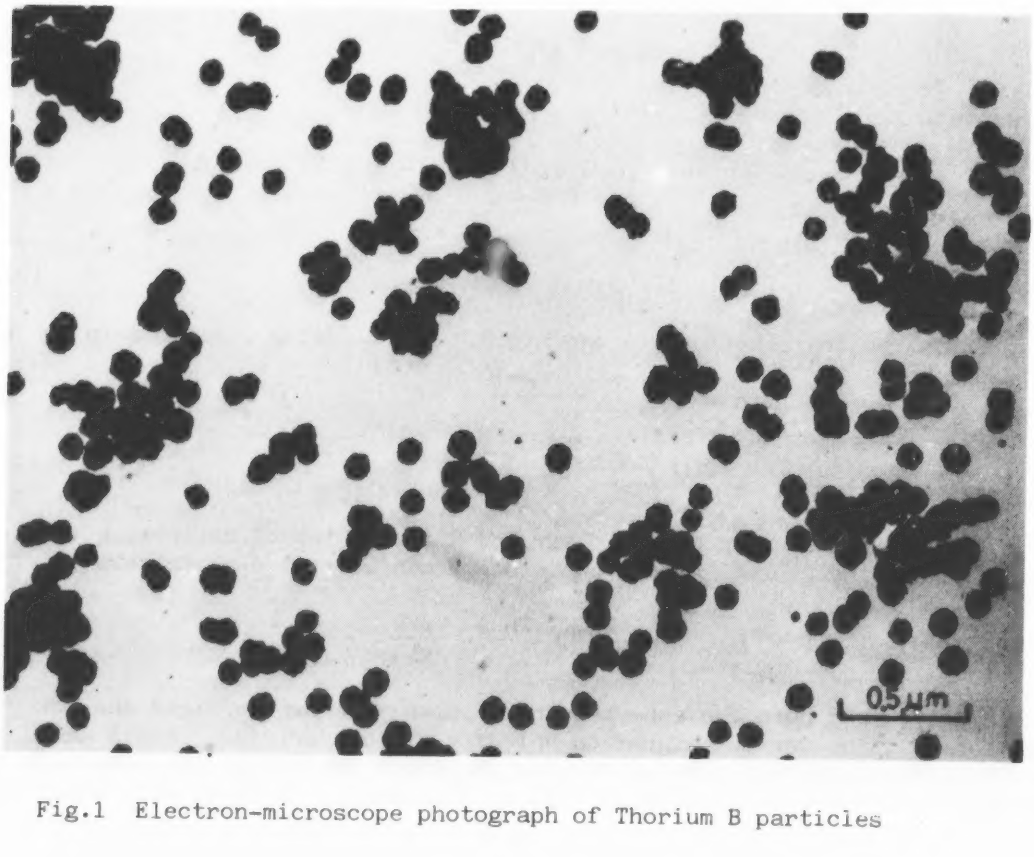

Fig.1 Electron-microscope photograph of Thorium B particles

EXPERIMENTAL RESULTS AND ITS INVESTIGATION

As shown in Fig.2, one of the representative examples in these experimental results, the Thorium B particles deposition rate per unit area of collecting electrode toward down stream represents a tendency which increases rapidly and reaches a peak point, after that, on the contrary, decreased exponentially toward the down stream.

The experimental results with such a tendency were found in the data of Mierdel and Seeliger[7] (1935) and Robinson[8] (1967) who had measured the deposition rate distribution on the collecting wall of a model precipitator using a usual testing dust. However, the effect of corona current density on the deposition rate was not clearly stated in these references.

The analysis in this paper were carried out within the zone showing an exponential decay of the deposition rate. Further, the required time to reach a peak deposition rate as mentioned above is suited for the so-called Pauthenier saturation charging time for a single sphere particle.

Now, the collecting electrode is divided into n segments having an equal length of ΔL along the down stream and the inlet particles concentration is C, volumetric treating gas flow rate Q, furthermore when the probability of deposition rate $\Delta\eta$ per unit length ΔL is kept constant, thus the deposition rate Wn for the nth segment can be given as follows

$$Wn = C\,Q\,(1-\Delta\eta)^{n-1}\cdot\Delta\eta, \qquad (2)$$

correspondingly,

$$\begin{aligned} \ln Wn &= \ln C\,Q\Delta\eta + (n-1)\ln(1-\Delta\eta) \\ &= a + (n-1)\,b, \end{aligned}$$

hence,

$$\Delta\eta = 1 - \exp - (b). \qquad (3)$$

Thus, from the equation (1) and Fig.2, the following relationship can be derived

$$\begin{aligned} b &= \frac{\ln(Wn_{-1}/Wn)}{d(n)} \\ &= \omega\,\frac{2\cdot\Delta L}{Vg\cdot R}, \end{aligned} \qquad (4)$$

where, Vg is the treating gas velocity and R the radius of collecting electrode. Hence, the Deutsch migration velocity can be stated as follows

$$\omega = \frac{\ln(Wn_{-1}/Wn)}{d(n)}\;\frac{Vg\cdot R}{2\cdot\Delta L} \qquad (5)$$

accordingly, from both the experimental results as shown in Fig.2 and the equation (5), the Deutsch migration velocity can be derived. Fig.3 shows such Deutsch migration velocity for the Thorium B aerosol particles versus the corona current density with the S.C.A. as parameter. It is clearly shown

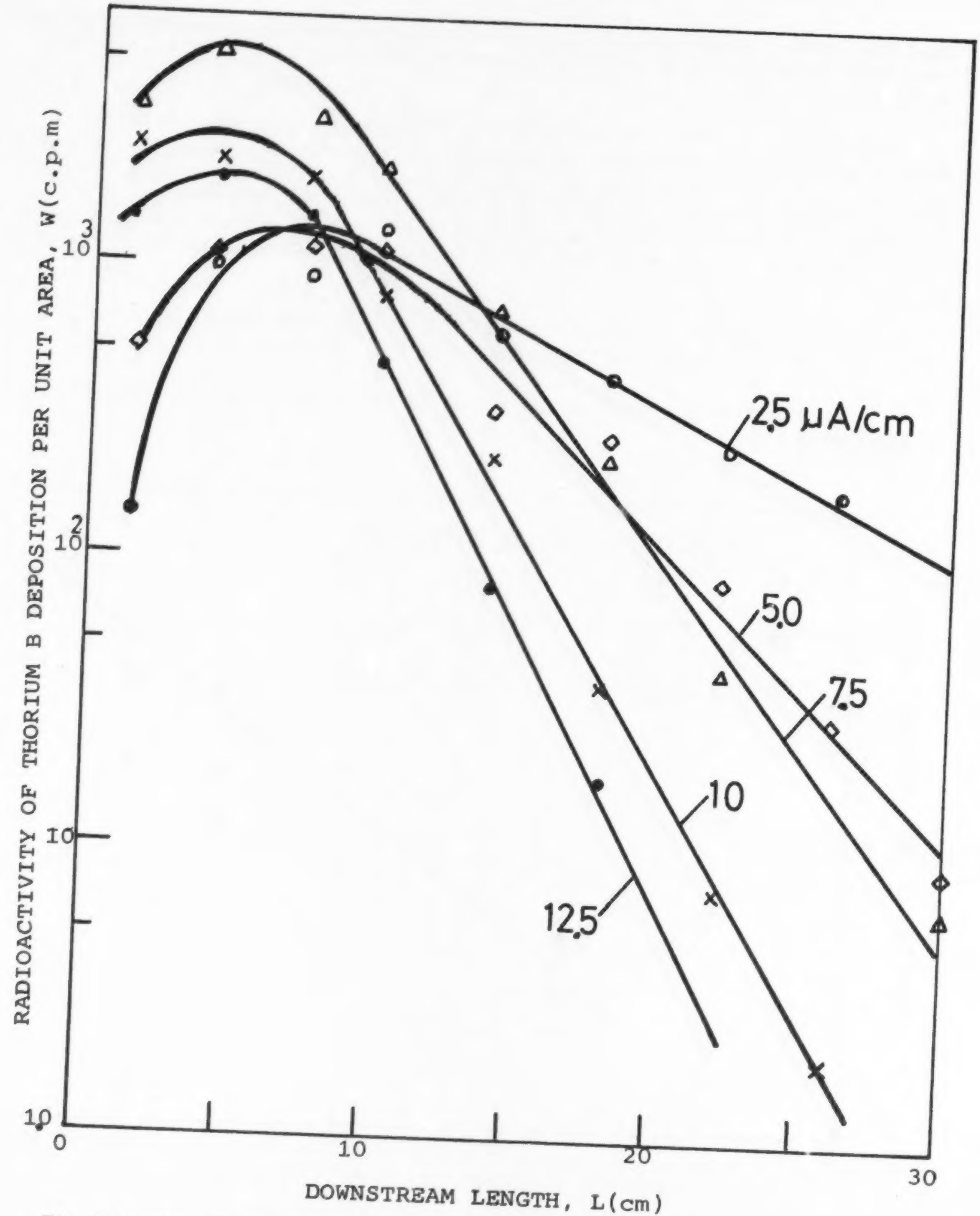

Fig.2 Thorium B particles deposition rate versus downstream location of collecting electrode with corona current density as parameter

that the Deutsch migration velocity is strongly dependent upon the corona current density and has a propotional relation, while it is practically independent upon the S.C.A..

In accordance with the equation (1), the Deutsch migration velocity should be held an unchangeability independently of the S.C.A. or treating gas velocity when a particle size is uniform, properly speaking. Such a relationship is almost consist with this experimental result in the range of the treating air velocity of approximate 0.35 - 1.0 m/s, S.C.A. of approximate 35 - 106 s/m and corona current density of approximate 2.5 - 13 μA/cm as shown in Fig.3.

CORRECTION METHOD OF MIGRATION VELOCITY IN DEUTSCH EFFICIENCY EQUATION FOR CONVERSION OF PRECIPITATOR SIZING FROM A PILOT-SCALE TO FULL-SCALE

In the practical operating condition for an industrial electrostatic precipitator,

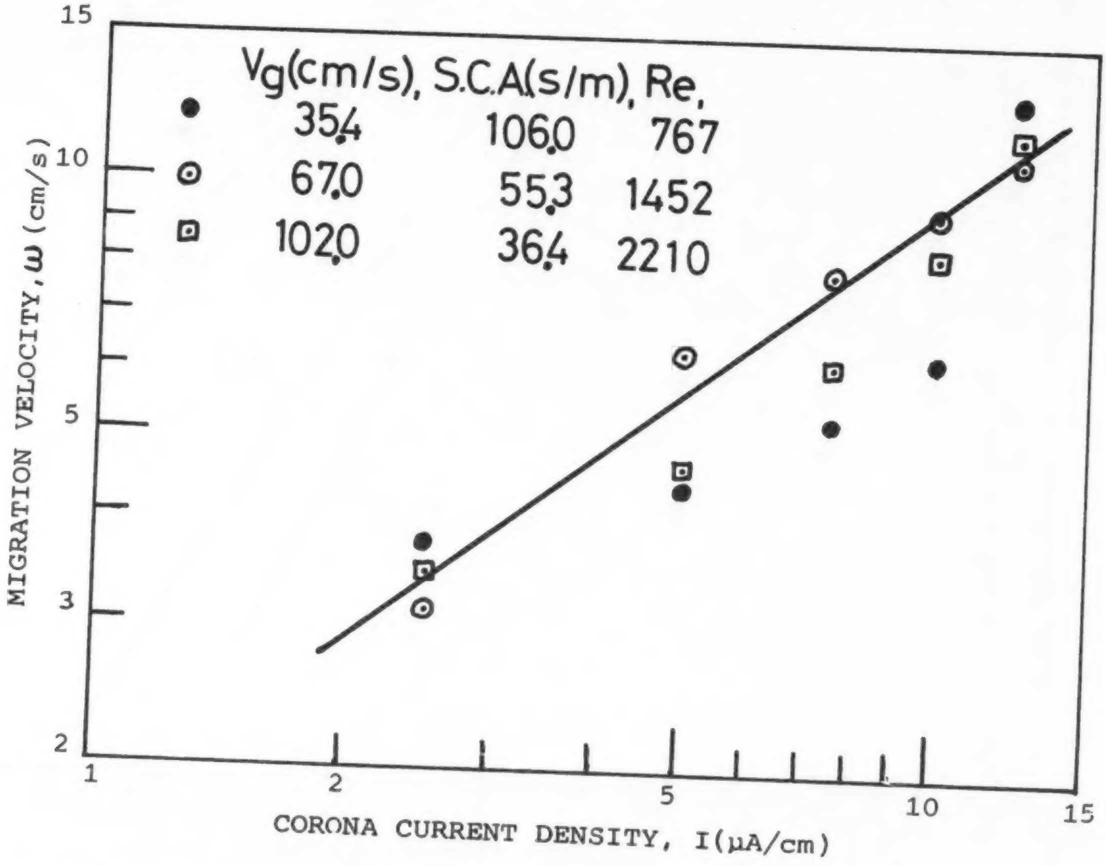

Fig.3 Deutsch migration velocity of Thorium B particles versus corona current density with S.C.A. as parameter

(1) the particles cloud has an wide range of size distribution, approximated to a logarithm normal,
(2) the Deutsch migration velocity is decreased with increasing the S.C.A. or length of the collecting electrode,
(3) a re-entrainment occurs when rapped the collecting electrode or because of the influence of aerodynamics flow disturbance and this also is under a strong influence of the gas velocity and aspect ratio of collecting electrode,
(4) an aerodynamic behaviour of the charged particles cloud is influenced by a particle coagulation, degree of flow turbulence[9] and ionic wind,
(5) an average corona electric field intensity is affected by the geometric configuration and spacing of the collecting and discharging electrode, furthermore a corona current suppression caused by the space charge effect of charged particles cloud,
(6) due to a high resistivity dust layer deposited on the collecting electrode , a back corona, irregular corona discharge and reducing of space potential occurs,
(7) a treating gas velocity in practical use of precipitators should be limited to the approximate 0.6 m/s or more because of the avoidance for a free convectional flow, furthermore the approximate 1.6 m/s or less which is so-called a critical velocity because of the avoidance for an aerodynamic re-entrainment on the collecting electrode.

Considering these matters as stated above, the Deutsch migration velocity should be corrected with the following concepts,

(1) in the items of (1) and (2), the coefficient "α" as a function of the gas flow Reynolds number acting on the aerodynamic behavior of particle represented in a geometric mass median diameter and the coefficient "β" as a function of the geometric standard deviation for the particle size distribution at the inlet of precipitator was introduced as shown in Fig.4 and 5,
(2) in the item of (3), the re-entrainment coefficient given by Isahaya[10] (1979) which was defined as a function of the aspect ratio of collecting electrode, treating gas velocity and effective gravity settling velocity of dislodging dusts from collecting electrode was introduced and this settling velocity is represented as a function of the S.C.A. as shown in Fig.6,
(3) in the item of (4), it is not necessary to correct with each other because these aerodynamic situations between a pilot-scale and full-scale are assumed to be in the same conditions,
(4) in the item of (5), applying the concept for a spread angle of the corona electric field model given by Isahaya[11,12] (1963, 64), an average corona electric field intensity was corrected with the collecting and discharging electrode spacing, furthermore the space charge effect of particles cloud,
(5) in the term of (6), the coefficient "γ" as a function of the resistivity of dust layer on the collecting electrode, dust layer thickness and applied voltage was introduced as shown in Fig.7, then the corona current density was corrected with this coefficient "γ" .

In accordance with the concepts as mentioned above, a new correction formula for the Deutsch migration velocity was proposed as follows,

$$\omega_f = \omega_p\left(\frac{\bar{d}_f}{\bar{d}_p}\right)^{\alpha}\left[\left(\frac{S.C.A._p}{S.C.A._f}\right)\left\{\sqrt{\frac{D_f^2+P_f^2}{D_p^2+P_p^2}}\;\frac{K_p(3+k_fS_fC_fD_f)}{K_f(3+k_pS_pC_pD_p)}\left(\frac{I_f}{I_p}\right)^{\gamma}\right\}^{-1}\right]^{\beta}$$

$$\times\left\{\sqrt{\frac{D_f^2+P_f^2}{D_p^2+P_p^2}}\;\frac{K_p(3+k_fS_fC_fD_f)}{K_f(3+k_pS_pC_pD_p)}\left(\frac{I_f}{I_p}\right)^{\gamma}\right\}\frac{1-\exp-\left(\frac{V_{Gf}}{V_{gf}}\frac{L_f}{H_f}\right)}{1-\exp-\left(\frac{V_{Gp}}{V_{gp}}\frac{L_p}{H_p}\right)}$$

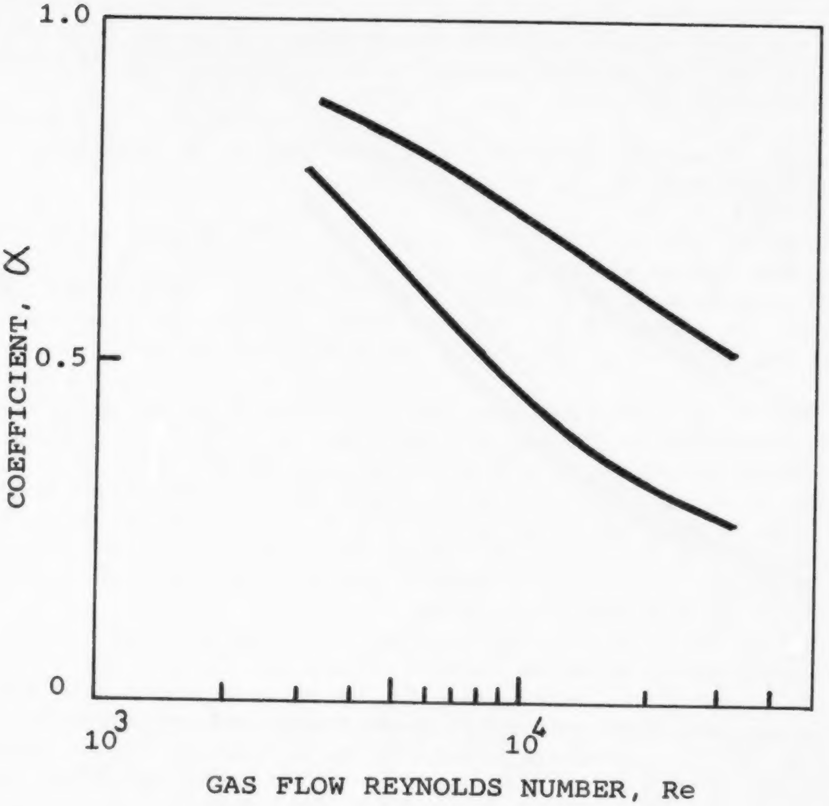

Fig.4 Coefficient α as a function of gas flow Reynolds number in parallel plate collecting electrode

$$=\omega_p \underbrace{\left(\frac{\bar{d}_f}{\bar{d}_p}\right)^{\alpha}\left(\frac{S.C.A._p}{S.C.A._f}\right)^{\beta}}_{\text{Particle Size Distribution and Aerodynamic Behaviour Effect}} \underbrace{\left[\underbrace{\sqrt{\frac{D_f^2+P_f^2}{D_p^2+P_p^2}}}_{\text{Spread Angle of Corona Electric Field Effect}} \underbrace{\frac{K_p(3+k_f S_f C_f D_f)}{K_f(3+k_p S_p C_p D_p)}}_{\text{Space Charge Effect}}\right]^{(1-\beta)} \underbrace{\left(\frac{I_f}{I_p}\right)^{\gamma(1-\beta)}}_{\text{Corona Discharge Mode Effect}}}_{\text{Wide Spacing Effect}}$$

$$\times \underbrace{\frac{1-\exp-\left(\frac{V_{Gf}}{V_{gf}}\,\frac{L_f}{H_f}\right)}{1-\exp-\left(\frac{V_{Gp}}{V_{gp}}\,\frac{L_p}{H_p}\right)}}_{\text{Re-entrainment Effect}} \tag{6}$$

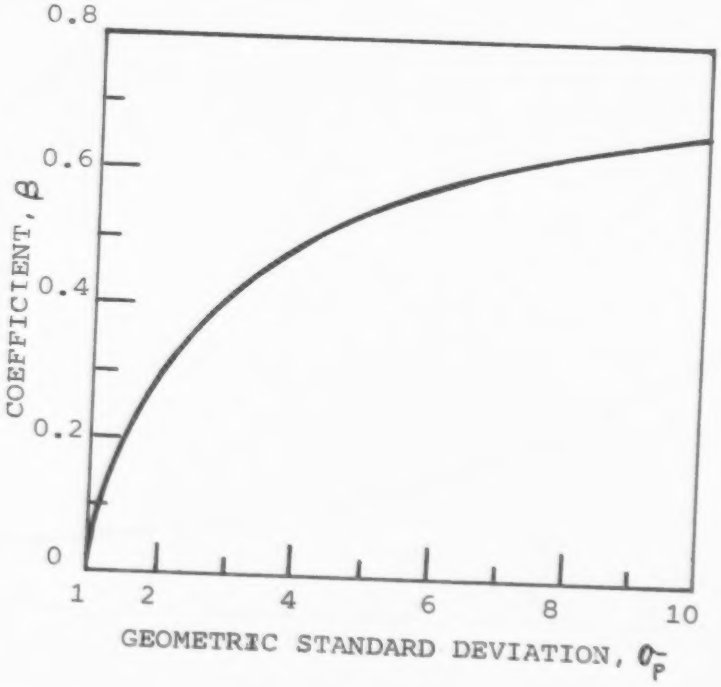

Fig.5 Coefficient β as a function of geometric standard deviation of particle size distribution

where sub-p is the basic design parameter of a pilot-scale precipitator, sub-f the basic design parameter of a full-scale precipitator, $\bar{d}$ the geometric mass median diameter of particle size distribution at the inlet of precipitator, σ_p the geometric standard deviation of particle size distribution at the inlet of precipitator, S the specific surface area of particles cloud, D the spacing of collecting electrode, P the spacing of discharging electrode, L the effective length on gas flow direction of treating chamber, H the effective height of collecting electrode, K the gas ion mobility, k the dielectric coefficient of particle, C the mass concentration of particles cloud, Vg the treating gas velocity, V_G the effective gravity settling velocity of dust dislodged from collecting electrode and I the corona current density on collecting electrode.

In the formula (6), the terms with regard to a space charge effect in the usually practical operating condition for a coal-fired boiler plant will be given as the following relation and it can be unaccounted without a hitch,

$$\frac{K_p\ (3 + k_f S_f C_f D_f)}{K_f\ (3 + k_p S_p C_p D_p)} \doteqdot 1.0\ , \tag{7}$$

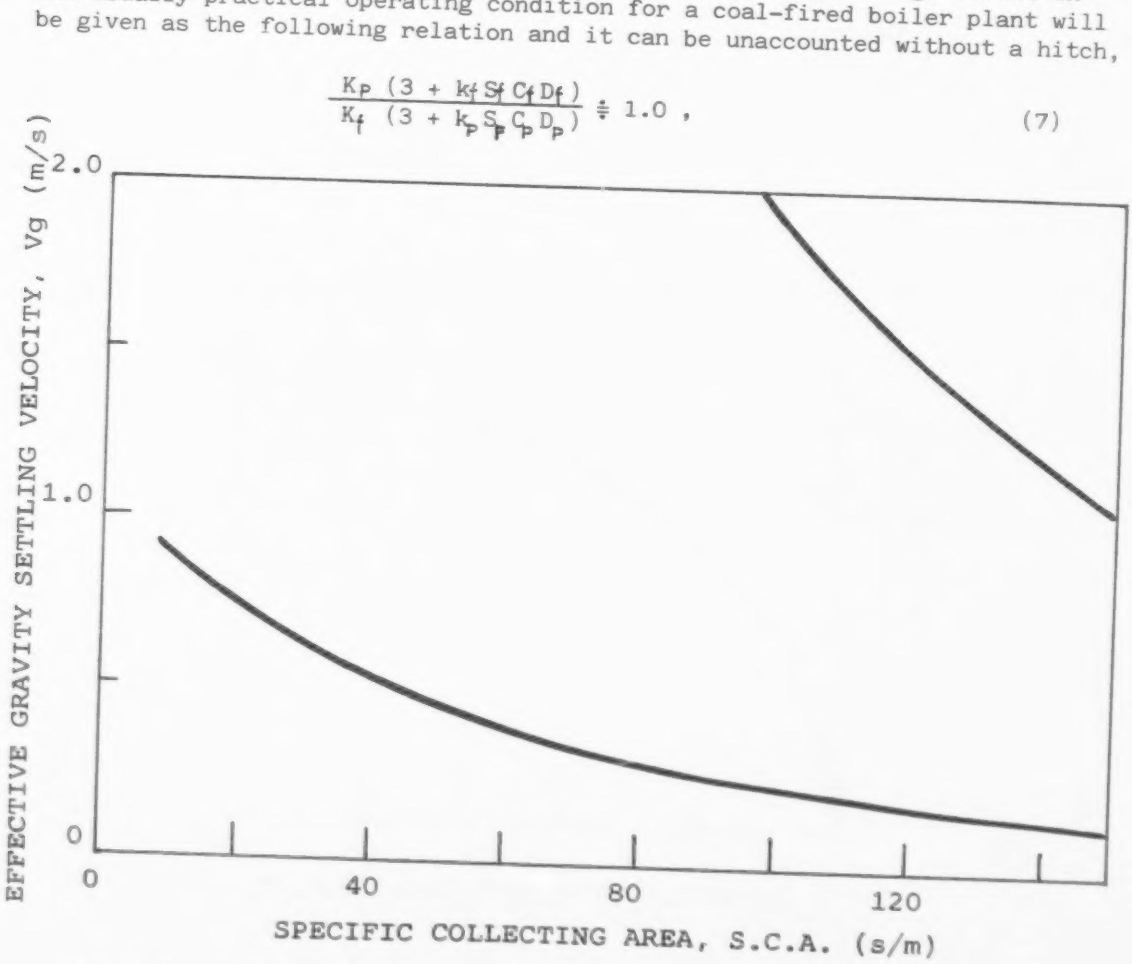

Fig.6 Effective gravity settling velocity of dusts dislodged from collecting electrode as a function of S.C.A.

furthermore, when the spacing of collecting and discharging electrode of a pilot-scale precipitator is designed to be the same as one of a full-scale, the formula (6) can be simplified as follows,

$$\omega_f = \omega_p \left(\frac{\bar{d}_f}{\bar{d}_p}\right)^{\alpha} \left(\frac{S.C.A_p}{S.C.A_f}\right)^{\beta} \left(\frac{I_f}{J_p}\right)^{\gamma(1-\beta)} \frac{1 - \exp - \left(\frac{V_{Gf}}{V_{gf}} \frac{L_f}{H_f}\right)}{1 - \exp - \left(\frac{V_{Gp}}{V_{gp}} \frac{L_p}{H_p}\right)} \tag{8}$$

From the formula (6) or (8) and on the basis of test results in a pilot-scale precipitator, the representative examples of the performance characteristics curves of collection efficiency versus the S.C.A. for the pilot-scale precipitator in comparison with the full-scale one are shown in Fig.8 and Fig.9.

CONCLUSION

The investigation described in this paper have led to the following conclusions,

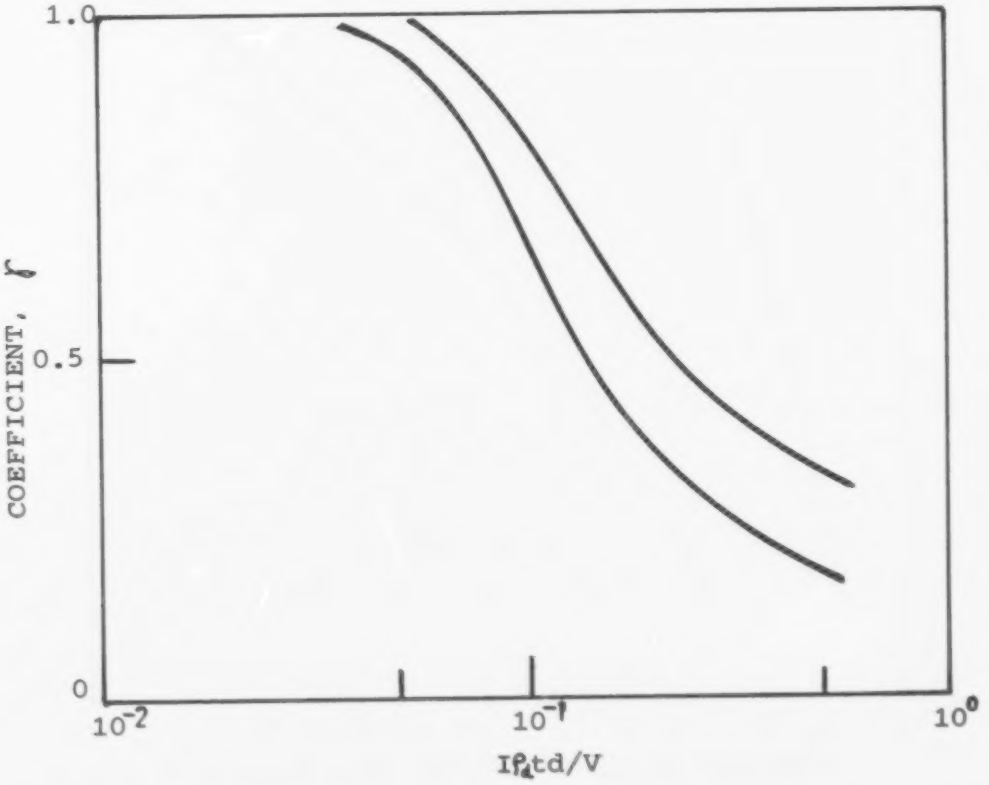

Fig.7 Coefficient γ as a function of ratio of dust layer potential on collecting electrode to applied voltage

(1) The Deutsch migration velocity for a pilot-scale precipitator will be different from one of a full-scale precipitator, when the S.C.A. is even the same between the both while the coefficient of re-entrainment is the difference between the both. In general, the Deutsch migration velocity for a full-scale precipitator will become to be lower, compared with one of a pilot-scale, since the aspect ratio of the full-scale precipitator is smaller than one of the pilot-scale, particularly when the bulk density or electric resistivity of dust layer on collecting electrode is a relatively low .

(2) The Deutsch migration velocity is decreased with increasing the S.C.A. because of the influence of the geometric standard deviation of particle size distribution at the inlet of precipitator, however the Deutsch migration velocity will be kept constant in independent of the S.C.A. when the particle size

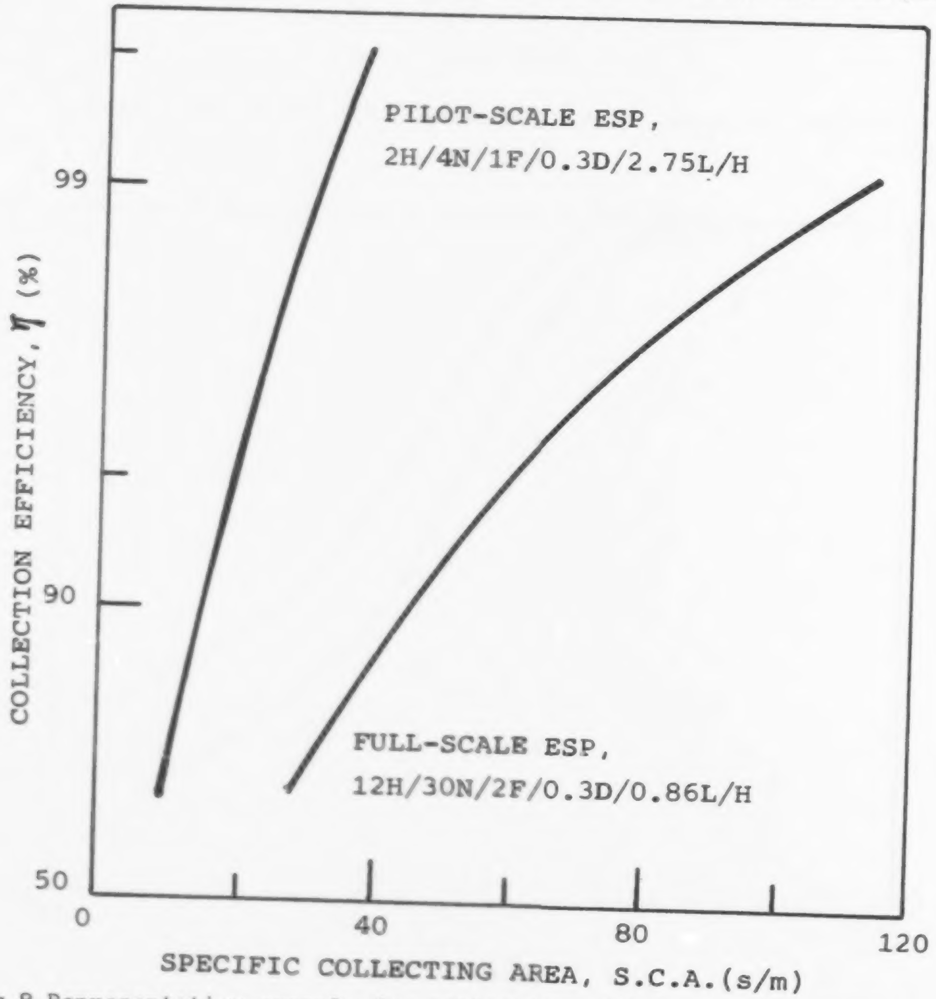

Fig.8 Representative example for collection efficiency performance characteristics curve as a function of S.C.A. in correspondence of a full-scale to pilot-scale

is almost uniform.

(3) The Deutsch migration velocity is increased with increasing the spacing of the collecting electrode. A so-called wide spacing effect is caused by the enhancement of an average corona electric field intensity as a predominant factor. Therefore, the validity of an wide spacing effect should be assessed in consideration of a space charge effect, corona current density, resistivity of dust layer on collecting electrode, coefficient β , γ and both a spacing of collecting and one of discharging electrode.

(4) Applying the formula (6)or(8) and on the basis of the Deutsch migration velocity obtained from the test results in a pilot-scale precipitator, the performance characteristics of collection efficiency versus the S.C.A. for a full-scale precipitator can be predicted and evaluated.

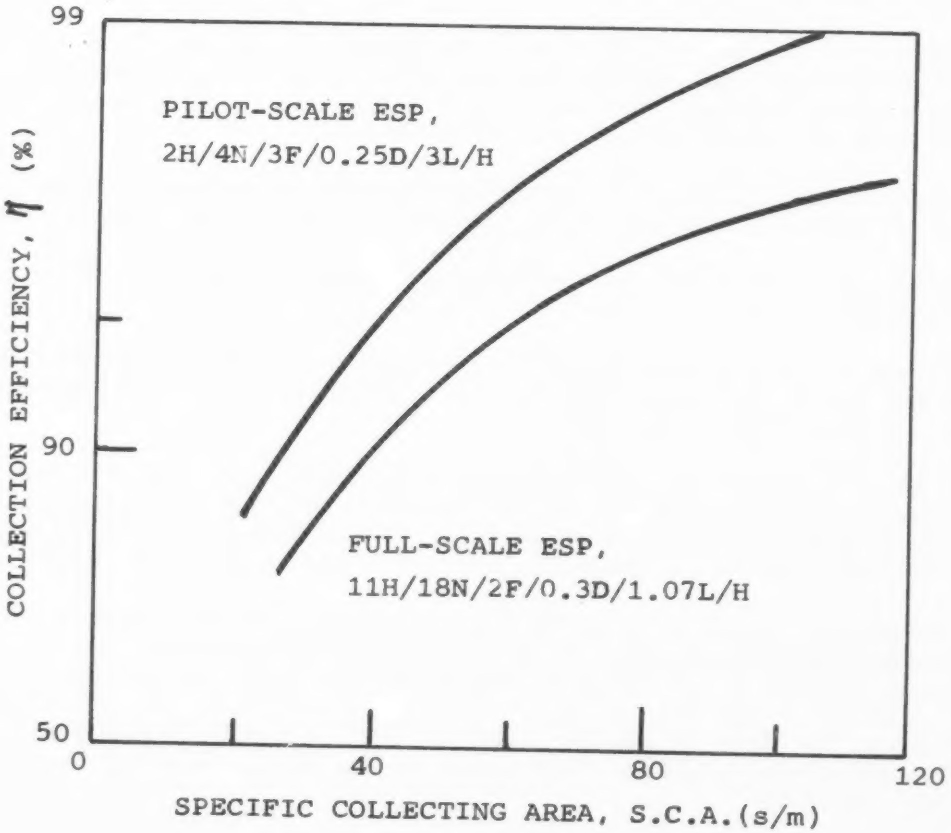

Fig.9 Representative example for collection efficiency performance characteristics curve as a function of S.C.A. in correspondence of a full-scale to pilot-scale

REFERENCES

1. Deutsch, W. Bewegung und Ladung der Elektrizitätstrager im Zylinderkondensator. Annln. Phys. 68, 1922. p.335-344.

2. White, H.J. Industrial Electrostatic Precipitators, Chap. 6, Addison Wesley, New York, 1963.

3. Masuda, S. Motion of Charged Particles with Difference Sizes Inside an Electrostatic Precipitator. In: Proceedings of the Fourth Conference of the Institute of Eletrostatics of Japan, Tokyo, 1980. p.97-99.

4. McDonald, J.R. A Mathematical Model of Electrostatic Precipitation, Revision 1, Vol.1, Modeling and Programing. EPA-600/7-78-111b, 1978.

5. Isahaya, F. Analysis of Corona Electric Field for Electrostatic Precipitator and its Industrial Application. Doctor Thesis of Tokyo Univ.. 1961. p.116-190.

6. Isahaya, F. Analysis of Efficiency Performance Characteristics of Electrostatic Precipitator by Utilizing Radioactive Tracer Technique Using Thorium B Aerosol Particles. In: Proceedings of Conference of Inst. Elect. Eng. of Japan, Tokyo, 1961. p.415-416.

7. Mierdel, G. und Seeliger, R. Untersuchungen über die Physikalischen Vorgänge bei der Elektrofilterung. Arch Elektrotech., 29, 1935. p.149-172.

8. Robinson, M. A Modified Deutsch Efficiency Equation for Electrostatic Precipitation. Atom. Envi., 1, 1967. p.193-204.

9. Cooperman, P. Efficiency Theory and Practice in Electrostatic precipitation. In: Proceedings of the Fourth International Clean Air Congress. Tokyo, Japan, 1977. p.835-838.

10. Isahaya, F. Electrostatic Precipitator by Using Ionic Wind for Very Low Resistivity Dusts from High Temperature Flue Gas of Petroleum-cokes Calcining Kiln. The First Symposium on the Trasfer and Utilization of Particulate Control Technology. EPA-600/7-79-044a, 1979. p.453-466.

11. Isahaya, F. Analysis of the Corona Field Intensity Distribution in Electrostatic Precipitator by a Steel Ball Dropping Method. Elecrtrotechnical Jl' of Japan, Vol.8, No.3/4, 1963. p.151-157.

12. Isahaya, F. Study on New Air Cleaning and its Testing method for Cleaning Effects. Special Publication of the Hitachi Hyoron. 1964. p.44-48

The work described in this paper was not funded by the U.S.Environmental Protection Agency and therefore the contents do not necessarily reflect the view of the Agency and no official endorsement should be inferred.

DISTORTION OF PULSE VOLTAGE WAVE FORM ON CORONA WIRES DUE TO CORONA DISCHARGE

by: Senichi Masuda and Hajime Nakatani
Department of Electical Engineering, University of Tokyo
7-3-1, Hongo, Bunkyo-ku, Tokyo, JAPAN 113

ABSTRACT

A very short pulse voltage travelling on a corona transmission line producing streamer coronas is subjected to a time-dependent distortion of its wave form owing to energy consumption by corona. There are two different streamers in the case of a parallel-wire transmission line. The first streamer is launched from the negative wire at the leading part of the pulse crest voltage, while the second streamer emitted from the positive wire at its rear part. The first (negative) streamer produces a small distortion in the leading part, whereas the second (positive) streamer causes a great lowering of voltage wave form in the rear part. The time-dependent equivalent surge impedance of the line also shows a concurrent lowering owing to these streamer activities.

1. INTRODUCTION

The specific advantages of using an extremely short pulse high voltage with several tens to several hundreds nanoseconds duration time have been recognized in twin-electrode type ESP's (1,2) and tri-electrode type ESP's (3), and also a precharger called Boxer-Charger developed by the authors (4). Such a short pulse voltage proceeds in a form of a travelling wave along a corona transmission line consisting of either a corona wire and a collecting electrode, a corona wire and a third non-corona electrode, or two parallel corona wires, and produces streamer coronas as a plasma ion source uniformly distributed on the line. One of its largest advantages is a simplicity in the construction of its pulse power supply. Another large advantage is its low power consumption compared with that producing a long duration pulse voltage. This is due to an effective conversion into corona discharge of the pulse energy, concentrated in a travelling wave packet and not distributed along the total length of the wire in a form of capacitive energy. The residual energy after losing its power to produce coronas remains also small. In a parallel corona wire transmission line, two different streamers appear. The first (negative streamer) is launched from the negative wire towards the positive one. In the case when the pulse voltage is sufficiently high, the second streamer (positive streamer) is subsequently emitted from the positive wire in the opposite direction to bridge across the gap. A more detailed description on these streamers is given in the separate reports (5,6). The travelling pulse voltage loses its energy as a result of corona production and, partly, of the skin-effect enhanced resistance loss in the line. Hence, ite wave form undergoes a gradual modification and attenuation, finally to become inactive so as not to produce coronas. The active length of the transmission line producing negative streamers is greatly increased with the aid of a dc field externally applied to the corona wires (5). In other words, more energy for negative streamer formation can be squeezed out of the pulse by the aid of dc field in this case.

The largest matter of concern in the use of an extremely short pulse high voltage is to understand the role of each streamer in the modification and attenuation of the voltage wave form, and in the concurrent change in the surge impedance of the transmission line. In this paper are reported the results of the investigation directed to this target.

2. EXPERIMENTAL APPARATUS

Fig. 1 illustrates an experimental set-up used in this experiment consisting of 35 m long parallel corona wires shaped in a form of a double-helix transmission line with 10 m in length. This is located horizontally between a long grounded (lower) plate and an isolated (upper) high potential electrode. The dimensions of the double-helix are given in the figure. The position on the double-helix line is expressed in terms of its distance, x, from the inlet as shown in Fig.1-(a). Hence, the actual wire length from the inlet is L = 3.5 x. One of the two wires (mother wire) of the double-helix is connected to the grounded plate at each 0.5 m distance, and the pulse voltage is applied through a feeder cable between the two wires in a polarity that another wire (daughter wire) is negative in reference to the mother wire. The main voltage wave travels along the helix wires, while two parasitic waves along the transmission lines (daughter wire / grounded plate) and (daughter wire / upper plate). The magnitude of the pulse current of the former parasitic wave amounts to 37.5 % of that of the main wave. The main wave proceeding along the double-helix line produces streamer coronas along its wires, with concurrent distortion and attenuation in its wave form. Two transmission lines, (double-helix) and (daughter wire / grounded plate), are terminated respectively by the matching resistances R_1 = 260 ohm and R_2 = 690 ohm. The ratio of R_1 and R_2 is 0.377, exactly equal to the inverse of the current ratio. The surge impedance of the feeder cable is either 50 ohm (section 3.1) or 75 ohm (sections 3.2, 4 and 5), and its length 50 m except in the section 4.2. A positive dc voltage, V_{dc}, is applied to the upper plate to form a dc field, E, between the double-helix and upper plate for extracting negative ions from the streamers to the upper plate. The magnitude of this field is expressed in terms of an average value, $E = V_{dc}/80$ mm, throughout this paper.

The voltage wave form is measured by a high voltage probe (Tektronix: P 6015) in combination with a high-speed dual-beam oscilloscope (Tektronix:7844), and the current wave form by a Rogowski-coil having a sensitivity of 2.2 mV/A in a passing band between 80 kHz and 30 MHz. The development of streamers between the double-helix wires is observed by a streak photograph taken through a 7 mm slit with an image converter camera (John Hadland: HE 700) combined with an image intensifier (EMI : 9912) (Fig.1-(b)). The light signal from the corona wires is detected with a photomultiplier tube (Hamamatsu : R 212) and compared with the wave form of the pulse voltage applied to the wires, so as to determine the starting point of the pulse voltage on the streak photograph.

Fig.2 shows the pulse generator used, consisting of a coaxial cable A. The cable A is charged from a dc high voltage source, B, through a resistance, R, and, then, discharged through a sphere gap to an initially uncharged feeder cable, C, connected to the double-helix wires. The duration time of the pulse voltage produced is twice the transient time of a travelling wave voltage across the cable A. The pulse wave form at the inlet of the double-helix is approximately rectangular, as shown in Fig.3-(a). The surge impedance of the cable A is 50 ohm and its length is 20 m. A ceramic capacitor of 1700 pF is also used in place of the cable A. The voltage wave form in this case is as shown in Figs. 6-(a) and 7-(a). The variation of the pulse rise time is made by inserting an inductance after the spark gap. The rise time and duration time of the pulse voltage wave are defined, respectively, by T_r = time of rise from 10 % to 90 % of the crest voltage, V_p, and T_h = half-peak duration time.

3. DISTORTION OF PULSE VOLTAGE WAVE FORM

Prior to this experiment the exact values of R_1 and R_2 are determined by supplying to the double-helix a very short pulse voltage with a duration time less than half of the time of reflection and observing the reflected wave at its inlet. The values of R_1 and R_2, thus obtained, are 260 and 690 ohms, respectively. The travelling speed of this voltage wave is 0.28 m/ns, 93 % of the light velocity in this particular case.

3.1 DISTORTION OF RECTANGULAR PULSE VOLTAGE WAVE FORM

A rectangular pulse voltage with T_r = 70 ns and T_h = 200 ns produced using the cable-type pulse generator is applied at the inlet of the double-helix. Fig.3-(a) shows the pulse voltage wave forms in the absence of corona activity measured at the inlet, center and terminal of the double-helix wires with a low inlet pulse voltage (V_p = -29 kV) and zero dc field (E= 0). The wave form remains almost unaltered, with a slight attenuation of ca. 3.5 % at the terminal. This is ascribable to a skin-effect enhanced resistance loss in the wires, specific to a fast rising pulse.

When E is raised from 0, keeping V_p = -29 kV, the negative streamers begin to develop at E = -2 kV/cm from the upper edge of the daughter wire in a region close to the inlet towards the upper electrode (Fig.4-(a)). As E is further raised, the negative streamers are enhanced in length, appearing finally on the whole length of the double-helix. The streak photograph of this negative streamer taken at x = 0.27 m and E = -5 kV/cm is shown in Fig. 5-(a), indicating the existence of a time lag T_- = 50 ns. The distortion of the voltage wave-forms in this case is indicated in Fig.3-(b). It can be recognized that the negative streamer erodes the region ahead of the pulse crest voltage from $t = T_-$.

When V_p is raised to -36 kV with E = 0 kV/cm, the positive streamers begin to develop to bridge across the two wires as shown in Fig.4-(c). In this case the voltage wave form becomes greatly distorted even at the inlet with the rear portion of its crest greatly eroded as shown in Fig.3-(c). It rapidly attenuates to V_p = -33.5 kV at x = 1.5 m and the positive streamers disappear beyond x = 1.5 m. Between x = 1.5 m and 10 m, only negative streamers, weak in luminosity and short in length, develop from the daughter wire with substantially smaller attenuation of the voltage (Fig.3-(c)).

Fig.3-(d) indicates the distortion occuring at a high inlet pulse voltage (V_p = -35 kV) and a high dc field (E = -5 kV/cm). The phenomena occuring in the region $x \leqq 1.5$ m are almost the same as in the case of Fig.3-(c) where E = 0. Beyond x = 1.5 m, the positive streamers again disappear, leaving only the negative streamers spreading along the entire length of the daughter wire. Hence, the positive streamers are not enhanced by the dc field. The difference exists, however, in a stronger luminosity and increased penetration length of the negative streamers (Fig.4-(b)), resulting in an enhanced energy loss. The negative streamer in this case causes the erosion not only in the region ahead of the crest voltage, but also in the crest itself. As a result, the pulse crest voltage attenuates more rapidly than in Fig.3-(c). This also leads to a change in the appearence of corona from Fig.4-(b) to Fig.4-(a) in a region near the terminal.

Figs.5-(b) and (c) are the streak photographs of the negative and positive streamers occured at a high pulse voltage in Figs.3-(c) and (d), respectively. The time lags of the negative and positive streamers, T_- and T_+, are 70 ns and 110 ns for E = 0 kV/cm, and 40 ns and 100 ns for E = -5 kV/cm.

It is recognized in Fig.3-(c) that the negative streamer starting from $t = T_-$ causes a small but continued erosion in the region ahead of the crest voltage. Whereas the positive streamers starting from $t = T_+$ first erode rapidly the subsequent region behind the crest to produce a very large dip. This dip formation is likely to be due to a large energy consumption required for formation of the second streamer plasma channel in its propagation process (leader formation). This is followed by a steady after-glow accompanied by a subsequent recovery in voltage up to a level slightly lower than -30 kV (plasma sustaining voltage). In other words, a large dip in a wave form subsequent to a high crest voltage (initiation voltage) and followed by a voltage recovery (plasma sustaining voltage) generally represents a distinct sign indicating the occurrence of positive streamers. A large distortion of the wave form occurring at x = 0 from the ideal lossless wave form depicted in this figure is considered to be caused by the time-dependent decrease in the voltage transmission rate of the double-helix line due to the corona-induced lowering of its effective surge impedance as described later.

A drastic change occurs in the wave form in the presence of an adequately high externally applied dc field (Fig.3-(d)). In accordance with the increased activity of negative streamer enhanced by E (see Fig.5-(c)), the erosion of the region ahead of the pulse crest starts at a lower voltage with a smaller time lag T_-. The erosion continues successively with an increased rate even at the stage when the pulse voltage has dropped to a much lower level. In other words, the externally applied dc field enhancing the local field around the negative wire assists the extraction of the more energy from the leading part of the pulse voltage to convert into negative streamers. In contrast, the dc field in this particular case has an effect of relaxing the pulse-induced local field around the positive wire. As a result the positive streamers are somewhat hampered (see Fig.5-(c)), and the erosion starting at

$t = T_+$ by these streamers at the subsequent region behind the crest is also diminished. It should be added that the undistorted wave forms depicted in Figs.3-(c), 3-(d), 6-(b) and 7-(b) are estimated from those at the output of the pulse generator by inserting a 50 m long feeder cable (delay line), and thereby eliminating the interference by coronas in the double-helix completely.

3.2 EFFECT OF RISE TIME AND CREST VOLTAGE

The capacitor type pulse generator with a capacitor C = 1700 pF is used. A fast rising, narrow pulse wave form (sharp pulse) with T_r = 38 ns and T_h = 150 ns is produced by removing the inductance L_r (Fig.2). A slow rising, wider pulse (moderate pulse) with T_r = 100 ns and T_h = 320 ns is produced by inserting L_r = 10 μH. These values of T_r and T_h are those measured at the output of the pulse generator.

Figs.6 and 7 show the distortion of the pulse wave form at E = -5 kV/cm for these sharp and moderate pulses, respectively. The pulse crest voltage, V_p, undergoing attenuation in these figures is plotted against x in Fig.8, where two solid curves show the results for the moderate pulse and two dotted curves for the sharp pulse.

When the inlet pulse voltage is low (V_p = -32 kV; Fig.6-(a) and Fig.7-(a)), only negative streamers are produced along the whole length of the double-helix, and they erode the front side of the pulse crest, independent of the pulse wave form. However, the sharp pulse voltage is more easily subjected to the erosion of the pulse crest because of its narrow pulse width (Fig.6-(a)). It can be recognized from Fig.7-(a) that the moderate pulse wave has enough energy distributed in a time-domain to produce coronas even after x = 10 m. This results in a great difference in the attenuation rate V_p between the sharp and moderate pulses (see the two curves starting from V_p = -32 kV at x = 0 in Fig.8).

Fig.6-(b) and Fig.7-(b) show the distortion occurring at a higher pulse voltage to produce active positive streamers bridging across the double-helix wires in the region close to x = 0. After the pulse voltage travels a certain length (1 m for the sharp pulse and 1.5 m for the moderate pulse), the positive streamers disappear because of the decrease in pulse voltage. In both the sharp and moderate pulses, the effective pulse duration time becomes decreased at x = 0, owing to the drop in transmission rate caused by the positive streamer induced lowering of the effective surge impedance. This diminished pulse duration time causes in turn a continued rapid attenuation of V_p after the positive streamers disappear. Thus, in the case of moderate pulse, its crest voltage attenuates from -38 kV at x = 0 to -30 kV at x = 10 to meet another solid curve starting from a lower level of V_p at x = 0 (Fig.8). In the case of the sharp pulse, even the reversal of its crest level occurs as indicated by two dotted curves in Fig.8 crossing each other at x = 5 m. These erosions lead to the flattening of the pulse voltage and lowering of its rise time.

Hence, the selection of the pulse wave form and its crest voltage must be made in consideration of its overall corona producing performance in its entire propagation process. In the case of a long transmission line, the selection of a too sharp pulse voltage loses its meaning, since it rapidly loses its peak region to turn into a broader, inactive pulse.

4. EFFECT OF REFLECTION OF TRAVELLING WAVE AT TERMINAL

When the terminals of the double-helix wires are open instead of being terminated with matching resistances, a reflection of pulse occurs at the terminal. As a result the terminal voltage is theoretically doubled when no corona loss exists, and this reflected wave is superimposed to the oncoming wave to enhance the overall apparent pulse voltage on the line. The effect of this reflection is investigated with a special attention to its technical importance, using the moderate pulse voltage (T_r = 100 ns and T_h = 320 ns) with different levels of its crest at the inlet, V_p, and with effectively open terminals (R_1 = 100 kilo-ohm and $R_2 = \infty$).

4.1 CHANGE OF OVERALL PULSE CREST VOLTAGE

The overall apparent pulse crest voltage, including both the forward and reflected travelling waves superimposed, is plotted against the distance, x, in Fig.9. In the case when no corona occurs (bottom line), the overall crest voltage continues to rise to become almost doubled at x = 10 m as expected. Fig.10-(a) indicates one of the examples of wave form modification in the similar corona-free case but with E = -5 kV/cm. The reflected wave can be clearly distinguished from the forward wave at x = 0 and x = 5 m.

When the inlet pulse crest voltage is raised, the positive streamers begin to occur at the terminal region, and the wave forms at x = 5 and 10 m indicate a typical dip specific to the positive streamers (Fig.10-(b)). The crest levels prior to these dips at x = 0, 5 and 10 m are limited to -35 kV which is the initiation threshold of the positive streamers in this case. This voltage limitting effect is clearly indicated also in Fig.9. The upper three curves starting from different levels of V_p at x = 0 come to meet at around V_p = -35 kV at x = 5 m, and remain flat up to x = 10 m. As soon as the voltage, enhanced by reflection, exceeds this threshold, the positive streamers are produced to cause a large dip, and a subsequent recovery in voltage, as described before.

4.2 RELATIONSHIP BETWEEN RESIDUAL DC VOLTAGE AND POSITIVE STREAMERS

In an open-ended transmission line, the voltage wave propagates back and forth many times between the pulse generator and the open terminal of the line through the feeder cable, undergoing multiple reflections. The wave dissipates its energy owing to the corona loss, skin-effect enhanced resistance loss, and the loss at the spark gap by passing through its arc plasma. The wave is gradually broadened by the energy dissipation to lose its nature as a travelling wave, finally to be converted into a dc residual voltage remaining on a transmission line.

This dc voltage is measured at t = 6 μs to estimate approximately the conversion ratio of pulse energy into corona energy. In Fig.11 the residual dc voltage is plotted against the pulse crest voltage, V_p, at the inlet of the double-helix line where the solid curve is for E = 0 kV/cm and the dotted curve for E = -5 kV/cm. Both solid and dotted curves coincide very well to each other, indicating a linear rise in the residual voltage with V_p up to V_p = -20 kV. With E = -5 kV/cm the negative streamer begin to occur at V_p = -14 kV, whereas no streamers occur with E = 0 up to V_p = -20 kV. Thus, it can be seen that the energy consumption of negative streamers is so small that no appreciable change occurs in the residual dc voltage. At $V_p = -20$ kV the positive streamers begin to occur, with both $E = 0$ and 5 kV/cm, in the terminal region of the double-helix line. With increasing V_p from -20 to -41 kV, the positive streamer region spreads gradually from the terminal to the whole length of the line. Concurrently, the curves begin to deviate from the straight line, taking maximum at $V_p = -25$ kV, and drop rapidly to become zero at $V_p = -41$ kV. This again indicates a large energy consumption of the positive streamers, probably because of their very conductive plasma channels bridging across the wires to bleed the charge and energy of the pulse voltage wave.

5. SURGE IMPEDANCE OF DOUBLE-HELIX WIRES AND ITS MODIFICATION BY CORONAS

The surge impedance, Zo, of a transmission line is modified by corona loss during the propagation of the pulse voltage. The effective value of Zo can be obtained by measuring the lacal time-dependent values of the pulse voltage V(x,t) and current I(x,t) as

$$Zo(x,t) = V(x,t)/I(x,t) \qquad \text{----------}(1)$$

The pulse voltage and current wave forms at the inlet, V(0,t) and I(0,t), are measured with a dual-beam oscilloscope for different levels of inlet pulse crest voltage to obtain Zo(0,t). A square-waved pulse voltage (T_r = 50 ns and T_h = 240 ns) is used, and the end of the double-helix line is terminated with the matching resistances. To eliminate the current of the parasitic pulse described in section 2, the Rogowski coil (current probe) is wound around the mother wire. The surge impedance of the feeder cable used is 75 ohm and its length 50 m.

The wave forms of V(0,t) and I(0,t) thus obtained are shown in Fig.12. In the case when no corona occurs, V(0,t) and I(0,t) indicate the same wave form as shown in Fig.12-(a). With V_p kept constant and increasing E from 0 to -6 kV/cm, the negative streamers occur along the whole length of the double-helix wires. The wave forms indicate a slight concurrent change (Fig.12-(b)). The voltage crest decreases from -34 kV to -33 kV and the current crest increases from -133 A to -140 A. In the case when the positive streamers occur, the voltage indicates the typical dip, and current shows a concurrent abrupt rise (Fig.12-(c)).

The time-dependent surge impedance Zo(0,t) is calculated by Eq.(1) from measured wave forms of V(0,t) and I(0,t) at different levels of V_p, and plotted against time in Fig.13. In the case when no corona activity takes place ($V_p = -26$ kV) the value of Zo(0,t) remains almost constant at about 270 ohm during the entire pulse duration time. In the case when only the negative streamers occur ($V_p = -33$ kV and -35 kV), it shows a very small time-dependent drop from 250 ohm to 240 - 200 ohm. In the case when the positive streamers occur ($V_p = -39$ kV and -41 kV), Zo(0,t) drops sharply after a certain delay time from 250 ohm to 80 - 100 ohm. This delay time coincides with the time lag for positive streamer initiation.

The drop of the effective surge impedance does not mean the abrupt jump of the pulse current from the pulse generator, but it produces a local jump of current in the cost of local attenuation of the pulse voltage.

3. CALCULATION OF CORONA LOSS

We consider a simple case when no reflection occurs. The power of a forward travelling wave at an arbitrary position x and time t is given by:

$$P(x,t) = V(x,t) \times I(x,t) \qquad \text{----------}(2)$$

Therefore, the pulse energy, $E(x)$, carried by the wave in the forward direction is

$$E(x) = \int P(x,t)dt \qquad \text{----------}(3)$$

$$= \int V(x,t) \times I(x,t)\, dt \qquad \text{----------}(4)$$

$$= \int V(x,t)^2 / Zo(x,t)\, dt \qquad \text{----------}(5)$$

The energy converted to the corona loss in a region between x_1 and x_2 is

$$\text{Corona Loss} = E(x_1) - E(x_2) \qquad \text{----------}(6)$$

This corona loss is estimated for the negative and positive streamers separately from the measured voltage wave forms and time-dependent change of surge impedance by using the Eqs. (5) and (6). The following simplified conditions are taken for this estimation:

Negative streamers:

1) $x_1 = 0$ m and $x_2 = 10$ m.
2) $Zo(x,t) = 240$ ohm (constant).
3) In the absence of positive streamers, the integration of Eq.(5) is made only in a time interval for the corona-induced wave distortion to appear.
4) In the presence of positive streamers in the inlet region of the line, the integration is made from $t = 0$ to the time of the crest voltage.

Positive streamers:

1) $x_1 = 0$ m and x_2 = position at which positive streamers disappear.
2) $Zo(x_1,t) = 100$ ohm and $Zo(x_2,t) = 240$ ohm.
3) The integration of Eq.(5) is made from the time of crest voltage to the time at which positive streamer induced wave distortion disappears at $x = x_2$, i.e. $V(x_1,t) = V(x_2,t)$.

The estimated value of corona loss by negative streamers per unit length of the double-helix, $\nabla E_-/\nabla x$, ranges from 0.005 to 0.010 J/m and increases with increasing inlet pulse voltage. The corona loss per unit length of wires is

$$\nabla E_-/\nabla L = 0.010/3.5\ [\text{J/m}] = 0.0029\ [\text{J/m}] \qquad \text{----------}(7)$$

On the other hand, the corona loss by positive streamers per unit length of the double-helix, $\nabla E_+/\nabla x$, is 0.40 - 0.58 J/m, about fifty times as high as $\nabla E_-/\nabla x$. The loss per unit length of the wires is $\nabla E_+/\nabla L = 0.11 - 0.17$ J/m. It should be noted that 27 - 44 % of the inlet pulse energy is consumed by the positive streamers after propagation of only 1.0 or 1.5 m from the inlet.

It is confirmed by other experiments that, in spite of this high energy consumption of positive streamers, their emission ability of ionic current is almost equal to the negative streamers (5,6). Hence, the occurrence of the positive streamers should be avoided in order to produce as much monopolar ions as possible along a longest possible corona transmission line with a limited pulse energy.

8. CONCLUSIONS

The corona-induced wave-form distortion of an extremely short pulse voltage travelling on a long transmission line is investigated, and the following conclusions derived:

1) The negative streamer is launched at the leading part of the pulse crest voltage, and erodes its front side. Whereas the positive streamer, subsequently emitted at a higher pulse voltage, bridges across the wire gap, and causes a great dip in the voltage wave form in the region behind its crest.
2) The positive streamers occur primarily in the inlet region of the line, as it rapidly disappear after propagation of say 1.0 or 1.5 m, because of their large energy consumption to produce a sharp attenuation of the pulse voltage. The negative streamers consume much less energy, and can develop along a long distance of the line when assisted by an externally applied dc negative field for extraction of negative ions. This dc field plays a role of squeezing more negative corona energy out of the pulse voltage wave, but produces no enhancing effect for the positive streamers.
3) Even at the inlet of the line, the region behind the crest is greatly eroded when the positive streamers occur. This is because of a concurrent abrupt drop of the line surge impedance.
4) The shorter the pulse duration time, the faster the pulse crest voltage attenuates.
5) In the case when the pulse voltage is high enough at the inlet so as to produce intensive positive streamers at the inlet region, the attenuation of pulse crest is more rapid than in the case when only negative streamers occur. This is because of a great erosion in the region behind the crest by positive streamers to produce also a great decrease in an effective pulse duration time.
6) The corona losses per unit length of the double-helix line due to negative and positive streamers are 0.005 - 0.010 J/m and 0.45 - 0.58 J/m, respectively. In the case when positive streamers occur, 27 - 44 % of the inlet pulse energy is consumed after propagation of only 1.0 or 1.5 m from the inlet. Therefore, the occurrence of positive streamers must be avoided in order to provide as much monopolar ions as possible along a longest possible length of a transmission line with a limited pulse energy.
7) When the line is open-ended, the reflection of the wave can raise the overall pulse voltage. But it dose not exceed the positive streamer initiation threshold as a result of a strong crest-trimming effect of the positive streamers consuming large energy. In the case when the pulse voltage is very high to produce positive streamers along almost whole length of the double-helix line, the pulse energy can be completely converted to corona loss after the multiple reflection of the wave on the line.
8) The base line surge impedance, Zo, at the inlet of the double-helix is 270 ohm. The negative streamers produce a slight time-dependent decrease

of its value from 250 to 240 - 200 ohm. The positive streamers, on the other hand, produces after a certain delay time a sharp abrupt drop from 250 to the level of 80 - 100 ohm, as a result of concurrent drop in voltage and rise in current.

REFERENCES

1 Milde, H.I. and VanHoesen, H.E., Application of Fast Rising Pulses to Electrostatic Precipitators, Conf. Rec. IEEE/IAS Annual Meet. 1979, pp.158-162 (1979).

2 Masuda, S. and Hosokawa, S., Corona Characteristics of Travelling Waves in the Pulse Energized ESP, Conf. Rec. of the Institute of Electrostatics Japan Annual Meet. 1982 (Nov. 1982 to be presented).

3 Masuda, S. and Hosokawa, S., Travelling wave Pulse Energization in A Tri-Electrode Type Electrostatic Precipitator, to be published separately.

4 Masuda, S., Mizuno, A., Nakatani, H. and Kawahara, H., Application of Boxer-Charger in Pulsed Electrostatic Precipitator, Conf. Rec. IEEE/IAS Annual Meet. 1980, pp.904-911 (1980).

5 Masuda, S., Nakatani, H., Yamada, K., Arikawa, M. and Mizuno, A., Production of Monopolar Ions by Travelling Wave Corona Discharge, Conf. Rec. IEEE/IAS Annual Meet. 1981, pp.1066-1073 (1981).

6 Masuda, S. and Shishikui, Y., Pulse Corona as Ion Source and Its Behaviours in Monopolar Current Emission, The Fourth EPA-Symposium on the Transfer and Utilization of Particulate Control Technology (Oct. 1982 to be presented).

The work described in this paper was not funded by the U.S. Environmental Protection Agency and therefore the contents do not necessarily reflect the views of the Agency and no official endorsement should be inferred.

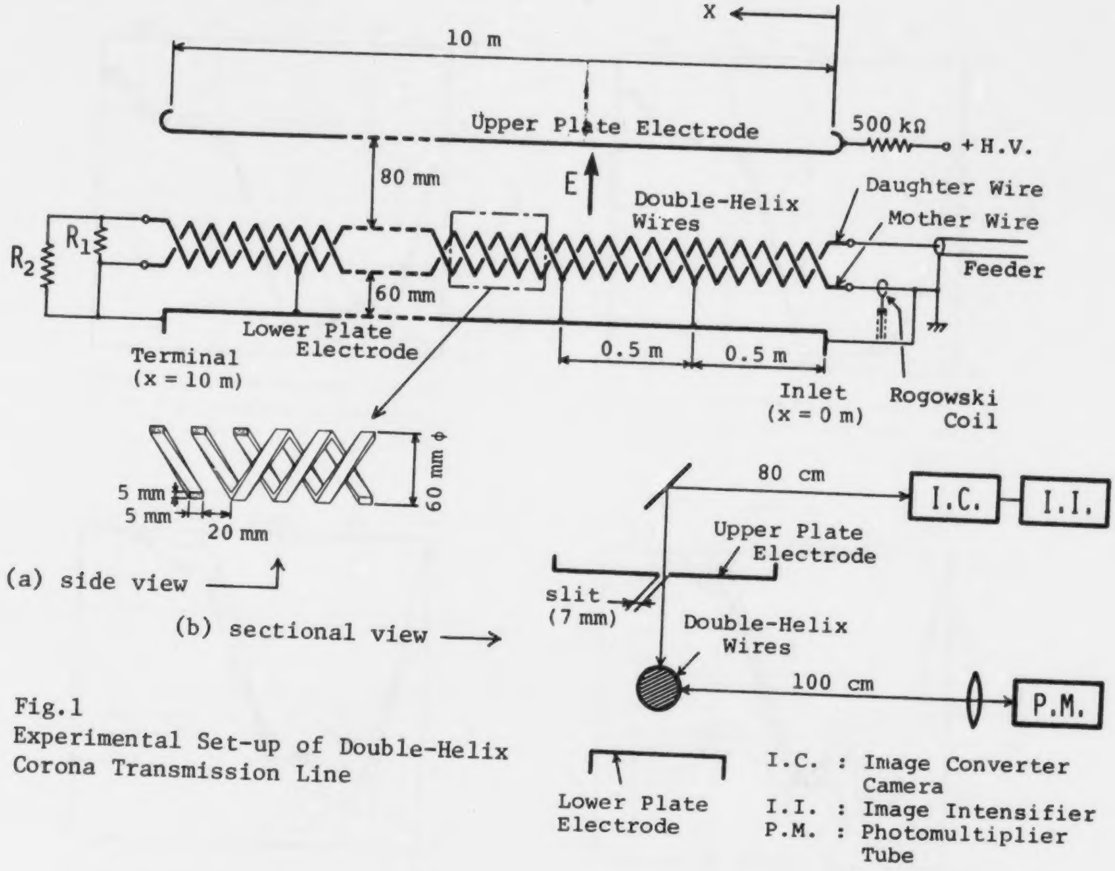
X
10 m
Upper Plate Electrode
500 kΩ
+ H.V.
80 mm
E
Double-Helix Wires
Daughter Wire
Mother Wire
Feeder
R_2
R_1
60 mm
Lower Plate Electrode
Terminal (x = 10 m)
0.5 m
0.5 m
Inlet (x = 0 m)
Rogowski Coil
5 mm
5 mm
20 mm
60 mm ϕ
(a) side view
(b) sectional view
80 cm
I.C.
I.I.
Upper Plate Electrode
slit (7 mm)
Double-Helix Wires
100 cm
P.M.
Lower Plate Electrode

Fig.1
Experimental Set-up of Double-Helix Corona Transmission Line

I.C. : Image Converter Camera
I.I. : Image Intensifier
P.M. : Photomultiplier Tube

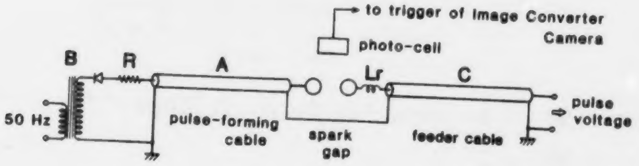
to trigger of Image Converter Camera
photo-cell
B
R
A
Lr
C
50 Hz
pulse-forming cable
spark gap
feeder cable
pulse voltage

Fig.2
Pulse Generator

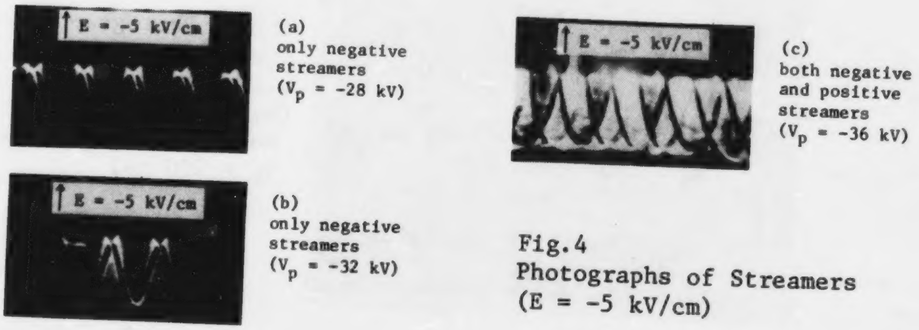
E = -5 kV/cm
E = -5 kV/cm
E = -5 kV/cm

(a)
only negative streamers
(V_p = -28 kV)

(b)
only negative streamers
(V_p = -32 kV)

(c)
both negative and positive streamers
(V_p = -36 kV)

Fig.4
Photographs of Streamers
(E = -5 kV/cm)

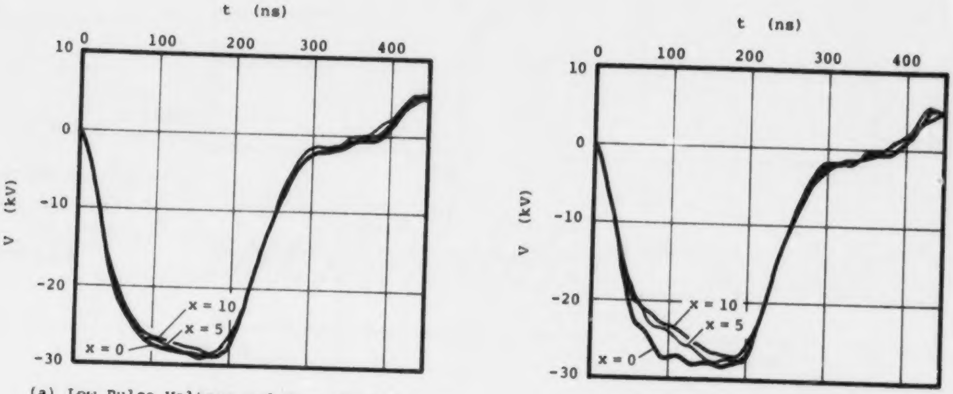

(a) Low Pulse Voltage and Zero DC Field (no corona discharge; V_p = -29 kV at x = 0)

(b) Low Pulse Voltage and High DC Field (only negative streamer; V_p = -28 kV at x = 0; E = -5 kV/cm)

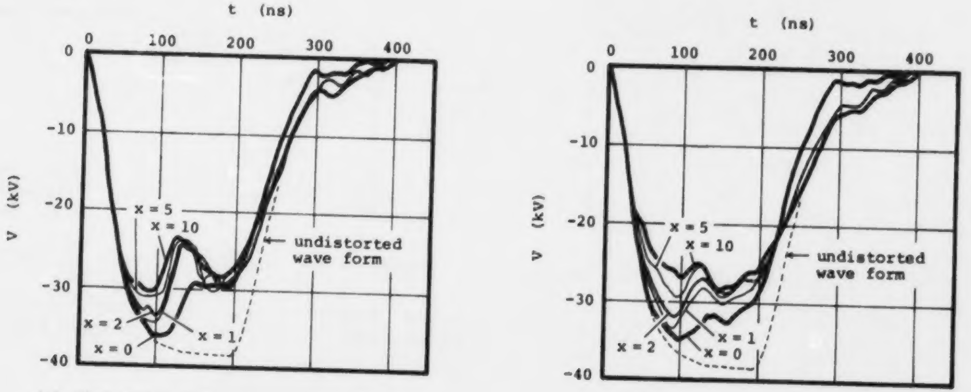

(c) High Pulse Voltage and Zero DC Field (positive streamers only in the region: x ≤ 1.5 m; V_p = -36 kV at x = 0)

(d) High Pulse Voltage and High DC Field (negative and positive streamers in region: x ≤ 1.5 m ; V_p = -35 kV at x = 0 ; E = - 5 kV/cm)

Fig.3 Wave Form Distortion of Rectangular Pulse Voltage (T_r = 70 ns, T_h = 200 ns)

(a) V_p = -28 kV (at x = 0)
E = -5 kV/cm

(b) V_p = -36 kV (at x = 0)
E = 0 kV/cm

(c) V_p = -35 kV (at x = 0)
E = -5 kV/cm

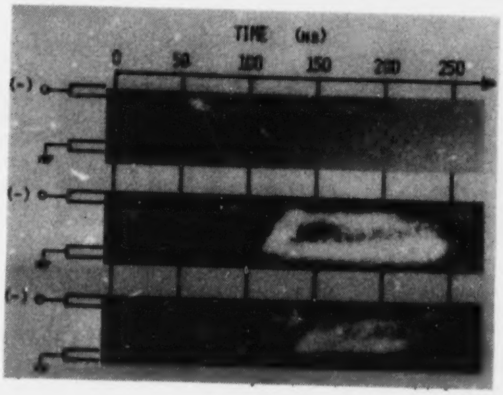

Fig.5

Streak Photographs of Streamers Taken at x = 0.27 m (square-waved pulse voltage : T_r = 70 ns, T_h = 200 ns)

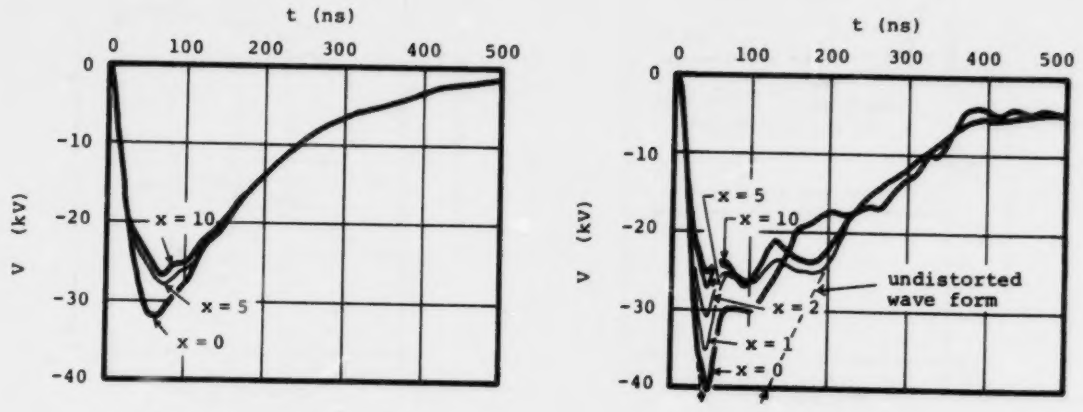

(a) negative streamer only

(b) negative and positive streamers

Fig.6 Distortion of Voltage Wave Form
(sharp pulse voltage : T_r = 38 ns,
T_h = 150 ns ; E = -5 kV/cm)

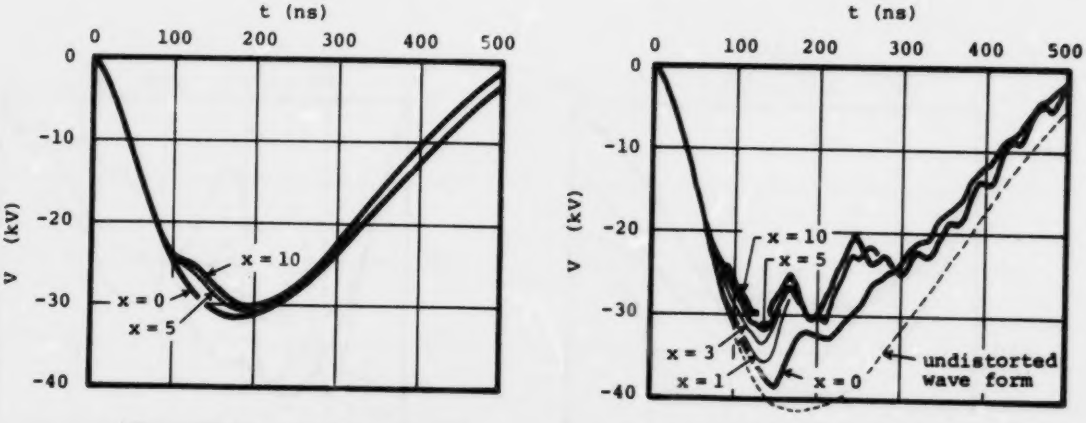

(a) negative streamer only

(b) negative and positive streamers

Fig.7 Distortion of Voltage Wave Form
(moderate pulse voltage : T_r = 100 ns,
T_h = 320 ns ; E = -5 kV/cm)

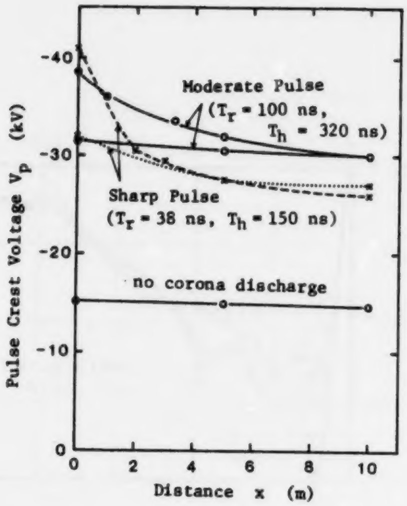

Fig.8
Effects of Inlet Crest Level of Pulse Voltage and its Sharpness on Attenuation of Pulse Crest Voltage
(E = -5 kV/cm)

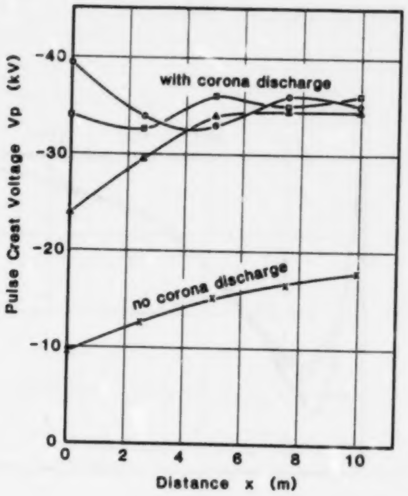

Fig.9
Change of Overall Pulse Crest Voltage, V_p, with Open Terminal
(moderate pulse : T_r = 100 ns, T_h = 320 ns ; E = -5 kV/cm)

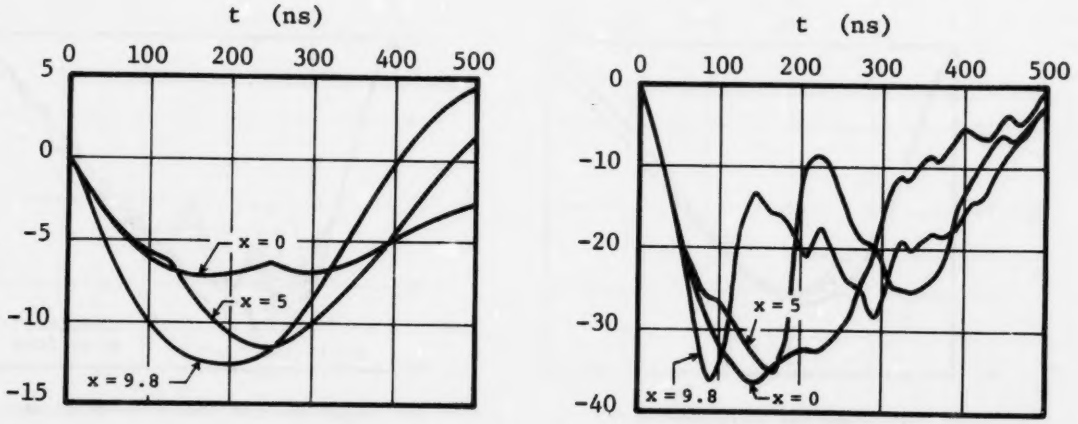

(a) without coronas
(E = -5 kV/cm)

(b) with coronas
(E = -5 kV/cm)

Fig.10 Distortion of Voltage Wave Form with Open Terminal
(moderate pulse : T_r = 100 ns, T_h = 320 ns)

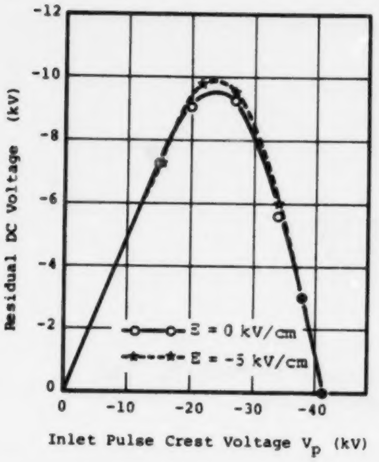

Fig.11
Residual DC Voltage after Multi-Reflection of Travelling Wave Pulse Voltage on an Open-Ended Line
(pulse generator : capacitor type (C = 2500 pF) ; feeder:75 Ω cable (6 m long) ; residual dc voltage : measured at t = 6 μs)

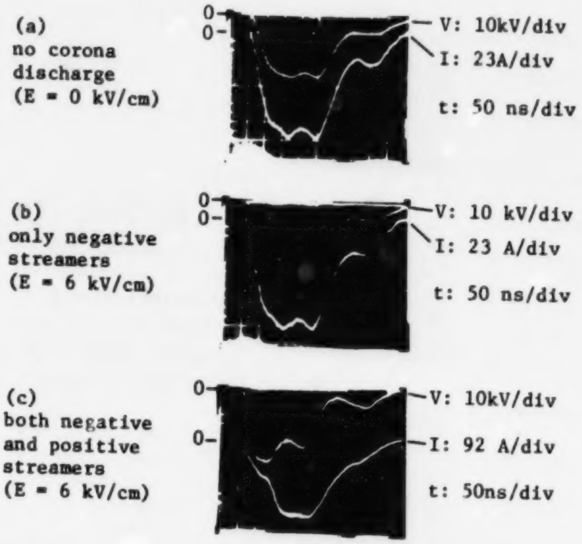

(a)
no corona discharge
(E = 0 kV/cm)

(b)
only negative streamers
(E = 6 kV/cm)

(c)
both negative and positive streamers
(E = 6 kV/cm)

Fig.12
Distortion of Voltage and Current Wave Forms Due To Streamer Coronas
(T_r = 50 ns, T_h = 240 ns)

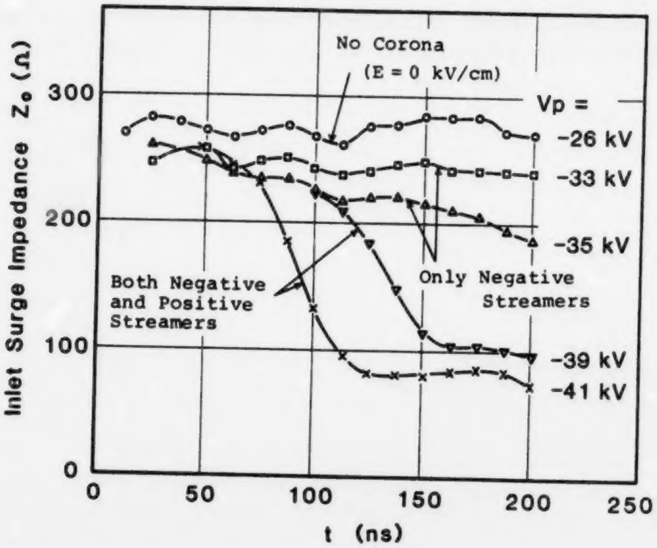

Fig.13 Time-Dependent Change in Inlet Surge Impedance, Zo(0,t), for Different Streamer Modes
(square-waved pulse voltage : T_r = 50 ns, T_h = 240 ns ; E = -6 kV/cm)

ELECTROSTATIC PRECIPITATOR ANALYSIS AND SYNTHESIS

by: Ta-Kuan Chiang
Thomas W. Lugar
General Electric Environmental Services, Inc.
Lebanon, Pennsylvania 17042

ABSTRACT

An analytic model using the modified Deutsch approach has been developed to describe the overall performance of an electrostatic precipitator comprising two different configurations or energization methods in tandem. Measurements of the overall collection efficiency and the collection efficiency of either configuration provide sufficient information to isolate the performance contributed by the other. Field data, obtained with pulse energization at the outlet half of the plate area and conventional dc energization at the inlet half of a full-scale utility precipitator, are presented to illustrate the method.

INTRODUCTION

In electrostatic precipitation technology, pilot-scale testing under actual flue gas conditions has been used for obtaining full-scale sizing data for new applications or fuel sources. It has also been used for field demonstration of new improved electrostatic precipitator designs. Typically, a scaled-down version of the conventional or improved design is set up in parallel with the existing flue gas control device. This parallel arrangement is often referred to as a slipstream pilot. A slipstream pilot is generally small and compact in size and thus transportable from site to site. To obtain meaningful test results, conditions of gas flow, particle size distribution and electrical sparkover levels experienced in a full-scale installation must be closely duplicated in the slipstream pilot. Even if these conditions are satisfied, prior operating experience of full-scale installations is required to provide empirical guidelines to correlate slipstream pilot observations to full scale with acceptable accuracy. Thus, unless reliable scaling means exist for direct extrapolation of slipstream pilot performance to full-scale design, the method of slipstream pilot testing cannot be extended without reservation for testing a new or improved precipitator concept since prior experiences on full-scale installations would not exist.

This paper discusses the methodology of evaluating an alternate on-stream full-scale pilot test wherein a portion of the existing full-scale precipitator is modified with a new or improved precipitator design or energization concept. Where space is available, an electrical section could be added in series to test a new design concept. Following the modified Deutsch approach (1,2) for both configurations, an analytic model capable of separating precipitator performances of each individual configuration can be established. With the assistance of this analytic model, full-scale sizing information for a new or improved precipitator can thus be obtained directly without the prerequisite of empirical guidelines derivable only from existing full-scale installations. Obviously, a properly selected testing site on a small full-scale unit would be ideal to minimize on-stream full-scale pilot testing costs in the case where a new precipitator design is to be evaluated. The size of the full-scale unit would not be a critical consideration in testing of new methods of energization such as pulse powering which requires no internal modifications to the precipitator.

STATEMENT OF PROBLEM

Similar to the circuit analysis and synthesis in electrical engineering practices, on-stream electrostatic precipitator pilot testing comprising two different configurations or energization means in tandem is also a problem of analysis and synthesis. Following the modified Deutsch representation, the input and output of the problem are the corresponding volumetric gas flow rate v, the particle loadings or the collection efficiency η, and k values for mainly particle dispersion characterization. The precipitators are completely and uniquely described by modified migration velocity ω_k, collection area A, or the plate area to flow rate ratio A/v.

The problem of electrostatic precipitator synthesis is to find two precipitator configurations in tandem characterized with a different ω_k and A/v to provide a resultant efficiency of $\tilde{\eta}$, or a combined modified migration velocity of $\tilde{\omega}_k$ at the conditions of flow rate v, and particle dispersion k. To state briefly, the problem of synthesis becomes:

Given: Particle dispersion k; upstream precipitator characterized by ω_k, A_1/v; downstream precipitator characterized by ω_k', A_2/v.

Find: The required performance, $\tilde{\omega}_k$ or $\tilde{\eta}$, has indeed been achieved.

Schematically, the problem can be represented conveniently in a block-diagram form as shown in Figure 1 where size of each block indicates the relative size of each precipitator configuration with parameters of interest contained inside each block as illustrated.

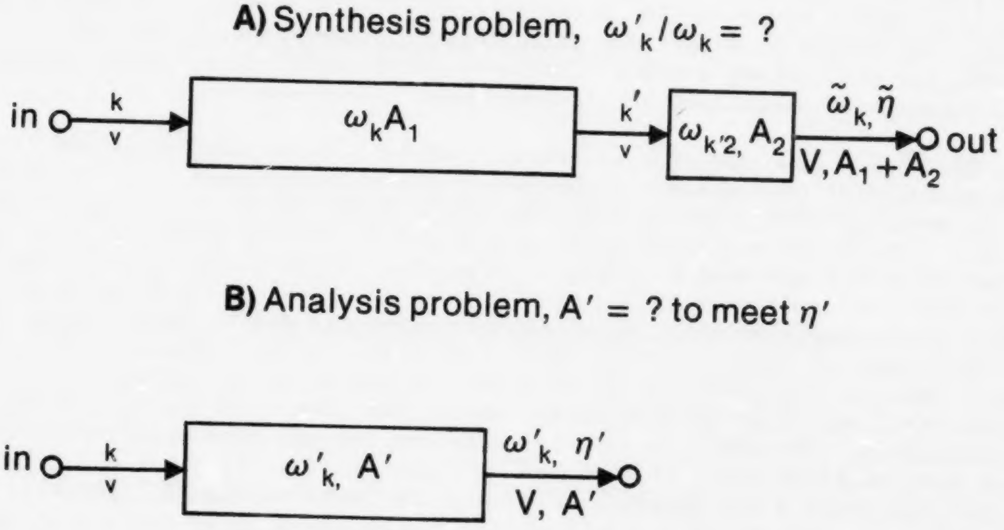
A) Synthesis problem, $\omega'_k/\omega_k = ?$

B) Analysis problem, $A' = ?$ to meet η'

Figure 1. Block-diagram representation of on-stream pilot testing.

The problem of electrostatic precipitator analysis of particular interest here is to scale up the pilot data of an on-stream full-scale pilot testing directly to a full-scale design. Briefly stated the analysis problem is:

Given: Downstream precipitator characterized by ω_k', A_2/v.

Find: A'/v size of downstream precipitator required to achieve a design efficiency of η', using the downstream precipitator only.

Block diagram representation of the corresponding analysis problem is also illustrated in Figure 1.

EXPERIMENTAL AND ANALYTICAL PROCEDURES

To implement an on-stream full-scale pilot testing, a pilot designed with all aspects of a full-scale unit except a much reduced length in its flow direction is to be installed directly downstream following an existing full-scale conventional configuration or installed to the outlet section of the existing unit by retrofit.

Utilizing correct analytical procedures, the pilot performance thus obtained can be used directly to size a full-scale unit. Experimentally, performances of the conventional unit alone and together with the pilot combined will be used to establish the baselines respectively. Analytically, normalization procedures will be followed to reduce performance of the combined configuration at an equal footing. These experimental and analytical procedures are best illustrated via block-diagram illustrations as shown in Table 1.

TABLE 1. PROCEDURES OF PRECIPITATOR PERFORMANCE SYNTHESIS AND ANALYSIS

Step	**Block Diagram**	**Remark**
I	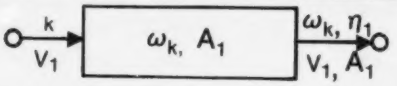 k V_1 ω_k, A_1 ω_k, η_1 V_1, A_1	Baseline ω_k, Conventional
II	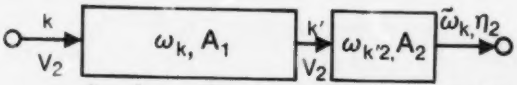 k V_2 ω_k, A_1 k' V_2 $\omega_{k'2}, A_2$ $\tilde{\omega}_k, \eta_2$ $A = A_1 + A_2, A_1 = fA, A_2 = (1-f)A$	Baseline $\tilde{\omega}_k$, New/improved
III	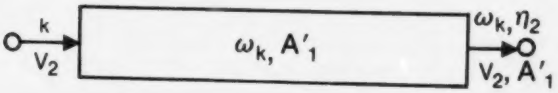 k V_2 ω_k, A'_1 ω_k, η_2 V_2, A'_1	Normalization, A'_1
IV	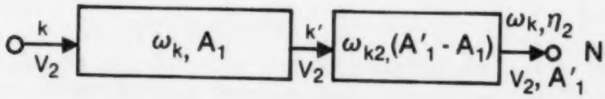 k V_2 ω_k, A_1 k' V_2 $\omega_{k2}, (A'_1 - A_1)$ ω_k, η_2 V_2, A'_1	Normalization, $\omega_{k'2}/\omega_{k2}$
V	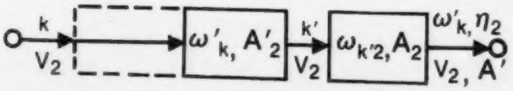 k V_2 ω'_k, A'_2 k' V_2 $\omega_{k'2}, A_2$ ω'_k, η_2 V_2, A'	Normalization, A'
VI	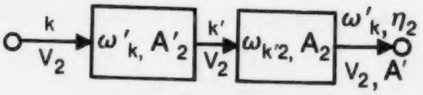 k V_2 ω'_k, A'_2 k' V_2 $\omega_{k'2}, A_2$ ω'_k, η_2 V_2, A'	Normalization, ω'_k/ω_k

Beginning at Step I, Table 1, the pilot is deenergized. A baseline of the existing full-scale conventional precipitator ω_k, A_1/v_1, η_1, is first established experimentally at an operating condition of k and v_1. Similarly, Step II establishes experimentally a baseline of the combined performance, $\tilde{\omega}_k$, A/V_2, η_2, at an operating condition of k and v_2. Steps I and II thus complete the experimental procedures.

Step III starts the normalization procedures. Based on ω_k established in Step I, it proceeds to find out the increased plate area to flow rate ratio, A_1'/v_2, that is required to generate equal performance η_2 as obtained at the combined baseline condition. At Step IV, the actual normalization begins by introducing an artificial new particle dispersion value k′ immediately following the conventional precipitator. The k′ introduced in Step IV is made to equal the k′ contained in Step II. By accomplishing these steps, performance of the conventional precipitator has thus been separated into two parts consisting of an upstream section and a downstream section, the downstream section is normalized in such a way that a comparison of performance with the new improved electrostatic precipitator can be made directly.

Similarly, assuming that the new or improved electrostatic precipitator is to take the place of the existing full-scale conventional precipitator as well, Step V starts the normalization at the inlet by reducing artificially the plate area to flow rate ratio such that the overall performance is equal to that in Step II. With conditions at the outlet section remaining unchanged, Step VI concludes the analytical procedure with a direct comparison of performances, ω_k'/ω_k.

MATHEMATICAL REPRESENTATION

Using modified Deutsch equation, precipitator performance is described in terms of a modified migration velocity ω_k, and a k value varying from 0.4 to 0.8 to account for particle size dispersion, electrical energization, non-uniformity in gas flow, and others representative of a typical operation of a conventional precipitator. To simplify the mathematical representation of an on-stream pilot performance, k value here is assumed to be predominately particle size dependent whereas other factors are of minor concern. Typically, if the existing full-scale conventional precipitator is represented with value k, then the pilot improved precipitator which is downstream of the existing conventional unit has to be represented with a different value k′ to describe the effect of reduced particle sizes.

In Figure 1, let ω_k be the modified migration velocity of the conventional unit having plate area A_1, and also for that particular application, particle size dispersion is represented by value k. If the overall collection efficiency with the on-stream pilot unit is η_2 at flow rate of v_2, then, from the conservation of mass, and in accordance with modified Deutsch approach,

$$\eta_2 = 1\text{-EXP}\{-(\omega_k A_1/v_2)^k\}\ \text{EXP}\{-(\omega_{k'2} A_2/v_2)^{k'}\} \tag{1}$$

also,

$$\eta_2 = 1\text{-EXP}\{-(\tilde{\omega}_k A/v_2)^k\} \tag{2}$$

where $\omega_k'2$ corresponding to value k' is the modified migration velocity of the pilot unit having plate area A_2, $\tilde{\omega}_k$ corresponding to value k is the combined modified migration velocity having a combined plate area of $A = A_1 + A_2$. Note that the full-scale improved precipitator, i.e., without the upstream conventional unit, would have a modified migration velocity ω_k' corresponding to value k. It is invariably true that physically the modified migration velocity $\omega_k' \neq \omega_k'2$. Following the experimental and analytical procedures outlined in Table 1, the relationship of ω_k'/ω_k can be established following the sequence of manipulations illustrated below.

Step I in Table 1 provides a baseline operation of the existing full-scale conventional unit when its downstream pilot is not energized. Analytically, its performance η_1 is,

$$\eta_1 = 1\text{-EXP}\{-(\omega_k A_1/v_1)^k\} \tag{3}$$

or,

$$\omega_k = \{-\ln(1-\eta_1)\}^{1/k}/(A_1/v_1) \tag{4}$$

Step II provides a baseline operation of the combined configuration when the pilot unit is energized. Its analytical expressions have already been described in Equations (1) and (2). Let $A_1/A \equiv f$, and $A_2/A \equiv (1-f)$,

$$\eta_2 = 1-e^{-(\omega_k fA/v_2)^k}\ e^{-\{\omega_k'2(1-f)A/v_2\}^{k'}} \tag{5}$$

In Step III, results of Step I are used to establish the required plate area A_1', for the conventional unit with an equal performance η_2 as described by the combined configuration. That is,

$$\begin{aligned}\eta_2 &= 1\text{-EXP}\{-(\omega_k A_1'/v_2)^k\}\\ &= 1\text{-EXP}\{-(\tilde{\omega}_k A/v_2)^k\}\end{aligned} \tag{6}$$

or,

$$A_1'/v_2 = (\tilde{\omega}_k/\omega_k)(A/v_2) \tag{7}$$

Normalization in Step IV provides the same k' value to describe a conventional unit having plate area of $\{(\tilde{\omega}_k/\omega_k)-f\}A$ downstream of the existing full-scale conventional unit. Let the modified migration velocity in the section of $\{(\tilde{\omega}_k/\omega_k)-f\}A$ be ω_{k2} corresponding to k' for a conventional unit, Equation (6) becomes,

$$\eta_2 = 1-e^{-(\omega_k fA/v_2)^k} \; e^{-\{\omega_{k2}(\frac{\tilde{\omega}_k}{\omega_k}-f)\frac{A}{v_2}\}^{k'}} \tag{8}$$

Comparison of Equations (5) and (8) results in,

$$\omega_k{}'_2/\omega_{k2} = \frac{f}{1-f}\left(\frac{\tilde{\omega}_k}{f\omega_k} - 1\right) \tag{9}$$

where quantities at the right-hand side of Equation (9) are all known.

Similarly, Step V establishes the required size of an improved precipitator for achieving equal efficiency as the combined unit. Let ω_k' be the modified migration velocity of a full-scale improved precipitator, and also defining an enhancement factor $\varepsilon \equiv \omega_k'/\omega_k$, the required size A'/v_2, can be found from,

$$\begin{aligned}\eta_2 &= 1-\mathrm{EXP}\{-(\tilde{\omega}_k A/v_2)^k\} \\ &= 1-\mathrm{EXP}\{-(\omega_k' A'/v_2)^k\}\end{aligned} \tag{10}$$

or,

$$A'/v2 = (\tilde{\omega}_k/\varepsilon\omega_k)(A/v_2) \tag{11}$$

With Equation (11), performance of the new improved precipitator can also be expressed in the form,

$$\eta_2 = 1-e^{-\{\omega_k'(\frac{\tilde{\omega}_k}{\varepsilon\omega_k}-(1-f))\frac{A}{v2}\}^k} \; e^{-\{\omega_k{}'_2(1-f)\frac{A}{v2}\}^{k'}} \tag{12}$$

Comparison of Equations (5) and (12) establishes,

$$\begin{aligned}\varepsilon &\equiv \omega_k'/\omega_k \\ &= \frac{f}{1-f}\left(\frac{\tilde{\omega}_k}{f\omega_k} - 1\right)\end{aligned} \tag{13}$$

From Equations (9) and (13), it is also shown that the enhancement factor ε is invariant with respect to its positions in a setup as long as the inlet conditions, e.g., flow rate v, and dispersion value k, remain the same. This conclusions is in agreement with the fundamental precipitation process for which the precipitator performance is known to be characterized with flow rate and dispersion value k.

ILLUSTRATIVE EXAMPLE

On-stream full-scale pilot testing examined in this paper is new, and thus it has not been actually carried out in the field. However, the recent demonstration of pulse energization on a full-scale utility electrostatic precipitator (3) provides an illustrating example of on-stream full-scale pilot testing. During that field demonstration, pulse energization was only applied at the outlet half of the plate area of an existing conventional precipitator whereas the inlet, or the upstream, half of plate area operated as a conventional precipitator. Thus, f in this case was 0.5. Use of Equation (13) and assuming k = 0.5, the pertinent data contained in Table I of Reference (3) are reduced accordingly and are tabulated in Table II

TABLE II. FIELD RESULTS (3)

$k = 0.5$, $\varepsilon = \omega_k'/\omega_k$, $F = \omega_k/\omega_k(0)$, $\omega_k(0) = .7092$ m/s

Date	ω_k (m/s)	$\tilde{\omega}_k$ (m/s)	$\tilde{\omega}_k/\omega_k$	ε	1/F
11/12/80	.1576				4.50
11/13/80	.1576	.2484	1.5761	2.15	4.50
11/20/80	.3480				2.04
11/20/80	.3480	.3905	1.1221	1.24	2.04
11/24/80	.2282				3.11
11/24/80	.2282	.3027	1.3264	1.65	3.11
11/25/80	.2292				3.09
11/25/80	.2292	.2999	1.3086	1.62	3.09

Modified migration velocities:

$\omega_k(0)$, dc, conventional, washdown baseline
ω_k, dc, conventional, operating
ω_k', pulse energization, operating

To avoid the ambiguity in the enhancement factor ε, a dc performance factor F, defined as the ratio of modified migration velocity at the operating condition over the maximum possible modified migration velocity at the unseasoned condition or the washdown condition, is also introduced in Table II. Figure 2 is a plot of the ε vs. 1/F. Surprisingly, experimental data thus reduced and plotted fit almost exactly according to a straight line intercepting the line $\varepsilon = 1.0$ at $(1/F) = 1.361$ or $F = 0.735$. From Figure 2, it is seen that the on-stream full-scale pilot testing was indeed an effective means for obtaining directly the full-scale sizing data for new improved precipitators.

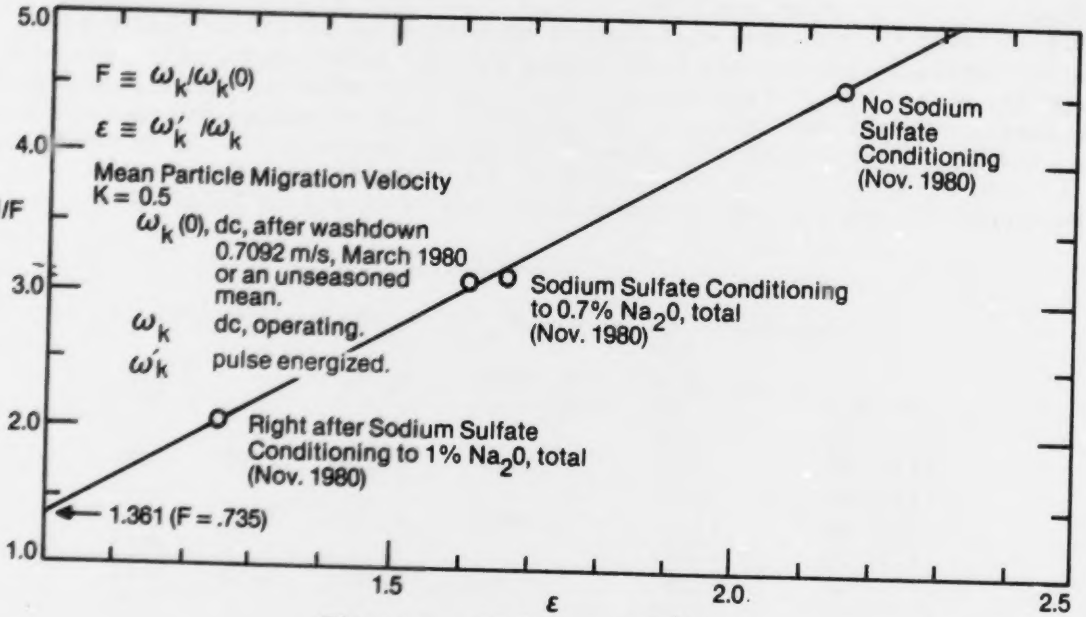

Figure 2. Field results (3).

DISCUSSIONS AND CONCLUSIONS

Although a great deal of research effort has been devoted in the past on the subject of electrostatic precipitation modeling, reliable scaling means still do not exist for direct extrapolation of laboratory results to pilot-plant performance, and pilot-plant performance to full-scale design. It is generally observed that a laboratory precipitator outperforms a pilot-plant precipitator, and a pilot-plant precipitator outperforms a full-scale installation. Direct scaling factors, however, have not been found. Thus, to avoid pitfalls inherent in arbitrary and improper interpretation of slipstream pilot-scale observations, empirical guidelines derived from operating experiences of existing full-scale units of similar application or fuel source are provided, and are strictly observed for obtaining sizing information with acceptable accuracy. With diversified, long-term experiences existing for full-scale conventional wire-duct precipitators, this empirical approach for sizing data has been successful for introducing the conventional precipitator for new applications or fuel sources, but, definitely, it has failed to realize new improved precipitator for full-scale applications.

To promote advancement in modern electrostatic precipitation technology, new ideas of improved precipitator need to be encouraged and introduced timely and economically. To accomplish this goal, this paper investigated the problems of an on-stream full-scale pilot testing scheme in which a one-to-one scale pilot with a short axial length in the flow direction is introduced or retrofitted downstream of an existing full-scale conventional precipitator. Because the size of this pilot is nearly a full-scale replica, pilot data of the new improved precipitator if separable from the combined performance would thus unquestionably represent a full-scale design; no prior experience on an operating full-scale unit would thus be needed. Following the modified Deutsch approach, the method of analysis and synthesis of the combined on-stream full-scale pilot testing has been indeed established providing means to separate the combined performances. The combined field data taken from recent development on pulse energization comprising a conventional dc energization upstream and a pulse energization downstream were used to demonstrate the utility of this analytical method.

To assure practical and economical on-stream full-scale pilot testing, the importance of the testing site selection must be emphasized. An ideal site for on-stream full-scale pilot testing would thus satisfy all or at least one of the conditions listed below:

- An operating full-scale conventional precipitator with an adequate flow capacity.
- An operating full-scale conventional precipitator requiring upgrading to meet emission standards.

The former condition prevents an unnecessarily large, and consequently costly, pilot fabrication and erection; whereas the latter justifies a full-scale installation of an improved precipitator.

The work described in this paper was not funded by the U.S. Environmental Protection Agency and therefor the contents do not necessarily reflect the views of the Agency and no official endorsement should be inferred.

REFERENCES

1. Allander, C. and Matts, S. Einwirkung der Korngrossenverteilung auf den Abscheidungsgrad von Elelctrofiltern. Staub, 52: 738, 1957.
2. Matts, S. and Ohnfeldt, P.O. Efficient Gas Cleaning with SF Electrostatic Precipitators. Flakt Review, 1963-64.
3. Piulle, W., Marchant, G.H. and Gooch, J.P. Evaluation of Performance Enhancement Obtained with Pulse Energization Systems on a Hot-side Electrostatic Precipitator. Paper presented at the Third Symposium on the Transfer and Utilization of Particulate Control Technology, U.S. Environmental Protection Agency, Orlando, Florida, March 9-12, 1981.

COMPUTER MODEL USE FOR PRECIPITATOR SIZING

by G. W. Driggers
A. A. Arstikaitis
L. A. Hawkins
Environmental Systems Division
Combustion Engineering, Inc.
Birmingham, Alabama 35243

ABSTRACT

The design of utility industry precipitators is typically based on a historical data base of performance and operating characteristics gathered from full scale units. Development over the last ten years of first principle analytical models for performance prediction offer new tools for the precipitator designer. The EPA/SORI model has been selected by the Combustion Engineering Environmental Systems Division for refinement to the C-E precipitator design. The current historical data sizing procedure and performance prediction approach is described followed by a discussion of the EPA/SORI model and refinements required to make it fit the C-E design.

INTRODUCTION

The selection of specific collection area (SCA) for utility precipitators is based throughout the industry on extrapolation from existing data.(1,2) Information collected on operating full scale units, including net penetration, electrical characteristics, type of coal fired, type of boiler, flyash chemistry, and resistivity, are typically used to draw correlations to new utility requirements. It is normal in the analytical design of a precipitator to use the traditional or modified Deutsch-Anderson equation relating precipitator size and collection efficiency to a known or extrapolated precipitation parameter ("migration velocity") to predict SCA needed to meet a specified level of performance.(1) The Environmental Systems Division of Combustion Engineering, Inc. has been able to use this approach with success when designing new units. However, changes in the industry--requirements for very high efficiency, new sources of coal, power consumption guarantees, and stricter opacity limits--have made it necessary to look at more sophisticated analytical techniques for predicting operating characteristics. Expanding the data base to cover fully all these variables through pilot, prototype, and full scale testing, would be prohibitively expensive.

In the last ten years, under Environmental Protection Agency sponsorship, Southern Research Institute (SORI) has developed a mathematical model of the precipitation process and computerized it.(3) Use of the current model to synthesize a particular precipitator is limited, however, by certain implicit assumptions that were necessary to make the model a general process simulation. To make the model fit a specific precipitator manufacturer's design requires that modifications be made and certain input variables specified. C-E/ESD has identified these required changes and developed predicted values for the input variables based on a variety of tests on C-E precipitators. The refined model is being used to assess predicted efficiency, fractional penetration (which is, in turn, input to an opacity prediction program), and power consumption on new and proposed units.

The following sections discuss the existing data base and sizing procedure, the basic EPA/SORI computer model, required changes to the model, how these were implemented, and an example of results that have been obtained analyzing operating units.

DATA BASE AND SIZING PROCEDURES

The C-E data base consists of design and performance information on over twenty-five installations with the number growing yearly as new units are commissioned and tested. These test data have been used to develop sizing guidelines based on use of the calculated precipitation parameter W_K (commonly called the "modified migration velocity"). These W_K values are cross referenced to coal source and chemistry, particularly sulfur, moisture and sodium content. Other parameters, such as inlet dust loading, operating temperature, ash resistivity, gas analysis and particle size distribution, are also correlated to W_K. Boiler operating parameters, geometry of the precipitator and a historical chronology are, of course, also included in the computerized data base management program.

To evaluate sizing on a new application the first step is to select a generic coal type and/or chemistry in the data base that best approximates the new specification. A value for W_K is drawn specifically from the data. Subsequently, if an inlet total dust loading is not specified, one is calculated based on given ash content and Btu values for the coal, the plant size and an assumed carryover value. Pitot correction factors from the published ASME literature and C-E data base are applied to the stoichiometric calculations to determine the total flow anticipated for the new precipitator. From these values a specific inlet dust (or "grain") loading can be determined and a total efficiency requirement calculated for a specified outlet concentration. This is compared to the efficiency requirement (if one is specified) and the more stringent value is used in subsequent calculations.

The parameter W_K is then modified by correction factors based on the comparison of the specific values for sulfur, sodium, temperature, moisture, and inlet dust loading in the data base vs. the specification. The final value for W_K is used in the equation

$$SCA = \frac{\{-\ell n(1-\eta)\}^{\frac{1}{x}}}{W_K}$$

(where η is the required efficiency and x is the exponent of the Matts-Ohnfeldt modification to the Deutsch-Anderson equation) to determine the required collection efficiency. With the specific collection area known, the remaining geometrical parameters can be calculated.

The approach being used by C-E to improve on this process is twofold. First, the correction factors used to modify W_K are being defined based on theoretical modeling as well as empirical data to allow better interpolation and extrapolation. Second, the theoretical model is being coupled with empirical data to derive a more rigorous predictive technique. The basis for these efforts is the EPA/SORI model.

EPA/SORI COMPUTER MODEL

Over the past decade, Southern Research Institute (SORI) has been developing a computer-oriented mathematical model of the electrostatic precipitation process.(3) The model is necessarily general so that it can be applied to most wire-plate geometries. The model can be a powerful tool for the ESP manufacturer, particularly when modified to apply to a specific precipitator design.

Required inputs to the SORI ESP model include important dimensions of the precipitator internals, such as wire-to-plate spacing, wire-to-wire spacing, and collecting surface per electrical section; operating voltage and current in each electrical section; and gas stream parameters, such as inlet dust loading, particle size distribution, gas volume flow rate, gas viscosity, and gas temperature. The model gives an ideal prediction of collection efficiency and outlet particle size distribution. The model also predicts ESP performance corrected for nonideal conditions, such as non-uniform gas flow distribution, gas sneakage, and reentrainment with and without rapping.

The model is built around the traditional Deutsch-Anderson equation,

$$\eta = 1-e^{(-W \cdot SCA)}$$

where η = collection efficiency,
W = "traditional" migration velocity near collecting surface,
SCA = specific collection area

The derivation of this equation assumes (among other things) that the particle migration velocity (W) is constant near the collecting surface since the migration velocity is calculated from

$$W = \frac{q\ E_pC}{6\ \Pi\ a\mu}$$

where q = particle charge,
E_p = electric field at the collecting plate,
C = Cunningham correction factor,
a = particle radius,
and μ = gas viscosity.

The assumption implies that the particles are all of the same size and that electrical conditions are constant. To satisfy the first condition, the particle size distribution is divided into discrete size bands, each having a representative particle size and all calculations are performed for each particle size band. To satisfy the second condition, the precipitator is divided into length increments that are small enough that electrical conditions remain essentially constant over the increment.

In order to calculate the particle migration velocities, the electric field at the collecting electrode and the charge on each particle size must be determined in each increment. Particle charge is calculated from the unipolar, ionic-charging theory formulated by Smith and McDonald.(4) The electric field distribution in the interelectrode space is determined from classical equations, assuming a round wire discharge electrode and flat plate collecting electrode geometry. The results are used to calculate the average electric field at the collecting electrode in a particular length increment. However, few precipitators have round wire, flat plate geometries and for enhanced accuracy the model must be modified to account for actual voltage and current conditions. This can be accomplished by determining the corona current distribution at the collecting plate as a function of the discharge and collecting electrode geometries. This distribution is used in the computer model as a boundary condition for calculation of the interelectrode electric field and the associated gradient near the plate. A theoretical correction is also required for space charge density near the DE if a non-round wire geometry is used.

Also, it is necessary to collect data sufficient to predict particle size distribution, voltage-current characteristics and non-ideal parameters (sneakage per field, reentrainment and gas flow distribution). Through various measurements on utility precipitators by C-E and others, sufficient data have been accumulated to make the computer model highly accurate with regard to performance correlation.

COMPUTER MODEL CHANGES AND INPUT

The EPA/SORI precipitator performance prediction program has been modified to model the specific geometry and electrical characteristics of the C-E precipitator. Non-ideal factors have been determined based on the data base discussed earlier after modeling of the electrical characteristics. Since the majority of the utility data base was obtained on designs with identical mechanical characteristics, (plate spacing, sneakage baffles, aspect ratio, rapping system, etc.), the model can be calibrated very accurately. The key element in assuring that the values determined for non-ideal parameters were not just "Kluge factors", was establishing real electrical operating characteristics and particle size distributions. The former came from specific measurements, the most involved of which was corona current distribution on the collecting plate. The latter was based on measurements or the existing data base.

CORONA CURRENT DISTRIBUTION DETERMINATION

Combustion Engineering uses the collecting electrode (CE) configuration shown in Figure 1. The contours provide rigidity and help to reduce reentrainment. Two discharge electrodes (DEs) are currently in use, a barbed electrode and a "star" electrode. The barbed electrode is used extensively in inlet fields when an ash with high resistivity is being collected. The star electrode is used to achieve higher interelectrode voltage for a given corona current.

The points on the barbed electrode are corona current sources and the collecting surface is irregular, thus current density distribution different from that produced by the round wire on a flat plate is expected. This distribution was measured for comparison to the round wire distribution. These data were then used to develop a correction to the predicted electric field at the plate as discussed earlier.

The current density distribution at the collecting electrode surface for the C-E wire-plate geometry was measured using the apparatus shown schematically in Figure 2. An array of metal squares arranged in a horizontal

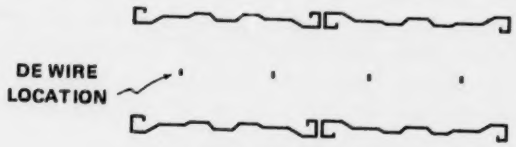

TYPICAL GAS PATH SHOWING COLLECTING ELECTRODE CROSS SECTION AND DE WIRE LOCATION.

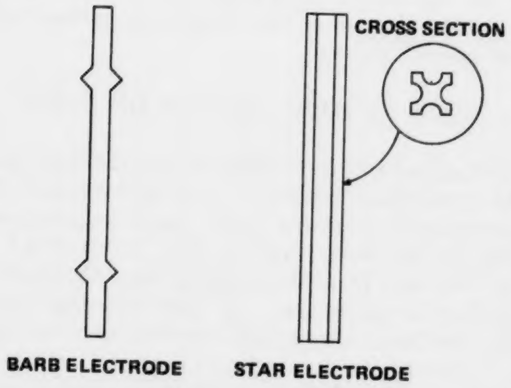

Figure 1. Discharge and collecting electrode configurations

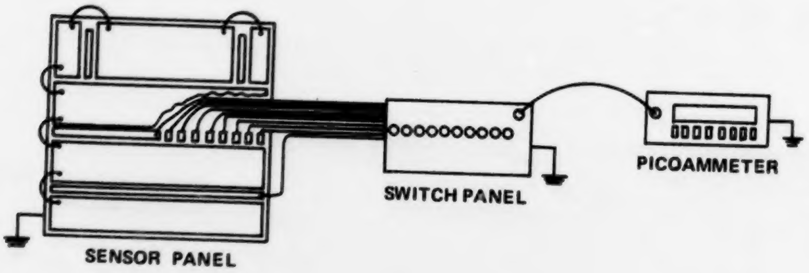

SCHEMATIC

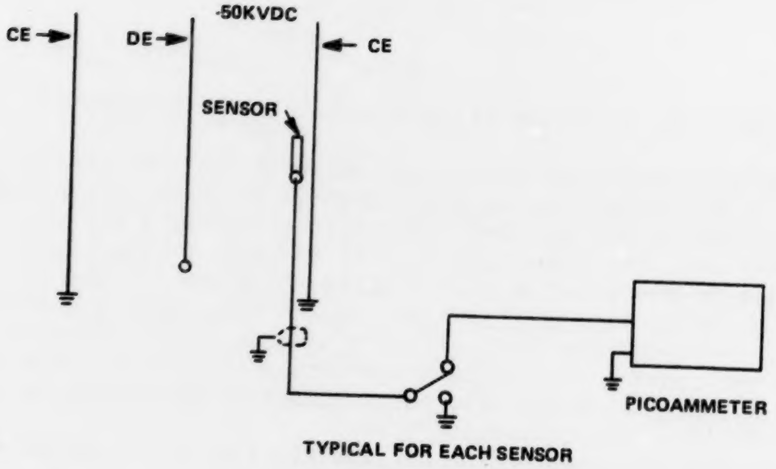

Figure 2. Current density measurement apparatus.

row across the CE panel and a horizontal strip served as current sensing elements. A sheet of plastic formed to the shape of the CE panel served as a movable mount for the sensors and as a dielectric to isolate the sensors from the grounded CE panel. Each sensor was connected by shielded cable to a switch panel located outside the precipitator. The panel was connected by shielded cable to a picoammeter which was grounded directly to the CE panel.

The panel was attached to a CE plate in a utility precipitator so that the sensors were initially in the same horizontal plane as a barb on the DE wire. A voltage-current curve was obtained and the current at each sensor was recorded at each point on the curve. The sensor panel was subsequently moved down five times in one-quarter inch increments and a V-I curve was taken at each position. The last increment placed the sensors in a horizontal plane halfway between two DE points. Specific locations for measurements are shown in Figure 3.

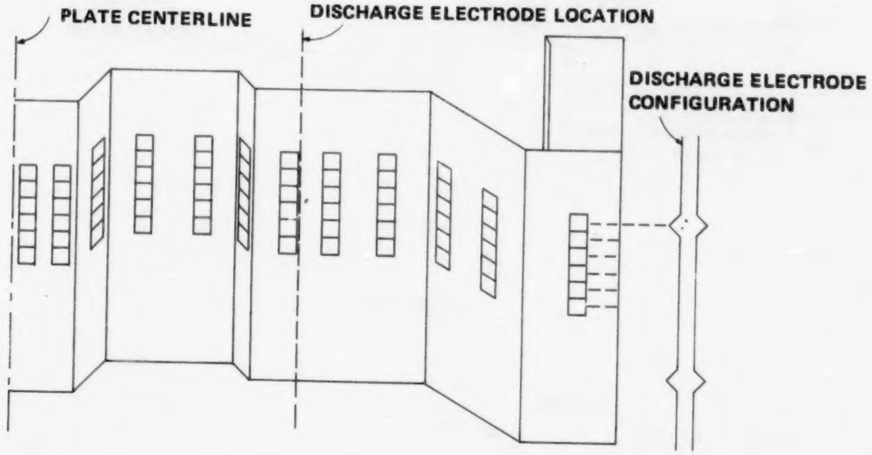
PLATE CENTERLINE
DISCHARGE ELECTRODE LOCATION
DISCHARGE ELECTRODE CONFIGURATION

Figure 3. Location of current density measurements.

Based on these measurements, it was observed that the current density is about twice the average in the region around the barb on the wire. Moving away from the wire in the horizontal plane, the current falls off rather slowly at first and then drops quickly near the edge of the plate in a fashion similar to the round wire/flat plate geometry. In the vertical direction, the current is about constant in the first quarter distance between the points and then falls off to a minimum halfway between the barbs. It is the latter contour that differs most significantly from the assumptions of the basic model. The model uses three different techniques to calculate the electric field at the collecting plate:

(1) an estimation based on the average electric field across the interelectrode space;
(2) a rigorous calculation of the electric field distribution in the interelectrode space, used when operating voltage and current are known; and
(3) a calculation procedure similar to technique (2) used when operating voltage and current are unknown.

The third technique is the only one sensitive to the geometry of the DE wire. It was used to find the equivalent round wire radius necessary to produce the measured current density in each horizontal section at the applied voltage. An overall equivalent radius was then found to give the same field at the plate as the average from the horizontal sections. After establishing an equivalent round wire medium, correction factors were developed to modify the predictions of electric field at the plate made by techniques (1) and (2).

The computer model was subsequently modified to take these corrections into account. The modified computer model was then used to quantify non-ideal factors on a consistent basis using the C-E data base.

VOLTAGE-CURRENT MODEL

Voltage-current (V-I) characteristics of a specific wire and plate geometry will vary as the dust loading varies and as the resistivity of the dust layer changes. To analyze an existing precipitator, the measured values from transformer-rectifier (T-R) set instruments can be used. For predicting performance of a new unit, some estimating procedure must be used. For a new unit, C-E has developed and is refining an empirical model based on data collected from operating units with various inlet dust loading and ash resistivity. Ash resistivity is being characterized by laboratory measurements and prediction using the computer program of Bickelhaupt.(5) Correlations between ash chemistry using ASTM coal ashing techniques and hopper ash samples are being developed. Thus, the very extensive coal ash data base at C-E can be used to predict flyash resistivity for new applications.

V-I curves from several paralled electrical cells at a facility are plotted together (as illustrated in Figure 4) and a best fit is established.

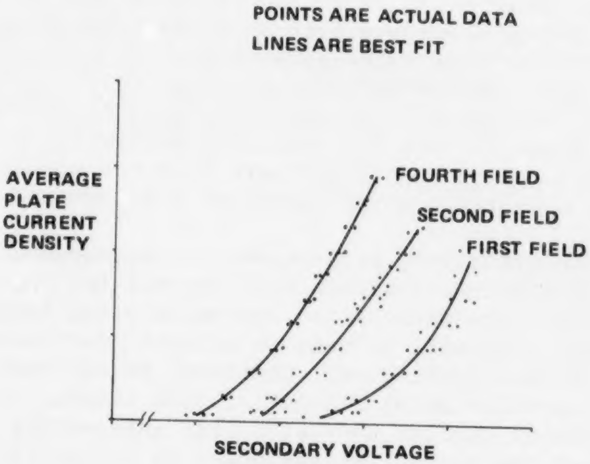

Figure 4. Voltage-current model for a C-E precipitator with barbed electrodes operating on a 10^{11} ohm-cm lignite ash and 2.5 grain/ACF inlet loading.

These data are then correlated to dust loading and resistivity as a function of electrical cell location (inlet, second, third, etc.). Thus, using a specified flyash chemistry and inlet dust loading, a prediction of the operating electrical characteristics of a particular section can be obtained by working from the first field to subsequent fields. Special attention is given to recording flashover (sparking) points and conditions, particularly repetition rate. This has only been significant on inlet fields, since second fields typically experience only occasional sparking and all subsequent cells operate at current limit for the T-R set in a well constructed unit. Tolerances are tightly controlled on new units to assure this condition.

For a new application, an operating point resistivity is obtained from the data base or predicted using the program of Bickelhaupt. This is used in combination with the predicted inlet dust loading and anticipated electrical section size to project the probable voltage-current characteristics and operating point.

PARTICLE SIZE DISTRIBUTION MODEL

The statistical model developed by SORI under EPRI sponsorship is used to estimate the inlet particle size distribution for the new application where a coal type is specified. Nominal and worst case distributions are analyzed on Western sub-bituminous coals to assess possible impacts to both total collection efficiency and opacity prediction. This portion of the analysis is gaining significance as fractional efficiency guarantees are being specified by some customers.

COMPUTER MODEL APPLICATION

The modified computer model is currently being used in conjunction with the data base design procedure both as a cross check and a predictor of performance parameters not otherwise obtainable. In particular, fractional penetrations are being computed and used as input to a numerical opacity prediction program. The program is also being used in conjunction with the flyash resistivity predictor and V-I model for determination of power consumption expectations, precipitation parameter correction factor computation, and energy management system control algorithm development.

Total collection efficiency predictions and measurements made during past performance tests agree to within 0.05 percent for three cases examined in detail. Performance projections for new units being brought on line in late 1982 and through 1983 will be made to enhance confidence in the models and refine the predictive techniques. Continual development of various aspects of the C-E specific model are anticipated leading ultimately to a design approach based on process understanding; integrating the electrodynamic, gas dynamic, chemical and mechanical variables to obtain the most cost-effective precipitator.

The work described in this paper was not funded by the U.S. Environmental Protection Agency and therefore the contents do not necessarily reflect the views of the Agency and no official endorsement should be inferred.

REFERENCES

1. White, Harry J. Review of the state of the technology. In: Proceedings of the International Conference on Electrostatic Precipitation, October

1981; published by APCA, Pittsburgh, PA.

2. Nichols, Grady B. Electrostatic precipitator design. In: Proceedings of the International Conference on Electrostatic Precipitation, October 1981; published by APCA, Pittsburgh, PA.

3. McDonald, Jack R. A mathematical model of electrostatic precipitation. EPA-600/7-78-111b, U.S. EPA, Washington, D.C. 1978.

4. Smith, W. B. and McDonald, J. R. Development of a theory for the charging of particles by unipolar ions. J. of Aerosol Science, 7:151-166, 1976.

5. Bickelhaupt, Roy E., A technique for predicting flyash resistivity, EPA-600/7-79-204, U.S. EPA, Washington, DC, 1979.

IMPROVEMENTS IN THE EPA/SRI ESP PERFORMANCE MODEL

by

M. G. Faulkner
Southern Research Institute
Birmingham, Alabama 35255

R. B. Mosley; J. R. McDonald
Crestmont Associates, Inc.
Central City, Kentucky 42330

and

L. E. Sparks
Industrial Environmental Research Laboratory
U.S. Environmental Protection Agency
Research Triangle Park, North Carolina 27711

ABSTRACT

Revision 3 of the ESP performance model developed for the EPA at Southern Research Institute has been completed. This version features a reduction in required computer time of about a factor of 10 over revision 1 for the rigorous calculation of collection efficiency. In addition, several new procedures have been added to the model. One of these allows the calculation of plume opacity. Another calculates the effects of rapping reentrainment through a dynamic process which examines the results of each rap as it occurs. These changes and others will be described.

This paper has been reviewed in accordance with the U.S. Environmental Protection Agency's peer and administrative review policies and approved for presentation and publication.

Revision 3 of the electrostatic precipitator (ESP) performance model developed by Southern Research Institute (SRI) for the Environmental Protection Agency (EPA) has been completed. Since the model was released in 1975 (1), it has been widely used to study and troubleshoot existing precipitators and to validate proposed new precipitators. The revisions (2, 3, 4) to the original model have increased its usefulness and convenience of operation. Revision 3 further increases the model's utility by offering a significant reduction in required computation time plus several new features which are described in the following paragraphs.

The ESP model predicts precipitator performance by first performing the collection efficiency calculation under ideal conditions and then correcting the results for non-ideal conditions and unmodeled effects. For calculation purposes, the precipitator is divided into sections, permitting different electrical conditions in each section, and then further divided into a maximum of 45 incremental lengths on the order of the ESP's wire-to-wire spacing. The efficiency calculation is performed sequentially on each incremental length to determine the total collection efficiency. To compensate for the different charging and collection rates of large and small particles, the input dust load is divided into a maximum of 20 size bands, each of which is handled separately in the efficiency calculation.

The ESP model uses the Deutsch equation to calculate the collection efficiency for each particle size band in each incremental length. The Deutsch equation is given by

$$\eta = 1 - \exp(-Aw/Q) \qquad (1)$$

where

η = the fractional collection efficiency,
A = the collection plate area,
Q = the gas volume flow rate, and
w = the migration velocity of the charged particles.

The migration velocity is calculated from

$$w = \frac{qE_pC}{6\pi au} \qquad (2)$$

where

q = the charge on the particle,
E_p = the electric field at the plate,
C = the Cunningham slip correction factor,
a = the radius of the particles, and
u = the viscosity of the gas.

Thus the calculation of collection efficiency requires the calculations of the charge on each size particle in each incremental length and of the electric field at the plate. This can be done simply by estimation formulas or more rigorously by using a more complete charging theory developed by Smith and McDonald (5) and a detailed analysis of the field at all points in the precipitator. The more rigorous process yields better accuracy over a wide range of applications and is the more frequently used routine. However, it involves many lengthy calculations and requires much more computer time than the estimation process. The changes resulting in reduced computer time for Revision 3 affect the electric field and particle charge calculations of the rigorous calculation procedure.

Table 1 contains a summary of ESP model features including the changes due to the various revisions. These features are discussed below in the order in which they are presented in Table 1.

1. The estimation procedures for calculating particle charges and the electric field at the plate remain unchanged.

2. The rigorous calculation of the electric field at the plate has been changed in Revision 3. Although the general procedure used to solve the field equations remains the same, the convergence of the iterative technique used to achieve a solution is accelerated using the dominant eigenvalue method. This method has previously been applied to various chemical processes and was applied to the electric field calculation by Felder and Arce-Medina. (6)

The procedure used in the rigorous calculation of the field at the plate consists of simultaneously solving two field equations relating the electric potential and the space charge density at every point inside the precipitator. These are:

$$\frac{\Delta^2 V}{\Delta x^2} + \frac{\Delta^2 V}{\Delta y^2} = -\frac{\rho}{\varepsilon_0}, \text{ and} \tag{3}$$

$$\rho^2 = \varepsilon_0 \left(\frac{\Delta v}{\Delta x}\frac{\Delta \rho}{\Delta x} + \frac{\Delta v}{\Delta y}\frac{\Delta \rho}{\Delta y}\right) \tag{4}$$

where

ρ = the space charge density,
V = the potential,
x = the coordinate from wire to plate,
y = the coordinate along the gas flow, and
ε_0 = the permittivity of free space.

In the model, the calculation is performed at every point on the grid shown in Figure 1. The initial estimate of the potential at each grid point, V_{ij}, is made using Cooperman's solution to the field equations. (7) Following this, the space charge density at each grid point ρ_{ij}, is calculated from V_{ij}. V_{ij} is then recalculated from ρ_{ij}. The process of alternately calculating ρ_{ij} and V_{ij} continues until the change in V_{ij} between iterations is less than a preset value at every grid point. At this point the current density at the plate is calculated and compared to the measured value. If the values differ by more than 1 percent, the space charge at the corona is adjusted and the calculation of ρ_{ij} and V_{ij} begins again. Otherwise the potential solution is considered to have converged, and the value of the electric field at the plate is obtained.

TABLE 1. ESP MODEL REVISION SUMMARY

Process	Revision
Estimation procedure	1,2,3
Electric field calculation	
rigorous calculation	1,2
same with dominant eigenvalues (faster)	3
analytic approximation	2
Particle charging calculation	
Simpson's rule integration	1
Gaussian integration (faster)	2,3
Correction for non-ideal effects	
sneakage, velocity distribution	1,2,3
empirical rapping calculation	1,2,3
dynamic rapping calculation	3
Opacity calculation	3
Option of metric input data	3
Option to reduce printed output	3
Internal data set	3
VI curve generation	1,2,3
option to stop after printing VI curve	3
Routine to check input data	3

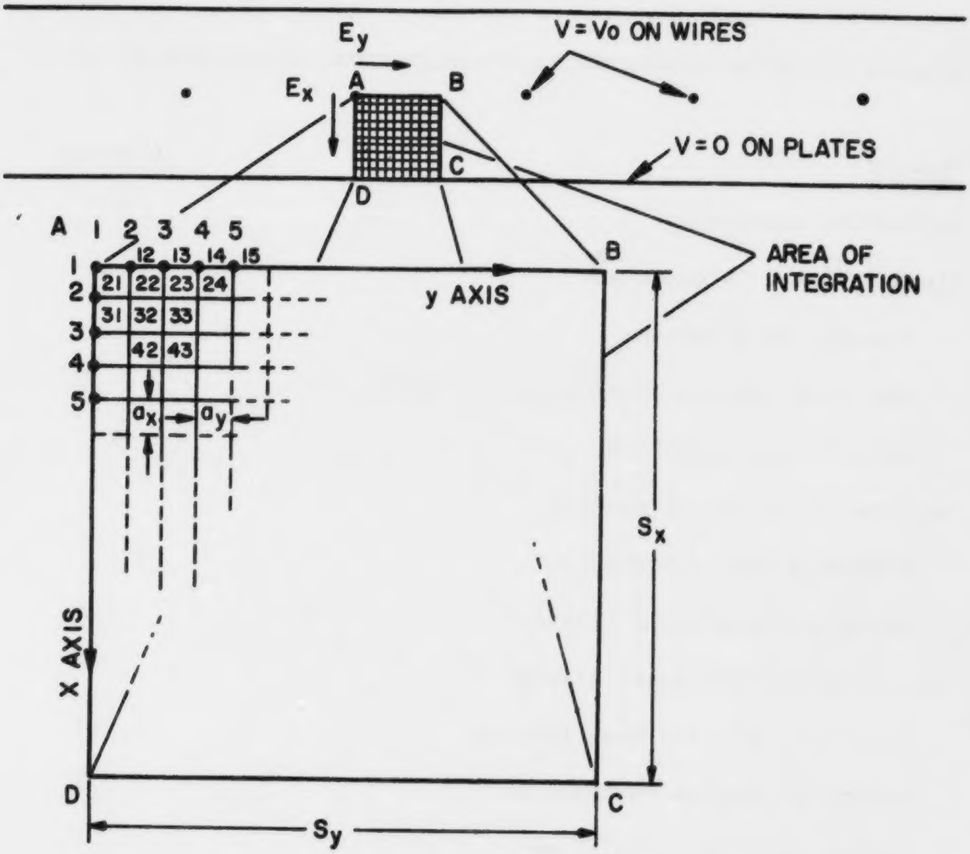
Ey
V = Vo ON WIRES
Ex
A
B
C
D
V = 0 ON PLATES
A 1 2 3 4 5
12 13 14 15
1 2 3 4 5
21 22 23 24
31 32 33
42 43
ax
ay
y AXIS
B
AREA OF INTEGRATION
X AXIS
Sx
D
C
Sy

S_y = ONE HALF WIRE TO WIRE SPACING
S_x = WIRE TO PLATE SPACING
a_x a_y = INCREMENT SIZES FOR INTEGRATION
V_0 = APPLIED VOLTAGE
E_x = COMPONENT OF ELECTRIC FIELD PERPENDICULAR TO PLATE
E_y = LONGITUDINAL COMPONENT OF ELECTRIC FIELD

4102-92

Figure 1. Nomenclature used in the numerical analysis of the electrical conditions in wire-plate precipitators.

In Revision 3, the convergence rate has been accelerated by the dominant eigenvalue method. Using the new procedure, two criteria are applied to the calculated potential after each iteration. These are (1) at least five iterations must have taken place since the last acceleration step, and (2) the change in the potential between the last two iterations must be less than a preset value at every grid point. These criteria ensure that each acceleration step has sufficient time to produce a stable solution before a new acceleration step is applied. If both of these criteria are met, the potential is adjusted at every point by a factor derived from the potential changes due to the last two iterations. The potential adjustment has the form:

$$V_{ij}^{(n+1)} = V_{ij}^{(n-1)} + \alpha(V_{ij}^{(n)} - V_{ij}^{(n-1)})/(1 - \lambda) \qquad (5)$$

where

$V_{ij}^{(n)}$ = the potential at point i,j calculated in the last iteration,

$V_{ij}^{(n-1)}$ = the potential calculated in the previous iteration,

$V_{ij}^{(n+1)}$ = the adjusted potential for use in the next iteration,

α = a damping factor, $0 < \alpha < 1$, used to prevent instability, and

λ = the dominant eigenvalue.

λ is given by

$$\lambda = \| \Delta V^{(n)} \| / \| \Delta V^{(n-1)} \| , \qquad (6)$$

where

$$\| \Delta V^{(n)} \| = ({}_i\sum{}_j \, [V_{ij}^{(n)} - V_{ij}^{(n-1)}]^2)^{1/2}. \qquad (7)$$

Following the adjustment, the mutual calculation of ρ_{ij} and V_{ij} is resumed until either the potential converges or the conditions for another acceleration step are met. Since the convergence criteria are not altered by this process, the accuracy of the calculation remains high. The effect of a potential adjustment is greater than the effects of many iterations, as shown in Figure 2. (8) Note that after the fourth acceleration step in Figure 2, the error increases for one iteration, after which it drops sharply and stabilizes before the next acceleration step. The reduction in the number of iterations required for convergence is clearly displayed in Figure 2. In the ESP model, the inclusion of the dominant eigenvalue method reduced the number of V-ρ iterations required for the complete efficiency calculation from 16,000 to 1,400 in a study of a power plant. This is a 91 percent reduction in the number of iterations.

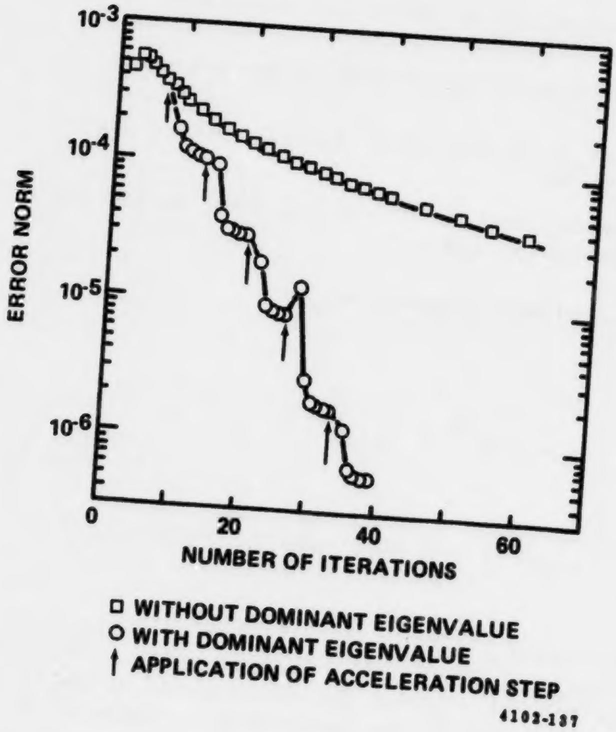

Figure 2. Effect of dominant eigenvalue convergence acceleration.

Table 1 shows the inclusion of an analytic approximation to the electric field in Revision 2. This approximation offered almost the same calculation accuracy as the rigorous calculation while using much less computer time. With the incorporation of the dominant eigenvalue procedure in Revision 3, the rigorous field calculation is now as fast as the approximation. Consequently, the approximation procedure was not included in Revision 3.

3. The speed of the particle charging routine is also reduced. In order to calculate the charge on each size particle in each incremental length using the more exact ionic charging theory, many integrations are required. The change to the Gaussian integration scheme in Revision 2 greatly reduced the integration time.

The net effect of the changes to the electric field calculation and the particle charging routine is a reduction in computer time of about 90 percent with no loss in accuracy.

4. As previously mentioned, after the ideal collection efficiency is calculated, the model corrects the efficiency for various non-ideal effects. Corrections for sneakage, non-rapping reentrainment, and non-uniform gas velocity are applied by adjusting the migration velocity for each size particle by a factor based on theoretical and experimental studies of a pilot scale precipitator. (1) This method of correction has not been changed in Revision 3.

Also unchanged is the empirical calculation of losses due to rapping reentrainment. This efficiency correction is based on the amount of mass collected in the last section of the ESP. A fraction of the collected mass is fit to a log-normal size distribution and added by size bands to the ESP penetration dust predicted by the ideal efficiency calculation. The collection efficiency is then recomputed based on the combined effluent. The log-normal size distribution used to describe the reentrained particles has default parameters of a 6 μm mass median diameter with a standard deviation of 2.5. Other size distribution data may be used in addition to these values if desired. However, the total mass of the reentrained particles is fixed by a relationship based on data derived from a study of rapping reentrainment in six power plants. (9) The subroutine which performs these operations requires a negligible amount of computer time relative to the ideal calculation and occurs automatically unless the new dynamic rapping routine is selected.

The new dynamic rapping routine utilizes a different process to calculate the effects of rapping reentrainment. This routine keeps track of dust layer growth at every point in the ESP as a function of time. At a user specified time of rap, the collected dust is removed from the rapped precipitator increments. A specified fraction of the removed dust is fit to a log-normal size distribution and stored for the calculation of reentrainment. The entire collection efficiency calculation is then repeated with the difference that the reentrained dust particles are reintroduced into the gas flow during the calculation. The mechanism for this is that the number of particles in each size band per m^3 of gas which are to be reentrained due to the rap of increment i is added to number of particles/size band/m^3 already present in the gas flow immediately before the calculations for increment i+1 begin. Thus the efficiency calculation in increment i+1 is performed on an increased amount of dust due to the reentrainment from the preceding increment. Inherent in this mechanism is the assumption that the reentrained particles instantaneously acquire the charge found on particles of the same size at that point in the gas flow.

The calculation of rapping reentrainment effects using the dynamic rapping routine is a very lengthy procedure due to the fact that the ideal collection efficiency calculation must be performed at least twice for each rap. The first time is to find the dust layer thickness at the time of the rap, and the second is to calculate the effects of the reentrainment. Depending on the complexity with which the reentrained dust is specified, up to seven additional efficiency calculations may be required. Therefore it is recommended that the estimation procedure be used to reduce computer time. The dynamic rapping calculation process is very flexible in that the user may vary the times of the raps, the rapping sequence, the fraction of the collected dust that gets reentrained, the size distribution and the density of the reentrained dust, and the duration of the rapping puff. This flexibility should be of use when comparing different rapping schemes. As of this time, no experimentally supported data set, such as that used in the empirical rapping correction, exists for the dynamic rapping calculation. A study should be performed to determine whether such a data set can or should be developed. Currently, the data for dynamic rapping must be matched to each application. Figure 3 shows the results of using dynamic rapping on power plant data.

5. A plume opacity calculation procedure has been added to Revision 3 of the model. This routine calculates differential and total extinction efficiencies and the total opacity of the ESP outlet plume calculated by the model. These are related by:

$$\text{Opacity} = 1 - \exp(-EL) = 1 - \exp(-NAQ_{ext}L), \qquad (8)$$

where

E = the extinction coefficient,
L = the pathlength of the light beam,
N = the particle concentration,
A = the projected area of the particle, and
Q = the extinction efficiency.

Figure 4 shows the extinction efficiency as a function of the particle size parameter, $x = \pi D/\lambda$, for four complex indices of refraction. D and λ are the particle diameter and the wavelength of the light beam, respectively. The calculation, which is based on Mie theory, (10) is performed at 10 wavelengths weighted according to the photopic response of the human eye. EPA-approved opacity monitors must simulate this color response, which is maximum at $\lambda = 0.55$ μm and has a width at half maximum of 0.1 μm. The required input data are stack diameter and complex index of refraction. A single wavelength-dependent index of refraction or up to 10 values of wavelength-independent indices of

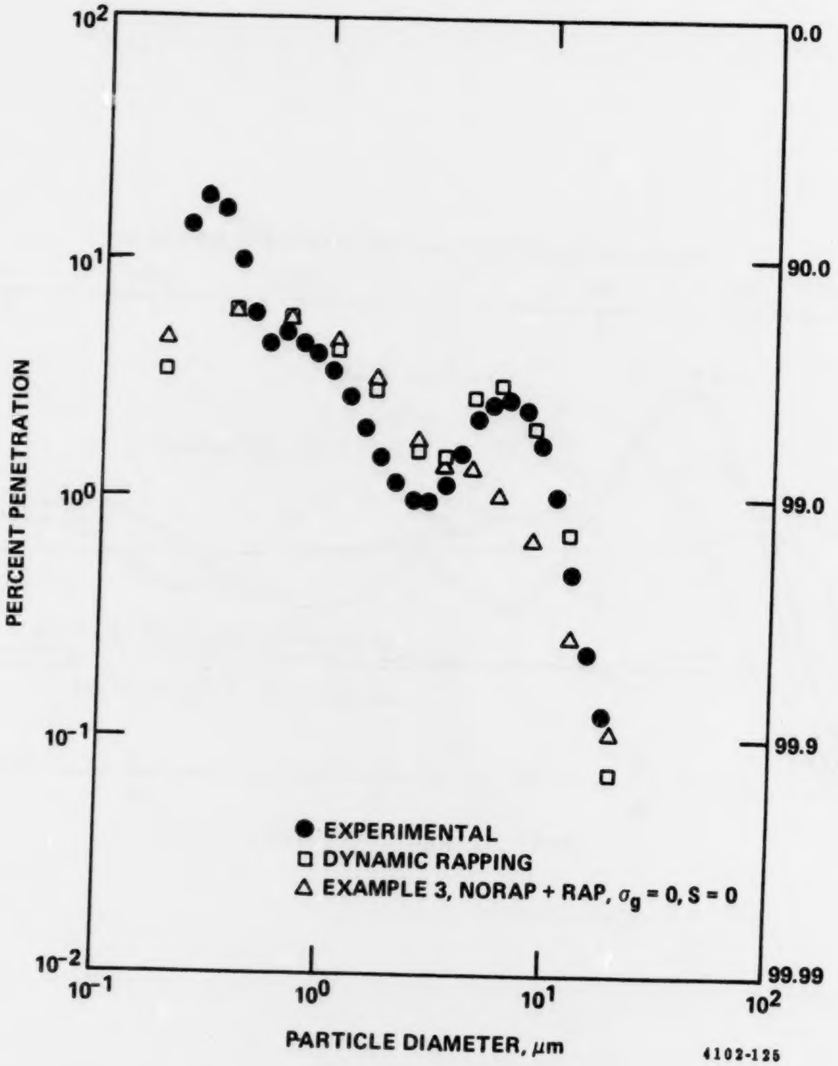

Figure 3. Comparison of standard and dynamic rapping reentrainment calculations.

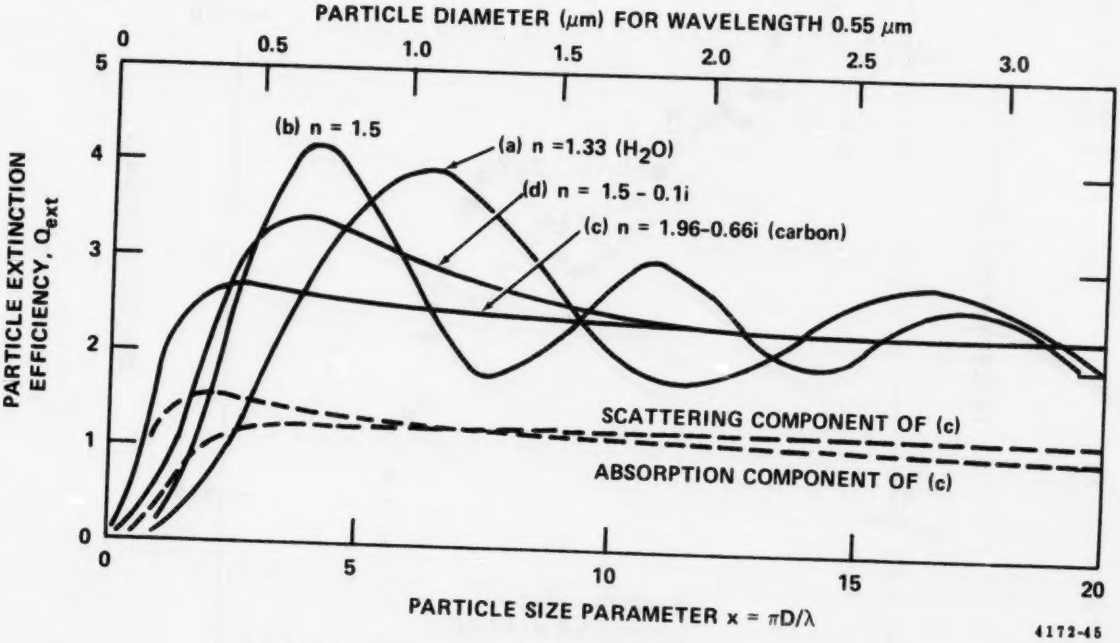

Figure 4. Extinction efficiency as a function of particle size parameter.

refraction may be entered. Alternatively, the refractive index may be omitted, in which case the calculation is performed using the default values of 1.5 and 1.5-0.1 i.

6. To facilitate the use of the model in other countries, the data entry routine has been modified to receive data in metric units if desired. However, unless all-metric data is specified, the data must be in the mixed metric/ English units used in previous versions of the model.

7. The option of reducing the amount of printed output data is provided. This will be of use in cases where only data summaries are of interest.

8. A built-in data set is provided in Revision 3. This data set contains nearly complete data based on a "typical" power plant. The only input data required are the resistivity of the collected particle and the collection plate spacing. From this, the model calculates a set of V-I curves and operating points for an ESP based on a study of 17 cold-side utility fly ash precipitators. (11) The length of the ESP is varied so that efficiency calculations may be performed for SCA values of 40 to 158 m^2/m^3/sec (200-800 ft^2/1000 acfm). This routine will be of use for verifying the operation of the model and for establishing a starting point for a more detailed examination of ESP design.

9. The model may be used as a V-I curve generator. The ability to calculate V-I curves has been in the model since Revision 1 as part of a routine which calculates the operating conditions and electric fields in the precipitator if the actual operating conditions are not available. This is a very lengthy calculation which may be more frequently used in Revision 3 due to the significantly reduced computer time resulting from the dominant eigenvalue procedure. In addition, there is now a switch which causes the program to terminate after the V-I curve is printed, in the event that only V-I data are required. Alternatively, if the ESP for which V-I curves are desired is similar to a utility fly ash precipitator, the V-I curves may be generated in the routine which calculates the internal data set. Again, there is a switch which causes the program to terminate after the V-I curves are printed.

10. A routine for checking the input data has been included in Revision 3. This routine checks each item of input data for variables which are out of the allowed range, such as having too many size bands, and for operating conditions which have allowed but unusually large or small values, such as found in a laboratory scale ESP. If anomalies in the data are discovered, diagnostic messages will be printed stating that an error has been made, or, in the second case, that certain values are unusual and should be checked for correctness.

Revision 3 requires only 12 percent more memory than Revision 1. On the SRI Digital Equipment Corporation (DEC) System 20 computer, Revision 3 uses 206 kilobytes of 7 bit memory. To facilitate model usage on computers having less memory available, the code is marked so that some of the less essential functions may be easily removed. The minimum program length, with all of the marked statements removed, is 135 kilobytes, which is approximately 65 percent of the entire program.

The data format for Revision 3 is largely the same as for previous versions of the model. Old data sets may be used without changes to yield the same results in less time. Only the additions, such as opacity and dynamic rapping, require additional input data.

The EPA/SRI ESP model has proven to be a useful tool in the design and evaluation of electrostatic precipitators. Revision 3 of the model offers greater utility through greater flexibility and added features such as the opacity calculation and dynamic rapping. Revision 3 is also much faster than previous model versions, which results in significantly reduced computer costs. This should encourage wider use of the model. As with Revision 1, Revision 3 will be complete in two volumes. Volume 1 will contain a description of the physical processes being modeled, the algorithms used, a description of the necessary input data, and a listing of the FORTRAN code. Volume 2 will be a user's manual which will contain complete explanations of the input and output data, examples of programs which illustrate the various options available, and a tutorial of the effects of varying some of the computer operating parameters, with supporting examples.

REFERENCES

1. Gooch, J. P., J. R. McDonald, and S. Oglesby, Jr. A Mathematical Model of Electrostatic Precipitation. EPA- 650/ 2-75-037 (NTIS PB246-188), U.S. EPA, IERL, Research Triangle Park, NC, 1975.

2. McDonald, J. R. A Mathematical Model of Electrostatic Precipitation (Revision 1): Volume I. Modeling and Programming. EPA-600/7-78-111a (NTIS PB284-614), U.S. EPA, IERL, Research Triangle Park, NC, 1978.

3. McDonald, J. R. A Mathematical Model of Electrostatic Precipitation (Revision 2): Volume II. User Manual. EPA- 600/ 7-78-111b (NTIS PB284-615), U.S. EPA, IERL, Research Triangle Park, NC, 1978.

4. Mosley, R. B., M. H. Anderson, and J. R. McDonald. A Mathematical Model of Electrostatic Precipitation (Revision 2). EPA-600/7-80-034 (NTIS PB80-190994), U.S. EPA, IERL, Research Triangle Park, NC, 1980.

5. Smith, W. B., and J. R. McDonald. Development of a Theory for the Charging of Particles by Unipolar Ions. J. Aerosol Sci., 7:151-166, 1976.

6. Felder, R. M., and E. Arce-Medina. Improvements in an Algorithm for Calculating the Potential Field Distribution and Current Density in a Parallel Plate Electrostatic Precipitator. J. Electrostatics. (To be published.)

7. Cooperman, P. The Dependence of the Electrical Characteristics of Duct Precipitators on Their Geometry. Progress Report No. 46, Research Corp., Bound Brook, NJ, 1952.

8. Orbach, O., and C. M. Crowe. Convergence Promotion in the Simulation of Chemical Processes with Recycle: the Dominant Eigenvalue Method. Can. J. Chem. Eng. 49:509, 1971.

9. Gooch, J. P., and G. H. Marchant, Jr. Electrostatic Precipitator Rapping Reentrainment and Computer Model Studies. EPRI Contract RP413-1, The Electric Power Research Institute, Palo Alto, CA, 1978.

10. Mie, G. Beitrage zur Optik truber Medien, Speziell Kolloidaler Metallosunge. Ann. Physik. 25:377-455, 1908.

11. DuBard, J. L., and R. F. Altman. Prediction of Electrical Operating Points for use in a Precipitator Sizing Procedure. Presented at the EPRI Conference on Electrostatic Precipitator Technology for Coal-Fired Power Plants, Nashville, TN, July 14-16, 1982.

NUMERICAL SIMULATION OF THE EFFECTS OF VELOCITY FLUCTUATIONS ON ELECTROSTATIC PRECIPITATOR PERFORMANCE

by: Eric A. Samuel
General Electric Environmental Services, Inc.
Lebanon, Pennsylvania 17042

ABSTRACT

A numerical scheme for including the effects of velocity fluctuations in plate-wire electrostatic precipitators arising from turbulent diffusion, within the framework of the already developed trajectory method for precipitator performance evaluation, is described. The predictions of the scheme are shown to be in agreement with classical solutions based on Fickian diffusion for some simple configurations.

INTRODUCTION

The turbulent flow in plate-wire precipitators may be regarded, in a restrictive sense, as comprising eddies of a range of diameters, with the number of eddies having diameters comparable to the plate spacing being small. The time fluctuations observed in the velocity distributions within gas passages may be explained within the above model as due to the random movement and relocation of the eddies. The motion of particles in a turbulent velocity flow field may be likened to the Brownian motion of gas molecules which is governed by random collisions. The above analogy suggests that particle motion in a turbulent field may be regarded as governed by random collisions, with the mean-free path between collisions being of the order of the average eddy diameter.

The microscopic motion of gas molecules have been shown to be described by a macroscopic diffusive transport operation known by Fick's Law(1), which relates the gas molecule flux to the gas molecule concentration gradient through a proportionality constant known as the diffusion coefficient. Analytical descriptinns of the effect of turbulence on the precipitator collection efficiency have centered on an analogous diffusive transport equation(2). The eddy diffusivity model for treating particle motion in turbulent flows yields analytically tractable results for only idealized precipitator configurations.

The purpose of the present study is to demonstrate an alternative computational method for including the effects of turbulence in theoretical predictions of the performance of precipitators, having realistic configurations, within the framework of an existing numerical simulation method based on particle trajectory calculations(3,4,5). This simulation method has been used previously to study theoretically the effect of precipitator geometrical parameters (plate spacing, wire spacing, and wire diameter) on the scaling of precipiator performance. The central idea in this alternative formulation is to superimpose a random component, attributable to the fluctuating component of the velocity flow field, on the particle trajectories calculated for the mean velocity field. The random component of the particle motion is calculated in incremental steps using a simple solution to the convective diffusion equation.

The present study is devoted to demonstrating the favorable comparison between the simulation method and analytical results for idealized precipitator configurations.

The present description of the above study is structured as follows. The bext section will contain a description of the alternative scheme for factoring the effects of turbulence into the already developed numerical simulation code based on the trajectory method. The following section will compare the predictions based on the tarjectory method with analytical results for turbulent flows in simple configurations. Concluding remarks are given in the final section.

NUMERICAL SCHEME

The numerical simulation code based on the trajectory method has been described elsewhere(3,4,5). Briefly, the method consists first of obtaining the electrical characteristics of the precipitator by simultaneously solving Poisson's Equation and the Continuity Equation together with the corona condition suggested by Leutert and Böhlen(6), and by McDonald, Smith, Spencer, and Sparks(7). The performance of the precipitator is then evaluated by following the trajectories of particles of known size distribution entering uniformly across a gas passage. The computer model as described above has been used to study the effect of varying the geometrical parameters which characterize a plate-wire precipitator; namely, the plate and wire spacings, and the wire diameter, on precipitator performance. The model predicted improved performance with decreasing wire spacing and increasing plate spacing and wire diameter. Configurations which increased corona power appeared to also yield improved collection efficiencies.

If D is the eddy diffusivity, and L the mean-free path (or mean eddy diameter), it can be shown that(1):

$$D = L\ v/3 \tag{1}$$

where v is the mean flow velocity. Also, by solving the Diffusion Equation, it can be shown thatthe mean square displacement between the positions r and r_o of a particle seperated by a time increment, Δt, is given by(1):

$$<(r - r_o)^2> = 2\ D\ \Delta t \qquad (2)$$

The effect of turbulence is included within the trajectory method by superimposing on the trajectory calculated for the mean velocity flow field a random component attributable to the velocity fluctuations. The random component is calculated as follows:

1. Assume that the motion of a perticle within an eddy is governed by Equation 2, which gives the random displacements in the x and y directions for motion within the eddy, as:

   $$\Delta x = (2\ D\ \Delta t)^{\frac{1}{2}} \sin \theta \qquad (3)$$

   $$\Delta y = (2\ D\ \Delta t)^{\frac{1}{2}} \cos \theta \qquad (4)$$

   where θ is the angle between the direction of particle motion within the eddy and the direction of mean particle flow. The angle, θ, lies in the range, $0 \leq \theta \leq 360$, due to the requirement that the time average of the fluctuating component of the velocity flow field is zero.

2. The angle, θ, is initially selected arbitrarily. The motion of a particle between eddies, however, is assumed to result in a random change in the value of θ. Once the local eddy size, L, is known, the effective local eddy diffusivity may be calculated on the basis of Equation 1 using the local mean velocity, v. The time increment, Δt, for calculating the random motion is selected such that:

   $$L = v\ \Delta t \qquad (5)$$

   The time increment, Δt_m, for calculating the mean particle motion is selected such that:

   $$\Delta t = N\ \Delta t_m \qquad (6)$$

   N being a sufficiently large integer. A random direction change and displacement due to turbulence is calculated once in N displacements calculated for the mean particle flow. Isotropic turbulence is invoked by assuming the mean eddy diffusivity to be the same everywhere within the precipitator gas passage.

In the absence of turbulence, it is necessary to calculate the trajectory of a particle of given diameter only once for each entrance position in the precipitator. In the presence of turbulence, however, it is necessary to calculate several trajectories for each entrance position, since no two random trajectories will be exactly the same.

COMPARISON OF COMPUTER PREDICTIONS WITH ANALYTICAL RESULTS

Table 1 describes four simple configurations in which the above method for including the effects of turbulence on particle trajectories was applied.

The configurations were chosen because analytical solutions for the particle concentration profiles in the presence of diffusion are available in the literature. The four configurations are:

1. Diffusion of particles originating from a point source in a flowing gas, ignoring wall effects. This case to the effect of turbulence in the central region of a precipitator gas passage in the absence of electrical energization.

2. Diffusion of particles originating from a point source in a flowing gas close to a plate boundary, the plate being assumed to be perfectly reflecting. This case corresponds to diffusion of particles close to a collecting plate, in the absence of electrical energization, and assuming complete specular reentrainment of the particles arriving at the plate (complete absence of collection).

3. Same as Case 2 above, but assuming the plate boundary to be completely absorbing. This case corresponds to diffusion of particles close to a collecting plate, in the absence of electrical energization, and assuming complete retention of particles which impact the plate (complete absence of reentrainment).

4. Diffusion of charged particles, all of the same diameter and carrying the same charge, in a gas passage across which a uniform static electric field is maintained. This case corresponds to the effect of diffusion in the collecting stage of a two-stage precipitator, the first stage of which is the charging stage.

Figures 1 to 4 summarize the comparison between predictions of the computer model and analytical theory based on Fick's Law. The agreement between the two methods are seen to be reasonably good. Two sources of discrepancy between the analytical and numerical methods are: (i) finite number of test particles in the numerical scheme, as opposed to limit of infinitely large particles assumed in the analytical method, and (ii) the lack of complete randomness in the random number generator used in the computer method (see Figure 5). The good agreement between the analytical and numerical methods, especially in the case of the two-stage precipitator, demonstrates the validity of the numerical scheme for calculating the effect of turbulence on precipitator performance.

CONCLUSION

Through comparison with classical solutions to the Diffusion Equation, the proposed numerical scheme for including the effect of velocity fluctuations on calculations of precipitator performance appears to have been validated. Use of the scheme to study the scaling of precipitator performance on its goemetrical parameters, including the effect of turbulence, is planned.

REFERENCES

1. Chandrasekhar, S. Rev. Mod. Phys. 15, 1, 1943.

2. Leonard, G. L., Mitchner, M., and Self, S. A. Experimental Measurements of Turbulent Diffusion on Precipitator Efficiency. In: Proceedings of the Third Symposium on the Transfer and Utilization of Particulate Control Technology, Volume II. Electrostatic Precipitators. EPA-600/9-82-005b. U. S. Environmental Protection Agency, Research Triangle Park, N. C. 27711, July 1982. p 120 - 129.

3. Kim, Y. W. and Samuel, E. A. Electrostatic Precipitators II. The Efficiency and Wire-to-Plate Spacing Ratio. Physics of Fluids Technical Report No. 27, Department of Physics, Lehigh University, Bethlehem, Pa. 18018, 1978.

4. Samuel, E. A. Collection Efficiency of Electrostatic Precipitators by Numerical Simulation. In: Proceedings of the Second Symposium on the Transfer and Utilization of Particulate Control Technology, Volume II. Electrostatic Precipitators. EPA-600/9-80-039b. U. S. Environmental Protection Agency, Research Triangle Park, N. C. 27711, September 1980. p 1 - 30.

   Samuel, E. A. Collection Efficiency of Electrostatic Precipitators by Numerical Simulation. Environment International. 6, 137 - 152, 1981.

5. Samuel, E. A. Computer Simulation of the Wide Plate Spacing Effect. In: Proceedings of the Third Symposium on the Transfer and Utilization of Particulate Control Technology, Volume II. Electrostatic Precipitators. EPA-600/9-82-005b. U. S. Environmental Protection Agency, Research Triangle Park, N. C. 27711, July 1982. p 149 - 159.

6. Leutert, G. and Böhlen, B. The spatial Trend of Electric Field Strength and Space Charge Density in Plate-Type Electrostatic Precipitators. Staub-Reinhalt. Luft. 32(7),27 - 33, July 1972.

7. McDonald, J. R., Smith, W. B., Spencer, H. W. and Sparks, L. E. A Mathematical Model for Calculating Electrical Conditions in Wire-Duct Electrostatic Precipitation Devices. J. Appld. Phys. 48(6), 2231 - 2243, June 1977.

Table 1. Simple configurations used for comparing the numerical method for calculating the effects of velocity fluctuations with the analytical method based on Fickian diffusion.

Configuration	Schematic	Analytical Expression	Reference
1. Point source in flowing gas without boundary effects (diffusion in center of unenergized gas passage).	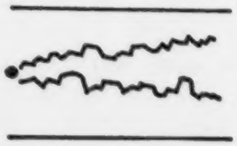	$W(x,t)^{\dagger} = \frac{1}{2(\pi Dt)^{1/2}} \exp\{-x^2/(4Dt)\}$	Chandrasekhar(1)
2. Point source in flowing gas near reflecting wall (diffusion near collecting plate of unenergized gas passage with complete specular reentrainment at plate).	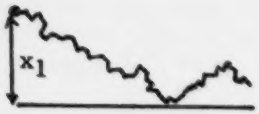	$W(x,t;x_1)^{\dagger\dagger} = \frac{1}{2(\pi Dt)^{1/2}} \{ \exp[-x^2/(4Dt)] + \exp[-(2x_1-x)^2/(4Dt)] \}$	Chandrasekhar(1)
3. Point source in flowing gas near absorbing wall (diffusion near collecting plate of unenergized gas passage with complete collection at plate).	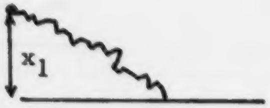	$W(x,t;x_1)^{\dagger\dagger} = \frac{1}{2(\pi Dt)^{1/2}} \{ \exp[-x^2/(4Dt)] - \exp[-(2x_1-x)^2/(4Dt)] \}$	Chandrasekhar(1)

Table 1 (Continued)

Configuration	Schematic	Analytical Expression	Reference
4. Uniform source in parallel plate collecting stage with uniform static electric field in two-stage precipitator.	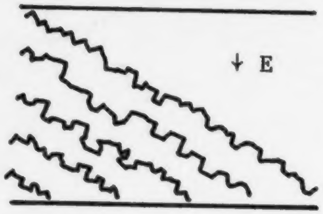	$W(y,t;\omega_y)^* = \frac{1}{(2\pi Dt)^{\frac{1}{2}}} \int_0^y \exp\{-[(y'-\omega_y t)/(2Dt)^{\frac{1}{2}}]^2\} dy'$	Leonard, Mitchner, and Self(2)

---

† $W(x,t)$ is the normalized probability of finding a particle at position x and time t, knowing that the particle source is located at the origin ($x = 0$) and emits particles at time $t = 0$. The time t is given by: $t = x/v$, v being the mean gas velocity.

†† $W(x,t;x_1)$ is the normalized probability of finding a particle at position x and time t, knowing that either a reflecting or absorbing wall is located at $x = x_1$, and the point source is located at the origin, and emits particles at time $t = 0$.

* $W(y,t;\omega_y)$ is the normalized probability of finding a particle at coordinate position (x,y), knowing that a uniform flux of particles having the same drift velocity, ω_y, entered the collecting stage at $x = 0$ and time $t = 0$. The time t is given by: $t = x/v = y/\omega_y$.

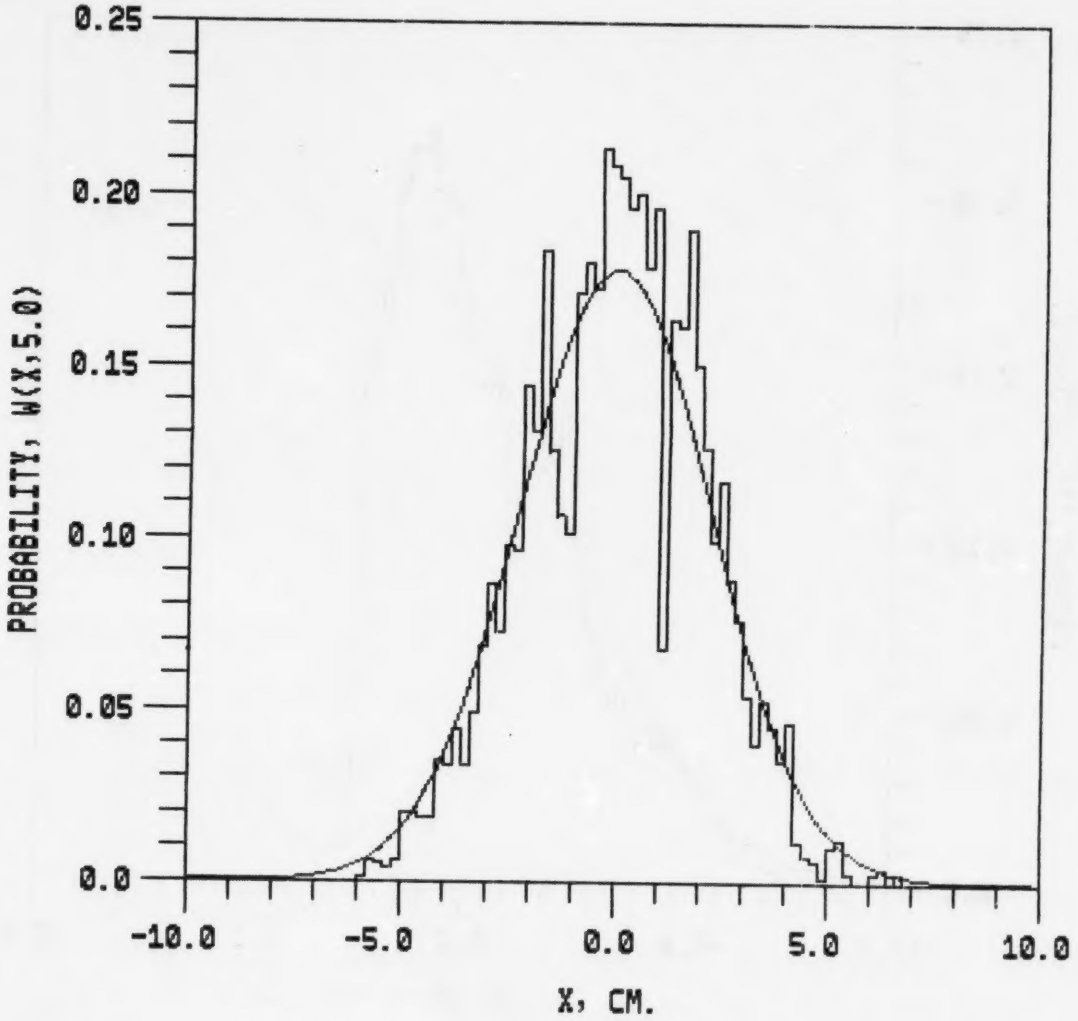

DIFFUSION TIME = 2.5 SECONDS
STEP SIZE = 0.10 CM.
NUMBER OF RANDOM JUMPS PER SECOND = 200
THEORETICAL DIFFUSION COEFFICIENT = 1.00 CM**2/SEC
TOTAL NUMBER OF PARTICLES SAMPLED = 4000

Figure 1. Comparison of the predictions of the numerical scheme for the inclusion of turbulence effects with the analytical result from diffusion theory for the case of a point source with no boundaries (Case 1).

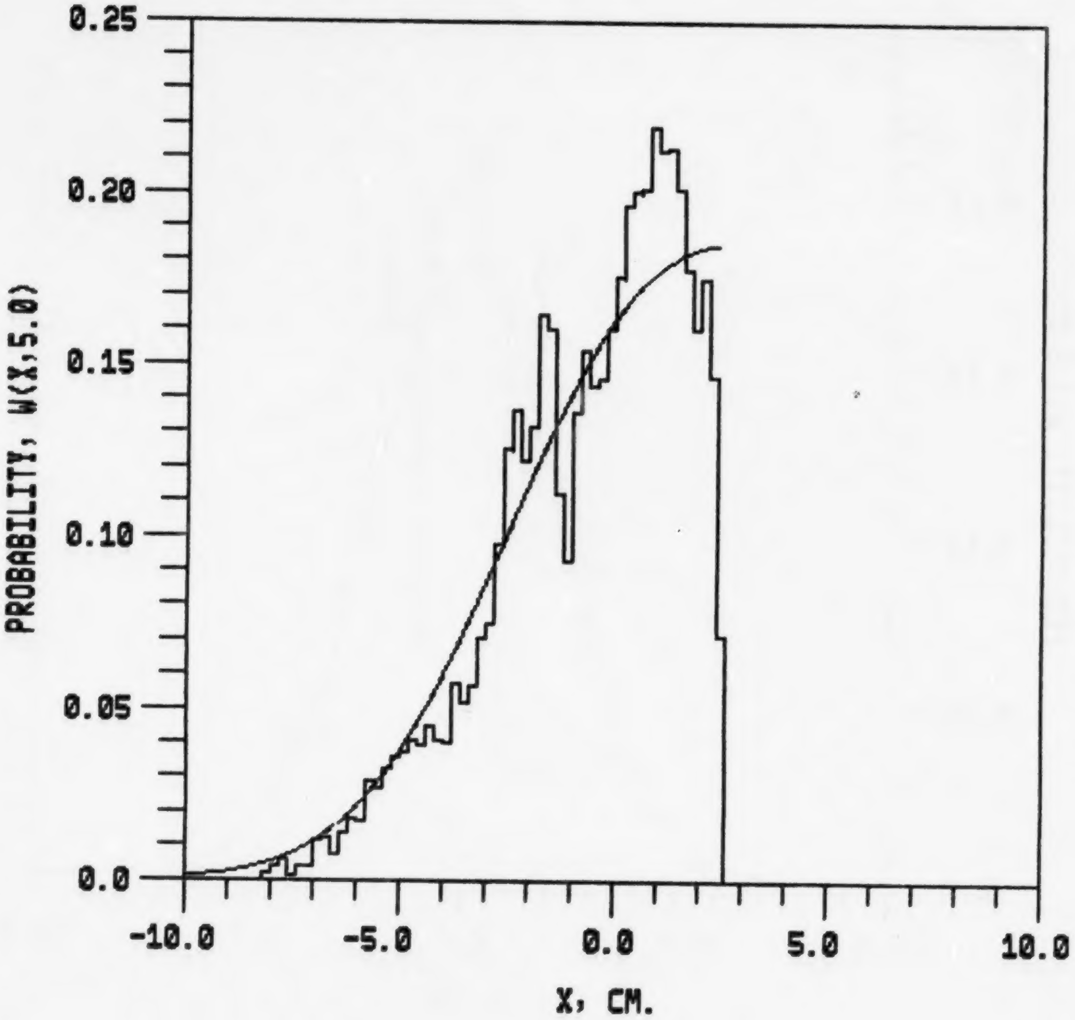

DIFFUSION TIME = 5.0 SECONDS
STEP SIZE = 0.10 CM.
NUMBER OF RANDOM JUMPS PER SECOND = 200
THEORETICAL DIFFUSION COEFFICIENT = 1.00 CM**2/SEC
TOTAL NUMBER OF PARTICLES SAMPLED = 10000

Figure 2. Comparison of the predictions of the numerical scheme for the inclusion of turbulence effects with the analytical result from diffusion theory for the case of a point source near a reflecting wall (Case 2).

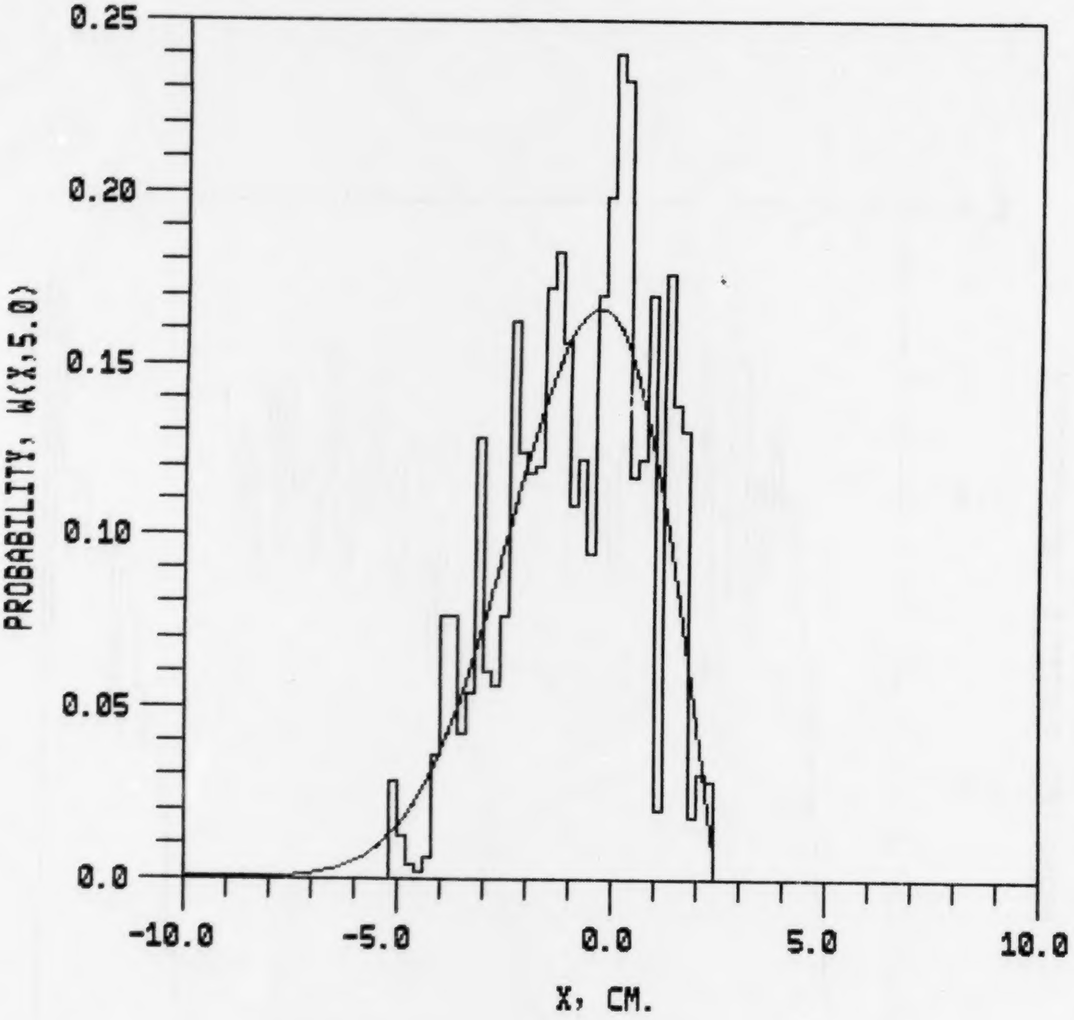

```
DIFFUSION TIME =  2.5 SECONDS
STEP SIZE = 0.10 CM.
NUMBER OF RANDOM JUMPS PER SECOND =  200
THEORETICAL DIFFUSION COEFFICIENT =   1.00 CM**2/SEC
TOTAL NUMBER OF PARTICLES SAMPLED =   2500
```

Figure 3. Comparison of the predictions of the numerical scheme for the inclusion of turbulence effects with the analytical result from diffusion theory for the case of a point source near an absorbing wall (Case 3).

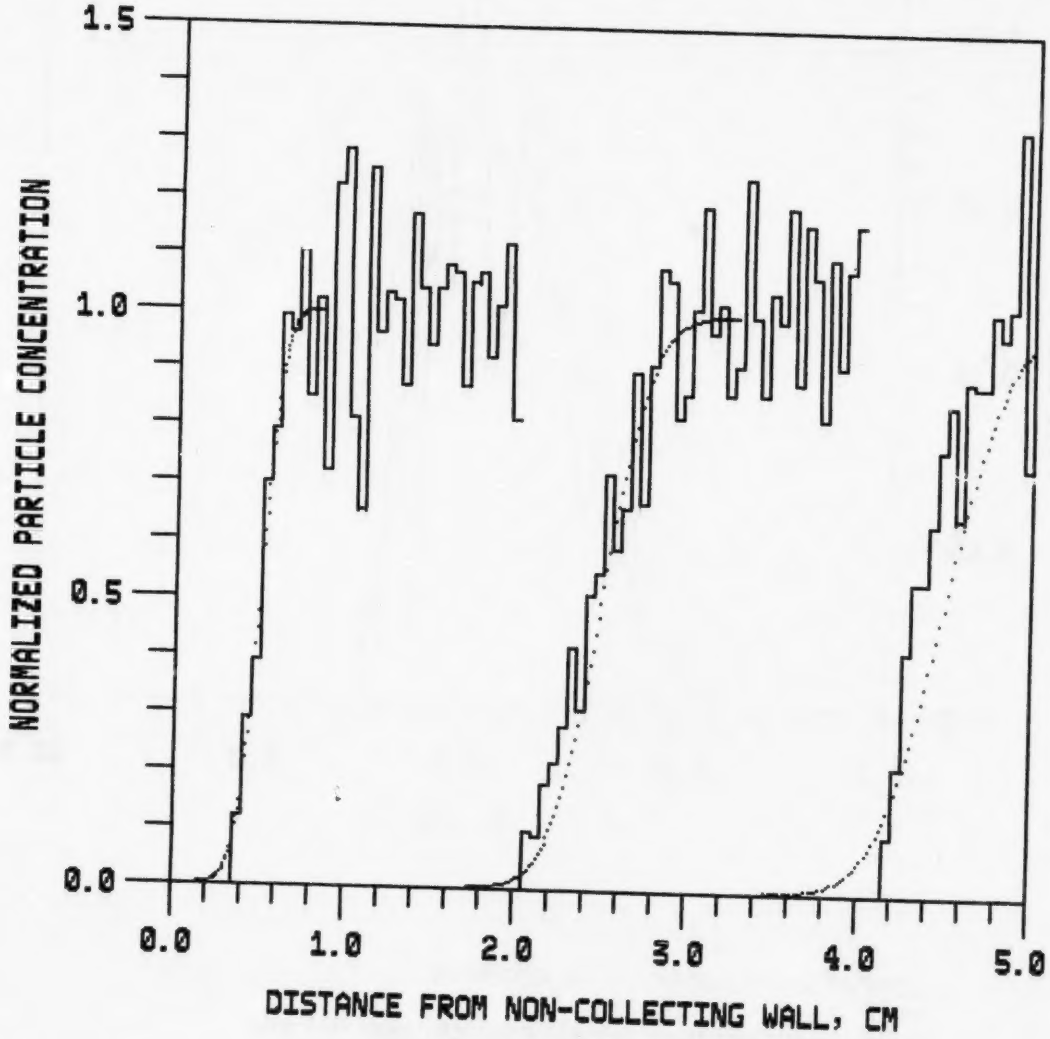

Figure 4. Comparison of the predictions of the numerical scheme for the inclusion of turbulence effects with the analytical result from diffusion theory for the case of a uniform flux of identically charged particles entering a parallel plate collecting stage in which a uniform electric field is maintained (Case 4).

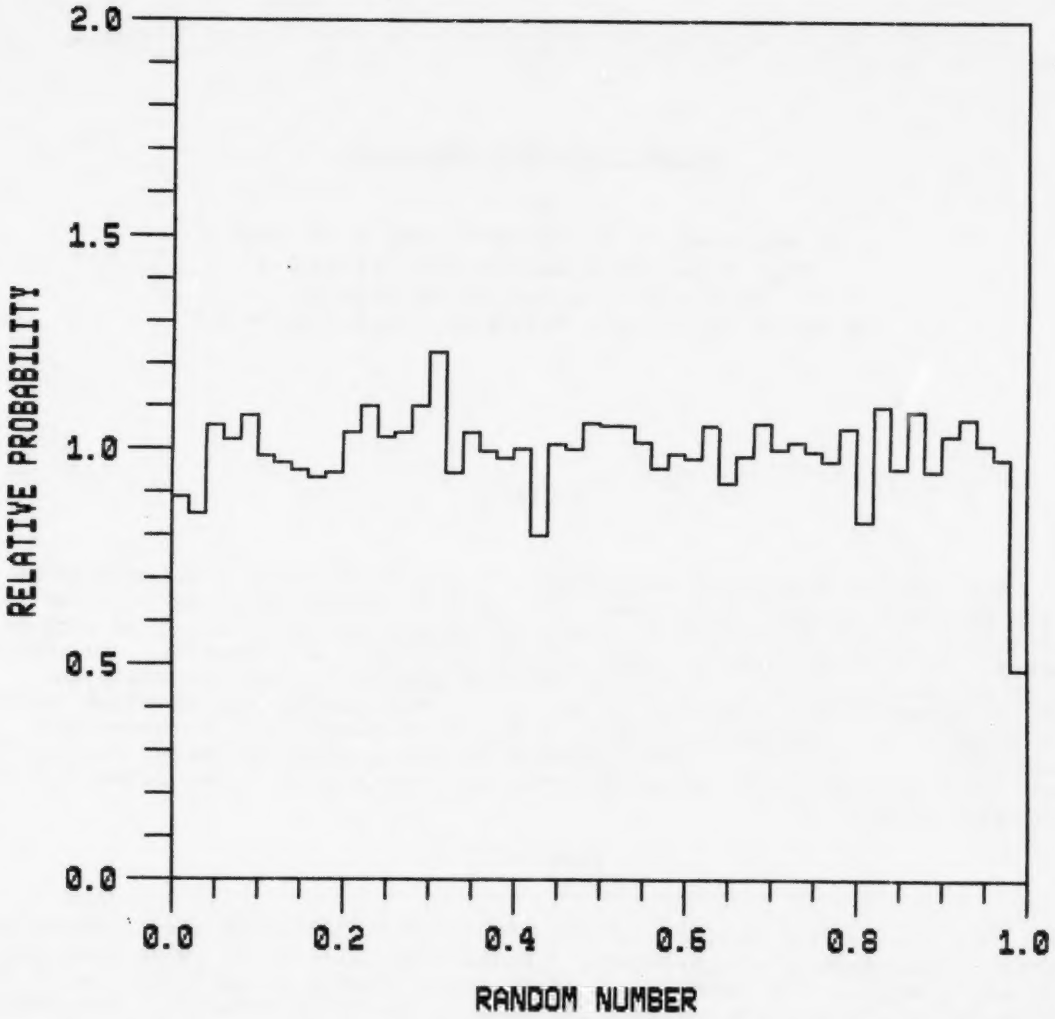

Figure 5. Distribution of random numbers from the random number generator used in the present investigation.

CORONA - INDUCED TURBULENCE

by
M. Mitchner, G. L. Leonard[1], and S. A. Self
High Temperature Gasdynamics Laboratory
Mechanical Engineering Department
Stanford University, Stanford, California 94305

ABSTRACT

The results of previous experiments with a bench-scale precipitator (5 cm plate-to-plate spacing) have shown that moderate levels of turbulence can be maintained in the presence of a corona discharge, and that in accord with theory, significant gains in precipatator efficiency are possible. In this paper hot-wire anemometer measurements in a laboratory-scale precipitator (25 cm plate-to-plate spacing) are presented that support the previous results and suggest that similar improved performance is possible in larger-scale commercial precipitators. The measurements also provide a further explanation for the reduced migration velocity previously reported by other workers at low gas velocities.

INTRODUCTION

In a theoretical analysis of the effect of differing levels of turbulence on the performance of electrostatic precipitators (1) it was shown that even for moderate levels of turbulence, efficiences significantly in excess of that predicted by the Deutsch-Anderson (2) formula should be possible. Experiments conducted in the collection stage (no corona discharge) of a bench-scale (5cm plate-to-plate spacing) two-stage precipitator yielded results in excellent agreement with the theory (3). With no corona discharge present, and therefore no possibility of corona-induced turbulence, the level of turbulent mixing could be controlled with standard flow-conditioning elements such as a well-designed entrance nozzle and turbulence-producing grids.

In a single-stage precipitator, particle collection occurs in the presence of a corona discharge, and the question arises as to the level of turbulence produced by the corona wind. In a study of the basic fluid mechanical effects of the corona wind (4) it was shown that a uniform positive corona discharge does not generate turbulence (5) but that turbulence could result from the instability of a pair of counter-rotating vortices produced at each end of the discharge wire, that propagate into the main flow.

---

[1] Currently at General Electric Corporate Research and Development, Schenectady, N.Y. 12345

For a negative corona, because of the characteristic non-steady tuft-like discharge structure, it was shown (4) that turbulence was generated throughout the precipitator volume. The intensity of the negative corona-induced turbulence was comparable or less than the background turbulence present without electrical energization for gas velocities exceeding approximately 1.5 m/s but increased rapidly for decreasing gas velocities.

The experiments to be described were undertaken to examine how the aforementioned corona wind effects scaled in a larger facility (25 cm plate-to-plate spacing), more nearly approximating the dimensions of commercial precipitators. The results, like those obtained for the bench-scale precipitator, show that moderate turbulence-level precipitator flows are achievable in the presence of a corona-discharge. In addition, results obtained for low gas velocities appear to offer a further explanation for the decreased migration velocities observed by other workers (6,7) for these conditions.

EXPERIMENTAL APPARATUS

Experiments were performed in a laboratory-scale electrostatic precipitator test facility described more fully by Pejack (8). The precipitator duct used in these experiments was 0.75 m high, 1.75 m long, and had seven 2.77 mm diameter uniformly spaced discharge wires. The mean gas velocity at the precipitator inlet plane was uniform to within ±2% and the rms of the free stream turbulent velocity was less than 2% of the mean velocity.

Hot-wire anemometer measurements were made 0.40 m downstream of the last corona wire. Time and space resolved values of the gas velocity component in the flow direction, $u(\vec{x},t) = \bar{u}(\vec{x}) + u'(\vec{x},t)$, were made with a 5μm diameter tungsten hot-wire sensor operated with a TSI model 1050 anemometer and linearizer. (Here $\bar{u}(\vec{x})$ denotes the local mean velocity and $u'(\vec{x},t)$ is the local fluctuation velocty. We shall denote by $u_o \equiv u_o(x)$ the value of $u(\vec{x})$ averaged over a transverse plane located at the streamwise location x. The rms value of $u'(\vec{x},t)$ will be written as $u'(\vec{x})$ or as u' (without an argument), and the turbulence intensity will refer to either $u'/\bar{u}(\vec{x})$ or to u'/u_o.) Values of $\bar{u} \equiv \bar{u}(\vec{x})$ were measured with a Hewlett Packard integrating digital voltmeter. The fluctuation velocity (not linearized) was processed with a TSI model 1076 true rms voltmeter to obtain values of u'.

EXPERIMENTAL RESULTS

Transverse profiles of $\bar{u}(y)$ and $u'(y)$, measured at mid-height downstream of the unenergized precipitator, are presented in Figure 1. These data show the turbulent boundary layer extending approximately 7 cm from each wall, and a turbulent wake with a centerline turbulence intensity of about 5%. Voltage-current characteristics for both negative and positive corona are given in Figure 2.

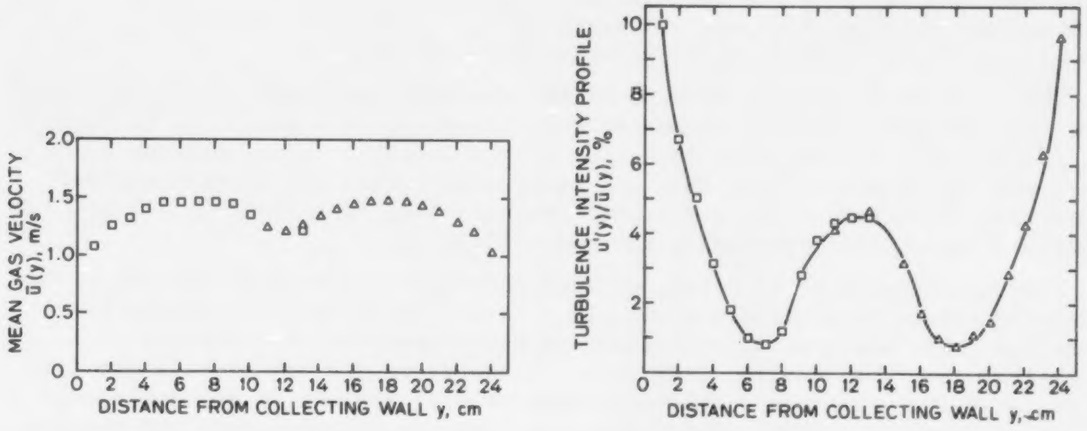

(a) Mean Gas Velocity Profile

(b) Turbulence Intensity Profile

Figure 1. Transverse mean velocity and turbulence intensity profiles at the exit of the unenergized precipitator.

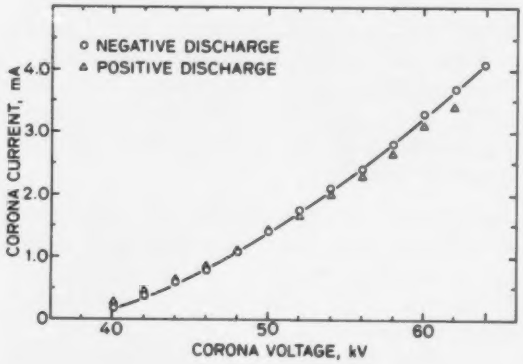

Figure 2. Voltage-current corona characteristics.

Turbulence intensity profiles measured at the centerline of the exit of the precipitator for several corona voltages and for gas velocities of 3,2, and 0.9 m/s are shown in Figure 3 for negative corona, and in Figure 4 for positive corona. The voltages correspond to current densities at the collector in the range from 0.08 to 1.3 mA/m^2, and approximately span the operating range of most power-plant precipitators (0.05 to 0.7 mA/m^2). For u_o = 3 m/s, these results show relatively little change for negative corona, and essentially no change for positive corona, from the corresponding turbulence intensity profiles for the unenergized precipitator. When the gas velocity is reduced to 1.5 m/s, the turbulence intensity for the negative corona becomes comparable to that produced by the turbulent wake from the unenergized discharge wires. This increased turbulence appears to result from the instability of localized vorticies generated by large localized body forces induced by the discrete discharge tufts (9), and by the nonuniform and nonsteady behavior of these tufts. For u_o = 1.5 m/s, very little change is produced in the turbulence intensity profile for the positive corona case.

For a gas velocity of 0.9 m/s both the negative and positive corona produce very marked increases in turbulence intensity. In the negative corona case this additional

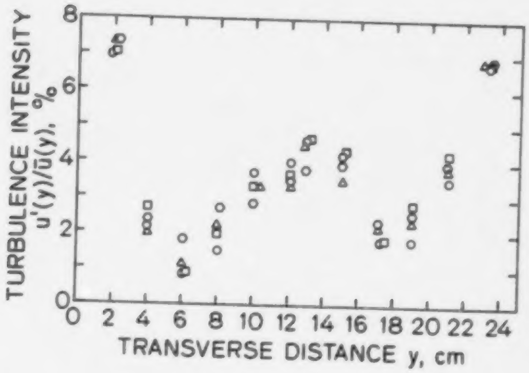

(a) u_o = 3 m/s

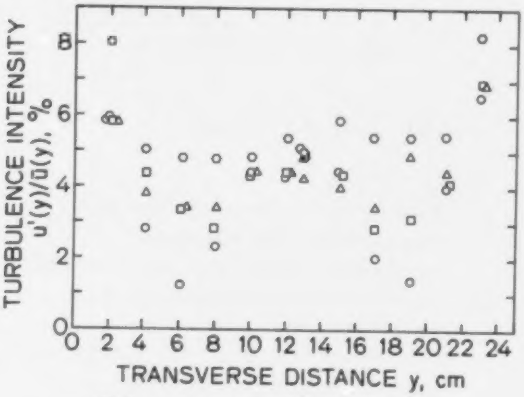

(b) u_o = 2 m/s

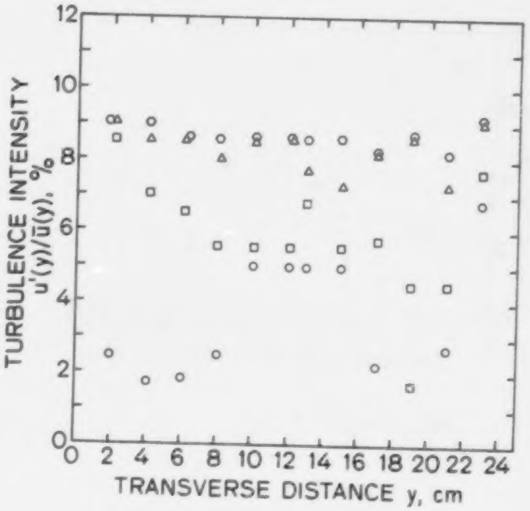

(c) u_o = 0.9 m/s

Figure 3. Dependence of transverse turbulence intensity profiles at the exit of the precipitator on gas velocity for negative corona. The symbols correspond to the following voltages: ○ 0kV, □ -40 kV, Δ-50kV, ○-60kV.

increase can be attributed to an increase in the relative strength of the discharge tufts and to the accompanying increase in localized flow instabilities produced by corona wind effects. In the positive corona case, the very large increased turbulence level is believed to result from the spread to the precipitator centerline of unstable axial vortex pairs generated near the ends of the discharge wires.

The turbulence-producing mechanism at low gas velocities for positive corona would appear to be dependent on the nature of the discharge wire termination, as well as on the height or perhaps aspect ratio of the precipitator, whereas for negative corona the dependence on these features should be much weaker or absent. Further measurements at low velocities with changes in these aspects of the precipitator design are necessary to examine this hypothesis.

In Figure 5, the turbulence intensity u'/u_o measured at one exit location (7 cm from one wall) is shown plotted as a function of linear current density for two different values of mean gas velocity, for each type of corona discharge. For negative corona, the turbulence intensity increases rapidly with increasing current for u_o = 1.5 m/s, but increases slowly for u_o = 3 m/s. For positive corona the turbulence intensity increases rapidly with increasing current for

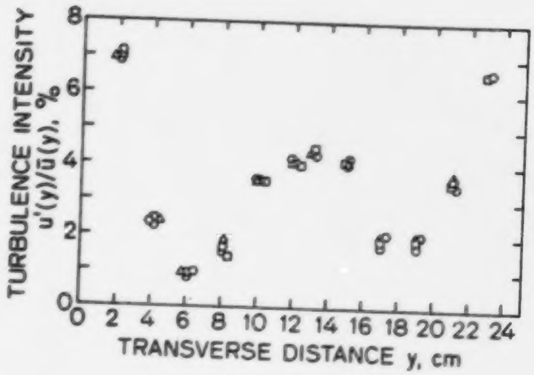

(a) $u_o = 3$ m/s

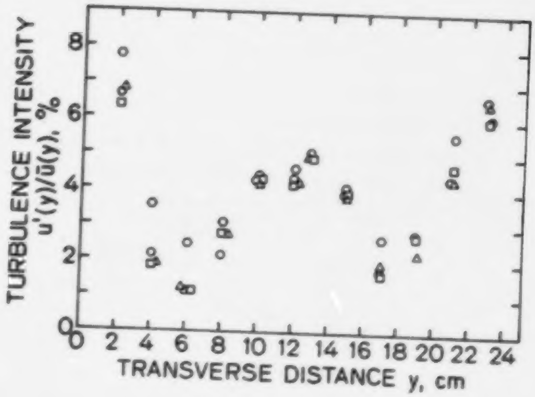

(b) $u_o = 2$ m/s

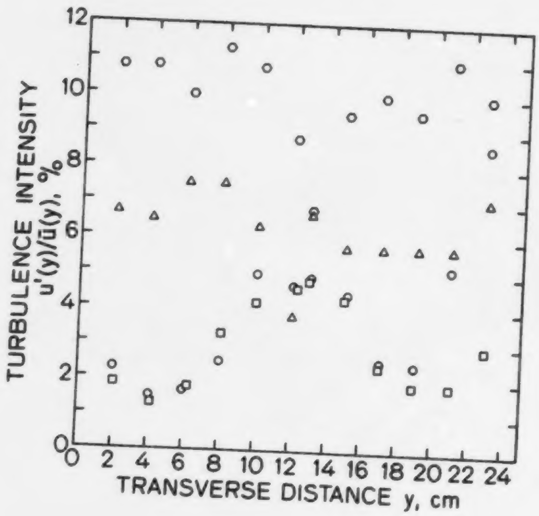

(c) $u_o = 0.9$ m/s

Figure 4. Dependence of transverse turbulence intensity profiles at the exit of the precipitator on gas velocity for positive corona. The symbols correspond to the following voltages: ○ 0 kV, □ 40kV, △ 50kV, ○ 60kV.

$u_o = 0.9$ m/s, but increases slowly for $u_o = 1.5$ m/s.

INTERPRETATION OF THE RESULTS

The experiments show that corona wind effects become important for larger currents and for smaller gas velocities. This behavior can be understood in terms of a dimensionless number which characterizes the strength of the interaction of the corona wind relative to the inertial force associated with the motion of the gas.

The force per unit volume that acts on the fluid to produce the corona wind is $\rho_i E$, where ρ_i and E are characteristic values of the ion charge density and electric field, respectively. The electric field is related to the ion current density J by the relation $J = \rho_i bE$, where b is the ion mobility. In terms of the total ion current i from a discharge wire of length ℓ and wire-to-plate spacing d, $J \simeq (i/\ell)/2\pi d$. We may therefore write $\rho_i E \simeq (i/\ell)/bd$.

The inertial force per unit volume acting on the fluid over a characteristic distance d is of order $\rho u_o^2/d$, where ρ is the mass density and u_o is the velocity of the gas. A measure of the relative

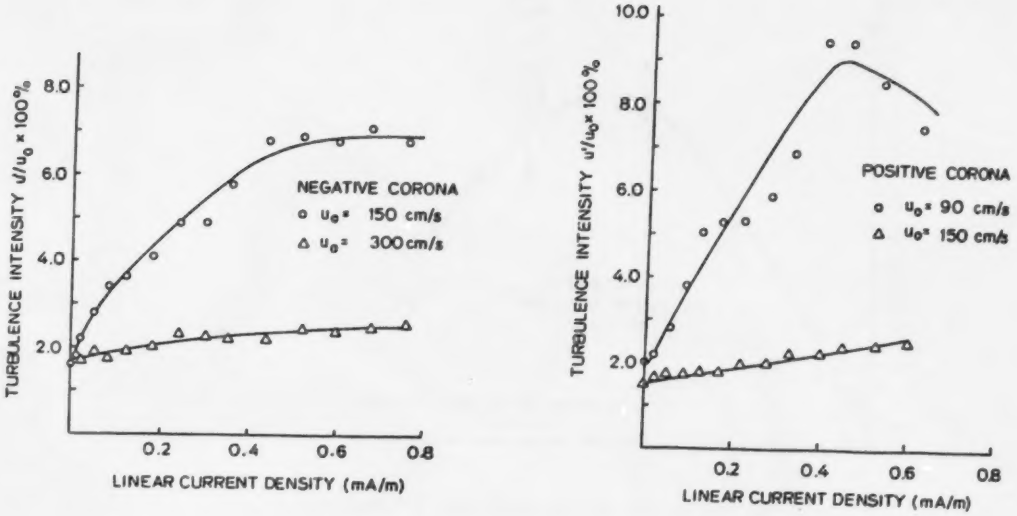

(a) negative corona

(b) positive corona

Figure 5. Effect of gas speed on turbulence intensity (7 cm from wall) as a function of linear current density.

importance of corona wind effects is provided by the dimensionless parameter

$$\frac{\text{electric body force/unit volume}}{\text{inertial force/unit volume}} = \frac{(i/\ell)/bd}{\rho\ u_o^2/d} = \frac{i/\ell}{b\rho u_o^2}$$

The experimental results reported here behave qualitatively in accord with this number, and in fact several other features of corona wind effects (9) may be correlated with the aid of this parameter.

LOW GAS VELOCITY EFFECTS

The Deutsch theory (2) of electrostatic precipitation does not predict any variation of migration velocity with gas speed, although it is generally appreciated that there will be a progressive deterioriation at high speeds owing to reentrainment. What is not well understood is the reduction in effective migration velocity observed by many workers for lower gas speeds. Examples of previously reported results are shown in Figure 6.

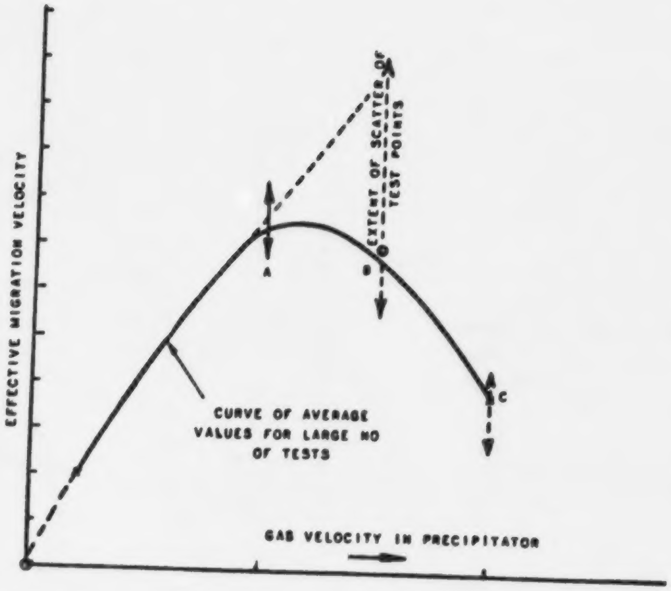

(a) Results of Busby and Darby (6)

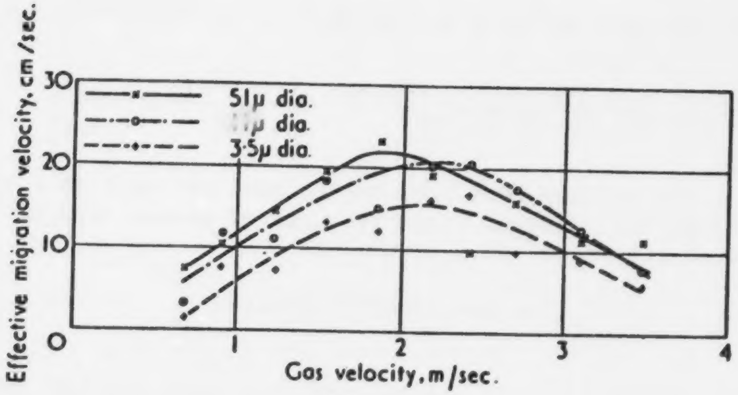

(b) Results of Dalmon and Lowe (L/d ≃ 20) (7)

Figure 6. Example of measurements of the variation of the effective migration velocity with gas speed reported by previous workers.

There are at least three different mechanisms that have been suggested to explain these observations. The Deutsch theory is strictly applicable to particles of one size whereas most observations have been made for polydispersions. In qualitative terms one might expect that at higher gas speeds the precipitator electric field acts on the average on particles of larger average size (and charge) and should therefore exhibit a larger effective migration velocity. A second explanation proposed by Cooperman (10) is that increasing axial turbulent diffusion relative to convection at decreasing gas speeds should reduce the effective migration velocity. A third explanation offered by Busby and Darby (6) is that the effect results from transverse turbulent diffusion (although the conjecture that the turbulence intensity increases with gas speed is not in accord with measurements reported in this paper).

In what follows, each of these mechanisms will be examined separately. The central feature of the experimental results on which we shall focus, is that the effective migration velocity at lower gas speeds is approximately increased by a factor of two for a doubling of the gas speed.

If $f(x)dx$ denotes the fraction of particles in a polydispersion with diameters between x and $x + dx$, then using the Deutsch formula, the penetration from a precipitator having a ratio of collection area to volume flow rate (A/V) is

$$Q = \int_0^\infty \exp[-(A/V)w(x)]\ f(x)dx.$$

The apparent migration velocity w_a of the polydispersion is defined by the equation $Q = \exp[-(A/V)w_a]$. Following the procedure of Allander and Matts (11), if we assume that field charging is dominant so that $w(x) \propto x$ and that $f(x)$ is a log-normal distribution, the integral may be evaluated numerically. The result is a function of two dimensionless parameters, the Deutsch No. $\mathscr{D}_g \equiv (L/d)(w_g/u_o)$ and the geometric standard deviation σ_g. Here L is the precipitator length and $w_g = w(\bar{x}_g)$ is the migration velocity of a particle having a diameter equal to the geometric mean $\bar{x}_g$ (equal to the median) of the distribution. For the apparent migration velocity one then obtains the formula $w_a/w_g = [\ell n\ (1/Q)]/\ \mathscr{D}_g$.

The quantity $\mathscr{D}_g^{-1} = (d/L)(u_o/w_g)$ may be viewed as dimensionless gas speed. Shown in Figure 7a are values of w_a/w_g plotted as a function of the dimensionless gas velocity (or equivalently, $\mathscr{D}_g$), for some representative flyash values for $\ell n\ \sigma_g$. For a fixed value of $\ell n\ \sigma_g$ if w_{a1} denotes the apparent migration velocity corresponding to a gas velocity u_1, then the apparent migration velocity w_{a2} corresponding to a gas velocity $u_2 = 2u_1$ may be obtained directly from this figure, as a function of $\mathscr{D}_g = (L/d)(w_g/u_1)$ and $\ell n\ \sigma_g$. The results of such a calculation for w_{a2}/w_{a1} are shown in Figure 7b. Laboratory precipitators usually have values of $\mathscr{D}_g$ of the order of one or larger, whereas large efficient commercial precipitators have values of $\mathscr{D}_g$ at the upper end of the scale. The main conclusion to be drawn from this figure is that polydispersion effects alone are too small to be able to account for the observed dependence of the effective migration velocity on gas speed.

To assess the possible effects of axial turbulent diffusion, we may employ the theoretical result (1) that the penetration of monodisperse particles, for the dominant mode (i.e. the mode that decreases least rapidly

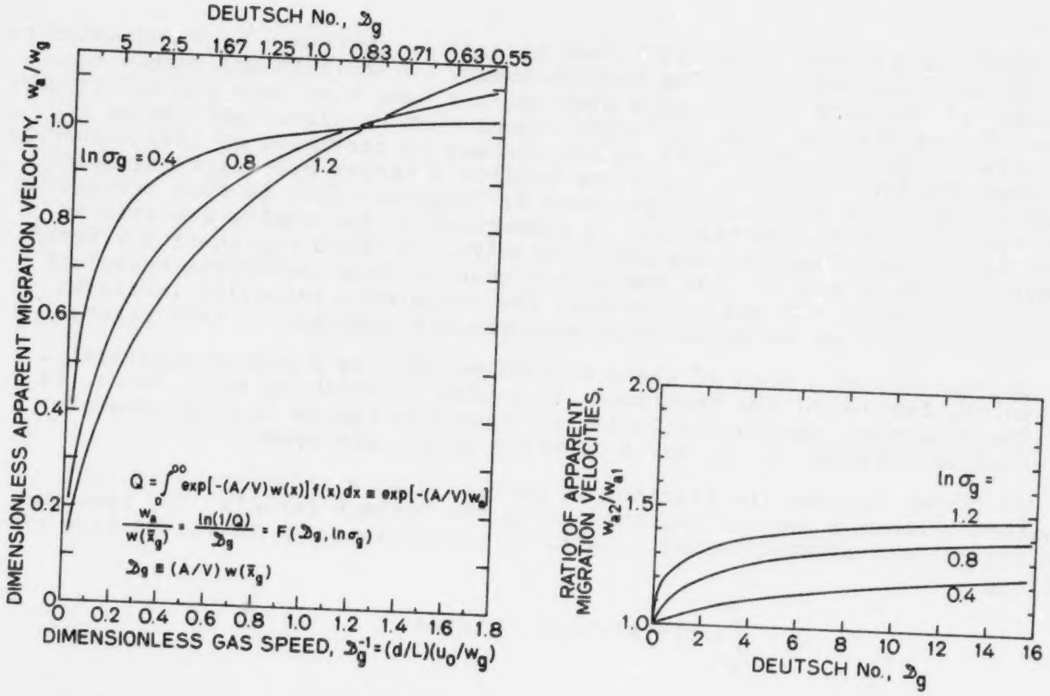

(a) Dependence of apparent migration velocity w_a on gas velocity u_o, for a log-normal polydispersion of particles $f(x)$ having a geometric mean diameter $\bar{x}_g$ and a geometric standard deviation σ_g. Here $w_g \equiv w(\bar{x}_g)$ is the actual migration velocity for a particle of diameter $\bar{x}_g$, and $\mathscr{D}_g \equiv (L/d)(w_g/u_o)$ is the corresponding Deutsch No. for a precipitator length L and wire-to-plate spacing d. The ratio of plate area to volume flow rate is A/V and Q denotes the penetration.

(b) Effect of a polydispersion of particles when the gas velocity is doubled ($u_2 = 2u_1$) on the ratio $w_{a2}/w_{a1} \equiv w_a(u_2)/w_a(u_1)$ of the apparent migration velocities. Shown is the dependence on the Deutsch No. $\mathscr{D}_g \equiv (L/d)[w(\bar{x}_g)/u_1]$ for a log-normal distribution with geometric mean diameter $\bar{x}_g$, for several values of the log of the geometric standard deviation, $\ell n\ \sigma_g$.

Figure 7. The gas speed effect of a polydispersion on apparent migration velocity.

with precipitator length), is given by the modified Deutsch formula $Q = \exp[-(A/V)w_a]$, where

$$w_a = w_a(u_o) = \frac{P}{2}\left(\frac{u_o}{w}\right)^2 \{[1+4\frac{F_1(P)}{P}\left(\frac{w}{u_o}\right)^2]^{1/2}-1\}$$

Here $P = wd/D$, the electric Peclet No., provides a measure of the ratio of particle transport by the electric field to that by turbulent diffusion. The quantity D is the turbulent diffusivity and $\mathscr{D} = (L/d)(w/u_o)$ is the Deutsch No. The function $F_1(P)$ must be determined numerically, but is given to a good approximation by the expression $F_1(P) = 1 + 0.2P$.

If w_{a1} and w_{a2} denote the apparent migration velocities corresponding to gas velocities u_1 and $u_2 = 2u_1$, the ratio w_{a2}/w_{a1} may be calculated directly from the formula $w_a(2u_1)/w_a(u_1)$. This ratio is shown in Figure 8 as a function of (w/u_1). The effect of increasing turbulent diffusivity D_1 is expressed through the effect of decreasing $P_1 = wd/D_1$. Curves are shown for $P_1 = 1, 10^{-2}$, and 10^{-4}. The corresponding values, $D_1 = 10^{-2}$ m²/s, 1 m²/s, and 10^2 m²/s are obtained using the typical values $w = 0.1$ m/s and $d = 0.1$ m. Typical values of the abscissa fall in the range from about 0.1 to 0.2.

These values of D_1 may be compared with values found in fully-developed turbulent pipe flow, where the correlation $u_o d/D \approx 1000$ has been developed (12). Using as typical values $u_o \approx 1$ m/s and $d \approx 0.1$ m, we obtain $D = 10^{-4}$ m²/s. Thus in relative terms, the values of D_1 shown in Figure 8 that are needed to obtain significant values for w_{a2}/w_{a1} are extremely large. Futhermore, the maximum value of w_{a2}/w_{a1} that can be obtained corresponding to $D_1 \to \infty$, is 2. It therefore seems highly unlikely that axial diffusion effects alone could be responsible for the experimental data shown in Figure 6.

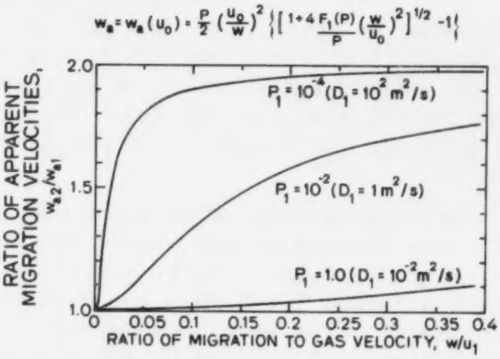

Figure 8. Effect of the axial turbulent diffusivity D when the gas velocity is doubled ($u_2 = 2u_1$) on the ratio $w_{a2}/w_{a1} \equiv w_a(u_2)/w_a(u_1)$ of the apparent migration velocities, for the dominant mode.

Shown is the dependence on the ratio (w/u_1) of the migration to the gas velocity, for several values of the electric Peclet No. $P_1 = wd/D_1$. Here d is the wire-to-plate spacing. Values shown for D_1 are for $w = 0.1$ m/s and $d = 0.1$ m.

A third possible mechanism is based on the effects of transverse turbulent diffusion. But in contrast to Busby and Darby (6), we propose an explanation based on the very large increase in the rms value of the turbulent velocity u' that the previously described experiments show occurs at lower gas speeds. Since the turbulent diffusivity is approximately proportional to u'L* (where L* is a measure of the size of the larger energy-containing eddies in the flow), if follows that D is significantly increased and therefore the electric Peclet No. is significantly decreased, at lower gas speeds. From theory (1) the penetration, and therefore the apparent migration velocity, is significantly decreased.

According to the theory of the effect of turbulence, the penetration Q is a function of the Deutsch No. $\mathscr{D}$ and the Peclet No. P — i.e. $Q = Q(\mathscr{D},P)$. The apparent migration velocities w_{a1} and w_{a2} corresponding respectively to the gas velocities u_1 and $u_2 = 2u_1$, and to the Peclet Nos. P_1 and P_2, are given by the equations $Q_1 \equiv Q(\mathscr{D}_1, P_1) = \exp[-(A/V_1)w_{a1}]$ and $Q_2 \equiv Q(\mathscr{D}_1/2, P_2) = \exp[-(A/2V_1)w_{a2}]$ and therefore $w_{a2}/w_{a1} = 2\,\ell n\,(1/Q_2)/\ell n\,(1/Q_1)$.

Performing this calculation one obtains the results shown in Figure 9, where the effects of gas speeds are shown as a function of $\mathscr{D}_1 = (L/d)(w/u_1)$, for several values of $P_2/P_1 = D_1/D_2$, and for $P_1 = 1.25$ or $P_1 = 2.5$. The values selected for D_1/D_2 approximately span the range inferred from the experiments. The main uncertainty hinges on the values for P_1, but the values selected are believed to be not unreasonable. It is apparent from these results that the proposed mechanism is certainly capable of explaining the magnitude of the reported effects of gas speed on migration velocity. Further work on this question is in progress.

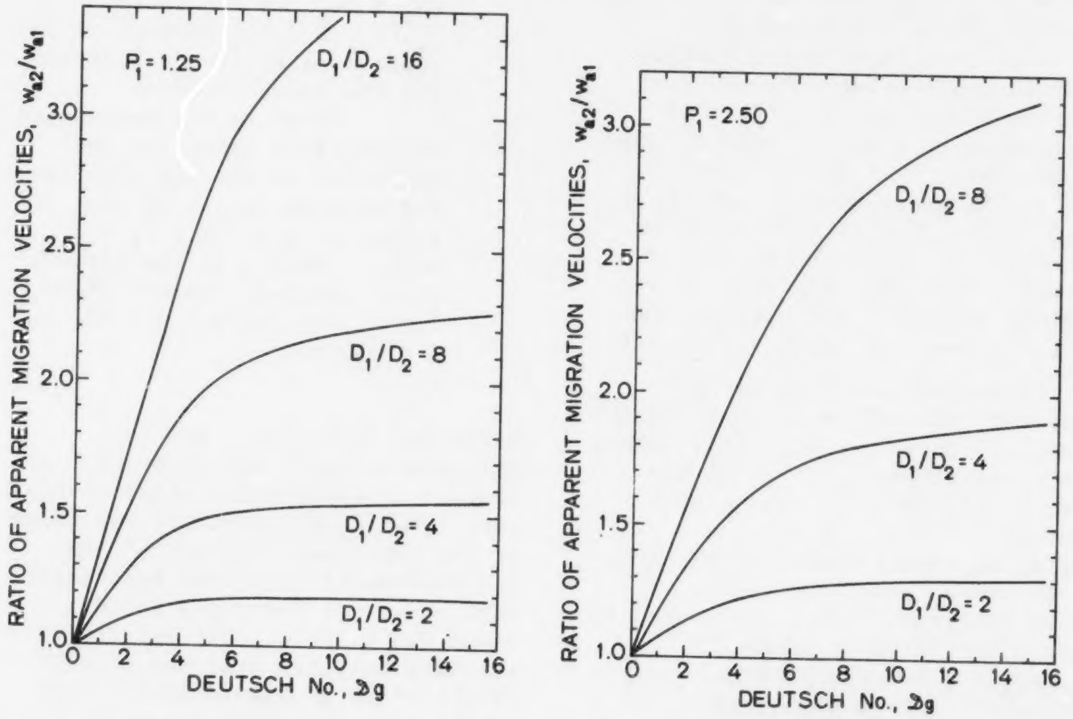

(a) $P_1 = 1.25$

(b) $P_1 = 2.50$

Figure 9. Effect of the transverse turbulent diffusivity D when the gas velocity is doubled ($u_2 = 2\,u_1$) on the ratio $w_{a2}/w_{a1} \equiv w_a(u_2)/w_a(u_1)$ of the apparent migration velocities. Shown is the dependence on the Deutsch No. $\mathscr{D}_1 \equiv (L/d)\,(w/u_1)$, for several values of the turbulent diffusivity ratio $D_1/D_2 \equiv D(u_1)/D(u_2)$. Here $w = w(x)$ is the migration velocity, d is the wire-to-plate spacing, and $P_1 = wd/D_1$ is the electric Peclet No.

CONCLUSIONS

For gas speeds in excess of about 3 m/s and currents of practical interest, corona-induced turbulence appears to have little influence on the background fluid mechanical turbulence generated in the boundary layer and by the discharge wire wakes. For gas speeds of about 1.5 m/s, negative corona-induced turbulence appears to be of the same magnitude as the background turbulence; positive corona-induced turbulence appears to be small except possibly near the top and bottom of the precipitator. At lower gas speeds negative corona-induced turbulence becomes increasingly intense with decreasing gas speeds, and methods for achieving moderate turbulence levels in single-stage precipitators are unlikely to be effective. To achieve improved precipitator performance with negative corona through turbulence control, it appears that gas speeds need to be approximately equal to or larger than 1.5 m/s. This value is reduced somewhat for smaller corona currents. Attainment of moderate turbulence levels at lower gas speeds with positive corona may be possible. An explanation of previously reported reductions of effective migration velocity at lower gas speeds is suggested by the large increase in turbulence intensity observed at lower gas speeds.

ACKNOWLEDGEMENTS

This work was supported by the National Science Foundation under Grant Number CPE-7926290 and by the Electric Power Research Institute under Contract RP-533-1.

The work described in this paper was not funded by the U. S. Environmental Protection Agency and therefore the contents do not necessarily reflect the views of the Agency and no official endorsement should be inferred.

REFERENCES

1. Leonard, G. L., Mitchner, M., and Self, S. A. Particle Transport in Electrostatic Precipitators. Atmospheric Environment 14, pp 1289-1299, 1980.

2. White, H. J., Industrial Electrostatic Precipitators. Addison-Wesley, 1963.

3. Leonard, G. L., Mitchner, M., and Self, S. A. Experimental Study of the Effect of Turbulent Diffusion on Precipitator Efficiency. Jour. Aerosol Science 13, pp 271-284, 1981.

4. Leonard, G. L., Mitchner, M., and Self, S. A. Experimental Study of the Electrohydrodynamic Flow in Electrostatic Precipitators. Accepted for publication by Jour. of Fluid Mechanics. See also Precipitation from Turbulent Flows. Proceedings of the Int. Conf. on Electrostatic Precipitation, pp 208-256. Monterey, Calif., October 14-16, 1981.

5. Yamamoto, T., and Velkoff, H. R. Electrohydrodynamics in an Electrostatic Precipitator. Jour. of Fluid Mechnics 108, pp 1-18, 1981.

6. Busby, H.G.T., and Darby, K. Characteristics of Electrostatic Precipitators. In: Proceedings of La Physique des Forces Electrostatiques, pp 229-253. Grenoble, France. September 27 - October 1, 1960.

7. Dalmon, J., and Lowe, H. J. Experimental Investigations into the Performance of Electrostatic Precipitators for P. F. Power Stations. In: Proceedings of La Physique des Forces Electrostatiques, pp 363-379. Grenoble, France. September 27 - October 1, 1960.

8. Pejack, E. R. An Aerosol Tunnel Test Facility. Jour. Environmental Sciences May/June, 1981.

9. Leonard, G. L. Effect of Turbulence on Electrostatic Precipitator Performance. Ph.D. Dissertation, Department of Mechanical Engineering, Stanford University, 1982.

10. Cooperman, P. A New Theory of Precipitator Efficiency. Atmospheric Environment 5, pp 541-551, 1971.

11. Allander, C., and Matts, S. The effect of Particle Size Distribution on Efficiency in Electrical Precipitators. Staub 52, p 738, 1957.

12. Becker, H. A., Rosensweig, R. E., and Gwodz , J. R. Turbulent Dispersion in a Pipe Flow. A. I. Ch. E. Jour. 12, pp 964-972, 1966.

VELOCITY AND TURBULENCE FIELDS IN NEGATIVE CORONA WIRE-PLATE PRECIPITATOR

by: H.P.Thomsen, P.S.Larsen, E.M.Christensen, J.V.Christiansen
Department of Fluid Mechanics
Technical University of Denmark
DK-2800 Lyngby

ABSTRACT

Back-scatter laser Doppler anemometry has been used to obtain distributions of mean and rms values of particle velocity in horizontal planes perpendicular to electrodes in a 0.3 m wide by 0.6 m high wire-plate electrostatic precipitator for four types of electrodes and a mean velocity of 1 m/s. Particle motion reveals complex three-dimensional flow patterns with rolls of axial vorticity which are most regular for barbed wire electrodes with axial needles. The turbulence level is shown to depend on current density and mean velocity and to disappear when the inverse electrical Froude number is below about 0.2 . However, rolls persist. Results are discussed in terms of the turbulent kinetic energy production.

INTRODUCTION

Further improvement of the modeling of particle transport in electrostatic precipitators requires detailed experimental studies of the ionized gas flow and the motion of charged particles under the influence of electric field and prevailing gas flow. Laser Doppler anemometry (LDA) provides a means for in-situ measurements of instantaneous velocity components of individual particles. Time averaging such results provides mean and rms velocity components of particles as well as particle concentrations. The extend to which such particle data reflect the gas motion depends on the governing parameters.

In the absence of an electrical field (or particle charge) uniformly distributed micron-sized particles closely follow the instantaneous motion of the gas phase to a sufficiently high frequency that the LDA-technique provides an adequate description of the turbulent gas flow (Durst, Melling & Whitelaw 1981). The governing parameter is the Stokesian time constant $\tau = (2a^2/9\nu)(\rho_s/\rho)$, which is less than 10^{-4} s , for example, for $2a = 5$ μm diameter drops, $\nu = \mu/\rho$, ρ and ρ_s denoting kinematic viscosity, fluid density and particle material density, respectively.

Net particle drift owing to non-uniform concentration distributions in turbulent flows may be inferred from the changes in concentration profiles along a flow. Actual drift velocities of particles relative to gas are usually too small to measure directly with any accuracy. For a turbulent diffusivity of, say $D_T = 10^{-4} - 10^{-3}$ m^2/s in a channel of small dimension $L = 0.1$ m, the drift velocity associated with turbulent diffusion will be on the order of $D_T/L \sim 0.001 - 0.01$ m/s.

Drift velocities resulting from the Coulomb force on charged particles in an electrical field, on the other hand, are typically on the order of $W_E \sim 0.05 - 0.5$ m/s and can be readily measured in a laminar parallel flow. The terminal drift velocity of small particles of radius a and charge q in a locally uniform electrical field of strength E may be calculated from $W_E = qEC/(6\pi\mu a)$, where C denotes the Cunningham correction factor.

In view of the smallness of the Stokesian time constant τ and for weak turbulence, terminal drift W_E can be assumed to exist locally throughout inhomogeneous fields. LDA-measurements therefore are expected to reflect the result of particle drift relative to the local gas motion. In general, when turbulent diffusion can be ignored, particle velocity components perpendicular to the local Coulomb force equal the gas velocity components. Specifically, when the electrical drift velocity is small, particle velocities approximately describe the gas velocity. The foregoing remarks are useful when interpreting LDA-data.

During the last few years LDA has been used in a number of experimental precipitator studies. Employing pre-charged particles in small parallel plate precipitators, Jurewicz, Stock & Crowe (1977) and Ross (1980) measured axial velocity and drift velocities at selected conditions, while Leonard, Mitchner & Self (1982a) made extensive measurements of concentration distributions for comparison with their mathematical model (1980) describing the effect of turbulent diffusion on collection efficiency. Results of this study infer the magnitude of particle diffusivity. Masuda, et al (1979) studied the velocity and turbulence in a long 1:1 aspect ratio, negative corona, wire-plate precipitator, finding turbulence to develop from the central part of the flow. Grass (1979), in a similar study of a 2:1 aspect ratio precipitator, found wall turbulence to increase with the application of the electrical field, and evaluated the turbulent kinetic energy production due to the near-wall shear flow associated with the observed distortion of the axial velocity profile. Data on drift velocity in a positive corona, wire-plate precipitator has been presented by Lawless, et al (1981). Kawase, et al (1980) and Tedjojuwono, et al (1981) observed increasing turbulence levels with increasing electrical field in a small, axial flow, single-wire precipitator, studying both positive and negative corona, and presented velocity vector maps for particles at different current densities. Leonard, Mitchner & Self (1982b) carried out a comprehensive study in a small scale wire-plate precipitator for positive and negative corona, combining LDA, hot-wire and visualization studies to determine flow patterns and turbulence levels to ascertain the role of turbulence on precipitator efficiency. Positive corona was found to yield plane secondary flows with wall-confined turbulence while non-uniformities of the negative corona produced three-dimensional secondary flows and bulk turbulence. The latter effect was shown to decrease with increasing mean velocity through the precipitator, and to disappear for a mean velocity of 2 - 3 m/s at a mean current density, which corresponds to an inverse electrical Froude number of $f_E = (J'/b)/(\rho U_o^2) \sim 0.5$. Here b denotes the ion mobility, ρ the gas density and U_o the mean gas velocity. The inverse Froude number, being the ratio of electrical force on the ionized gas to inertial force, was shown to be a useful parameter for correlating the onset on turbulence at the centerline for the case of positive corona.

It appears to be well established that increased turbulent mixing lowers the parallel plate precipitator efficiency (Leonard, Mitchner & Self 1980, and discussion by Cooperman 1982). For negative corona, wire-plate precipitators, irregular corona discharge induces three-dimensional secondary flows enhancing turbulence and mixing. These effects are further enhanced by baffles usually incorporated into industrial type wire-plate precipitators (Crowe, Stock & Bernstein 1978). Aside from the problems associated with deposition and reentrainment, it appears that improvement of collector efficiency requires further knowledge and search for possible means of control of secondary flows and mixing. It is the purpose of the present study to provide new experimental data on distributions of mean and rms velocity of particles in a full-width, negative corona, wire-plate precipitator.

EXPERIMENTAL FACILITY

The present experimental study has been performed in a full-width, 2:1 acpect ratio, negative corona, wire-plate type laboratory precipitator facility (Figure 1). The 0.30 m wide by 0.60 m high by 5.0 m long test section has grounded aluminium side walls and perspex bottom and top. Vertical, 3 mm diameter wire electrodes are positioned along the centerline of the channel at a 0.20 m spacing, normally starting at x = 0.35 m , where x = 0 denotes the inlet. The wire voltage can be adjusted over the range - 35 kV to - 50 kV. Electrode voltage and current to groups of discharge electrodes can be measured. In addition a portion (0.60 m long by 0.30 m high) of one side wall is subdivided into 6 sections (each 0.10 m long by 0.30 m high) to which the plate current can be measured individually, essentially eliminating inhomogeneous field effects from bottom and top.

Air is drawn into the test section through a contraction (1.2 by 1.2 m inlet) equipped with two screens (0.5 mm wire, 18 mesh per inch). The flow is driven by the fan of a bag filter connected to the test section exit, yielding test section velocities in the range 0.1 - 2.5 m/s . Aerosol particles (80 - 90 °C hot glycerin, atomized into 2 - 5 μm diameter drops) are feed over the width on the inlet contraction in the midplane and serve as seeding particles for LDA-measurements.

Velocity and concentration measurements are made with a two-color, dual beam, back-scatter laser Doppler anemometer, equipped with frequency shift (DISA 55X), amd employing a Spectra Physics 165-03 argon-ion laser, 2:1 beam expander and a 600 mm focal length front lens to access the test section through its perspex bottom (Figure 2). A rigid traversing bench supports the LDA-optics and permits three-axes positioning of the measuring volume to within 0.2 mm accuracy. The measuring volume has a diameter of 0.16 mm and a length of 0.17 mm . Data is referred to x,y,z-coordinates, where axial coordinate x = 0 at the test section inlet, transverse coordinate y = 0 on the one collector plate, and vertical coordinate z = 0 at the bottom.

Photomultipliers (DISA 55X08) incorporate preamplifiers and low output impedance for low sensitivity to external electrical noise. Signal processing involves computer interfaced counters (DISA 55L) operated in combined mode, allowing for bias-free residence time averaging of velocity and relative concentration. Averages were based on 500 samples in most cases, after establishing the level of accuracy based on 1000 samples. Since the LDA-system has been only recently expanded to a full two-color operation, most data were obtained with a one-color system. Consequently, axial and transversal components of velocity were measured separately. To obtain reliable turbulence data requires careful operation of the LDA-system for optimum S/N-ratio (greater than 15 - 30 dB). Comparison to hot-wire data in reference flows and in the test section were carried out to ascertain the accuracy of the data. Such tests show a 2 - 5% accuracy on mean velocity and 5 - 10% accuracy on rms-velocity without electrical field.

EXPERIMENTAL RESULTS

The measured electrical characteristics of the precipitator for four types of discharge electrodes (Table 1) having axial spacing 0.20 m is shown in Figure 3. The low currents measured for electrode A show an anticipated scatter, but are within 10% of predictions based on numerical calculations of two-dimensional electrical fields. Electrode B was not found to improve uniformity of corona discharge. The current on the rough side (shown) is much higher than on the smooth side (not shown), hence giving an asymmetrical electrical field. Electrodes C_a and C_t yield nearly the same current with little scatter in results, but C_a was found to give more stable and uniform discharge as seen from the velocity distributions. Because of the low particle concentrations (about 10^{10} particles per m^3) currents were insensitive to variations experienced in concentrations, and Figure 3 applies to all data presented.

TABLE 1. ELECTRODE TYPES

type	cross section	description
A		polished 3.0 mm diameter brass wire.
B	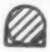	M4/4 mm threaded brass wire, ground to leave two threaded edges. Flat side facing collector plate.
C_a	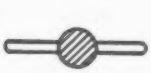	Barbed wire electrode. Polished 3.0 mm diameter wire fitted with 1 mm dia. by 12 mm long pins spaced 100 mm apart. Pins point in axial direction.
C_t		Barbed wire electrode as C_a. Pins point in transversal direction towards plates.

The uniformity of velocity profiles in the precipitator without and with electrodes, for zero current, is shown in Figure [illegible]. Except for the regions of wall boundary layers and electrode wake (0.02 m downstream of the second electrode) the turbulence intensity is uniform at about 2.5% for a mean velocity $U_o = 1.1$ m/s . This is typical of a wind tunnel of the present design. The accuracy of this data is better than 2% on $\bar{u}_x$ and 5% on $u_{x,rms}$.

With a 50 kV negative corona voltage a comprehensive experimental program was undertaken to determine the velocity field of particles in the upstream and central part of the test section where effects of bottom and top should be small. The accuracy of the following data, because of the inherent irregularity of negative corona discharge, is on the order of 10% for mean velocities of the more regular flows and about 20% on the rms-values. The accuracy is less on irregular flows.

Figures 5.1 - 5.8 show the velocity vector and turbulence intensity at a number of points in a horizontal plane between the second and third electrode for a number of condictions. Figure captions give electrode type (Table 1), z-coordinate for horizontal plane, mean velocity U_o (1 m/s for the first six figures), and the inverse electrical Froude number $f_E = (J'/b)/(\rho U_o^2)$, where $J' = JL$, L denoting the electrode spacing.

Regarding mean velocities, as expected for negative corona, smooth or rough electrodes (Types A and B) give irregularly distributed corona discharge along wires, resulting in irregular ionic wind distortions of the axial flow in a given plane (Figures 5.1 - 5.3). Although irregular, the recorded flow appeared to remain unchanged during the period of measurements.

Barbed wire electrodes with axial needles (Type C_a) give a fairly regular flow distortion which is towards the collector plate in the horizontal plane of needles (Figure 5.4) and away from it in the horizontal plane between needles (Figure 5.5). This implies the existence of vertical velocity components, which has been verified by a local check of data for the divergence of the velocity in a horizontal plane. No measurements of vertical velocity components has been made so far. Yet, distributions of transverse velocity components in vertical planes (Figure 6.2) clearly show the existence of a regular pattern of secondary flow, forming rolls of axial vorticity of alternating sign. The precipitator height being 0.6 m and the distance between needles 0.1 m , suggest enough rolls that end effects from bottom and top may be small.

Barbed wire electrodes with transverse needles (Type C_t) give more irregular secondary flows due to ionic wind which appears to vary in intensity from needle to needle (Figure 5.6). However, results indicate to secondary flows as rolls of axial vorticity (Figure 6.1).

Two cases of low mean velocity $U_o = 0.5$ m/s (Figure 5.7) and $U_o = 0.1$ m/s (Figure 5.8) are included to show pronounced effects of ionic wind, leading also to particle and gas flow reversals in a horizontal plane. The results imply three-dimensional flow and only partial periodicity, probably owing to less regular corona discharge.

In no case of a mean velocity of $U_o = 1$ m/s (Figures 5.1 to 5.6) were negative axial velocity components of particles measured. Assuming the axial component of the electrical field to be zero in y,z-planes through electrodes, the axial velocity component here equals the gas velocity. It appears that gas recirculation zones are suppressed at an axial velocity of 1 m/s , but not at 0.1 - 0.5 m/s . Also apparent from several figures is the weakly pointed distributions of axial gas velocity in y,z-planes through electrodes with reduced values near the wall and increased values near the center. For the data as a whole, increasing values of f_E yield increasing transversal flow and rolls of axial vorticity induced by ionic wind. In view of the smallness of the Stokesian time constant of particles, the velocity distributions of the gas phase may be inferred by subtracting computed values of the electrical drift velocity vector W_E of particles from the measured particle velocity vector. Near the collector plate W_E is essentially perpendicular to the plate and on the order of 0.2 m/s , for example, for the data of Figure 5.6.

Measured values of turbulence intensity $u_{x,rms}/U_o$ are indicated in Figures 5.1 - 5.6 by circles at each point according to the adjoining scale. Of the several features, turbulence increases with increasing f_E , it appears to be high in areas of high ionic wind and strong shear layers, and it appears to reach a maximum intensity in a region some distance from the wall. To study further the development of turbulence, the flow was traversed in axial direction at three values of y , starting well upstream of the first of the type C_a electrodes placed at x = 750 mm . Figure 7 shows the increase of $u_{x,rms}$ from the typical no-field level of 0.02 - 0.03 m/s , which persists to a position of about 150 mm upstream of the first electrode. Although irregular, the variation of data shows $u_{x,rms}$ between electrodes to be highest, on the average, at the intermediate plane at y = 220 mm . Note that the rise in turbulence near the wall occurs well downstream of the first electrode.

Figure 8 shows the rise in $u_{x,rms}$ at two axial positions as the current density is increased from its lowest attainable value (at - 35 kV). Figure 9 shows $u_{x,rms}/U_o$ versus mean velocity U_o without and with full electrical field at one location between the first two electrodes. The turbulence intensity without field is about 2% except for velocities less than about 1 m/s, where it is 3 - 5%. Note the suppression of field induced turbulence with increasing mean velocity, as found also by Leonard, Mitchner & Self (1982b). The suppression appears to be complete for $f_E < 0.2$.

Figure 10 shows the same data of turbulence intensity, now plotted versus f_E . Beyond a threshold, there is first a rapid increase in turbulence with increasing f_E , followed by a nearly linear increase which may level off for $f_E > 2$.

DISCUSSION AND CONCLUSIONS

On essential points the present results obtained by in-situ velocity measurements corroborate the often indirect findings of recent studies of negative corona, wire-plate precipitator flows. In horizontal planes, the ionic wind produces flow distortions of the type suggested by Yamamoto & Velkoff (1981) for low mean velocity and smooth electrodes, but flow reversal and recirculation was not found to exist at mean velocities at or above 1 m/s. Here, the flow is strongly three-dimensional and most regular for barbed wire electrodes with axial needles. In vertical y,z-planes, the three-dimensionality of flow is revealed as rolls of alternating axial vorticity, as suggested by the study of Robinson (1976). Turbulence appears to develop first in the bulk flow at electrodes, and between electrodes and wall (where it attains the highest average levels), and later near the wall. While turbulence dissappears for mean velocities above about 2 m/s ($f_E < 0.2$) rolls persist for type C_a electrodes. These results imply that turbulent mixing can be effectively reduced by increasing the mean velocity, but that mixing associated with three-dimensionality of flow persists.

For an explanation of the influence of mean velocity on turbulence level we turn to the balance of turbulent kinetic energy $k = \frac{1}{2}\overline{u'_j u'_j}$ of the gas phase, which for steady mean flow is of the form

$$\bar{u}_i \, \partial k/\partial x_i = P_k + D_k - \varepsilon \qquad , \tag{1}$$

expressing the change as contributions from production, diffusion and dissipation. Since any increase in k is due to increased production, we here confine attention to this term. For an ionized gas, including the electrical body force $\rho_e E_j$ into the momentum balance, the usual derivation of Eq.(1) (see for example Hinze 1975) then yields the production

$$P_k = P_{k,s} + P_{k,b} = -\overline{u'_i u'_j}\, \partial \bar{u}_j/\partial x_i + \overline{\rho'_e u'_j}\, \bar{E}_j \qquad , \tag{2}$$

where the electrical field E_j has been assumed to be steady while velocity u_j and charge density per unit mass ρ_e are expressed in the usual way as the sum of mean and fluctuating components, $u_j = \bar{u}_j + u'_j$ and $\rho_e = \bar{\rho}_e + \rho'_e$. Obvious additional electrical terms arise if fluctuations E'_j correlate with those of ρ'_e and u'_j .

The first term in Eq.(2) describes shear production. In view of

$$-\overline{u'_i u'_j} = \nu_T \, \partial \bar{u}_j/\partial x_i \quad , \text{ hence } \quad P_{k,s} = \nu_T (\partial \bar{u}_j/\partial x_i)^2 \qquad , \tag{3}$$

where ν_T is the turbulent (eddy) diffusivity of momentum, any distortion of an initially uniform flow produces velocity gradients, hence a turbulent momentum flux in a velocity gradient, yielding production and increased turbulence level. At low mean velocity, the ionic wind distortions of the mean flow are large, giving a significant shear production. Grass (1979) examined his data for the increase in shear production in the near-wall layer associated with the distortion of the mean velocity distribution here. At high mean velocity, however, we find that ionic wind distortions are reduced to ondulations on the mean flow, yielding small velocity gradients, hence small production.

The second term in Eq.(2) describes body force production, originating from a turbulent charge flux $-\overline{\rho'_e u'_j}$ in electrical field $\bar{E}_j$. A similar term is known in thermally stratified flows, where buoyancy production, however, may be positive or negative depending on direction of heat flux. In view of the large velocities of ions, it is not clear to what extend body force production is important. Assuming ρ'_e to be associated with the turbulent motion, we estimate $P_{k,b}$ by use of the Prandtl mixing length arguments as

$$P_{k,b} = \overline{\rho'_e u'_j}\,\bar{E}_j \sim u'\ell\,(\partial\bar{\rho}_e/\partial x_j)\bar{E}_j \sim \nu_T\,\vec{\nabla}\bar{\rho}_e\cdot\vec{E} \quad . \qquad (4)$$

Employing the electrical field equations

$$\vec{\nabla}\cdot\vec{E} = \bar{\rho}_e/\varepsilon_o \quad , \quad \vec{J} \cong \bar{\rho}_e b\vec{E} \quad , \quad \vec{\nabla}\cdot\vec{J} = 0 \quad , \qquad (5)$$

where b is assumed to be constant, Eq.(4) may be expressed, for example, as

$$P_{k,b} \sim \nu_T\,(\bar{J}/(b\bar{E}))^2/\varepsilon_o \qquad (6)$$

Present estimates of $P_{k,b}$ and $P_{k,s}$ suggest that shear production created by ionic wind distortion of the mean flow is principally responsible for the increased turbulence production at large values of f_E . However, further study is required to explain the phenomena near electrodes and differences between positive and negative corona turbulence.

ACKNOWLEDGEMENTS

The present study was supported by research grant 20138.M-654 from the Danish Council of Scientific and Industrial Research (STVF) and by contributions to the precipitator facility from F.L.Smidth & Co A/S. The authors are indepted to Messrs. L.Barlebo and P.Carlslund for their contributions to the planning phase, preliminary hot-wire studies, and field calculations, and to Dr. L.Lind for advice and many constructive discussions.

The work described in this paper was not funded by the U.S. Environmental Protection Agency and therefore the contents do not necessarily reflect the views of the Agency and no official endorsement should be inferred.

REFERENCES

Cooperman,P. 1982 Particle Transport in Electrostatic Precipitators. Discussion, Atmos.Environ., 16, 1568-1571.

Crowe,C.T., Stock,D.E. & Bernstein,S. 1978 Numerical simulation of the Fluid Mechanic, Electrodynamic and Particle Dynamic Interaction in Wire-and-Plate Electrostatic Precipitators, Model.Simul., Proc.(ISA), 9, 149-153.

Durst,F., Melling,A. & Whitelaw,J.H. 1981 Principles and Practice of Laser-Doppler Anemometry, 2nd ed., Academic Press Inc., London.

Grass,H. 1979 Zur Wirkung der Turbulenz in Elektroabscheidern, Staub-Reinhalt.Luft, 39, 197-202.

Hinze,J.O. 1975 Turbulence, 2nd Ed., McGraw-Hill Book Comp., New York.

Jurewicz,J.T., Stock,D.E. & Crowe,C.T. 1977 Particle Velocity Measurements in an Electrostatic Precipitator with a Laser Velocimeter, AIChE Symp.Ser., 73:165, 138-141.

Kawase,Y., Tedjojuwono,K. & Asakura,T. 1980 Application of Laser Doppler Velocimeter to Velocity Measurement of Charged Dust Particles in High Electric Field, Optik, 56, 283-292.

Lawless,P.A., Damle,A.S., Viner,A.S., Shaughnessy,E.J. & Sparks,L.E. 1981 Laser Doppler Anemometry Measurements of Particle Velocity in a Laboratory Precipitator, 3rd Symp.Transfer Util.Part.Control Techn., Orlando, Florida.

Leonard,G.L., Mitchner,M. & Self,S.A. 1980 Particle Transport in Electrostatic Precipitators, Atmos.Environ., 14, 1289-1299.

Leonard,G.L., Mitchner,M. & Self,S.A. 1982a Experimental Study of the Effect of Turbulent Diffusion on Precipitator Efficiency, J.Aerosol Sci., 13, 271-284.

Leonard,G.L., Mitchner,M. & Self,S.A. 1982b An Experimental Study of the Electrohydrodynamic Flow in Electrostatic Precipitators, (to appear in J.Fluid Mech.).

Masuda,S., Akutsu,K., Kanno,Y. & Ko,M. 1979 Motion of Small Charged Particles inside an Electrostatic Precipitator, IEEE, IAS 14th Annu.Meet., Cleveland, Ohio, 139-145.

Robinson,M. 1976 Effects of Corona Discharge on Electrical Wind Convection and Eddy Diffusion in an Electrostatic Precipitator, Ph.D. Thesis, The Cooper Union University.

Ross,J.N. 1980 Studies of an Electrostatic Precipitator using Laser Doppler Anemometry, Optica Acta, 27, 19-23.

Tedjojuwono,K., Kawase,Y. & Asakura,T. 1981 Studies of the Dynamic Behaviour of Charged Dust Particles in High Electric Fields using Laser Doppler Velocimetry, Opt.Laser Technol., 13, 187-192.

Yamamoto,T. & Velkoff,H.R. 1981 Electrohydrodynamics in an Electrostatic Precipitator, J.Fluid Mech., 108, 1-18.

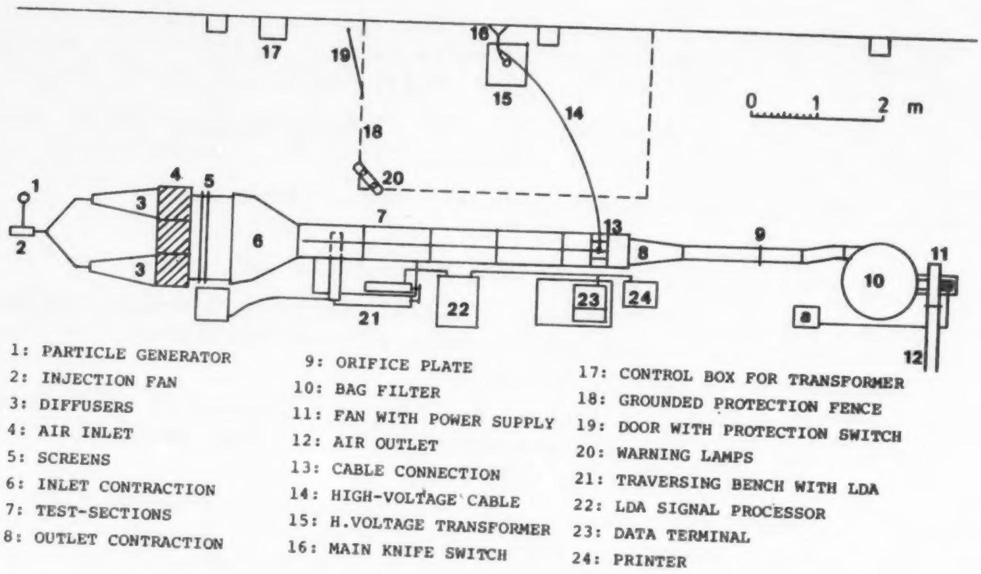
1
2
3
3
4
5
6
7
8
9
10
11
12
13
14
15
16
17
18
19
20
21
22
23
24
0 1 2 m
1: PARTICLE GENERATOR
2: INJECTION FAN
3: DIFFUSERS
4: AIR INLET
5: SCREENS
6: INLET CONTRACTION
7: TEST-SECTIONS
8: OUTLET CONTRACTION
9: ORIFICE PLATE
10: BAG FILTER
11: FAN WITH POWER SUPPLY
12: AIR OUTLET
13: CABLE CONNECTION
14: HIGH-VOLTAGE CABLE
15: H.VOLTAGE TRANSFORMER
16: MAIN KNIFE SWITCH
17: CONTROL BOX FOR TRANSFORMER
18: GROUNDED PROTECTION FENCE
19: DOOR WITH PROTECTION SWITCH
20: WARNING LAMPS
21: TRAVERSING BENCH WITH LDA
22: LDA SIGNAL PROCESSOR
23: DATA TERMINAL
24: PRINTER

Figure 1. Plan view of precipitator facility.

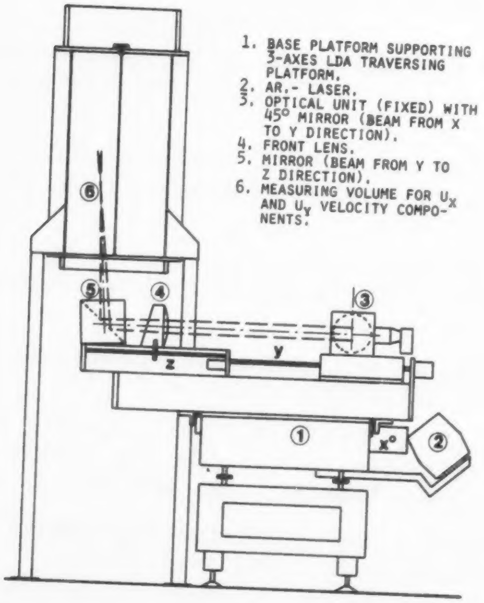
1. BASE PLATFORM SUPPORTING 3-AXES LDA TRAVERSING PLATFORM.
2. AR.- LASER.
3. OPTICAL UNIT (FIXED) WITH 45° MIRROR (BEAM FROM X TO Y DIRECTION).
4. FRONT LENS.
5. MIRROR (BEAM FROM Y TO Z DIRECTION).
6. MEASURING VOLUME FOR U_X AND U_Y VELOCITY COMPONENTS.
⑥
⑤
④
③
y
z
①
x°
②

Figure 2. Cross section of test section with optical traversing bench for positioning the x,y,z-coordinates of the LDA measuring volume.

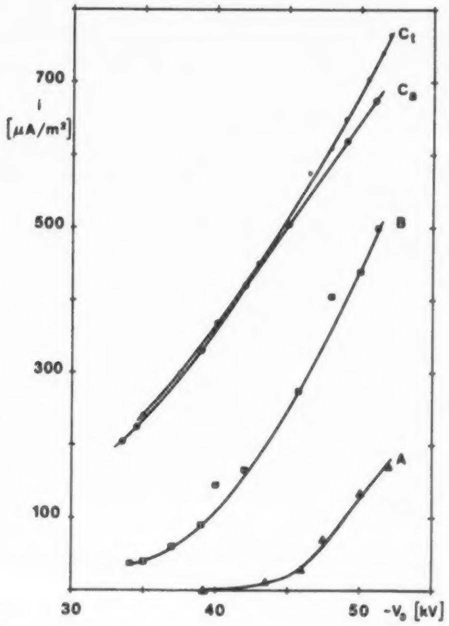

Figure 3. Mean current density versus negative corona voltage for four types of electrodes (Table 1).

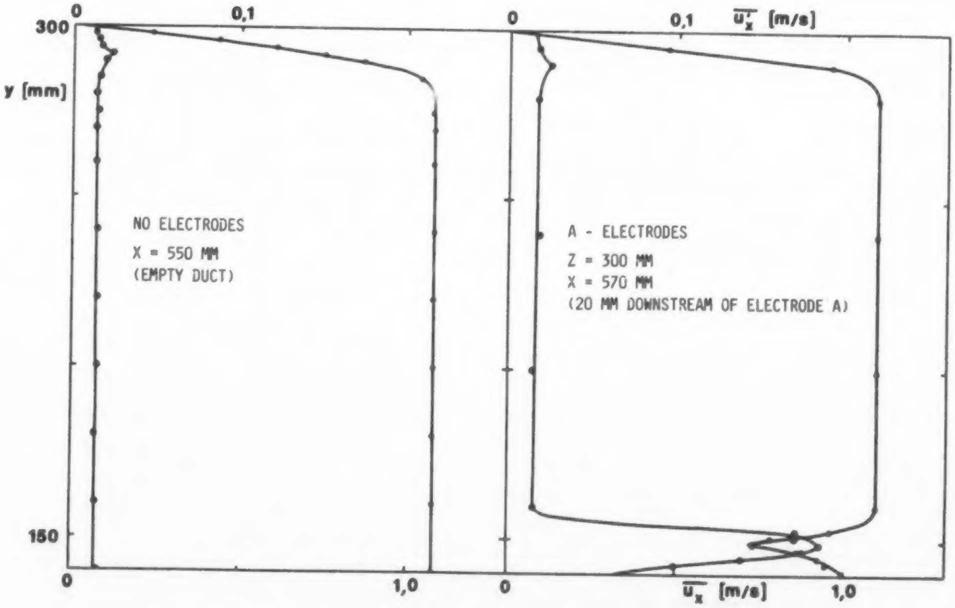

Figure 4. Distributions of mean and rms axial velocity, J=0.

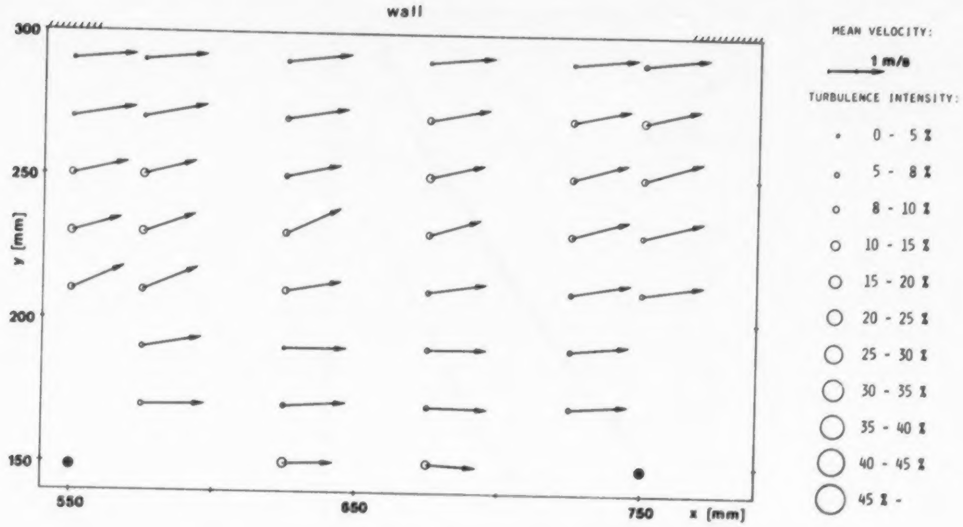

Figure 5.1 Velocity vectors and turbulence intensity in horizontal plane between 2nd and 3rd electrode.
Type A, $f_E = 0.11$, $U_o = 1$ m/s, z = 300 mm.

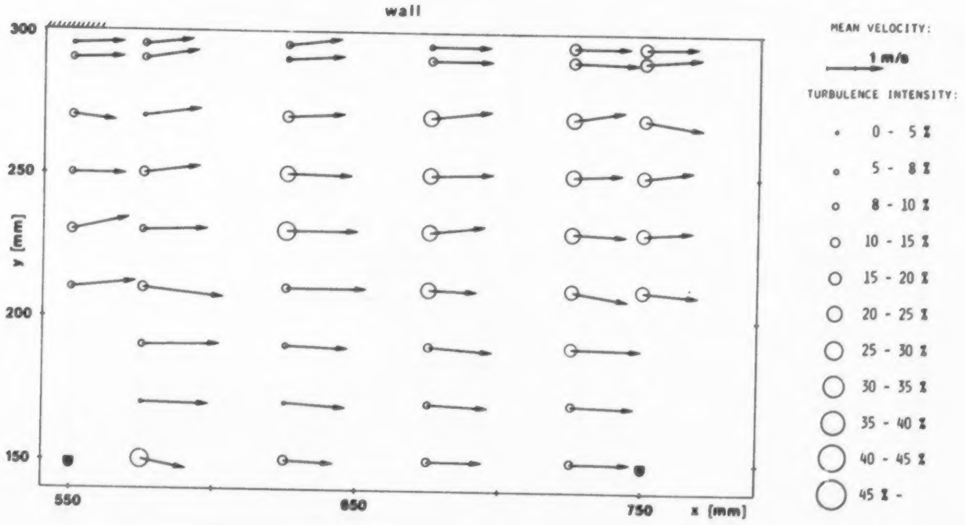

Figure 5.2 Velocity vectors and turbulence intensity in horizontal plane between 2nd and 3rd electrode.
Type B, $f_E = 0.36$, $U_o = 1$ m/s, z = 300 mm.

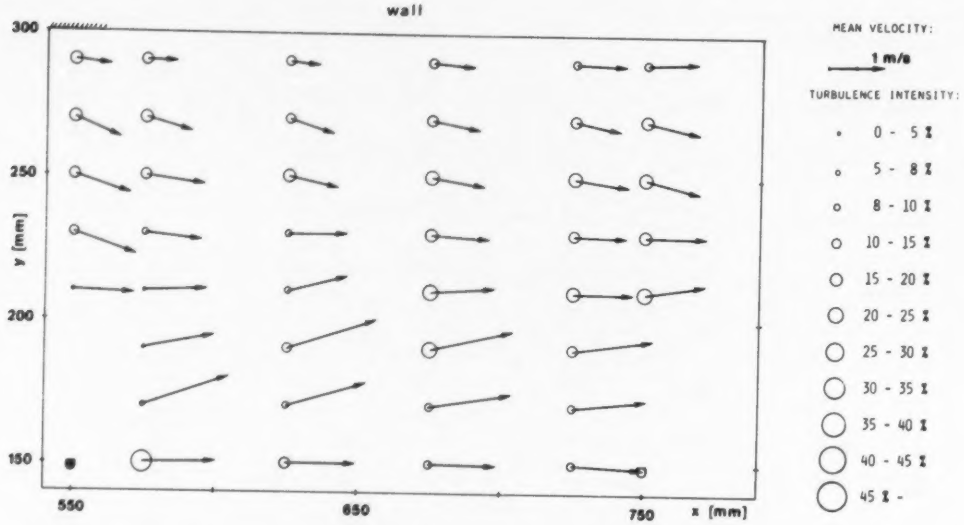

Figure 5.3 Velocity vectors and turbulence intensity in horizontal plane between 2nd and 3rd electrode.
Type B, $f_E = 0.36$, U_o = 1 m/s, z = 270 mm.

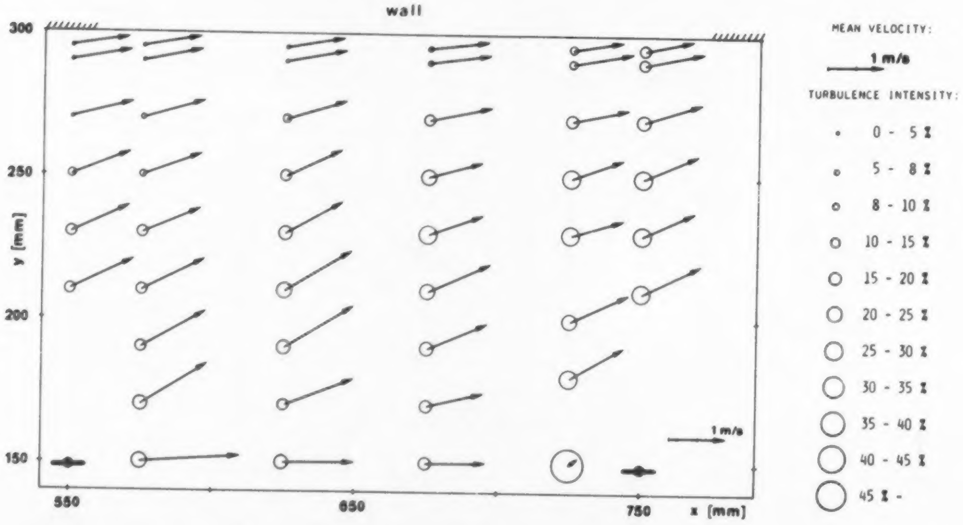

Figure 5.4 Velocity vectors and turbulence intensity in horizontal plane between 2nd and 3rd electrode.
Type C_a, $f_E = 0.54$, U_o = 1 m/s, z = 300 mm.

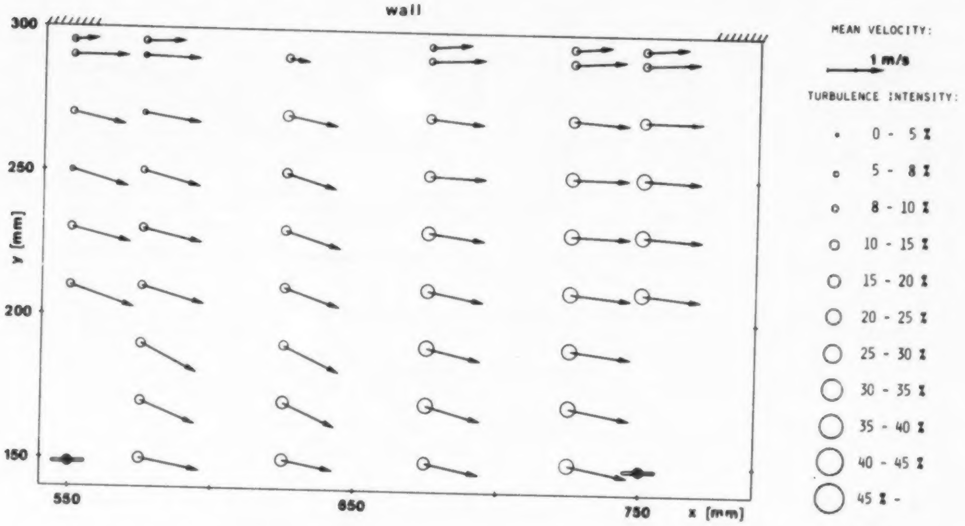

Figure 5.5 Velocity vectors and turbulence intensity in horizontal plane between 2nd and 3rd electrode. Type C_a, $f_E = 0.54$, U_o = 1 m/s, z = 250 mm.

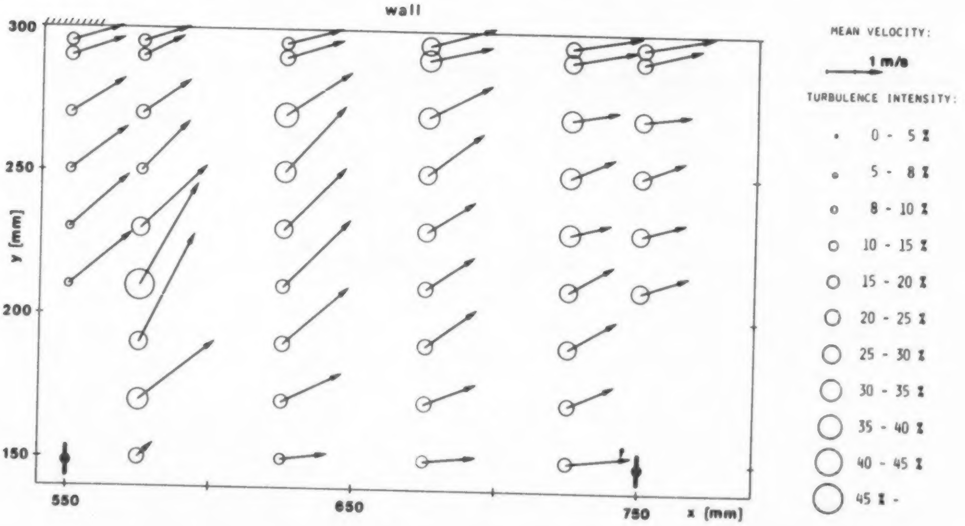

Figure 5.6 Velocity vectors and turbulence intensity in horizontal plane between 2nd and 3rd electrode. Type C_t, $f_E = 0.58$, U_o = 1 m/s, z = 300 mm.

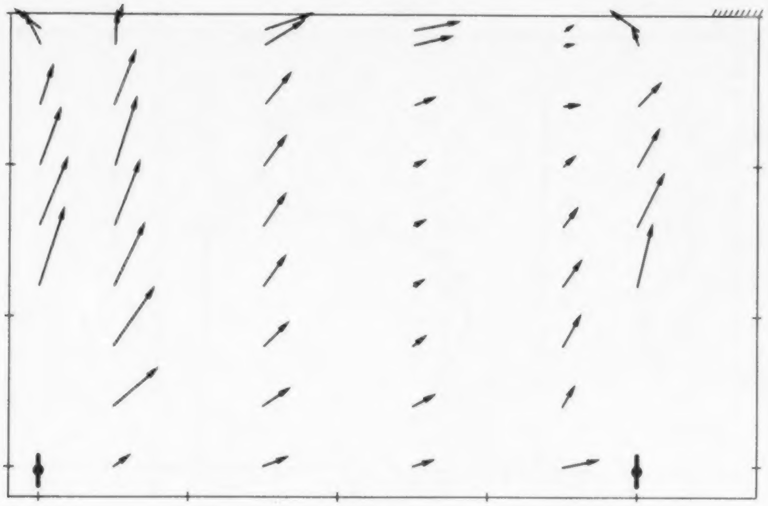

Figure 5.7 Velocity vectors and turbulence intensity in horizontal plane between 2nd and 3rd electrode.
Type C_t, f_E = 2.23, U_o = 0.5 m/s, z = 300 mm.

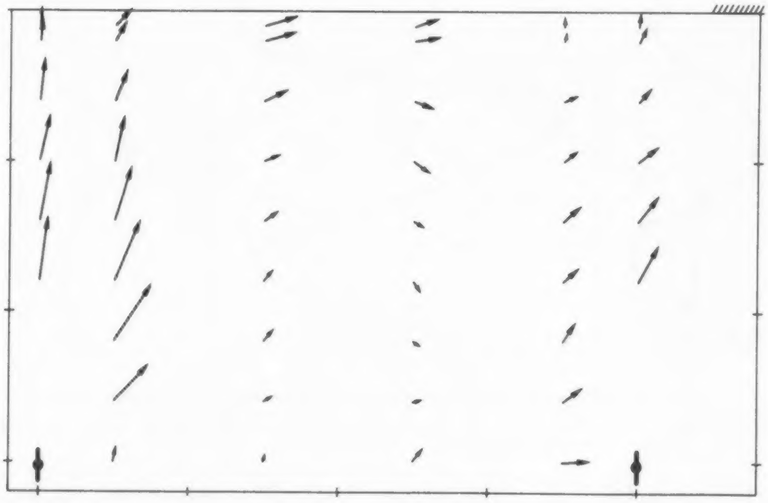

Figure 5.8 Velocity vectors and turbulence intensity in horizontal plane between 2nd and 3rd electrode.
Type C_t, f_E = 58 , U_o = 0.1 m/s, z = 300 mm.

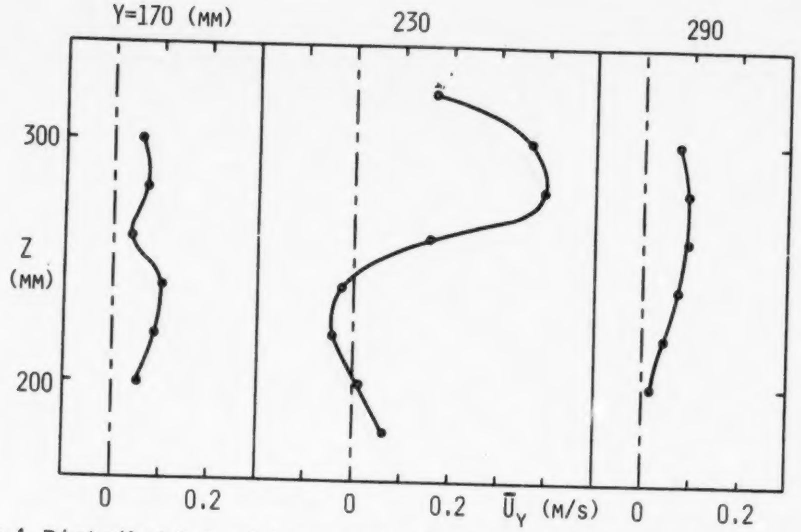

Figure 6.1 Distribution of transversal velocity component $\bar{u}_y$ in three vertical planes, y = 170, 230 and 290 mm at x = 575 mm. U_o = 1.0 m/s, Type A electrode.

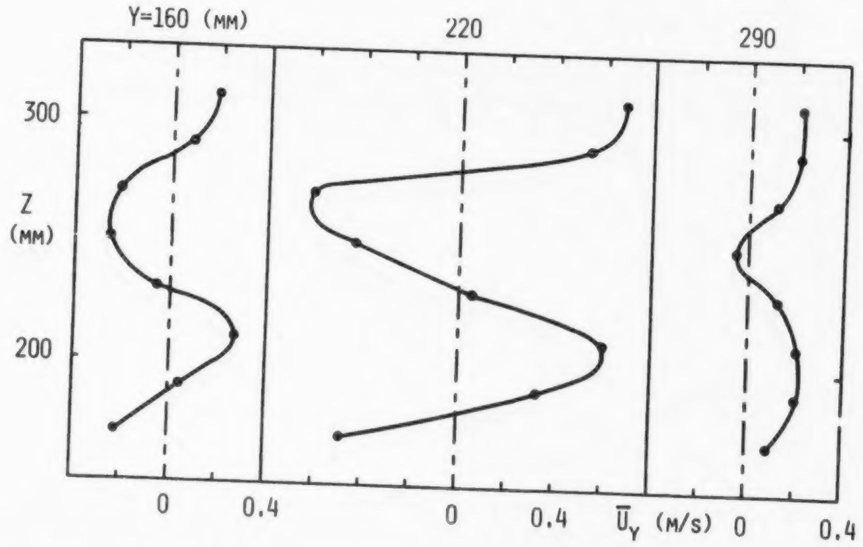

Figure 6.2 Distribution of transversal velocity component $\bar{u}_y$ in three vertical planes, y = 160, 220 and 290 mm at x = 575 mm. U_o = 1.0 m/s, Type C_a electrode.

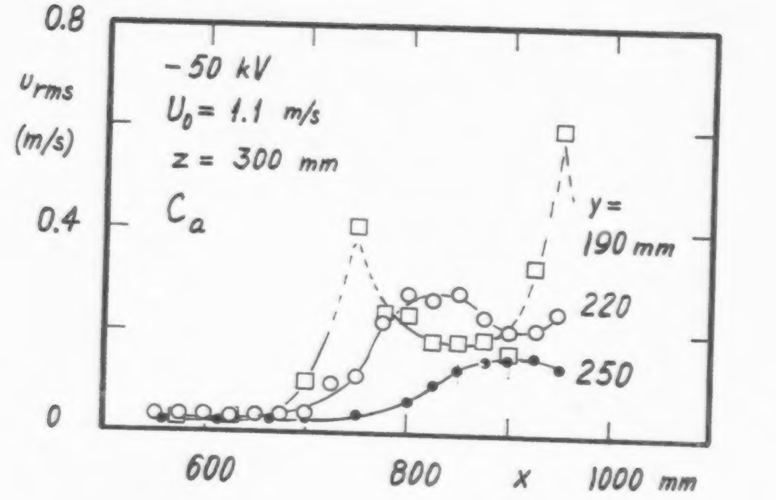

Figure 7. $u_{x,rms}$ versus x at y = 190, 220 and 250 mm. Type C_a electrodes at x = 750 and 950 mm.

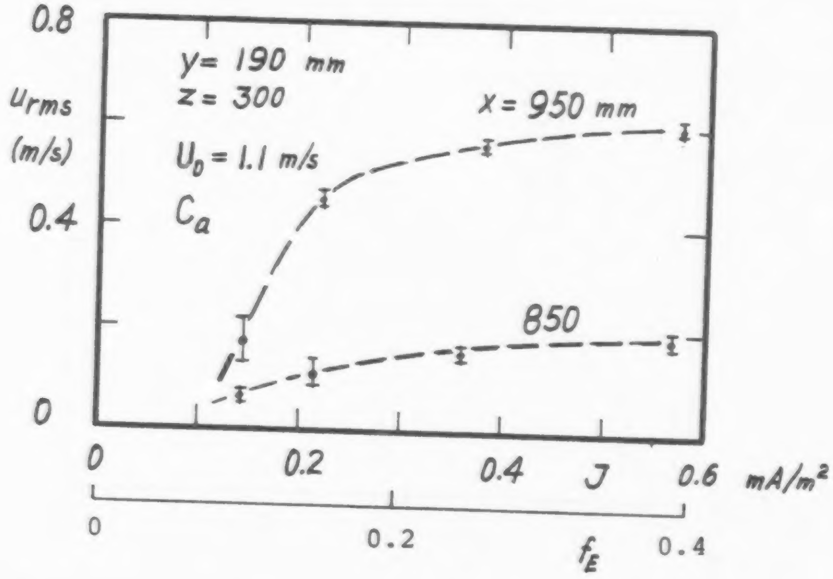

Figure 8. $u_{x,rms}$ versus $f_E = (J'/b)/(\rho U_o^2)$ at two points between first and second electrode, Type C_a.

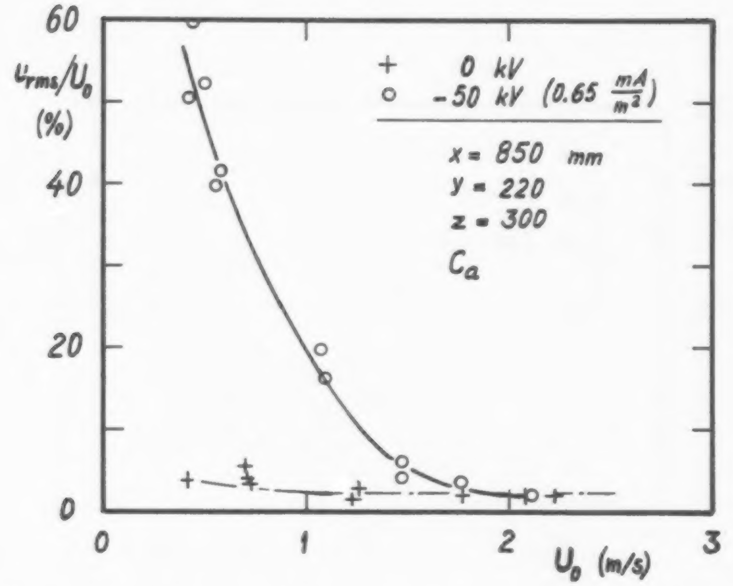

Figure 9. Turbulence intensity $u_{x,rms}/U_o$ versus U_o with and without electrical field at point between first and second electrode, Type C_a.

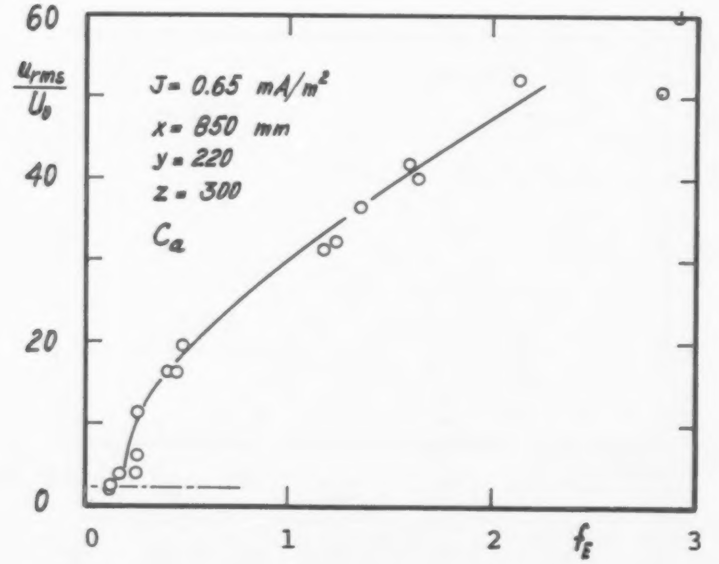

Figure 10. Turbulence intensity versus $f_E = (J'/b)/(\rho U_o^2)$ (data of Figure 9.)

THE EFFECT OF TURBULENCE ON ELECTROSTATIC PRECIPITATOR PERFORMANCE

D. E. Stock
Department of Mechanical Engineering
Washington State University
Pullman, WA 99164 - 2920

ABSTRACT

The turbulent character of the gas flow found in an electrostatic precipitator (ESP) affects the motion of the particles (dust) and, therefore, the unit's performance through two mechanisms. The mean velocity profile found in an ESP conveys the particles both longitudinally through the precipitator and in the transverse direction. Particle motion is also strongly affected by turbulent diffusion. The magnitude of the turbulent diffusion is expressed through a particle turbulent diffusivity which depends on the turbulent character of the gas, particle size, and the crossing trajectories effect.

A particle diffusion equation is developed and the coupling with the gas flow field and electric field is discussed. Finally, techniques for estimating the particle diffusivity are presented.

The work described in this paper was not funded by the U. S. Environmental Protection Agency and therefore the contents do not necessarily reflect the views of the Agency and no official endorsement should be inferred.

INTRODUCTION

An ESP is an extremely complex mechanical system. Beyond the complexity of the physical unit with its requirements for correct plate and wire spacing, for minimum gas leakage around the plates, and for controlled rapping; the physical phenomena controlling the particle motion is a coupled system which is difficult to model. The particle motion depends on the interaction between particles, electric field, and the turbulent gas flow field.

When trying to understand and to predict the operation of such a complex system, one would like to isolate the various phenomena and then carry out some form of parametric study on each variable separately. The success of this technique strongly depends on the insight of the modeler.

The Deutsch Equation [1], developed in 1922 and widely used to scale ESP until a few years ago, is an example of a model which did not include all the physical phenomena. It neglects the change in space charge and assumes infinite mixing. The use of this equation has limited the investigation of the importance of turbulent mixing and wide plate spacing. Only recently have these topics started to attract interest. In this paper the equations governing particle motion is presented along with a discussion of coupling between the electric field, the gas flow field, and the diffusion coefficient for the particles.

BACKGROUND

Considering the flow in a wire and plate precipitator to be two-dimensional and treating the particles as a dilute, continuous phase, we can write the differential equation for particle continuity as

$$\frac{\partial}{\partial x}(U_pC) + \frac{\partial}{\partial y}(V_pC) = 0 \qquad (1)$$

where both the particle velocity, U_p and V_p, and particle concentration are instantaneous values which depend on both location and time. If the equation is time-averaged, we obtain

$$\frac{\partial \overline{U}_p\overline{C}}{\partial x} + \frac{\partial}{\partial y}(\overline{V}_p\overline{C}) + \frac{\partial}{\partial x}(\overline{U'_pC'}) + \frac{\partial}{\partial y}(\overline{V'_pC'}) = 0 \qquad (2)$$

Now, assuming the longitudinal time-averaged particle velocity is equal to the gas velocity $\overline{U}$, and transverse particle velocity is equal to the sum of the gas velocity, $\overline{V}$, and the particle velocity relative to the gas due to the electrostatic forces on the particle, $\overline{W}$, we can write

$$\frac{\partial(\overline{UC})}{\partial x} + \frac{\partial}{\partial y}(\overline{VC}) + \frac{\partial}{\partial y}(\overline{WC}) = -\frac{\partial}{\partial x}(\overline{U'_pC'}) - \frac{\partial}{\partial y}(\overline{V'_pC'}) = 0 \qquad (3)$$

Using the gas phase continuity equation for incompressible flow

$$\frac{\partial\overline{U}}{\partial x} + \frac{\partial\overline{V}}{\partial y} = 0 \qquad (4)$$

gives

$$\overline{U}\,\frac{\partial \overline{C}}{\partial x} + \overline{v}\,\frac{\partial \overline{C}}{\partial y} + \overline{w}\,\frac{\partial \overline{C}}{\partial y} + \overline{C}\,\frac{\partial \overline{w}}{\partial y} = -\frac{\partial}{\partial x}(\overline{U'_pC'}) - \frac{\partial}{\partial y}(\overline{V'_pC'}). \tag{5}$$

For a simple velocity field, the two velocity–concentration correlation terms on the right hand side can be modeled with the Boussinesq approximation, Fick's Law gradient diffusion model, to give

$$\overline{U}\,\frac{\partial \overline{C}}{\partial x} + \overline{V}\,\frac{\partial \overline{C}}{\partial y} + \overline{W}\,\frac{\partial \overline{C}}{\partial y} + \overline{C}\,\frac{\partial W}{\partial y} = +\frac{\partial}{\partial x}D\,\frac{\partial \overline{C}}{\partial x} + \frac{\partial}{\partial y}D\,\frac{\partial \overline{C}}{\partial y} \tag{6}$$

Now, neglecting changes in the particle diffusion coefficient, D, neglecting gradient in the migration velocity, W, and agreeing all symbols stand for average values, we get

$$U\,\frac{\partial C}{\partial x} + V\,\frac{\partial C}{\partial y} + W\,\frac{\partial C}{\partial y} = D\,\frac{\partial^2 C}{\partial x^2} + D\,\frac{\partial^2 C}{\partial y^2} \tag{7}$$

Boundary conditions suitable for an electrostatic precipitator include assuming no net transverse mass flux at the centerline,

$$D\,\frac{\partial C}{\partial y} - WC = 0 \text{ at the centerline} \tag{8}$$

and assuming that very near the collecting wall turbulent dispersion effects on the particle vanish giving

$$\frac{\partial C}{\partial y} = 0 \quad \text{at the wall.} \tag{9}$$

The boundary condition at the wall assumes that in the viscous sublayer near the wall, the particle velocity due to electrostatic force dominates all other forces acting on the particle. In the absence of the electric field, this boundary condition could no longer be used. Under such conditions, particle stopping distance in the sublayer must be considered.

Two assumptions used in developing equation (7) need to be examined in more detail. Modeling the concentration-velocity correlation with Fick's Laws assumes that particle dispersion is governed by a single characteristic length scale and a single turbulent velocity scale [2]. These assumptions are met for a smooth wall precipitator with a well-controlled inlet. Gradient diffusion is often used for more complex geometries since the more correct model, 2nd order turbulence model [3], is much more complex to develop. The validity of the second assumption, neglecting the gradient in the migration velocity, depends on the gradient in the electric field normal to the plate and on the gradient of the concentration profile normal to the plate. Large particle concentration gradients toward the wall would cause the electric field to increase slightly and the migration velocity and particle concentration to increase. Under such conditions, this term could be important. We have neglected this term in past work, but will investigate its importance in future studies.

Many of the past studies [4,5,6] have assumed uniform longitudinal velocity, U, constant migration velocity, W, and constant particle diffusion coefficient, D. Using these assumptions, insight into the operation of ESP has been obtained, but also some important aspects have been neglected.

MODELING COUPLING

To use equation (7), the gas velocity must be known and the motion of the particle due to the electric field must also be known. We assume the particle velocity due to the electric field is equal to the equilibrium velocity attained by a particle charged to saturation in a field equal to the local field. This is given by

$$W = \frac{E_c E_p d \varepsilon_o}{\mu} . \tag{10}$$

where E_c is the charging field and E_p is the local field. Since particle history is unknown E_c is set equal to E_p. The justification for assuming local equilibrium and for neglecting forces other than drag on the particles is given by Eschbach [7].

To use equation (10) the local electric field must be determined. We assume the field is uniform except for the influence of the particle space charge. The details of the modeling of the electric field are given by Eschbach and Stock [8].

MEAN GAS FLOW EFFECTS

The diffusion equation (7), which governs particle concentration, requires the gas phase mean velocity, U and V, to be specified. Most of the simpler numerical models [4,6,8] assume the axial velocity is uniform in the transverse direction and constant in the axial direction. This simplification allows major trends to studies. More complete, and therefore complex, models [9] take into account variation in the U and V velocity, but often provide more information than can be easily assimilated.

In the initial region of the channel formed by two plates the velocity profile goes through a development stage from a near uniform profile to a rounded profile typical of low Reynolds number turbulent flow. This development occurs over the initial half of the stage with its length and flow character depending on the initial velocity profile and turbulence characteristic. Given the initial conditions, numerical codes can predict the flow field development. Measurements need to be made at the inlet plane of full scale precipitators to determine velocity profile, turbulence level and length scale. In the initial region, the transverse gas velocity is toward the centerline with typical velocities of 2% of the mean flow but 50% of the particle migration velocity, W. The effect of the transverse gas velocity must be evaluated for a particular installation.

Most ESP are built with some form of baffles or stiffeners. These stiffeners can greatly change the gas flow field. We have modeled one particular geometry [10]. Figures 1-4 show the concentration profiles for the geometry given in Table 1. Figure 1 shows how the smooth plate configuration is more efficient than one with stiffeners. It is also interesting to find that the stiffeners cause the concentration to decay in an exponential manner which explains why many commercial ESP's follow the trend given by the Deutsch Equation [1] with a modified particle migration velocity. Figures 2-4 show the transverse concentration profile. The stiffeners make the concentration more nearly uniform. The shape and magnitude of concentration profile would probably change with changes in the turbulence of the gas flow.

TURBULENT GAS FLOW EFFECTS

The turbulent characteristics of the gas flow affect particle motion through its influence on mean flow as discussed above and through the affect of turbulent dispersion. Turbulent dispersion enters the diffusion equation (7) through the particle diffusion coefficient, D . The diffusion coefficient enters the equation when the gradient diffusion assumption is made. In simple flow fields where only one length scale and velocity scale exist, this assumption is known to work well. Grid generated turbulent flow in a wind tunnel is one case where gradient diffusion can be used. In a well-conditioned tunnel, the flow is isotropic and decays in turbulent intensity as the flow moves through the tunnel. A smooth wall ESP with a well-conditioned inlet as found in the last stage of a multiple stage precipitator comes close to meeting these requirements except the passage is not square.

Particle dispersion is determined by the gas phase turbulence, the particle inertia, and by the crossing trajectory effect. The crossing trajectory effect [11] refers to a particle which has a velocity relative to the fluid phase (due to gravity or electric field) and moves from one eddy to another at a rate faster than the average eddy decay rate. Therefore, particles with a drift velocity lose velocity correlation faster than a fluid point and diffuse less than a particle which follows the flow. Wells [12] built a wind tunnel which, through the use of an electric field, could control the drift velocity of charged particles. He measured the particle drift velocity and mean squared dispersion with a laser Doppler anemometer for two particle sizes, 5μm and 57μm, glass beads. Figure 5 shows the particle dispersion coeffients measured in this study. Dispersion is seen to depend only on the drift velocity, not on particle size. With no drift velocity both particles have the same diffusion as a fluid point. These measurements were taken in a 35 x 35 cm tunnel with a 2.5 cm grid. Measurements were taken between .5 and 2.2 m from the grid with a gas velocity of 6.5 m/s. The gas turbulence intensity fell from 4% to 1.5% in the test section. These results support the work by Csanady [13] where the effect of crossing trajectories is given by

$$\frac{D_p}{D_f} = \left[1 + \frac{4\beta^2 V_t^2}{U'^2} \right]^{-\frac{1}{2}}$$

where β is a parameter describing the relationship between the Lagrangian and Eulerian integral scales and $\sqrt{U'^2}$ is the gas RMS velocity and V_t is the particle drift velocity. This relation shows that crossing trajectories will become important when the particle drift velocity is comparable to the gas RMS velocity. For an ESP with typical drift velocities of 8 cm/s and mean gas velocities of 2 m/s at turbulence levels above 4% crossing trajectories effects can probably be neglected and the particle diffusion coefficient assumed equal to the gas turbulent diffusivity. For lower turbulence levels, as might be found in the last few stages of a smooth wall ESP, crossing trajectories effects would reduce the particle diffusion coefficient below that of the gas and result in higher collection efficiencies than expected.

SUMMARY AND DISCUSSION

Numerical models can be used to help understand ESP operation, but the models must include the important physical phenomena. The turbulent character of the gas flow is one such physical phenomena. If we know the physical geometry of the precipitator and the velocity and turbulence distribution of the gas entering each stage of a precipitator, then the mean gas flow and gas turbulent diffusivity can be calculated [14]. Using these results in the particle continuity equation (7), the concentration and efficiency can be calculated. If only small particles are considered, then the particle diffusion coefficient can be set equal to the gas diffusion coefficient except for modification to account for the crossing trajectories effect. Considering only particle collection on the plates, reducing the turbulence level and using smooth walls will improve collection efficiency.

REFERENCES

1. Deutsch, W., Bewegung und Ladung der Eteletrizitatstrager. Annalen der Physik, IV, Folge 68, pp.335-344, 1922.
2. Tennekes, H. and Lumley, J.T., A First Course in Turbulence, MIT Press, 1972.
3. Lumley, J.T., Computational modeling of turbulent flows. in Advances in Applied Mechanics, Vol.18, Academic Press, pp.124-176, 1978.
4. Williams, J.C. and Jackson, R., The motion of solid particles in an electrostatic precipitator. Proceedings of the Symposium on Interaction of Fluids and Particles, Institute of Chemical Engineering, pp.282-288, 1962.
5. Feldman, P.L., Kumar, K.S. and Cooperman, G.P., Turbulent diffusion in electrostatic precipitators. AIChE, Symposium Series, Atmospheric Emissions and Energy Source Pollution, Vol.73, No.1651, pp.120-130, 1977.
6. Leonard, G.L. Mitchner, M. and Self, S.A., Particle transport in electrostic precipitators, Atmospheric Environment, Vol.14, No.11, pp.1289-1299.
7. Eschbach, E.J., Numerical prediction of electrostatic precipitator performance, M.S. Thesis, Washington State University, 1982.

8. Eschbach, E.J. and Stock, D.E., Optimization of collection efficiency by varying plate spacing within an electrostatic precipitator. Environmental Inter., Vol.6, pp.177-180, 1981.

9. Stock, D.E. and Crowe, C.T., The effect of electrodynamic secondary flow on the performance of electrostatic precipitators, Proceedings, 1974 Heat Transfer and Fluid Mechanics Institute, Stanford University Press, 1974.

10. Stock, D.E. and Eschbach, E.J., "Prediction of electrostatic precipitator performance, Proceedings, Gas Bourne Particles, C76/81 Institute of Mechanical Engineering, London, 1981.

11. Yudine, M.I., 'Physical considerations on heavy-particle diffusion, Advances in Geology, Vol.6, Academic Press, 1959, pp.185-191.

12. Wells, M.R., The effects of crossing trajectories on the diffusion of particles in a turbulent fluid, Ph.D. dissertation, Washington State University, 1982.

13. Csanady, G.T., Turbulent diffusion of heavy particles in the atmosphere, Journal of Atmospheric Science, Vo.20, 1963, pp.201-108.

14. Barriga, A.N., Effect of protruding normal dividers on the turbulent flow between plane boundaries, Ph.D. Dissertation, Washington State University, 1978.

Table 1

Operating Conditions

Wire to Plate Spacing	0.10 m
Stiffener Height	.028 m
Distance between Stiffeners	0.40 m
Inlet Gas Velocity	.28 m/sec
Inlet Particle Concentration	4.57×10^{-2} kg/m³
Applied Potential	8×10^{4} volts
Particle Diameter	2×10^{-6}m

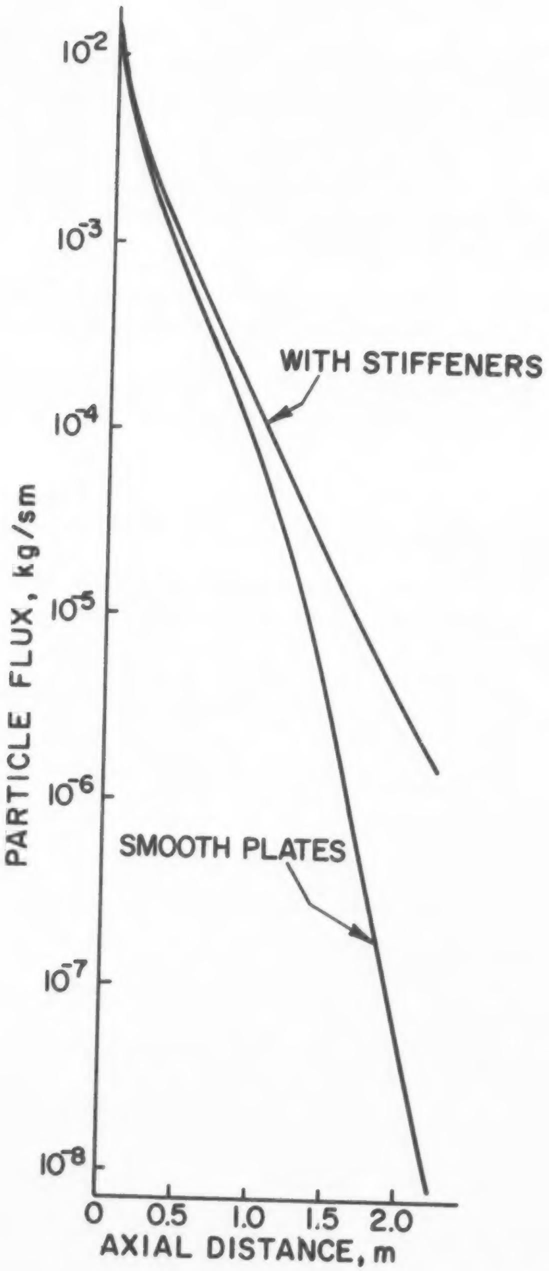

Figure 1. Net particle flux at various longitudinal locations

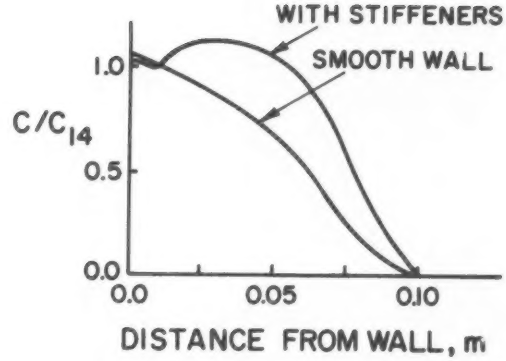

Figure 2. Concentration at .375 m from inlet normalized by concentration at node 14

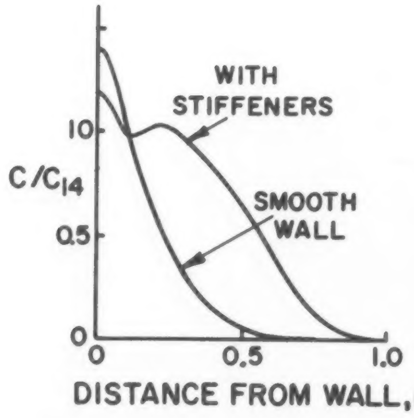

Figure 3. Concentration at 1.175 m from inlet normalized by concentration at node 14

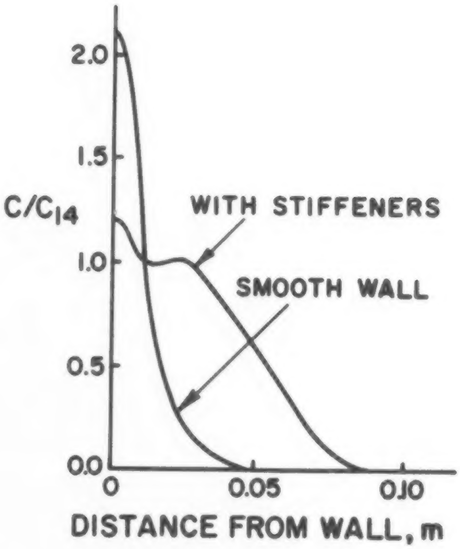

Figure 4. Concentration at 1.975 m from inlet normalized by concentration at node 14

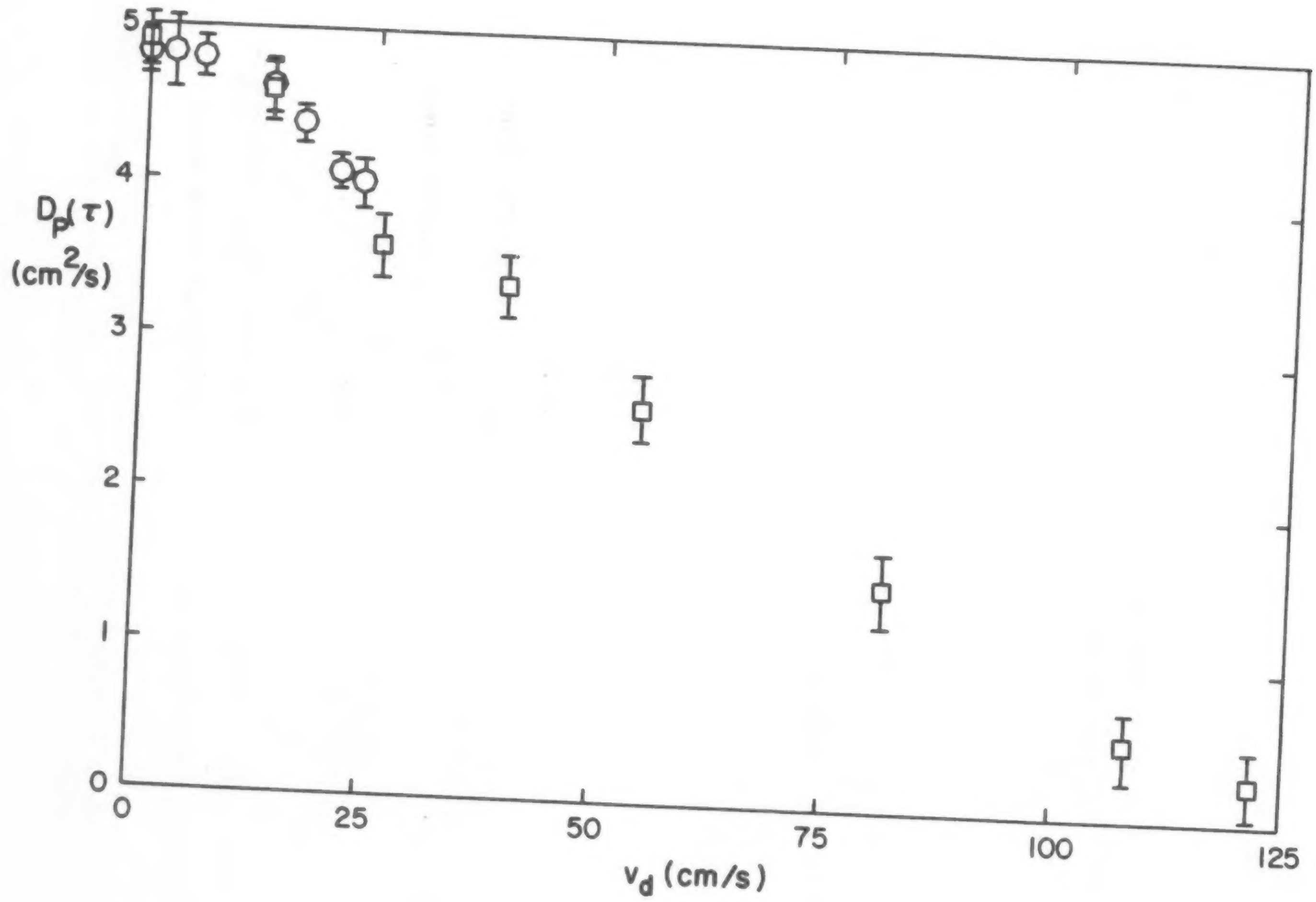

Figure 5. Particle dispersion coefficients from $\overline{Y}^2$ measurements.
, 57 µm particles; , 5 µm particles.

FACTORS LEADING TO ELECTRICAL BREAKDOWN OF RESISTIVE DUST LAYERS AND SUSTAINED BACK CORONA

By: Phil A. Lawless
Research Triangle Institute
P. O. Box 12194
Research Triangle Park, North Carolina 27709

Leslie E. Sparks
Industrial Environmental Research Laboratory
U. S. Environmental Protection Agency
Research Triangle Park, North Carolina 27711

ABSTRACT

Recent theoretical work modeling the resistive dust layer has shown considerable enhancement of the electric field at the points of contact between particles. These theories are examined with regard to evaluating the conditions leading to electrical breakdown and sustained back corona discharge via the Townsend avalanche mechanism. Among other factors, the particle size distribution is shown to have a significant effect on the internal field in the layer. The resulting breakdown characteristics of the resistive layer can be used to obtain the proper operating current density for the precipitator and to evaluate the effects on collection of excursions into the back corona regime.

This paper has been reviewed in accordance with the U. S. Environmental Protection Agency's peer and administrative review policies and approved for presentation and publication.

INTRODUCTION

Back corona is an electrical breakdown of a resistive dust layer which results in the injection of ions (of the polarity opposite to that from the "charging" electrode) into the gas space of a precipitator. The presence of ions of both polarities leads to a reduction of charge on the suspended particles and to a lowering of the operating voltage of the precipitator. Both effects are deleterious to collection performance, with the severity of degradation in proportion to the resistivity of the material.(1)

The problem of determining the effects of back corona has two basic parts: describing the conditions which lead to breakdown of the dust layer and evaluation of the effects of back corona on particle charge and operating voltage. An earlier paper (2) described the sustained breakdown, and methods for calculating the effects on particle charge and operating voltage are available.(3) This work is aimed at improving the estimation of layer breakdown conditions and extending the calculation of degradation effects to more realistic conditions than previously described.

The previous model of back corona discharge (2), called the "pore breakdown model," assumed that the electric field existing in a resistive dust layer could sustain a continuous generation of ions in pores in the layer by means of the Townsend avalanche mechanism. The resistivity of the layer was assumed to be uniform and ohmic in character, and, based on those assumptions, the values of the electric field in the dust required to sustain back corona were several times higher than experienced in practice. The equation relating electric field, E; current density, j; and resistivity, ρ; is:

$$E = j\rho. \tag{1}$$

The interaction of the ions, the electric field in the layer, and the electric field in the pore is shown in Figure 1.

In recent years, research on the nature of conduction paths in particle layers (4,5,6,7) has emphasized the local enhancement of electric fields at the points of contact between particles. The results of these investigations show that all phenomena which depend on electric field in nonlinear fashions will have very different behavior in a particulate layer from a homogeneous layer. Since the Townsend avalanche mechanism is a highly nonlinear function of the electric field, the particulate nature of fly ash layers is expected to play a very important role in the pore breakdown model.

TOWNSEND GAS DISCHARGE IN A PORE

The Townsend avalanche ionization of a gas is a process caused by free electrons.(8) Because electrons are so much less massive than gas molecules, they lose very little energy in collisions with them. In the presence of an electric field, electrons may gain more energy between collisions than is lost during collisions. If the electrons gain sufficient energy, there is a definite probability for ionizing a gas molecule during a collision. When ionization occurs, two electrons (the original one and the ionized one)

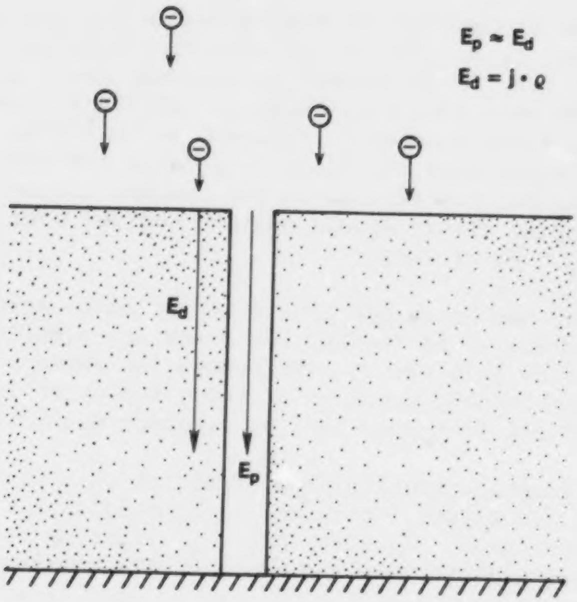

Figure 1. Evaluation of electric field, E_p, in a pore.

are available for further ionizing collisions. In this way, a single free electron can produce a population of several million in a distance of a few millimeters. The number of new electrons created by a single electron traversing a 1-cm path is called the first Townsend coefficient, α.

A factor opposing the growth of the free electron population is electron attachment, a process by which a free electron and a molecule form a stable negative ion, incapable of further ionization. The attachment coefficient, η, is the average number of free electrons forming negative ions in 1 cm of travel.

Because of the rapid growth of the number of free electrons, the total gain of electrons, G, is an exponential function of the distance, x, over which the avalanche occurs:

$$G = \frac{\alpha \exp[(\alpha - \eta)x] - \eta}{\alpha - \eta} . \qquad (2)$$

Both α and η depend on the value of electric field moving the electrons. When the "effective Townsend coefficient," $\alpha - \eta$, is negative, no multiplication can occur. When $\alpha - \eta$ is positive, the avalanche will proceed. For air at standard conditions, α and η are equal at an electric field of 24 kV/cm.

As indicated by Equation 2, a given value for the gain can be achieved over any distance, x, as long as the effective Townsend coefficient is large enough. This is true for distances larger than about 10 μm, but below that length (about 100 mean free path lengths), the finite probability the electron has for ionizing a given molecule reduces the effective Townsend coefficient and requires a higher electric field to produce the same gain. This phenomenon is the basis for the minimum in the Paschen discharge curve.(8) As a result, the Townsend theory should only be applied over macroscopic distances of the order of 10 μm or larger.

The Townsend mechanism can provide an enormous multiplication from a single electron; but if no further electrons are supplied, only a single burst of ionization will occur. Continuous ionization, such as called for in the pore breakdown model, requires a steady supply of initiating electrons. These must originate from some sort of feedback mechanism.

The usual feedback mechanisms operational in a corona discharge are photoionization and impact ionization. Photoionization occurs because some of the free electrons or negative ions may recombine with positive ions, releasing high energy photons in the process. The photons travel in all directions and may ionize neutral molecules to provide a new source of electrons. Only those photons which travel upstream of the electron flow direction will be useful in renewing the ionization process, although all photons will contribute to the total ionization. Impact ionization occurs when the positive ions gain enough kinetic energy from the electric field to cause emission of secondary electrons from any surface they may strike. Impact ionization is only effective for renewing a negative avalanche, one in which the electrons move away from the surface (e.g., a negative corona wire).

Masuda (9) has suggested that a third mechanism, negative ion detachment, may be responsible for providing the free electrons in a dust layer. In this mechanism, the presence of the large electric fields near the dust pore destabilizes approaching negative ions, liberating an electron from each one. Within the confines of a dust pore, it is reasonable to expect contributions from all these sources.

If the fraction of electrons (or ions) in the avalanche which are effective in renewing the process is denoted by γ, the gain equation is modified to become:

$$G = \frac{\exp[(\alpha - \eta)x]}{1 - \gamma\{\exp[(\alpha - \eta)x] - 1\}} . \qquad (3)$$

As the feedback factor, γ, approaches 1, the value of $(\alpha - \eta)$ needed for a given gain decreases. This can lead to a significant reduction in the value of electric field required to maintain the ionization, but in no case can the field decrease below the value for which $(\alpha - \eta) = 0$. A plot of the effect of feedback on the electric field required to produce a gain of 10^8 is shown in Figure 2. The gain of 10^8 is chosen because of estimates that there are about 10^8 ions in a corona Trichel pulse.(8)

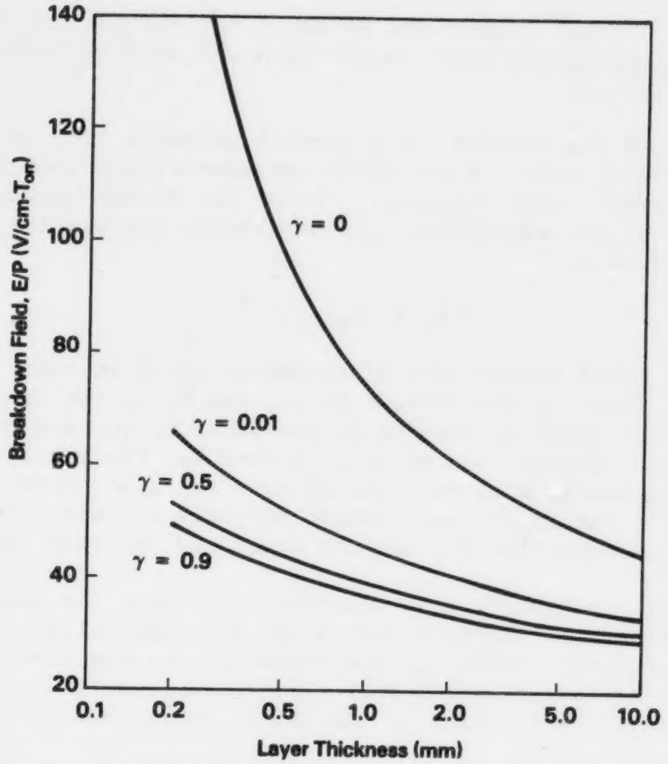

Figure 2. Breakdown field as a function of layer thickness for various feedback factors.

When negative corona is used in a precipitator, the positive ions produced by back corona can emerge from the dust layer at a high enough density to form a streamer. A streamer is a self-propagating Townsend avalanche that advances by photoionization. Streamers can lead to sparks by creating an ionized channel between the corona electrode and ground plate. Streamers also can charge dust particles positive to a significant degree, resulting in their moving away from the collecting plate.(9)

Because streamer formation is a positive ion phenomenon, it cannot occur as a manifestation of back corona with positive corona. Also, because there is a certain density of positive ions required to achieve the high local electric fields, low current density back corona does not form streamers. High resistivity materials reach breakdown conditions at low current densities and fall into this category. The remainder of this investigation is concerned with only low current density back corona, without the formation of positive streamers.

PARTICLE SIZE DISTRIBUTION EFFECTS

Theories of the conduction of electric currents through an array of spherical particles all assume that there is a very strong constriction of the current at the points of contact between spheres.(4,5,6,7) In order to maintain the same current through all parts of the sphere, the electric field in the contact region must be much larger than the average field over the diameter of the sphere.

The presence of the intense field greatly enhances the cohesiveness of the particulate layer, modifies its field dependence, and produces a resistivity which is mildly field dependent. Using the theory developed by Dietz (6) because of its simplicity, the expression for the resistivity, ρ, of a layer of spheres is:

$$\rho = \rho_s R (E_m/E_o)^{0.2}, \tag{4}$$

where ρ_s is the surface resistivity of the material, R is the radius of the sphere, E_m is the field at the contact point, and E_o is the average applied field. Although the model is derived on the basis of surface resistivity alone, monodisperse spheres, and an undetermined E_m, the trends indicated in Equation 3 do hold fairly well for precipitated fly ash. More complex theoretical results (7) modify the dependences slightly and distinguish between volume and surface conduction but are not necessary for this work.

The principal conclusions from Equation 4 are that the effective resistivity is proportional to particle radius and decreases slightly with applied field. The former result indicates the potential for size-dependent effects in a polydisperse mixture of particles. The latter result should be used to correct the effective resistivity to conditions other than those under which it was measured.

There is some experimental evidence for this size dependence. Figure 3 shows the size-dependent resistivity of glass spheres (10), for several conditions of temperature and humidity, and resistivity measurements on fly ash classified into narrow size ranges.(11) Both plots are consistent with the linear dependence of resistivity on particle diameter indicated by Equation 4.

Evaluating the effects of size distribution on the Townsend avalanche is done by comparing a uniform average field producing a certain gain with the average field producing the same gain with a nonuniform set of field values. This situation is illustrated in Figure 4, showing the effect of including a single large particle in an otherwise monodisperse array.

The average field in both arrays is determined by the current flowing down each chain of particles. For the monodisperse chain, it is uniform from particle to particle (but not along the surface of each particle). For the second chain, the same current must flow through the large particle as through the smaller ones, leading to a higher field across it because of its higher effective resistivity (Equation 4). This region of higher electric field enhances the gain for two reasons: $(\alpha - \eta)$ increases with field strength, and the increased multiplication is effective over a larger than normal distance. Because of the local field enhancement, the polydisperse particle chain can produce the same total gain at a lower average field than the monodisperse chain.

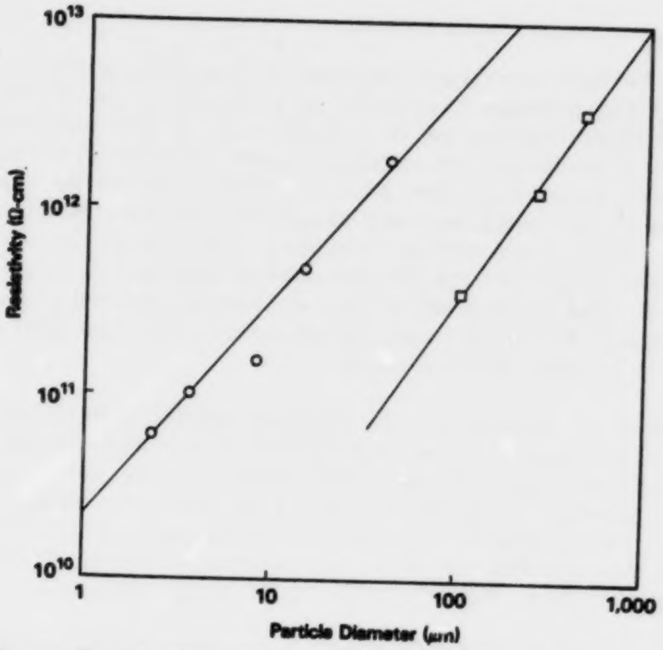

Figure 3. Resistivity variation with particle diameter (○ - Reference 3; □ - Reference 4).

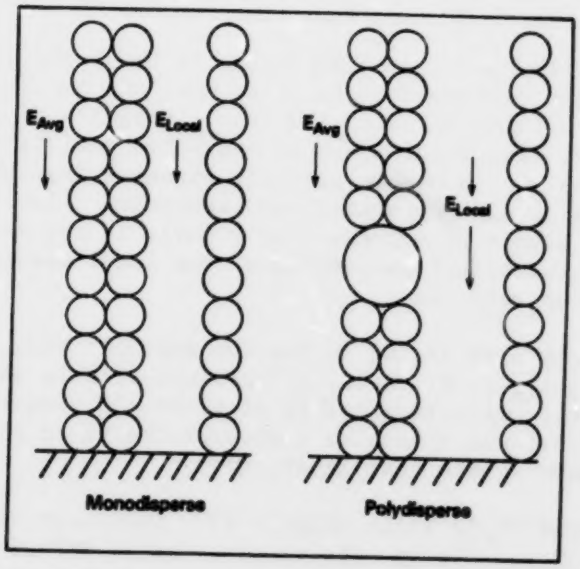
E_Avg
E_Local
E_Avg
E_Local
Monodisperse
Polydisperse

Figure 4. Effect of polydispersity on local field.

Two limiting factors have been assumed in evaluating this model. The first is that only the average field across a particle can be effective in maintaining the Townsend discharge in a pore next to the particle. Even though the electric fields in the contact region between particles may be orders of magnitude larger than the average value, the close separation of the particles effectively encloses any electrons and leaves room for few ionizing collisions. Thus, even though ionization may occur in the gap, it is not capable of sustaining the discharges characteristic of back corona. Some of the initial free electrons may come from microdischarges in the gaps, but unless the average field is high enough to sustain the avalanche, the ionization will not produce back corona.

The other limit is imposed on the maximum enhancement that can be associated with a large particle. Because Equation 3 was derived on the assumption of only one contact area in each hemisphere of the particle, it cannot be expected to be correct if there are multiple contact points. Multiple contacts are the norm in a randomly packed polydisperse layer. Therefore, a limiting function was invoked to keep the maximum electric field to some multiple of the average field, and the effects of this limitation were tested.

The previously used values for α and η (2) were fitted graphically, resulting in the following power law expressions for $\alpha - \eta$:

$$(\alpha - \eta)/P = B\ (E/P - 31.3)^{C}, \tag{5}$$

where: $B = C = 0$, $(E/P < 31.3)$;
$B = 7.47 \cdot 10^{-4}$, $C = 1.30$, $(31.3 \leqslant E/P < 39.6)$;
$B = 2.54 \cdot 10^{-4}$, $C = 1.81$, $(39.6 \leqslant E/P)$;

E is the electric field (V/cm); and P is the pressure (torr).

For the size distribution of particles in the layer, lognormal parameters were used: the mass median diameter, MMD; and the geometric standard deviation, σ. With lognormal distributions, integrals of power law expressions over the size distribution can be evaluated analytically. This is useful for finding the most probable particle diameter from the MMD, but the nature of Equations 2 and 5 prevents easy analysis. Also, the limitation on the maximum field cannot be expressed as a power in the particle diameter. For these reasons, numerical evaluation of the local electric fields and equivalent gains was required.

Four parameters were varied in the evaluation: MMD, σ, E/P, and the upper field limit, E_{max}. Of these, E/P produced little change in the enhancement of the electric field from values of 40 to 400 V/cm-torr; therefore, a value of 90 V/cm-torr was chosen to represent the field that might be expected to break down a thin dust layer.(2)

Since the upper field limit plays a very important role in determining the enhancement, Figure 5 shows the results for an MMD of 10 μm and a σ of 3. It is evident that the enhancement grows less rapidly than the maximum field. This is due to the nature of the size distribution: the higher

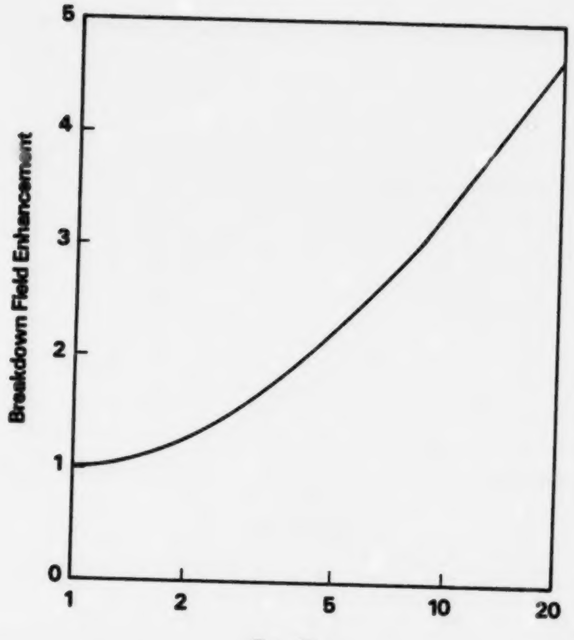

Figure 5. Effect of maximum local field on enhancement.

local fields are associated with larger particles, but the number of large particles decreases rapidly for sizes larger than the MMD.

For examining the remaining relationships, the maximum field was set to a value 5 times the average field, yielding an enhancement of about 2 at this MMD and σ. This choice may seem large, but it yields observable variations in the effects of the other parameters. From considerations of geometry, it can be taken as an upper limit on the local field.

On the basis of the model assumptions, the enhancement should not depend on the MMD of the dust layer (although the resistivity does, Equation 4). The reason for this expectation is that the calculation of the average field is based upon a monodisperse layer of particles having the diameter most likely to be found in the polydisperse layer; and the most probable diameter is always in a fixed ratio to the MMD in a lognormal distribution.

The numeric integration must use definite limits for its upper and lower bounds; as a result, if the most probable diameter approaches those boundaries, significant amounts of the enhancement contribution may be ignored. This is borne out in Figure 6, where significant changes begin to occur for MMDs greater than 20 percent of the largest size in the integration, 50 µm. Therefore, the original expectation of particle size independence is realistic.

The variation of geometric standard deviation would be expected to have effects on the enhancement for the same reason that MMD variations should not: the most probable diameter changes its relationship to the MMD when

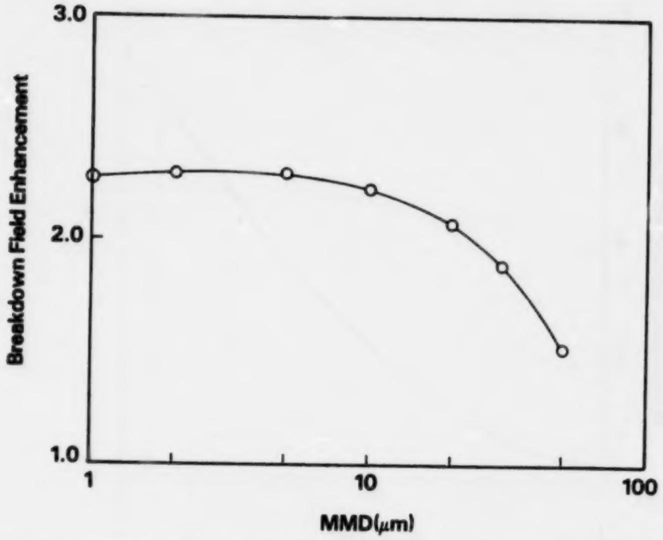

Figure 6. Effect of mass median diameter on enhancement.

σ is varied. When σ is 1, the particles are monodisperse, with the most probable diameter and MMD coincident. As σ increases, the most probable diameter decreases in relation to the MMD. As in the case with the MMD, the particle size distribution may spread so much that the finite limits of integration affect the enhancement.

Figure 7 shows the trend of enhancement with σ over the range from 1 (monodisperse) to 5 (very polydisperse). The relationship can be described as approximately linear, with much of the curvature caused by the numerical methods used.

The conclusions drawn from this application of particle-contact theories to the pore breakdown process are as follow. Field inhomogeneities around large particles may enhance the local electric field to the degree that breakdown into sustained back corona is possible for average fields 2 to 5 times smaller than for homogeneous layers. The actual reduction depends very strongly on the maximum value of local field that can be attained in relation to the average field. The reduction also depends strongly on the geometric standard deviation of the particle size distribution, but not on its MMD.

In practice, if a fly ash with σ = 3 is well distributed in a precipitator, a reduction in back corona sustaining field of about 2 is reasonable. A reduction in sustaining electric field by a factor of 2 is a significant reduction because it corresponds to a reduction in the current density required to cause the back corona by almost the same amount (allowing for the resistivity to change as well, according to Equation 4).

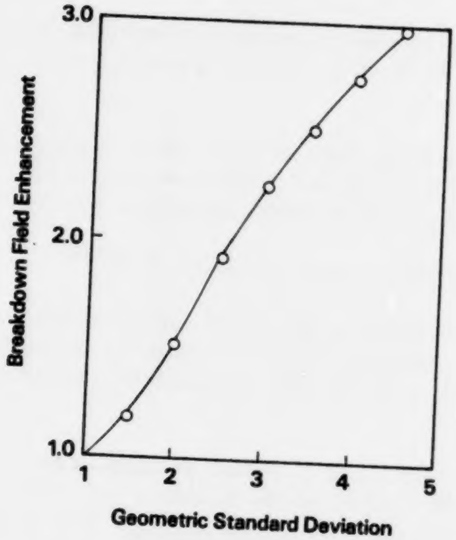

Figure 7. Effect of σ on enhancement.

CURRENT DENSITY DISTRIBUTION EFFECTS

Since the local current density acts in concert with the resistivity to produce the field for breakdown, it is important to know how much the current density differs from its average value at various locations in the ESP. Numerical techniques (3) are available for calculating the variation in the case of uniform corona, such as occurs in the positive glow mode. The calculations, which are in good agreement with experimental measurements, show that geometrical effects can be substantial.

For a geometry with wire-wire spacing equal to the plate-plate spacing, the maximum current density at the plate occurs directly opposite a corona wire and is about 1.2 to 1.5 times the average value; the higher factors occur at higher current densities.

For wire-wire spacings less than plate-plate spacings, the maximum ratio is somewhat less, 1.1 to 1.2, and less dependent on current density. In effect, the corona wires approximate a uniform sheet of ions, delivering an almost uniform corona current.

For wire-wire spacings of twice the plate-plate spacing, the peak current density ranges from 2.2 to 2.4 times the average. For wire-wire spacings of 4 or more times the plate-plate spacings, the peak current density is about 4.5 times the average. At the widest separations, each corona wire is essentially uninfluenced by the presence of the other corona wires.

In common use the wire-wire spacing is between 1 and 2 times the plate-plate spacing, meaning that with uniform positive corona the maximum current density would be 1.2 to 2.4 times the average value. Since negative corona is most often used, the uniformity of corona assumed in the calculation is not even valid. Negative corona is found to emanate from distinct spots on a corona wire, resulting in a very spotty generation of current along the wire.

As a first approximation, each corona spot emits current toward the plate in a manner similar to a point-to-plane electrode. The current density distribution on the plate under a point is given by the Warburg distribution:

$$j(\theta) = j(0) \cos^5\theta, \ \theta \leqslant 60^\circ, \tag{6}$$

where $j(\theta)$ is the current density measured at an angle, θ, with respect to the point, and $j(0)$, the current density directly opposite the point.(12) By integrating $j(\theta)$ over all angles, the calculated ratio of $j(0)$ to the average current density is 1.89.

Since the corona wire is not a point source, the actual distribution will be distorted from that of a point electrode. Experimental measurements of corona from a point embedded in a plate (13) show a current density distribution with a sharper cutoff at a limiting angle which is a function of the applied field. Under a corona wire tuft, the distribution of current could be considered a combination of the two types of distributions, with the Warburg distribution dominating in a direction perpendicular to the wire and the embedded point distribution dominating in the direction parallel to the wire.

It has been observed that negative corona tufts interfere with one another, and the movement of one toward another is limited to some minimum distance. This is interpreted as a mutual repulsion of the ion clouds emitted from each tuft and implies that current density distributions on the plate do not overlap. Because of the nonoverlapping, the average current density on the plate will contain substantial areas of zero contribution; and this means that the ratio of peak current density to plate average current density will be higher than indicated by Equation 6.

Figure 8 shows an arrangement of Warburg tuft distributions along corona wires, corresponding to the closest approach of areas without overlapping. The wire-wire spacing is equal to the plate-plate spacing for this figure, and the ratio of the total plate area to the area covered by current is 1.2. This ratio reaches a maximum of 1.27 when the wire-wire spacing is about 1.2 times the plate-plate spacing. When the spacing ratio (wire-wire/plate-plate) equals 1.73, the total area is 1.27 also and increases with further increases in the spacing ratio. For the spacing ratios commonly found in precipitators, an area ratio of 1.25 is a reasonable average value. If the corona tufts were not densely packed, as at low current densities, then the area ratio could be much larger.

Multiplying the area ratio by the ratio of peak to average value of the Warburg distribution provides the factor relating the maximum negative current density (under the corona tufts) to the average plate current density: 2.36 for spacing ratios from 1 to 1.7. This ratio represents a conservative estimate of the peak current density in terms of the average current density.

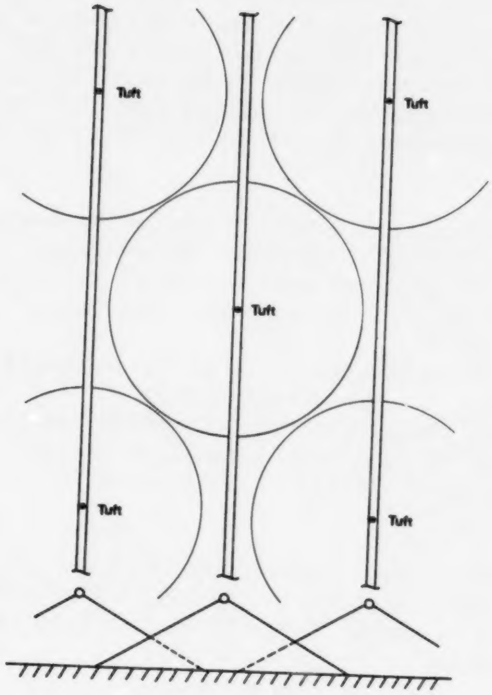

Figure 8. Idealized arrangement of negative corona tufts on wires.

COMBINING FACTORS TO CALCULATE BREAKDOWN

It is now possible to relate the back corona sustaining field and current density for a real fly ash layer in a negative corona precipitator. To calculate the initial homogeneous layer breakdown, the thickness of the dust layer in Equation 2 is used to to find an $(\alpha - \eta)$ that produces a gain of 10^8. For reasonable thicknesses, 1 to 10 mm, the field required will be large enough that $\alpha >> \eta$ and Equation 2 can be rewritten:

$$G \simeq \exp\left[(\alpha - \eta)x\right]. \tag{7}$$

This can be solved for $(\alpha - \eta)$:

$$\alpha - \eta = \ln G/x, \tag{8}$$

with x being the dust layer thickness. Equation 5 is then used to determine the E/P required to produce that $(\alpha - \eta)$. Using the notation of Equation 5:

$$E/P = 31.3 + \left(\frac{\alpha - \eta}{PB}\right)^{1/C} \tag{9}$$

Recall that E/P is the standard variable used in gas ion measurements, with the field, E (in V/cm) and the temperature-reduced pressure, P (in torr). As an example, assume a thickness of 1 mm, a pressure of 760 torr, and a temperature of 150° C. Then, $\alpha - \eta$ would be 184 and E/P would be 87.7. At the reduced pressure of 490 torr, E is 43 kV/cm. This value of electric field is much higher than usually calculated from dust resistivity and current density values: breakdown fields of 5 to 10 kV/cm are expected in operating precipitators.

But assume that the particle size distribution has a σ of 3 and that the maximum local field is limited to 5 times the average. Then, from Figure 7, the field enhancement in the pore is a factor of 2.25; this means the back corona would be sustained by an average field of only 19.1 kV/cm.

The average pore breakdown field is given by Equation 1, relating current density and resistivity. Assume a resistivity of $5 \cdot 10^{11}$ Ω-cm, as measured at an electric field of 10 kV/cm; then the effective resistivity at 19.1 kV/cm, calculated with the aid of Equation 4, would be $4.4 \cdot 10^{11}$ Ω-cm. The current density required to produce a field of 19.1 kV/cm in a resistive layer of $4.4 \cdot 10^{11}$ Ω-cm is $4.35 \cdot 10^{-4}$ A/m^2.

Presuming that this current density is produced directly under a negative corona tuft, the average plate current density corresponding to that peak value is $1.84 \cdot 10^{-4}$ A/m^2 because of the factor of 2.36 between the peak and average current densities.

The apparent electric field in the layer at breakdown, given by the product of the average plate current density and the measured dust resistivity, is 9.2 kV/cm, a value well within the range encountered in common practice.(11)

Until the back corona is fully established, there can be no feedback mechanism operating to reduce the electric field. However, once the pore channel has enough gain to initiate the Townsend avalanche, the intense photoionization and impact ionization within the channel will provide very high feedback factors, close to 1 in value. There is evidence for this in the surface potential measurements in Reference 14. In that work, Teflon® filter paper was used as a resistive layer under a point-plane electrode.

The layer was able to sustain an average E/P of 105 V/cm-torr without breakdown, with the breakdown field evaluated by Equations 8 and 9 as 112 V/cm-torr. When the breakdown was firmly established by using a higher corona point potential, the surface potential on the layer dropped to the point that the average E/P was only 44 V/cm-torr. This corresponds to a feedback factor of 0.8, using Equation 3. Thus, these measurements support both the initial breakdown calculation and the use of heavy feedback after breakdown occurs.

The feedback lessens the current density required to maintain the discharge, and, according to the pore breakdown model, the excess current density flows directly into the pore. The same factors may apply to the sustaining field as were previously calculated for the breakdown field.

Therefore, continuing the hypothetical layer example, at a feedback value of 0.8, the average enhancement corrected electric field is 8.8 kV/cm. The corresponding layer resistivity is $5.13 \cdot 10^{11}$ Ω-cm, and the local current density required is $1.7 \cdot 10^{-4}$ A/m^2. The heavy ionization in the pore may upset these calculations, but the drop in E/P to 44 V/cm-torr will be reflected in a drop of local current density.

At present it is not possible to relate this local current density to the plate average current density. The back corona generates additional ionic carriers which not only increase the total current but also change the distribution of current by neutralizing some of the ionic space charge.

CONCLUSIONS

The pore breakdown model for back corona generation predicts average layer electric fields which are much higher than usually accepted for operating precipitators, but which are in agreement with laboratory determined values. It is shown that the size distribution of particles in the dust layer can account for about half of the discrepancy and that current density distribution effects can account for the other half.

The size distribution has been shown to have an effect on the initiation of back corona only through the range of sizes encountered, characterized by the geometric standard deviation. For lognormal, or approximately lognormal, distributions, the MMD does not have a noticeable effect. Layers composed of monodisperse particles should have the same back corona initiation point as homogeneous porous layers of the same average resistivity.

The distribution of current density along the plate of a precipitator is equally important because back corona will always be initiated at the areas of maximum current density. The tuft structure of negative corona works against achieving uniform current densities, but the spacing of the corona wires can also be important in determining the inhomogeneity of the current density.

The ionic feedback that occurs within a pore after back corona begins is so large that the field required to sustain the back corona may drop to less than half the value required to initiate it. This process results in a considerable hysteresis in the conditions required to turn on and turn off back corona. The Townsend avalanche conditions set an upper bound on the amount of hysteresis.

The pore breakdown model has proven to be a useful and accurate model for describing the back corona process. It provides quantitative values for layer breakdown, for the degree of hysteresis, and for the amount of back corona current generated. When applied with electric field models and bipolar particle charging models, it should be capable of describing adequately the motion of particles in precipitators operating in back corona.

REFERENCES

1. White, H. J. Industrial Electrostatic Precipitation. Addison-Wesley, Reading, Massachusetts, 1963.
2. Lawless, P. A. Progress in modeling back corona. In: Third Symposium on the Transfer and Utilization of Particulate Control Technology: Volume II. Electrostatic Precipitators. EPA-600/9-82-005b. U. S. Environmental Protection Agency, Research Triangle Park, North Carolina, 1982. pp. 35-43.
3. Lawless, P. A., and Sparks, L. E. A Mathematical model for calculating effects of back corona in wire-duct electrostatic precipitators. Journal of Applied Physics. 51:242, 1980.
4. McLean, K. J. Electrical conduction in high resistivity particulate solids. Doctoral dissertation, University of New South Wales, December 1969.
5. McLean, K. H. Cohesion of precipitated dust layer in electrostatic precipitators. JAPCA. 27:1100, 1977.
6. Dietz, P. W. Cohesive force and resistivity between electrostatically-precipitated particles. J. Electrostatics. 6:273, 1980.
7. Moslehi, G. B., and Self, S. A. Electromechanics of precipitated particulate layers. In: Conference Record IEEE-IAS Annual Meeting, 1981. Library of Congress No. 80-640527. p. 1102.
8. Loeb, L. B. Basic Processes of Gaseous Electronics. University of California Press, Berkeley, California, 1961.
9. Masuda, S. Back discharge phenomena in electrostatic precipitators. In: Symposium on the Transfer and Utilization of Particulate Control Technology: Volume I. Electrostatic Precipitators. EPA-600/7-79-044a (NTIS No. PB295226). U. S. Environmental Protection Agency, Research Triangle Park, North Carolina, 1979. pp. 321-333.
10. Masuda, S. The influence of temperature and moisture on the electrical conductivity of high-resistivity dusts. Staub. 25:1, 1965.
11. Spencer, H. W., III. Electrostatic precipitators: relationship between resistivity, particle size, and sparkover. EFA-600/2-76-144 (NTIS No. PB257130). U. S. Environmental Protection Agency, Research Triangle Park, North Carolina, 1976.
12. Sigmond, R. S. Simple approximate treatment of unipolar space-charge-dominated coronas: the Warburg law and the saturation current. J. Appl. Phys. 53:891, 1982.

13. Collins, L. F., Self, S. A., and Shearer, D. D. Point-source corona current distribution in an external field. IEEE Trans. on Ind. Appl. Vol. IA-14:506, 1978.

14. Thanh, L. C. Back corona--Part I: its formation. J. Electrostatics. 6:139, 1979.

ELECTRICAL BREAKDOWN OF PARTICULATE LAYERS

By: G. B. Moslehi and S. A. Self
High Temperature Gasdynamics Laboratory
Mechanical Engineering Department
Stanford University
Stanford, CA 94305, U.S.A.

ABSTRACT

A theoretical analysis of electrical breakdown of a current-carrying particulate layer modeled as a regular array of equi-sized resistive spheres having combined surface and volume conduction, is presented. This analytical treatment is based on an extension of a theory of electromechanics of the layer and predicts the onset of electrical breakdown of the layer in the form of intermittent microsparks in the gap between the contacting particles when the electric field at the contact or in the surrounding gap exceeds the threshold breakdown value. The occurrence of breakdown is due to the existence of a very strong electric field in and around the contact region as a result of current constriction at the contact area. Two possibilities of breakdown are examined: i) breakdown in the gap where the gap height, d, is larger than the gas mean free path, λ, and ii) vacuum breakdown at the contact where $d < \lambda$.

The electrical behavior of the layer after breakdown is also analyzed in terms of a simplified equivalent lumped circuit using methods of conventional transient circuit theory. In this analysis the layer is modeled as a number of capacitive spark gaps in series, separated by high resistances. In effect, the discharge propagates through the layer as a cascade of microsparks, which discharges the layer locally. The theory predicts increases of sparking frequency and average current as the applied average field E_A, exceeds the threshold average field for the onset of breakdown, E_{AB}.

Experiments with glass beads demonstrate the existence of intermittent microsparks after the onset of breakdown, whose frequency of occurrence increases with increasing E_A.

INTRODUCTION

Back discharge, which seriously impairs the precipitation of high resistivity ash, is poorly understood and not satisfactorily incorporated into computational codes or design procedures for precipitators. It is generally attributed to electrical breakdown of the ash layer when the average electric field

$$E_A = \rho_A J_A \tag{1}$$

exceeds some critical breakdown value of the order of 10^6 V/m. Here, ρ_A is the apparent layer resistivity and J_A is the average current density passing through the layer.

This macroscopic view of the phenomenon, while undoubtedly correct as far as it goes, treats the layer as a homogeneous medium subject to uniform current and field. However, to understand back-discharge breakdown in more detail, and to explain the remarkably low value of dielectric strength, it is essential to consider the particulate structure of the layer.

It is generally accepted that the onset of back discharge is due to electrical breakdown in the interstices of the ash layer (as a result of a large field enhancement in the contact region), since it occurs at average fields of the order of a few kV/cm which is many orders of magnitude less than the inherent dielectric strength of glassy materials such as fly ash.

ONSET OF BACKDISCHARGE

In a particulate layer carrying an ion current from the discharge space to the grounded collector, the current must flow through the small contact areas between particles (Figure 1a). Therefore, the current and field lines are concentrated near the contacts and most of the resistance and voltage drop is associated with these regions. This current constriction in the contact, results in a strong field enhancement above the average value of the applied field, E_A, in and around the contact region, which gives rise to a remarkably large electrical compressive stress, P_E, in the layer. Furthermore, the apparent resistivity of the layer, ρ_A, decreases with increasing J_A or E_A as a result of self-compression (electrostriction).

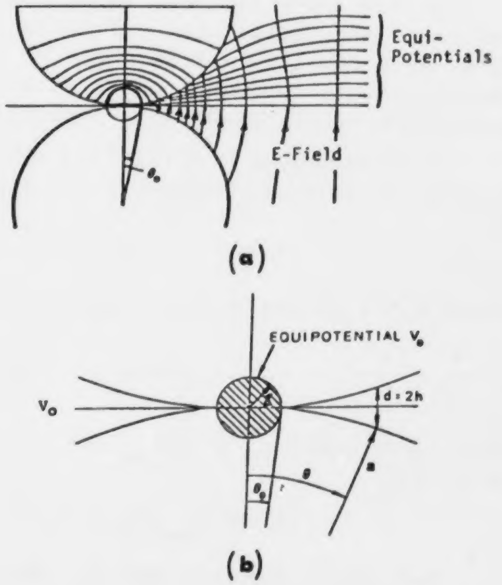

Figure 1. Geometry for current flow through resistive spheres. (a) potential and field distribution; (b) geometry in contact region.

The existence of a very strong electric field in and around the contact region, results in the onset of electrical breakdown of the layer (or back-discharge) in the form of intermittent microsparks in the gap between the contacting particles when the (local) electric field at the contact or surrounding gap exceeds the threshold breakdown value, E_B. At the onset of microspark breakdown the average field across the layer, E_A, is equal to the average (threshold) breakdown onset field, E_{AB}. At higher fields ($E_A > E_{AB}$), microsparks occur with increasing frequency so that the average current increases (and hence the apparent resistivity decreases) more rapidly than is the case prior to breakdown. However, the decrease in the apparent resistivity, ρ_A, is steady rather than catastrophic.

Clearly, a homogeneous leaky dielectric model for the layer fails to represent the true structure of the layer and is not able to explain and predict the behavior of the particulate layer.

In this section we outline an analysis of the onset of back-discharge breakdown of a current-carrying particulate layer by coupling the results of our analysis for the field distribution in the layer reported in References 1 and 2, with certain well-established results for electrical breakdown in small gaps. This allows one to predict, in terms of the basic parameters of the system, the average current density, J_{AB}, or average electric field, E_{AB}, at which the onset of microspark breakdown occurs and its location in the gap.

ELECTRIC FIELD DISTRIBUTION IN THE GAP BETWEEN TWO CONTACTING SPHERES

In the past we have developed a comprehensive theory of the electromechanics of precipitated particulate layers (1,2). The basic model treats the layer as a regular cubical array of equal size resistive spheres through which the current is conducted to the collector either by volume conduction, surface conduction or, in general, a combination of both.

In References 1 and 2, the electric field in the gap between two equal spheres in contact (Figure 1) having a (finite) contact angle θ_o is shown to be

$$E\,(\theta,\theta_o) \equiv E_{max}\,G\,(\theta,\theta_o) \tag{2}$$

where $G = 1$ in the contact region itself and for $\theta>\theta_o$,

$$G(\theta,\theta_o) \equiv \frac{[1 - F(\sigma,\theta)/F(\sigma,\theta_o)]}{[(\mu_o - \mu)(FEF)]}\ . \tag{3}$$

Here, $\mu \equiv \cos\theta$, $\mu_o \equiv \cos\theta_o$ and the field enhancement factor (FEF) is defined as (1,2)

$$FEF \equiv E_{max}/E_A = b_E D^{(\alpha/4\,-\,1/2)}\ (E_A)^{(\alpha/2\,-\,1)}\ . \tag{4}$$

For small angles θ and θ_o, the function F is approximately given by (2)

$$F(\sigma,\theta) \simeq a_F(\theta)^n \tag{5}$$

and

$$F(\sigma,\theta_o) \simeq a_F(\theta_o)^n\ . \tag{6}$$

TABLE 1 VALUES OF COEFFICIENTS AND EXPONENTS IN THE POWER LAW EQUATIONS

$F = a_F(\theta_o)^n$; $\theta_o = b_\theta D^{\alpha/2} (E_A)^\alpha$; $E_{max} = b_E D^{(\alpha/4 - 1/2)} (E_A)^{\alpha/2}$

σ	a_F	n	b_θ	b_E	α	$A(\sigma)$
0	1.5865	-0.1628	0.6767	0.8226	0.4279	2.139
1	1.2057	-0.1867	0.7484	0.8651	0.4314	2.115
10	4.3475	-0.2859	1.0391	1.0194	0.4430	1.976
10^2	3.8322	-0.5492	1.5103	1.2289	0.4502	1.582
10^3	1.0545	-0.8927	1.2112	1.1005	0.4184	1.299
10^4	0.6970	-0.9860	0.9865	0.9932	0.3996	1.274
∞	0.6879	-0.9889	0.9766	0.9882	0.3987	1.274

NOTE:

1. In all cases θ_o is in radians. All values are in (MKS) SI Units.
2. Value of F for $\sigma = 0$ is actually F_s where $F_s \equiv \lim_{\sigma \to 0} (F/\sigma)$. For $\sigma \lesssim 10^{-4}$ the approximate expression $F = \sigma F_s$ may be used.
3. For intermediate values of σ, which are not given in the table, the functions F, θ_o and E_{max} may be evaluated using a logarithmic interpolation procedure.

(The exponent n used in the above expressions is identical to n_F in Ref. 2.) Values of a_F, n and α for different values of σ are given in Table 1.

For a spherical particle of radius a the non-dimensional resistivity ratio σ is defined as

$$\sigma \equiv sa/\rho \tag{7}$$

where ρ is the (intrinsic) material volume resistivity and s is the surface resistivity of the particle. Pure surface conduction corresponds to $\sigma = 0$ and for pure volume conduction $\sigma \to \infty$.

In Eq. 2, E_{max} is the maximum electric field in the gap and is expressed by (1,2)

$$E_{max} = \lim_{\theta \to \theta_o} [E(\theta, \theta_o)] = b_E D^{(\alpha/4 - 1/2)} (E_A)^{\alpha/2} \quad . \tag{8}$$

The contact angle θ_o is given by (2)

$$\theta_o(\sigma, E_A) = b_\theta \, D^{\alpha/2} (E_A)^\alpha \quad . \tag{9}$$

In Eqs. 4, 8 and 9 the material constant D is defined as

$$D(\sigma) \equiv \pi \varepsilon_o A(\sigma) B \tag{10}$$

where ε_o is the vacuum permittivity, $A(\sigma)$ is a constant and B depends only on the elastic properties of the particle and is given by

$$B \equiv 3(1-\nu^2)/4Y \quad . \tag{11}$$

Here, Y is the Young's modulus and ν is Poisson's ratio.

Values of b_θ, b_E and $A(\sigma)$ for different values of σ are also given in Table 1.

Using Eqs. 4, 5 and 6 with Eq. 3 gives an expression for G in terms of E_A, which together with Eqs. 2 and 8 results in

$$E(x,\sigma,E_A) = \frac{2[(1 - x^n)/(x^2 - 1)]}{[b_\theta^2 \, D^\alpha (E_A)^{(2\alpha-1)}]} \tag{12}$$

where $x \equiv \theta/\theta_o$ is a measure of location in the gap between two contacting spheres.
The gap height between spheres can be written (for small angles)

$$d = 2a(\mu_o - \mu) \simeq a\theta_o^2(x^2 - 1) = a \, b_\theta^2 \, (x^2 - 1)(D^\alpha)(E_A)^{2\alpha} \tag{13}$$

where use is made of Eq. 9.

Substitution for (x^2-1) from Eq. 13 into Eq. 12 gives

$$E(x,\sigma,E_A) = (1-x^n)\left[\frac{2a \, E_A}{d}\right] \quad . \tag{14}$$

Equations 12 and 13 give the values of the electric field in the gap and gap height as a function of the average electric field, E_A, the normalized location x and the resistivity ratio σ, and are necessary inputs for determining the breakdown condition from gas-discharge considerations, as discussed below.

BACKDISCHARGE ONSET CONDITIONS

The condition for back-discharge onset can be estimated by using the field in the contact area and surrounding gap together with results from the literature for electrical breakdown of small gaps between parallel plane electrodes in air. There are two mechanisms to consider, namely, gas discharge breakdown for gaps of height $d \gtrsim \lambda$ and vacuum breakdown for $d < \lambda$, where λ is the gas mean free path. Which mechanism occurs first with increasing E_A, and where it occurs, will be determined by which threshold field for breakdown is first exceeded.

Figure 2 shows the composite breakdown curve, $E_B(d)$, for the threshold breakdown field E_B as a function of gap height d. This curve is plotted using the data taken from literature and applies to metallic parallel plane electrodes in air at STP. The method of construction of this composite breakdown curve is explained in Reference 1. For $d \gtrsim \lambda$, in the gas discharge regime, the curve of $E_B(d)$ is a monotonically decreasing function of d. For $d \lesssim \lambda$, in the vacuum breakdown regime, for short gaps the local field initiating breakdown is quoted (3) as $E_{B_0} = E_{VB} \sim (6.5 \pm 1) \times 10^9$ V/m. For the purpose in hand we take $E_{VB} = 6.5 \times 10^9$ V/m for gaps less than $d \sim 1$ µm where the data for gas discharge breakdown yields the same value. This is a reasonable assumption because at this point d is close to the gas mean free path $\lambda \sim 0.06$ µm (for air at STP).

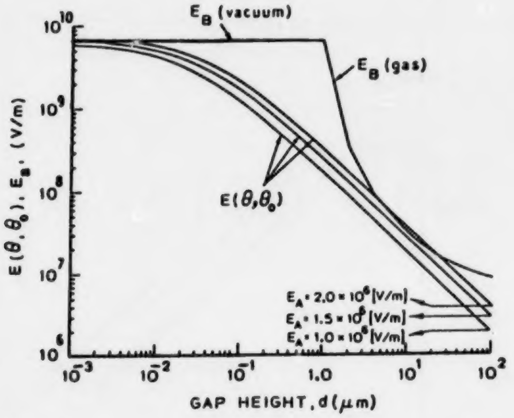

Figure 2. Graphical procedure for determining breakdown field E_{AB} (Volume Conduction).

From the expression for the electric field in the gap between contacting spheres, summarized in the previous section and the conditions for electrical breakdown in uniform gaps for the two distinct mechanisms discussed above, we can now calculate the conditions for breakdown in the gap between spheres.

The case of vacuum breakdown is relatively straightforward. Because breakdown can be assumed to occur when a certain field E_{VB} is reached anywhere in the gap, and since the maximum field in the gap occurs at the edge of the contact area x = 1, then we have from Eq. 8 the vacuum breakdown condition for the average layer field

$$E_{AB} = (D)^{\left(\frac{1}{\alpha} - \frac{1}{2}\right)} \cdot [E_{VB}/b_E]^{\left(\frac{2}{\alpha}\right)} \cdot \qquad (15)$$

It may be noted that, for a given σ, this condition is independent of particle radius, and that breakdown occurs at the edge of the contact area (or in the contact region itself, where $x \leqslant 1$, if it is assumed that, due to microprojections, it contains microscopic gaps.)

Taking B ~ 9.4 x 10^{-12} m^2/N for a typical glassy material (with Y ~ 7.5 x 10^{10} N/m^2 and ν ~ 0.25) in Eq. 10, and using the data given in Table 1, together with E_{VB} ~ 6.5 x 10^9 V/m one can calculate from Eq. 15 the average electric field for vacuum breakdown, E_{AB}. For the limiting case of volume conduction ($\sigma \to \infty$) one obtains E_{AB} ~ 13 kV/cm, whereas for the case of pure surface conduction ($\sigma = 0$) one calculates E_{AB} ~ 170 kV/cm, an exceedingly high value. Thus on the basis of the value E_{VB} ~ 6.5 x 10^9 V/m derived from the literature, one concludes that in practice for typical precipitation conditions vacuum breakdown is not likely to be responsible for backdischarge onset in the case of surface conduction. The basic reason for this is that, for a given E_A, the field enhancement factor FEF ($\equiv E_{max}/E_A$) is very much smaller in the case of surface conduction compared with volume conduction. The ratio of the vacuum breakdown values of average field in the two cases is $(E_{AB})_s/(E_{AB})_v$ = 170/13 ~ 13.

Vacuum breakdown in the contact region can be expected to be responsible for the onset of breakdown of the layer at average fields of the value estimated above, provided that, with increasing E_A, gas (discharge) breakdown somewhere else in the gap does not occur first.

Turning now to the mechanism of gas discharge breakdown, we use the results of previous subsection for the field in the gap together with data for breakdown fields $E_B(d)$ in order to calculate a condition for gas breakdown in the gap. However, one does not know, a priori, at what position in the gap (i.e. x value) the breakdown condition is first attained.

The method for determining the onset condition for back-discharge breakdown is best illustrated by the graphical procedure shown in Figure 2. For a given particle radius, a, and material properties, the field in the gap $E(\theta,\theta_0)$ can be calculated for given values of average field E_A using the formulae developed earlier. Three such curves are shown in Figure 2 for the case of volume conduction ($\sigma\to\infty$), a = 100 μm, B ~ 10^{-11} m^2/N and for $E_A = 1.0 \times 10^6$, 1.5×10^6 and 2.0×10^6 V/m. It is seen that the first curve does not intersect the $E_B(d)$ curve, the second curve intersects $E_B(d)$ in the vacuum breakdown regime, while the third curve additionally intersects $E_B(d)$ in the gas discharge breakdown region. Interpolation from these curves shows that for these conditions breakdown occurs first in the contact region (d ~ 0) at an average field for breakdown $E_{AB} \sim 1.3 \times 10^6$ V/m followed by breakdown in the surrounding gap (at a position where the gap height is ~ 10 μm) at an average field of $E_{AB} \sim 1.8 \times 10^6$ V/m.

To avoid the tedium and inaccuracy of the graphical procedure illustrated above, a computer program has been developed to calculate the gas-discharge breakdown condition. Using this method, values of E_{AB} for gas discharge breakdown have been obtained for the two limiting cases of surface and volume conduction as a function of particle diameter D_p = 2a (for atmospheric pressure air at 25°C and 150°C, respectively) as shown in Figure 3.

It is found that for the case of volume conduction, with B ~ 10^{-11} m^2/N, and for air at 1 atm, then for a < 140 μm, breakdown always occurs first as vacuum breakdown in the contact region (d ~ 0) at $E_{AB} \sim 1.3 \times 10^6$ V/m, independent of particle size (Figure 3). For larger particles, however, breakdown occurs first as gas discharge breakdown in the surrounding gap where the gap height is ~ 10 μm and at a field which decreases roughly inversely with radius.

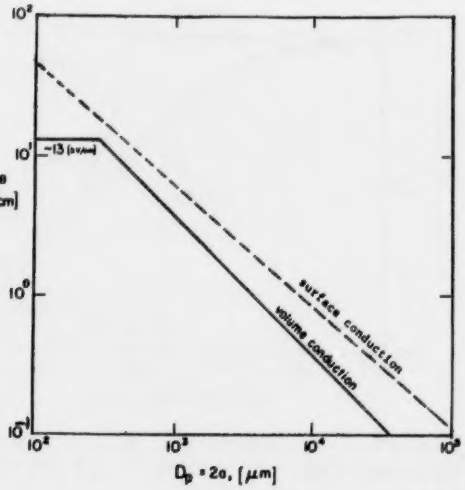

Figure 3. Average electric field E_{AB} for the onset of breakdown versus particle diameter D_p. Volume conduction case. For $D_p \lesssim 280$ μm, vacuum breakdown occurs first at E_{AB} ~ 13 kV/cm.

Calculations of the conditions for the onset of back-discharge breakdown for the case of surface conduction lead to generally similar results. However, because the field enhancement factor is lower for the case of surface conduction, an appreciably larger value of average layer field E_{AB} is required for breakdown. For instance for a = 150 μm, B = 10^{11} m^2/N, gas discharge breakdown occurs in the surrounding gap (at d ~ 15 μm) at an average field of $E_{AB} \sim 2.0 \times 10^6$ V/m, a factor ~ 1.7 higher than in the volume conduction case.

While the model on which these conclusions are based is idealized and the breakdown data we have employed are only approximate, especially for vacuum breakdown, we expect these conclusions to be valid in general form even though the predicted values of E_{AB} for onset of microsparks and back-discharge may be only approximate.

Because of the form of Eq. 15, which, (for $\alpha \sim 0.4$, from Table 1) shows $E_{AB} \propto E_{VB}^5$ the results are extremely sensitive to the value assumed for the local vacuum breakdown stress, E_{VB}, which is a quantity whose value for non-metallic electrodes is difficult to establish from the literature. What values are available were obtained for small gaps between (parallel plane) metal surfaces, and since the breakdown mechanism undoubtedly depends on the surface state, the appropriate value of E_{VB} (or $E_B(d)$ in general) for glassy materials is difficult to know with any certainty.

EXPERIMENTS WITH GLASS BEADS

Using a standard resistivity cell under various conditions of temperature and humidity, measurements of the apparent resistivity ρ_A of the layer were made as a function of the (applied) average field, E_A. In these tests glass beads (450-500μm dia.) were used. In each test a new layer of beads was used from the same supply sample. The mechanical pressure due to the weight of the upper electrode was ~ 10 g wt./cm^2 and the layer thicknes was about 5mm.

The results of these experiments are discussed in some detail in Ref. 2. Table 2 gives the values of (dry bulb) temperature, t_{db}, and relative humidity, P_r, for each test. In the high temperature tests ($t_{db} > 30°C$) the ambient air was heated to the specified temperature. Other tests were made under ambient conditions. Only in experiment #1 was the humidifier used, in order to achieve a relative humidity of $P_r \sim 100\%$ at $t_{db} \sim 28°C$.

Figures 4a and b show a few examples of the measured apparent resistivity, ρ_A, of the layer as a function of the (applied) average field, E_A, given in Table 2. Figures 4a and b are identical, with the exception that the former has a log-log scale and the latter a semi-log scale.

Generally in all of these experiments, the $\rho_A(E_A)$ characteristic is composed of two distinct regimes: pre- and post- microspark breakdown.

The pre-microspark breakdown regime has two regions. In region I, for E_A in the range $10^4 \lesssim E_A \lesssim 2\times10^4$ to 3×10^4 V/m, ρ_A is approximately constant. This is due to the fact that the compression as a result of the electric stress in the layer is less than that due to the weight of the upper electrode. In region II, for E_A between $\sim 4\times10^4$ V/m and $\sim 2\times10^5$ V/m, the $\rho_A(E_A)$ characteristic follows a power law ($\rho_A \propto E_A^m$) with the exponent having a value somewhere between -0.077 for the case of surface conduction ($t_{db} = 28°C$, $P_r \simeq 100\%$) and -0.4 for the case of volume conduction (hot and dry conditions). These values are in agreement with our theoretical predictions which are reported in Reference 2.

In the third region (Figure 4a), at $E_A = E_{AB} \sim (2-4) \times 10^5$ V/m, the $\rho_A(E_A)$ curve starts to deviate from the power law dependence, with ρ_A decreasing more rapidly with increasing (applied) field E_A. This is due to the electrical breakdown of the layer which occurs in the form of intermittent microsparks. For E_A between $(4-5) \times 10^5$ V/m and the value for gross breakdown of the layer, the $\rho_A(E_A)$ dependence is exponential in form (Region III in

TABLE 2. RESULTS OF RESISTIVITY CELL MEASUREMENTS ON GLASS BEADS AT DIFFERENT VALUES OF TEMPERATURE

No.	Oven Conditions		Region I ρ_A = const.	Region II $\rho_A = b\,E_A^m$ ρ_A in [Ω - cm]; E_A in [kV/cm]		Region III $\rho_A = \rho_o \exp(a_o E_A)$ ρ_A in [Ω - cm]; E_A in [kV/cm)		Gross Breakdown
	t_{db}, [°C]	P_r, (%)	ρ_A, [Ω-cm]	b	m	ρ_0, [Ω-cm]	a_o, [cm/kV]	E_{GB}, [kV/cm]
1	28	100	$9.24\text{x}10^7$	$7.54\text{x}10^7$	-0.077	----	----	----
2	23	~ 88.5	$4.56\text{x}10^{10}$	$3.53\text{x}10^{10}$	-0.172	$2.60\text{x}10^{10}$	$-2.88\text{x}10^{-2}$	15.8
3	22.5	~ 82	$5.84\text{x}10^{10}$	$4.97\text{x}10^{10}$	-0.175	$3.46\text{x}10^{10}$	$-3.53\text{x}10^{-2}$	16.0
4	23	~ 81	$9.82\text{x}10^9$	$6.95\text{x}10^9$	-0.21	$4.15\text{x}10^9$	$-2.65\text{x}10^{-2}$	13.4
5	22.5	~ 80	$3.07\text{x}10^{10}$	$2.07\text{x}10^{10}$	-0.23	$1.36\text{x}10^{10}$	$-2.16\text{x}10^{-2}$	16.0
6	22	~ 78	$9.83\text{x}10^{10}$	$7.92\text{x}10^{10}$	-0.23	$6.15\text{x}10^{10}$	$-3.25\text{x}10^{-2}$	----
7	22.5	~ 81.6	$4.25\text{x}10^{10}$	$3.37\text{x}10^{10}$	-0.235	$3.16\text{x}10^{10}$	$-5.52\text{x}10^{-2}$	15.8
8	29	~ 70	$5.17\text{x}10^{10}$	$4.44\text{x}10^{10}$	-0.259	$3.46\text{x}10^{10}$	$-4.01\text{x}10^{-2}$	16.0
9	46	23.2	----	$6.28\text{x}10^{11}$	-0.352	$4.71\text{x}10^{11}$	$-6.06\text{x}10^{-2}$	16.0
10	46	22.9	----	$5.56\text{x}10^{11}$	-0.337	$4.07\text{x}10^{11}$	$-5.45\text{x}10^{-2}$	16.0
11	61	12.1	$1.27\text{x}10^{12}$	$6.14\text{x}10^{11}$	-0.344	$4.43\text{x}10^{11}$	$-6.74\text{x}10^{-2}$	15.4
12	119	1.2	$7.12\text{x}10^{12}$	$3.55\text{x}10^{12}$	-0.408	$2.50\text{x}10^{12}$	$-8.95\text{x}10^{-2}$	13.8
13	133	0.8	----	$3.64\text{x}10^{12}$	-0.407	$2.72\text{x}10^{12}$	$-8{,}50\text{x}10^{-2}$	12.6
14	151	0.5	----	$3.41\text{x}10^{12}$	-0.382	$2.46\text{x}10^{12}$	$-8.92\text{x}10^{-2}$	13.4
15	162	~ 0.4	$4.54\text{x}10^{12}$	$2.71\text{x}10^{12}$	-0.337	$2.09\text{x}10^{12}$	$-8.98\text{x}10^{-2}$	12.0
16	185	~ 0.2	$4.60\text{x}10^{12}$	$2.12\text{x}10^{12}$	-0.420	----	----	----

(-) means: (i) "No Data Taken" or (ii) "No Data Available".

Figure 4b). The gross breakdown of the layer occurs at $E_A = E_{GB} \sim (12\text{-}16) \times 10^5$ V/m, with the lower values corresponding to higher temperatures and drier conditions. These values are much lower than $\sim 4 \times 10^6$ V/m required for breakdown across a 5 mm air gap between two parallel electrodes at STP. Table 2 gives the values of ρ_o and a_o for the exponential form

$$\rho_A = \rho_o \exp\,(-\,a_o E_A) \qquad (16)$$

in Region III which applies to the range $4 \times 10^5 \text{ V/m} \lesssim E_A \lesssim E_{GB}$. These values are calculated using a least squares fit to the experimental results. This form of functional dependence of ρ_A on E_A has also been observed by McLean and Huey (4). In these experiments, for the cases close to volume conduction the microspark breakdown of the layer occurs at $E_{AB} \sim 2$ to 4 kV/cm which is close to the theoretical value of ~ 7.2 kV/cm for 500 μm diameter beads and volume conduction, taken from Figure 3. The difference is mainly due to the lack of accurate breakdown data for non-metallic electrodes in nonuniform fields and, partly due to the approximations of the theory.

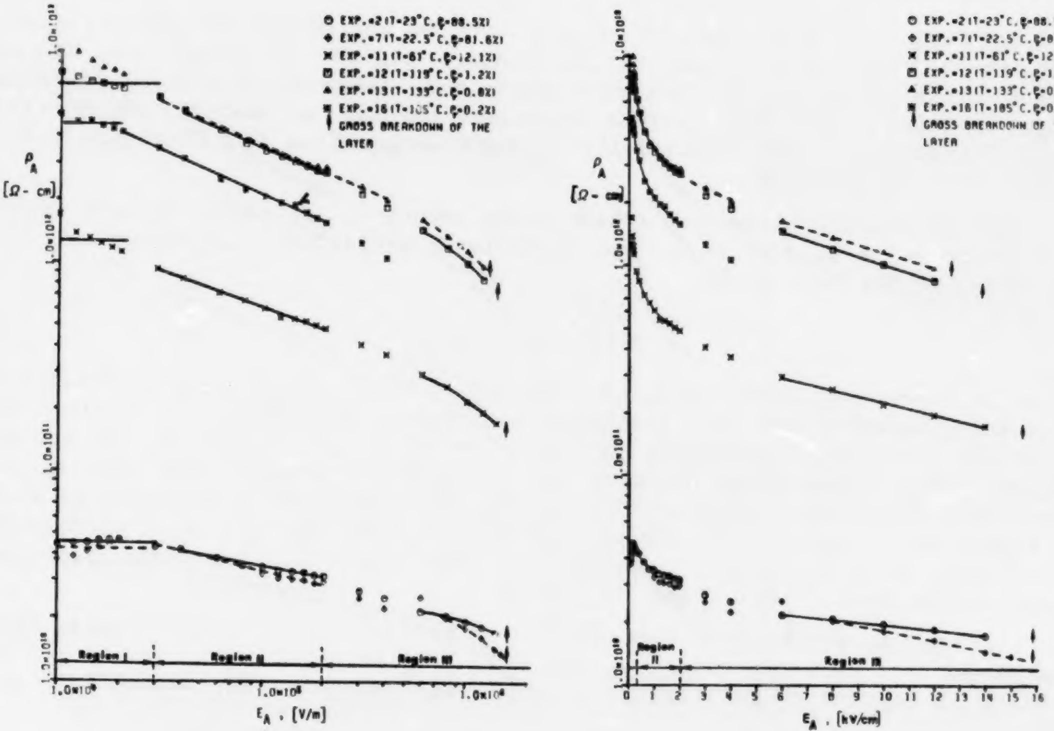

(a)

(b)

Figure 4. Resistivity cell measurements at different values of temperature; Glass beads; $D_p \sim 450$ μm. Solid (or dotted) lines are the best fit to the experimental results in the corresponding region. Experimental conditions and results are given in Table 2. (a) log-log scale showing $\rho_A \sim$ const. in Region I and $\rho_A = b(E_A)^m$ in Region II (Power law form). (b) Data points of Figure 4a plotted in semi-log scale showing the exponential dependence of $\rho_A = \rho_o \exp(-a_o E_A)$.

POST-MICROSPARK BREAKDOWN REGIME

Our theory of the electromechanics of a particulate layer (1,2) shows that there is a strong field enhancement in and around the contacts due to the current concentrations there. As a result the cohesive electrical stress is much larger than one would calculate for a given average field, E_A, on the basis of a homogeneous dielectric having a permittivity of the order of the layer material. This is because the cohesive stress is $\langle(1/2)\ \varepsilon_o\ E^2\rangle$, and for a highly inhomogeneous field $\langle E^2\rangle$ is much greater than $\langle E\rangle^2$.

Alternatively, one can regard the layer as having a greatly enhanced effective permittivity ε_A such that $(1/2)\ \varepsilon_A\ \langle E\rangle^2 = (1/2)\ \varepsilon_o\ \langle E^2\rangle$. Moreover, because the stored energy density in the field is also $\langle(1/2)\ \varepsilon_o\ E^2\rangle$, the energy stored for a given average field is much larger than one would calculate for a uniform dielectric. (It may be noted that energy density in J/m^3 and stress in N/m^2 have the same dimensions).

Both the enhanced cohesive stress and the energy stored are associated with the strong fields local to the contact region. In effect the contact region and surrounding gap act as a capacitor. There is also a large resistance associated with the current concentration in the contact region which makes the average layer resistivity ρ_A much larger than the intrinsic resistivity ρ of the material.

Our previously presented steady state theory (1,2) takes account of the self-compression of the layer and predicts a resistivity characteristic for the layer of the form (1,2)

$$\rho_A \propto E_A^m \; ; \; m < 0 \tag{17}$$

prior to breakdown. Also, using the calculated field enhancement together with literature results for gas discharge and vacuum breakdown, we predict the onset of electrical breakdown in the form of a microspark in the contact region. These theoretical results can be used to explain the form of the measured resistivity characteristic ρ_A (E_A) for layers of glass beads as shown in Figure 4. On theoretical grounds one expects that for $E_A > E_{AB}$, microsparks will occur with increasing frequency so that the average current increases more rapidly than in the power law region.

To analyze the layer's current-voltage characteristic in the region after the onset of microsparking, we model the distributed real system of two spheres in contact (Figure 5a) by a simple equivalent circuit shown in Figure 5b.

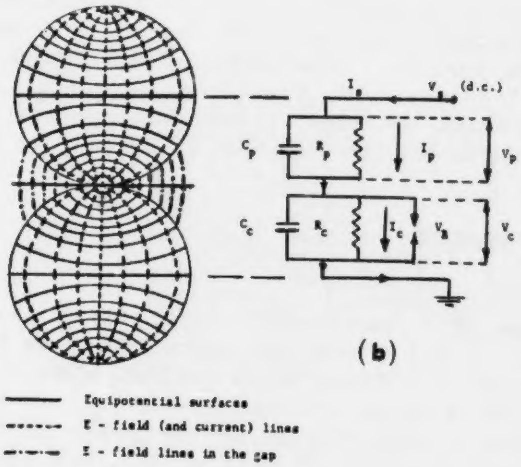

(b)

(a)

Figure 5. Two current-carrying particles in contact and their equivalent circuit. (a) Contacting particles and their contact region. (b) Equivalent circuit.

The contact region is represented by a capacitor C_c in parallel with a contact resistance R_c together with a parallel spark gap having a sparking voltage V_B. These elements are in series with a parallel combination of C_p and R_p representing the capacity and resistance of the bulk of the sphere, away from the contact region. The total circuit is connected between a supply voltage V_s and ground.

This division of the distributed system into separate parts representing the contact region and the bulk of the sphere is, of course, somewhat arbitrary. In practice the distributed system consists of infinitely many series-parallel R-C combinations. However, it does represent the fact that the bulk of the resistance and capacity is associated with the local region in and around the contact where the spark occurs.

ANALYSIS OF THE EQUIVALENT CIRCUIT

In the steady state, for applied voltages V_s such that sparking does not occur, the voltage across the contact region and spark gap as

$$V_c = V_s R_c/(R_c + R_p) \quad . \tag{18}$$

For $V_c < V_B$ no sparking occurs. As V_s is slowly raised so that $V_c = V_B$, a spark will occur which discharges the contact capacitance C_c rapidly and reduces V_c to essentially zero.

A transient analysis of the circuit gives the voltage V_c across the parallel combination of R_c, C_c and spark gap as

$$V_c\ (t) = A_0 \exp\ (-t/\tau) + V_s R_c/(R_p + R_c) \quad , \tag{19}$$

where

$$\tau \equiv \frac{R_p R_c\ (C_p + C_c)}{R_p + R_c} = \left(\frac{R_c}{R_p + R_c}\right) \tau_p + \left(\frac{R_p}{R_p + R_c}\right) \tau_c \tag{20}$$

and

$$\tau_p \equiv R_p C_p \tag{21}$$

$$\tau_c \equiv R_c C_c \tag{22}$$

are the time constants of the component circuits. Normally we expect the condition $\tau_c >> \tau_p$ to be satisfied. The coefficient A_0 depends on the initial condition assumed.

BEHAVIOR IN THE REPETITIVE SPARKING REGIME

Immediately following a spark, the initial condition is $V_c(t=0)=0$. Then Eq. 19 gives for the increase of V_c:

$$V_c\ (t) = V_s \left(\frac{R_c}{R_p + R_c}\right) \left[1 - \exp(-t/\tau)\right] \quad . \tag{23}$$

The total current (through the parallel combination) is given by

$$I_s\ (t) = \frac{V_s}{(R_p + R_c)} \left[1 + \left(\frac{\tau_c}{\tau} - 1\right) \exp\ (-\ t/\tau)\right] \quad . \tag{24}$$

In Eq. 23 , when $V_s > V_B\ (R_p + R_c)/R_c$, the voltage $V_c\ (t)$ reaches V_B and a spark occurs after a time given by

$$t_B = \tau\ \ln \left(\frac{\mathcal{V}}{\mathcal{V}-1}\right) \quad , \tag{25}$$

where

$$\mathcal{V} \equiv \frac{V_s}{V_B} \left(\frac{R_c}{R_p + R_c}\right) \tag{26}$$

is a normalized supply voltage such that $\mathcal{V} = 1$ corresponds to onset of sparking and $\mathcal{V} > 1$ corresponds to an overvoltage where repetitive sparking occurs. With increasing $\mathcal{V}$, the time t_B decreases and the rate of sparking increases.

The forms of the voltage $V_c(t)$ and of the total current $I_s(t)$ are shown in Fig. 6a and 6b respectively. In Fig. 6a, the voltage across the spark gap is assumed to fall instantaneously to zero at $t = t_B$ and then repeat its previous increase. Figure 6b is drawn for the case $R_c C_c > R_p C_p$, when

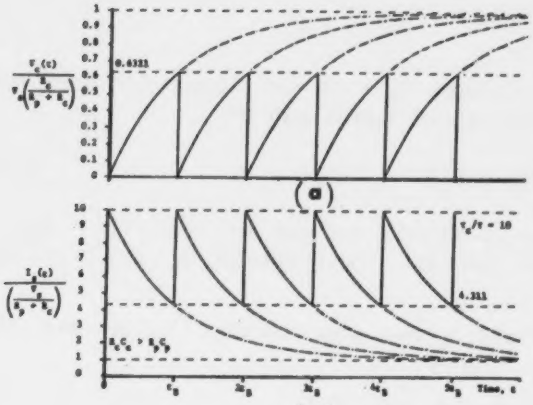

Figure 6. The forms of the voltage $V_c(t)$ and of the total current $I_s(t)$. (a) Dependence of $V_c(t)$ on time. (b) Dependence of $I_s(t)$ on time with $R_cC_c > R_pC_p$, for $\tau_c/\tau = 10$.

$I_s(t = 0) > I_s(t = t_B)$. This is the condition to be normally expected and shows a current overshoot immediately following the spark.

TIME-AVERAGE CURRENT IN THE SPARKING REGIME

In conventional resistivity cell measurements on powders, only the time-average current is measured. In the sparking regime we expect the average current to increase more rapidly than if sparks did not occur.

The time-average total current is by definition

$$\langle I_s \rangle = \frac{1}{t_B} \int_0^{t_B} I_s(t)\, dt \quad . \quad (27)$$

Using I_s (t) from Eq. 24, together with Eq. 26, this can be expressed as

$$\langle I_s \rangle = \left(\frac{V_B}{R_c}\right) . \mathcal{V} . \left[1-\left(\frac{\tau_c}{\tau} - 1\right) \frac{(1/\mathcal{V})}{\ln (1 - 1/\mathcal{V})}\right] \quad . \quad (28)$$

Note that at the onset of sparking, when $\mathcal{V} = 1$, $\langle I_s \rangle = (V_B/R_c)$ and defining a normalized current $\mathcal{I} = \langle I_s \rangle R_c/V_B$ we can write the normalized time-average $\mathcal{I} - \mathcal{V}$ characteristic above the point ($\mathcal{V} = 1$, $\mathcal{I} = 1$) for the onset of sparking as

$$\mathcal{I} = \mathcal{V}\left[1-\left(\frac{\tau_c}{\tau}-1\right)\frac{(1/\mathcal{V})}{\ln (1 - 1/\mathcal{V})}\right] . \quad (29)$$

Above the point of sparking onset, the characteristic $\mathcal{I}(\mathcal{V})$ departs gradually from the linear form $\mathcal{I} = \mathcal{V}$ and for $\mathcal{V} \gg 1$ tends to an asymptote $\mathcal{I} \rightarrow \mathcal{V}(\tau_c/\tau)$. Two cases are distinguished according as τ_c/τ is greater or less than unity. For the case of interest, when $C_c \gg C_p$ and $R_c \gg R_p$, one obtains $(\tau_c/\tau) \approx (R_c/R_p) \gg 1$. Thus, the current rises more rapidly than linearly for $\mathcal{V} > 1$ tending eventually to a steeper linear asymptote for $\mathcal{V} \gg 1$.

TIME-AVERAGE RESISTANCE IN THE SPARKING REGIME

Defining a normalized resistance $\mathcal{R} = \mathcal{V} / \mathcal{I}$ such that $\mathcal{R} = 1$ for $\mathcal{V} < 1$, below the onset for sparking, we have from Eq. 29

$$\mathcal{R} = \left[1-\left(\frac{\tau_c}{\tau}-1\right)\frac{(1/\mathcal{V})}{\ln (1 - 1/\mathcal{V})}\right]^{-1} . \quad (30)$$

As $\mathcal{V}$ increases above unity, $\mathcal{R}$ changes smoothly from the value $\mathcal{R} = 1$ to a new asymptotic constant value (τ/τ_c). For the case of interest, when $\tau_c/\tau \sim (R_c/R_p) \gg 1$, the resistance falls to a lower asymptotic value for $\mathcal{V} \gg 1$.

SPARK REPETITION RATE

The discharge repetition rate f_B is given by

$$f_B = \frac{1}{t_B} = - \frac{1}{\tau \ln (1 - 1/\mathcal{V})} . \quad (31)$$

For $\mathcal{V} = 1$ at sparking onset $f_B = 0$ and increases rapidly to an asymptotic rate

$$f_B \to \mathcal{V}/\tau \quad , \text{for } \mathcal{V} \gg 1 \quad . \tag{32}$$

DISCUSSION OF THEORETICAL RESULTS

From the foregoing it is seen that our simple equivalent circuit predicts, for the reasonable condition $R_c \gg R_p$ and $C_c \gg C_p$, that the time-average resistance should decrease for voltages above the onset voltage for sparking and is *qualitatively* capable of explaining the observed decrease in resistivity of the layer of glass beads below the power law (E_A^m where $m < 0$) form for voltages above sparking onset. Of course the equivalent circuit model does not take account of self-compression of the layer as the steady state theory does for applied voltages below that for sparking onset.

The transient analysis also predicts that the sparking frequency increases quite rapidly for voltages greater than the onset voltage, eventually becoming linearly proportional to $\mathcal{V}$ for $\mathcal{V} \gg 1$.

It must be admitted, of course, that the model is a simplification and, as with all equivalent lumped circuit representatives of distributed systems, it is difficult to clearly identify appropriate values of the circuit parameters.

EXPERIMENTAL OBSERVATIONS OF MICROSPARKS

A direct observation of the occurrence of microsparks in a particulate layer for applied fields $E_A > E_{AB}$, the onset field, would provide strong evidence of the correctness of the theoretical explanation derived in the last section for the decrease of the apparent resistivity characteristic ρ_A (E_A) below the power law form for high fields.

Using the resistivity cell, there are basically two techniques available for detecting sparks. The first is to detect the electrical pulses (due to microsparks) superimposed on the average current in the resistivity cell circuit. The second is to detect the light pulses emitted by the individual microsparks. Both techniques have been employed in exploratory experiments described below.

To detect the electrical pulses, a signal resistor (of 100 kΩ) is inserted in the ground return from the cell to the high voltage power supply. The light pulses are detected by a photomultiplier tube (UV enhanced RCA 1P28B) with a signal resistor (of 10 kΩ) in conjunction with a 1 mm diameter optical fiber to collect light from the cell. The voltages developed across these signal resistors associated with the electrical pulse detection system and the light pulse emission detection unit can be displayed on a storage oscilloscope and photographed, independently or simultaneously.

Using this setup, we have performed experiments with 500 μm diameter glass beads under ambient conditions in which both the electrical pulses and the light pulses emitted by the individual microsparks were observed and recorded. The thickness of the layer was about 5 mm.

Figure 7 shows oscilloscope traces of the electrical pulses for different values of the applied field E_A across the layer, for 500 μm beads under ambient air conditions. In Figure 7 (a) at $E_A \sim 10$ kV/cm, there are tens of low amplitude forward pulses with a smaller number of reverse pulses. Figures 7 (b) and (c) for $E_A \sim 12$ and 14 kV/cm, respectively, show a progressive increase in the number of microspark pulses and their amplitude with increasing applied field. The upward or forward pulses correspond to current flow in the same sense as the average current through the layer, and are current pulses due to microsparks. They are dominant and have the effect of increasing the time-average current through the layer. The downward or reverse pulses have, generally, a much lower amplitude and occur less frequently than the upward pulses. They are fast and similar in form to the upward pulses except for their sign. At present, we do not understand the mechanism responsible for this phenomenon.

Figure 7(d) shows the waveform of an individual (forward) pulse at $E_A \sim$ 14 kV/cm which has a very sharp rise (~ 15 to 20 μs), corresponding to the discharge period, followed by an exponential decay (corresponding to the charging period) having a time constant of ~ 160 μs. The fast rise time in the discharge period, supports our assumption of instantaneous discharge in our theoretical analysis.

Similar experiments were carried out using a single layer of glass beads of 6mm diameter, under ambient air conditions, which, generally, give the same form of results.

The measured spark repetition rate, f_B, as a function of the (applied) average field, E_A, for a single layer of 6mm glass spheres under ambient conditions is shown in Figure 8, which indicates that f_B increases (linearly) with increasing E_A, in qualitative agreement with the theoretical predictions. Here, f_B has a value between ~5 to 25 Hz.

In addition, a few experiments were carried out in which the oscilloscope traces for both light and electrical pulses were recorded for different values of the applied field, E_A, across the layer. Figure 9, shows an example of these tests with (one layer of) 6mm beads under ambient conditions at $E_A \sim$ 11.67 kV/cm. Here, the lower trace shows the electrical pulses and the upper trace represents their corresponding light pulses.

In this photograph a single light pulse is shown which is clearly associated with an electrial pulse. However, there are two other electrical pulses for which no corresponding light pulse can be observed in the photograph. This is due to the fact that the 1mm optical fiber, used for transmission of the emitted light pulses to the PM tube, only "sees" a small portion of the sample exposed to it and cannot detect the light pulses occurring at a distant location. In Figure 9, the light pulse has a sharp rise corresponding to the discharge period, followed by a relatively slow exponential decay having a time constant of ~ 10 to 20 ms, as opposed to ~ 100 μs for electrical pulses.

This photograph and the results of other similar experiments clearly indicate the existence of microsparks and pulsed light emission in a particulate layer for applied fields $E_A > E_{AB}$, the breakdown onset field. Furthermore, it is found that the spark repetition rate increases with increasing E_A.

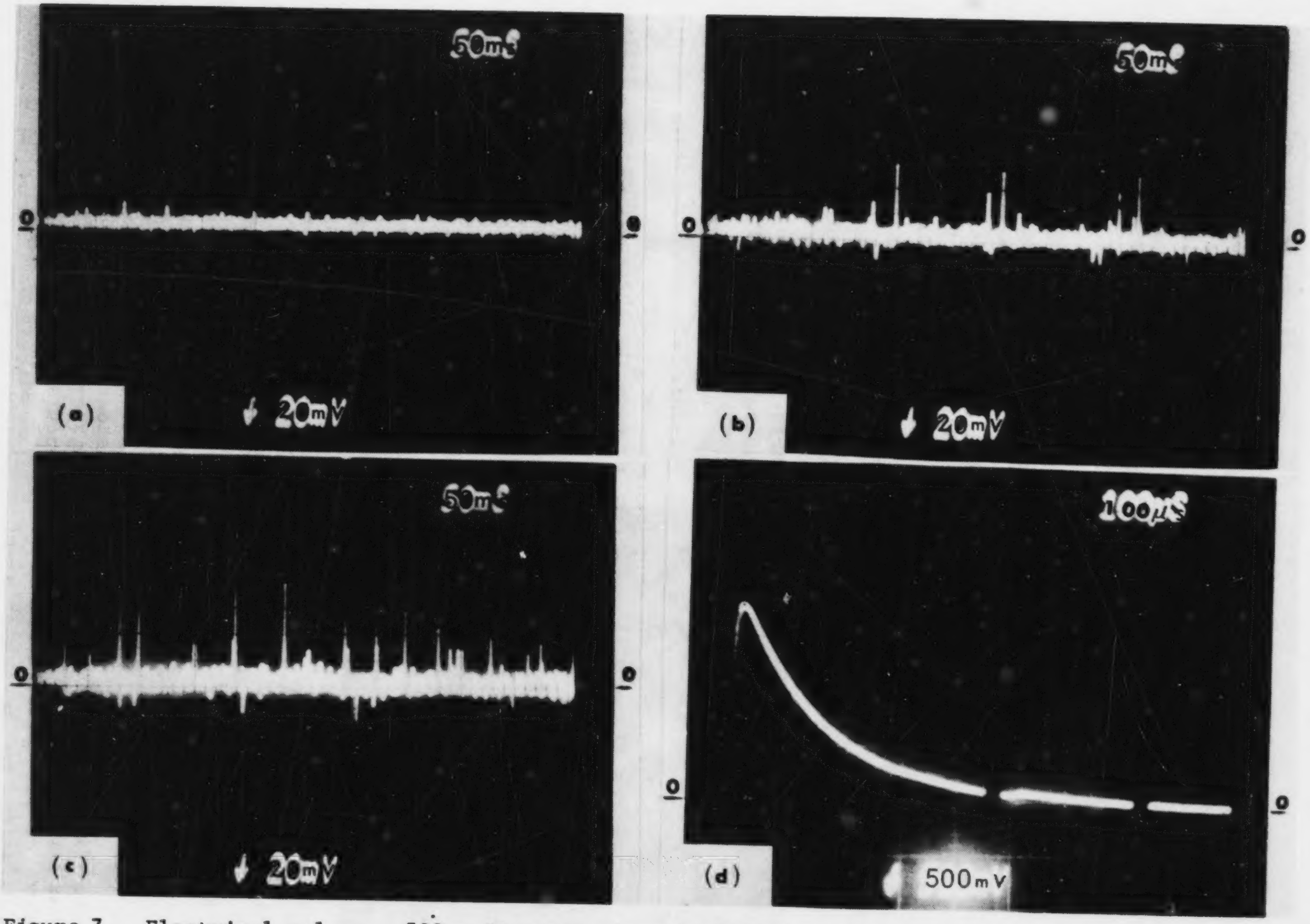

Figure 7. Electrical pulses. 500μm diameter glass beads under ambient conditions. (a) $E_A \sim$ 10 kV/cm; (b) $E_A \sim$ 12 kV/cm; (c) $E_A \sim$ 14 kV/cm; (d) waveform of forward electrical pulses at $E_A \sim$ 14 kV/cm.

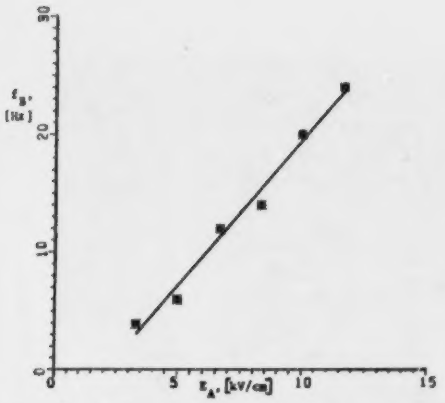

Figure 8. Experimental increase in the average spark repetition rate, f_B, with increasing the applied E_A. The solid line is the best fit to the data points.

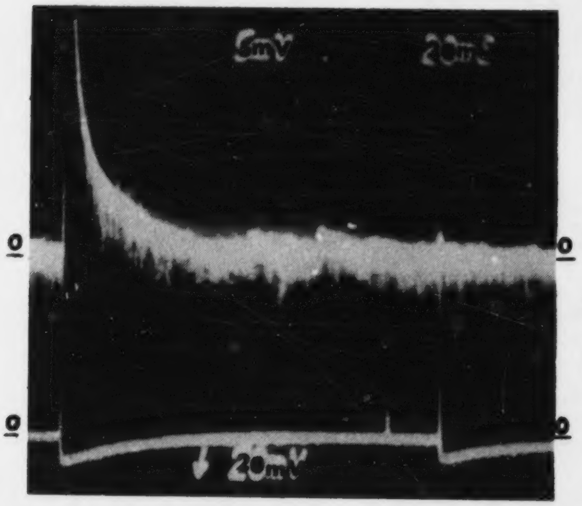

Figure 9. Upper trace, light pulses; lower trace, electrical pulses. 6 mm beads, ambient conditions. $E_A \sim 11.67$ kV/cm.

SUMMARY AND CONCLUSION

The first part of this paper presents a theory of electrical breakdown of precipitated ash layer which appears to be capable of explaining quantitatively, in terms of fundamental parameters, the onset of back discharge as microspark breakdown in and around the contacts between particles where the field is greatly enhanced above the average layer value. This theory enables one to predict the conditions required for the onset of the microspark breakdown of the layer and our calculations are in reasonable agreement with the experimental results. The theory treats the generalized case of combined surface and volume conduction and can be easily extended to consider the effect of different modes of compaction (2).

In an extension of the theory, the post-microspark breakdown behavior of the layer is qualitatively explained, in terms of a simplified equivalent lumped circuit. The theory predicts increases of sparking frequency and average current (and hence decrease of ρ_A) as the applied average field, E_A, exceeds the threshold average field, E_{AB}, for the onset of breakdown.

Experimental observations of microsparks confirm the existence of electrical and light pulses associated with them. Moreover, in all cases the spark repetition rate increases (linearly) with increasing E_A, as predicted by our theory.

ACKNOWLEDGEMENTS

This work was supported by the Electric Power Research Institute.

The work described in this paper was not funded by the U.S. Environmental Protection Agency and therefore the contents do not necessarily reflect the views of the Agency and no official endorsement should be inferred.

REFERENCES

1. Self, S. A., Moslehi, G. B., Mitchner, M. and Leach, R., "Electromechanics and Reentrainment of Precipitated Ash," Proc. International Conference on Electrostatic Precipitation, Monterey, CA, October 14-16, 1981.

2. Moslehi, G. B. and Self, S. A., "Electromechanics of Particulate Layers," 4th Symposium on Transfer and Utilization of Particulate Control Technology, Houston, Texas, October 11-15, 1982. (Session C-6, this conference)

3. L. L. Alston, editor, High-Voltage Technology, Chapter 4, Oxford University Press (1968).

4. McLean, K. J. and Huey, R. M., "Influence of Electric field on the Resistivity of a Particulate Layer," Proc. IEE, Vol. 121, No. 1, pp. 76-80 (Jan. 1974).

ELECTROMECHANICS OF PARTICULATE LAYERS

By: G. B. Moslehi and S. A. Self
High Temperature Gasdynamics Laboratory
Mechanical Engineering Department
Stanford University
Stanford, California 94305, U.S.A.

ABSTRACT

In previously reported work, a comprehensive theory of the electromechanics of a particulate layer was developed, treating it as a regular cubic array of equi-sized resistive spheres, allowing for both volume and surface conduction, and taking account of self-compression of the layer. The theory gives expressions for various quantities of interest including the contact angle θ_o, the maximum electric field E_{max}, the average compressive stress P_E and the apparent resistivity ρ_A, all in terms of the average layer current density J_A (or average field $E_A = \rho_A J_A$) and the system parameters.

In the present paper this theory is extended in two ways. First, explicit expressions for the quantities θ_o, E_{max}, P_E and ρ_A are given in the form of power laws (in E_A) in which the coefficients and exponents depend on the system parameters, in particular the resistivity ratio $\sigma = sa/\rho$, where a is the particle radius and s and ρ are, respectively, the (intrinsic) surface and volume (material) resistivities of the particles. These expressions should be operationally useful for interpreting experimental data. Second, the theory has been extended to include all of the six classical modes of compaction for equi-sized spheres. The results are qualitatively similar to those for the cubic array and are related to them by a set of multiplicative constants which are of order unity.

Measurements of the resistivity characteristics ρ_A (E_A) of layers of glass beads confirm the theoretical results both qualitatively and quantitatively.

BACKGROUND

In this section, the results of the theory of electromechanics of a current-carrying particulate layer are summarized. A detailed account of this theory is given in References 1 and 2, where the particulate layer is modeled as a regular cubic array of uniform spheres through which a steady current is flowing, as illustrated in Figure 1, which shows the distribution of electric field and current lines. Because the current must flow through the small contact areas between spheres, the current and field lines are concentrated near the contacts, and most of the resistance and voltage drop is associated with these regions.

The theory for the cubical array was based on the distribution of potential V for a single sphere of radius a with point contacts at opposite poles where current I enters and leaves (Figure 2). For combined volume and surface conduction the potential is (1,2)

$$V(r,\theta) = \left(\frac{\rho I}{4a}\right) F(\sigma,z,\mu) \equiv \frac{sI}{4}\left[\frac{F(\sigma,z,\mu)}{\sigma}\right] \quad . \tag{1}$$

Here $z \equiv (r/a)$, $\mu \equiv \cos\theta$, ρ is the volume resistivity, s is the surface resistivity and the nondimensional resistivity ratio $\sigma \equiv (sa/\rho)$; a measure of the relative contributions of surface and volume conduction. Figure 3 shows computed results for $F(\theta)$, for points on the surface with σ as a parameter.

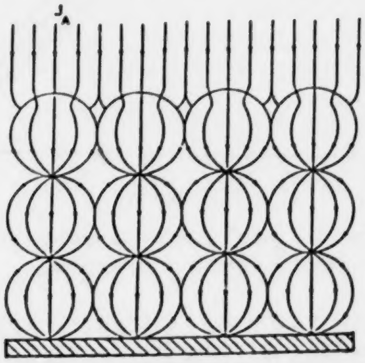

Figure 1. Model for current flow through array of resistive spheres.

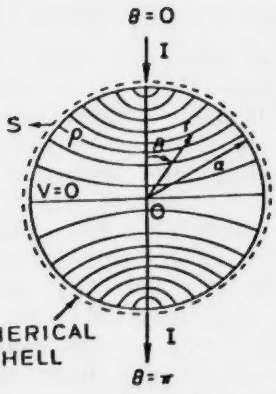

Figure 2. Model for current flow through single sphere with point contacts showing equipotentials.

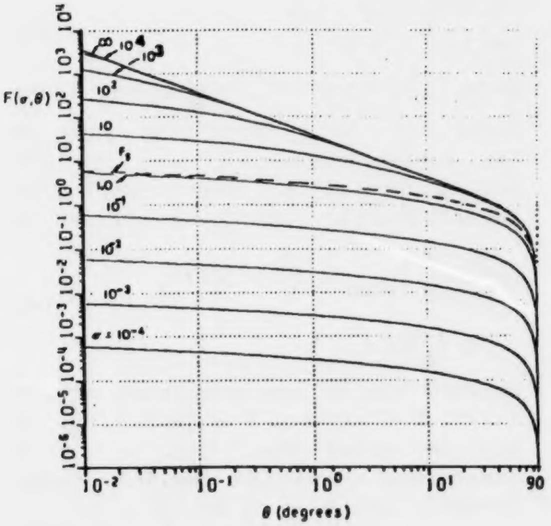

Figure 3. Function $F(\sigma,\theta)$ for potential distribution at the surface (r=a) for current flow across a sphere. For comparison F_s is shown as a broken line, where $F_s \equiv \lim\limits_{\sigma\to 0} (F/\sigma)$.

This solution for $V(r,\theta)$ was used to find an approximate solution for the case of a finite contact angle θ_0, from which the electric field distribution in and around the contact between spheres was calculated. From this field the electrical attractive force between two spheres was calculated as a function of contact angle θ_o. Then using the Hertz formula from elastic deformation theory, the contact angle θ_o due to self-compression was determined.

In this manner self-consistent equations (with respect to self-compression) were derived for the following quantities of interest: (i) the contact angle θ_o between spheres; (ii) the average resistivity ρ_A of the layer; (iii) the average compressive stress P_E in the layer and the attractive electrical force between two contacting particles F_E and (iv) the maximum electric field E_{max} in the gap between contacting spheres (2)

$$\theta_o = D^{1/5} \mathscr{E}^{2/5} \tag{2}$$

$$\rho_A = \begin{cases} \rho F(\sigma,\mu_o), \text{for} \sigma \neq 0 \\ saF_s(\mu_o), \text{for} \sigma = 0 \end{cases} \tag{3}$$

$$P_E = \frac{F_E}{4a^2} = \frac{\pi}{4} \varepsilon_o A(\sigma) D^{-2/5} \mathscr{E}^{6/5} \tag{4}$$

$$E_{max} = D^{-2/5} \mathscr{E}^{1/5} \tag{5}$$

Here $F_s \equiv \lim_{\sigma \to o}(F/\sigma)$, and D and A are constants, being functions only of the sphere radius, a, and its material properties. The characteristic electric field $\mathscr{E}$ is defined as

$$\mathscr{E} \equiv \theta_o^2 E_{max} \equiv \theta_o^2 (F'/F) E_A$$
$$\equiv E_A / K(\sigma,\theta_o) \tag{6}$$

where F and F' are evaluated at z = 1, $F' \equiv dF/d\mu$ and $K \equiv (F/F')/\theta_o^2$. It may be noted that Eqs. 2 and 6 constitute a pair of implicit equations determining θ_o and $\mathscr{E}$.

The field enhancement factor FEF $\equiv (E_{max}/E_A)$ as a function of contact angle θ_o and resistivity ratio σ is numerically evaluated and the results are shown in Figure 4.

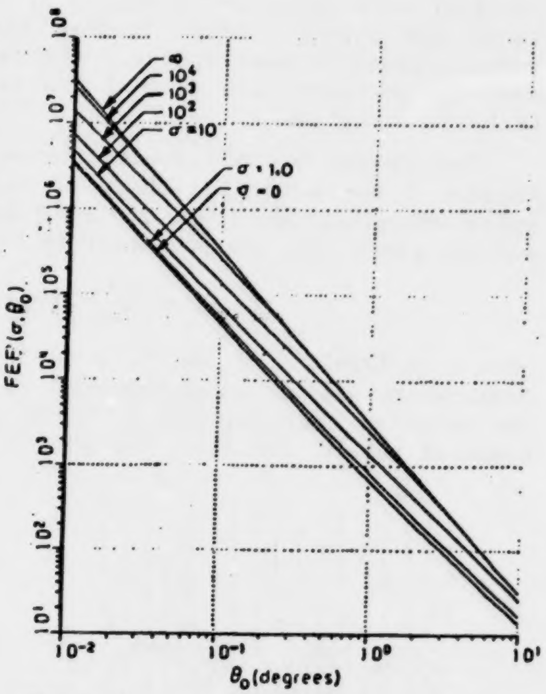

Figure 4. Field enhancement factor (FEF) dependence on σ and θ_o.

The value of D in Eqs. 2-5, can be evaluated from $D = \pi \varepsilon_o AB$, where $\varepsilon_o \sim 8.854 \times 10^{-12}$ F/m is the vacuum permitivity, $A(\sigma)$ is a constant given in Table 1, and B is given by $B \equiv 3(1 - \nu^2)/4Y$. Here, Y is Young's modulus and ν is Poisson's ratio.

In the special case of pure volume conduction ($\sigma \to \infty$), which applies for high temperature and low humidity, we have $K \to K_v \simeq 1$, so that $\mathscr{E} \approx E_A$ which when substituted in Eqs. 2-5 results in a set of explicit equations (2). Here, the values of A (and hence D) at $\sigma \to \infty$, denoted by A_v and D_v, should be used. In the case of pure surface conduction (σ=0), which applies for low temperature and high humidity, the quantity $K \to K_s$ is not a universal constant but is weakly dependent on E_A and on the material

TABLE 1. EXPLICIT FORM OF THE SET OF SELF-CONSISTENT ELECTROMECHANICAL EQUATIONS OF A PARTICULATE LAYER

$$\theta_o = b_\theta \, D^{(\alpha/2)} \, (E_A)^{\alpha}$$

$$\rho_A = \begin{cases} b_F \rho D^{(m_F/2)} (E_A)^{m_F} , & \text{for } \sigma \neq 0 \\ b_F (sa) \, D^{(m_F/2)} (E_A)^{m_F} , & \text{for } \sigma = 0 \end{cases}$$

$$P_E = b_P (\pi/4) \, A(\sigma) \, \varepsilon_o D^{(3\alpha/2-1)} (E_A)^{3\alpha}$$

$$E_{max} = b_E \, D^{(\alpha/4 - 1/2)} (E_A)^{\alpha/2}$$

σ	b_θ	b_F	b_P	b_E	α	m_F	$A(\sigma)$
0	0.6767	1.6906	0.3099	0.8226	0.4279	-0.0697	2.139
1	0.7484	1.2727	0.4191	0.8651	0.4314	-0.0805	2.115
10	1.0391	4.3000	1.1221	1.0194	0.4430	-0.1267	1.976
10^2	1.5103	3.0557	3.4451	1.2289	0.4502	-0.2473	1.582
10^3	1.2112	0.8887	1.7766	1.1005	0.4184	-0.3735	1.299
10^4	0.9865	0.7064	0.9600	0.9932	0.3996	-0.3940	1.274
∞	0.9766	0.7042	0.9314	0.9882	0.3987	-0.3942	1.274

NOTES: (i) All values in (MKS) SI Units.

(ii) For intermediate values of σ, which are not given in the table, and for a given E_A the parameters θ_o, ρ_A, P_E and E_{max} may be evaluated using a (logarithmic) graphical interpolation procedure.

(iii) Value of D in the above table can be evaluated from $D = \pi\varepsilon_o AB$, with $\varepsilon_o \sim 8.854 \times 10^{-12}$ F/m. The constant B is given by $B = 3(1 - \nu^2)/4Y$. For a typical glassy fly ash we take $Y \sim 7.5 \times 10^{10}$ N/m^2 and $\nu \sim 0.25$, therefore $B = 9.4 \times 10^{-12}$ m^2/N $\sim 10^{-11}$ m^2/N.

properties. Here, the values of D_s and A_s are evaluated at σ=0. As a result, $\mathscr{E} = E_A/K_s$, which when used in Eqs. 2-5 provides explicit results (2).

EXPLICIT FORM OF THE SET OF ELECTROMECHANICAL EQUATIONS

In the previous section we outlined the results of an extensive analysis of the electromechanics of a particulate layer prior to the onset of micro-spark breakdown. In particular, for the two special cases of pure volume and pure surface conduction explicit analytical expressions were derived which each provide a set of operationally useful tools for prediction of the behavior of the layer under these limiting conditions. Equations for the general case of combined volume and surface conduction were also given. However, these relationships are not explicitly expressed in terms of the (applied) average field E_A (or the average current density J_A). They are in the form of a set of transcendental equations which must be solved numerically. This complexity of the governing equations of the layer clearly creates some inconvenience in practical applications.

In this section we numerically solve the set of general equations of the layer. It is shown that in the range of contact angles of practical importance all the quantities of interest depend on the average field E_A according to a power law. Applying a least squares curve fit to the numerical results the set of electromechanical equations of the layer are derived in the form of power law relationships whose exponents are functions (of σ and hence) of temperature and humidity. These explicit expressions are useful from an operational point of view in interpreting ash resistivity characteristics, for example.

POWER LAW EQUATIONS

A close examination of Figures 3 and 4, where log-log scales are used, reveals that, to a close approximation, in the range of the contact angles of practical interest ($\theta_o \sim 0.05°$ to $1°$) the functions $F(\sigma,\theta_o)$ and $FEF(\sigma,\theta_o)$ depend on θ_o according to a power law of the form

$$F\,(\sigma,\theta_o) = a_F(\theta_o^{\,n_F}) \tag{7}$$

and

$$FEF\,(\sigma,\theta_o) = a_{FEF}\,(\theta_o^{\,n_{FEF}}) \tag{8}$$

It follows from the definitions of FEF ($\equiv F'/F$) and K ($\equiv (F/F')/\theta_o^2$) that the dependence of the functions $F'(\sigma,\theta_o)$ and $K(\sigma,\theta_o)$ on θ_o also have power law forms

$$F'\,(\sigma,\theta_o) = a_{F'}(\theta_o^{\,n_{F'}}) \tag{9}$$

$$K\,(\sigma,\theta_o) = a_K(\theta_o^{\,n_K}) \tag{10}$$

In the above relationships both the exponents n and the numerical coefficients a are functions of σ. A least squares curve fit procedure is applied to the numerical results for F,F', FEF and K (for the contact angles between 0.05° and 1°) and values of a and n are determined for each case.

The next step is to relate the contact angle θ_o and the applied average field E_A in an explicit manner. Using Eqs. 6 and 10, with Eq. 2, after some simplifications, gives

$$\theta_o = b_\theta\, D^{(\alpha/2)}(E_A)^\alpha \tag{11}$$

where

$$b_\theta \equiv (a_K)^{-\alpha} \tag{12}$$

and

$$\alpha \equiv 2/(5 + 2n_K) \tag{13}$$

Substitution of Eq. 11 into Eqs. 7-10 results in a set of explicit expressions for the functions F, F', FEF and K in terms of E_A

$$F\left(\sigma, E_A\right) = b_F\, D^{(m_F/2)} \left(E_A\right)^{m_F} \tag{14}$$

and

$$K\left(\sigma, E_A\right) = b_K\, D^{(m_K/2)} \left(E_A\right)^{m_K} \; . \tag{15}$$

The expressions for $F'(\sigma, E_A)$ and $FEF(\sigma, E_A)$ are similar to Eqs. 14 and 15. In Eq. 14, $b_F \equiv a_F \left(b_\theta\right)^{n_F}$ and $m_F \equiv \alpha\, n_F$ where b_θ and α are given by Eqs. 12 and 13, respectively. The coefficients $b_{F'}$, b_{FEF} and b_K and the exponents $m_{F'}$, m_{FEF} and m_K are given by identical relationships with the exception that in each case the index F should be replaced by the appropriate index (F', FEF or K) corresponding to the parameter of interest.

At this point, from Eqs. 6 and 15 the dependence of the characteristic field $\mathcal{E}$ on the average field E_A can be determined which when substituted into Eqs. 4 and 5 gives the explicit equations for P_E and E_{max} in the following form:

$$P_E = b_P\, (\pi/4)\, A(\sigma)\, \varepsilon_o D^{(3\alpha/2-1)} \left(E_A\right)^{3\alpha} \; . \tag{16}$$

and

$$E_{max} = b_E D^{(\alpha/4\, -\, 1/2)} \left(E_A\right)^{\alpha/2} \tag{17}$$

Here $b_P \equiv \left(a_K\right)^{-3\alpha}$ and $b_E \equiv \left(a_K\right)^{-\alpha/2}$.

Values of b_θ, b_P, b_E and α are evaluated and the results are given in Table 1. Also given are the values of the constant $A(\sigma)$. For the sake of completeness the explicit equation for ρ_A is also given as

$$\rho_A = \begin{cases} b_F \rho D^{(m_F/2)} \left(E_A\right)^{m_F}, & \text{for } \sigma \neq 0 \\ b_F (sa)\, D^{(m_F/2)} \left(E_A\right)^{m_F}, & \text{for } \sigma = 0 \end{cases} \tag{18}$$

where use is made of Eqs. 3 and 14. Values of b_F and m_F are also given in Table 1.

Table 1 presents the complete set of self-consistent electromechanical relationships of a current-carrying layer of uniform resistive spheres, in an explicit form. These expressions relate the values of θ_o, ρ_A, P_E and E_{max}, to the (externally applied) average electric field E_A (or current density J_A) with the resistivity ratio σ as a parameter. These explicit expressions are all in the form of power law relationships whose exponents are functions of σ. The coefficients b which arise from the least squares curve fit to the numerical solutions of the implicit equations governing the behavior of the layer, are also functions of σ.

To evaluate the parameters of interest (θ_o, ρ_A, P_E, E_{max}, etc.) as a function of E_A, for a given value of σ, one can find the values of $A(\sigma)$, α, m_F and coefficients b_θ, b_F, b_P, and b_E from Table 1. Then one can calculate the values of the elastic properties constant B and the material properties constant D. Finally, for the specified value of σ, the functions $\theta_o(E_A)$, $\rho_A(E_A)$, $P_E(E_A)$ and E_{max} (E_A) can be established, using Eqs. 11, 18, 16 and 17, respectively. In general, a knowledge of particle radius, a, surface resistivity, s, and (intrinsic) volume resistivity ρ of the particle material and their variation with temperature and humidity is necessary for evaluation of σ (and ρ_A).

From Table 1 one may note that the power law dependence of θ_o, P_E and E_{max} on E_A are rather insensitive to σ, because α varies very slowly with σ (by a maximum factor of ~ 1.13). The coefficients b vary rather more (by maximum factors of ~ 2.2 and ~ 1.5 for b_θ and b_E, respectively) but no more than a factor of ~ 11 (in the case of b_P). In the case of ρ_A, the power law dependence on σ is more pronounced. Here, the exponent m_F decreases from ~ - 0.07 for surface conduction (σ=0) to ~ - 0.4 for pure volume conduction ($\sigma \rightarrow \infty$); a factor of ~ 5.7 difference. The variation of b_F with σ is relatively slight (a maximum factor of ~ 6).

THE EFFECT OF PACKING MODE ON THE ELECTROMECHANICS OF THE LAYER

Our analysis so far applies to the case of a regular cubic array of uniform spheres. However, in practice the particles are usually more densely packed which suggests the necessity of studying the effect of packing mode of spheres on the behavior of the layer.

In this section, the electromechanical equations for all six classical regular arrays of equi-sized spheres are derived in a unified form.

Of the many types of packing of identical spheres, we consider here only regular stable arrays. Such arrays are composed of repeated planar layers which are geometrically systematic (3).

The parameter which characterizes the type of a (single) layer is the base angle, α_b, which is the angle between the two sets of rows having different directions. This angle has a value between 60° and 90°. In the following analysis we consider only the two particular cases of a square base layer (α_b = 90°) and a simple rhombic base layer (α_b = 60°). It may be noted that the number of contacts N_b between any sphere and its neighbors in the layer is N_b = 4 for the square based layer and N_b = 6 for the rhombic based layer (Figures 5a and 6a).

For each of these cases there are three simple geometric ways of stacking adjacent layers, thus producing a total of six different types of array. Topologically, only four of these are distinct, since two of the square based arrays are equivalent to two of the rhombic based arrays, but have different spatial orientations (3,4). However, since we are interested in the application to current flow normal to the base plane (resting for instance on an electrode), we must consider the six cases as distinct. In this connection it may also be noted that the N_b contacts, mentioned above, do not carry current, since they lie on the equipotential mid-plane of the layer.

These six classical modes of packing for spheres are illustrated in Figures 5 and 6 for the cases of square and rhombic bases, respectively (3,4,5). Each mode is designated by a letter, S (≡ square) or R (≡ rhombic), followed by a number 1, 2 or 3 which refers to one of the three ways of stacking the next layer. The two pairs of cases (S-2 and R-1) and (S-3 and R-3) are the ones mentioned earlier which are topologically identical but have different spatial orientations.

At this point an additional complication should be mentioned; that is the concept of twinned or tripled packings, as opposed to the basic or standard packing.

Figures 7(a) and 7(b) illustrate two alternative ways of stacking (I and II) for orthorhombic (S-2) and rhombohedral (R-3) arrays, respectively. In the standard packing either one of these ways is used exclusively, and the whole array is symmetric about the mid-plane of any layer. However, it is possible to create twinned arrays with the sequence 0 I II or 0 II I where 0 denotes the base layer, which do not have the basic symmetry. In the case of the tetragonal-sphenoidal array (Figure 7(c)) there are three alternative ways of constructing the next layer which gives rise to two types of twinned packing and one type of tripled packing, with the sequence 0 I II III for example (3).

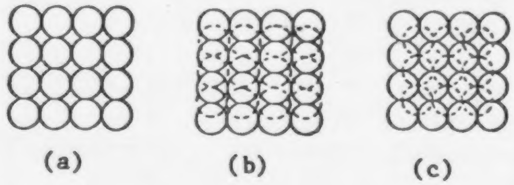

Figure 5. Regular arrays of identical spheres (3,4). Square base layers (S). (a) simple cubic (S-1); (b) orthorhombic (S-2); (c) pyramidal (S-3). Top view; solid lines represent the first layer and dotted lines the second layer.

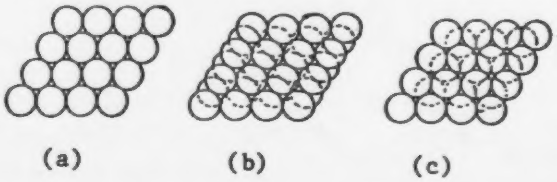

Figure 6. Regular arrays of identical spheres (3,4). Rhombic base layers (R). (a) cubical-tetrahedral (R-1); (b) tetragonal-sphenoidal (R-2); (c) rhombohedral (R-3). Top view; solid lines represent the first layer and dotted lines the second layer.

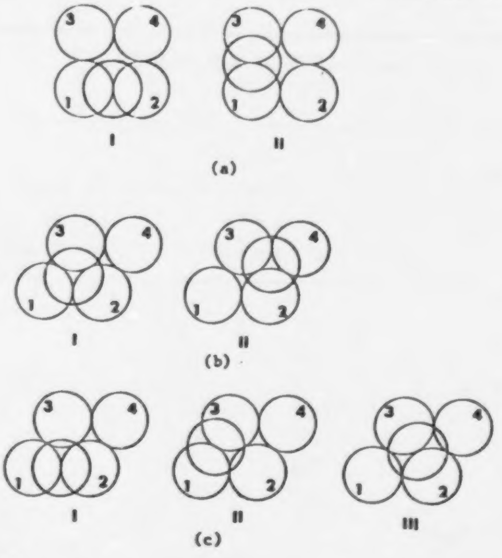

Figure 7. Alternative ways of stacking of identical spheres (3). (a) orthorhombic array (S-2); two alternative ways. (b) rhombohedral array (R-3); two alternative ways. (c) tetragonal-sphenoidal (R-2); three alternative ways. Top view; numbered spheres represent the lower layer, denoted by 0.

In the analysis which follows, we consider only the standard packing for all cases except for the rhombohedral array (R-3), where we treat only the twinned packing. The reason for this exception is that from the electrical point of view the twinned rhombohedral array has the desired form of symmetry which is amenable to a simple analysis.

For the set of packings considered, the 2N current-carrying contacts that each sphere makes with the layer above and the layer below can be arranged in pairs which form current paths lying along a diameter of the sphere. Furthermore, when $N = 1$ the colatitude angle α_c that this path makes with the z-axis normal to the layers is zero, while when $N > 1$, the angles α_c for each current path are identical but the paths have different azimuthal angles. This fact is essential for the electrical analysis, developed later, and is the reason for restricting the class of arrays to those mentioned.

In general each sphere has a total of N_t ($= N_b + 2N$) contacts with other spheres, which is sometimes called the coordination number. Values of N_t, N_b, N and cos α_c for the six arrays considered are listed in Table 2.

Table 2. CHARACTERISTICS OF REGULAR ARRAYS OF IDENTICAL SPHERES.

BASE →	SIMPLE SQUARE BASE (S) $N_b = 4$			SIMPLE RHOMBIC BASE (R) $N_b = 6$		
Type of → Array	Simple Cubic (S-1) Standard	Orthorhombic (S-2) Standard	Pyramidal (S-3) Standard	Cubical-Tetrahedral (R-1) Standard	Tetragonal-Sphenoidal (R-2) Standard	Rhombohedral (R-3) Twinned
N_t	6	8	12	8	10	12
N	1	2	4	1	2	3
$\cos \alpha_c$	1	$\sqrt{3}/2$	$\sqrt{2}/2$	1	$\sqrt{3}/2$	$\sqrt{2}/\sqrt{3}$
P	0.4764	0.3954	0.2595	0.3954	0.3019	0.2595
A_c	$4a^2$	$4a^2$	$4a^2$	$2\sqrt{3}a^2$	$2\sqrt{3}a^2$	$2\sqrt{3}a^2$
ℓ_c	$2a$	$\sqrt{3}a$	$\sqrt{2}a$	$2a$	$\sqrt{3}a$	$2\sqrt{2}a/\sqrt{3}$
V_c	$8a^3$	$4\sqrt{3}a^3$	$4\sqrt{2}a^3$	$4\sqrt{3}a^3$	$6a^3$	$4\sqrt{2}a^3$
$\theta_o/(\theta_o)_c$	1	0.9441	0.8706	1	0.9441	0.9221
$E_{max}/(E_{max})_c$	1	0.9716	0.9330	1	0.9716	0.9603
$P_E/(P_E)_c$	1	1.4575	1.8661	1.1547	1.6829	2.2176
$\rho_A/(\rho_A)_c$	1	0.5774	0.3536	0.8660	0.5000	0.3536

For our purposes we define a unit cell with an effective base area A_c, effective height ℓ_c and volume $V_c = A_c \ell_c$.

By geometry it can be shown that

$$A_c = [N_b \tan (\pi/N_b)]a^2 \tag{19}$$

and

$$\ell_c = 2 a \cos \alpha_c \tag{20}$$

Since the volume of a single sphere occupying the cell is $V_s = (4/3)\pi a^3$, the porosity P can be evaluated from $P \equiv 1 - V_s/V_c = 1 - V_s/A_c\ell_c$. The values A_c, ℓ_c, V_c and P are listed in Table 2 for the six simple arrays considered.

ELECTROMECHANICAL EQUATIONS - GENERAL FORM

For the basic cubic array each sphere has a single diametral current path ($N = 1$) parallel to the z-axis (normal to the layer) so that $\cos \alpha_c = 1$, and the basic electromechanical equations were solved to give the derived quantities θ_o, ρ_A, P_E and E_{max} (Eqs. 2-5) for this case.

For the other five regular arrays to be considered now, the number of diametral current paths N varies up to $N = 4$ and they make different colatitude angles α_c to the z-axis with the N paths disposed at different azimuthal angles ϕ around the z-axis. We now have to take these facts into account to determine the modifications to the expressions 2-5 for the derived quantities for the five additional cases considered.

The basic solution for the potential due to current flow between one pair of diametrically opposed point contacts (Eq. 1) can be used to find the total potential due to a set of N diametrically opposed point contacts (at different angles α_c and ϕ) by superposition. However, because the potential only varies rapidly in the neighborhood of each current-carrying contact, it is a good approximation for calculating the fields and stresses around each contact, to ignore the contribution to the potential due to the other current-paths. Thus, the behavior in the region of each contact can be treated as decoupled from the effects of the presence of the other contacts. With this approximation the treatment for the simple cubic array may be generalized as follows.

The potential drop across each half unit cell is obtained from Eq. 1 with $z = 1$ and $\mu = \mu_o$ as

$$V_o = \begin{cases} \rho\ [(I/N)/(4a)]\ F\ (\sigma,\mu_o) & , \quad \text{for } \sigma \neq 0 \\ (sa)\ [(I/N)/(4a)]\ F_s(\mu_o) & , \quad \text{for } \sigma = 0 \end{cases}$$

where (1/N)th of the current I per cell flows through each contact. Hence, the resistance per sphere is $R = 2\ V_o/I$. Equating this to the average resistance per unit cell $\rho_A\ell_c/A_c$, we find for the average layer resistance

$$\rho_A = \begin{cases} [(A_c/\ell_c)/(2aN)]\ \rho\ F\ (\sigma,\mu_o) & , \quad \text{for } \sigma \neq 0 \\ [(A_c/\ell_c)/(2aN)](sa)\ F_s(\mu_o) & , \quad \text{for } \sigma = 0 \end{cases} \tag{21}$$

The average compressive stress is given by

$$P_E = [NF_E\ (\cos\ \alpha_c)]/A_c \tag{22}$$

where F_E is the attractive electrical force at one contact, in the direction of the current path.

In the earlier work for a cubic array, we defined a characteristic field (via Eq. 6) in terms of E_A (which in that case was parallel to the current path) to determine (via Eq. 2) the contact angle θ_o. In the general case, when the current path makes an angle α_c to E_A, it is clear that we can use the same formalism to calculate θ_o, but that we should use ($E_A \cos \alpha_c$) in place of E_A in Eq. 6. Thus in general, E_{max} and F_E can be evaluated in a similar way. Collecting together the results for the derived quantities of interest, making use of Eqs. 19 and 20, we have in general, in place of Eqs. 2-5 for the basic cubic case:

$$\theta_o = D^{1/5} (\cos \alpha_c)^{2/5} \mathscr{E}^{2/5} \tag{23}$$

$$\rho_A = \begin{cases} \{N_b \tan(\pi/N_b)]/[4N(\cos\alpha_c)]\}\rho F(\sigma,\mu_o) & \text{, for } \sigma \neq 0 \\ \{[N_b \tan(\pi/N_b)]/[4N(\cos\alpha_c)]\}(sa)F_s(\mu_o), & \text{for } \sigma = 0 \end{cases} \tag{24}$$

$$P_E = \{N/[N_b \tan (\pi/N_b)]\} \pi \varepsilon_o A (\sigma) D^{-2/5} (\cos \alpha_c)^{11/5} \mathscr{E}^{6/5} \tag{25}$$

$$E_{max} = D^{-2/5} (\cos \alpha_c)^{1/5} \mathscr{E}^{1/5} \quad . \tag{26}$$

In these equations $\cos \alpha_c$ is given by Table 2, and $\mathscr{E}$ is given by Eq. 6.

For the simple cubic array, $N_b = 4$, $N = 1$, $\cos \alpha_c = 1$, and Eqs. 23-26 reduce to Eqs. 2-5 as they should.

For comparison, these derived quantities can be normalized on the expressions for the simple cubic case (Eqs. 2-5)to give multiplicative factors which are functions only of $\cos \alpha_c$, N and N_b which define the various packing arrangements. Thus

$$\theta_o/(\theta_o)_c \simeq (\cos \alpha_c)^{2/5} \tag{27}$$

$$\rho_A/(\rho_A)_c = [N_b \tan (\pi/N_b)]/[4N \cos \alpha_c] \tag{28}$$

$$P_E/(P_E)_c \simeq [4N (\cos \alpha_c)^{11/5}]/[N_b \tan (\pi/N_b)] \tag{29}$$

$$E_{max}/(E_{max})_c \simeq (\cos \alpha_c)^{1/5} \tag{30}$$

Here $(\ )_c$ refers to the parameter of interest for the cubic array. It should be noted that these relations are only approximate because for a given E_A, Eqs. 6 and 23, solved together to find $\mathscr{E}$ and θ_o, will give values that depend weakly on $\cos \alpha_c$.

The multiplicative factors for the various packing modes considered are evaluated numerically and listed in Table 2. From Table 2 it is seen that the factors relating the derived quantities for the various packing modes to those of the simple cubic array are all of order unity. For a given average field E_A, the contact angle θ_o and maximum field at the contacts E_{max} are quite insensitive to packing mode. In general the cohesive stress in the layer increases with the number of current-carrying contacts N, as might be expected, being a maximum for the close-packed rhombohedral array (a factor~2.2

higher than for the simple cubic array). On the other hand the average layer resistivity decreases with increasing number of parallel current paths N, as might be expected, being lowest for the pyramidal and rhombohedral arrays (a factor ~ 3 lower than the cubic array).

When equi-sized spheres are packed under gravity, for instance in a resistivity cell, it is probable that the packing mode approximates the rhombohedral or pyramidal types which have the minimum porosity, so that the quantitative results for these cases are most appropriate to use for comparison with measurements.

EXPERIMENTS WITH GLASS BEADS

The theory described in the preceeding sections applies to equi-sized spherical particles which is, admittedly, rather idealized. However, treatment of the case of a randomly packed bed of polydisperse spheres appears to be quite intractable. Therefore, it is important to devise some experimental tests of the theory to check how far it describes the behavior of particulate layers in practice.

One aspect of the theory which is amenable to a fairly straightforward test is the prediction of the dependence of the apparent layer resistivity ρ_A on the applied field E_A, and how this varies with the ambient conditions through the ratio, σ, of volume to surface conduction.

Using a standard resistivity cell (ASME Power Test Code 28) we have made measurements of ρ_A, as a function of E_A. For these experiments, glass beads (450-500 μm dia.) are used rather than fly ash, which is a glassy material. Since the beads are monodisperse, smooth spheres of uniform properties, it is to be expected that more reproducible and interpretable results should be obtained. In each experiment a new layer of beads was used from the same supply sample. The procedure used was standard. In particular the weight loading the top electrode was designed to compress the layer to the standard compressive stress of ~ 10 g wt./cm^2. In addition, the layer was ~ 5mm thick. In each experiment sufficient time (~ 1 hour) was given to the sample in order to reach equilibrium with the conditions of the oven (i.e. temperature and humidity). The electric current readings were also performed after a period of ~ 2 minutes following each step change made in the magnitude of the applied voltage. This period is found to be long enough to let transients die out.

Figure 8a shows a few examples of the measured apparent resistivity, ρ_A, of the layer as a function of the (applied) average field, E_A, for different values of (dry bulb) temperature, t_{db}, in range of ~ 20° to 185°C. Table 3 summarizes the experimental conditions in these tests and a number of additional experiments which are not shown in Figure 8a. This table gives the values of t_{db} and relative humidity P_r for each test. For the cases in which $t_{db} < 30°C$ the conditions of the oven were identical to those of ambient air, except for Experiment #1 in which the humidifier was used in order to achieve a humidity of ~ 100% at $t_{db} \sim 28°C$. In all the other cases where $t_{db} > 30°C$, the ambient air was heated to the specified oven temperature, without any change in the specific humidity. However, the relative humidity in these cases is varied, with the lower values corresponding to a higher oven temperature. The general features of $\rho_A(E_A)$ characteristics are as follows.

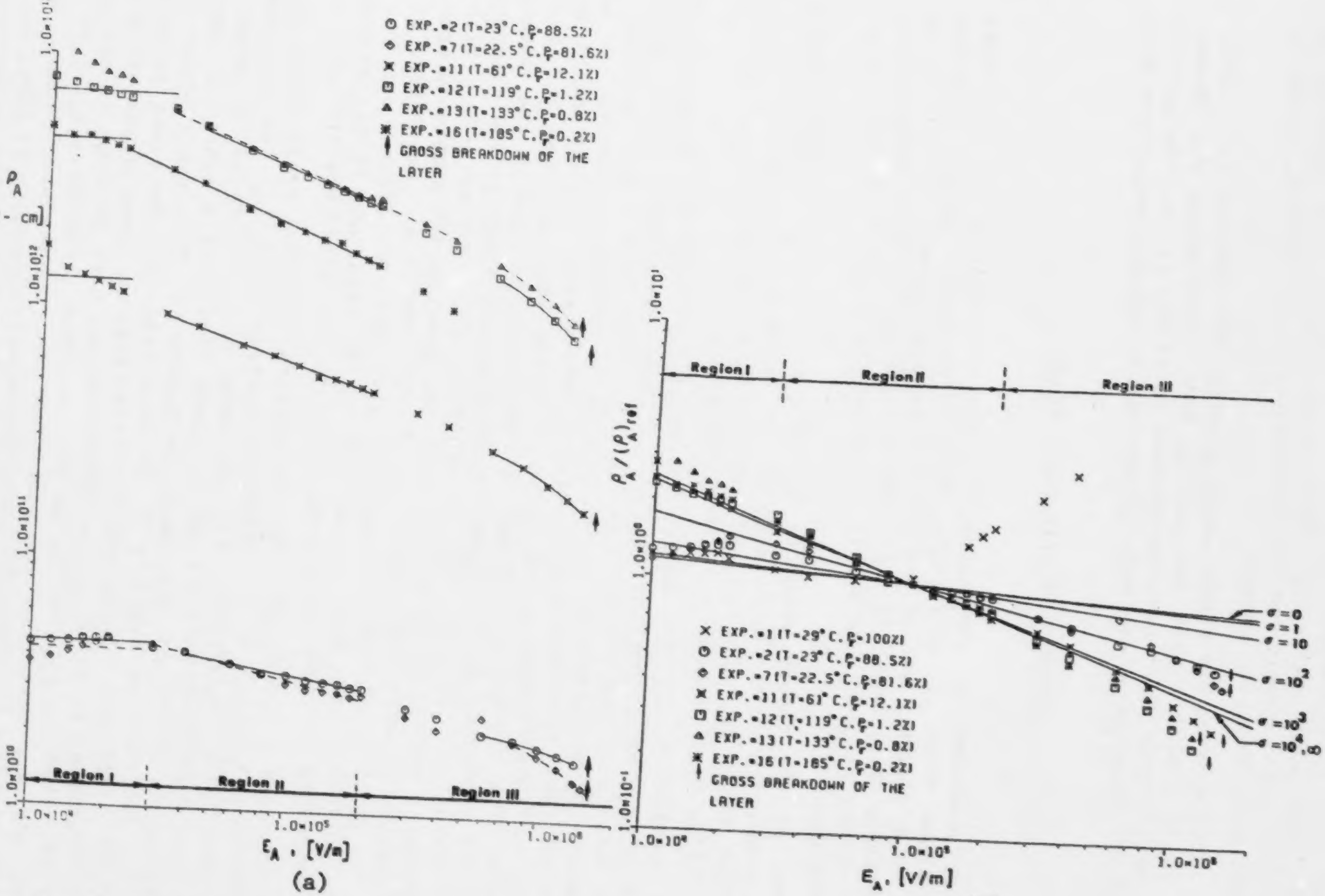

(a)

(b)

Figure 8. Resistivity cell measurements at different values of temperature; Glass beads; $D_p \sim 450 - 500\ \mu m$. Experimental conditions and results are given in Table 3. (a) log-log scale showing $\rho_A = b(E_A)^m$ in Region II (power law form). Solid (or dotted) lines are the best fit to the experimental results. (b) Normalized resistivity data. Solid lines represent the theoretical results of power law expressions (for Region II).

TABLE 3. RESULTS OF LEAST SQUARES CURVE FIT TO THE EXPERIMENTAL DATA POINTS

	Oven Condition		Region I, $\rho_A \approx$ const.	Region II $\rho_A = b(E_A)^m$ ρ_A in [Ω - cm] E_A in [kV/cm]		Region III, Gross Breakdown
No.	t_{db}, [°C]	P_r, [%]	ρ_A, [Ω - cm]	b	m	E_{GB}, [kV/cm]
1	28	100	9.24×10^7	7.54×10^7	-0.077	----
2	23	~ 88.5	4.56×10^{10}	2.53×10^{10}	-0.172	15.8
3.	22.5	~ 82	5.84×10^{10}	4.97×10^{10}	-0.175	16.0
4	23	~ 81	9.82×10^9	6.95×10^9	-0.210	13.4
5	22.5	~ 80	3.07×10^{10}	2.07×10^{10}	-0.230	16.0
6	22	~ 78	9.83×10^{10}	7.92×10^{10}	-0.230	----
7	22.5	~ 81.6	4.25×10^{10}	3.37×10^{10}	-0.235	15.8
8	29	~ 70	5.17×10^{10}	4.44×10^{10}	-0.259	16.0
9	46	23.2	----	6.28×10^{11}	-0.352	16.0
10	46	22.9	----	5.56×10^{11}	-0.337	16.0
11	61	12.1	1.27×10^{12}	6.14×10^{11}	-0.344	15.4
12	119	1.2	7.12×10^{12}	3.55×10^{12}	-0.408	13.8
13	133	0.8	----	3.64×10^{12}	-0.407	12.6
14	151	0.5	----	3.41×10^{12}	-0.382	13.4
15	162	~ 0.4	4.54×10^{12}	2.71×10^{12}	-0.337	12.0
16	185	~ 0.2	4.60×10^{12}	2.12×10^{12}	-0.420	----

(--) means: (i) "No Data Taken" or (ii) "No Data Available"

We can divide the $\rho_A(E_A)$ graph into three regions:

i. For an average field between 10^4 V/m and $(3-4)\times10^4$ V/m, the apparent resistivity in most cases is approximately constant (Region I in Figure 8a). This is due to the fact that the compression resulting from the electric stress is less than that due to the weight of the upper electrode. In fact, from our theory the average compressive stress of ~ 10 g wt./cm^2, corresponds to $E_A \sim 3.6 \times 10^4$ V/m for the case of pure volume conduction ($\sigma \rightarrow \infty$) and $E_A \sim 1.73 \times 10^5$ V/m for the case of pure surface conduction ($\sigma \rightarrow 0$). For intermediate values of σ, the value of E_A required falls between these two limits; for instance, from Table 1, for $\sigma = 10^2$ one obtains $E_A \sim 6.26 \times 10^4$ V/m, for $P_E \sim 10$ g wt./cm^2. Values of ρ_A in Region I for each experiment are given in Table 3.

ii. In the second region (Figure 8a), for $4 \times 10^4 \text{ V/m} \lesssim E_A \lesssim 2 \times 10^5$ V/m, the $\rho_A(E_A)$ characteristic follows a power law form, $\rho_A = b\,(E_A)^m$, with the exponent m ($= m_P$) having a value somewhere between - 0.077 for the case of surface conduction in Experiment #1 ($t_{db} \approx 28$°C, $P_r \approx 100\%$) and - 0.4 for the case of volume conduction (hot and dry conditions with low relative humidity P_r). Values of m and b, for each test are evaluated by applying a least squares curve fit to the experimental data points in the aforementioned range of E_A and are given in Table 3. These values of m are in reasonable agreement with our theoretical predictions (for m_F) which are summarized in Table 1. In may be noted, from Table 3 that the value of m decreases with temperature as expected from theory. These results clearly confirm both qualitatively and (approximately) quantitatively the power law dependence of ρ_A on E_A in the second region of the $\rho_A(E_A)$ characteristic, as is explicitly predicted by our theory. This non-ohmic behavior is due to self-compression of the layer.

iii. In the third region (Figure 8a), at $E_A = E_{AB} \sim (2-4) \times 10^5$ V/m, the $\rho_A(E_A)$ curve starts to deviate from the power law dependence, with ρ_A decreasing more rapidly with increasing (applied) field E_A. This is due to the electrical breakdown of the layer which occurs in the form of intermittent microsparks, as discussed in the companion paper (6). The gross breakdown of the layer occurs at $E_A = E_{GB} \sim (12-16) \times 10^5$ V/m, with the lower values corresponding to higher temperatures and drier conditions.

In Figure 8b the results of Figure 8a are compared with each other by plotting the normalized resistivity $(\rho_A/\rho_{A_{ref}})$ versus E_A, where $\rho_{A_{ref}}$ is taken as the (reference) resistivity for $E_A = 10^5$ V/m. Also shown are the theoretical lines for Region II of the $\rho_A(E_A)$ characteristic (the power law forms) with σ as a parameter, from Table 1. In addition, the results of Experiment #1 ($T \sim 28°C$, $P_r \sim 100\%$) are also plotted.

Generally, it is seen that in the pre-breakdown regime the experimental results fall within the envelope of the limiting theoretical lines for volume and surface conduction and follow a power law form. Particularly, the data for the hot and dry cases lie close to the theoretical curve for volume conduction ($\sigma \to \infty$), as is to be expected. On the other hand the data for the ambient condition and more humid cases fall between the theoretical curves for the volume and surface conduction cases. This indicates that under the given ambient conditions, both volume and surface conduction are contributing to the effects. Finally, the data for Experiment #1, where $T \sim 28°C$ and $P_r \sim 100\%$, lie close to the theoretical curve for surface conduction ($\sigma = 0$).

An interesting phenomenon observed during Experiment #1, for the case of surface conduction, was that for $E_A \gtrsim 10^5$ V/m, ρ_A started to increase. This behavior is attributed to the Joule heating of the contact region. Calculations show that in the case of surface conduction at $E_A \sim 10^5$ V/m the true current density in the contact area is $J_c \sim 2.3$ A/cm^2, which is a factor of $\sim 1.8 \times 10^5$ higher than the measured apparent current density $J_A \sim 12.6$ μA/cm^2. Typically, for the case of volume conduction with $J_A \sim 5 \times 10^{-4}$ μA/cm^2 and $E_A \sim 10^5$ V/m, one obtains $J_c/J_A \sim 5 \times 10^4$ and $J_c \sim 25$ μA/cm^2, a low value (a factor of $\sim 10^5$ lower than the case of surface conduction). Therefore, for surface conduction the local Joule heating at higher current densities dries out the contact region, causing an increase in the apparent resistivity with increasing E_A.

DISCUSSION AND CONCLUSIONS

Tables 1 and 2 summarize the set of self-consistent electromechanical equations governing the behavior of a (monodisperse) particulate layer *prior to microspark breakdown*. A close examination of these tables reveals that the dependence of θ_o and E_{max} on E_A and packing mode is rather weak. Also, their variation with σ at a specified value of E_A is slow. However, the dependence of ρ_A on σ and mode of packing is more pronounced. In this case, the value of σ also determines the strength of the dependence of ρ_A on E_A through its influence on the power law exponent m_F. The compressive stress P_E is proportional to E_A raised to a power of 1.2 to 1.35, instead of E_A^2 which arises from a homogeneous leaky dielectric model for the layer.

The experimental results are in agreement with the theoretical prediction regarding the $\rho_A(E_A)$ characteristic in the power law region (Region II), where $\rho_A \propto (E_A)^m$. Here, m (= m_F) lies in the predicted range and has the correct dependence on temperature and humidity.

ACKNOWLEDGEMENTS

This work was supported by the Electric Power Research Institute.

The work described in this paper was not funded by the U.S. Environmental Protection Agency and therefore the contents do not necessarily reflect the views of the Agency and no official endorsement should be inferred.

REFERENCES

1. Moslehi, G. B. and Self, S. A., "Current Flow across a Sphere with Volume and Surface Conduction," J. Electrostatics (in Press).

2. Self, S. A., Moslehi, G. B., Mitchner, M. and Leach, R., "Electromechanics and Reentrainament of Precipitated Ash," Proc. International Conference on Electrostatic Precipitation, Monterey, California, October 14-16, 1981.

3. Graton, L. C. and Fraser, H. J., "Systematic Packing of Spheres," J. Geology, Vol. 43, No. 8, Part I, pp. 785-909, (Nov.-Dec. 1935).

4. Deresiewicz, H., "Mechanics of Granular Matter," in *Advances in Applied Mechanics*, Vol. 5, Academic Press (1958).

5. McLean, K. J., "Electrical Conduction in High Resistivity Particulate Solids," Ph.D. Thesis, E. E. Dept., Wollongong Univ. College, Univ. of New South Wales, Australia, Chap. 7 (Dec. 1969).

6. Moslehi, G. B. and Self, S. A., "Electrical Breakdown of Particulate Layers," 4th Symposium on Transfer and Utilization of Particulate Control Technology, Houston, Texas, October 11-15, 1982. (Session C-6, this conference).

LATERAL PROPAGATION OF BACK CORONA IN TWIN-ELECTRODE TYPE PRECIPITATORS

by: Senichi Masuda and Toshifumi Itagaki
Department of Electrical Engineering,
University of Tokyo
7-3-1 Hongo, Bunkyo-ku, Tokyo, Japan 113

ABSTRACT

The lateral propagation of back corona, discovered to occur in a tri-electrode corona system, also occurs in a conventional electrostatic precipitator of the twin-electrode system under certain circumstances. The primary factor in initiating this phenomenon is the mutual excitation of the wire corona discharge and back corona. At high resistivity of dust deposit and with small discharge wire diameter, this mutual excitation becomes dominant and the lateral propagation occurs from a single back corona on a plate appearing at a local spot. The dc base voltage in a pulse charging system must be selected in a careful consideration of this phenomenon. The detailed conditions of its initiation and extinction in air at NTP are presented in relation to various modes of corona discharge.

INTRODUCTION

Investigations on the back corona occurring in a tri-electrode system revealed that its lateral propagation takes place to cover the whole collection and third electrodes in the case when the magnitude of field intensity in its collection field exceeds a certain threshold (1). This threshold is a level to cause streamer-mode in the original back corona. The wide-spread secondary back corona, thus produced, is self-sustaining and cannot be eliminated unless the field intensity be lowered well below its initiation threshold.

In the observation of back corona made at a large scale twin-electrode precipitator for a sinter machine, one of the authors found with the aid of a portable image intensifier that back corona occasionally occurs on the dust-covered supporting frames of discharge wires. This phenomenon results from positive ionic current induced by the original back corona on the plate and accumulating on the dust-covered frames similar to the lateral propagation in the tri-electrode system. This finding motivated a careful observation of time-dependent development of back corona in a test precipitator of twin-electrode system in the authors' laboratory. As a result, the occurrence of the lateral propagation of back corona and the concurrent hysteresis in voltage-current (V-I) curves were confirmed in the twin-electrode system, when dust resistivity was extremely high. Again in this case, the lateral propagation starts to occur when the average field intensity in the collection field exceeds a certain threshold. It was further confirmed in the laboratory precipitator being operated by pulse-energization that the level of dc base voltage, Vb, is subjected to the limitation posed by the lateral propagation of back corona possible to occur by chance somewhere on the collection plate. In other words, although it is possible to raise Vb by modification of corona electrodes so as to increase corona initiation voltage, Vc, there is another essential constraint of limitting the operating field intensity beyond which the collection performance is drastically deteriorated by the lateral propagation and the pulse-energization loses its control. This paper is a preliminary report on the lateral propagation of back corona specific to the twin-electrode system occurring in air at NTP.

METHOD OF EXPERIMENT

The experimental apparatus consists of two parallel plates (25cm in width, 15cm in length and spaced at 15cm) and a single discharge wire as illustrated in Fig. 1. One of the plates has a rectangular probe (14.9cm in width and 7.9cm in length) at its center for measurement of corona current. The plates are covered with paper towels (1.2mm in thickness and 0.034g/cm^3 in volume density) to simulate the dust layer. Resistivity of the paper towel is adjusted by controlling the humidity of its ambient air at room temperature and normal pressure, and its value measured with ordinary parallel plate electrodes. Three wires with different diameters 0.5mm, 1.1mm and 2.0mm respectively, and a stranded wire out of 0.35mm wire elements with a total diameter of 3.2mm are used. The corona discharge on the wire and back corona are observed with the aid of an image intensifier (EMI type 9912 with maximum photon gain of 10^6) and a portable image intensifier (HITACHI HS-690 with photon gain of 3.5×10^4). The experiment is made only for negative corona discharge on the wire.

RESULTS OF EXPERIMENT

Corona Wire with 0.5mm Diameter

Figures 2 (a), (b) and (c) show the voltage versus current density (V-J) curves obtained with a 0.5mm discharge wire for three different resistivities $\rho = 1.1\times10^{15}$, 1.4×10^{13}, and 2.7×10^{12} ohm-cm.

When the resistivity of the layer is very large at $\rho = 1.1\times10^{15}$ ohm-cm, a distinct hysteresis in the V-J curve occurs (Fig. 2 (a)). As the voltage is raised, negative corona appears on the wire at point B, and the corona current begins to flow. The current gradually increases to reach point C even though the source voltage is kept unaltered. The corona points concurrently appear one after another propagating in both directions along the wire, and moving back and forth (Fig. 3). Glow of the back corona, on the other hand, is so weak in this case that it does not allow a visual confirmation of its lateral propagation on the plate electrodes even with the aid of the EMI image intensifier. At point C, the time-dependent increase in number of the corona points stops. At the initial stage when only a few corona points exist on the wire, no distinct back corona activity can be observed. At the final stage (point C), back corona as a dim light is observed with the EMI image intensifier, covering the entire surface of the plate electrodes(Fig.4).

As the voltage is reduced from point C, the current decreases slowly with decrease in the number of the corona points. The coronas do not disappear and back corona cannot be eliminated unless the voltage is reduced to point D much lower than point B. If the voltage is raised from a point between D and C, the current density J follows a curve on or close to the original curve D-C. In this case, the number of the corona points varies with the variation in voltage. These results provide a strong evidence that the lateral propagation of back corona has occurred in this case.

Further raising the voltage beyond point C results in a current density increase following the extrapolated curve of D-C. The number increase of corona points remains small in this case, but each corona point becomes increasingly brighter.

The initiation point B of back corona and its lateral propagation can vary by about 1kV, with the concurrent fluctuation of point C.

Fig. 2 (b) shows V-J curve measured at $\rho = 1.4\times10^{13}$ ohm-cm. At this lower resistivity level, back corona first occurs at point B' with a substantially larger corona current being required to produce the layer breakdown. Once back corona starts, it again propagates laterally with the concurrent rise in corona current up to point C'. Raising or lowering the voltage from point C' causes the same effect as in the case of Fig. 2 (a). When ρ is about 10^{14} ohm-cm, almost the same V-J curve as shown in Fig. 2 (b) is obtained. Velosity of lateral propagation of back corona in these cases is slow. It takes 10 to 15 seconds from points B and B' to points C and C'.

When ρ is smaller than 5×10^{12} ohm-cm, no hysteresis occurs in V-J curve (Fig. 2 (c)). The number of corona points remains unchanged at constant voltage, and neither increase in current nor propagation of the coronas is observed unless the voltage raised. The lateral propagation of back corona does not take place at this resistivity in this particular case of the experiment.

Corona Wire with 1.1mm Diameter

In the experiment using 1.1mm wire, neither hysteresis in the V-J curve nor propagation of the coronas along the wire occurs at constant voltage in the resistivity range of 10^{11} to 6×10^{14} ohm-cm, indicating no lateral propagation of back corona to occur. An example of V-J curve is shown in Fig. 5.

Instead, two remarkable phenomena are observed in this case. One is that the negative coronas on the wire take a form of diffused glow in the lower resistivity range $\rho < 10^{13}$ ohm-cm. The other is that the back corona on the collection electrodes takes a form of separate domains at higher resistivity range $\rho \geq 10^{13}$ ohm-cm. The negative corona at onset manifests itself as a few number of small motionless spots, or the diffused glow surrounding a small portion of the wire. In the range $\rho < 10^{13}$ ohm-cm, the increase in voltage produces the transition of these corona spots into the diffused glow so that it extends along the wire (Fig. 6 (a)). A photograph taken with a shorter exposure (Fig. 6 (b)) reveals this diffused glow to be consisting of very small corona spots. These spots are moving very fast along the wire to produce the outlook of a diffused glow. Fig. 7 shows back corona in this case uniformly spreading over the collection plate.

At high layer resistivity $\rho \geq 10^{13}$ ohm-cm, the diffused glow turns into separate corona spots with voltage increased (Fig. 8). The spots move around back and forth along the wire. As is clearly seen in Fig. 9, each corona spot on the wire produces its own domain of back corona on the plate, which also moves concurrently with the corona spot. The back corona domains are separated from each other, and behave as if they are repelling each other. When the voltage is increased over 35kV with the current density beyond $2mA/m^2$, the number of corona points becomes too large and makes it difficult to recognize one-to-one correspondence between the corona points and the back corona domains. But the discrete nature of back corona domains still exists although their contours become partly indistinct.

Corona Wire with 2.0mm Diameter

When ρ is in the order of 10^{14} ohm-cm, the time-dependent rise in corona current, much faster in speed, occurs at a constant voltage beyond back corona initiation, and a slight hysteresis occurs in V-J curve (Fig. 10). But it differs from the hysteresis in Fig. 2 (a) and (b) for 0.5mm wire diameter in that this time-dependent current rise is not caused by the increase in number of the corona points but by the mode change of corona in each original spot. At the onset, corona appears in a form of tiny active lumps of glow on the wire, but the current remains practically zero. When the voltage is slightly increased these active lumps of glow suddenly turn into a motionless corona spot, raising the current at a constant voltage, and back corona appears at a small region opposit to this corona spot. The corona spot abruptly disappears when the voltage is lowered about 1kV below corona initiation threshold. This presents a striking contrast to the case of Fig. 2 (a) and (b) with 0.5mm wire where the corona extinguishing voltage lies far below its initiation voltage. The time required for the rise or drop of the current in this case is less than 1 second, much shorter than that for 0.5mm wire. In spite of the hysteresis in V-J curve, the lateral propagation of back corona does not occur in this case. When the voltage is further increased after the formation of one single corona spot, active lumps of glow appear renewed on both sides of this spot. The spot and the lumps of glow repel each other leaving dark portions in between. Back corona in this case also takes a form of separate domains, each corresponding to a spot or the lumps of glow.

At a lower resistivity in the order of 10^{13} ohm-cm, no corona point appears unless voltage exceeds, say, 45kV. Below this threshold, the corona forms active lumps of glow (Fig. 11), each being accompanied by its own domain of back corona (Fig. 12). The lumps of glow move around rapidly along the wire with the concurrent movement of the back corona domains. When the voltage is raised beyond 40kV, the current density exceeds $2mA/m^2$ at which value the lumps of glow turn into corona spots moving back and forth along the wire. Concurrently, the boundaries of the back corona domains are blurred.

When the layer resistivity is less than 10^{13} ohm-cm, corona after onset takes a diffused form along the wire to have the same appearance as the diffused corona with 1.1mm wire at a low value of ρ. In this case, back corona becomes also diffused losing its boundary of each region, and uniformly distributed on the collection plates (Fig. 13).

Stranded Wire with 3.2mm Outer Diameter

No lateral propagation of back corona occurs in this case in the entire resistivity range between 10^{11} to 3×10^{14} ohm-cm.

One-to-one correspondence between back corona domains and corona points appears at a higher resistivity $\rho \geq 10^{13}$ ohm-cm (Fig. 14). Corona motion, similar to those of the active lumps of glow appearing with 2.0mm wire, occurs, and it is enhanced with increasing resistivity.

Fluctuation of current density at a constant voltage is very large. For example, it fluctuates between $2.5mA/m^2$ and $0.1mA/m^2$ at $V = 30kV$ and $\rho = 1.5\times10^{13}$ ohm-cm. When a large domain of back corona happens to cover a major portion of the current probe, the current increases concurrently. But the domain rapidly moves out of the probe area following its corona point to cause a sharp drop in current.

Fig. 15 indicates the appearance of both negative coronas and back coronas at a lower resistivity $\rho = 8.8\times10^{11}$ ohm-cm. Boundaries of the back corona domains are blurred, and one-to-one correspondence between the wire corona and back corona disappears. However, the flicker of a corona point is accompanied by the concurrent change in the brightness of back corona, causing a slight fluctuation in the current density. Both wire coronas and back coronas at this lower resistivity are very static, so that no large current fluctuation is produced.

DISCUSSION

It must be emphasized that the present investigation is a preliminary one made in air at NTP with clean negative corona wires, far from the realistic conditions. Hence, the results obtained are primarily for understanding the basic phenomena, and should never be extended to the practical precipitators in operation.

With these factors born in mind, one can recognize from the results so far obtained that the lateral propagation of back corona in this particular case occurs only when the diameter of negative corona wire is very small ($d = 0.5mm$) and the layer resistivity very high ($\rho \geq 10^{13}$ ohm-cm). The propagation proceeds with a concurrent increase in number of discrete corona points along a negative wire, and not with a continual extention of diffused negative corona. No distinct effect of the level of average field in corona space is observed, unlike in the case of a tri-electrode system (1). This effect is likely to be masked by the fact that, in this particular case when the lateral propagation can occur only at $\rho \geq 10^{13}$ ohm-cm, the initiation of back corona immediately produces its lateral propagation.

In general, it is hypothesized for the lateral propagation to occur that both of the following conditions must be met. First, lateral diffusion of charge carriers (positive ions, negative ions, electrons) should occur in the original back corona either in gas space or on the surface of dust layer and/or corona wire. Second, the neighbouring region of both wire and dust layer must be ready for initiation of new corona and back corona activities, respectively. It can be imagined that the first condition is easily met in most of the cases.

In consideration of the experimental results described above, the second condition is met in this particular case by a very high resistivity ρ in the layer easy to cause its breakdown and a very small wire diameter to produce a very high local field enhanced by ion sheath of oncoming positive ions.

In the case of practical precipitators in operation, the following factors are to be taken into account. First, the operating temperature is much higher to increase gas mean free path, thereby enhancing the lateral diffusion of charge carriers, and also reducing the breakdown threshold at both dust layer and corona wire. Second, the corona wires are not clean and covered with high resistivity dust deposit which will easily experience breakdown by accumulation of oncoming positive ions, similar to back corona occurring on the collection electrodes. As a result, the wire diameter may have a much less effect. Under these otherwise relaxed threshold values the effect of field intensity in gas space may again take the most essential role as the initiation condition of streamer-mode back corona which is actually observed in our laboratory precipitator, and a more detailed investigation is being attempted. The importance of this field criterion in the twin-electrode system is that it poses a strict constraint on the dc base voltage to be applied to the corona electrodes in pulse-energization.

CONCLUSIONS

The preliminary investigations are made on the lateral propagation of back corona in a twin-electrode system in air at NTP with clean negative corona wires. The results obtained lead to the following conclusions:

(1) The occurrence of lateral propagation of back corona under a negative clean corona wire is strongly dependent on the diameter of wire, d, and the layer resistivity, ρ. In air at NTP, it appears only when the wire diameter is very small ($d = 0.5$mm) and the layer resistivity very high ($\rho \geq 10^{13}$ ohm-cm). No distinct effect of the field level in gas space is observed in air at NTP, unlike the case of the tri-electrode system. In other words, as soon as back corona appears, it starts lateral propagation in this particular case.

(2) At a higher operating temperature of an ESP with a larger gas mean free path, the lateral propagation is expected to occur at a larger wire diameter and/or lower dust resistivity. The contamination of the corona wire with deposition of high resistivity dust also may result in the same tendency.

(3) The lateral propagation of back corona produces at a constant voltage both a time-dependent increase in number of corona points extending along the wire and a concurrent gradual rise in corona current. Once appeared, a negative corona point and back corona stabilize each other through their mutual action, so that they cannot be extinguished unless voltage be lowered to a level much lower than the back corona initiation threshold. As a result, a very distinct hysteresis in V-J curve occurs in the case when the lateral propagation of back corona takes place.

(4) Irrespective of whether or not the lateral propagation occurs, a strong correlation exists between the appearance and motion of back corona and those of the negative corona points. At a very high resistivity $\rho \geq 10^{13}$ ohm-cm and with a larger wire diameter $d \geq 1.1$mm, back corona takes a form of separate domains, each corresponding to a discrete corona spot or a lump of glow on the wire. At a lower resistivity $\rho < 10^{13}$ ohm-cm and with a larger wire diameter, d = 1.1mm and 2.0mm, the negative corona takes a diffused form surrounding the wire, and the boundary of the back corona domains becomes also blurred. This diffused negative corona consists of very small corona spots moving around at high speed along the wire.

A further investigation is attempted to clarify the initiation conditions of the lateral propagation of back corona under the conditions prevailing in a practical precipitator, with a special attention to pulse-energization technology.

REFERENCE

1. Masuda, S., Obata, S. and Ogura, Y. Lateral propagation of back-discharge in a tri-electrode system. Electrostatics 1979, Inst. Phys. Conf. Ser. No. 48, Institute of Physics (1979)

The work described in this paper was not funded by the U.S. Environmental Protection Agency and therefore the contents do not necessarily reflect the views of the Agency and no official endorsement should be inferred.

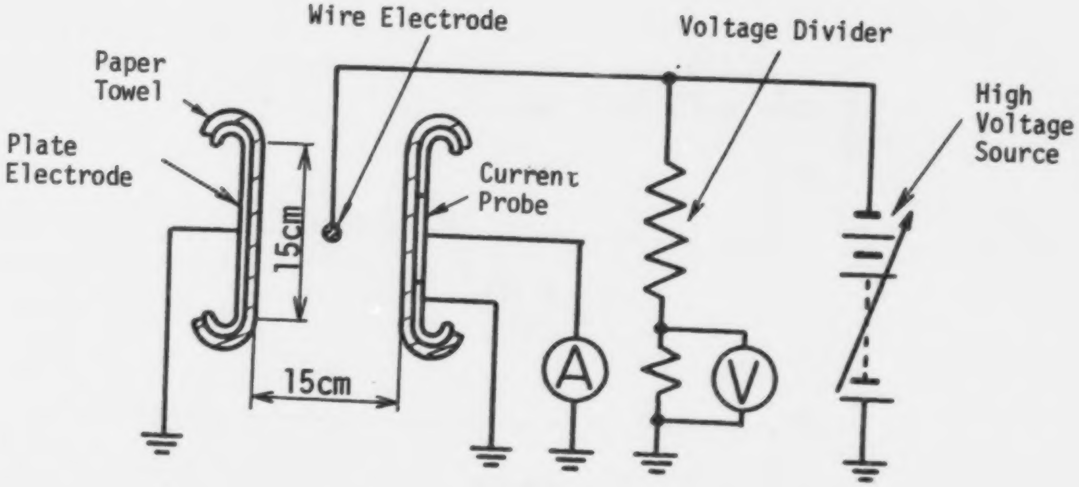
Wire Electrode
Voltage Divider
Paper Towel
Plate Electrode
High Voltage Source
Current Probe
15cm
15cm
A
V

Fig. 1. Experimental Set Up.

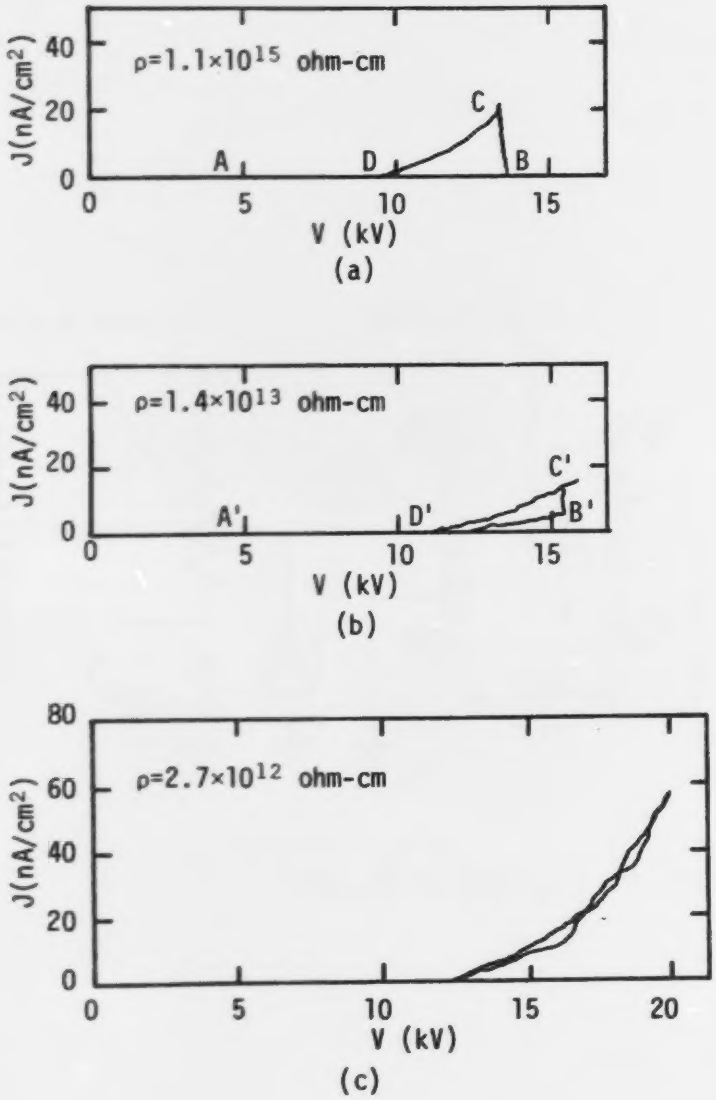

Fig. 2. V-J curve with 0.5mm negative wire

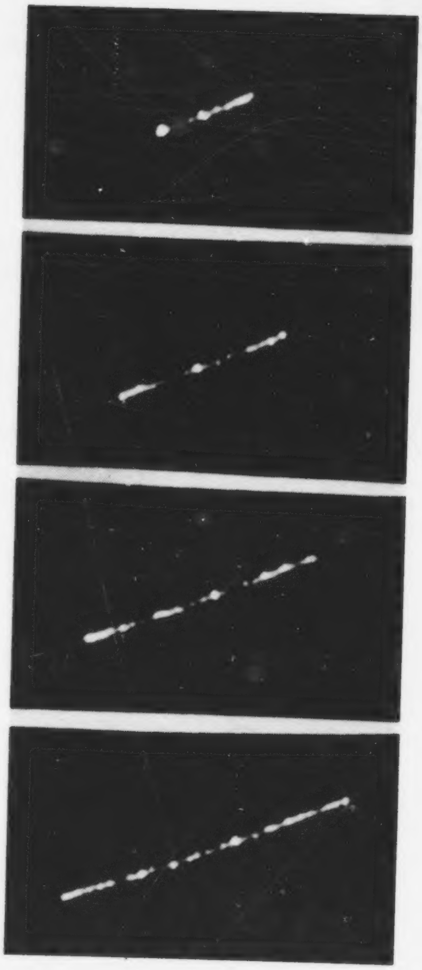

(a) t = 0 second

(b) t = 2 seconds

(c) t = 4 seconds

(d) t = 10 seconds

Fig. 3. Time-dependent growth in number of negative corona points on wire observed with a portable image intensifier.

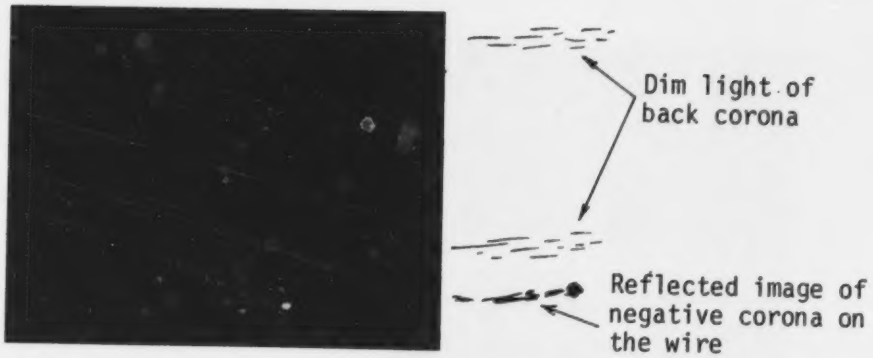

Dim light of back corona

Reflected image of negative corona on the wire

Fig. 4. Back corona under 0.5mm negative wire at the final stage of growth in corona points (point C in Fig. 2 (a)) at $\rho = 1.1\times10^{15}$ ohm-cm observed with EMI image intensifier.

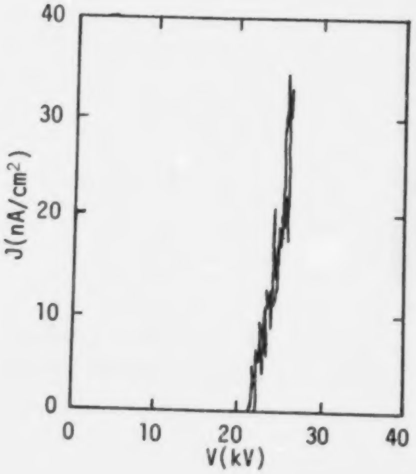

Fig. 5. V-J curve with 1.1mm negative wire at $\rho = 1.1\times10^{14}$ ohm-cm.

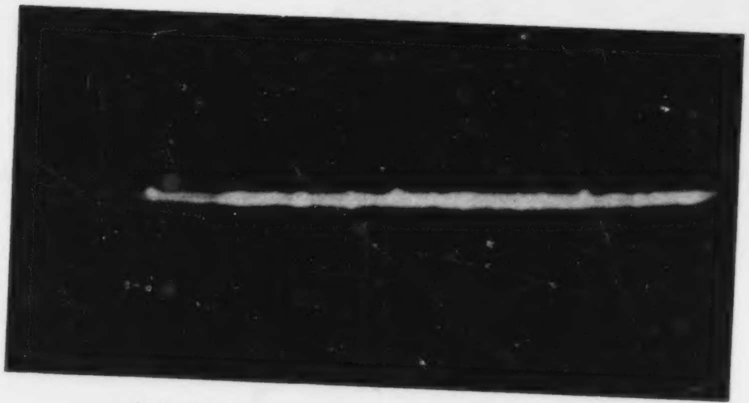

(a) Exposure time: 1/4 second

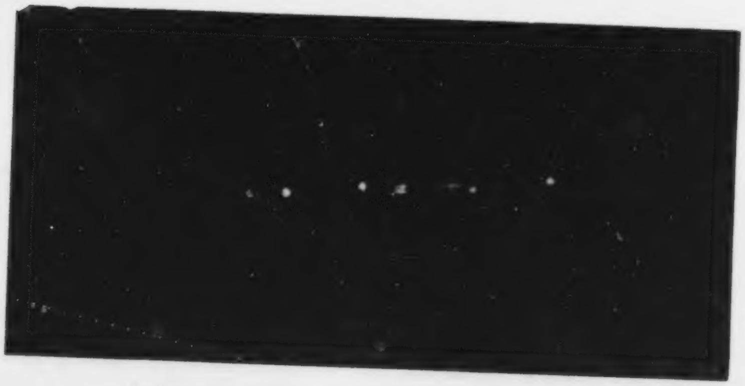

(b) Exposure time: 1/500 second

Fig. 6. Negative coronas on 1.1mm wire at $\rho = 5.4 \times 10^{11}$ ohm-cm observed with a portable image intensifier.

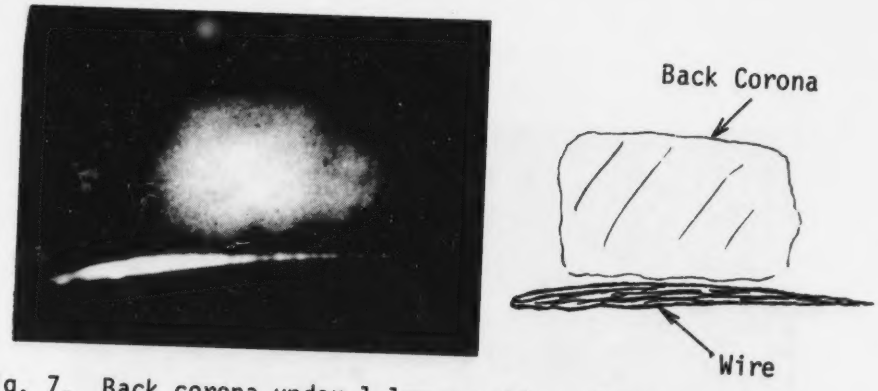

Fig. 7. Back corona under 1.1mm negative wire at $\rho = 5.4\times10^{11}$ ohm-cm observed with a portable image intensifier. (Exposure time: 1/4 second)

Fig. 8. Negative coronas on 1.1mm wire at $\rho = 5.5\times10^{14}$ ohm-cm observed with a portable image intensifier. (Exposure time: 1/2 second)

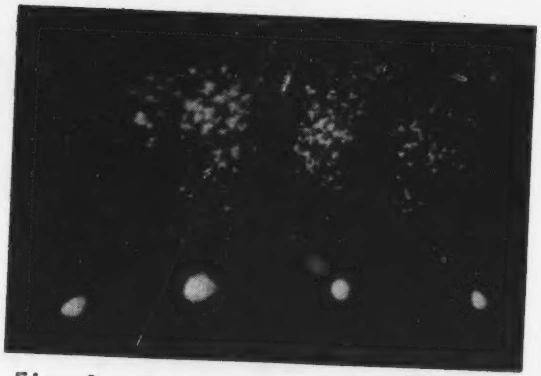

Fig. 9. Back corona under 1.1mm negative wire at $\rho = 1.1\times10^{14}$ ohm-cm observed with a portable image intensifier. (Exposure time: 1/4 second)

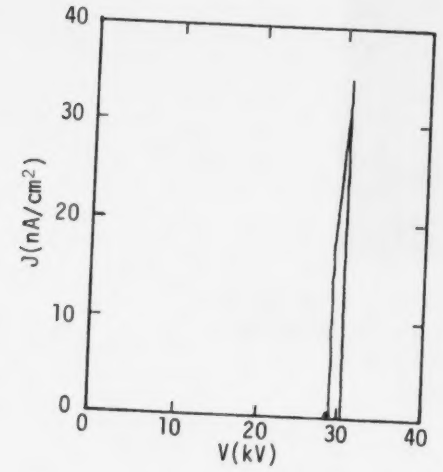

Fig. 10. V-J curve with 2.0mm negative wire at $\rho = 4.0\times10^{14}$ ohm-cm.

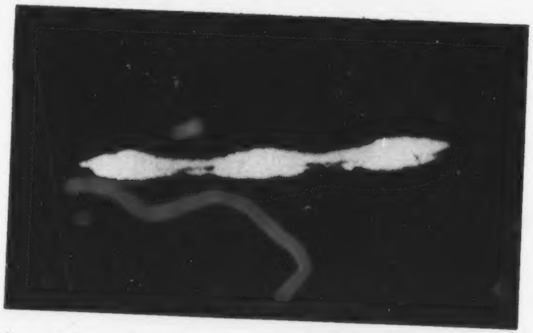

Fig. 11. Negative coronas on 2.0mm wire at $\rho = 4.1\times10^{13}$ ohm-cm observed with a portable image intensifier.
(Exposure time: 1/4 second)

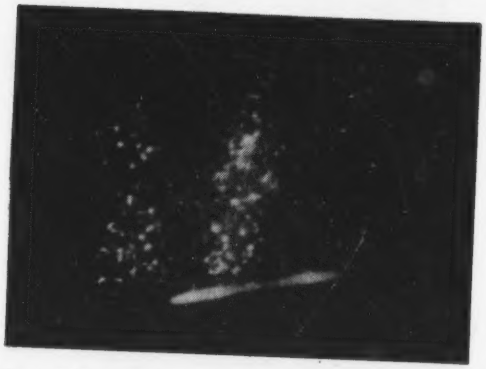

Fig. 12. Back corona under 2.0mm negative wire at $\rho = 1.5\times10^{13}$ ohm-cm observed with a portable image intensifier.
(Exposure time: 1 second)

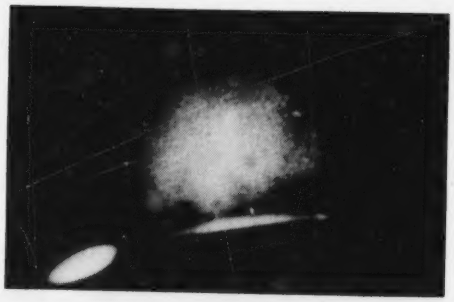

Fig. 13. Back corona under 2.0mm negative wire at $\rho = 4.2\times10^{12}$ ohm-cm observed with a portable image intensifier. (Exposure time: 1 second)

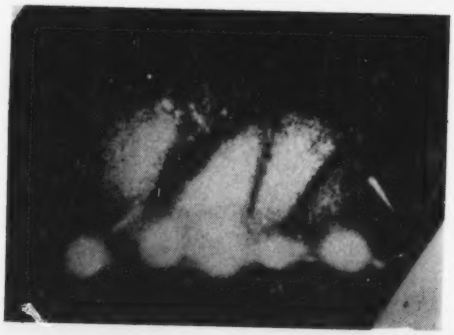

Fig. 14. Back corona under 3.2mm negative stranded wire at $\rho = 1.6\times10^{13}$ ohm-cm observed with a portable image intensifier. (Exposure time: 1/4 second)

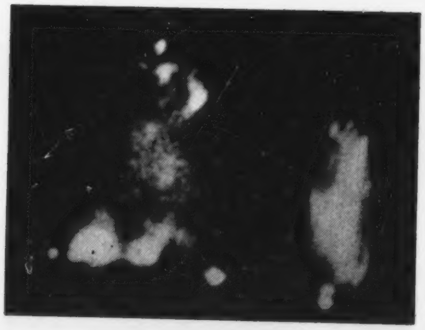

Fig. 15. Back corona under 3.2mm negative stranded wire at $\rho = 8.8\times10^{11}$ ohm-cm observed with a portable image intensifier. (Exposure time: 1/4 second)

FIRST MEASUREMENTS OF AEROSOL PARTICLE CHARGING BY FREE ELECTRONS

James L. DuBard and M. G. Faulkner
Southern Research Institute, Birmingham AL 35255

Leslie E. Sparks
Industrial Environmental Research Laboratory
U.S. Environmental Protection Agency
Research Triangle Park, NC 27711

ABSTRACT

The charging of fine aerosol particles by free electrons has been isolated from negative ionic charging and measured for the first time. The charge and size of individual particles were measured in a Millikan cell, with charging electric field from 0.82 to 8.2 kV/cm. In the particle size range 0.5 to 3.0 μm diameter, the particle charge values are much larger, and increase much faster with particle size, than those predicted and observed for negative ionic charging. The particle charge values show only slight dependence on the charging electric field.

INTRODUCTION

A number of techniques for removing particles from gas streams involve electrically charging the particles. Particles may be charged by impact of positive or negative molecular ions produced from a high voltage corona discharge in the carrier gas. The physical mechanisms associated with ionic charging have been determined experimentally and described theoretically (1,2,3). Ionic charging theory has been applied in a mathematical model which describes the cleaning of industrial process gas streams by electrostatic precipitation (4). In a negative corona discharge, particles may be charged also by free (unattached) electrons. The mechanisms associated with free electron charging have not been determined.

Ionic charging theory was tested by direct measurements of the charge acquired by fine particles, 0.5 μm to 3.0 μm diameter, using a Millikan cell (5). The charge and size of individual fine particles escaping laboratory precipitators were measured at air temperatures from 38°C to 343°C. The data for positive ionic charging were in good agreement with theory at all temperatures. However, the measured particle charge with negative corona was significantly higher than the predicted charge at temperatures above 200°C. At 343°C, the negative charge enhancement was about a factor of two for 2.0 μm diameter particles, as shown in Figure 1. The negative charge enhancement was attributed to a contribution from free electrons which had escaped attachment to electronegative gas molecules because of the reduced gas density. The top curve in Figure 2 shows the ratio of the negative-to-positive charges in the laboratory data of Figure 1. For comparison, the bottom curve in Figure 2 shows the numerator of that ratio (that is, the measurements of negative charge) replaced by data from field tests on a hot-side precipitator. The charge and size of individual fly ash particles escaping the precipitator were measured with a Millikan cell. In the diameter range 1 to 2 μm, 100 to 150 particles were measured in each 0.1 μm interval. The data were obtained at a sampling port downstream of the precipitator outlet. Particle collisions with duct walls may account for the lower charge enhancement, and much greater scatter in the data, than that observed in the laboratory. However, there remains a strong suggestion of enhanced negative charging of fine fly ash particles. The plausibility of fly ash particle charging by free electrons can be shown by an estimate of the surviving free electrons in the flue gas. Using the calculated electric field distribution in the hot-side precipitator and using electron attachment coefficients measured in pure oxygen (6) (and adjusted to the flue gas density and composition) it can be estimated that 2% to 4% of the electrons leaving the negative corona discharge will survive halfway to the collecting plate.

In applications to industrial electrostatic precipitation, it is particularly important to understand the charging and collecting of fine particles because they are the most hazardous to human health, the most difficult to precipitate from a gas stream, and the most responsible for visible emissions. Although laboratory data and field data suggest that conventional negative ionic charging of fine particles may be significantly enhanced by electronic charging, there have been no data that isolate electronic charging from ionic charging. The preliminary data on electronic charging reported in this paper show that free electrons are much more effective than negative ions in charging fine particles. However, the electronic charging process cannot be aequately described by adaptation of the established ionic charging theory.

EXPERIMENTS

The experiments were performed in commercial ultrapure nitrogen gas having 1 ppm residual O_2. In electric fields the order of 5 to 10 kV/cm, the electron attachment coefficient in 1 ppm O_2, at 20°C, is 4.2 to 6.5 x 10^{-5} cm^{-1} (6). Within the dimensions of the aerosol charging apparatus, the probability of an electron attachment was less than 4 x 10^{-4}. A flux of free electrons was obtained from a single needle point pressed into a cold cathode plate and energized with negative dc high voltage. The electrical discharge from the needle point was an intense streamer, pulsating at 6.0 Hz. (The stability of a conventional negative corona discharge results from the negative ionic space charge surrounding the emitting point. In a gas that is not electronegative, that space charge control is missing.) The electrical parameters of the discharge were independent of the power supply and were controlled entirely by the electrode geometry. The maximum cathode voltage between pulses was about 7.5 kV, and the maximum cathode current during a pulse was about 0.6 mA. The electrical discharge was extremely sensitive to residual traces of ambient air in the experimental chamber. However, once the chamber was cleared of electronegative gases, the unusual character of the electrical discharge was entirely reproducible.

The aerosol charging apparatus was contained in a standard cylindrical vacuum chamber, fitted with a viewport and with gas and electrical feedthroughs. The flux of free electrons was obtained in a uniform electric field between two parallel metal plates, 20 cm in diameter and separated by 4 cm. There was a rectangular cutout in the center of the grounded plate opposite the cathode plate, to accommodate the aerosol charging assembly. This cutout was covered with wire cloth having 49% open area. The aerosol charging region was a rectangular void in a teflon block set into the rectangular cutout in the grounded plate. The grounded wire cloth formed the front boundary of the aerosol charging region. The back boundary was a metal anode plate set into the teflon block. The separation between the grounded wire cloth and the anode plate, across which the charging electric field was developed, was 1.2 cm. The aerosol generator was a Collison nebulizer operated with ultrapure nitrogen gas. In a preliminary series of three experiments, a dilute water suspension of 0.8 μm diameter polystyrene latex (PSL) particles was used in the nebulizer. The nebulizer was followed by a dessicator and a polonium-210 strip irradiating the gas stream. The charge and size of individual particles exiting the chamber were measured with a Millikan cell. In every experiment, the Millikan cell was operated before and after energization of the cathode needle point to be sure that no frictionally charged particles were contained in the gas stream.

Three experiments, with different voltages on the anode, were performed in order to investigate the effect of the charging electric field on the particle charge. The experimental parameters are listed in Table 1. In order to investigate the variation of particle charge with particle size, the driving gas pressure from the gas cylinder was set such that the gas stream passed through the dessicator quickly enough for the particles to be incompletely dried. The residual water surface resulted in a particle size range, measured in the Millikan cell, of 1.1 to 1.7 μm diameter. The dielectric constant of water was used in calculations of particle charge.

In order to minimize precipitation of charged particles, the high voltage on the anode was applied in the form of a square wave, alternately positive and negative. The square wave frequency was 100 Hz. Thus, as shown in Table 1, the 5 ms period of positive high voltage on the anode was just slightly longer than the estimated maximum aerosol exposure time of 4.1 ms. Both times were short compared to 83 ms, which was half the cathode streamer pulsing period. Thus, some particles had the opportunity to be exposed to the maximum electron flux and to experience a uniform charging electric field during the entire exposure. Measurements were made on the most highly charged particles observed in the Millikan cell.

Each data point for particle charge and particle size was calculated from an average of three up and three down velocity measurements of the particle, acquired within 30 seconds of charging the particle. The stability of the water surface on the particles was investigated for some particles by observing the up and down motions in the Millikan cell for several minutes. These data showed a trend in successive measurements of particle velocity; the particles were growing by condensation. However, the data acquired within 30 seconds gave no evidence of a changing particle size.

In the theoretical description of ionic charging of particles, the critical parameters are the particle radius (a), the charging electric field (E), and the product of ion density (N_o) and the aerosol exposure time (t) (2). For example, the charge acquired by a large conducting particle as a result of electric field charging is given by (8)

$$en = 12\pi\varepsilon_o \, a^2 E \, \frac{N_o t}{N_o t + 4\varepsilon_o / eb} \text{, coulombs,} \tag{1}$$

where b is the electrical mobility of the ions. In these experiments, the analogous free electron density (N_e) was calculated from the measured electron current density which penetrated the grounded wire cloth and collected on the anode, as

$$J = e \, N_e \, v\text{, A/cm}^2\text{,} \tag{2}$$

where v is the drift velocity of a thermalized electron swarm. Several of the electronic charging parameters, listed in Table 1, had to be estimated in these preliminary experiments. The particle exposure time depended on the estimated average aerosol velocity in the aerosol charging region. The electron flux from a streamer discharge was estimated (from visual observations) to be uniform over one square centimeter of the aerosol charging region.

Data points for individual particles in the three preliminary experiments are shown in Figure 3, along with dashed straight lines least-squares-fitted to the data points to guide the eye. The fits to the two data sets obtained with 8.2 and 4.1 kV/cm were so nearly the same that only one dashed line is shown. Also shown in Figure 3, for comparison with the data, are calculated curves for negative ionic particle charging under similar conditions. Three interesting features of Figure 3 may be noted:

a) The measured values of particle charge are very much larger than those predicted for analogous negative ionic charging. The three curves in Figure 3 were calculated using ion density N_o the same as the estimate of free electron density N_e, and using established ionic charging theory (2).

b) There is no dependence on electric field strength shown in the data obtained with 8.2 and 4.1 kV/cm and only a slight dependence shown at 0.82 kV/cm. For negative ionic charging of particles in this size range, there is a strong field dependence, as shown in the three calculated curves in Figure 3.

c) Accumulated electron charge increases more rapidly with increasing particle diameter than accumulated negative ion charge.

If the same physical mechanisms were assumed for electronic charging as for ionic charging, the three curves of Figure 4 would result. In Figure 4, the experimental data are represented by the two fitted straight lines. The three curves were calculated in the same manner as for ionic charging, but with the ion mobility replaced with the much larger electron mobility obtained from the electron drift velocity in Table 1.

A second series of experiments was performed to obtain a direct experimental comparison between electronic charging and negative ionic charging, using a non-volatile aerosol. Di (2-ethylhexyl) sebacate (DES) was used in the Collison nebulizer. The resulting aerosol included fine particles spanning the entire size range (0.5 to 3.0 μm diameter) that could be measured in the Millikan cell.

The experimental objective was to achieve the same value of $N_e t$ for free electrons in ultrapure nitrogen gas as the value of $N_o t$ for negative ions in dry air. All of these experiments were performed with 5 kV/cm electric field in the aerosol charging region. The high voltage on the cathode needle point was adjusted to control the discharge current so that the measured anode current in the aerosol charging region was different for electrons and ions by approximately a factor of 300 in order to compensate for the difference in mobility. With ultrapure nitrogen in the chamber, the cathode discharge was current-limited by the external high voltage supply in order to change the pulsating streamer into a low-intensity steady streamer giving a steady dc current (which was nearly the same as the average current with the pulsating streamer.) The parameters for this second series of experiments are listed in Table 2. It should be noted that the value $Nt \sim 10^6\ \mathrm{cm}^{-3}\mathrm{s}$ achieved in all experiments is lower by about an order of magnitude than the typical charging parameter in an industrial precipitator.

Individual data points for two different pairs of experiments are shown by the open and closed symbols in Figure 5. Again, only the most highly charged particles found in the Millikan cell are shown on the graph. (The values of anode current for the closed symbols were lower than those shown in Table 2, due to a systematic measurement error, but the ratio remained approximately correct at 300:1.) The particle size range shown in Figure 3 is only a small slice of that shown in Figure 5. However, a close comparison of measurements and calculations shows that the results of the two sets of experiments are consistent.

SUMMARY

These experiments have isolated the charging of fine particles by free electrons for the first time. Although the data are of a preliminary nature, they clearly cannot be interpreted with the theory of negative ionic charging, not even when the value of mobility is corrected to represent free electrons. This indicates that the physical mechanisms involved in electronic charging differ from those applying to ionic charging. The estimated experimental values of the charging parameter $N_e t$, shown in Table 1 and used as $N_o t$ in the calculations of Figure 3, are believed to be a conservative upper limit. A more accurate determination of that charging parameter may result in an even larger difference between ionic charging and electronic charging. At least for the rather low values of Nt achieved in these experiments, the difference between ionic charging and electronic charging increases rapidly with particle size. This trend is consistent with the cases of negative charge enhancement described in the INTRODUCTION. In those cases, the density of unattached electrons averaged over the wire-plate spacing would have been a small fraction of the negative ion density. Although the work presented here demonstrates that particle charging by free electrons can be investigated in a conclusive manner, further experiments are needed to define the physical parameters and to determine the dependence of electronic charging on $N_e t$, a, and E. The data from these experiments should lead to an understanding of the physical mechanisms, a capability to develop a theoretical model, and a basis for advantageous use of electronic charging.

REFERENCES

1. Hewitt, G. W. The Charging of Small Particles for Electrostatic Precipitation. Trans. AIEE 76:300 (1957).

2. Smith, W. B., and J. R. McDonald. Development of a Theory for the Charging of Particles by Unipolar Ions. J. Aerosol Sci. 7:151 (1976).

3. Smith, W. B., L. G. Felix, D. H. Hussey, D. H. Pontius, and L. E. Sparks. Experimental Investigations of Fine Particle Charging by Unipolar Ions - A Review. J. Aerosol Sci. 9:101 (1978).

4. McDonald, J. R. A Mathematical Model of Electrostatic Precipitation (Revision 1). EPA-600/7-78-111a,b. NTIS PB284-614 and -615. U.S. Environmental Protection Agency, Research Triangle Park, NC (1978).

5. McDonald, J. R., M. H. Anderson, R. B. Mosley, and L. E. Sparks. Charge Measurements on Individual Particles Exiting Laboratory Precipitators with Positive and Negative Corona at Various Temperatures. J. Appl. Phys. 51:3632 (1980).

6. Grünberg, R. Anlagerung von Elektronen in Luft und in Gemischen aus O_2 mit He, N_2 und CO_2. Z. Naturforschung 33A:1346 (1978).

7. Dutton, J. A Survey of Electron Swarm Data. J. Phys. Chem. Ref. Data 4:577 (1975).

8. Pauthenier, M. M. and M. Moreau-Hanot. La Charge des Particules Sphériques dans un Champ Ionisé. J. Phys. et Radium 3:590 (1932).

TABLE 1. APPROXIMATE PARAMETERS FOR MEASURED ELECTRONIC CHARGING AND CALCULATED IONIC CHARGING OF PSL-H_2O PARTICLES

Anode positive voltage	kV	1	5	10
Duration of anode positive voltage, with 100 Hz square wave on anode	ms	5	5	5
Charge electric field E	kV/cm	0.82	4.1	8.2
Electron current through screen into charging region	μA	14	128	182
Electron drift velocity in charging region, assuming thermalized electrons (7)	10^6 cm/s	0.8	2.5	4.5
Free electron density N_e in charging region, assuming electron current distributed over 1 cm^2	10^8 cm^{-3}	1.09	3.20	2.52
Aerosol velocity	cm/s	268	268	268
Estimated maximum aerosol exposure time	ms	4.1	4.1	4.1
Charging parameter $N_e t$	10^6 cm^{-3} s	0.44	1.31	1.03

TABLE 2. APPROXIMATE PARAMETERS FOR AN EXPERIMENTAL COMPARISON OF ELECTRONIC CHARGING AND IONIC CHARGING OF DES PARTICLES

	Negative ions in dry air	Free electrons in ultrapure nitrogen
Electric field	5 kV/cm	5 kV/cm
Ion mobility	2 $cm^2/V \cdot s$	
Electron E/N		20 Td
Drift velocity	10^4 cm/s	3×10^6 cm/s
Anode current	1 μA	300 μA
Charge density	6×10^8 cm^{-3}	6×10^8 cm^{-3}
Charging Nt	10^6 cm^{-3} s	10^6 cm^{-3} s

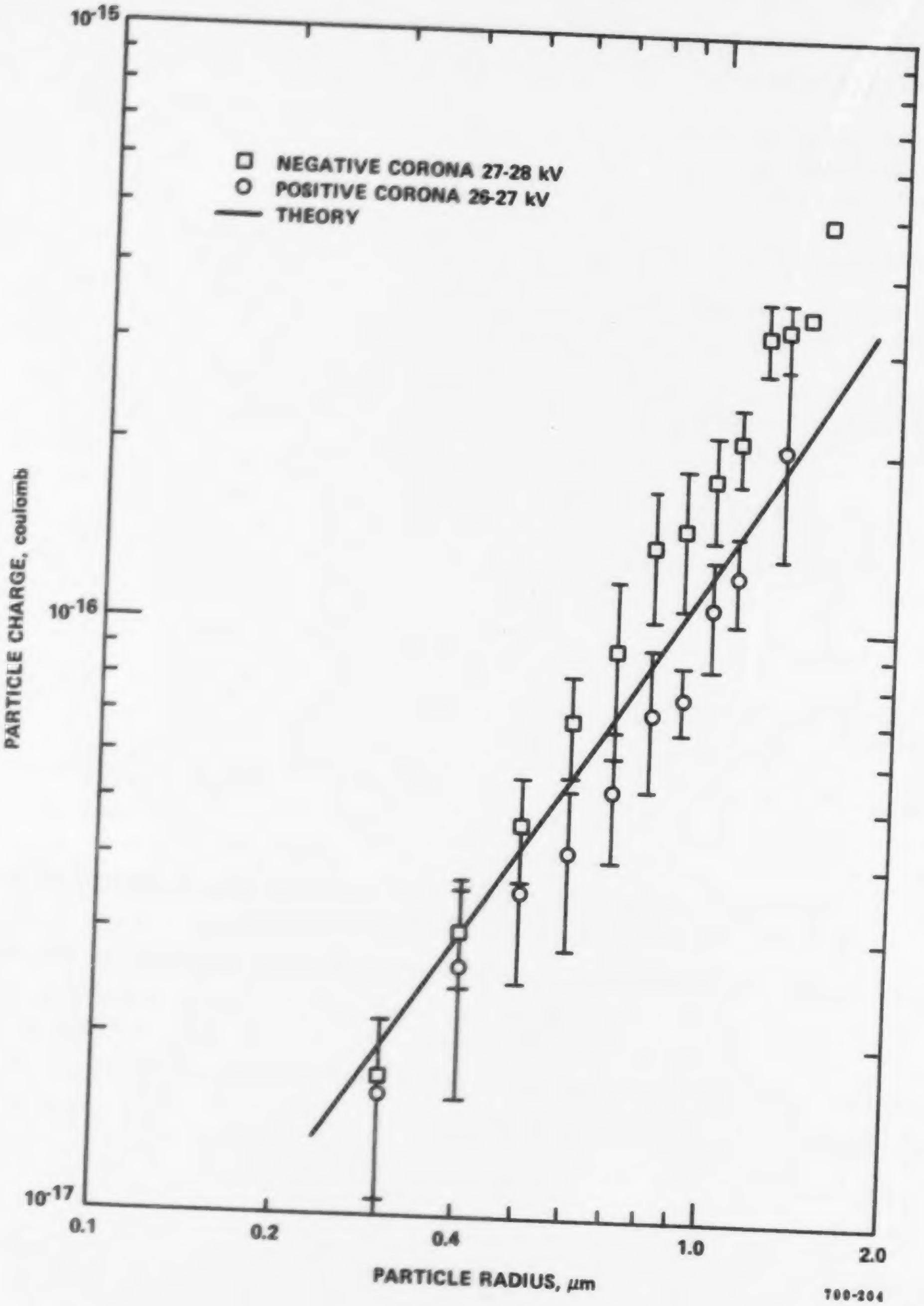

Figure 1. Measured positive and negative particle charge and comparison with ionic charging theory, at 343°C and 30 nA/cm^2 plate current density.

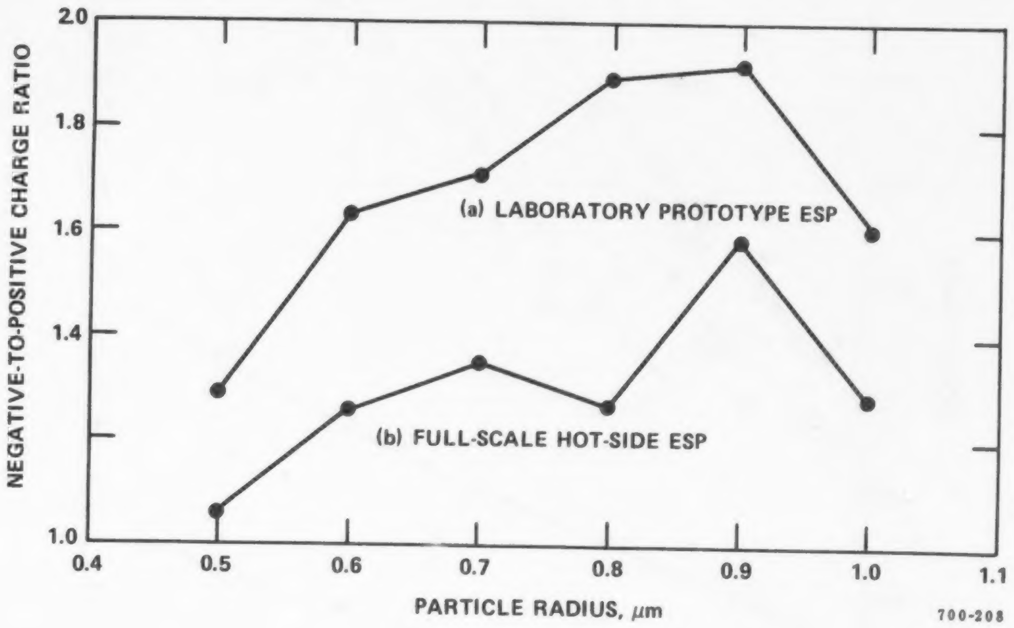

Figure 2. Measured negative particle charge, in proportion to the positive charge measured in a laboratory precipitator at 343°C and 30 nA/cm^2. (a) Laboratory precipitator at 343°C and 30 nA/cm^2. These data are the ratio of average values plotted in Figure 1. (b) Hot-side precipitator (Lansing Smith Plant) at 360°C and 20 nA/cm^2.

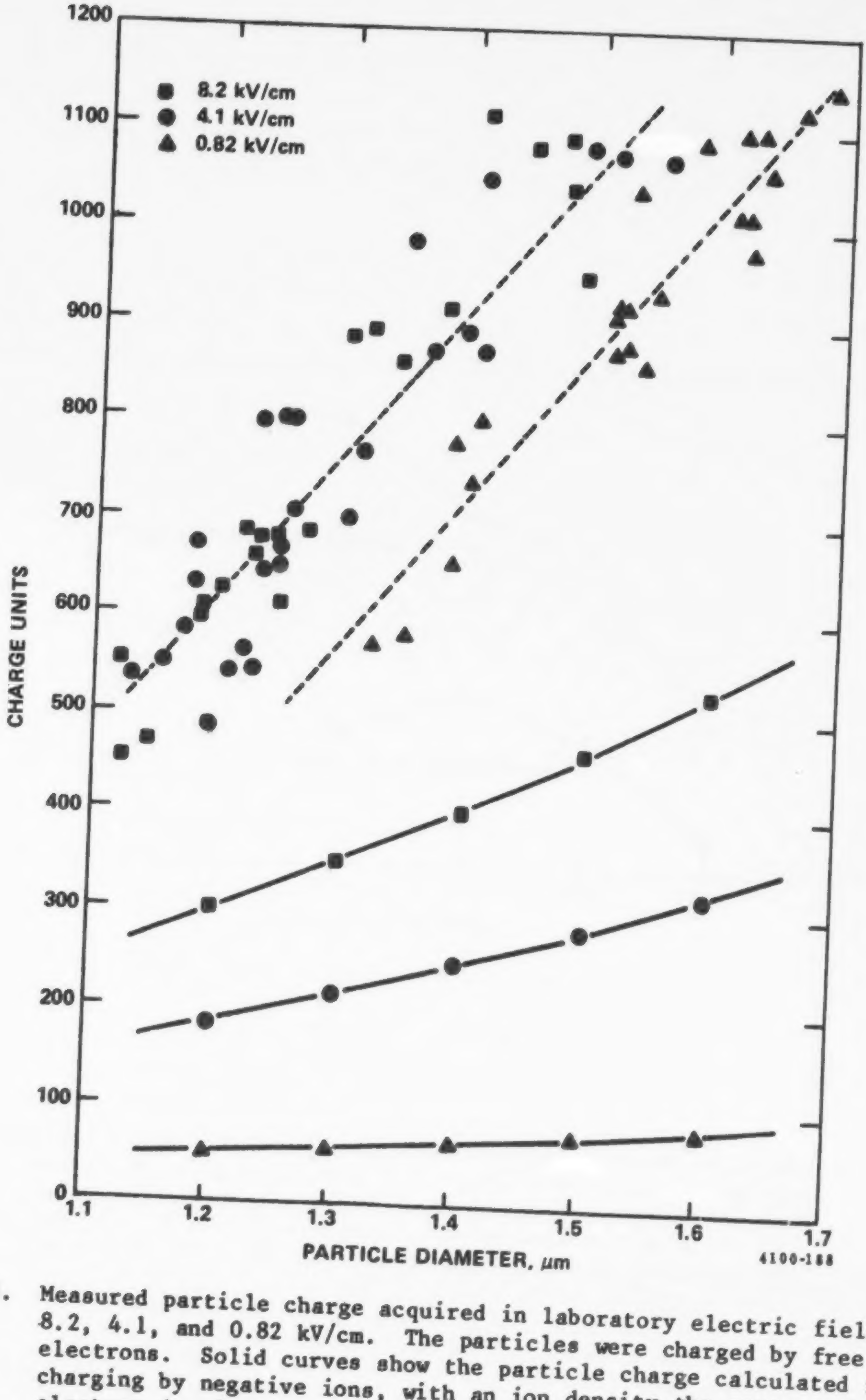

Figure 3. Measured particle charge acquired in laboratory electric fields of 8.2, 4.1, and 0.82 kV/cm. The particles were charged by free electrons. Solid curves show the particle charge calculated for charging by negative ions, with an ion density the same as the electron density.

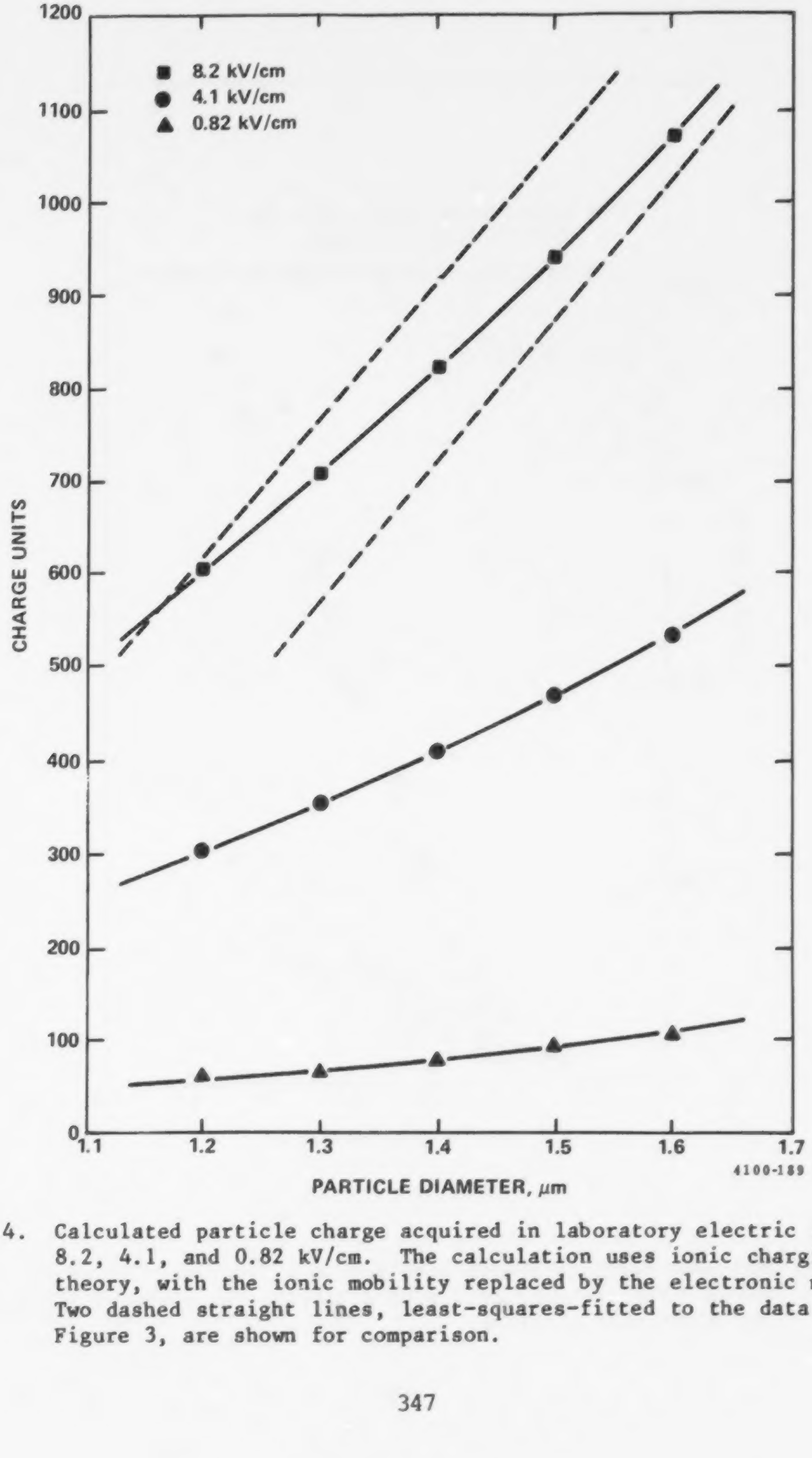

Figure 4. Calculated particle charge acquired in laboratory electric fields of 8.2, 4.1, and 0.82 kV/cm. The calculation uses ionic charging theory, with the ionic mobility replaced by the electronic mobility. Two dashed straight lines, least-squares-fitted to the data points in Figure 3, are shown for comparison.

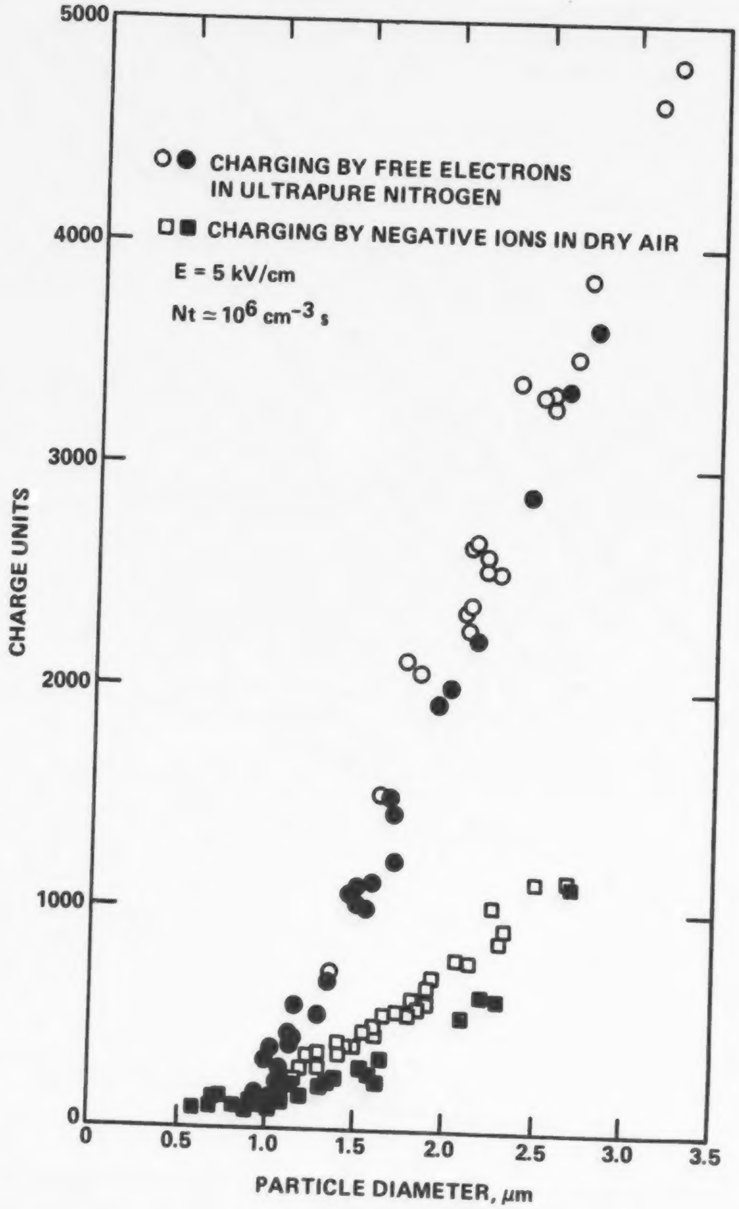

Figure 5. Measured particle charge acquired in a laboratory electric field of 5 kV/cm. The two data sets give a direct comparison of ionic charging and electronic charging.

GAS FLOW DISTRIBUTION MODEL TESTING

by: D. R. Cook
J. M. Ebrey
D. Novogoratz
Lodge-Cottrell/Dresser
Houston, Texas 77002

ABSTRACT

Uniform gas distribution is critical to the operational efficiency of both electrostatic precipitators and structural baghouses.

The relationship of collection efficiency to gas distribution criteria is discussed. The Deutsch-Anderson equation modelled into a computer gas distribution program indicates the effects of gas distribution deviations on efficiency performance.

Unique characteristics of the Lodge-Cottrell approach to gas flow distribution, pressure loss, and dust fallout testing are discussed, as are the proprietary distribution devices used. Test objectives and methods used are described.

These preceding discussions identify the need for gas flow correction technology and its role in fulfilling todays technological requirements.

The need for gas flow correction in structural baghouses is discussed, and some results presented.

Finally, model vs. field test results will be compared for both the electrostatic precipitator and the structural baghouse.

ACKNOWLEDGEMENTS

The authors wish to express their appreciation to Dresser Industries, Inc. for granting permission to publish this information and also our thanks to our colleagues at Lodge-Cottrell U.K. and U.S. for their assistance.

INTRODUCTION

Todays Plant Manager has to live in an environment of highly regulated emission control standards. The requirements for efficiencies of 99.5% and higher for particulate control devices on a continuing basis places a heavy responsibility on both the plant owner and the original equipment supplier.

In support of these demands, original equipment manufacturers must respond by offering control devices where every facet of the design is thoroughly scrutinized. One such critical area is the need for controlled gas distribution and minimized pressure losses.

Consider now, two devices widely used in industrial gas cleaning; the electrostatic precipitator and the fabric filter. While these are very different in their method of collecting dust, similar considerations hold for the need to control gas flow within the filtration zone. In our experience, devices relying on resistance to flow only succeed in improving gas distribution to the required standards with an unwelcome increase in pressure loss. In contrast, when the gas distribution is controlled by use of guide vanes, etc., then not only will the best distribution pattern be obtained, but also the pressure loss for the system will be minimum.

Our basic contention, therefore, is that a correctly designed gas distribution system does not rely on excessive use of resistance devices to control flow.

ELECTROSTATIC PRECIPITATORS

The critical need for controlled gas distribution in precipitators is self-evident. Consider a fifty-duct precipitator and imagine that with the flow control condition existing, one duct is completely devoid of gas flow. This has the effect immediately equivalent to a loss of 2% of the effective plate area. If the precipitator has been designed for an efficiency of 99.5% then the effect of the mal-distribution would be to increase dust emissions by 10%.

It is essential, therefore, that the gas distribution across the face of the electrode system be reasonably uniform. This can be illustrated by consideration of the Deutsch-Anderson formula used to calculate the efficiency for different gas velocities existing in different parts of the field as determined by a survey. A weighted mean efficiency is then produced which shows how much the efficency falls below that attained when the distribution is normally uniform. Fig. 1 shows such a uniform velocity survey and the associated mean efficiency. Fig. 2 indicates the effects of gas mal-distribution at this same position for the same flow rate. Efficiency is reduced from 99.03% to 98.6% while the RMS deviation increases from 15% to 35%. To achieve the same efficiency with the degree of mal-distribution present, the collector plate area would need to be increased in the order of 10%.

In addition to the uniformity of velocity profile, the gas must not bypass the field via the roof and hopper regions. As a simple example, if 1% of the gas completely bypasses the field, the efficiency can never exceed 99%

even when the dust removal from the remaining gases passing through the electrical field approaches 100%, which is equivalent to an infinite migration velocity.

Another variable condition which distorts gas distribution is the effect of dust buildup within the system. As the gas flue approaches a precipitator, the gas velocity must be reduced from the duct velocity of 15-23 meters/second to about 1.5 m/s. This must be achieved with the knowledge that as the gas velocity falls, so will dust tend to fallout. Failure to take this into consideration can result in partial blockage of the final gas distribution system with the consequent serious effects on gas distribution across the face of the precipitator.

For example, with flat resistance plate distributors, the probability of dust fallout is high behind the flat plate, effectively blocking a significant area of gas flow at the lower end of the collecting electrode. Another side effect of such fallout was experienced with the chevron arrangement widely used by some equipment suppliers a few years ago. This was a very compact gas distribution system used on large boiler installations. However, due to the low gas velocity, the inlet flares had substantial dust deposition which in some cases resulted in structural failure of the duct system.

The prerequisite for all correction devices installed in the system is that their ultimate effect on flow distribution is accomplished with minimum pressure loss and dust fallout. Three typical examples which achieve these criteria are; the proprietary top inlet mouthpiece (Fig. 3), with its triangular splitters followed by the tubular distributors which act as final smoothing devices. This system has the virtue of compactness and the ability to remain free of buildup with relatively adhesive dusts such as high-sulphur fly ash or cement dust, and has been widely used.

Another example is the patented high-velocity wedge type inlet (Fig. 4), which lends itself to a very compact mouthpiece so that the risk of fallout is at a minimum. This inlet is extremely valuable in retrofitting plants with space limitations.

Fig. 5 illustrates a typical horizontal straight inlet system. This uses honeycomb splitters and tubular distributors as the final smoothing device. The honeycomb splitters are of a spreading eggcrate configuration installed in the upstream position of the flare where controlled spreading of the gas takes place while still in a relatively high velocity area. By keeping the splitter in a high velocity area, the device is essentially self-cleaning, thus eliminating the need for external rapping. This is a particularly low pressure loss system, and remains free of fallout problems to an acceptable degree.

DECISION TO PERFORM A MODEL STUDY

Having highlighted some of the relationships between controlled gas distribution and particulate removal efficiency, it follows that flow correction must be considered an important aspect of equipment design and technology. The question is now asked, how can we most economically produce a system design to insure acceptable gas flow distribution? It is not possible to reliably calculate the total effects of gas flow correction devices, and, in view of todays large plant, on-site flow correction is not economically feasible.

The alternative is to accurately construct a scaled-down version of the system and to study the effects that various distribution devices have on the gas flow through the modelled system.

SELECTION OF MODEL SIZE

If scale modelling techniques are to be used to identify and provide solutions, then the first step is to decide the scale to which the model will be constructed.

To obtain useful results which can be interpreted to predict full-scale or prototype performance, modeling techniques have to attempt to satisfy certain laws of similarity.

Basically these are: Geometric, Kinematic and Dynamic similarity.

Geometric similarity means that the ratios of all corresponding dimensions on the model and prototype shall be equal. This condition is easily satisfied irrespective of the model scale.

Kinematic similarity exists between model and prototype when the ratios of corresponding velocities and accelerations are the same throughout the flow.

Dynamic similarity between the two flows occurs when the ratios of all forces acting on corresponding fluid masses are similar.

Satisfying the requirements of dynamic similarity of model and prototype in typical gas cleaning systems would require that the force ratios, as represented by Reynolds, Euler and Froude numbers, be the same in both systems. To simultaneously match these three force ratios is impractical in this type of model study and only becomes attainable as the model to prototype ratio approaches 1:1.

In most industrial flue systems, the flow is said to be turbulent, characterized by Reynolds numbers above the transition range of 2,000-4,000. This transition range has been the topic of some controversy and it has been argued that due to internal geometric configuration, flow separation probably takes place at a much lower calculated Reynolds numbers than those stated, and when this has taken place, flow patterns will remain the same over a wide range of Reynolds numbers.

It has, therefore, been concluded by many that the velocity profile pattern within a precipitator model is independent of the calculated Reynolds number providing that number is above 4,000. This has lead to the widespread use of small-scale models. Our experience, however, has been that only when operating high into the turbulent range does the pattern become less dependent of Reynolds number.

Figure 6 illustrates the relationship between the model scale, the treatment velocity within the precipitator model and the associated calculated Reynolds number. For this particular example a model constructed at 0.58:1 scale and operating at the prototype design treatment velocity, will duplicate the Reynolds number of the prototype. For a precipitator of todays dimensions, a model scale of 0.58:1 is neither practical nor economic. A more acceptable compromise might be to construct the model 1/8 full-size and operate at 2x the design velocity with a resultant calculated Reynolds number of 12,000, i.e. high into the turbulent range. However, in order to test at design velocity the Lodge-Cottrell approach would be to install every other collector plate, thus increasing the cross section to wetted perimeter ratio, and maintain a Reynolds number of 12,000.

For the above reasons it is recommended that the largest practical model scale size be utilized.

DISTRIBUTION CRITERIA AND MODEL STUDY OBJECTIVES

Today, with the demand for higher operating efficiencies, some customers and consulting engineers are specifying flow distribution criteria to which they feel the supplier must conform in order to obtain design efficiency.

Typical of some recent specifications are the following extracts:

1. The precipitator study shall conform to the most recent IGCI recommendations.
2. RMS deviations of 15% or less shall be achieved.
3. Collecting plates to be modelled in all fields.
4. Tests shall be performed at equivalent velocity, i.e., model gas velocity = site gas velocity.
5. Additional velocity surveys within the precipitator model will be performed at gas flow rates equivalent to 25, 50, 75, 100, 125 and 150% design flow rate.

Velocity surveys at significantly reduced velocities are not justified from a performance viewpoint since the effective S.C.A. would increase proportionately. However dust fallout in the ducting at low velocities is of concern and should be considered.

In addition to meeting these typical criteria, the model study needs to satisfy other specific objectives. Some of these are:

1. Obtain specified velocity distribution within the precipitator.
2. Minimize systems overall total pressure loss.
3. Identify and minimize dust fallout area.
4. Eliminate gas bypass of electrode system.
5. Optimize gas distribution to I.D. fan inlets.

Let's now address each of these points.

Velocity Distribution

1. Velocity surveys within the model are performed using hot-wire and electronic direct-reading vane anemometers. Measurement positions correspond to 4 ft. centers of equal area on the prototype. Signals generated by each sensor are interfaced to a computer via a digital voltmeter and stored. On completion of a survey, the results are immediately printed out on the computer terminal for assessment.

Pressure Loss

2. Pressures and velocities within the ducting system are determined with the use of a standard pitot tube and inclined manometer. Static and velocity pressure measurements together with ambient conditions are entered into the computer for rapid calculation of both velocity and total pressure at each position in the system of significant potential pressure loss.

Dust Fallout

3. Cork dust is used as an evaluation tool for identifying areas of potential dust fallout. Dust is injected into the flue system at a relatively low gas velocity sufficient to allow fallout to occur. When the pattern of dust deposit has become stable, the gas velocity is incrementally increased and the clearing effect upon the dust noted for each velocity increment. As a separate exercise, dust is introduced into the system at a sufficiently high gas velocity to remain entrained. By incrementally lowering the gas flow rate, areas can be identified where initial fallout is likely to occur. Fallout can be controlled in many cases by simple adjustment of existing turning vanes. By allowing the dust to be transported to the precipitator, an indication of the distribution across the face of a unit can be also made by measurement of the amount of dust fallout in each inlet hopper. In a recent study, the dust mal-distribution across the face of the precipitator was resolved by extending the trailing edge of the turning vanes at a critical position in the inlet ducting.

During the dust test, no attempt is made to either quantify the amount of fallout or predict the flow rate at which this would occur on the prototype installation. The dust is used as a visual aid to identify stagnant areas within the ducting system.

Gas Bypass of Electrode System

4. In practice, less than ideal flow conditions exist across the collecting electrodes, particularly at the upper and lower extremities. It is very important that the full collector height be utilized while preventing gas bypassing of the electrostatic field. This is achieved by horizontal top and bottom baffles across the full face of each field. Gases receiving partial treatment due to looping in and out of successive fields can be reduced to an acceptable level by this method. Smoke or neutral buoyancy

bubbles are used to evaluate gas bypass, particularly in the vicinity of the last field. To a large extent, evaluation of this condition is by visual means and is not quantitative. Relating gas behavior observed in this area on the model to the gas behavior predicted on the prototype should be made with caution, as the extent of looping and disturbance will be a function of time proportional to the model scale.

I.D. Fan Gas Distribution

5. The development of high efficiency I.D. fans has increased their sensitivity to velocity distribution at the fan inlet. Consequently, to maintain efficiency, fan manufacturers are imposing gas distribution standards as additions to the model study. Fortunately, these criteria are not too difficult to achieve because the measurement positions are normally in areas of high velocity.

MODEL CONSTRUCTION PROCEDURES

Prior to the commencement of a model study, the precipitator designer has studied both contract specifications and plant site real estate constraints to produce the most economic ducting arrangement. Economic, in this sense, does not imply the cheapest, but the most efficient arrangement to transport the gases and remain within the limitations placed upon him by site constraints. It is extremely rare for ducting modifications to result from model study findings. In fact, it becomes the model study departments' responsibility to "make the layout work".

Lodge-Cottrell started model study work in 1947. This practical experience combined with theories discussed in earlier sections of this paper led to the adoption of a 1/8 scale minimum model size.

Construction materials are wood, masonite, plexiglass and aluminum, with the modelled system extending normally from the air pre-heater outlet to the inlet side of the I.D. fan. The flue system from the outlet of the I.D. fan to and including a length of chimney are also modelled when requested. Where necessary, turning vanes and internal bracings are installed in the inlet and outlet ducting. Depending upon the configuration of the precipitator inlet mouthpiece, a particular type of distribution device selected from various proprietary designs is selected and installed in a starting pattern. In the precipitator outlet mouthpiece, proprietary sawtooth distributors are installed in a starting pattern. The sawtooth distributors ensure that gases in the final stages of cleaning remain within the confines of the electrode system and are not prematurely drawn towards the high velocity outlet ducting in the vertical plane. Within the precipitator roof and hopper levels, baffles are installed and unless specified to the contrary, collecting electrodes are simulated only in the first and last fields of the precipitator model. As mentioned in the previous section, some specifications require that each field of collectors be modelled. This is based on the argument that "the plates act to preserve existing horizontal distributions and that the absence of several groups of plates could make the modelled outlet velocity distribution different than it is in the actual unit."(1) Our experience shows that in large models operating at relatively low treatment velocities, collector plates downstream of the first field have a negligible influence on preservation of the velocity profiles measured at the outlet of the first field. If a relatively uniform velocity distribution is achieved at the outlet of the first field, then this degree of distribution will progressively improve through the precipitator.

Collector plates installed in the last field of the precipitator model, however, do play a role in controlling gases by minimizing the tendency of the gas to horizontally converge towards the outlet ducting. Avoiding vertical convergence of the gases to the outlet ducting is achieved with sawtooth distributors as discussed earlier.

Following the installation of turning vanes, flow correction devices, and distributors in the "starting pattern", the model is connected to one or more of three test fans. Each fan is rated at 9.4 m^3/s at 406 mm w.g., offering the capability of testing to 1/8th scale a prototype designed for handling over 1,415 m^3/s.

LIMITATIONS TO OPTIMUM DISTRIBUTION

1. In October 1981, the Industrial Gas Cleaning Institute (IGCI) revised its Publication No. EP-7, Gas Flow Model Studies. This standard for acceptable gas distribution states, "Within the treatment zone near the inlet and outlet faces of the precipitator collection chamber the velocity pattern shall have a minimum of 85% of the velocities not more than 1.15 times the average velocity, and 99% of the velocities not more than 1.40 times the average velocity."

The revised standard does not impose any limitations on areas of low velocity within the precipitator. In an extreme case, Fig. 7, the survey obviously does not follow any "normal" or Gaussian distribution but nevertheless conforms to the IGCI standard. The effect of low velocity areas is illustrated by the potential loss of efficiency from 99.15% to 98.6%. This would result in a 65% increase in dust emissions. It is important to note that the high efficiencies obtained in the low velocity areas are not compensated by the lowered efficiencies at the higher velocities, due to the exponential relationship between efficiency and velocity.

Our recommendation is that the old IGCI standard "85% of the velocity readings, within ±25% of the average velocity, and all readings within ±40% of the average velocity"(2) together with the imposition of the 15% RMS deviation at the end of the first field, is more than adequate for todays needs. We have used the above criteria for years and have many high efficiency operational units to prove the veracity of our recommendation.

2. Unless specified differently, the model assumes that the gas distribution at the inlet to the flue system--in the case of a boiler, the air pre-heater outlet--is uniform. There is no alternative to this since the data is rarely available, but in practice not only is distribution at this plane rarely uniform, it can also change as some degree of buildup occurs in the air pre-heater. Accepting that this condition exists, mal-distribution is deliberately induced at the air pre-heater outlet to check effects upon

precipitator distribution. There is some smoothing due to turbulence as the gas is progressed through the flue system, but even so the very fact that this situation exists implies that very fine correction of gas flow in the precipitator on the flow model is not justified.

3. None of the flow distribution criteria or work carried out takes any account of the turbulence induced by the ionic or electric wind. It is known that this produces gas movements of up to 3 m/s, that is higher than the mean gas velocity in the average commercial precipitator. The dramatic effect of this phenomena is demonstrated on Figs. 8 and 9. Note the vertical spread of the gas as the electric field is applied. This phenomena is currently being studied and we hope to have the opportunity to report the results of this study in the near future.

The cost of flow correction devices on the prototype and cost of carrying out the flow model work escalates rapidly as distribution criteria becomes more stringent. In view of the pratical limits to optimum distribution discussed above, the pre-1981 IGCI recommendations together with a 15% RMS criteria at the end of the first field constitute a reasonable practical limit, based on our experience on 1/8 scale models.

GAS FLOW CORRECTION FOR FABRIC FILTERS

Unless corrective work is performed on precipitators, mal-distribution of gas flow within the precipitator treatment zone will remain there indefinitely. In the case of a fabric filter, initial mal-distribution to the thimble plate will be improved to some degree as filter cake develops back pressure. However, this infers that for some period of time, higher than designed air to cloth ratios are experienced. This is due to the lack of equal flow to filter bags. These thoughts prompted a recent model study of a single compartment within a multicompartment fabric filter.

The model was constructed 1/4 full size, with 234 thimbles installed. Fig. 10 shows the extent of the model construction. An additional simulated second compartment was constructed. The purpose of this addition was to allow simulation of gas flow take off, as experienced in a multicompartment baghouse.

It should be mentioned that this exercise is part of an overall development program associated with multicompartment fabric filters. However, this discussion is limited to the following objectives:

1. Determine the velocity distribution of inlet gases to the filter thimbles.

2. Determine the distribution of "reverse gas cleaning" gases to the filter thimbles.

3. Assess the disturbance and/or re-entrainment of hopper dust during filtering and reverse gas cleaning.

4. Determine system pressure loss.

Before Flow Correction

Initial observations and measurements were made without flow correction devices, and the hoppers were partially filled with cork dust to a level below the inlet entrance.

Figure 11 shows the turbulent gas path with the resultant scouring and re-entrainment of hopper dust. Negative flow during normal filtering mode was observed over 54% of the thimble area, as shown in Figure 12.

The total pressure differential across the model system was measured at 142 mm w.g.

After Flow Correction

Continued tests led to the inclusion of flow distribution devices developed from our precipitator distribution technology and similar to those used during the model study for the EPRI Fabric Filter Pilot Plant.

The results of the final tests with the inclusion of flow correction devices showed that:

1. Positive gas flow through the thimbles gave an RMS deviation of 14% across the cell plate.
2. A 23% RMS deviation during reverse gas cleaning.
3. The hopper dust remained undisturbed.
4. The pressure differential across the system was reduced to 91 mm w.g., a decrease of 51 mm or 36%.
5. Negative gas flow through the thimble plates was eliminated.

With the addition of a few simple flow correction devices, it is possible to achieve acceptable flow distribution, eliminate disturbance of previously captured dust and reduce overall pressure loss.

CONCLUSIONS

The approaches to flow model studies which have been discussed here have consistently resulted in excellent correlation between onsite measurements, and those predicted from the model.

Figure 13 demonstrates the onsite measurements of two recent precipitator installations with those determined from their respective model studies and confirms our previous statement.

Figure 14 (3) shows the comparison between thimble plate velocity surveys carried out on the Lodge-Cottrell designed EPRI Fabric Filter Pilot Plant at

Arapahoe Station as compared to the models test surveys. These comparisons are shown with and without gas distribution devices.

The improvement in velocity profile using distribution devices is evident, and the close similarity in velocity contour between model and prototype for both conditions supports our confidence in large scale modelling.

Our experience in flow model studies has led to the following conclusions:

1. A correctly designed gas distribution system does not rely upon excessive use of resistance devices to control flow.
2. The largest practical size model should always be utilized to ensure reasonable correlation between the model and the full-size installations.
3. More stringent distribution criteria is not justified until existing practical limitations have been addressed.
4. Flow correction devices in fabric filters can reduce re-entrainment of previously captured dust, and reduce overall pressure loss.

It is Lodge-Cottrell policy to conduct gas flow studies for large precipitator and fabric filter contracts. Operating units have consistently met or exceeded contract performance specifications.

The work described in this paper was not funded by the U.S. Environmental Protection Agency and therefore the contents do not necessarily reflect the views of the Agency and no official endorsement should be inferred.

REFERENCES

1. Gas Flow Model Studies, Publication EP-7, Industrial Gas Cleaning Instutute, Revision 4

2. Gas Flow Model Studies, Publication EP-7, Industrial Gas Cleaning Institute, Revision 3

3. Cusing, Kenneth M., Wilson, Rufus Ray Jr., Smith, Wallace B., Belkus, Paul and Carr, Robert. Arapahoe Fabric Filter Pilot Plant, Air Load-Flow Distribution Test Results, EPRI RP 1129, November 1980

4. Darby, Ken. Criteria for Designing Electrostatic Precipitators, EPA Second Symposium on the Transfer and Utilization of Particulate Control Technology, July 1979.

1.22 99.74%	1.30 99.64%	1.37 99.50%	1.45 99.34%	1.52 99.15%	1.52 99.15%	1.60 98.94%	1.68 98.69%	1.75 98.42%	1.83 98.13%
1.22 99.74%	1.30 99.64%	1.37 99.50%	1.45 99.34%	1.52 99.15%	1.52 99.15%	1.60 98.94%	1.68 98.69%	1.75 98.42%	1.83 98.13%
1.22 99.74%	1.30 99.64%	1.37 99.50%	1.45 99.34%	1.52 99.15%	1.52 99.15%	1.60 98.94%	1.68 98.69%	1.75 98.42%	1.91 97.80%
1.13 99.84%	1.30 99.64%	1.37 99.50%	1.45 99.34%	1.52 99.15%	1.52 99.15%	1.60 98.94%	1.68 98.69%	1.75 98.42%	1.92 97.73%
1.13 99.84%	1.30 99.64%	1.37 99.50%	1.45 99.34%	1.52 99.15%	1.52 99.15%	1.60 98.94%	1.68 98.69%	1.75 98.42%	1.92 97.73%
1.07 99.89%	1.30 99.64%	1.37 99.50%	1.45 99.34%	1.52 99.15%	1.52 99.15%	1.60 98.94%	1.68 98.69%	1.75 98.42%	1.92 97.73%
1.07 99.89%	1.30 99.64%	1.37 99.50%	1.45 99.34%	1.52 99.15%	1.52 99.15%	1.60 98.94%	1.68 98.69%	1.75 98.42%	1.98 97.45%
1.02 99.92%	1.22 99.74%	1.37 99.50%	1.45 99.34%	1.52 99.15%	1.52 99.15%	1.60 98.94%	1.68 98.69%	1.83 98.13%	1.98 97.45%
1.02 99.92%	1.22 99.74%	1.37 99.50%	1.45 99.34%	1.45 99.34%	1.60 98.94%	1.60 98.94%	1.68 98.69%	1.83 98.13%	1.98 97.45%
1.02 99.92%	1.22 99.74%	1.37 99.50%	1.45 99.34%	1.45 99.34%	1.60 98.94%	1.60 98.94%	1.68 98.69%	1.83 98.13%	1.98 97.45%

DESIGN MIGRATION VELOCITY
= 8.0 cm/sec

EFFECTIVE CSA = $102m^2$

COLLECTOR PLATE AREA
= $9290m^2$

AVERAGE VELOCITY = 1.52 m/sec

RMS DEVIATION = 15%

AVERAGE EFFICIENCY = 99.03%

FIGURE 1 NORMAL DISTRIBUTION

0.51 100.00%	0.51 100.00%	1.73 98.52%	1.73 98.52%	1.73 98.52%	1.52 99.15%	1.73 98.52%	1.73 98.52%	1.73 98.52%	2.11 96.82%
0.51 100.00%	0.51 100.00%	1.73 98.52%	1.73 98.52%	1.73 98.52%	1.52 99.15%	1.73 98.52%	1.73 98.52%	1.73 98.52%	2.11 96.82%
0.51 100.00%	0.51 100.00%	1.73 98.52%	1.73 98.52%	1.73 98.52%	1.52 99.15%	1.73 98.52%	1.73 98.52%	1.73 98.52%	2.11 96.82%
0.51 100.00%	0.51 100.00%	1.73 98.52%	1.73 98.52%	1.73 98.52%	1.52 99.15%	1.73 98.52%	1.73 98.52%	1.73 98.52%	2.11 96.82%
0.51 100.00%	0.51 100.00%	1.73 98.52%	1.73 98.52%	1.73 98.52%	1.52 99.15%	1.73 98.52%	1.73 98.52%	1.73 98.52%	2.11 96.82%
0.51 100.00%	0.51 100.00%	1.73 98.52%	1.73 98.52%	1.73 98.52%	1.52 99.15%	1.73 98.52%	1.73 98.52%	2.49 94.62%	2.11 96.82%
0.51 100.00%	0.51 100.00%	1.73 98.52%	1.73 98.52%	1.73 98.52%	1.52 99.15%	1.73 98.52%	1.73 98.52%	2.11 96.82%	2.11 96.82%
0.51 100.00%	0.51 100.00%	1.73 98.52%	1.73 98.52%	1.73 98.52%	1.52 99.15%	1.73 98.52%	1.73 98.52%	2.11 96.82%	2.11 96.82%
0.51 100.00%	0.51 100.00%	1.73 98.52%	1.73 98.52%	1.73 98.52%	1.52 99.15%	1.73 98.52%	1.73 98.52%	2.11 96.82%	2.11 96.82%
0.51 100.00%	0.51 100.00%	1.73 98.52%	1.73 98.52%	1.73 98.52%	1.52 99.15%	1.73 98.52%	1.73 98.52%	2.11 96.82%	2.11 96.82%

DESIGN MIGRATION VELOCITY
= 8.0 cm/sec

EFFECTIVE CSA = $102m^2$

COLLECTOR PLATE AREA
= $9290m^2$

AVERAGE VELOCITY = 1.52 m/sec

RMS DEVIATION = 35%

AVERAGE EFFICIENCY = 98.60%

FIGURE 2 NON-UNIFORM DISTRIBUTION

FIGURE 3

TOP ENTRY NOZZLE

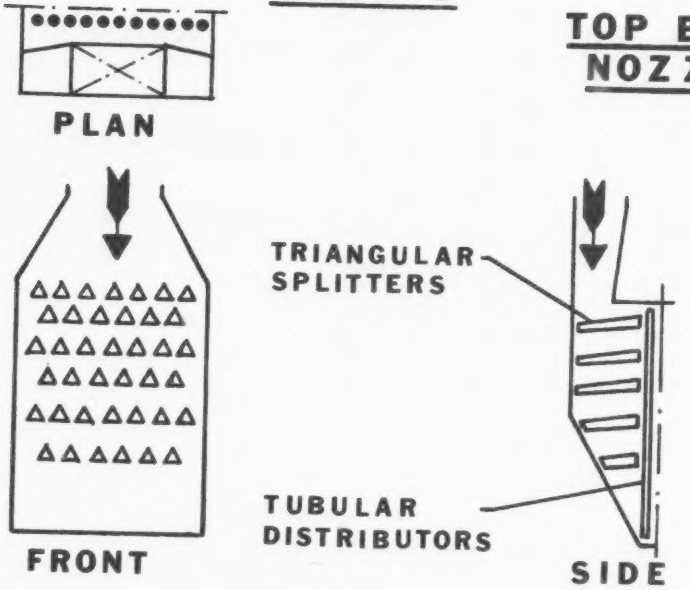
PLAN
TRIANGULAR SPLITTERS
TUBULAR DISTRIBUTORS
FRONT
SIDE

FIGURE 4

HIGH VELOCITY WEDGE INLET

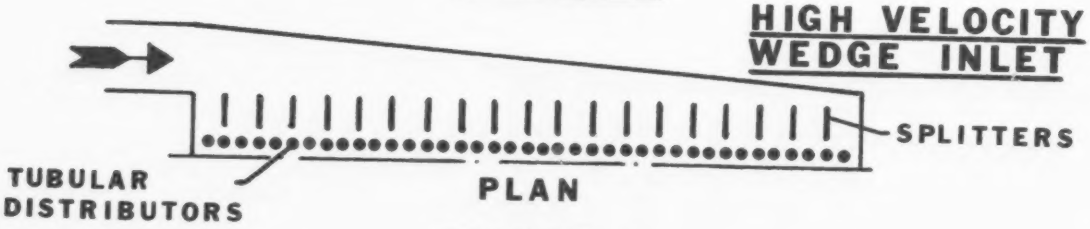
SPLITTERS
TUBULAR DISTRIBUTORS
PLAN

FIGURE 5

HORIZONTAL INLET

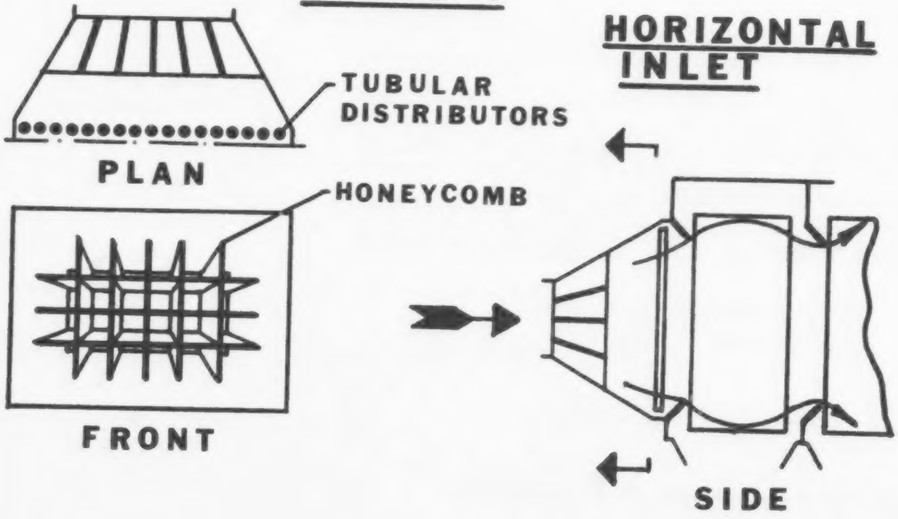
TUBULAR DISTRIBUTORS
PLAN
HONEYCOMB
FRONT
SIDE

FIGURE 6

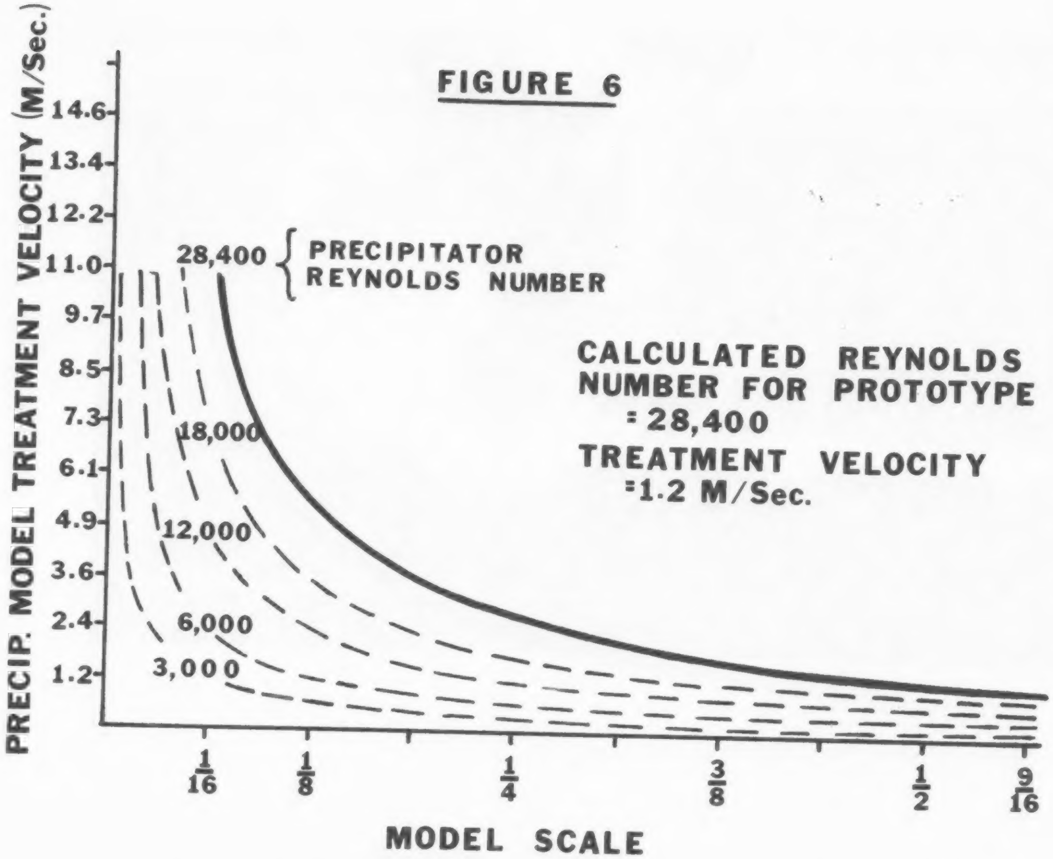

CALCULATED REYNOLDS NUMBER FOR PROTOTYPE
= 28,400
TREATMENT VELOCITY
= 1.2 M/Sec.

FIGURE 7

DESIGN:-

TREATMENT VELOCITY = 1.52 M/Sec.
MIGRATION VELOCITY = 8.00 Cm/Sec.
EFFICIENCY = 99.15%

ACTUAL:-

AVERAGE VELOCITY = 1.52 M/Sec.
VELOCITIES ABOVE 15% = 15%
VELOCITIES ABOVE 40% = 1%
RMS % DEVIATION = 35
AVERAGE EFFICIENCY = 98.60%

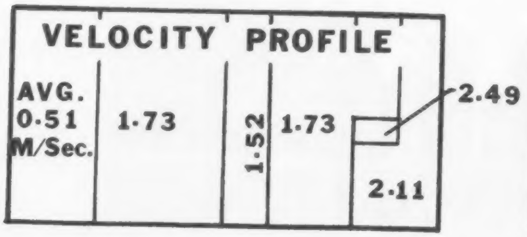
VELOCITY PROFILE
AVG. 0.51 M/Sec.
1.73
1.52
1.73
2.49
2.11

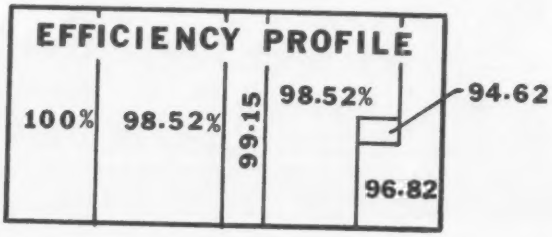
EFFICIENCY PROFILE
100%
98.52%
99.15
98.52%
94.62
96.82

EFFECT OF IONIC WIND

FIGURE 8

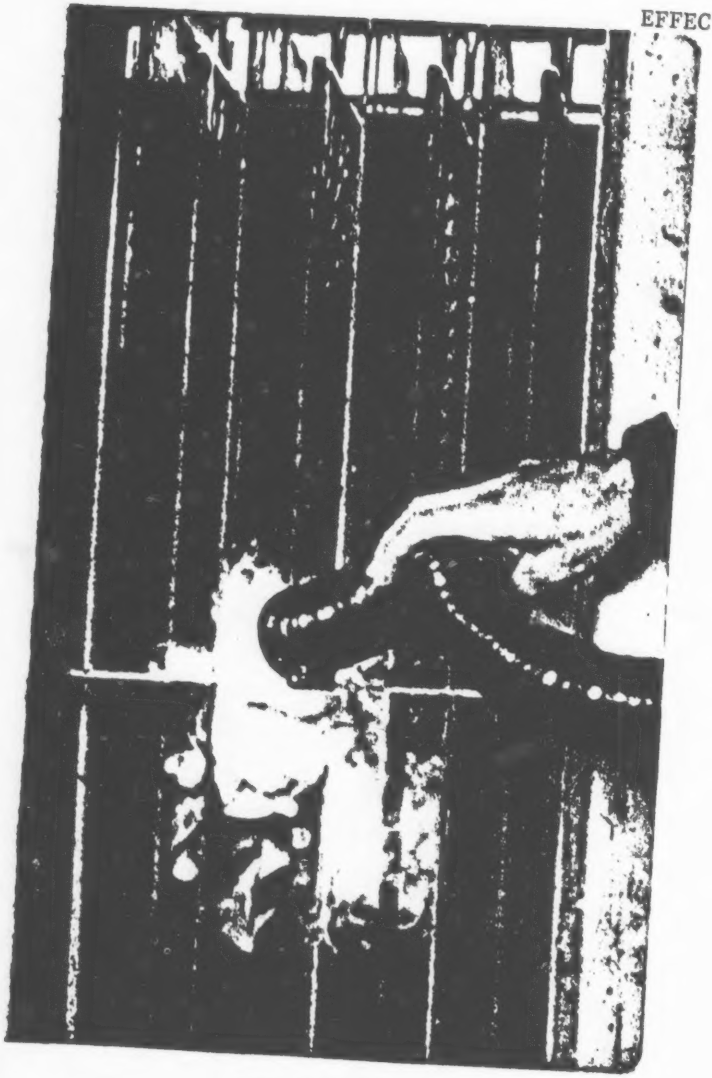

DEENERGIZED

FIGURE 9

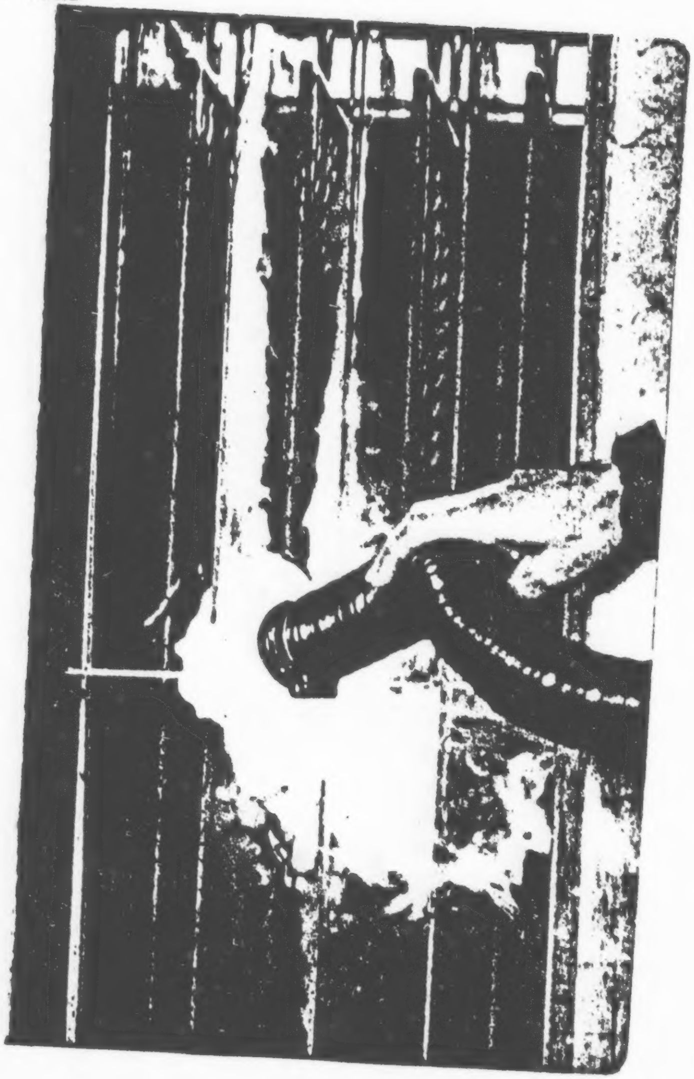

ENERGIZED

Reproduced from
best available copy.

FIGURE 10

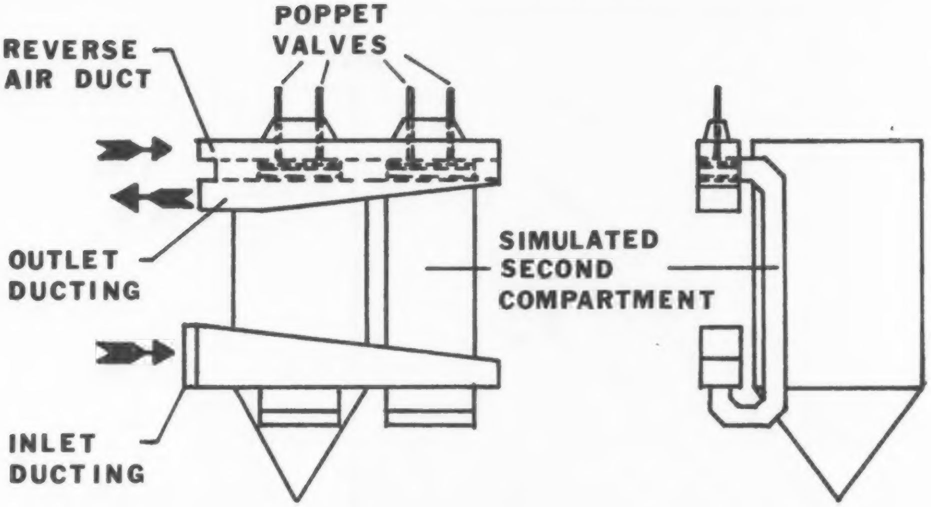
POPPET VALVES
REVERSE AIR DUCT
OUTLET DUCTING
SIMULATED SECOND COMPARTMENT
INLET DUCTING

EXTENT OF MODEL CONSTRUCTION

FIGURE 11

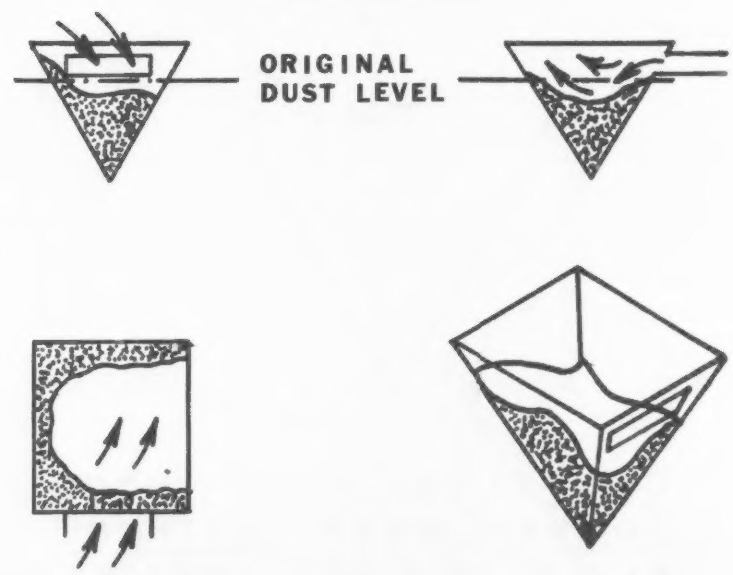
ORIGINAL DUST LEVEL

DISTURBANCE OF HOPPER DUST WITHOUT FLOW DEVICES INSTALLED

FIGURE 12

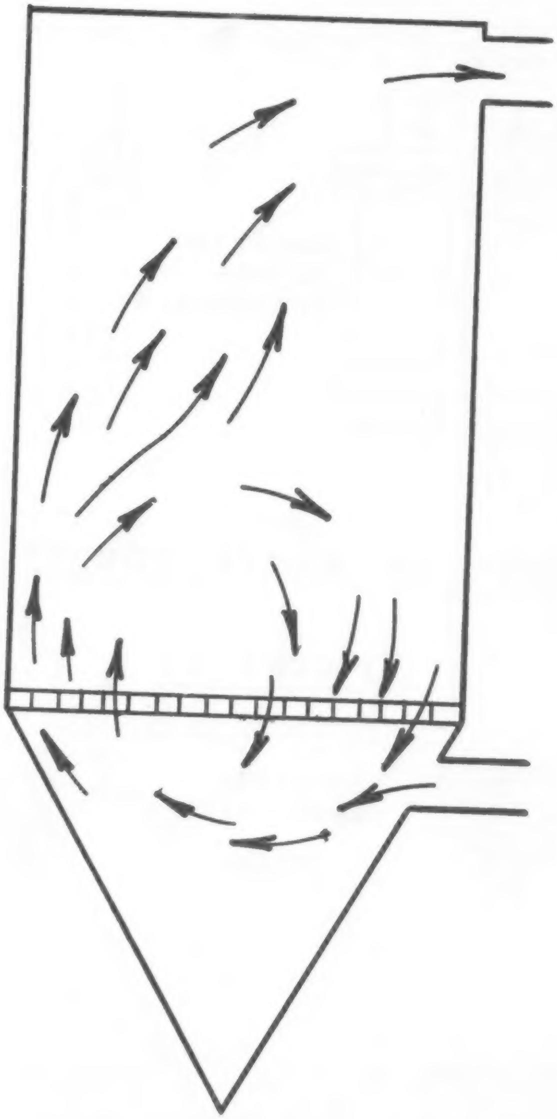

GAS FLOW PATH THROUGH COMPARTMENT WITHOUT FLOW DEVICES INSTALLED

FIGURE 13

490MW BOILER:-

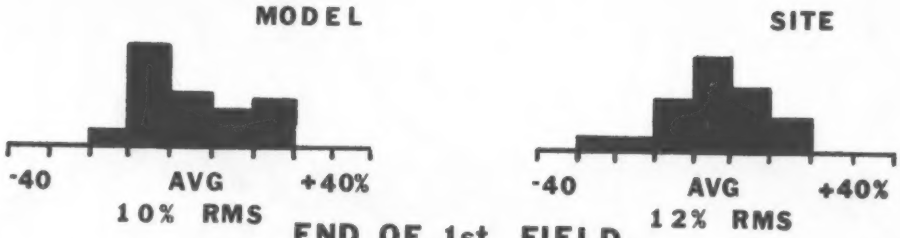

END OF 1st FIELD

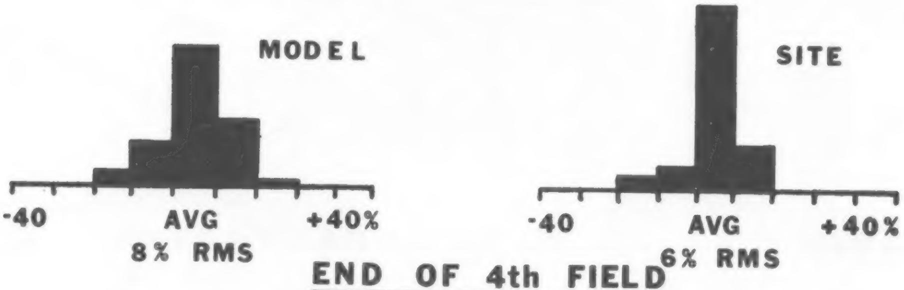

END OF 4th FIELD

120MW BOILER:-

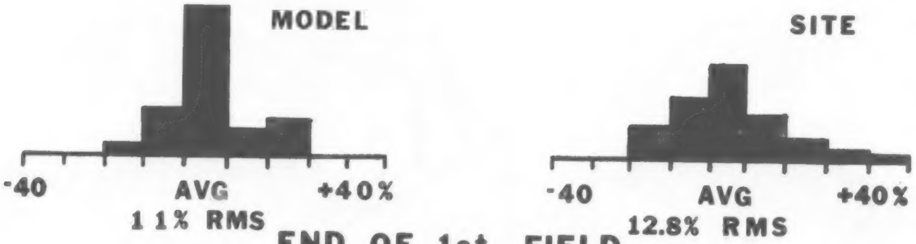

END OF 1st FIELD

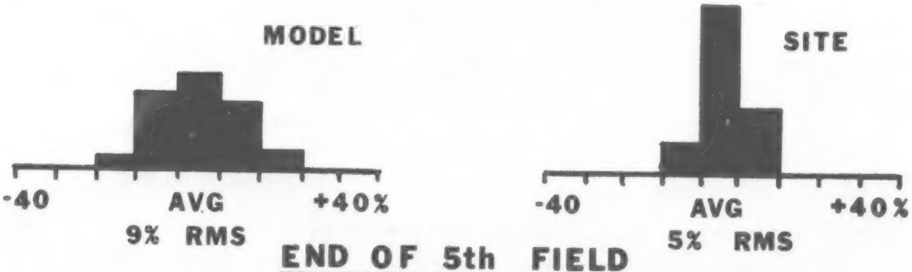

END OF 5th FIELD

FIGURE 14

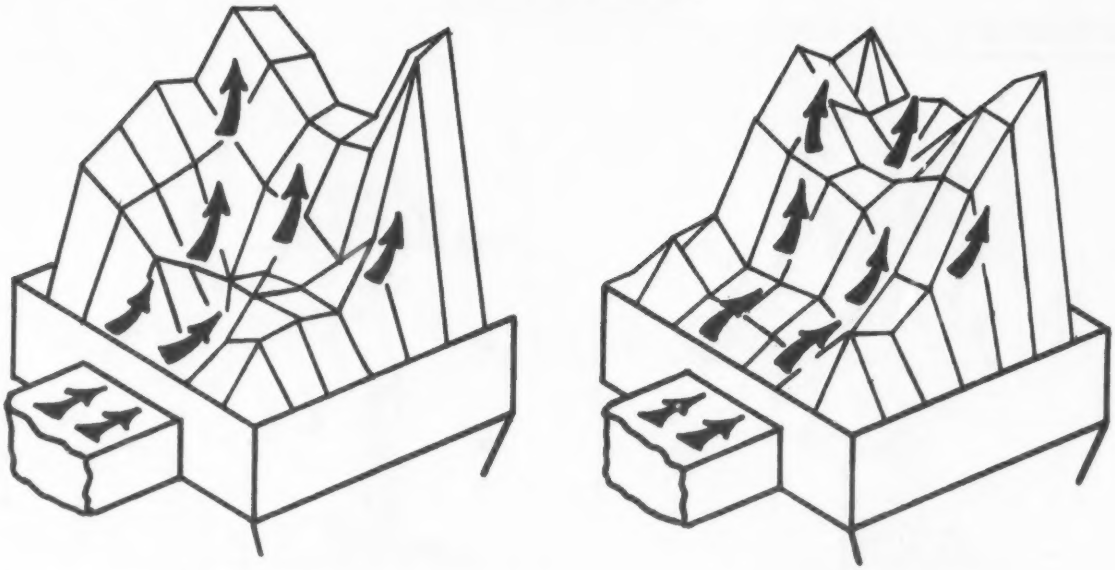

MODEL PROTOTYPE

WITHOUT DISTRIBUTORS

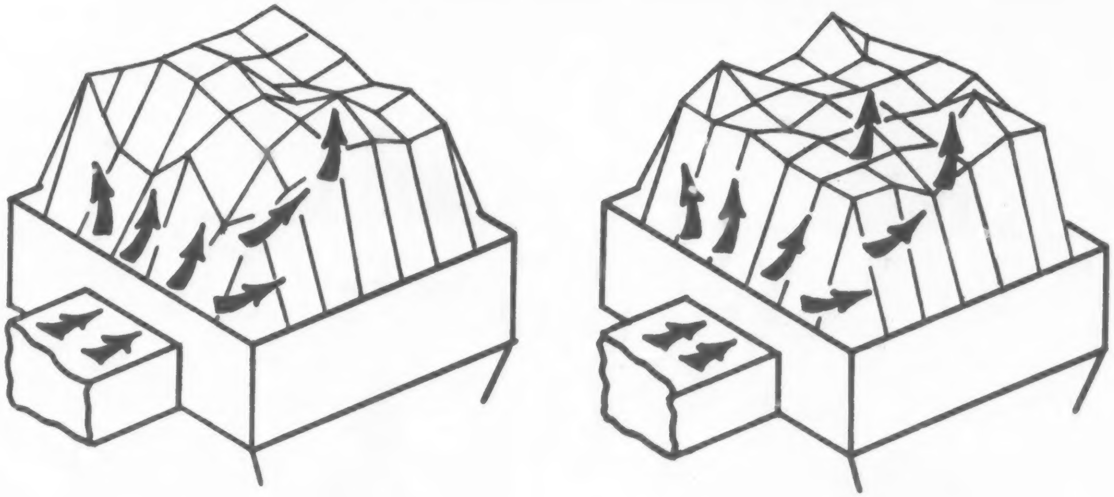

MODEL PROTOTYPE

WITH DISTRIBUTORS

AIR FLOW MODEL STUDIES

by: L. H. Bradley
United Engineers and Constructors
Philadelphia, Pennsylvania 19101

ABSTRACT

This paper establishes the need for strict control of air flow model studies and the higher acceptance standards for test results which are required to obtain the collection efficiencies needed to satisfy regulatory requirements. The importance of flow patterns and minimum pressure losses is reviewed and discussed including the importance of dimensionless ratios such as Reynolds Number, modified Fraude Number, and the momentum ratio. The requirements for design, scale, model limits, fabrications and test procedures as established by I.G.C.I. Standards and additional requirements are shown and discussed. Data collection methods including limitations and evaluation methods for test data are presented and discussed. Examples from recent air flow model studies are presented and reviewed to illustrate items which should be considered. Based on these results, a comparison of deviation from design collection efficiency as a function of root mean square deviation is shown.

The work described in this paper was not funded by the U.S. Environmental Protection Agency and, therefore, the contents do not necessarily reflect the views of the Agency and no official endorsement should be inferred.

1.0 INTRODUCTION

The use of scaled models for evaluation of flow distribution patterns and to establish expected pressure losses has been common practice for many years. Because of the varied opinions regarding the interpretation of the test data and the lack of field data to verify reproducibility in the prototype installations, the need for and the importance of model studies have been questioned for many years. However, over the last few years, numerous existing installations have improved the performance of the particulate collector by conducting model studies. In addition, two factors have combined to emphasize the need for detailed model studies. These factors are:

a The regulatory standards required a reduction in particulate emission level to 0.03 lbs/mm BTU. This, in turn, requires collection efficiencies ranging from 99.4% to 99.8% and

b The cost of energy has increased substantially.

To obtain the efficiencies mentioned in (a) above, excellent flow distribution must be assured. Item b above dictates that the system consisting of the collector and associated ducts be designed for a minimum pressure loss. For these reasons, United Engineers believes that detailed model studies are a necessity and therefore, includes this requirement for all particulate collection systems.

The requirements for a model study often have been expressed in a single paragraph contained in the equipment specification. This can and often does result in an inferior model study and misunderstanding between the owners, the Engineers, and the test personnel regarding the overall requirements. It is believed that a separate section of the specification should be devoted to the model study and this section should include the scope, the design requirements, the acceptance criteria for the test results, the preferred methods for data collection and the acceptable evaluation methods. United Engineers also insists on the right of witness and the review of test data. This paper will outline the requirements which are recommended for inclusion in the specifications for a model study and provides some example of data collected during a model study.

2.0 MODEL STUDY REQUIREMENTS

The requirements for a model study may be issued as a separate specification or as a separate section of the equipment specification. The following items are suggested as the minimum requirements to be included:

A) Purpose of the Study
B) Scope of the Study
C) Fabrication of the Model
D) Design and Acceptance Criteria
E) Data Acquisition

F) Data Evaluation
G) Special Requirements

The inclusion of and the compliance with the details of the above requirements will result in model study results which will dictate the design and placement of flow distribution devices at the inlet and the outlet of the precipitator for flow distribution as well as areas in the associated ducts which require the installation of turning vanes to correct flow disturbances. The incorporation of these items in the prototype unit will obtain minimum system pressure loss and will enable the collector to operate at the designed collection efficiency.

2.1 PURPOSE

The purpose of all model studies is simple: optimize the flow distribution through the use of flow corrective devices and to obtain minimum pressure loss. Both of the above must be consistent with acceptable engineering design standards.

2.2 SCOPE

To obtain full evaluation of the gas flow distribution and the associated pressure loss, the scope of the equipment to be modelled should include all ducts from the air heater outlet to the inlet transition box of the collector, the collector including the inlet and outlet transition box and the connecting ducts to the inlet of the induced draft fan. For installations with separate primary and secondary air heaters, both connecting ducts should be modelled and the flow should be adjusted to reflect the expected flows in the prototype unit. In addition, the ducts should include internal struts, trusses, etc. to fully duplicate the flow distribution and the pressure losses.

For units with more than one collector, both units should be modelled unless one is a mirror image of the other. If differences in ducts, turns, etc., exist, separate studies are required to determine both the flow distribution and the pressure loss. In some cases, the same collector can be used and the connected ducts are modified.

2.3 FABRICATION

To obtain similarity between the model and the prototype unit, the fabrication of the model and the associated ducts must be based on drawings of the prototype and be to the selected scale.

I.G.C.I. standard E.P.-7 specifies a scale of 1 to 16 or larger and is commonly used in the United States. A scaling factor of 1 to 12 is usually used in Canada, Great Britian, and the European Countries.

The fabrication of the system should include the inlet and the outlet transition boxes complete with flow distribution devices, the collector complete with plates in all electrical fields, ash collection hoppers and all associated ducts complete with internal struts, braces, etc. Provision should be incorporated into the design of the model to permit easy installation of turning vanes, flow distribution plates, etc. Some model studies have been conducted without installation of all internal collector plates, but the inclusion of all plates will provide a more accurate evaluation of internal drift or movement of gas flow within the collector between the inlet and the outlet.

The material for fabrication of the model should permit visual observation of the flow patterns as an integral part of the test program. Plywood or sheet metal may be allowed for fabrication of duct sections where visual observation of the flow pattern is not critical.

2.4 DESIGN CONSIDERATIONS

General guide rules for the design of the model are found in I.G.C.I. standard E.P.-7, however, depending upon the intent of the test and the variables being studied consideration must be given to the following dimensionless ratios to insure continuity between the model study results and the performance of the Prototype unit.

1) Reynolds Number $= \frac{\text{Inertia Forces}}{\text{Viscous Forces}}$

2) Froude Number $= \frac{\text{Inertia Forces}}{\text{Buoyancy Forces}}$

3) Momentum Ratio $= \frac{\text{Momentum - Stream 1}}{\text{Momentum - Stream 2}}$

The importance of these ratios to specific tests was discussed in a May 1974 article in Power Engineering[1] and additional information was contained in a November 1976 issue of Research-Development[2].

2.4.1 REYNOLDS NUMBER

The majority of model studies investigate only the gas flow distribution and the pressure loss and need only to consider the influence of the Reynolds Number. Due to the difference in effective diameters between the model and the prototype, a match of the Reynolds Number is not feasible and the normal procedure is to match the flow velocity and then to verify that the Reynolds Number is in the turbulent region. If this condition is met and dimensional similarity has been obtained, the flow patterns and the pressure losses existing in the model will be representative of the conditions to be expected in the prototype unit.

2.4.2 FROUDE NUMBER AND MOMENTUM RATIO

For model studies to determine the thermal mixing of two gas streams entering at different temperatures and to evaluate plume effects for atmospheric discharges, both the density modified Froude Number and Momentum Ratios need to be considered. For these studies, it is essential that the values used for the density modified Froude Number and the Momentum Ratio match the calculated values which are expected for the prototype installation. For normal cases, the frictional component will be small relative to the other forces and can be eliminated.

2.5 ACCEPTANCE CRITERIA

The acceptance criteria outlined in the October 1981 edition of I.G.C.I standard EP-7 represents a minimum criteria which is required to ensure that the high design collection efficiencies will be obtained. The requirement that 85% of all data points be within ± 15% of the average velocity is excellent and represents a level which has been specified by many consultants and some manufacturers for several years. Based upon a review of available test data and in consideration of the need to maintain high collection efficiency during extended periods of operation, it would seem that the requirement for 99% of all data points to be within ± 40% of the average velocity should be modified to require that 95% of all data points be within ± 25% of the average and except for a few scattered points, the balance within the ± 40% range. Based on actual test, we believe this criteria to be obtainable.

In addition to the recommended tolerance for flow distribution variations, the maximum root mean square (RMS) deviation may be specified and based upon present criteria for the high collection efficiencies, the RMS deviation should be in the 8 to 14% range to assure compliance.

2.6 DATA ACQUISITION

The collection of the raw test data is a critical item in the performance of a model study since incomplete erroneous or non-reproducible data can lead to improper evaluation of the results and, therefore, incorrect conclusions may be reached regarding flow distribution which could result in the installation of wrong flow corrective devices and non-performance of the prototype unit.

Calibration of all instruments used in the test is required and the calibration is to be verified before the start of each series of tests. Calibration records should be available for inspection and should be included in the final report of the model study.

For most applications, the raw test data for flow determination is secured using either a pitot tube or a hot wire anemometer with the selection being based on the existing velocity. A hot wire anemometers is normally used when the flows are below 40 ft. per second and are accurate to very low flows. The resultant data is usually recorded on a continuous strip chart and must be converted to velocity data at predetermined locations to assure continuity between all tests. The resultant data provides flow rate data but does not provide directional indications therefore other tests must be conducted to verify direction of flow.

Pitot tubes are used in areas where higher velocities exist and for static head measurements. Care must be taken to ensure that all readings are taken at consistent locations and that the probe is inserted with care to assure correct alignment.

To provide the directional component of the flow which is not obtained with a hot wire anemometer, it is common to use tufts of string or cotton attached to a small diameter wire which can be inserted through predrilled holes at selected locations to ascertain flow direction. The presence of eddies, reverse flow, dead spots, etc., can be determined and proper flow corrective devices can be installed to correct the undesireable condition which will also assist in obtaining the minimum pressure drop.

To assure proper evaluation of the velocity patterns, the minimum number of data points as prescribed by I.G.C.I. standard should include sampling in every third gas passage lane between collector plates and the vertical distance between data points should not exceed 10% of the plate height. The pattern of sampling should be repeated for the inlet, at the midpoint of gas passage through the unit and at the outlet. (The pattern is normally defined by assuming that the observer is in front of and facing the inlet. Row 1 is located at the unit left side. Vertical data points are recorded from top to bottom.)

The final configuration should also be tested at flows of 75% and 50% of the design flow rate to verify that acceptable flow distribution is being obtained. The unit is normally designed for the maximum expected flow based on the fan capability, therefore, testing at flows higher than the design rate is normally not done.

2.7 DATA EVALUATION

Careful and accurate evaluation of the raw test data obtained in the model study at each sample point is essential to assure that the conclusions reached will enable the prototype unit to operate in accordance with the specified requirements. As a minimum, the evaluation should include the following methods:

1) Iso-Velocity Profile Plots
2) Velocity Histogram Plots
3) Root Mean Square Deviation - RMS
4) Visual Observations

Examples of data collected during recent model studies are presented below with reference to each specific method of evaluation. These are included to illustrate suggested methods.

2.7.1 ISO-VELOCITY PROFILE PLOTS

The Iso-Velocity plot is an actual plot of the velocity existing at every sample point location and provides the best means of understanding the flow distribution existing in the model. By comparison of the actual velocity existing in the model for the inlet the midpoint and the outlet, determination of flow distribution can be made with respect to the following criteria which are of concern to ensure performance. Figures 1 through 6 are presented to illustrate specifically the following items which may be evaluated using the following:

a) Identification of areas within the model where either high or low velocities exist.

b) The velocity profile existing at the bottom of the model in the area just above the ash hopper.

c) A means to determine and to evaluate internal drift within the gas passage lanes as the flow proceeds from inlet to outlet.

d) The influence of internal obstructions.

e) The compliance with the specification requirements as they pertain to flow distribution.

Figure 1 represents a velocity profile plot for flow distribution existing at the inlet of an electrostatic precipitator model as it was recorded in a recent model study. In this instance, the velocities are shown as a percentage of average velocity, however, actual velocities as recorded may be used. Note that except for a few data points, the velocity points in the bottom rows are at or below the average velocity. This is desirable since it reduces the possibility of re-entrainment. For this profile, the root mean square (RMS) deviation is 10.2% and unless other problems are discovered in the evaluation, the profile as obtained represents good flow distribution and is acceptable.

Figure 2 represents an unacceptable flow pattern which was obtained from a different test series. Even though the RMS deviation is only 13.9%, the concentration of high flow velocities in the center of the unit with low velocities on the outer edges was not acceptable to the manufacturer or to United Engineers and corrective action was taken to modify the flow patterns.

Figure 3 has been included to illustrate objectionable condition existing at the bottom of the unit and represents an unacceptable condition.

Figure 4 has been included to illustrate the effects of an internal truss on flow distribution which was located upstream of the sample area and was observed in a recent study. The very low velocities as seen on the four sides are a result of the gusset plates used to secure the truss. In addition to the effects on flow distribution, each truss is a source of additional pressure loss. As an example, if the obstruction caused by a truss reduces the total area by 12 to 15%, each truss can cause an additional loss of 0.10 IN-WG.

Figures 5 and 6 have been included to illustrate internal drift of gas flow within a unit. Figures 4 represents the flow distribution at the inlet and Figure 5 indicates the distribution at the outlet. A comparison of Figures 5 and 6 indicate a definite drift of the gas flow as it proceeds through the unit. Because the majority of the velocities are within ± 15% of the average velocity and the RMS deviation are in the 8 to 12% range, this drift pattern can be accepted. If a wide variation in velocities existed with high velocities at the bottom, the flow patterns should be corrected.

2.7.2 HISTOGRAM VELOCITY PLOTS

A histogram is usually plotted as a bar graph and is plotted showing the number of data points existing as a function of the percent deviation from the average velocity. The plots provide a visual means of verifying compliance with specification compliance regarding the distribution of all velocities and also provide a ready reference to indicate the number of data points outside the specification limits.

Figures 7 and 8 are histogram plots taken from a recent study and represent conditions at the inlet and the outlet of the unit. In addition to verifying compliance with specification requirements for flow distribution, these plots provide an indication of internal drifts although exact location cannot be verified.

2.7.3 ROOT MEAN SQUARE (RMS) DEVIATION

This mathematical ratio provides a reliable indication of the capability of the measured flow distribution to obtain the specified collection efficiency.

The data used in plotting Figure 9 has been compiled from a number of model studies with different collection efficiencies. Using the actual velocity for each data point and the expected performance curves as furnished by the manufacturer, the collection efficiency for each point was calculated. The collection efficiency was compared to the design value and the deviation from the design value was established. This deviation from the design value has been plotted as a function of the root mean square deviation. From this plot, it would appear that to obtain and maintain the high collection efficiencies now required, the RMS deviation should be in the 8 to 14% range depending upon the specific job requirements.

2.7.4 VISUAL EVALUATION

The use of visual observations in the evaluation of flow patterns enables the test program to determine the direction of gas flow, to correct objectionable flow patterns in ducts and to evaluate drop out and re-entrainment potential.

The determination of flow direction is accomplished by using cotton tufts or string attached to a small diameter wire and inserted into the flow stream. Areas of concern can be identified and corrective action taken.

The evaluation of dead areas of drop out potential and hopper re-entrainment is performed using powdered cork which is deposited in the duct area upstream of the model. The unit is then operated at 50% flow, then at 75% flow and at 100% of design flow. Results are noted for all cases to determine the pickup potential as the flow rate is increased, the presence of any areas where dropout may occur and the potential for hopper re-entrainment. In a few cases, fly ash has been used and although good results were obtained, the procedure requires the addition of a small fabric filter to the outlet to avoid discharging fly ash into the laboratory area and also to protect the instrumentation.

2.8 PRESSURE LOSS

The pressure drop raw data is normally secured using a sensing type pitot tube and an inclined monometer to obtain static pressures at all locations. The model data is converted to expected pressure loss for the prototype unit by the square of the flow ratio and the ratio of the density.

2.9 SPECIAL REQUIREMENTS

This section should include the requirements for inspection of the model, witnessing of tests, review of data, and requirements for submission of the test report. The contents of this section may be varied depending upon the requirements of the owner and/or Engineer.

3.0 CONCLUSION

Operation of a number of installed units where the model studies were controlled to the standards as presented have demonstrated that the design collection efficiency and pressure loss requirements have been met. Therefore, the importance of a detailed model study has been verified, provided that careful attention has been given to the model specification, the collection of data and to the evaluation and interpretation of the results.

REFERENCES

1) Experimental Flow Modeling for Power Plant Equipment, Gerald B. Gilbert, Dynatech Corp. - Power Eng., May 1974.

2) Scale Model Flow Testing, David J. Gibson, Research Cottrell, Research/Development, November 1976.

89	87	83	93	106	113	109	100	106
92	95	89	91	109	117	112	102	109
104	104	99	90	87	105	115	100	124
99	98	78	96	101	111	78	105	117
106	89	81	93	103	111	96	110	114
106	91	84	95	96	109	83	109	114
107	101	87	99	96	104	94	104	118
109	101	88	106	98	115	98	106	114
93	92	90	105	102	106	94	106	107
96	91	105	102	96	99	106	103	118
87	90	112	98	91	95	116	105	108
84	99	110	93	96	95	115	102	87
71	87	102	101	95	101	115	103	80

FIGURE NO. 1
VELOCITY PROFILE PLOT

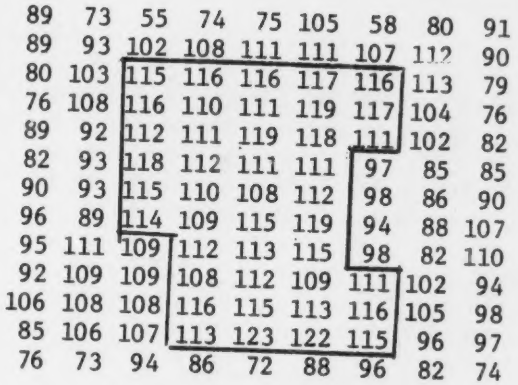

89	73	55	74	75	105	58	80	91
89	93	102	108	111	111	107	112	90
80	103	115	116	116	117	116	113	79
76	108	116	110	111	119	117	104	76
89	92	112	111	119	118	111	102	82
82	93	118	112	111	111	97	85	85
90	93	115	110	108	112	98	86	90
96	89	114	109	115	119	94	88	107
95	111	109	112	113	115	98	82	110
92	109	109	108	112	109	111	102	94
106	108	108	116	115	113	116	105	98
85	106	107	113	123	122	115	96	97
76	73	94	86	72	88	96	82	74

FIGURE NO. 2
VELOCITY PROFILE PLOT

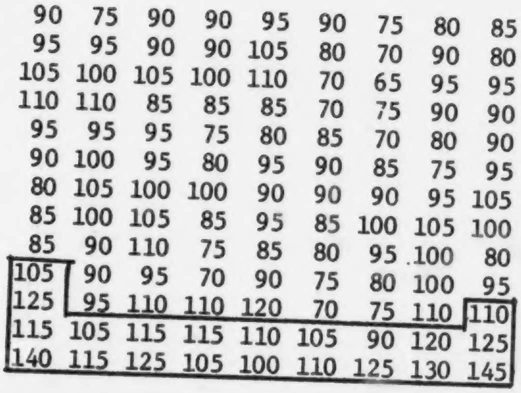

90	75	90	90	95	90	75	80	85
95	95	90	90	105	80	70	90	80
105	100	105	100	110	70	65	95	95
110	110	85	85	85	70	75	90	90
95	95	95	75	80	85	70	80	90
90	100	95	80	95	90	85	75	95
80	105	100	100	90	90	90	95	105
85	100	105	85	95	85	100	105	100
85	90	110	75	85	80	95	100	80
105	90	95	70	90	75	80	100	95
125	95	110	110	120	70	75	110	110
115	105	115	115	110	105	90	120	125
140	115	125	105	100	110	125	130	145

FIGURE NO. 3
PROFILE PLOT-HIGH BOTTOM VEL.
UNACCEPTABLE PROFILE

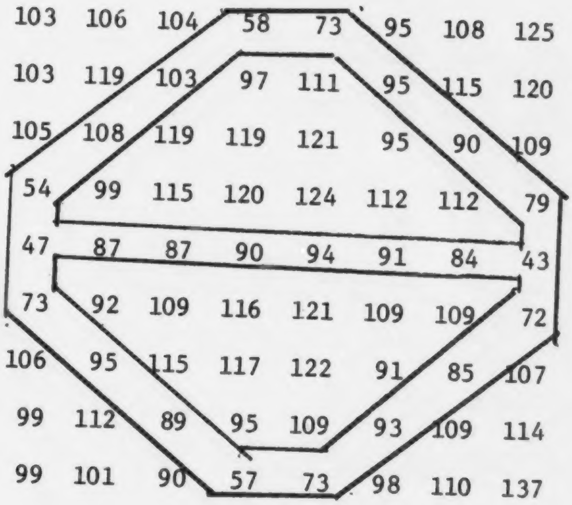

103	106	104	58	73	95	108	125
103	119	103	97	111	95	115	120
105	108	119	119	121	95	90	109
54	99	115	120	124	112	112	79
47	87	87	90	94	91	84	43
73	92	109	116	121	109	109	72
106	95	115	117	122	91	85	107
99	112	89	95	109	93	109	114
99	101	90	57	73	98	110	137

FIGURE NO. 4
PROFILE PLOT-TRUSS EFFECT

105	112	102	98	94	96	100	105	105	110	98	96
114	102	120	115	108	100	98	110	105	100	106	90
110	105	90	88	82	100	86	126	124	116	110	100
102	98	96	86	88	78	82	120	116	120	118	102
100	98	92	90	86	86	82	114	108	106	116	100
98	100	88	84	88	92	84	122	100	100	110	100
98	105	84	86	90	88	90	112	106	100	98	102
94	110	87	88	90	80	88	110	100	106	96	96
110	98	78	90	84	86	80	106	98	110	100	90
100	104	86	76	86	80	82	104	100	98	108	88
90	106	90	82	94	95	96	100	96	105	110	94
98	100	88	90	100	105	100	95	108	104	100	96
96	92	80	96	105	110	90	90	100	102	100	100
90	88	86	92	100	102	110	98	96	98	98	96
88	84	89	100	94	100	104	90	100	90	96	96

FIGURE 5
PROFILE PLOT-INLET

106	98	96	100	106	100	100	98	96	96	100	102
108	112	110	110	110	108	104	98	100	96	98	104
104	110	104	98	115	110	112	102	100	94	100	100
100	98	106	110	120	100	100	92	88	96	90	98
100	106	98	94	128	100	80	78	76	84	96	102
98	110	106	100	132	88	84	80	78	82	98	104
96	114	120	126	130	86	90	84	82	80	92	96
88	114	110	100	124	86	88	86	90	90	96	98
94	110	112	108	116	90	70	84	86	92	98	100
100	98	104	112	116	78	82	80	82	86	100	94
102	106	98	110	120	80	80	82	78	80	96	96
100	96	100	100	110	84	78	90	80	96	100	100
96	98	96	100	90	94	90	96	96	98	100	98
96	90	96	98	96	92	90	90	96	100	96	98
90	88	100	102	96	88	82	80	88	90	94	100

FIGURE NO. 6
PROFILE PLOT-OUTLET

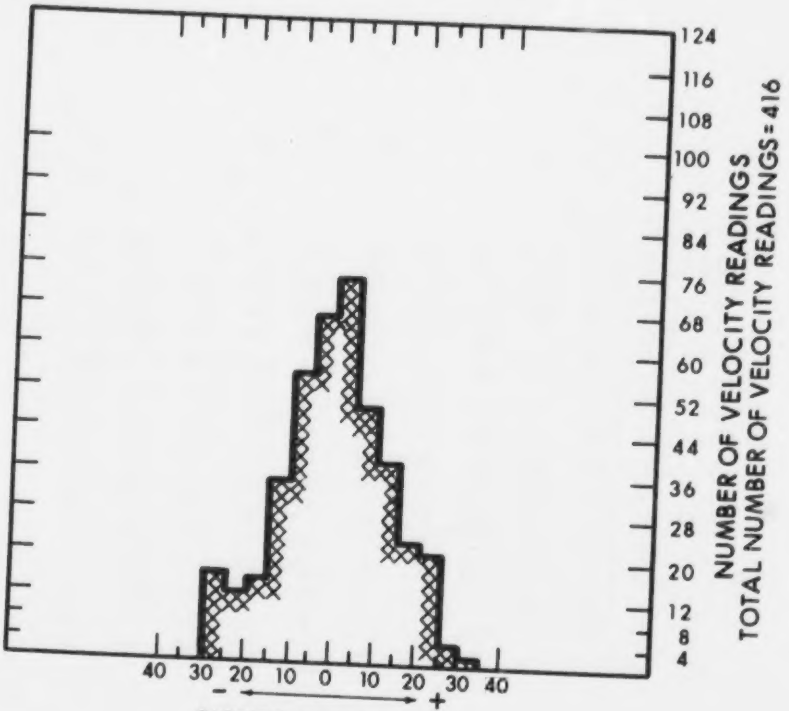

FIGURE NO. 7 INLET
HISTOGRAM PROFILE
% DEVIATION

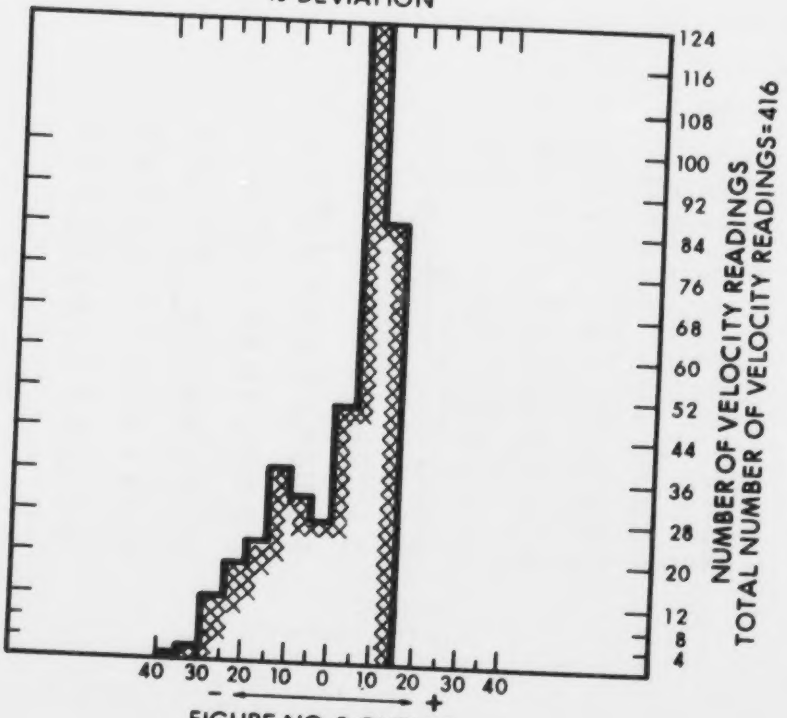

FIGURE NO. 8 OUTLET
HISTOGRAM PROFILE
% DEVIATION

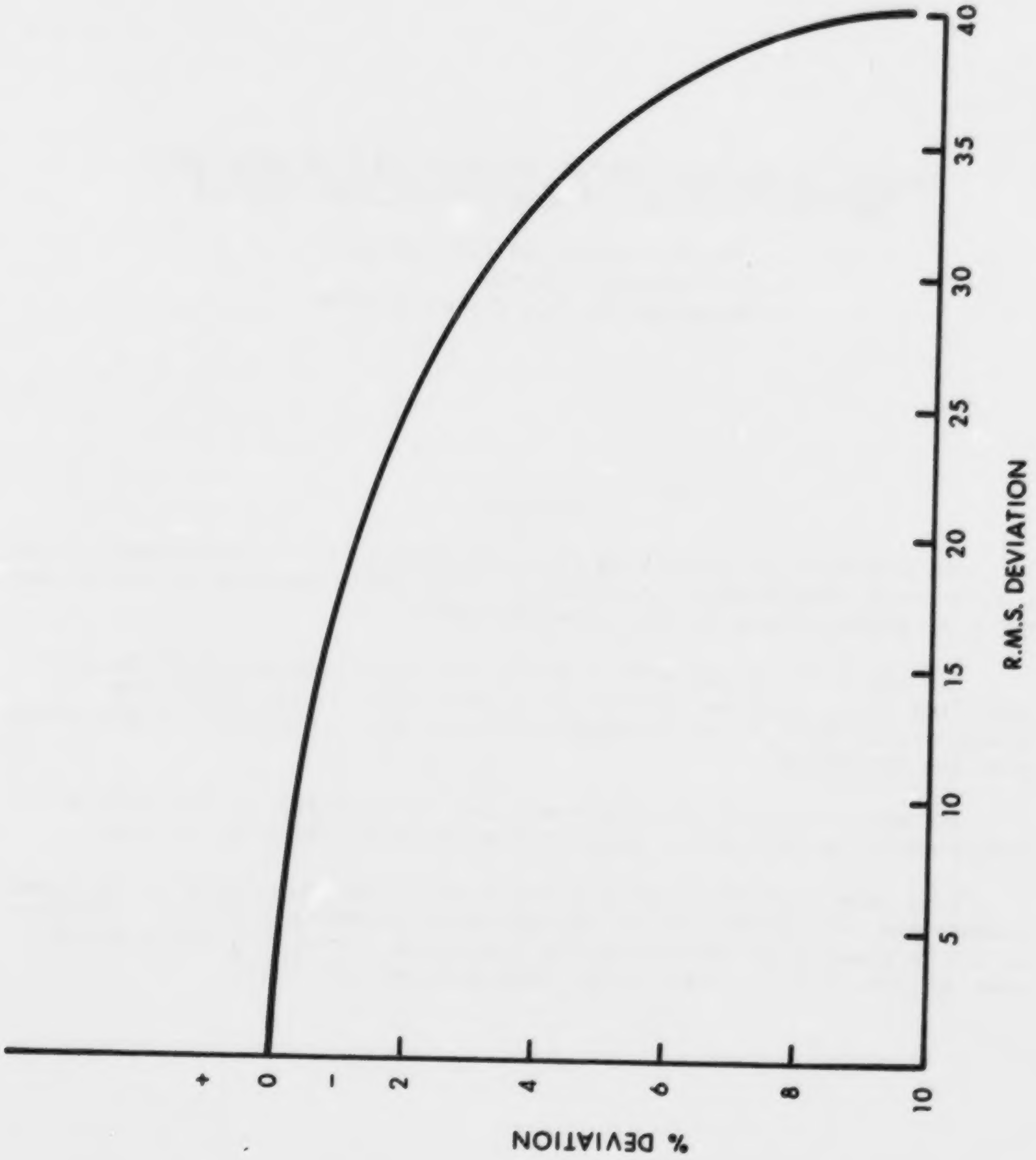

FIGURE NO. 9

AIR FLOW MODEL STUDIES

COLLECTING ELECTRODE RAPPING DESIGNED FOR HIGH EFFICIENCY ELECTRIC UTILITY BOILER ELECTROSTATIC PRECIPITATORS

by: A. Russell-Jones and A.P. Baylis
Lodge-Cottrell Limited
Birmingham, B3 1QQ, United Kingdom.

ABSTRACT

The influence of collecting electrode rapping on the efficiency of an electrostatic precipitator is examined. Particular emphasis is placed upon the limitations caused by dust re-entrainment.

The way in which the effectiveness of the dislodgement blow is often specified in terms of measured shock acceleration on the collecting electrode, is shown to be unsatisfactory in view of plate and accelerometer response variations.

The means by which re-entrainment can be minimised is discussed and a theory which can be used to explain observed performance is advanced.

Long term performance of Electric Utility gas cleaning plant designed to achieve the best compromise of rapping requirements is reviewed. Examples of 500 MW power plant precipitators, and larger, operating satisfactorily over periods up to 17 years after commissioning, are cited.

COLLECTING ELECTRODE RAPPING DESIGNED FOR HIGH EFFICIENCY ELECTRIC UTILITY BOILER ELECTROSTATIC PRECIPITATORS

INTRODUCTION

The overall process of dust removal from the flue gas stream by electrostatic precipitation can be considered to comprise 6 main stages:

1. Particle charging.
2. Migration through the gas to the collecting electrode.
3. Particle deposition on the collecting electrode.
4. Dislodgement of agglomerates.
5. Settlement into the hopper.
6. Withdrawal from the hopper.

Only when the dust has been withdrawn from the hopper can it be counted as "caught".

Dislodgement of the accumulated dust layer from the collecting electrode must be effected at regular intervals. It represents a series resistance on the surface, which reduces the effective field voltage, and hence the efficiency of dust removal.

In order that the dust layer is dislodged, a shock impulse must be applied to the collecting electrode. This shears the dust from the plate as agglomerates of the initially deposited fine dust. It is the means of achieving this end which we will discuss in this paper.

For some years, it has been fashionable to define the effectiveness of rapping of the electrode system in terms of a specified minimum acceleration measured on the surface. This specification is in multiples of 'g', the acceleration due to gravity (9.81 ms^{-2}). Such a system of specification is an over simplification of the requirements for dust dislodgement, since it ignores the inter-relationship between acceleration, displacement, and frequency. We will endeavour to show that such is the variation in these three factors that reliance upon acceleration alone as an indication of satisfactory rapping effect can be misleading.

The methods adopted by various manufacturers to effect dust dislodgement are to some extent dependent upon the construction of their collecting electrodes. Broadly speaking they fall into three main classes:

1. Top rapped.
2. Bottom rapped.
3. Multi-level rapped.

These can be further sub-divided in terms of prime mover:

a. Drop rod rapping.

b. Tumble hammer rapping.

c. Vibratory rapping.

These are illustrated in Figure 1.

Bottom rapped systems are generally of the long, rolled form electrode type and use internally mounted tumble hammers to produce the blow. Similar tumble hammers are used for multi-level rapping. Top rapped systems on the other hand can be found using all three types of prime mover. The difference in response brought about by these various constructions and rapping blows are also to be considered in this paper.

THE SHOCK IMPULSE

It has been generally assumed that the most important factor in assessing a rapping system is the minimum acceleration measured on the collecting electrode surface. This is based on the view that a mass of dust 'm' on the surface accelerated by an acceleration 'a' is subjected to a force 'F' according to the expression:

$$F = m.a$$

F = Force (N)
m = Mass (kg)
a = Acceleration (ms^{-2})

When the shock impulse is applied to the collecting electrodes, a range of forced vibrations is set up and propogated to the whole system. This impulse can be broken down into its constituent frequencies by Fourier transform analysis. Data have been variously reported showing how electrodes of differing construction exhibit different frequency response patterns. Zarfoss (1) showed data which are consistent with our own findings, viz. the frequency content of measurements made on a rolled form electrode are significantly higher than those found on a channel and plate type as used by Lodge-Cottrell. These differences are extremely important as we will demonstrate later.

EFFECT OF THE RAPPING BLOW

Work was carried out some years ago in the U.K. by the Central Electricity Generating Board (2) to try to determine the residual dust layer thickness on a collecting electrode as a function of the local level of acceleration when the electrode was rapped. The data which were obtained are shown in Figure 2.

It would seem from the data in Figure 2, that an acceleration level of at least 30'g' is required to ensure that only a small residual layer of dust remains. However, it is important to bear in mind that the data refer to one dust, on one type of electrode, and measured with a particular accelerometer. All three of these factors have a significance which we hope to demonstrate.

The effect of a 30'g' acceleration upon the dust layer is not in fact a predictable one. This was elegantly demonstrated by Juricic and Herrmann (3). In a small test cell, fly ash was deposited electrostatically onto a collecting electrode. Peak initial accelerations of 20 to 25'g' were applied to the deposited dust layers and observed by means of high speed cinematography. Two frequencies of vibration were used, viz. 100 and 500 Hz.

The differences observed between 20'g' acceleration for two frequencies were quite startling and enlightening. At 100 Hz. the dust layer was largely broken up into re-entrainable debris, whereas at 500 Hz. the layer slid off the plate in large agglomerates.

We interpret these observations in the following manner. The acceleration in the dust layer subjected to sinusoidal vibration is described by the equation:

$$a = 4\pi^2 f^2 d$$

a = Acceleration (ms^{-2})
f = Frequency (Hz)
d = Deflection (m)

For an acceleration of 20'g' at 100 Hz. and 500 Hz., the linear displacements are 5×10^{-4} m and 2×10^{-5} m respectively. The kinetic energy imparted to the dust is given by the equation:

$$E = \tfrac{1}{2}mv^2 = 4\pi^2 f^2 d^2 m$$

E = Kinetic Energy (J)
m = Mass of Dust (kg)
f = Frequency (Hz.)
v = Velocity (ms^{-1})
d = Displacement (m)

Thus at a constant level of acceleration (e.g. 20'g') the kinetic energy imparted to the dust at the two different frequencies is given by the ratio

$$\frac{E \text{ at } 100 \text{ Hz.}}{E \text{ at } 500 \text{ Hz.}} \qquad \frac{4\pi^2(100^2)(5 \times 10^{-4})^2 m}{4\pi^2(500^2)(2 \times 10^{-5})^2 m} \qquad \text{i.e. } 25:1$$

This significant difference in the kinetic energy terms can account for the observed behaviour on dislodgement under the conditions of similar applied peak acceleration, and hence similar applied force.

It is reasonable to expect that similar effects should be found in the dislodgement of dust in the full scale precipitator unit. In the light of these observations it is clear that the frequency content of the shock impulse is important.

Since it is well established that different forms of collecting electrode respond very differently to the impact blow in terms of the propogated shock impulse frequency content, it follows that the dislodgement of dust for a given acceleration level will be significantly different. Identical measured peak accelerations can therefore produce large agglomerates, or debris, depending on the frequency content of the local shock impulse.

For the reasons outlined above we maintain that it is misleading to apply a specification minimum of a specific number of 'g' and try to make comparisons between different forms of collecting electrode on that basis. Indeed the method of measurement can account for a variation of more than 3:1 in the 'g' levels.

RAPPING ACCELERATION MEASUREMENT

A major reason for disagreement between those supplying precipitators, and those specifying them, and in particular laying down minimum acceleration criteria, is that the measurement of acceleration is sensitive to the type of accelerometer used.

Accelerometers used for measurement of acceleration on collecting electrodes have ranged in weight from 4×10^{-2} kg downwards. Various reports on, and studies of, the mass/acceleration effect have been made (4, 5, 6). It might seem surprising that when measuring shock impulses on a structure weighing over 1000 Kg, the introduction of a 4×10^{-2} kg mass could affect the measured result. It must be recognised that the accelerometer will nevertheless interfere with the vibration at the point of attachment to the thin sheet material of the collecting electrode. The degree of interference will be dependent upon the material thickness, and the method of electrode construction. Only an accelerometer with zero mass could measure the true acceleration level. Figure 3 shows how the mass and acceleration are inter-related for a specific position on a 13.72 m x 4.57 m collecting electrode. The observed acceleration levels for identical rapping blows range from 18 'g' to 85 'g'.

Workers at Princetown University have attempted to explain this effect in terms of refraction of the incident shock wave and developed correction curves in terms of both frequency and accelerometer mass (4). The curves permit the calculation of the theoretical acceleration using an accelerometer with zero mass.

With the mass effect in mind we have used the lightest practicable accelerometers currently available. Both the major manufacturers of accelerometers - Endevco of California, U.S.A. and Bruell and Kjaer of Denmark - offer micro-miniature accelerometers with suitable characteristics, weighing less than 5 x 10^{-4} kg. For accelerometers of such a low mass no significant correction need be made.

Data obtained using a measuring system comprising an Endevco type 22 accelerometer and 'SMART' processing equipment, are shown in Figure 4 for a complete survey of a 13.72 m x 4.57 m collecting electrode. The data show a spread of acceleration level from 62'g' up to 285'g', with the point of lowest acceleration close to the bottom of the electrode. Fourier transform analysis of the frequency content of the shock impulses at the two extremes reveal much higher peak frequencies associated with the individual plates where high 'g' accelerations are measured. This serves to moderate the kinetic energy input to the dislodged dust, whilst at the same time producing a sufficient acceleration to ensure dislodgement of the thinner dust layer which tends to form at the top of each collecting electrode as compared to the bottom (see later).

DISLODGED AGGLOMERATE SIZE

Considering the six stages of precipitation listed earlier, it is obvious that the agglomerates dislodged from the collecting electrode will only reach the hoppers if their aerodynamic effective size is greater than a critical minimum. This minimum agglomerate size will vary according to the position on the collecting electrode and the field from which it is dislodged. The controlling factor is the residual contact time in the precipitation fields. This must exceed the time taken to fall into the hopper. The most critical field is therefore the outlet field.

Figure 5 shows the free fall terminal velocity as a function of agglomerate size. In order that a velocity of more than 7 ms^{-1} is achieved, the equivalent sphere diameter needs to be at least 10^{-3} m. The data plotted in the graph are for an apparent particle density of 1000 kg m^{-3} based on a dust with a density of 2000 kg m^{-3} with an agglomerate voidage of 50%.

Another way of looking at this effect is shown in Figure 6. Here are shown computer-calculated particle trajectories for various agglomerate sizes. The gas is typical flue gas at 150°C. The assumption is made that the dust is projected from the collecting electrode with no forward velocity. It is accelerated up to the gas velocity. The trajectories illustrate the important point that provided the agglomerate size can be kept large, tall collecting electrodes with a height of upto 15.24 m can be used with minimal re-entrainment risk. They also emphasise that badly designed rapping systems can result in excessive rapping re-entrainment losses from the outlet field of a precipitator.

In order that the size criterion can be met, the rapping equipment must be designed with attention paid to the interval between rapping blows - the "periodicity" of the rapping mechanism. It is essential that between rapping blows a cake of dust is allowed to build up. Since for the majority of dusts the adhesive strength of the dust to the plate exceeds the cohesive strength of the dust layers, dust will be sheared from dust. This leaves behind a tenacious layer referred to by Ruckelhausen as the "basic" layer (7).

Ideally, the periodicity of the rapping blow should be optimised so as to develop large dislodged agglomerates, but not so great as to upset the electrical operation of the plant. Setting of the periodicity is generally a compromise. Its significance can be appreciated by reference to Figure 7. The plant performance for a precipitator field with an inlet dust burden of approximately 1 gm^{-3} is shown by Darby (8) for a range of periodicity from seconds to hours. The performance factor (plotted as the effective migration velocity) shows a steady rise through to a peak and then a fall-of. The latter is due to the dust layer being of a thickness whereby it has started to affect the electrical performance of the precipitator.

Variation in boiler load and coal ash content both have an effect on the rapping periodicity requirements. To date, the settings of periodicity have been a fixed compromise. However, as Bradburn and Darby (9) point out, microprocessor-based control equipment for electrostatic precipitators open up the possibilities of programming in automatic compensation for changes of this type. The programming can also ensure that when an upstream field is de-energised the succeeding field rapping periodicities are adjusted to compensate for the change in dust loading. Only the last field would be left with periodicity unchanged in view of the increased risk of re-entrainment of debris in the event of premature rapping.

The work of Sproull (10) illustrated the advantages of allowing the dust 'cake' to build up on the receiving electrode surface. His experiment, although performed on a rigid "engine valve head" type of surface, rather far removed from a plate surface, showed 90% dislodgement of fly ash with a deposition of 2.17 kg m^{-2} on the 6 x 10^{-3} m^{-2} collection area, with an acceleration of 30'g'. With a deposition of only 3 x 10^{-1} kg m^{-2} the removal was only 40%. This ties up with the prediction made by Lowe and Lucas (11) who calculated that acceleration of the order of 10^5 'g' would be required to get down to clean metal, free of the "basic layer".

ELECTRICAL DUST DISLODGEMENT

At the stage referred to above, and illustrated in Figure 7, at which the precipitator performance starts to deteriorate due to excessive dust build up, other mechanisms of dust dislodgement come into play. Firstly, the mass of the dust can lead to local fracture of the cake. This self cleaning mechanism leaves a "basic layer" which can itself be quite thick.

The second mechanism which can dislodge the dust is arcing, i.e. electrical flash-over from the discharge electrode to the collecting electrode. We have carried out experiments to quantify the magnitude of the acceleration induced in the collecting electrode when flash-over takes place. We have found it to be a significant quantity when compared to the magnitude of the conventional mechanical rapping blow.

In Figure 8 are shown the shock impulse traces obtained using an Endevco "SMART" system. The accelerations were measured on a bottom row centre plate of a 13.72 m x 4.57 m collecting electrode of the standard Lodge-Cottrell catch space type. Values of acceleration, and general form of the impulse for the mechanical and electrical rapping can be seen to be of a similar order.

The level of acceleration induced in the sheet by the flash-over is adequate to effect dust dislodgement, suggesting that provided the plant is run with a high degree of arcing it would keep itself clean without mechanical rapping. This would be inadvisable, since frequent arcing results in decreased time-averaged field voltage, and hence reduced dust deposition efficiency. In addition, there is the possibility that a sudden surge of current to, and through, the dust layer may disrupt the 'cake' and produce excessive amounts of debris which are readily re-entrained.

DUST SEGREGATION

When each collecting electrode is rapped, most of the dust should fall as agglomerates. Some will be re-entrained as ultra-fine debris, and the remainder will be of an intermediate size which will settle only slowly. In all but the final field of the precipitator this dust will be recharged and reprecipitated. Hence, as we proceed down the length of the precipitator the lower halves of the collecting electrodes will be covered with progressively more and more reprecipitated intermediate size debris.

The agglomerate dislodged from an upstream plate has porosity, and thus when redeposited produces a layer of higher porosity still. The layer has consequently a reduced cohesive strength. This renders it more susceptible to break-up on being dislodged from the electrode surface. For this reason, it is best for the rapping blow to be applied at the top of the collecting electrode producing the higher accelerations where they are needed to dislodge the thinner, more compact dust layers, and the lower accelerations in the areas where the thicker layers with lower cohesive strength are located.

DISCHARGE ELECTRODE RAPPING

An electrostatic precipitator with the best design of collecting electrode rapping, perfectly tuned to the operating conditions of the boiler, would fail to perform well quite rapidly if equal attention were not paid to the discharge electrode rapping.

Accumulations of dust on the discharge electrode wires cause suppression of the corona and hence prevent proper charging of the dust particles in the gas stream. Thus, effective rapping blows must be transmitted to the discharge elements. At the same time the elements must not sway or bow, for any such movement adversely affects the plant alignment and results in reduction in field voltage due to premature flash-over. In addition, electrical arcing is detrimental to the integrity of long, small diameter electrode wires since each flash-over results in local spark machining. For these reasons, the U.S. Electric Utility Industry moved away from the use of weighted wires to the rigid frame design of discharge electrode.

Figure 9 shows the basic elements of a rigid design, and how the electrodes are incorporated into the precipitator in a rigid interconnected framework. This gives the best possible plant alignment, even with field heights upto 15.24 m. Maximum unsupported wire length is short, ensuring excellent transmission of the rapping blow to the wire elements and minimised risk of fatigue failure.

FATIGUE FAILURE

It has been observed on competitors plant that the use of over-weight hammers to produce high 'g' rapping has on more than one occasion led to fatigue failure of electrode components, leading to unscheduled shut-down of the power plant to permit rectification.

Any rapping system must introduce a risk of fatigue failure over years of continuous operation. The typical energy input level at the anvil position of a large collecting electrode is 30 J. By calculation and good design one can minimise the risk of fatigue failure, but the only really reliable method of assessment is an accelerated life test. For this reason we carry out an accelerated life test on any development on a full scale unit in our rapping test bay. There is provision for hanging pairs of collecting electrodes upto 15.24 m in height with a field length of 4.57 m.

High 'g' rapping is sometimes put forward as a solution to the problems resulting from high resistivity fly ash. Despite the high induced accelerations, there remains a "basic layer" of dust which in the case of high resistivity fly ash is still sufficient to affect the electrical performance of the plant adversely. In addition, since the dust layer retains charge unable to drain to earth due to the insulating nature of this "basic layer", the cohesive strength of the dust deposited onto the "basic layer" is reduced and high 'g' rapping can therefore result in increased production of re-entrainable debris and hence significantly increased emissions.

Lodge-Cottrell's approach to rapping systems design ensures that the risk of fatigue failure is small. This in turn means that provided regular maintenance is carried out, the precipitator performance is maintained over the lifetime of the plant.

LONG TERM HIGH EFFICIENCY PERFORMANCE

A newly constructed plant will always perform well when first on-line. After a period of 'running-in' of about 800 hours an initial assessment of the efficiency can be sensibly carried out. Even this test may give misleading data. The only meaningful acceptance test is that carried out after several months operation, since any poor design features will have made themselves apparent by then.

The performance of the precipitator could deteriorate over this period for a whole variety of reasons. One of the reasons would be failure of the electrode rapping system to prevent long term build up of dust on the collecting electrodes. If no such deterioration is observerable over this period of time it is almost certain that the same will be true after many years of operation, provided that regular plant maintenance is carried out.

By far the most reliable indicator of the adequacy of any manufacturer's rapping system is the long term high efficiency performance of the plant. Lodge-Cottrell is able to cite plant operating on a wide range of coal types throughout the world, and in particular plant in the U.S.A. in which low sulphur coal gives rise to the so called "difficult" dusts. Figure 10 shows the long term performance data for some typical precipitator installations.

CONCLUSIONS

Our experience in the design of electrostatic precipitator rapping systems for high efficiency operation has lead us to the following conclusions:

1. Rapping system must maintain adequate electrical operation.
2. Rapping must remove dust whilst minimising re-entrainment.
3. Mechanisms must be accessible and easy to maintain.
4. Rapping periodicity must allow adequate 'cake' build up.
5. Acceleration is a misleading measure of rapping adequacy.
6. High 'g' rapping does not solve high resistivity dust problems.
7. High 'g' rapping can increase rapping re-entrainment.
8. High 'g' rapping can induce major fatigue problems.

The Lodge-Cottrell precipitator has been scientifically designed on the basis of the data presented. The rapping systems for the collecting and discharge electrodes have been proven in the field over many years to be effective and reliable and to provide long term high efficiency performance of the dust collecting plant.

ACKNOWLEDGEMENTS

The authors wish to thank their colleagues for their help and assistance in the preparation of this paper, and the Management of Lodge-Cottrell Limited and Dresser Industries for granting permission for this paper to be published.

The work described in this paper was not funded by the U.S. Environmental Protection Agency and therefore the contents do not necessarily reflect the view of the Agency and no official endorsement should be inferred.

REFERENCES

1. Zarfoss, J.R.
New precipitator technology for particulate control.
Third Symposium on the Transfer of Particulate Technology, March 1981.

2. Madden, M. and Wrigley, W.
The relationship between dust accumulation on precipitator collector electrodes and hammer rapping forces.
Central Electricity Generating Board Report EPP.113, May 1968.

3. Juricic, D. and Herrmann, G.
Modelling and simulation of dust dislodgement on collecting plates in electrostatic precipitators.
Modelling and Simulation 9 (Published: Instrument Society of America) Proceedings of Ninth Annual Pittsburgh Conference (1) 161-166, April 1978.

4. Chang, N., Billington D.P. and Nagy, D.A.
Effect of accelerometer mass on the flexural vibration of plates.
International Journal of Solids and Structures 14 (10) 851-860 (1978).

5. Hardie, J. and Kelsell P.H.
Precipitator manufacturers methods of measuring acceleration levels induced by rapping precipitator plates and wires.
Central Electricity Generating Board Report EPP.93, December 1967.

6. Heiber, M.
Plane plate rapping experiment.
EPRI Plate rapping and reliability study.
Heiber Engineering, Wachung N.J. unpublished report June 1977.

7. Ruckelshausen K.
Uber entwicklungsstand der elektrostatischen staubabschieder unter besonderer berucksichtigung der abreinigungsprobleme.
Doctorate thesis, Technischen Hochschule, Stuttgart, No. DK-68511 Geise-Druck Kg. Offenbach/M 1957.

8. Darby, K.
Criteria for designing electrostatic precipitators.
Second Symposium on the Transfer of Particulate Technology, July 1979.

9. Bradburn, K.M. and Darby, K.
Electrostatic precipitator energization and control systems.
Fourth Symposium on the Transfer and Utilization of Particulate Technology, October 1982.

10. Sproull, W.T.
Fundamentals of electrode rapping.
Journal of the Air Pollution Control Association 15(2) 50-55, 1965.

11. Lowe, H.J. and Lucas, D.H.
The physics of electrostatic precipitation.
British Journal of Applied Physics Supplement No.2 S40-S47, 1953.

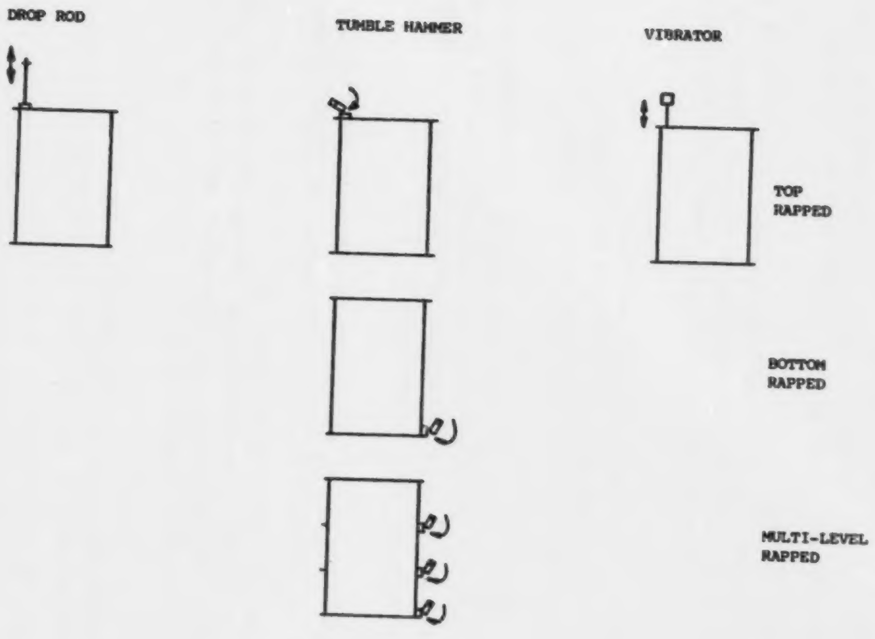
DROP ROD
TUMBLE HAMMER
VIBRATOR
TOP RAPPED
BOTTOM RAPPED
MULTI-LEVEL RAPPED

FIGURE 1
ALTERNATIVE RAPPING METHODS AND POSITIONS

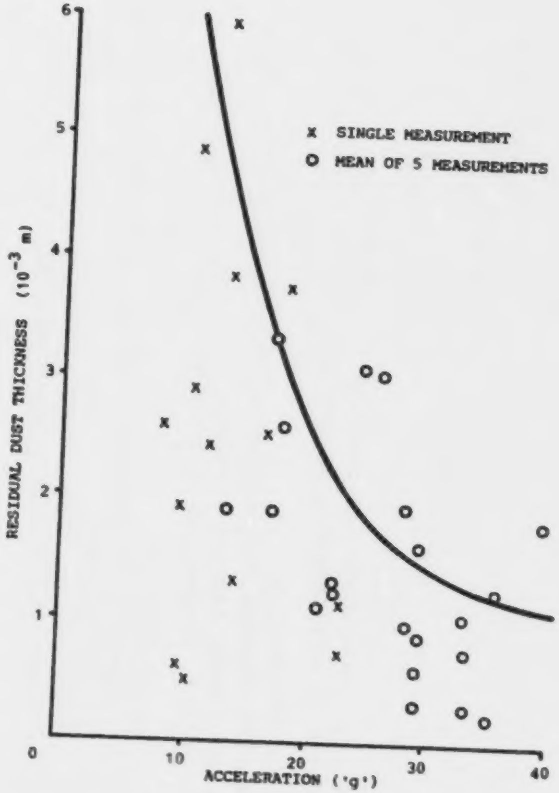

FIGURE 2
RESIDUAL DUST THICKNESS
AS A FUNCTION OF
MEASURED ACCELERATION LEVEL
(DATA SOURCE C.E.G.B. GREAT BRITAIN)

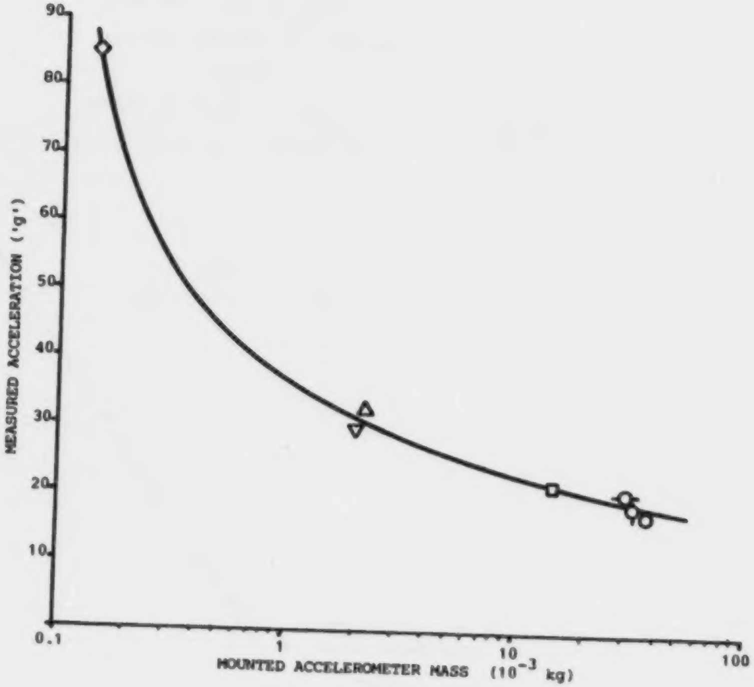

FIGURE 3

MEASURED ACCELERATION AS A FUNCTION OF MOUNTED ACCELEROMETER MASS

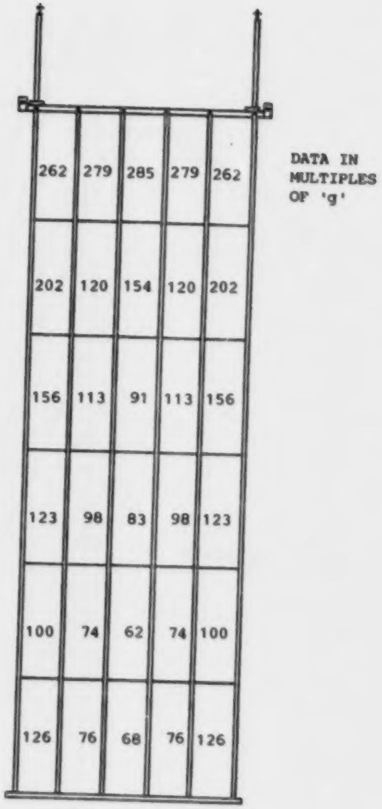

262	279	285	279	262
202	120	154	120	202
156	113	91	113	156
123	98	83	98	123
100	74	62	74	100
126	76	68	76	126

FIGURE 4

RAPPING ACCELERATION SURVEY FOR A 13.72 x 4.57 m COLLECTING ELECTRODE PAIR USING ENDEVCO TYPE 22 ACCELEROMETERS

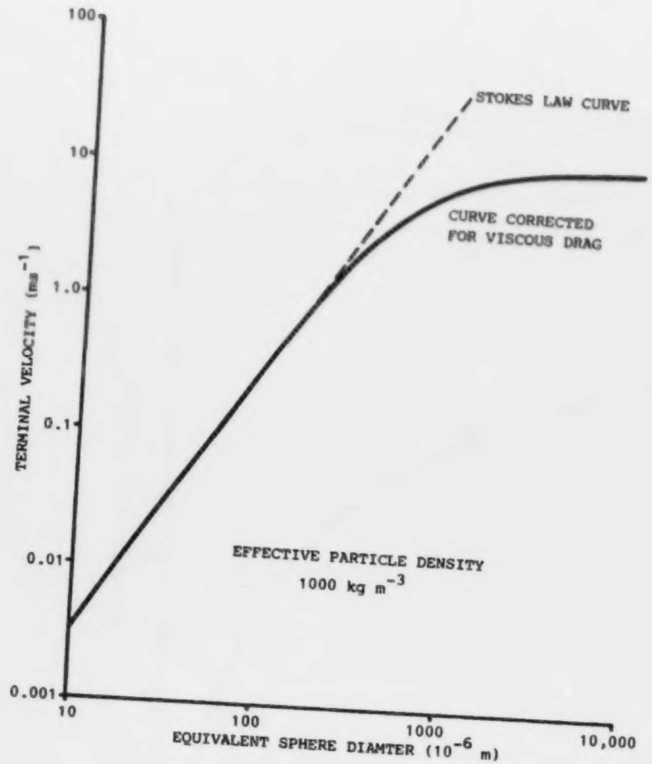

FIGURE 5

TERMINAL FREE-FALLING VELOCITY
AS A FUNCTION OF
EQUIVALENT SPHERE DIAMETER

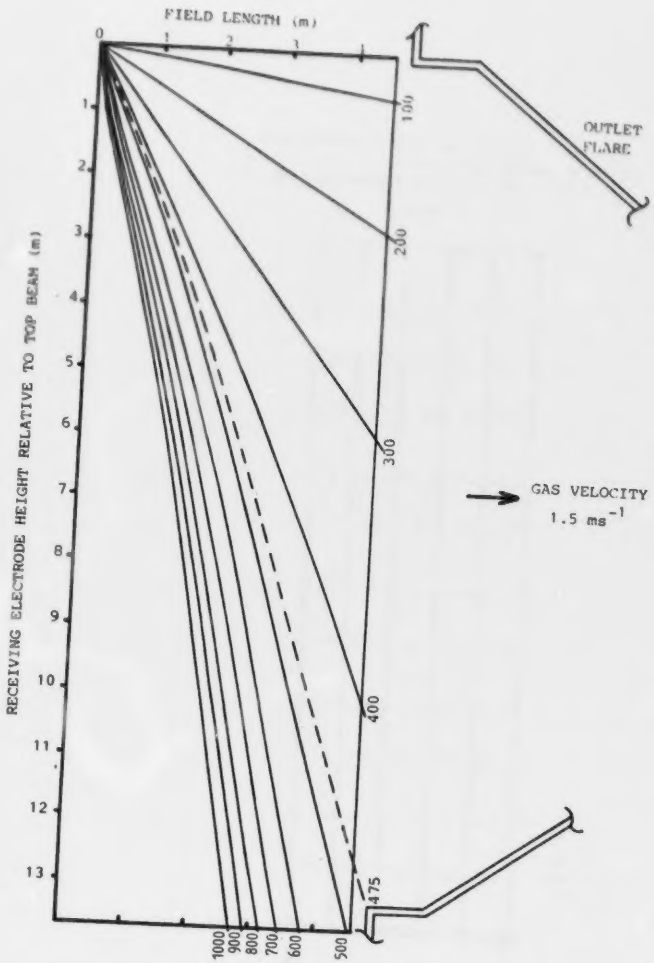

FIGURE 6
PARTICLE AGGLOMERATE TRAJECTORIES AS A FUNCTION OF THEIR
EQUIVALENT SPHERE DIAMETERS (10^{-6} m)

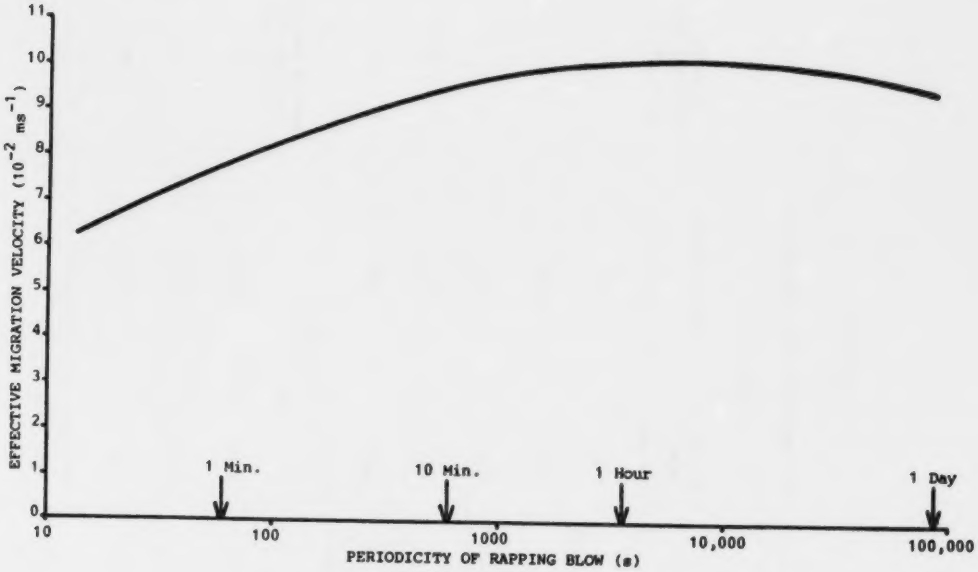

FIGURE 7

PRECIPITATOR PERFORMANCE AS A FUNCTION OF RAPPING PERIODICITY

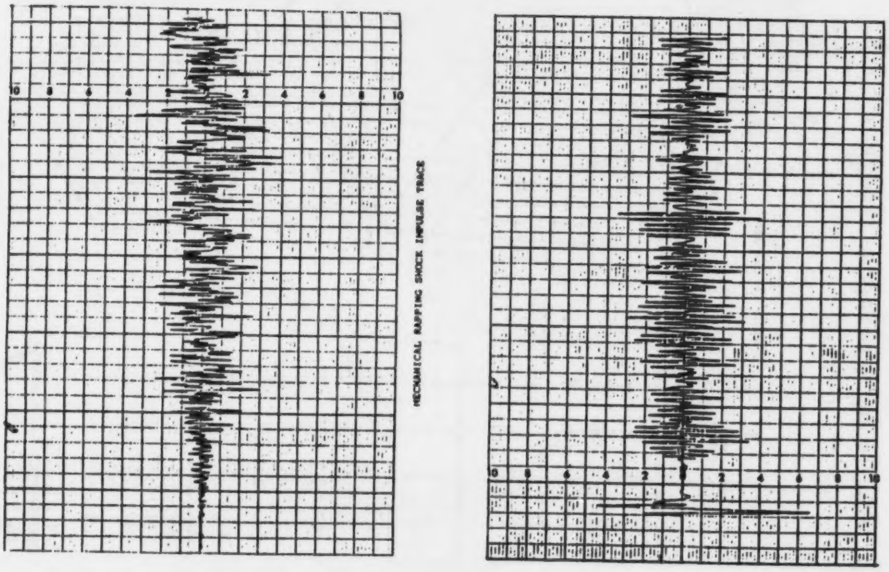

MECHANICAL RAPPING SHOCK IMPULSE TRACE

FLASH-OVER RAPPING SHOCK IMPULSE TRACE

FIGURE 8

DISCHARGE ELECTRODE ASSEMBLY

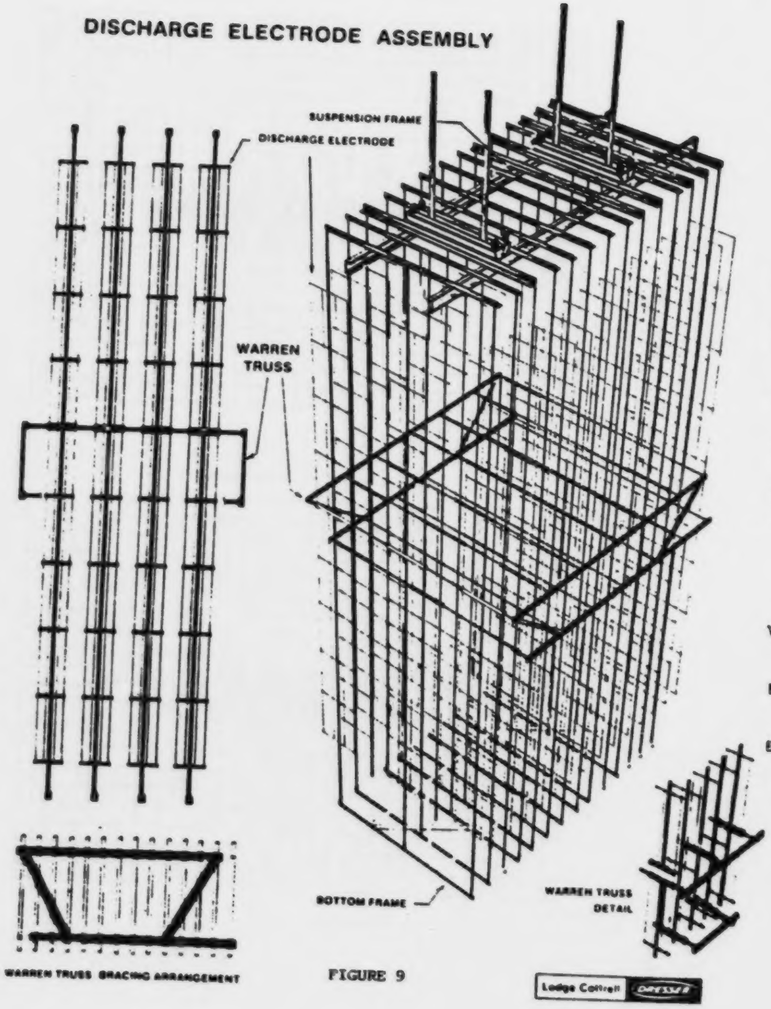
SUSPENSION FRAME
DISCHARGE ELECTRODE
WARREN TRUSS
BOTTOM FRAME
WARREN TRUSS DETAIL
WARREN TRUSS BRACING ARRANGEMENT
Lodge Cottrell
DRESSER

FIGURE 9

FIGURE 10

LONG TERM PLANT PERFORMANCE DATA

U.S. PLANT

	RATING (M.W.)	COMMISSIONING	CURRENT STACK OPACITY (PER CENT)
CENTRALIA Pacific Power & Light	700	1974	3.0
RUSH ISLAND Union Electric	550	1976	3.0
GEORGE NEAL Iowa Public Service	500	1975	8.0
IATAN Kansas City Power & Light	650	1979	2.5
LA CYGNE Kansas City Power & Light	650	1977	2.5

U.K. PLANT
(C.E.G.B.)

			CURRENT EMISSION (10^{-3} kg Nm^{-3})
WEST BURTON	500	1965	110
FIDDLERS FERRY	500	1969	115
EGGBOROUGH	500	1965	96

ELECTROSTATIC PRECIPITATOR AND FABRIC FILTER OPERATING AND MAINTENANCE EXPERIENCE

by: P. Goldbrunner
Burns and Roe
Oradell, NJ 07649

W. Piulle
Electric Power Research Institute
Palo Alto, CA 94303

ABSTRACT

This paper summarizes the "Reliability Assessment of Particulate Control Systems" (RP 1401) performed by Burns and Roe, Inc. for the Electric Power Research Institute. Its purpose was to determine the performance and availability of electrostatic precipitators and fabric filters used to control flue gas particulate emissions from coal fired electric utility power plants. Representative precipitator and fabric filter installations, with associated ash handling systems, were studied. Operation and maintenance histories were compared. The results are presented in graphic form.

INTRODUCTION

The utility industry has installed several hundred electrostatic precipitators (ESPs) for flue gas particulate removal in the past two decades to comply with the Clean Air Act of 1970 and its more stringent amendments of 1978. More recently, fabric filters have been installed to achieve required emission levels. Some of these ESP and fabric filter installations are retrofits to existing generating units, and others are original equipment on new plants. A large number of early ESPs were of "hot-side" design, particularly those in which fly ash resistivity was deemed to be a problem. Recently, there has been a trend towards rigid frame ESP designs instead of the weighted wire designs which served the industry well in the past. Fabric filter designs currently operating include reverse air, shake-deflate and pulse jet cleaning, with reverse air predominant in the utility industry today.

Many problems in achieving required outlet emissions are reported with ESPs of both hot-side and cold-side design and of rigid frame or weighted wire construction. These problems are often reported in a general way lacking specific details. The application of fabric filter technology to utility boilers for particulate removal has indicated problems as well. These problems are generally due to excessive pressure drop at startup or, as in the case of Clay Boswell and Monticello, are of specific nature and are discussed later in the text.

EPRI has just completed a program to better define and identify the specific details of these reported problems. Armed with this information, the utility will be better prepared to avoid or correct problems through proper engineering, design, operation and maintenance.

APPROACH

Operating and maintenance histories of ESPs and fabric filters at 22 generating stations were surveyed as part of this program. These stations had a total of 38 ESPs and 7 fabric filters installed on 13,233 MW of generating capacity. Selection criteria for ESP examination were that they be of modern designs, more than 99.5% efficient, no less than 100 MW in size, and having a minimum of four electrical fields. Fabric filters were selected primarily on the basis of cleaning method, unit size, and bag material. Representation of a variety of manufacturers, coals and lengths of operation were additional considerations in the selection process.

Table 1 lists the installations surveyed. They include five eastern hot-side, six eastern cold-side, four western hot-side, and four western cold-side installations. The intent was to reveal differences in operation, maintenance, and performance of the various applications. In-service dates for the ESPs range from 1971 through 1979. The four generating stations with fabric filters included in the study used western coals exclusively and began operation between 1977 and 1980.

TABLE 1. PRECIPITATOR AND FABRIC FILTER INSTALLATIONS

Utility	Plant	Unit No.	Unit Capacity MW	Hot Side	Cold Side	Design	Mfr.	Operating Date
Potomac	Potomac	1-5	5x100	E		WW	Joy-Western	1978
TECO	Big Bend	2	420		E	WW	Joy-Western	1974
TECO	Big Bend	3	420		E	WW	R-C	1976
Penelec	Homer City	3	640		E	WW	R-C	1978
TVA	Kingston	1-9	4x150/ 5x200		E	RF	AAF	1976
TVA	Widows Creek	1-4	4 x 130		E	RF	C-E	1977
TVA	Bull Run	1	950		E	RF	Carborundum	1978
CP&L	Sutton	1	105	E		WW	R-C	1975
CP&L	Sutton	2	110	E		WW	Buell	1975
AEC	Tombigbee	2,3	2x233	E		WW	R-C	1979
Buckeye	Cardinal	3	618	E		WW	R-C	1977
NIPSCO	Shanfer	14	520	W		RF	C-E	1977
NIPSCO	Shanfer	15	511	W		WW	Buell	1979
KCP&L	LaCygne	2	674		W	RF	L-C	1977
TUGCO	Monticello	3	750		W	RF	C-E	1977
Utah P&L	Hunter	1&2	2x420		W	WW	Buell	1977
P.S. of Colorado	Comanche	1&2	2x350	W		WW	R-C	1971
Colorado Ute	Hayden	1	192	W		WW	Buell	1974
Oklahoma Gas & Elec.	Muskogee	4&5	2x555		W	WW	R-C	1977
K.C. Board Pub. Util.	Kaw	1&2	2x44	Fabric Filter			ICA	1979
Minn. P&L	Clay Boswell	1&2	2x69	Fabric Filter			Joy Western	1978
TUGCO	Monticello	1&2	2x575	Fabric Filter			W-F	1977
Col.Springs Dept. Pub. Utils.	R.D. Nixon	1	200	Fabric Filter			Joy Western	1980

E = Eastern Fuel
W = Western Fuel

WW = weighted wire
RF = rigid frame

Since performance of the ash removal system directly affects ESP and fabric filter operation, it was included as part of the assessment.

To assess the problems with ESPs and fabric filters, meetings were held on-site at the selected generating stations with plant operating and maintenance personnel. The results presented here are primarily based on information received during these on-site meetings, augmented by data taken from specifications and performance tests. The on-site meetings concentrated on two areas:

- Review of maintenance records to obtain data on component failures frequency of failures, and repair times. Discussions with plant personnel to learn first-hand their problems with the ESP or fabric filter, its ash removal equipment, and auxiliaries, in order to supplement frequently incomplete data from user's files.
- Determination of the unit outages and load reductions resulting from ESP or fabric filter ash removal or related system malfunctions.

In this paper, the results are presented separately for ESPs and fabric filters.

ELECTROSTATIC PRECIPITATORS

A goal of the study was to find the causes of ESP operating and maintenance problems affecting reliability and availability. The on-site meetings concentrated on obtaining historical data on failures of ESP and ash handling components. Detailed records were not maintained at all plants, and variations existed between recordkeeping methods at those which did. Therefore comparisons of component failures between ESPs of different designs at different plants are not always definitive.

The ESPs surveyed were installed on units ranging in size from 100 to 950 MW. Specified and actual operating parameters are presented in Table 2. Specific collecting areas varied from 275 to 600 ft^2/1000 ACFM. Fuel ash contents ranged from 5 to 25%, sulfur contents from 0.3 to 3%.

Of the 38 precipitators reviewed, 26 meet or exceed their design efficiency, the remaining twelve either meet required emissions or use remedial methods to enhance ESP performance. At the Kingston plant, initial performance problems required use of a higher sulfur coal to maintain compliance outlet emissions. (This has since been corrected through modifications to the rapper systems.) The Comanche and Hayden stations use flue gas conditioning on their hot-side units to maintain emission requirements. The Hunter station has experimented with "off-line" rapping to minimize ESP performance degradation.

Failure frequency rates for the ESP components and associated fly ash handling system components are summarized graphically in Figure 1. It is apparent from this exhibit that the ESP has significantly lower failure rates than the fly ash handling system.

TABLE 2 Precipitator Specified versus Operating Conditions

Plant	Unit(s)	Heating value of Coal (Btu/lb)		Ash Content of Coal (%)		Sulfur Content of Coal (%)		Flow volume per boiler unit (acfm)		Inlet Temperature(°F)		Inlet Dust Loading (gr/acf)		SCA Rating (ft^2/1000 acfm)		Efficiency* %	
		Spec'd	Actual	Spec'd	Actual	Spec'd	Actual	Spec'd	Actual	Spec'd	Actual	Spec'd	Actual	Spec'd	Actual	Spec'd	Actual
Potomac River	1-2	11,000-12,700	13,000	10-25	8	0.5-1.0	0.8	585,000	562,000	550-650	N/A	4.5	1.42	413	430	99.5	99.81
	3-5	11,000-12,700	13,000	10-25	8	0.5-1.0	0.8	585,000	482,000	550-650	N/A	4.5	1.42	413	501	99.5	99.72
Big Bend	2	9,700-11,800	11,200	10.4-17.7	10.9	3.0-4.6	3.1	1,408,000	1,312,000	301	320	9.9	4.59	331	356	99.8	99.78
	3	11,400	11,800	11.0	11.0	2.9	1.6	1,420,000	1,150,000	291	N/A	4.7	4.5	322	398	99.78	99.73
Homer City	3	11,500	11,700	20	18.0	2.1	1.5	2,600,000	2,230,000	220-300	293	4.5	2.8	440	510	99.54	99.65
Kingston	1-4	12,288	11,600	15.5	16	0.9	2.1	500,000	558,000	325	318	2.3	2.0	475	427	99.2	99.47
	5-9	12,288	11,600	15.5	16	0.9	2.1	700,000	706,000	325	342	2.3	1.37	450	445	99.2	98.95
Widows Creek	1-4	11,030	11,600	30	13.8	0.7	0.7	575,000	534,000	320	337	6.8	3.59	561	604	99.6	99.84
Bull Run	1	10,700	11,500	16.3	15.	0.6	0.9	2,600,000	2,515,00	270	266	5.5	4.2	570	586	99.6	99.94
L.V. Sutton	1	12,000	12,400	19.0	12	0.7	1.0	667,800	507,000	625	622	2.6	3.6	275	377	99.5	99.79
	2	12,000	12,400	19.0	12	0.7	1.0	665,000	* 465,000	640	594	2.8	2.9	335	480	99.40	99.2
Tombigbee	2&3	12,009	11,550	12.90	14.7	1.41	1.95	1,353,000	1,140,000	775	730	1.98	2.1	326	385	99.5	99.2
Cardinal	3		11,900	25	14.8	0.5	1.11	3,900,000	3,100,000	750	641	2.0	2.30	492	619	99.8	99.84
Schahfer	14		10,400	11.0	10.0	0.5	0.6	4,948,000	NA	660	NA	.66-2.6	NA	326	NA	99.5	NA
Schahfer	15		10,400	11.0	9.8	.5	0.6	5,806,000	NA	750	NA	NA	NA	367	NA	99.5	NA
La Cygne	2	8,125	8,100	19.7	6.0	.32	0.48	2,926,000	3,000,000	302	314	3.6	1.01	603	576	99.4	99.7
Monticello	3	6,767	5,461	14.31	24.51	0.61	0.44	3,400,000	NA	NA	NA	6.0	NA	420	NA	NA	NA
Hunter	1&2	11,500	11,400	5-11	11.5	0.32-0.80	0.52	1,878,000	1,865,700	262	258	2.65	2.47	440	443	99.6	99.78
Comanche	1&2	7,883-9,108	8,500	3-8.5	.16-.9	0.3	NA	2,514,000	3,100,000	828	NA	1.89	NA	296	240	NA	NA
Hayden	1	10,500	9,600	9.54	13.5	0.47	1.5	1,555,000	1,666,000	775	706	2.45	1.52	377	373	99.6	98.85
Muskogee	4&5	8,700	8,793	5.0	5.54	0.31	0.67	2,080,000	2,180,000	264	294	3.84	.775	635	542	99.66	99.24

Note: Actual conditions taken from review of operating and test data.

The highest failure category in the ESP is the "high voltage system." Here the primary causes of failure are support insulators and discharge electrodes. The second highest failure category is "TR set tripout," the cause of which is normally external to the TR set itself. Very few actual TR failures were encountered. The TR trips were caused by high hopper levels, electrode failures, other ground-related occurrences, and malfunction of the protective relay designed into the TR control for low voltage protection.

Figure 1. SUMMARY OF FAILURE ANALYSIS PRECIPITATOR vs FLYASH HANDLING SYSTEMS

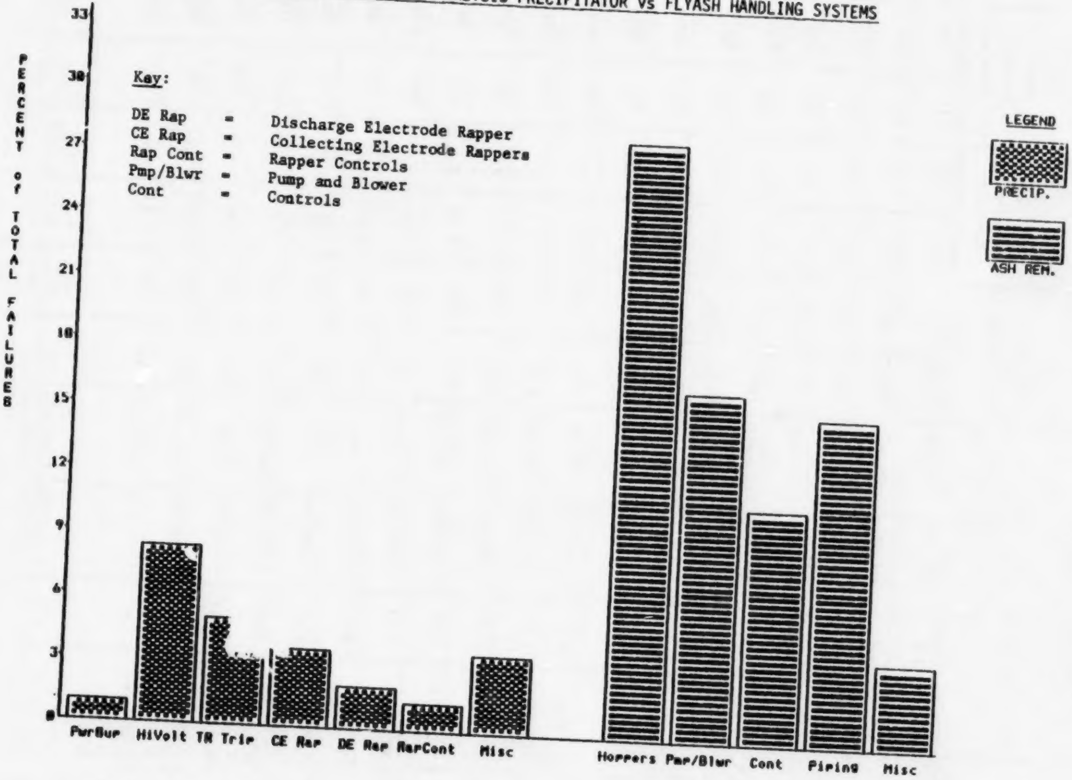

Fly ash handling system problems are the cause of approximately 75% of the total particulate removal system failures. The largest failure category is "hopper equipment" which includes hopper pluggages, the primary contributor to this category's high failure rate. On-site discussions indicated that continuous ash removal and auxiliary hopper equipment such as heaters, vibrators, and fluidizing air (when properly installed) reduce hopper pluggage problems.

During the on-site meetings, load reduction and outage data related to the ESP was requested of plant personnel. Records were not usually available, but in some cases oral information was used. Of 19 stations visited, only 6 (Potomac 1-5, Big Bend 2&3, Sutton 1&2, and Hayden 1) reported availability* reductions. These reductions ranged from a high of

---

$$* \text{ Availability } \% = \frac{\text{Boiler Avail. Hours - ESP Outage Hours}}{\text{Boiler Avail. Hours}} \times 100$$

2.6% to less than 1%. A number of plants indicated that sometimes ESP problems are corrected during outages which are charged to other pieces of equipment.

Basic ESP and ash handling system design differences were examined to determine their possible reliability variations. The following subsections present these comparisons.

RIGID FRAME VS. WEIGHTED WIRE DESIGNS

Figure 2 compares component failure rates between weighted wire and rigid frame ESPs surveyed in this study. The principal difference is in the category of TR set trips. The major contributor to higher TR set trips in weighted wire design ESPs was malfunction of the TR control unit, not wire failures. Most of the weighted wire designs investigated had "spark rate" controllers which contained printed circuit boards having high failure rates.

Figure 3 compares O&M costs of weighted wire and rigid frame designs. Electrical costs and maintenance labor are equal in both designs. Maintenance material and operating labor costs are somewhat higher for the weighted wire designs, but there is basically little difference in overall O&M costs between the two types.

HOT SIDE VS. COLD SIDE DESIGNS

Of the stations visited, those with hot-side ESPs burning western coal require remedial measures (usually flue gas conditioning) in order to meet emission standards. The stations burning eastern coal meet compliance requirements without gas conditioning. Figure 4 compares the average number of ESP component failures for the cold- and hot-side units. No conclusions can be reached although hot-side units have a higher failure rate in four of the six categories. Table 3 shows the average O&M costs for the hot- and cold-side ESPs. Total O&M costs are shown to be almost equal for both designs; these values may be biased by exclusion of gas conditioning from operating costs. No allowance has been made for the thermal losses inherent with hot-side designs.

TABLE 3. AVERAGE O&M COST (MILLS/KWH) FOR COLD-SIDE & HOT-SIDE ESP

Precipitator	Cold-Side	Hot-Side
Maint. material	0.011	0.012
Maint. labor	0.029	0.023
Subtotal	0.040	0.035
Fly Ash System		
Maint. material	0.043	0.038
Maint. labor	0.040	0.050
Subtotal	0.083	0.088
Operating Cost		
Labor	0.044	0.054
Electricity	0.070	0.072
Subtotal	0.114	0.126
Total	0.237	0.249

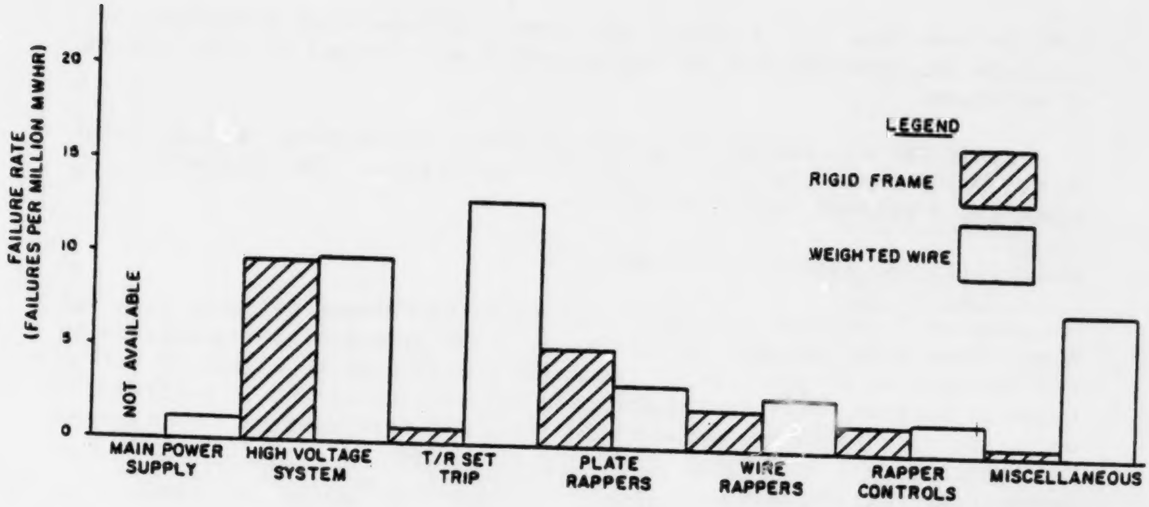

Figure 2. ESP FAILURE RATES, RIGID FRAME VS WEIGHTED WIRE

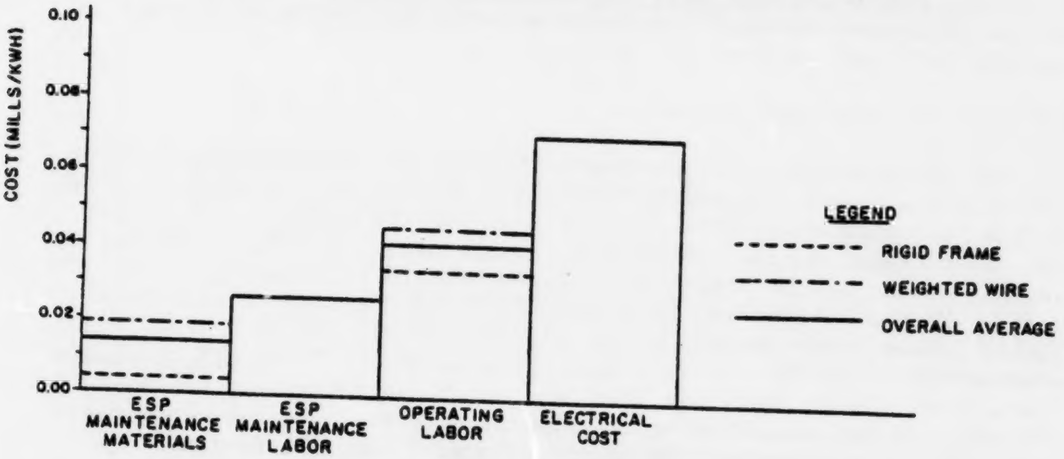

Figure 3. ESP O&M COST, RIGID FRAME VS WEIGHTED WIRE

FLY ASH REMOVAL SYSTEM

Figure 5 depicts, in bar chart format, the various types of fly ash system failures for vacuum and pressurized systems and their frequency of occurrence. Pressurized system hopper equipment failures are high, presumably because of the amount and complexity of the equipment. The pressurized system also has a higher control system failure rate. Vacuum hydraulic systems have a high frequency of piping system failures because the fly ash and water slurry causes system pluggage and erosion or corrosion. Both pressure and vacuum producing equipment also have relatively high failure frequencies. Failures are slightly higher with vacuum

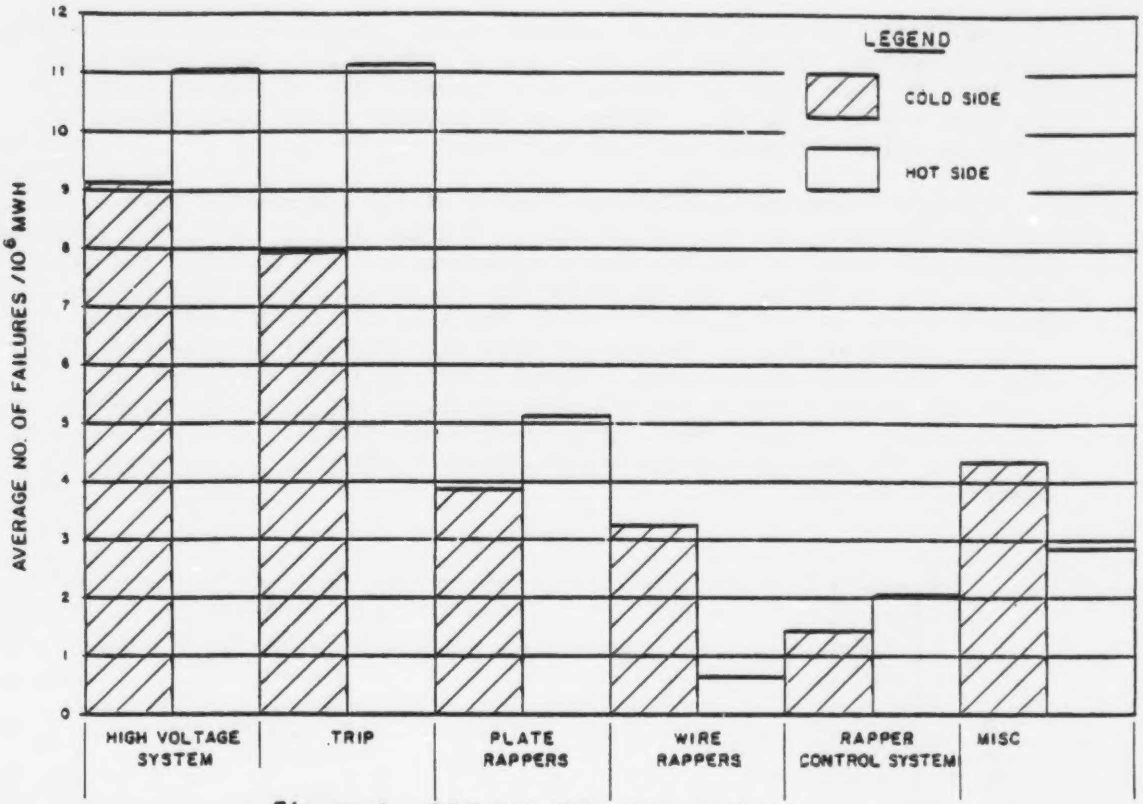

Figure 4. ESP FAILURES, HOT VS COLD

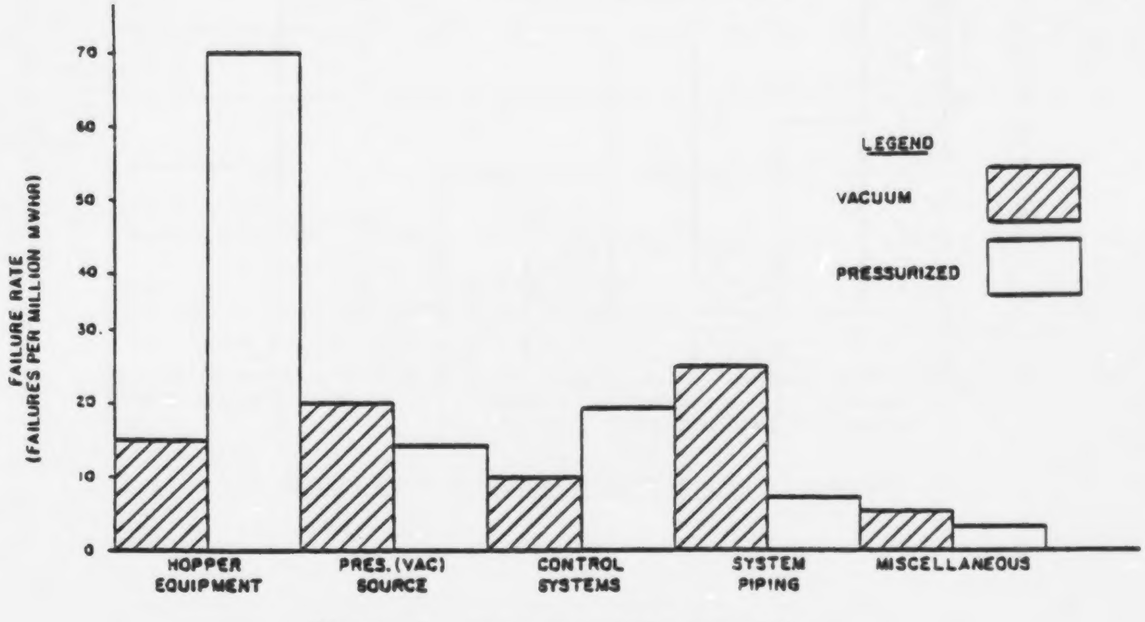

Figure 5. FLY ASH SYSTEM FAILURES

systems probably because in the plants studied they were usually of water jet eductor design, the pumps for which had a high failure rate. Blower failures in both types of systems were normally due to fly ash seepage into the lubricating oil. Vacuum system blowers also failed because of upstream filter pluggage and ash carryover.

Figure 6 compares the average number of fly ash removal system failures for hot- and cold-side units. The ash system components affected by this ESP location are the hopper equipment and the piping. For hot-side units, the hopper equipment failure rates are lower, presumably because there is less condensation in the ash, and the piping system failure rates are higher because of expansion problems encountered at higher operating temperatures. Figure 7 presents the breakdown of labor and material costs for O&M of pressurized and hydraulic vacuum type systems. It shows very little difference between labor and material costs for the two systems but a significant difference in the costs for electrical energy.

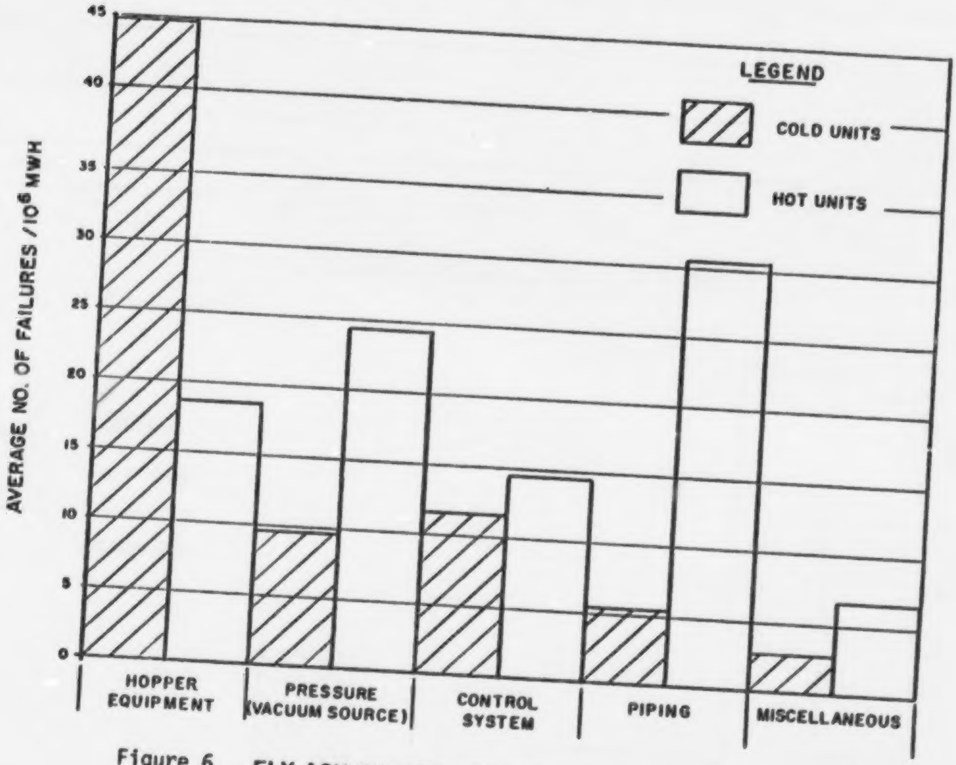

Figure 6. FLY ASH SYSTEM FAILURES, HOT VS COLD

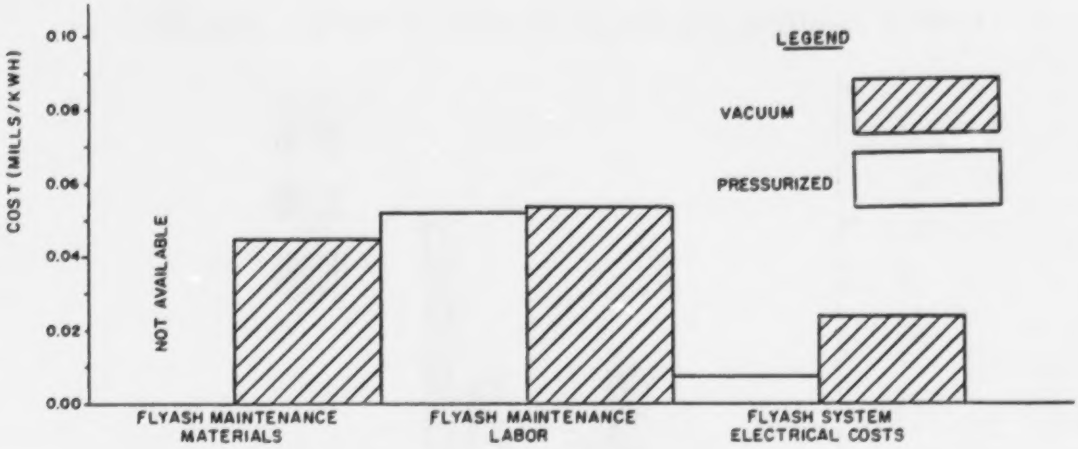

Figure 7. O & M COST OF FLY ASH REMOVAL SYSTEM

OPERATION AND MAINTENANCE COSTS

The O&M costs for the ESP installations studied are summarized in Figure 8. The largest portion of particulate removal system O&M costs, ESP electrical cost, is estimated at 70% of the installed TR set capacity. (Coal type, unit load, and other variables may cause actual power requirements to differ.) Fly ash system maintenance was considerably more costly than ESP maintenance. ESP maintenance is labor-intensive, while fly ash removal system maintenance is fairly evenly split between labor and materials.

FABRIC FILTERS

Relatively few utility boilers currently use fabric filter systems when compared with the number using ESPs; however, this situation is rapidly changing. In August 1982 there were 17,500 MW of fabric filter systems in operation, on order, or under construction. To establish a data base from which future design and operating improvements can be identified and from which changes to existing installations can be recommended, the operating and maintenance histories of four utility fabric filter installations were investigated.

On-site meetings were held at the plants to obtain first-hand operating and maintenance information. The plants were selected to be representative of typical design and operating conditions covering as wide a variety of parameters as possible. The four plants included fabric filter installations by three different manufacturers and cover extremes of climatic conditions. Table 4 presents the general design features of the four fabric filter installations and their ash handling systems.

Figure 8. PARTICULATE REMOVAL SYSTEM OPERATING AND MAINTENANCE COSTS

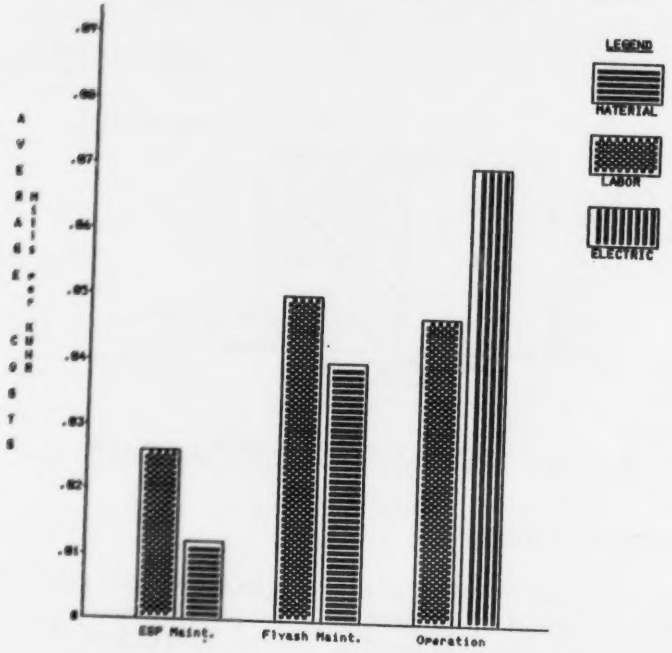

The Kaw, Clay Boswell, and R.D. Nixon fabric filter installations are cleaned by the reverse air cleaning method, Monticello by the shake-deflate method. All four plants currently use fiberglass bags with a 10% by weight coating of Teflon B.

For the units using reverse-air cleaning, the normal design gas-to-cloth ratio is between 2.02 and 2.26 to 1; for the unit that uses the shake-deflate cleaning method, it is 3.1 to 1. These ratios are within the typical range for the two respective bag cleaning methods. Normal gas-to-cloth ratio is based upon one or more fabric filter compartments out of service for cleaning or maintenance. The number out of service is dependent on the conservatism of the design. Higher gas-to-cloth ratios generally lead to greater pressure drops across the fabric filter, thus requiring more fan power to move the gas through the system and reducing bag life.

PERFORMANCE

All four installations visited are in compliance with the specified particulate emissions levels, although the systems at Kaw plant have not yet achieved their guaranteed collection efficiency. The collector at Clay Boswell station met guaranteed efficiency after some mechanical modifications which stopped particulate leakage around the bag thimbles. No performance tests have been run at Monticello. The R.D. Nixon station has an outlet dust concentration significantly lower than 0.03 lb/MBTU and a clear stack (opacity less than 5%).

Table 4. PARTICULATE REMOVAL SYSTEM DESIGN DATA

Station Name Units	Kaw 1 and 2 2 x 44 MW	Clay Boswell 1 and 2 2 x 109 MW	Monticello* 1 and 2 2 x 595 MW	R.D. Nixon 1 200 MW
Fabric Filter Design Data				
Manufacturer	ICA	Western Precipitator	Wheelabrator Frye	Western Precipitator
Coal Analysis				
Type	Bituminous	Sub-bituminous	Texas lignite	Western Sub-bit.
Moisture Content (% by wt.)	6-12	25	26-37	15
Ash Content (% by wt.)	15	10	23	6
Sulfur Content (% by wt.)	5	1.0	0.5	0.4
Heating Value (Btu/lb)	11,000	8,500	5,500	10,500
Normal Gas-to-Cloth Ratio	2.02:1	2.26:1	3.1:1	2.03:1
Gas Flow to Baghouse (ACFM)	200,000	348,000	1,840,000	1,071,000
Flue Gas Temperature (^oF)	350	240-390	400	295
Inlet Dust Loading (gr/acf)	-	1.0-3.5	9.0	5.25
Outlet Loading (gr/acf)	0.005	0.01	0.009	0.005
Outlet Loading (lb/10^6Btu)	-	-	-	0.022
Removal Efficiency	99.86	99.7	-	99.86
F to F Pressure Drop (in. water)	6	6	6.5	5
Bag Size (L x D)	36' x 8"	32' x 12"	30'-6" x 11"	31'-9" x 12"
Bag Material	Fiberglass	Fiberglass	Fiberglass	Fiberglass
Bag Finish	10% Teflon B	10% Teflon B	Silicon graphite**	10% Teflon B
Anticollapse Ring/Bag	3	7	0	7
Inlet Thimble Length	8"	4"	12"	12"
Bag Cleaning Method	Reverse air	Reverse air	Shake-deflate	Reverse air
Number of Compartments	9	8	36	36
Bags Per Compartment	248	240	204	156
Gross Cloth Area (ft^2)	111,600	176,275	671,936	527,825
Ash Handling System Design Data				
Manufacturer	A-S-H	United	United	A-S-H
Type	Pneumatic vacuum	Pneumatic vacuum	Pneumatic pressurized	Pneumatic vacuum
Hoppers per Baghouse	18	8	12	18
Level Detector	Capacitance	Nuclear	Capacitance	Capacitance
Warm Air Fluidizer	No	Yes	No	Yes
Hopper Heater	No	Yes	No	Yes
Insulation	3-in. Fiberglass	3-in. Fiberglass	2-in. Fiberglass	4-in. Fiberglass
Vibrators	Yes	No	Yes	No

---

* Fabric filters installed in parallel with ESPs.
** Being replaced by 10% Teflon B.

Table 5. OPERATING AND MAINTENANCE DATA FABRIC FILTER STUDY

	Kaw	Clay Boswell	Monticello	R.D. Nixon
Pressure Drop History				
Design W.G.	6	6	6.5	5
Operating W.G.	10-12	6	10-12	4
Bag Failure Data				
Bag Failures	Note 1	100 (1980) 300 (1979)	Note 1	9 (1980)
Points of Failure	Lower portion	Lower portion	Random	Thimble/lower half
Location in Baghouse	Random	Random	Random	Random
Replacement Bag Material	10% Teflon B/ fiberglass	10% Teflon B/ fiberglass	10% Teflon B/ fiberglass	10% Teflon B/ fiberglass
Component Failure Data				
Inlet Valves/Operators	None	Sticky damper limit switches	None	None
Outlet Valves/Operators	None	Viton boot failures	None	Seal replacement
Reverse Air Fans	Motor bearing	Motor bearing	Motor bearing	None
Flue Gas Dist. Problems	None Reported	None Reported	Extensive	None
Cleaning Effectiveness	Some problems during low loads	Some problems in winter and at low loads	Many problems	None
Baghouse Service Hours	N/A	7931 (1980) 8094 (1979)	N/A	6650 (1980)
Boiler Service Hours	N/A	7931 (1980) 8094 (1979)	N/A	6650 (1980)
Baghouse Restricted Load Hours	N/A	230 (1980) 200 (1979)	N/A	None
Baghouse Outages	None reported	None reported	None reported	None reported

NA = Not Available
Note 1: Definitive data not available; on-site reports indicate major problems.

OPERATION AND MAINTENANCE

Operating and maintenance data for the four fabric filter installations are presented in Table 5. Aside from pressure drop and bag life problems, there were reports of minor component failures, including failure of ductwork, valves, valve operators, and reverse air fan motor bearings. Some failures of ash handling equipment were also reported (not shown in table); however, ash removal system problems have not been great on fabric filters. Perhaps this is because the flue gas entrance to the bags is through the hoppers, which keeps them naturally warm and fluidized.

PRESSURE DROP

The reported flange-to-flange pressure drops range from 4 in. to 12 in. of water. The pressure drop of the system at the R.D. Nixon plant is 3.5 in. of water and within the design specification. The pressure drop at the Clay Boswell plant is normally within the specification (6 in. of water) but condensation during extremely cold weather has occasionally caused a hard-to-remove cake to form on the bags. This results in increased pressure drop, at times leading to a reduction in load due to insufficient fan capacity. High differential pressures, up to 12 in. of water, have been experienced at Kaw and Monticello, the reasons for which have not been completely determined. At Kaw, load is occasionally reduced. At Monticello, flue gas flow rate through the fabric filter system has been reduced to minimize pressure drop; to compensate, the flue gas flow rate through the parallel ESPs has been increased. Monticello also reports a unique problem of ash particles seeping through the bag cloth; as yet, this problem is unresolved.

BAG LIFE

The R.D. Nixon plant had been on line over 1-1/2 years with only a few bag failures, whereas Monticello reported a bag life of 6 months to a year, and of this writing, even two years. The Kaw plant has had some bag life problems. It operates at higher pressure differentials, is used for cyclic operation, and uses a high sulfur coal, all of which may affect bag life adversely. Clay Boswell's records show poor bag life during the first year of operation; meetings on-site revealed that considerably fewer bag failures now occur.

GENERAL

It is recognized that this is a sampling of a very limited number of installations. It is not representative of the overall performance of fabric filters as reported in other more broad based EPRI reports such as RP 1401 "Operating History and Current Status of Fabric Filters in the Utility Industry" dated July 1981 and currently being updated.

The work described in this paper was not funded by the U.S. Environmental Protection Agency and therefore the contents do not necessarily reflect the views of the Agency and no official endorsement should be inferred.

ECONOMICAL FLY ASH COLLECTION BY FLUE GAS CONDITIONING

by: E. L. Coe, Jr.
Wahlco, Inc.
Santa Ana, CA 92704

ABSTRACT

This paper discusses the application of sulfur trioxide flue gas conditioning to the collection of high resistivity fly ash in coal-fired power plants. A large portion of the world's coals produce ash falling in this category. Performance figures for a 600-Mw U.S. plant having this type of equipment in operation are given. This plant had conditioning installed as a part of the original plant equipment. A comparison of emissions to those of baghouses is included, along with data on maintenance and operating costs.

The work described in this paper was not funded by the U.S. Environmental Protection Agency and therefore the contents do not necessarily reflect the views of the Agency and no official endorsement should be inferred.

INTRODUCTION

Sulfur trioxide conditioning of flue gas to improve the dust collection performance of an electrostatic precipitator was first demonstrated in 1912 at a smelter in Garfield, Utah (1). Its application to fly ash collection dates back to 1950 (2). Increasing use of low-sulfur coal, reduction of permissible emission levels and the availability of practical operating equipment have combined to cause the installation of this type of system on approximately 130 boiler units world-wide in the past decade. There has been no instance of a failure of these units to control fly ash resistivity.

It is the purpose of this paper to show from actual experience that these conditioning systems can be advantageously applied to new plant installations and that their use should not be confined to retrofit situations.

SYSTEM DESCRIPTION

Systems for catalytic generation of sulfur trioxide for flue gas conditioning have been described in a number of publications (3, 4, 5). This description will therefore be brief. The basic process is the same as that used and proven in the manufacture of sulfuric acid. In the most widely used process, sulfur trioxide (SO_3) is made from sulfur dioxide (SO_2). SO_2 can be purchased as a liquid, or can be generated by burning elemental sulfur. Except for test work or for installations of limited life expectancy, the use of liquid SO_2 is uneconomical because its cost as a feedstock is three to four times as great as that of sulfur to produce a given amount of SO_3. This paper will therefore consider only the sulfur-burning system, a typical flow diagram for which is shown in figure 1.

Filtered ambient air is pressurized by a centrifugal blower and electrically heated to combine with sulfur in a refractory-lined burner compartment. The electric heaters are controlled so that their heat plus that from the combustion of the sulfur results in the temperature of the gas stream at the burner exit being about $800^{\circ}F$, suitable for catalytic conversion. The gas stream then passes through the converter compartment which is usually constructed as a part of the same enclosure in which the burner is located. Excess air in the combustion gas stream provides oxygen for the conversion of SO_2 to SO_3 over a vanadium pentoxide type catalyst. An additional rise in temperature occurs due to this oxidation, and the converter outlet temperature becomes 800 to $1200^{\circ}F$, depending on the rate at which sulfur is fed to the system. The gas conditioning stream contains air, SO_3 and a small amount of unconverted SO_2. Water vapor is also present, and this makes it necessary to keep the temperature above the acid dew point until the conditioning gas is combined with the boiler flue gas. For this reason the connecting piping and the injection probes are carefully insulated.

In the U.S., sulfur is conveniently available in molten form and is handled with steam-heated piping, vessels and pumps. A variable-rate metering pump controlled by a plant signal proportional to coal feed or boiler load delivers sulfur to the burner. Insertion of a ratio station in the feed rate signal circuit permits setting the injection rate as a percentage of maximum capability, and it is thereafter maintained at an essentially constant volume percentage of the flue gas as boiler load varies.

Commercial systems are instrumented and interlocked to be self-policing and highly automatic and normally operate unattended. As previously stated the basic system technology is taken from acid plant practice, but items not useful or essential in power plant operation, such as air dryers and multi-stage converters, have been omitted to gain reliability and simplicity of operation. Systems are pre-packaged as integral skid-mounted units appearing generally as shown in figures 2 and 3 for burner-converter and pump assemblies.

PLANT DESCRIPTION

One U.S. power plant to date has incorporated a cold-side electrostatic precipitator with flue gas conditioning in its original design. This is the Pleasant Prairie Station of the Wisconsin Electric Power Company, located near Kenosha, Wisconsin (6, 7). This 616 Mw unit (580 Mw net) was brought on line in June of 1980 and was extensively tested for acceptance and environmental compliance in the summer of 1981 without any unusual maintenance or adjustments preceding the tests. The precipitator is a wire-and-weight type of U.S. design constructed in a double-decked configuration of four precipitator units having two chambers each with eight electrical fields per chamber for a total of 64 electrical fields with 64 power supplies. The general arrangement of the precipitator is shown by figure 4. Design parameters are listed in table 1.

The coal supplied to this unit is Western sub-bituminous which originates in the Powder River Basin of Wyoming and, as shown in table 2, is relatively low in sulfur and ash content and somewhat high in moisture. Analysis of the ash shows high calcium and magnesium percentages and fairly low sodium content. It would be expected that this ash would exhibit a moderately high resistivity, and in-situ measurements as shown in table 3 determined this to be the case (8). It was necessary to make measurements without conditioning at reduced boiler load which caused a decrease in gas temperature. It is expected that the unconditioned resistivity would have been somewhat higher if 300°F could have been maintained for all measurements. Nevertheless the capability of SO_3 injection for adjusting ash resistivity to a value best suited to efficient precipitator operation is clearly shown. The quantity of SO_3 in the flue gas entering the precipitator was measured simultaneously with resistivity. At 15 ppm injection 1.7 ppm SO_3 was observed in the gas stream. At all other points, the quantities were too low to be experimentally significant; that is, they were less than one ppm. The difference between the observed concentration and the injected quantity indicates deposition on the fly ash.

TEST RESULTS

Acceptance tests conducted on June 9, 10 and 11 in 1981 gave the results shown in Table 4. These tests were conducted by a third party using EPA method 17 and were inlet/outlet tests of the complete precipitator installation. It will be noted that the design efficiency of 99.72% was exceeded by a wide margin, and that the precipitator migration velocities averaged 8.0 cm/s. Since it appeared that the design requirement could have been met by a smaller precipitator, it was of interest to determine the effect of reducing the effective collection area. Therefore the tests dated June 16 were conducted on a single chamber (one-eighth of the precipitator) with two fields nearest the outlet deenergized, leaving six in line of gas flow in service. As would be expected the efficiency decreased, but it continued to exceed the design value. The migration velocity increased to about 10 cm/s, presumably reflecting increased loss of ultra-fine particles.

In October of 1981, an additional single-chamber test run by the Southern Research Institute under EPRI sponsorship verified that the single chamber with all fields in service produced a collection efficiency of 99.975%, corresponding closely to the acceptance test performance of the full installation. It was thus determined that performance of the tested chamber fairly represents that of all four precipitator units. Inlet and outlet cascade impactor measurements on the chamber produced the fractional efficiency data illustrated in figure 5. Included for comparison on this figure is previously published data (9, 10) from EPRI sponsored tests of two baghouse installations. It is obvious that a properly sized and operated precipitator can match or exceed the fine particle emission and "clean stack" capabilities of baghouses.

All performance data for the Pleasant Prairie Station reported here was taken with the flue gas conditioning system injecting approximately 8.5 ppmv SO_3 into the flue gas stream. Without conditioning it has been determined that approximately 75% boiler load produces stack opacity exceeding 20%, the applicable limit at this station. It was therefore unacceptable to the owner and the surrounding community to operate for test purposes without conditioning. With conditioning, the stack opacity at full load is normally in the range of two to five percent. Visually the stack appears clear.

UNCONDITIONED COMPARISON PLANT

Published information on the Wyodak plant of Pacific Power & Light appears to present a reasonable comparison of the performance to be expected from an unconditioned precipitator system (11). This plant is located near Gilette, Wyoming, in the Powder River Basin and its coal analysis corresponds closely to that of the Pleasant Prairie fuel. The plant is rated 330 Mw and has a rigid-frame two-unit precipitator installation with 40 bus sections, 40 power supplies and five fields handling 1.954 million acfm. It has been tested with four of the five fields in operation which yields an SCA of 600. Performance tests during each of the past three years gave outlet emissions levels of 0.0044, 0.0057 and 0.0047 gr/acf respectively with an inlet loading of 1.34 gr/acf. Corresponding migration velocities range from 4.6 to 4.8 cm/s. When all five fields of the precipitator are in operation, giving an SCA of approximately 750, the outlet loading is stated to be 0.003 gr/acf which at the same inlet concentration indicates an efficiency of 99.78% and a migration velocity of 4.1 cm/s. It may be worth noting that at least one authority on the application of rigid-frame cold-side precipitators has indicated that migration velocities in the 4 cm/s range should be used on low-sulfur coal fly ash in high-efficiency situations (12). It might thereby be inferred that Wyodak performance is in the expected range.

Clearly, one should not carry comparisons between the Wyodak and Pleasant Prairie precipitators to a point of excessive refinement, because this is not an exact "apples to apples" situation. The Wyodak boiler is by Babcock and Wilcox, the Pleasant Prairie unit is a Riley Turbo type. The inlet loading to the Pleasant Prairie precipitator is slightly higher at approximately 1.5 gr/acf. Comparative particle size data is not at hand. Nevertheless, at two-thirds the size (in SCA) the Pleasant Prairie unit produces one-fourth to one-eighth the emission concentration of Wyodak and operates at a migration velocity twice as great in spite of having a higher efficiency. The two plants represent up-to-date practice and burn very similar coal. General comparison is not unwarranted.

ECONOMIC COMPARISON

For convenience, a 600 Mw plant is assumed, requiring cleaning of particulate matter from 2.6 million acfm of flue gas at 280°F. The fuel is low-sulfur coal, and the required collection efficiency is 99.9%. The precipitator may be of any design not having excessive sneakage, rapping, reentrainment or hopper losses; either rigid frame or wire-and-weight style. From the actual plant data in preceding sections of this paper it is determined that the precipitator design migration velocities (unmodified Deutsch equation) will be 4.0 cm/s for the unconditioned case and 8.0 cm/s for the conditioned case. Note that this is conservative in that it favors the unconditioned case, since the unconditioned plant did not achieve 99.9% efficiency at 4.0 cm/s migration velocity but the conditioned plant exceeded it at 8.0 cm/s.

CAPITAL COST

The cost of precipitators is assumed to vary as the 0.74 power of the size ratio (13). For 99.9% efficiency with a migration velocity of 8.0 cm/s the conditioned precipitator has an SCA of 440 ft^2/1000 acfm, giving a collecting area of 1.144 million ft^2. Assuming the purchaser will conservatively wish to add a ten percent safety factor, 1.258 million ft^2. will be purchased. At $20.00 per square foot installed, this precipitator will cost $25.2 million. The conditioning equipment adds $2.5 million for a total of $27.7 million.

By the ratio of migration velocities the unconditioned precipitator with the same safety factor will have twice the collecting area and by the 0.74 power rule its cost will be 1.67 times as great, or $42.0 million. It is assumed that ash handling connection costs, to the extent they vary with precipitator size, are covered in the assumed collecting area unit cost.

The conditioned installation shows a capital cost advantage in this example of $14.3 million.

ANNUAL COST

At 20 ppmv injection with an annual capacity factor of 70%, the example system will use 670 tons of sulfur. At $200/ton, the sulfur will cost $134,000 per year. This figure is relatively conservative, inasmuch as Pleasant Prairie uses less than half of this injection rate.

In calendar year 1981, the Pleasant Prairie plant used 323 man-hours in maintaining its conditioning system. A portion of this was applied to correction of a minor installation design problem, but taking into account the possibility of somewhat increased maintenance requirements as equipment ages, an average 350 man-hours per year is projected. At $30.00 per hour, the annual maintenance labor expense is $10,500.00. Annual cost for maintenance material is estimated at $20,000.00. This amount is somewhat speculative inasmuch as it exceeds experience to date by a wide margin, but looks toward the possibility of major overhauls which have not yet been encountered.

Operator expense is estimated at one man, one shift, 40 hours per week. At $30 per hour an annual cost of $62,400.00 is determined. No plant having this type of equipment, to the writer's knowledge, assigns a man to this duty full time, nor has added to the normal operating staff for this purpose. Nevertheless, some time is consumed in operating the equipment, and this amount is decidedly conservative.

Power is required to operate the blowers, heaters, and heat tracing of the conditioning system. The example plant will represent an average load of 165 kw. Year-round operation at $0.025/kwh will cost $36,135. Steam for heat tracing is included in this figure as though it were obtained from an electric boiler. This power consumption must be offset against the excess precipitator power required by the unconditioned unit. The relatively large fields in the Wyodak precipitator required the use of 40 power supplies to treat 1.954 million acfm. By gas volume proportion, the unconditioned unit of this example would have about 52 supplies, and the conditioned unit 26. Each supply will use about 60 kw and the reduction of 26 supplies saves 13.6 Mwh per year or $340,000.00. The difference of $304,000 is the net reduction in cost of power from use of the conditioned system.

The reduction in the number of precipitator power supplies reduces its load by approximately 1560 kw. The net reduction in load is thus 1395 kw, not including hopper heating. At a capacity charge of $1000/kw, the reduction in investment cost is $1.395 million. Table 5 is a summary of the economic effect of using the conditioned system.

This economic comparison is conservative. No credit has been taken for reduced maintenance, hopper heating power or simplification of the ash handling system due to reduced precipitator size with conditioning. Sulfur costs have been taken at about twice the usage rate experienced in service on Power River coal, and the tonnage price of sulfur is on the high side for present deliveries. Installed precipitator cost at $20 per square foot of collecting surface is conservative compared to some recent figures in the $30 range. The amount of money allocated to operation and maintenance is greater than that experienced by any FGC installation known to the writer. Refinement of these factors would be expected to increase the advantage shown for flue gas conditioned precipitators.

CONCLUSIONS

- The viability of sulfur trioxide flue gas conditioning in conjunction with cold-side electrostatic precipitators for collection of fly ash from low-sulfur coal has been demonstrated in full scale continuous new plant operation.

- Economics favor use of the conditioned system, based on comparison of full-size existing operating U.S. plants.

- Emissions less than those measured on certain baghouses are obtainable, economically and reliably.

Precipitator performance for moderate dust resistivity is highly predictable and reliable. For high dust resistivity predictions can be, and are being made but the degree of uncertainty is inherently greater. It is difficult to understand why one should accept random fluctuations at Mother Nature's whim when such variations affect the performance of pollution control equipment, and when it has been proven that they can be eliminated with net savings in money, space, energy and headaches.

REFERENCES

1. White, H.J. Industrial Electrostatic Precipitation. Addison-Wesley Publishing Co., Inc. Reading, MA. 1963 p. 12

2. White, H.J. Electrical Resistivity of Fly Ash. Air Repair 3: 2, 79 Nov. 1953

3. Archer, W.E. Fly Ash Conditioning Update Power Engineering 81: 6, 76 June, 1977

4. Brennan, J.H. and Reveley, R.L. Flue Gas Conditioning With SO_3 To Improve Precipitator Performance In: Proceedings of American Power Conference Chicago, IL 1977 p. 569.

5. Brines, H.G. and Reveley, R.L. Flue Gas Conditioning to Reduce Size and Costs of a New Precipitator at Public Service Company of Colorado - Arapahoe Station Unit No. 1 In: Proceedings of American Power Conference Chicago, IL. 1978 p. 742.

6. Eskra, B.J and McKiney, B.G. One Year's Operating Experience With SO_3 Conditioning on a Large Coal-Fired Unit's Electrostatic Precipitator. Paper 82 - 49.3 presented at the 1982 Annual Meeting of the Air Pollution Contol Association. New Orleans, LA June 1982

7. Coe, E.L. Jr. Conditioning Power Plant Flue Gas Pollution Engineering April, 1982 p.36.

8. Altman, R.F.; Gooch, J.P.; Bickelhaupt, R.E. and Dismukes, E.B. Flue Gas Conditioning Studies In: Proceedings International Conference on Electrostatic Precipitation. Air Pollution Control Association. Pittsburgh, PA. 1982 p. 131

9. Ensor, D.S.; Hooper, R.G. and Scheck, R.W. Determination of the Fractional Efficiency, Opacity Characteristics of the Fractional Efficiency Aspects of a Fabric Filter Operating on a Utility Boiler. EPRI-297 Electrical Power Research Institute, Palo Alto, CA 1976

10. Ensor, D.S. et al. Kramer Station Fabric Filter Evaluation. EPRI-CS-1669 Electric Power Research Institute, Palo Alto, CA 1981

11. (Unsigned) Cold-Side Precipitator Handles Low-SulfurCoal. Electric Light and Power August 1982 p. 21

12. Brandt, J. Exhaust Gas Dust Collection From Boiler-Furnaces for Fuels with a Low Sulphur - And High Ash Content In: Proceedings, Second Indo-German Power Plant Symposium v1, p22/IV-7 New Delhi, India January, 1982

13. Stenby, E.W.; Grimm, R.P. and Mora, R.R. Update on Economics for Particulate Control In: Proceedings of the Coal Technology '80 Conference Houston, TX November 1980 p. 559

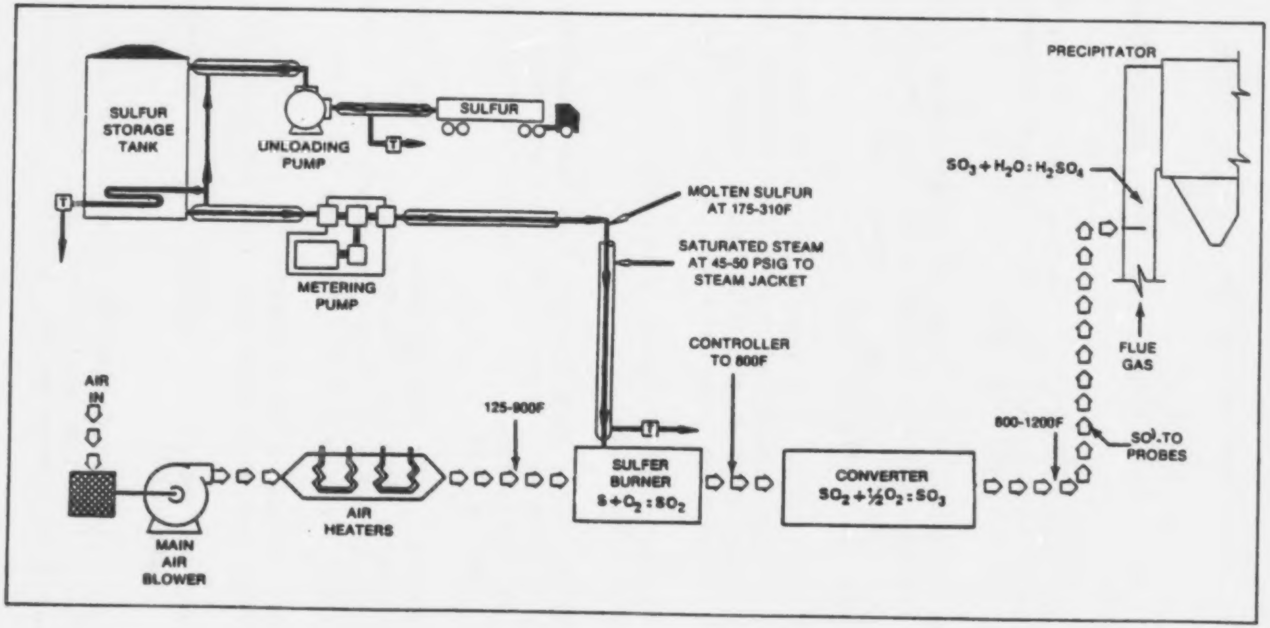
SULFUR STORAGE TANK
UNLOADING PUMP
SULFUR
METERING PUMP
MOLTEN SULFUR AT 175-310F
SATURATED STEAM AT 45-50 PSIG TO STEAM JACKET
CONTROLLER TO 800F
AIR IN
MAIN AIR BLOWER
AIR HEATERS
125-900F
SULFER BURNER $S+O_2:SO_2$
CONVERTER $SO_2+\frac{1}{2}O_2:SO_3$
800-1200F
SO_3 TO PROBES
FLUE GAS
$SO_3+H_2O:H_2SO_4$
PRECIPITATOR
T

Figure 1. Sulfur-burning flue gas conditioning system

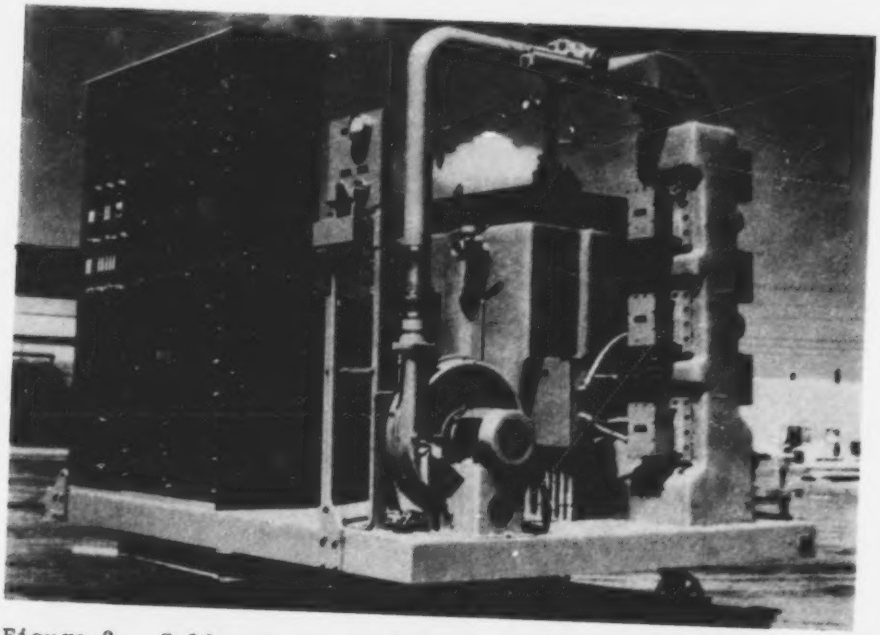

Figure 2. Sulfur Burner and Converter

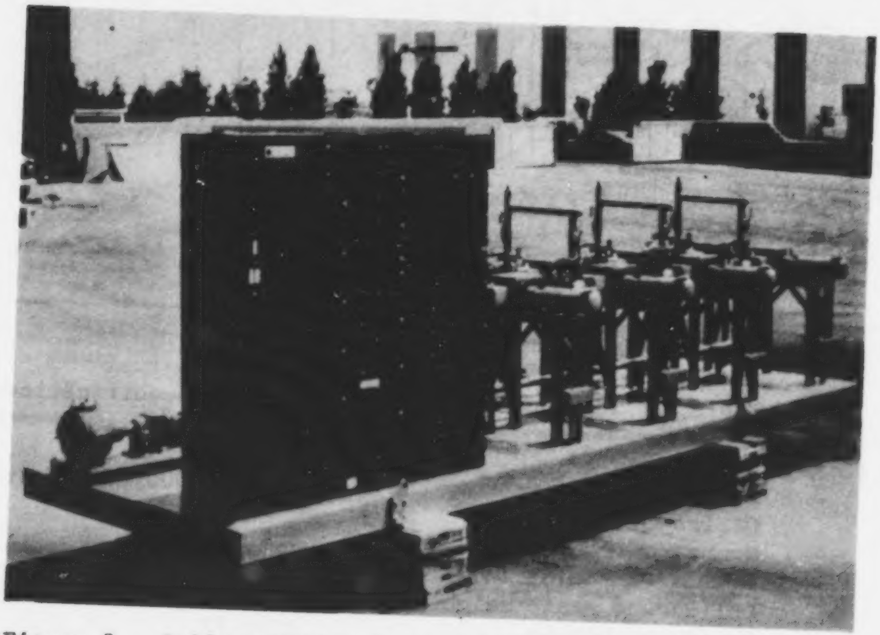

Figure 3. Sulfur Pumping Unit - Eight Pumps for Four Boilers.

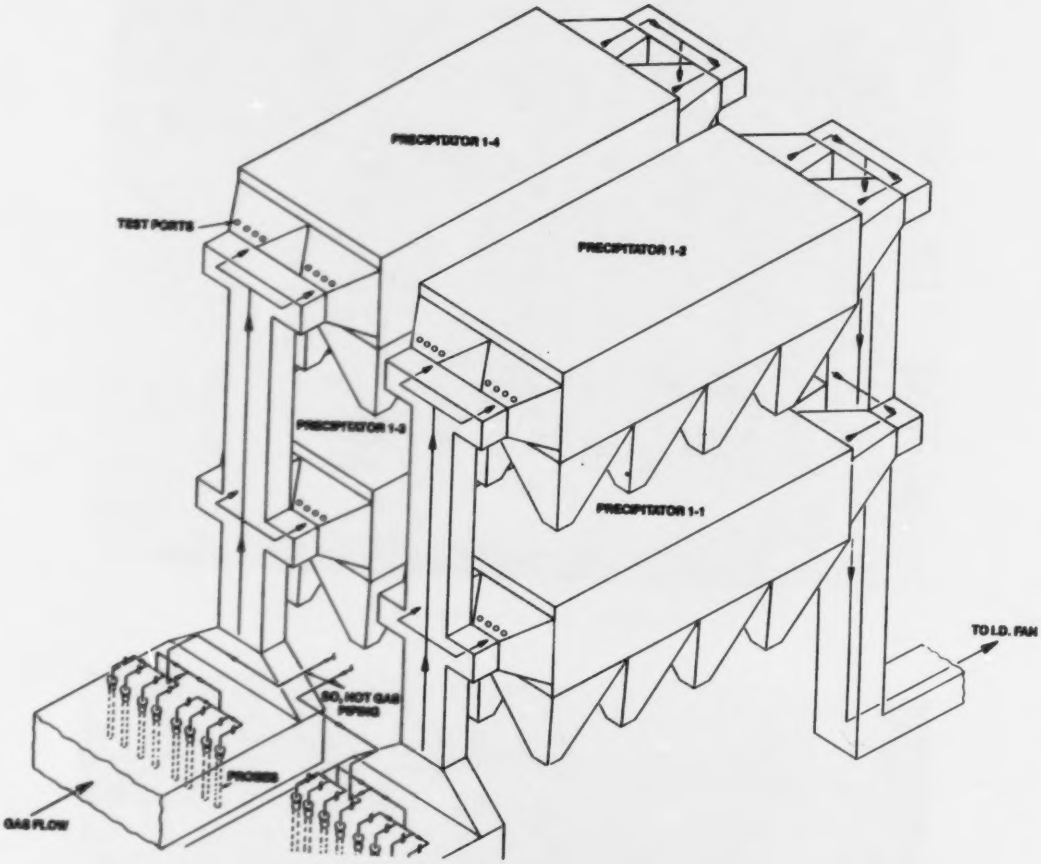
PRECIPITATOR 1-4
TEST PORTS
PRECIPITATOR 1-2
PRECIPITATOR 1-3
PRECIPITATOR 1-1
TO I.D. FAN
SO3 HOT GAS PIPING
PROBES
GAS FLOW

Figure 4. Pleasant Prairie Precipitator Arrangement

Table 1. Pleasant Prairie Precipitator Specifications

Design Gas Volume	2,600,000 ACFM @ 290°F
Design Collection Efficiency	99.72
Number of Precipitators	4
Number of Fields in Series	8 @ 4 1/2 Ft.
Collecting Plate Height	36 Ft.
Treatment Length	36 Ft.
Total Collecting Plate Area	1,223,424 Sq. Ft.
SCA	468 Sq. Ft./1000 ACFM
Drift Velocity, w	6.38 cm/sec.

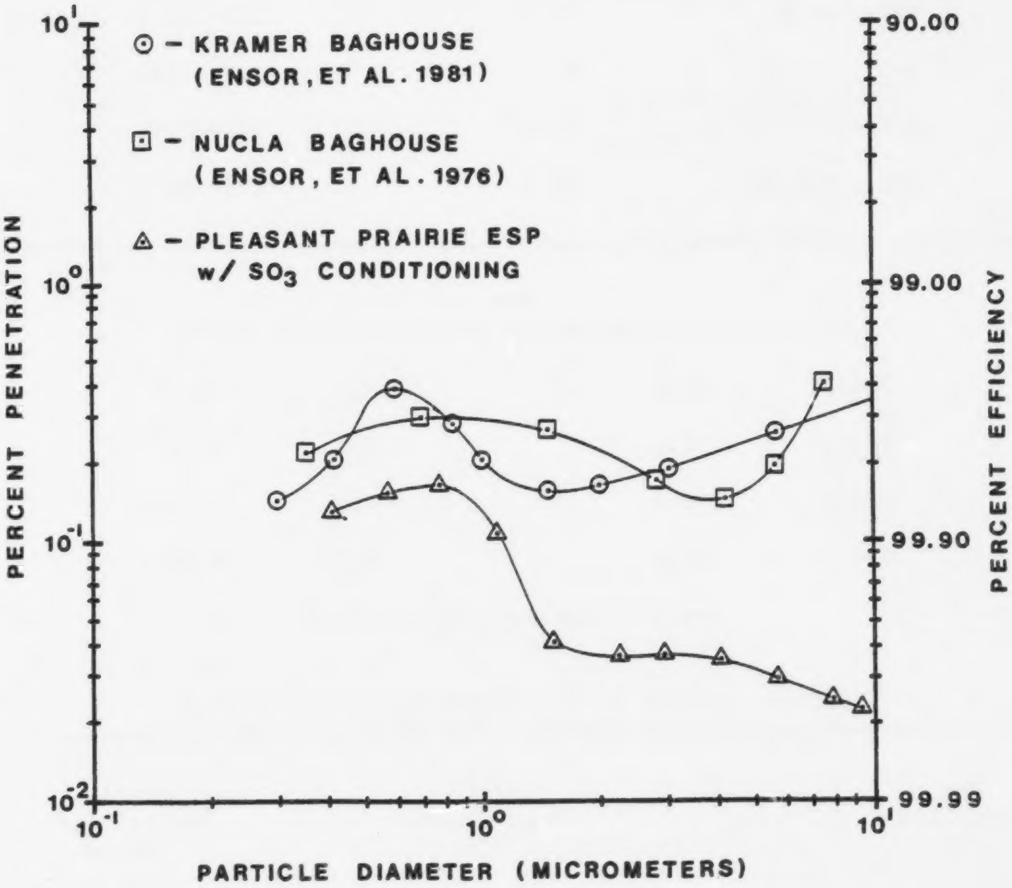

Figure 5. Particle size dependency of collection.

Table 2. Coal and Ash Analysis

	Average	Range
Moisture,%	29.2	20.9-32.1
Ash	6.12	5.31-7.26
Sulfur	0.47	0.19-0.58
HHV, BTU/Lb.	8213	8052-8376

ASH

SiO_2,%	30.6	MgO	8.1
Al_2O_3	12.6	K_2O	0.24
Fe_2O_3	7.2	TiO_2	1.1
CaO	22.2	Na_2O	0.90

Table 3. Effect of SO_3 Injection on Resistivity

SO_3 Injection ppmv	Gas Temperature ^oF	In-situ Resistivity ohm-cm
0	260	3×10^{10}
	280	1×10^{11}
5	300	5×10^9
7	300	1×10^9
15	300	7×10^7

Table 4. Pleasant Prairie Precipitator Tests with SO_3 Flue Gas Conditioning

Date 1981	MW	SCA Ft^2/1000 ACFM	Efficiency %	w cm/sec	gr/DSCF	Outlet Lb/10^{6}BTU
6/9	587	506	99.97	8.15	0.0008	0.0016
6/10	580	505	99.945	7.55	0.0017	0.0034
6/11	583	502	99.97	8.22	0.0012	0.0024
6/16*	572	354	99.93	10.42	0.0021	0.0042
	572	348	99.89	9.94	0.0034	0.0068

*Tests of 6/16 conducted with two fields (1/4) of precipitator de-energized.

Table 5. Economic Effect of Conditioning

Investment Cost	Unconditioned $1,000's		Conditioned $1,000's
Installed cost - precipitator	42,000		25,200
gas conditioner	-		2,500
Capacity charge	Base		(1,395)
TOTAL	42,000		26,305
Difference		15,695	
Annual Cost			
Fixed charges @ 20%	Base		(3,139)
Energy	Base		(304)
Sulfur	-		134
O & M	Base		93
TOTAL	Base		(3,126)

EXPERIENCES AT DETROIT EDISON COMPANY WITH DECLINING PERFORMANCE OF SULFUR TRIOXIDE FLUE GAS CONDITIONING EQUIPMENT

by: L. A. Kasik
W. A. Rugenstein
J. L. Gibbs
Detroit Edison Co.
Detroit, Michigan 48226

ABSTRACT

The generation of sulfur trioxide in some of our Company's sulfur-burning flue gas conditioning systems has been found to decrease significantly over a period of a few years. The deteriorating performance went undetected because SO_2 to SO_3 conversion efficiency was measured with what later proved to be an inadequate procedure. A fall-off in SO_3 output can seriously affect precipitator collection efficiency resulting in opacity and/or mass emission excesses. The vanadium pentoxide catalyst bed was suspected to be at fault because in some systems very little heat was being generated in the bed. A new test procedure, a modified EPA Reference Method 8, was used to overcome the inadequacies of the old procedure. Using the new procedure, conversion efficiency on one particular boiler was found to have dropped from about 80 percent to about 30 percent after five years of service.

BACKGROUND

COMPANY AND PLANTS

The Detroit Edison Company serves the Southeastern Michigan area with a system generation capability of 8450 MW. Pulverized coal firing accounts for approximately 72 percent of this generation capability. The Company employs cold-side electrostatic precipitators exclusively for particulate emission control. A number of different coal types are used system-wide, ranging from low sulfur western sub-bituminous to medium sulfur eastern bituminous.

To comply with the State of Michigan regulations on sulfur dioxide emissions, the amount of sulfur in the coal is limited. Of interest in this paper are those units which control SO_2 emissions by burning a variety of eastern coals having a sulfur content of 1.0 percent or less. This type of coal can be supplied from upwards of 10 different mines. All of the boilers were designed to burn coal of much higher sulfur content. The installed precipitators were, as a result, incapable of meeting particulate emission and opacity regulations, due primarily to the highly resistive ash (greater than approximately 10^{11} ohm-cm) produced by the low sulfur coals. The particulate emission problem has been solved by using manufactured sulfur trioxide to condition the flue gas and particles. A summary of those plants using SO_3 flue gas conditioning (FGC) is provided in Table I.

THE FGC SYSTEM

Most of the FGC systems used by Detroit Edison are the sulfur burning type supplied by Wahlco, Inc. Figure 1 shows in schematic the typical FGC system. Molten sulfur is delivered by truck and stored in a heated tank at ground level. Sulfur is transferred to an adjacent pump house which delivers a metered quantity of sulfur, by means of a reciprocating piston pump with check valves, to the burner. The sulfur burner is part of a skid-mounted package of components. The major components are: 1) a constant speed fan to deliver filtered air to the burner; 2) an air heater to maintain optimum thermal conditions in the burner at low sulfur delivery rates; 3) the burner, to oxidize sulfur to sulfur dioxide; and 4) the catalyst bed, which is vanadium pentoxide on a silica based substrate in pellet form, to further oxidize the sulfur dioxide to sulfur trioxide. The air/sulfur trioxide gas mixture, of approximately 4-5 percent concentration, is then piped to a grid of nozzles located in the flue gas duct just downstream of the air heater. All systems were sized to provide a maximum of 40 ppm sulfur trioxide at 100 percent boiler load.

It is important to note that considerable heat is generated when sulfur is burned, 3982 Btu/lb sulfur, and when sulfur dioxide is catalytically converted to sulfur trioxide, 1957 Btu/lb sulfur. The transport air serves two additional purposes: 1) to cool the gases and 2) furnish sufficient oxygen for burning the sulfur and further converting the SO_2 to SO_3. The air, in conjunction with the air heater, regulates thermal conditions in the burner. Burner thermal conditions are important and the temperature there should normally be between 800F and 825F for proper functioning of the catalyst. The catalyst manufacturer recommends keeping gas temperatures into the catalyst bed below 850F to avoid impairing catalyst performance.

PROBLEM IDENTIFICATION AND ANALYSIS

The Marysville Power Plant, as early as May, 1980, reported difficulty in controlling stack opacity to the low levels once achievable when the FGC system was new. To stay below the legal opacity limits it was now necessary to lower load on the unit. By the summer of 1981, plant personnel felt sufficient operating experience had been gained to conclude that opacity levels fluctuated depending on the source of the coal. The plant also reported that with the more troublesome coals they were unable to effect reductions in opacity by manipulating output from the FGC system.

An investigation was begun to determine the reason behind the opacity fluctuations and to find a method of control less costly than reducing load. Several factors have a bearing on stack opacity. In very general terms these are: the precipitator, boiler operation, the flue gas conditioning system and the coal, or more correctly, the ash. Study in the first two areas was not considered worthwhile, in the early stages at least, because very little correlation could be made between them and the observation that opacity changed when the coal changed. Boiler operation, especially as it relates to coal pulverizing however, was not completely forgotten as a factor. In addition, plant personnel reported both the precipitator and boiler equipment were in good working condition, having received special attention during the period that opacity had been a problem. The next two plant areas were to be the prime study targets. The coal, known to produce highly resistive ash, and for the reasons stated, could be cited as a source of the problem. However, flue gas conditioning should be able to compensate for the high ash resistivities. Ash resistivities were calculated for each coal source, using the techniques of Bickelhaupt (1), and found to range from 1.1×10^{11} to 1.5×10^{12} ohm-cm. The FGC system was identified as the primary study area.

Operating data on several FGC systems and precipitators were taken in an effort to isolate an area for further study. On some units precipitator current densities were found to be low, indicating high resistivity ash conditions. Furthermore, by increasing the sulfur rate of the FGC system on these units to slightly higher levels, current densities and stack opacity improved slightly. Following this, the sulfur burning rate was raised to the highest level possible without sounding the burner over-temperature alarm (1000F). This procedure of overconditioning should produce two very noticeable effects. First, a bluish-white plume should be seen emanating from the tip of the stack. Second, opacity degrades rapidly, particularly when the plates are rapped, due to the very low resistivity ash in the precipitator. Neither of these effects were noticed in our tests. Finally, it was noted that on some FGC systems there was very little increase in gas temperature through the catalytic converter. Recognizing that the reaction of sulfur dioxide to sulfur trioxide is exothermic, and by making adjustments for heat loss to the surroundings, a temperature increase proportional to the sulfur rate is expected. Based on the above observations it was concluded that there was sufficient sulfur as evidenced by high burner outlet temperatures and that catalytic conversion efficiency was likely very low on some of the systems. It was decided that tests would be performed to determine the efficiency.

CATALYST EFFICIENCY TEST

The FGC equipment manual contains a suggested procedure for testing for conversion efficiency. Several tests were performed using the procedure with disappointing results. Test efficiencies were consistently in the range of 93 to 96 percent. Some (2) (3) suggest conversion efficiencies for catalyst in new condition to be approximately 80 percent. Not only were our test results high by comparison but also inconsistent with our observation of very low heat release in some of the converters.

Consultation with technical experts from EPA, Southern Research Institute, and Monsanto Corp. resulted in our using a modified version of EPA Reference Method 8 to determine conversion efficiency of SO_2 to SO_3 in the FGC system. A representative sample of system outlet gas was taken through a sample line heated to at least 600F to prevent premature acid condensation. The EPA Method 8 was modified such that two impingers (bubblers) of 80 percent isopropyl alcohol (IPA) in water were used to remove SO_3, followed by two impingers of 5 percent hydrogen peroxide (H_2O_2) solution in water to remove SO_2. Both gaseous components are converted to sulfuric acid via the following reactions:

In the IPA/water solution

$$SO_3 + H_2O \rightarrow H_2SO_4$$

that used in FGC systems is not known with confidence. When the FGC equipment was first bought, the catalyst was believed to be good for the life of the equipment unless it was damaged in one of three ways: 1) exposure to temperatures in excess of 1200F, 2) plugging the bed of pellets with dust or ash, or 3) contamination with excessive moisture. The effects of such damage are usually immediate and quite noticeable. However, it is believed the catalyst can be damaged in a gradual, less noticeable manner. The catalyst manufacturer claims their product can function anywhere between 800-1200F, but at temperatures above approximately 850F, catalyst life and performance level is significantly diminished. It is preferable to have the gases (SO_2 and air) enter the catalyst at as low a temperature as possible to sustain catalytic action.

In addition, the manufacturer reported that catalysts can develop a temperature memory. If a catalyst bed is operated at a higher temperature, its performance remains approximately the same as it was at the lower temperature. However, after operating for a significant time at high temperature there is a reduction in conversion efficiency after lowering the operating temperature back to the original temperature. The long-term effect of such temperature cycling is not known but shortened life and reduced performance is suspected, especially when the temperature excursions are several hundred degrees and the temperature cycling is frequent.

The test results suggest that cycling of the FGC system between "run" and "standby" modes and over a range of sulfur burning rates may also contribute to poor catalyst performance. Trenton Channel Unit 9 is base-loaded and has one of the oldest FGC systems. Its tested conversion efficiency is also one of the highest. The other units, while not considered peaking type, are operated at several levels of load and undergo more frequent start-ups and shutdowns.

Indications are that stack opacity control has been substantially improved at our Marysville Plant since the catalyst was replaced. It has been reported that higher unit load at lower average opacity is now possible while burning the same coal once considered troublesome. Unfortunately, there has not been sufficient opportunity to perform any definitive testing to quantify the extent of improvement. Further work is planned along these lines.

CATALYST REPLACEMENT

The decision to replace catalyst material is dependent on several factors and not solely on an arbitrary level of efficiency. Acceptable stack opacity (and low particulate emissions) is possible with a catalyst bed having very low efficiency. Simply by burning more sulfur, needed levels of SO_3 can be generated to lower ash resistivity to the proper range. A limitation exists, however, because only an amount of sulfur can be burned that does not create excessive temperatures in the FGC system.

and in the peroxide solution

$$SO_2 + H_2O_2 \rightarrow H_2SO_4$$

Instead of the in-train filter between the IPA and the H_2O_2 impingers, quartz wool was used at the top of the IPA impingers to prevent crossover of acid mist into the H_2O_2 solution.

As a further modification of EPA Method 8, the respective samples were titrated with a standardized sodium hydroxide (NaOH) solution using a phenolphthalein indicator to simplify analysis for field technicians.

Catalyst bed conversion efficiency was determined as the ratio of the amount of NaOH necessary to neutralize the SO_3 solution to that required for both the SO_2 and SO_3 solutions, times 100 percent.

TEST RESULTS

Test results to date have confirmed that several of our FGC systems have very low conversion efficiency. Based on test results for systems using new catalyst, a conversion efficiency of 80 percent seems reasonable using fresh catalyst. Tested efficiencies for systems having catalyst from 3-1/2 to 6 years old range from 30 to 85 percent. Table II gives the efficiency test results for the old catalyst and the new catalyst plus the catalyst manufacturer's test results on samples of the old catalyst.

The catalyst manufacturer uses a test procedure slightly different than the test for efficiency but both are measures of conversion performance and give equivalent results. Their test results are reported as "activity". The test for activity consists of splitting a stream of SO_2 gas of a given concentration and sending one part through a sample of the old catalyst and the other through a fresh batch of catalyst of the same type. The amount of SO_3 in each outlet gas stream is then measured and used to form a ratio which relates the "activity" of the two catalysts. The conversion efficiency test consists of extracting a gas sample downstream of the catalyst bed of an operating unit and determining the relative amounts of SO_2 and SO_3. "Activity" and "efficiency" are related by a factor that derives from the fact that fresh catalyst is not 100 percent efficient in converting the SO_2 to SO_3. The equivalency factor between activity and efficiency should be approximately 0.8 based on the test results for new catalyst beds. This general relationship appears to be good for the limited number of tests performed to date.

Catalyst bed material has a finite life expectancy but the value for

The coal too, may be of a type that does not require much SO_3 for resistivity attenuation. Flue gas temperatures, which have a significant effect on ash resistivity, may be adjustable over a narrow range and by operating at a slightly lower temperature, less resistivity attenuation via FGC may be needed. This technique can have application on older boilers that typically operate at flue gas temperatures of 300F and higher. Unfortunately, these same boilers do not incorporate sufficient flexibility in gas temperature adjustability. However, should the coal change to one with significantly higher ash resistivity, the flue gas temperature be high with no provision for control, and the sulfur burning rate be near maximum level, then a marginal to poor catalytic converter will create opacity problems and need to be replaced.

Instructions on catalyst replacement is not covered in very great detail in the FGC equipment manual. For those contemplating catalyst replacement the following may be helpful:

.In the standby mode, purge the system of SO_2 and SO_3 gases for at least 30 minutes.

.Remove insulation from the top of the burner/converter box but only for that portion above the converter.

.Break the seal weld and remove the converter lid.

.Scoop the V_2O_5 pellets out of converter compartment and place them in an appropriate disposal container.

.Wire brush the compartment and lid brick surfaces of dust and debris, then vacuum.

.Inspect the internal brickwork for damage. In two units at Detroit Edison, cracks and compartment baffle wall separations from the main side wall were found and had to be repaired. In one case where baffle wall damage was severe, reconstruction resulted in an improved design by interlocking the baffle wall with the side walls.

.Screen new V_2O_5 pellets of dust and refill converter compartment following instructions in the equipment manual.

.Replace lid, seal weld, replace insulation and purge with hot air as soon as possible to prevent moisture contamination of the pellets.

As a guide to planning, catalyst bed replacement using the above procedures spanned four days, requiring a total of approximately 200 man-hours. In most instances, catalyst replacement is best done during a regularly scheduled boiler outage.

The catalyst pellets are fragile, dust easily, with the dust irritating to the eyes, skin and respiratory tract. Approved protective equipment including goggles, masks, gloves and other clothing were used during the operation. In addition, dust exposure testing was performed by a Company Hygienist that showed levels were well below the permissible exposure limits in the "Material Safety Data Sheet" (4).

CONCLUSIONS

Based on our test results, consultation with the catalyst manufacturer and observations of FGC unit operation, the following conclusions can be drawn:

- Catalyst conversion efficiency can decrease gradually to unacceptably low levels in as little as 3 to 4 years. Probable explanations for this are: 1) operating the catalyst bed at temperatures above 850F, 2) temperature cycling of the catalyst bed over several hundred degrees and 3) start-up/shutdown and sulfur burning rate cycling of the FGC system.

- Low converter efficiency alone is not justification for replacing the catalyst. The decision to replace the catalyst should be based on the ability of the FGC system to adequately condition the fly ash. However, to deal effectively with problem situations, conversion efficiency should be measured periodically.

- The amount of heat released in the catalytic converter, as evidenced by the difference between inlet and outlet temperatures, is a good indication of conversion efficiency. Each FGC system has slightly different physical characteristics and as a result, displays slightly different temperature profiles through the catalyst bed. As a result no general guidelines can be provided relating temperature increases to efficiency.

- The basic EPA Reference Method 8 using the modifications mentioned earlier is a satisfactory procedure for determining conversion efficiency.

- The ability of a particular FGC systm to overcondition the flue gas/ash i.e., produce a bluish-white plume at the tip of the stack and/or spikes on the opacity monitor, is an indication that 1) adequate sulfur is being pumped and 2) converter efficiency is sufficiently high for the particular coal being burned. If overconditioning is demonstrated, yet opacity is unacceptably high, then other problem areas should be explored. For example, there may be poor SO_3 gas distribution as a result of plugged injection ports.

ADDITIONAL STUDIES

Despite feeling that we have dealt effectively with the problem of poor catalyst performance, the work is not finished. Considerably more can be learned about the overall gas conditioning process. Additional activities are planned that will result in a better understanding of how FGC systems perform and how performance affects opacity. Following are steps we feel should be taken to achieve the above objective:

- Obtain more information on the theory and practical limitations of vanadium catalysts.
- Prepare one or more FGC systems for short-term testing by,
    1) calibrating flow and temperature measuring apparatus,
    2) performing current efficiency tests at several levels of sulfur burning, and
    3) cleaning SO_3 injection nozzles.
- Measure both equilibrium SO_3 levels and in situ ash resistivity for one or more
    1) coal types,
    2) flue gas temperatures, and
    3) SO_3 generation rates on the FGC system.
- Evaluate FGC system performance over the long-term by

1) performing periodic conversion efficiency tests,

2) obtaining historical information on temperature and duty cycle,

3) recording opacity data on systems before and after catalyst replacement to quantify improvement increment.

Information obtained from the outlined steps will help formulate better operating practices and problem solution guidelines resulting in more reliable plant operation.

The work described in this paper was not funded by the U. S. Environmental Protection Agency and therefore the contents do not necessarily reflect the views of the Agency and no official endorsement should be inferred.

Table I. SULFUR TRIOXIDE FLUE GAS CONDITIONING SYSTEMS AT DETROIT EDISON

Plant Name	Unit No.	Unit Size,MW	System Type*	Start-up Date
Conners Creek	15	62	SB	May, 1978
Conners Creek	16	62	SB	May, 1978
Conners Creek	17	62	SB	May, 1978
Conners Creek	18	62	SB	May, 1978
Marysville	9	37	SB	Dec. 1976
Marysville	10	37	SB	Jan. 1977
Marysville	11	37	SB	Jan. 1977
Marysville	12	37	SB	Nov. 1976
Trenton Channel	9	500	SB	June, 1976
Trenton Channel	16	44	SB	Oct, 1978
Trenton Channel	17	44	SB	Oct, 1978
Trenton Channel	18	44	SB	Oct, 1978
Trenton Channel	19	44	SB	Oct, 1978
Harbor Beach	1	103	SB	Sept, 1979
Monroe	1	750	SB	**
Monroe	2	750	SB	**
Pennsalt	-	14	SA	-
Port Huron	-	5	LSD	-

*SB - Sulfur Burner, SA - Sulfuric Acid, LSD - Liquid Sulfur Dioxide.

**Systems were started and subjected to brief acceptance/trial operation in November 1980; have not been operated since.

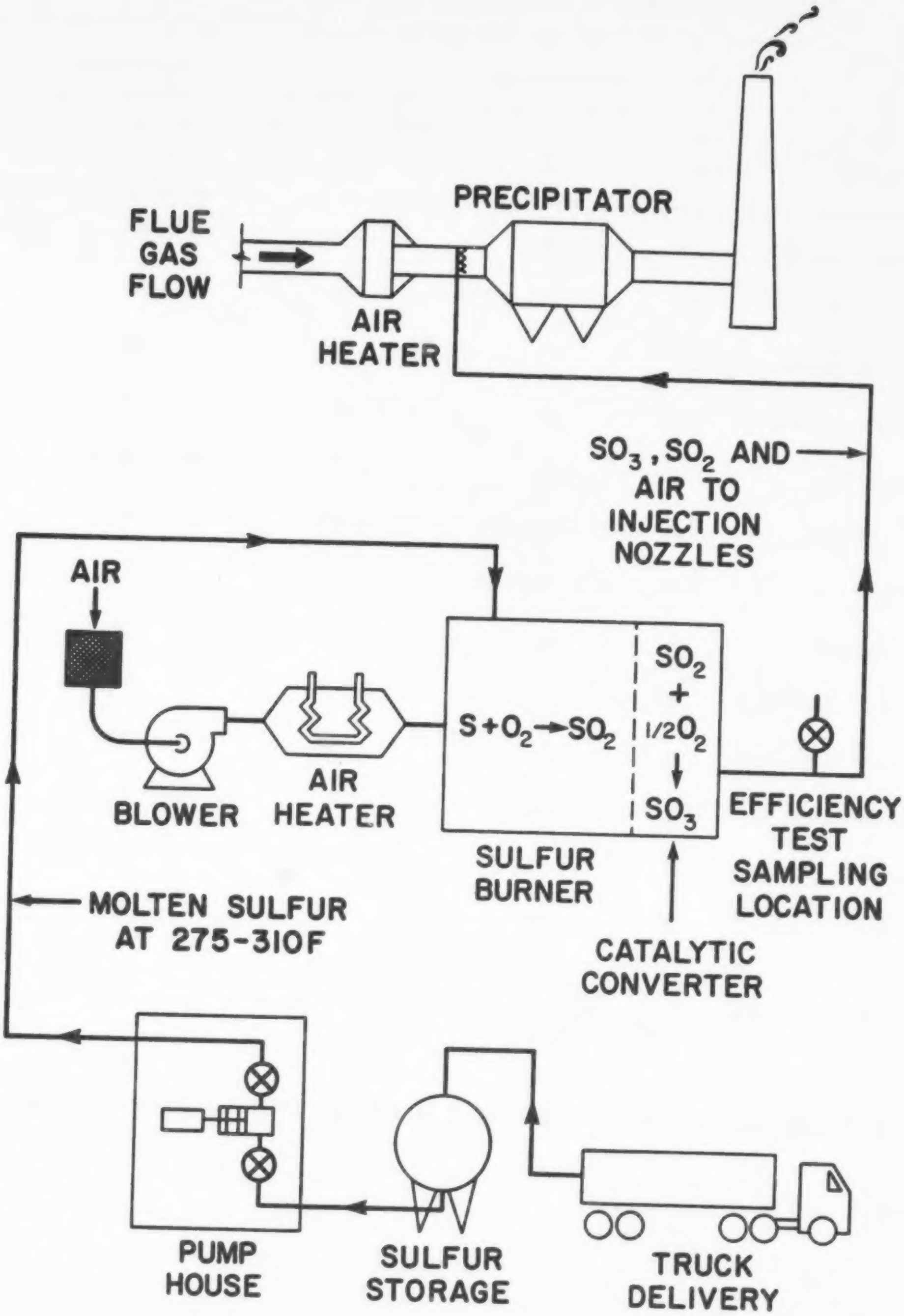
FLUE GAS FLOW
AIR HEATER
PRECIPITATOR
SO_3, SO_2 AND AIR TO INJECTION NOZZLES
AIR
BLOWER
AIR HEATER
$S+O_2 \rightarrow SO_2$
SO_2 + $1/2O_2$ ↓ SO_3
SULFUR BURNER
EFFICIENCY TEST SAMPLING LOCATION
CATALYTIC CONVERTER
MOLTEN SULFUR AT 275-310F
PUMP HOUSE
SULFUR STORAGE
TRUCK DELIVERY

FIGURE 1 SULFUR BURNING FLUE GAS CONDITIONING SYSTEM

Table II. SUMMARY OF FGC CATALYST TEST RESULTS*

Plant Name	Unit No.	Conversion Efficiency, Old Catalyst, %	"Activity", Old Catalyst, %	Conversion Efficiency, New Catalyst, %
Conners Creek	15	48	60	84
Conners Creek	16	49	66	82
Conners Creek	17	69	**	**
Conners Creek	18	73	**	**
Marysville	9	74	28	Not Tested
Marysville	10	Not Tested	68	81
Marysville	11	Not Tested	38	75
Marysville	12	30	45	76
Trenton Channel	9	83	**	**
Trenton Channel	16	70	**	**
Trenton Channel	17	56	84	Not Tested
Trenton Channel	18	85	**	**
Trenton Channel	19	68	**	**

$$\text{Conversion efficiency} = \frac{SO_3}{SO_2 + SO_3} \times 100$$

*Tests were performed over the period September, 1981 to October, 1982.

**Catalyst bed not replaced.

REFERENCES

1. Bickelhaupt, R. E., A Technique for Predicting Fly Ash Resistivity, EPA-600/7-79-204. U. S. Environmental Protection Agency, Research Triangle Park, N. C. 1979, 115 pages.

2. Klipstein, D. H., Atkins, R., Sulfur-Burning Recommended for Precipitator Gas Conditioning. Electric Light and Power, April, 1976.

3. Proposal to Detroit Edison Company, SO_3 Conditioning System for Pennsalt Power Plant, Wyandotte, Michigan, Joy Manufacturing Co. July 12, 1971.

4. Material Safety Data Sheet, equivalent to OSHA Form 20 and supplied by Monsanto Company, 800 N. Lindbergh, St. Louis, Missouri.

ESP CONDITIONING WITH AMMONIA AT THE MONROE POWER PLANT OF DETROIT EDISON COMPANY

by: E. B. Dismukes
J. P. Gooch
G. H. Marchant, Jr.
Southern Research Institute
Birmingham, Alabama 35255

ABSTRACT

An investigation of ammonia conditioning was conducted recently at Monroe Unit 1, a 720-MW unit burning coal with about 2% sulfur and collecting fly ash in cold-side ESPs around 270°F (132°C). Experience has shown that 8 ppm of ammonia substantially lowers stack opacity. Tests confirmed the effect on opacity and showed that ammonia increased the ESP efficiency, from 99.72 to 99.83% on an overall mass basis and from 99.20 to 99.68% for particle sizes below 6 μm. Particle-size data and ESP electrical data indicate that conditioning mechanisms include space-charge enhancement of the electric field by means of a fume of ammonium sulfate or bisulfate. The resistivity of the ash without conditioning ($<1 \times 10^{10}$ ohm-cm) was not altered by ammonia addition. Data on outlet particle sizes show evidence of reduced rapping reentrainment through increased ash cohesiveness.

ESP CONDITIONING WITH AMMONIA AT THE MONROE POWER PLANT OF DETROIT EDISON COMPANY

This paper discusses one of the most recent field studies of flue gas conditioning that have been performed by Southern Research Institute under sponsorship of the Electric Power Research Institute (RP724-2). This specific study was cosponsored by EPRI and the utility company concerned, Detroit Edison Company.

Ammonia is used at Monroe at an added concentration of 8 to 9 ppm to improve the efficiency of cold-side ESP collection of fly ash from a coal of moderate sulfur content (about 2%) and low alkalinity (less than 10% total of the oxides of alkali and alkaline earth metals in the fly ash). Ammonia is thus used at Monroe under quite different circumstances from those in which the classical conditioning agent, sulfur trioxide, is applicable. Details about the design of the ESPs at Unit 1 are given in Table 1; the scope of the test plan executed at one of the four ESPs (in November 1981) is described in Table 2.

The specific mechanisms of ammonia conditioning anticipated at Monroe, on the basis of prior research at other plants (1), were (a) space-charge enhancement of the electric field in the interelectrode space of the ESP and (b) suppression of rapping reentrainment from the ESP plates. Operation of both of these mechanisms was confirmed; neither a resistivity effect on the ash nor an agglomeration of ash particles prior to precipitation was indicated by the experimental data.

A major objective of the research was to quantify the degree of improvement in ESP performance achieved with ammonia addition. Data on mass efficiencies and stack opacities are presented in Table 3. The level of performance was unexpectedly high even without ammonia addition, but evidence of a significant improvement was nevertheless obtained with ammonia addition. The improvement in collection efficiency as a function of particle size observed with impactors is shown in Figure 1; the improvement was most pronounced for particle diameters smaller than 1 μm. During the time the ESP performance data were being acquired, the discovery was made that some of the outlet gas was probably bypassing the available sampling ports. Whether this was actually so and what its impact was on the reliability of the data cannot be ascertained until the next outage occurs.

The second major objective of the investigation was to identify the mechanisms by which ammonia is beneficial. Prior work (1) has shown that ammonia conditioning in a cold-side precipitator involves interaction with normally occurring sulfuric acid to produce a mist of ammonium bisulfate NH_4HSO_4 or, if the mole ratio is appropriate, the normal sulfate $(NH_4)_2SO_4$:

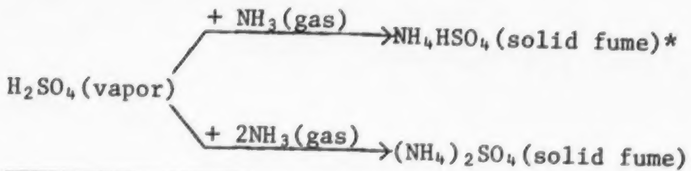

$$H_2SO_4(\text{vapor}) \xrightarrow{+\ NH_3(\text{gas})} NH_4HSO_4(\text{solid fume})^*$$

$$H_2SO_4(\text{vapor}) \xrightarrow{+\ 2NH_3(\text{gas})} (NH_4)_2SO_4(\text{solid fume})$$

---

*Occurs as a liquid above 300°F (150°C).

Data from Monroe bearing testimony to the occurrence of one or both of these chemical reactions are given in Tables 4 and 5. The sampling strategy for flue gases was such that one technique was designed to determine free, uncombined ammonia and sulfuric acid vapors whereas another technique was designed to determine the total of the free vapors and the combined forms as particulate substances. The data in Table 4 reveal that when ammonia was added little of either substance occurred in the free forms whereas roughly the expected amount of ammonia and sulfuric acid occurred in the combined forms. The analysis of fly ash from the ESP hoppers (Table 5) indicates a recovery of about 50% of the added ammonia in the ash. The data in this table for inlet and outlet hoppers were combined proportionally to obtain an estimate of 4 ppm accounted for out of the total of 8 to 9 ppm added; the calculated recovery in hoppers would have been higher, as it was in ash collected in the mass train, if allowance had been made for disproportionally higher collection of small, ammonia-containing particles in the outlet hopper.

The first mechanism of conditioning considered was resistivity modification. The in situ resistivity data obtained with and without ammonia addition fell within the two areas plotted in Figure 2. Although some of the resistivity values recorded with ammonia addition were considerably higher than any result obtained without ammonia addition, there was virtual coincidence of the points within the two areas corresponding to the "centers of mass" (i.e., the points representing the average values of the logarithm of resistivity and the reciprocal of absolute temperature). Hence, no effect of ammonia on resistivity was evident above the scatter in the data, which is attributed to several factors: (a) the customary lack of precision in field resistivity data, (b) the lack of constancy in the background concentration of sulfuric acid (also see Table 4), and (c) the high sensitivity of resistivity changes to even minor changes in the sulfuric acid concentration.

Documentation of three factors pointing to a space-charge effect is given in Table 6. This effect arises when the fume of NH_4HSO_4 or $(NH_4)_2SO_4$ is charged in the ESP and the electric field is thereby increased, with accompanying increases in the charge level of fly ash particles and the collecting field near the plates. The voltage effect, as the table indicates, was more prominent in the first field than in any of the following three fields in succession. The voltage effect is displayed differently in Figure 3, which was obtained with the inlet TR under manual rather than automatic control.

Data pertaining to the effect of ammonia on rapping reentrainment were obtained with a photoelectric device (Large Particle Sizing System) at the

ESP outlet. Figure 4 gives a graphic illustration of the suppression of the counting rate at a selected range of particle sizes (11.0 to 14.5 μm) with ammonia addition. Figure 5 compares relative counting rates as a function of particle size. The effect of ammonia is most logically attributed to a suppression in rapping reentrainment, for existing theories provide no basis for attributing effects of the observed magnitude to the alternative mechanism—a change in the effectiveness of the primary collection process.

A fourth possible mechanism of conditioning—agglomeration of fly ash particles in the gas stream before they are collected (2)—was considered, although there is no known evidence of ammonia as a specific agent causing this effect. The data in Figure 6 do not exclude this effect, but obviously they give no suggestion of it.

The third and final objective of this research was to compare the degree of improvement in ESP performance achieved with that theoretically predicted, using the principles incorporated in a computer model of ESP performance (3). This could only be done for the space-charge mechanism, in view of the limited ability of the model to predict any effects associated with rapping reentrainment. Accordingly, attention was focused on experimental fractional efficiency data from impactors for small particles and theoretical predictions for these particles in the absence of rapping reentrainment. Figure 7 compares the ratios of migration velocities based on experiment and theory.

Obviously, Figure 7 shows a serious discrepancy for particle diameters less than 2 μm. This discrepancy seems to be most logically attributed to an anomaly in the impactor data, which if operative would give a bias in the direction of an unfavorable collection efficiency when ammonia was absent. The operation of the impactors is associated with adiabatic cooling of the sample gas stream, which can be as great as 30°F (17°C). Such cooling could cause complete condensation of all of the sulfuric acid vapor present in the absence of ammonia and add materially to the apparent concentration of fine particulate matter present at the ESP outlet. The effect of cooling in the impactors in this respect would be minimal with ammonia present, on the other hand, because of the almost complete conversion of the acid vapor to a particulate form upstream from the ESP and its removal from the gas stream in the ESP.

In summary, ammonia was found to cause an improvement in ESP performance at Monroe even in the face of high performance even without ammonia treatment. The improvement is most graphically seen in terms of the reduction im mass penetration (about 40%) in the ESP tested. Data on stack opacity confirmed that a marked improvement in ESP performance occurred. The primary mechanisms identified were space-charge enhancement of the electric fields responsible for charging and collecting fly ash particles and suppression of the loss of collected ash by the process of rapping reentrainment. Alternative conditioning mechanisms—modification of fly ash resistivity and particle agglomeration prior to collection—seem to be inoperative or without consequence.

The work described in this paper was not funded by the U. S. Environmental Protection Agency and therefore the contents do not necessarily reflect the views of the Agency and no official endorsement should be inferred.

REFERENCES

1. Dismukes, E.B. Conditioning of fly ash with ammonia. J. Air Pollut. Contr. Assoc. 25: 152, 1975.

2. Potter, E.C. and Paulson, C.A.J. Improvement of electrostatic precipitator performance by carrier-gas additives and its graphical assessment using an extended Deutsch equation. Chem. Ind. 532, 1974.

3. McDonald, J.R. A mathematical model of electrostatic precipitation (Revision 1): Vol. I. Modeling and programming the electrostatic precipitation process. EPA-600/7-78-111a. U. S. Environmental Protection Agency, Research Triangle Park, North Carolina, June 1978.

TABLE 1. DESIGN FEATURES OF MONROE UNIT 1

Boiler	Babcock and Wilcox 5,700,000 lb steam/hr 750 MW
ESPs	Research Cottrell 4 parallel units 4 electric fields each unit 2,360,000 acfm (66,800 m^3/min) 240°F (115°C) SCA: 190 ft^2/1000 acfm (37 m^2/[m^3/sec])

TABLE 2. TEST PLAN FOR ONE OF FOUR ESPs

Week	NH_3	Temperature	Measurements/Samples
1	ON	"High"—ca. 280°F (138°C)	Schedule A
2	ON	"Normal"—ca. 250°F (121°C)	Schedules A and B
3	OFF	"Normal"—ca. 270°F (132°C)	Schedules A and B

NH_3 ON = 8-9 ppm.
A = Ultrafine particle sizing, large particle sizing, resistivity, flue gas analysis, fly ash and coal for analysis, ESP electrical data.
B = Mass train and impactors.

TABLE 3. ESP PERFORMANCE

	With NH_3	Without NH_3
Test conditions*		
Mass loading, gr/scf (g/m^3)	3.0 (6.9)	3.2 (7.3)
Temperature, °F (°C)	252 (122)	269 (132)
SCA, ft^2/1000 acfm (m^2/[m^3/sec])	156 (30.7)	154 (30.3)
Test results		
Mass efficiency, %	99.83	99.72
Stack opacity, %†	8.5	15.6
Emission rate, lb/10^6 Btu (ng/joule)	0.009 (3.9)	0.015 (6.4)

*Coal: % S = 1.9, % ash = 9.8, Btu/lb = 12,600 (joule/kg = 29,300).

†Values of stack opacity were related to the performance of the one ESP unit tested in a complex fashion. The value with ammonia on was achieved with ammonia addition in all four ESPs preceding the stack. The value with ammonia off was reached with ammonia off only in the one ESP tested and one other ESP but with ammonia addition continued in the other two ESPs.

TABLE 4. GAS ANALYSIS AT THE ESP INLET

	With NH_3	Without NH_3
Ammonia, ppm		
Vapor	0.2-0.4	0.1
Total	6.8-9.5	Not det'd
Sulfuric acid, ppm		
Vapor	0.1-0.9	0.3-1.8
Total	3.2-7.6	1.6-5.4

TABLE 5. ANALYSIS OF FLY ASH FROM ESP HOPPERS

	With NH_3	Without NH_3
Ammonia, wt %		
Inlet hopper	0.033*	0.007
Outlet hopper	0.095*	0.033
Sulfate, wt %		
Inlet hopper	0.67	0.55
Outlet hopper	1.4	1.1

*Equivalent to 4 ppm as vapor (mass train sample, equivalent to 7 ppm as vapor).

TABLE 6. DOCUMENTATION OF THE SPACE CHARGE EFFECT

	With NH_3	Without NH_3
Ultrafine sizing, 0.018-2.0 μm	3.1×10^{13}/DNm^3	2.6×10^{13}/DNm^3
Impactors, <0.5 μm	0.0138 gr/acf* (0.0316 g/m^3)	0.0041 gr/acf* (0.0094 g/m^3)
Voltage†, 1st field	44.2 kV	38.5 kV

*Compare difference = 0.0097 versus
calculated value = 0.0078 as $(NH_4)_2SO_4$
or = 0.0134 as NH_4HSO_4.

†At current limit (j = 38 nA/cm^2).

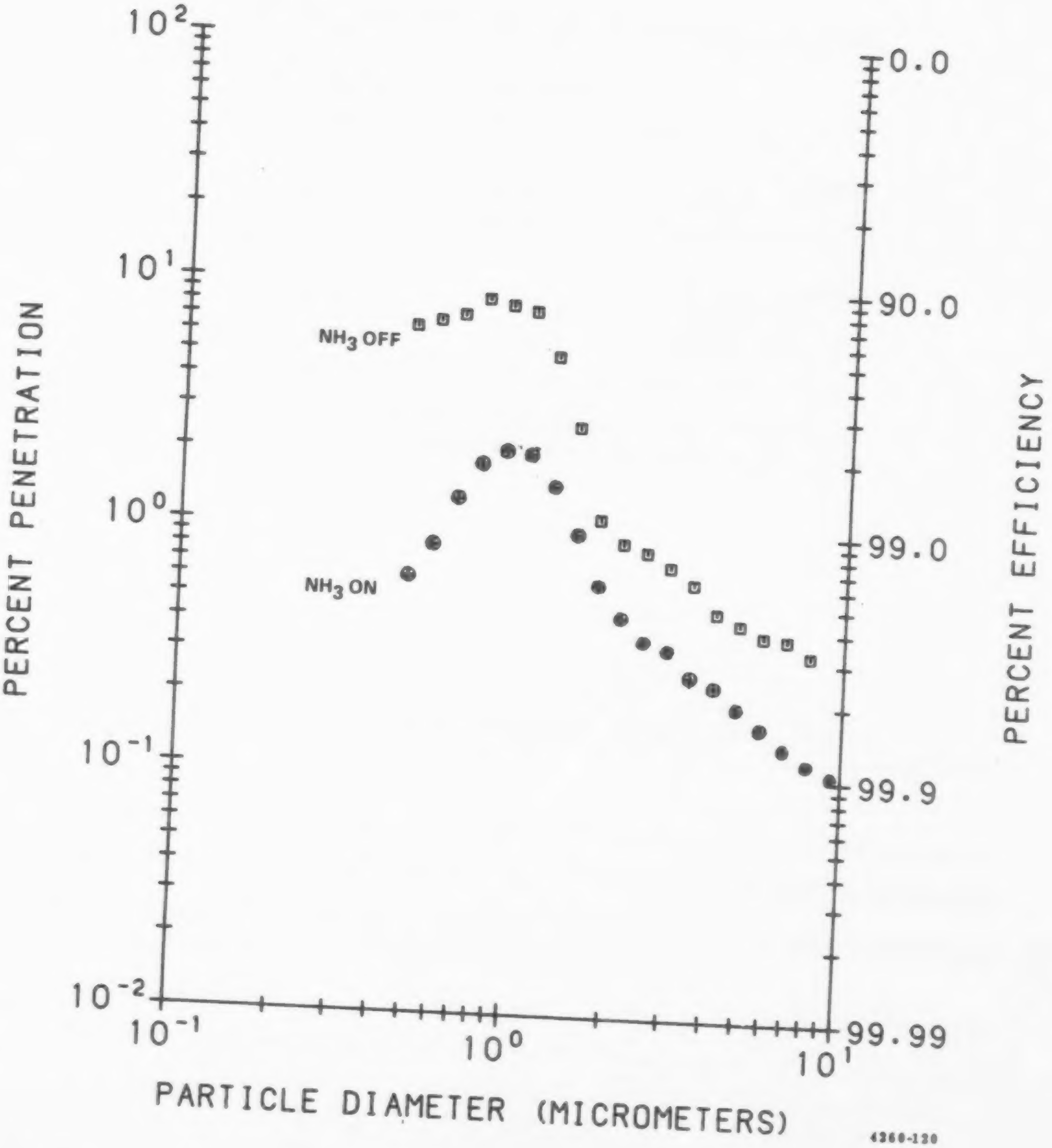

4260-120

Figure 1. Fractional efficiencies measured with impactors.

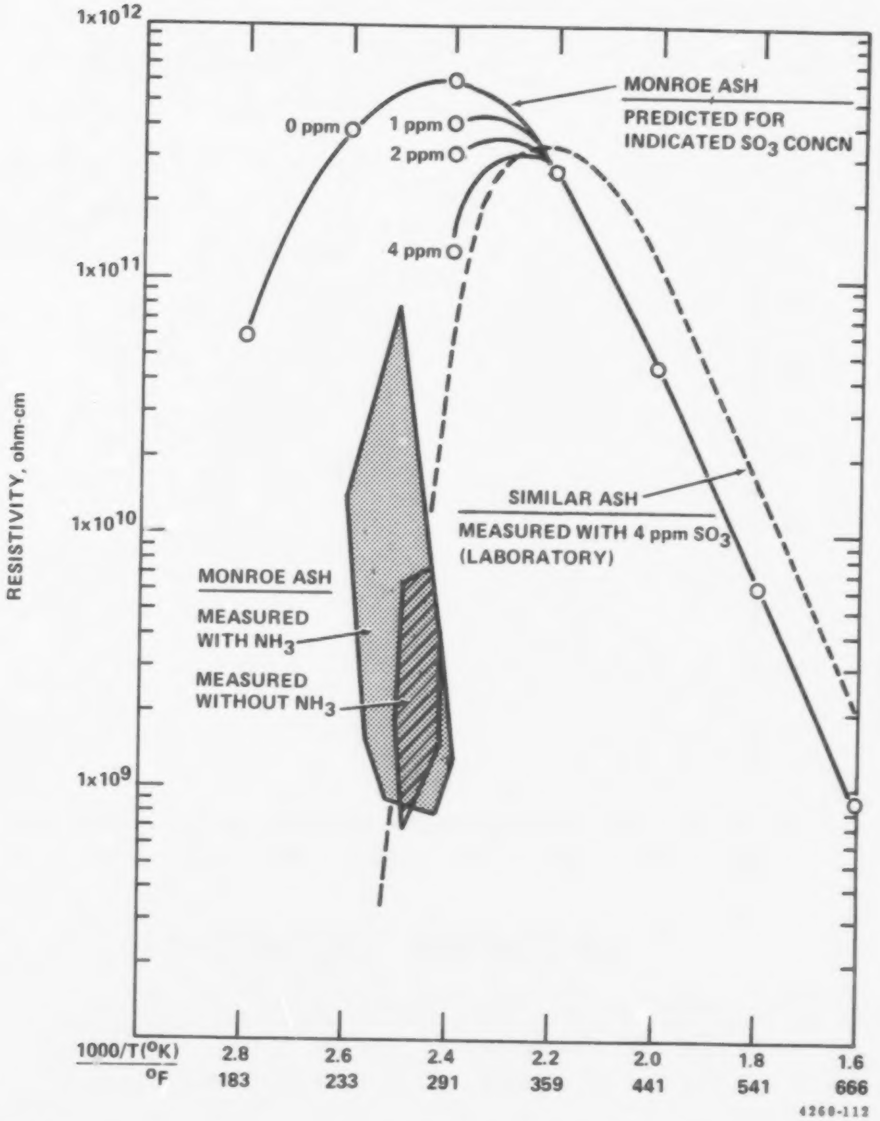

Figure 2. Comparison of observed and predicted resistivities of fly ash from Monroe Unit 1 and another similar fly ash.

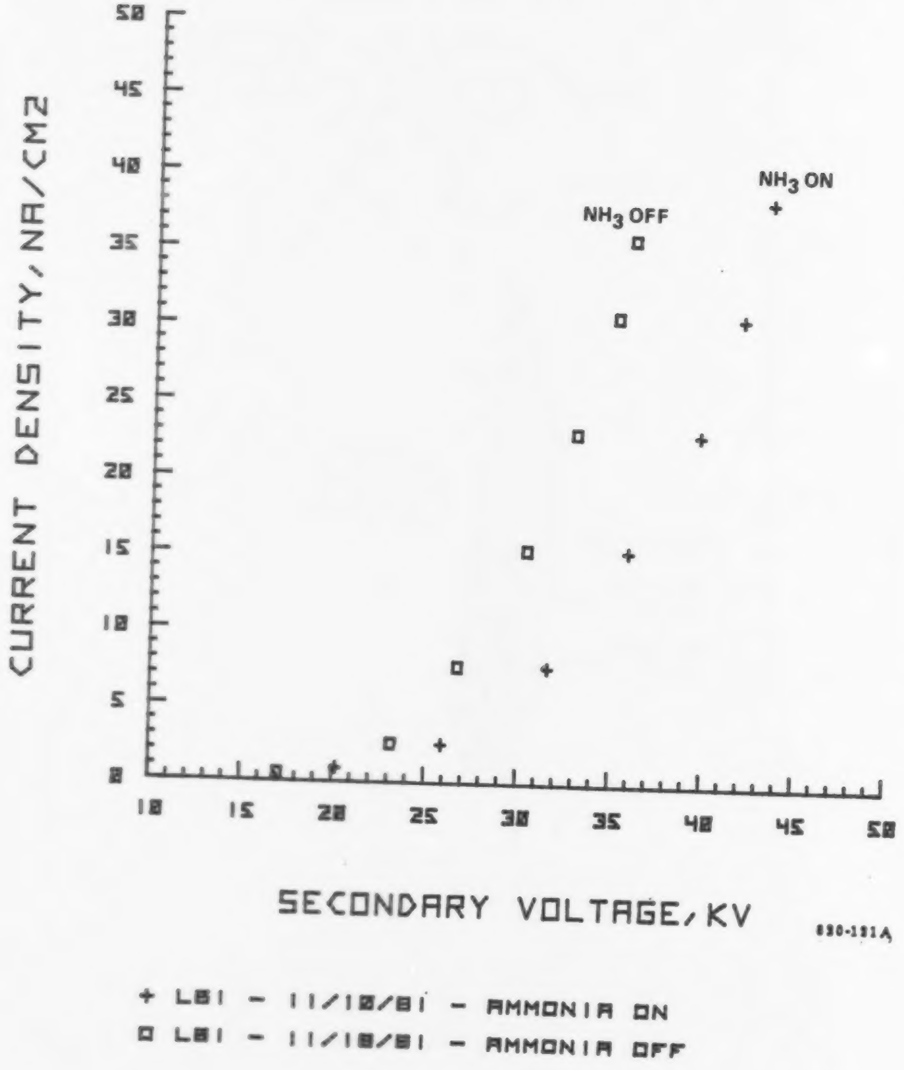

Figure 3. Current-versus-voltage in inlet field with and without ammonia addition.

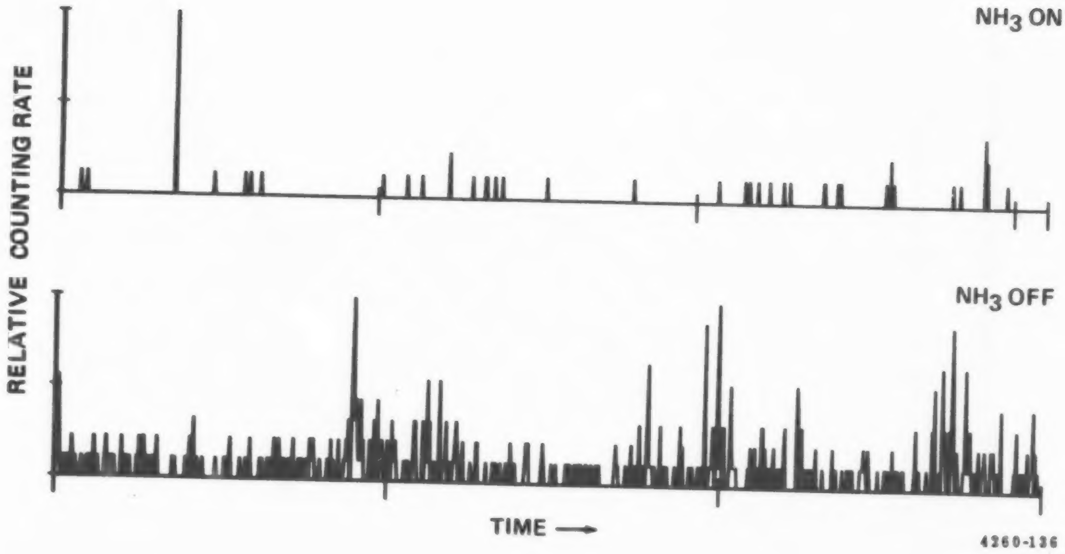

Figure 4. LPSS Data for particles 11.0 to 14.5 μm in diameter at the ESP outlet.

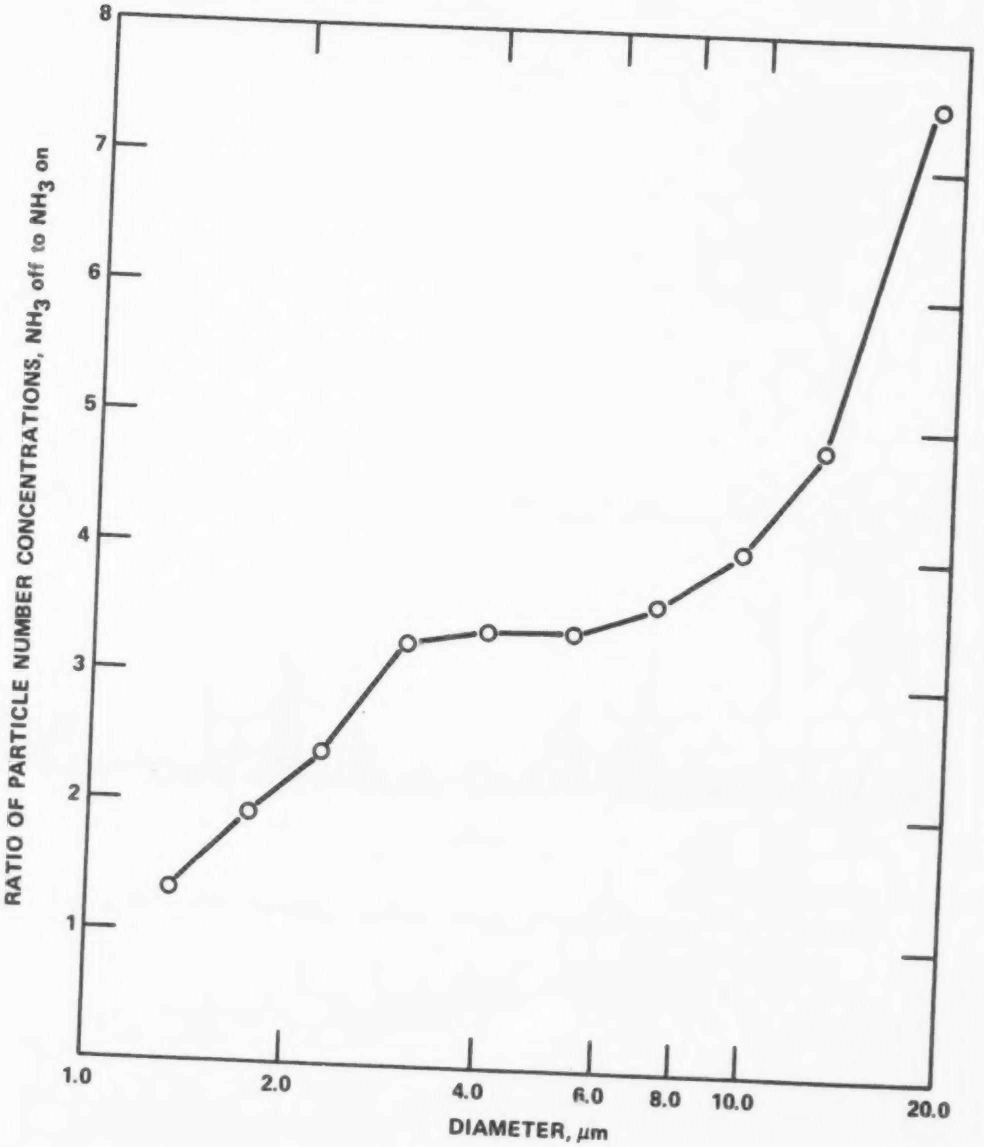

Figure 5. Relative number concentrations detected by the LPSS with ammonia on and off.

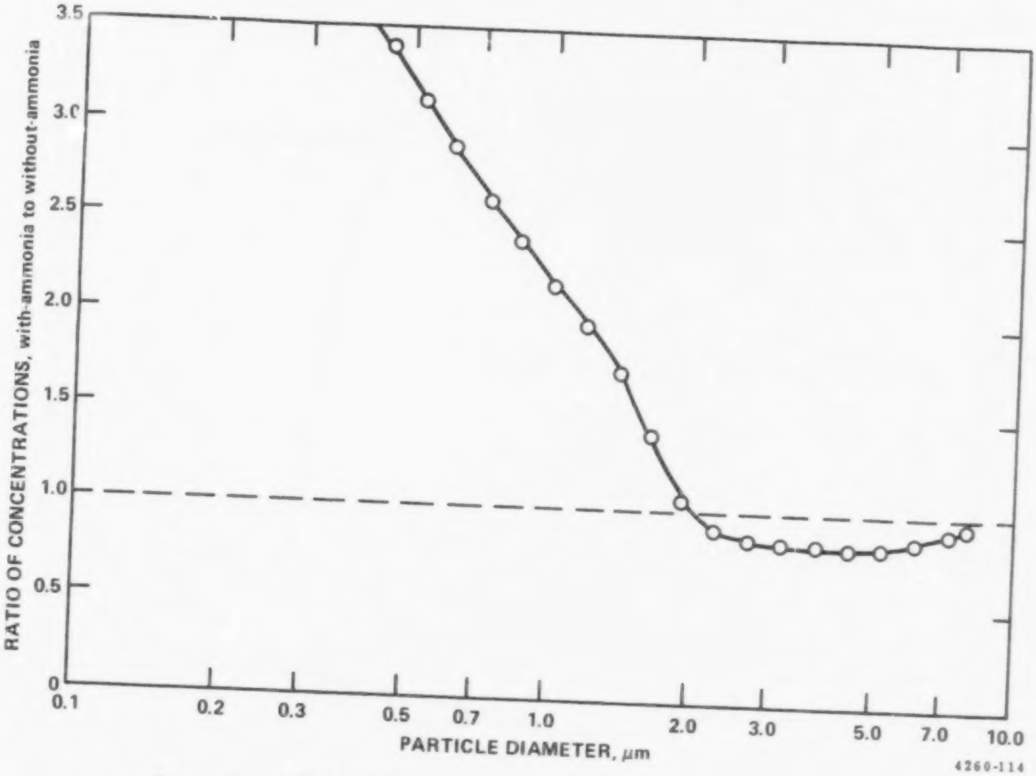

Figure 6. Ratios of inlet mass concentrations of fly ash with and without ammonia addition.

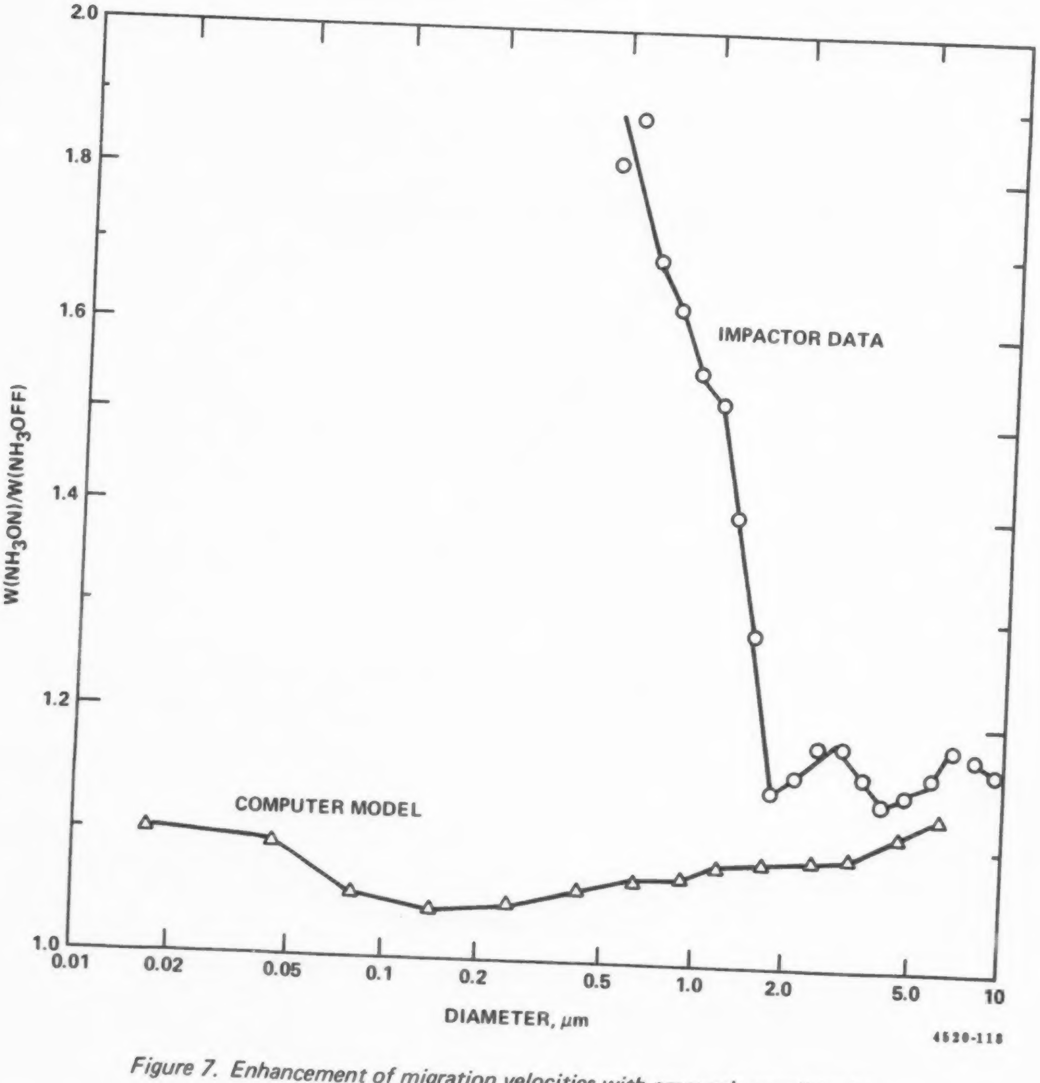

Figure 7. Enhancement of migration velocities with ammonia conditioning predicted and observed.

FLY ASH CHEMISTRY INDICES FOR RESISTIVITY AND EFFECTS ON ELECTROSTATIC PRECIPITATOR DESIGN AND PERFORMANCE

by: Herbert J. Hall
H. J. Hall Associates, Inc.
Princeton, New Jersey 08540

ABSTRACT

Field data on coal-ash properties and in situ fly ash resistivity measurements for 24 cases of cold side precipitators are correlated with various ash chemistry indices for resistivity prediction. Coals studied, principally low sulfur, are from eastern and western U.S.A., western Canada, and several other countries; boiler sizes 50-800 MW. Most universally applicable general indices for low S coals seem to be those based upon sodium content, per se, and on a silicate type index long used by the author. Under special conditions, other indices may also be useful. Ash chemistry indices proposed by investigators such as Selle, et al, Dunston, Matts, Soviet ESP designers, Bickelhaupt, Hall, and others are reviewed. Comparisons of useful indices with resistivity data calculated from a computer program based on Bickelhaupt's work are illustrated for an additional 16 cases which are also compared with the in situ field data. Some quantitative aspects of coal-ash properties as affecting precipitator design and performance are discussed.

INTRODUCTION AND BACKGROUND

In the last decade, high resistivity ash problems and effective precipitator design for very high, reliable performance (99.5-99.9+%) have received much attention in the ESP community worldwide. Earlier research by White and Hall (1946-58) explored and developed many fundamental aspects of this field - including ash chemistry factors, various physical and chemical conditioning systems, correlation of precipitator electrical operating parameters with ash resistivity factors and process conditions, and new equipments and automatic controls. Later work by the author included studies on high temperature/high pressure corona and resistivity effects, electrical waveform optimization for high ρ dusts, electron beam possibilities for high particle charging and in situ $SO_2 \rightarrow SO_3$ conversion, and the role of ash chemistry factors in resistivity problems. Over the past 13 years, I have been closely associated with precipitator design, operations and upgrading under a wide variety of high resistivity ash conditions in many different applications.

Earlier investigations have been continued and significantly advanced; new ones have been added, and some have reached a degree of maturity. An early recognition of the fact that western U.S.A. coals required a different approach to viable ESP design was that of Selle, et al (1) in the early 1960's. This work showed the critical effect of Na_2O ash content, per se, and some correlations of resistivity with other ash chemistry indices. Success with the hot precipitator at ≃700F (370C) for coping with resistivity problems in low S eastern coals, beginning circa 1968, was transferred as an expected solution to western coal problems by a number of vendors. Although some installations have worked well, many did not. The fine work of Bickelhaupt (2,3) beginning 1973-74, has indeed clarified the critical role of alkali metal ions, principally sodium, in determining low S coal, fly ash resistivity and in the phenomena of sodium depletion and deteriorating ESP performance over time. Some of the most difficult ashes for electrostatic precipitation include the highly lignitic types with low S, low Na, low Fe and very high CaO+MgO contents, as well as the high silica+high alumina content (80-90+%) bituminous types.

In addition to conditioning with various chemical additives, other approaches to high resistivity ash problems have surfaced recently - e.g., massive SCA, new pulse energization systems, hybrid two-stage ESP's, relooks at wet wall and cooled charger electrodes, wide duct technology; rigid frame type, high intensity rapping designs, and others. A recent paper (4) gives several references to results in progress on these techniques.

Regardless of precipitator design approach, it is first essential to assess ash resistivity conditions to ensure ultimate long-term, reliable, high performance at minimum size and cost. Recent advances in sampling techniques, particle size determinations, and specific chemical constituent analyses of industrial dusts (5), as well as new resistivity measurement standards (6), should be helpful. Coal and ash chemistry indices to assist in boiler-ESP operations analyses, in resistivity prediction, and in coal selections can be useful. Although over the years many investigators have developed such indices and techniques, no coordinated summary of these indices and their application exists. Many have not previously been published. Bickelhaupt's technique (2), now being widely used, has had only limited correlation with field data. It is our purpose here to try and shed some more light in these areas.

SUMMARY AND DEFINITIONS OF COAL-ASH INDICES

Various coal and ash chemistry indices for predicting fly ash resistivity and electrostatic precipitator operations may be summarized as follows:

1. COAL SULFUR CONTENT $< 1\%$ wgt = low S coal; $> 2.5\%$ wgt = high S coal. Coal sulfur content alone is not generally useful for predicting resistivity or ESP performance.

2. COAL S-ASH INDEX, α $\alpha = \frac{\#S/10^6 BTU}{\% \text{ ash}}$ - long used by the author for eastern bituminous type coals. For $\alpha < 0.1$, generally high resistivity ash at 300+F; $\alpha > 0.15$, generally good precipitation capability. Gas temperature, ash specific surface, and relative conversion of $SO_2 \rightarrow SO_3$ in the boiler are important concomitant influences.

3. COAL SODIUM-ASH YIELD RATIO (7) $\frac{\% \text{ Na}}{\% \text{ ash}} > 0.035$, (atomic sodium and ash contents by weight in coal), found boiler fouling problems in certain small Australian boilers. Loss of any available sodium in the coal due to fouling in boiler back passes can strongly influence ultimate sodium content of ash actually reaching the precipitator - hence bulk resistivity and ESP performance.

4. ASH TYPES Lignitic, where $CaO+MgO > Fe_2O_3$ (% wgt ash contents), is typical of many western U.S.A., western Canada, and some other country coals. Bituminous, where $Fe_2O_3 > CaO+MgO$, is typical of eastern and midwest U.S.A. coals - also some western coals. Bickelhaupt (2) defines these types on atomic number basis as $Ca+Mg > 3.5\%$ and $K < 1\%$ for western ash; $Ca+Mg < 3.5\%$ or $K \geq 1\%$ for eastern ash, respectively.

5. SLAGGING AND FOULING FACTORS

It is desirable to have a handle on slagging and fouling properties of ash related to specific coal sources and boiler conditions. These are complex subjects now receiving much attention. Of interest are such questions as the use of high excess air to help control slagging conditions and effects on gas temperature, gas flow rate, $SO_2 \rightarrow SO_3$ conversion; possible loss of alkali metals due to fouling; and overall effects on particle sizing, ash resistivity at the ESP, and performance vs boiler load. For eastern bituminous coals, ash base/acid ratios have long been used with coal sulfur and Na_2O ash contents for evaluation indices. Ash viscosity temperatures and alkali metal indices are now being more widely used for lignitic type coal ash. In assessing suitable coals by source and local areas of mines for good boiler and ESP performance, we recommend evaluation not only of probable ash resistivity properties, but also of potential slagging and fouling aspects. These latter interesting subjects are beyond the scope of this paper; hence, we fold their tents with brief words and steal away to more ash chemistry indices and resistivity matters.

6. ATOMIC PER CENT LITHIUM + SODIUM

Basis for Bickelhaupt (2,3) computer model for predicting resistivity from coal bore samples. It is applied to both western and eastern U.S.A. coals in combination with other ash components - Ca+Mg, K and Fe. Note that this refers to atomic per cent by number for the various chemical species present in the ash from coal fired in the laboratory at 1050C. Computer programs produce ρ as a function of temperature (with and without SO_3 effects), and include corrections for selected moisture content of gas, electric field (usually 10KV/cm), and surface conductivity based upon a known SO_3 content or on SO_3 calculated as 0.4% of SO_2 as determined from stoichiometric coal data with 30% excess air. Final resistivity prediction is the net result of chemical, moisture, and SO_3 surface resistivity operating in parallel with volume resistivity for gas temperatures $< \approx$350-400F (177-204C). The computer programs were derived from careful laboratory resistivity measurements in simulated flue gas environment. Some further correlation of this method with in situ resistivity field data are presented later.

7. SILICA + ALUMINA CONTENT, y $y = SiO_2 + Al_2O_3$ wgt % in ash. For y typically $\geq \approx 80\%$ of ash, high resistivity problems can be expected at 300F+ gas temperature.

8. x/y INDEX = $\frac{Fe+Na+K}{SiO_2+Al_2O_3}$ expressed as per cent, where Fe, Na, K are monoatomic wgt % of iron, sodium and potassium in the ash. This is a type of silicate index long used by the author, particularly for eastern bituminous coals. Useful correlations with resistivity and precipitator performance have been found.

9. SILICATE INDEX HSiO = $\frac{Na_2O}{y+CaO+MgO}$ expressed as per cent, where ash constituents are % wgts. We have used this index with low S, lignitic and bituminous ashes with fairly good results on resistivity prediction and precipitator operations - general applicability.

10. ALKALI-SILICATE INDEX ASi = $\frac{K+Na}{SiO_2+Al_2O_3}$, %, where K and Na are monoatomic wgt % in ash, gives fairly good general correlation within limits. Some anomolies have been found with certain bituminous type ashes.

11. Na_2O ASH CONTENT Shown as a primary index for ion conduction mechanism developed by Bickelhaupt. White (8) illustrates good in situ resistivity correlation for a group of western coal ashes.

12. SILICA-SODIUM INDEX We have found that cold side precipitators generally have good performance capability on low S, subbituminous, western type coals at ≈300F when the ratio Na_2O/SiO_2, as per cent wgts in ash, is equal to or greater than 0.05-0.07. Frisch (9) has indicated similar results in a plot of ρ vs SiO_2/Na_2O for western ashes from seven states.

13. ALKALI SULFATE INDEX (ASI) Matts (10) has described this index long

used by Flakt, Inc. The ASI is the sum of ash components, % wgt, of K_2O, Na_2O and P_2O_5 plus portions of the SO_3 content used in sulfating the potassium and sodium oxides. Any free SO_3 left after remaining chemical conversion of CaO to $CaSO_4$ is also added. The ASI was developed for assessing resistivity and ash precipitability from coal samples.

14. SOVIET INDEX (11) $K_s = \frac{(SiO_2+Al_2O_3)A}{(M+9H_2)S}$, where SiO_2 and Al_2O_3 are weight % in coal ash, and A, M, H_2, S are ash, moisture, hydrogen and sulfur contents % wgt in the coal as received. Some low moisture, low S, very high ash content coals are used in the U.S.S.R.

15. MODIFIED SOVIET INDEX $K_H = K_S/Na_2O$. We have sometimes used this variation to give weight to the sodium content of ESP ash expressed as Na_2O, % weight.

16. BUREAU OF MINES OXIDE INDEX (1) $BMO = \frac{CaO+MgO}{Na_2O+SO_3}$, where items are % wgt in ash. Used for western low S coals by Selle, et al.

17. DUNSTON OXIDE FACTOR (12) $DOF = \frac{Na_2O+Fe_2O_3+CaO}{Al_2O_3}$ wgt % ratio is correlated with ash softening temperatures. For DOF > 0.4, improved performance of small size precipitators is reported on industrial boilers burning low S eastern coals. Dunston gives an interesting discussion of mineral components of fly ash related to conditions under which various coals were formed.

18. SO_4 CONTENT OF WATER SOLUBLE ASH

For eastern U.S.A. coal precipitators, good performance at ≃300F+ with modest SCA typically requires a minimum of ≃0.6% SO_4 by weight of total ash. This reflects the amount of H_2SO_4 adsorbed on fly ash particle surfaces. It can be achieved either by combinations of adequate coal S-ash factors with suitable gas temperatures and normal SO_3 production in the boiler system, or by injecting SO_3/H_2SO_4 conditioning agent. Let us reiterate that sulfur content of coal, per se, is not very useful in assessing reliable resistivity and precipitator performance conditions. SO_3/H_2SO_4 adsorption processes are enhanced as temperature is reduced.

DATA SUMMARY

Table 1 summarizes basic coal and ash chemistry data together with in situ precipitator ash resistivity measurements for 24 cases among various coals and conditions. Ash chemistry is based upon samples of ESP inlet ash. The in situ data were carefully measured at ESP inlet with well-known point-plane apparatus. Most of the base data are from our files and private communications. Items 6-9, 16, 16a are from Gooch (13) and Bickelhaupt (2,14); item 15 is from Carr and Ensor (15); and lignite data are from Gronhovd, et al (16).

Table 2 summarizes coal-ash data for another 16 cases for which indices were calculated and compared with resistivities calculated as shown on the

TABLE 1. SUMMARY COAL-ASH PROPERTIES AND IN SITU RESISTIVITY DATA

		% by wgt. coal					% wgt. in ash										
Plant	Coal	M	Ash	S	H_2	K BTU lb	SiO_2 + Al_2O_3	Al_2O_3	Fe_2O_3	CaO	CaO + MgO	Na_2O	K_2O	SO_3	°F	H_2O Vol.	Resistivity ohm-cm	Size MW
1.	E. Bit.	6.4	13	0.9	4.6	12.3	84.6	29.1	7.2	2.3	3.3	0.3	1.1	0.5	300	≈7.0	10^{12}	375
2.	E. Bit.	6.0	17	0.99	4.4	10.6	81.0	31.0	6.7	1.5	2.2	0.61	2.7	0.31	257	≈7.0	$5x10^{11}$	200
2a.	E. Bit.	6.0	11	1.8	5.0	12.5	67.0	22.0	14.5	2.0	3.0	2.6	4.3	0.42	262	≈7.0	$3-5x10^{9}$	200
3.	E. Ky.	4.0	11.7	0.7	5.1	12.6	85.5	30.2	7.0	1.5	2.2	1.0	2.5	0.30	330	≈7.0	$3x10^{11}$	80
4.	E. Ky.	4.0	7.4	0.76	5.0	13.1	84.0	27.5	6.3	1.4	2.9	1.5	2.8		275	≈7.0	$≈3.5x10^{10}$	Small
5.	E. Bit.	7.5	18	0.5	≈5.0	11.2	80.5	27	6.5	7.7	9.1	0.45	1.5	0.3	300	7.0	10^{12}	250
6.	E. HiS	2.1	11	3.28	5.0	≈12.5	64	18.5	22.7	4.73	5.7	0.54	2.5	2.77	311	7.2	$1.7x10^{10}$	160
7.	E. HiS	10.84	11.2	2.05	3.95	11.05	72	21.7	13.1	4.95	6.0	0.67	2.1	2.29	315	8.2	$2x10^{10}$	122
8.	E. Bit.	11.7	10.9	0.81	3.87	12.01	82.8	29.3	7.1	3.7	4.6	0.27	2.1	0.70	325	9.0	$2.7x10^{11}$	350
9.	E. Bit.	8.4	25.8	0.79	3.74	≈10.6	84.6	27.2	7.0	0.8	2.1	0.45	3.4	0.10	290	8.1	$3x10^{11}$	250
10.	70% S.Afr. 30% WC	10.3	15.7	0.56	4.92	10	78	30	4.74	7.9	9.9	0.38	0.85	3.3	266	10.0	$2.4x10^{12}$	285
11.	W-SB	27.6	5.4	0.45	3.45	8.83	57	16	7.5	30	35.5	1.15	0.4	2.8	320	8-9	$1.1x10^{11}$	350
12.	W-SB	25.3	7.8	0.40	3.6	8.5	66.6	23.1	6.4	17.4	22.2	0.91	0.86	1.3	300	11	$1.5x10^{11}$	800
12a.	W-SB	25.3	7.8	0.40	3.6	8.5	64.3	22.3	7.3	18.8	22.6	1.4	0.80	1.5	300	11	$7x10^{10}$	800
13.	W-SB	23.4	6.0	0.48	2.86	8.77	68.5	21.3	4.0	16.2	19.7	0.75	0.53	4.5	300	10-11	$5x10^{11}$	480
14.	W-SB	28	5.6	0.40	3.5	8.25	48.2	15.4	5.8	26.1	30.8	2.10	0.30	11.6	300	11-12	$4x10^{10}$	650
15.	W-SB	12.7	10.6	0.61	4.93	10	62	17.4	5.72	16.1	18.9	0.33	1.13	8.7	300	10	$4x10^{12}$	525
16.	West						75.2	24.6	5.5	8.7	12.3	0.50	1.72	0.55	306	8.2	$1.4x10^{11}$	128
16a.	West	13.94	5.21	0.41	4.24	10.56	75.6	23.7	5.9	8.6	12.2	0.29	1.8	1.2	293	8.3	$3x10^{11}$	204
17.	Austr.	≈3	32.8	0.42	4.8	9.72	90	25	7.24	0.33	0.81	0.07	1.01	0.20	300	6.5	$3-5x10^{13}+$	
18.	W. Can.	20	14	0.20	4.8		77.4	22.6	4.5	11.7	13.5	0.36	1.3	1.1	350	≈10	$2x10^{12}$	150
19.	W. Can.	20	15.8	0.19	4.8		77.3	26.4	4.8	13.2	14.2	2.26	1.0	0.42	350	≈10	$4x10^{10}$	150
20.	Lignite ND						36.2	14.5	11.8	29.3	43.1	1.40		5.1	310		$2.3x10^{10}$	
21.	Lignite ND						34.1	13.0	9.5	25.4	34.3	6.9		9.9	335		$5x10^{9}$	

TABLE 2. SUMMARY COAL-ASH PROPERTIES AND RESISTIVITY DATA
CALCULATED ON BICKELHAUPT MODEL COMPUTER PROGRAM

Coal	M	Ash	S	H_2	BTU/lb	SiO_2 + Al_2O_3	Al_2O_3	Fe_2O_3	CaO	CaO + MgO	Na_2O	K_2O	SO_3	Resistivity, No SO_3				ρ with SO_3		
														300F	Max @	F	%H_2O Vol.	300F	Max	F
1. a. W. Can.	27.5	18.6	0.49	2.93	6800	78.6	22.71	3.86	7.57	8.5	0.47	1.28	6.06	5.4×10^{11}	9.3×10^{11}	360	12.7	9×10^{10}	6×10^{11}	400
b. W. Can.	27.5	23.4	0.45	2.67	6192	84.0	22.53	3.46	5.93	7.14	0.86	1.49	2.19	1.3×10^{11}	3×10^{11}	370	13.1			
c. W. Can.	27.5	23.4	0.45	2.67	6192	64.3	21.12	9.04	11.80	13.64	1.34	0.81	9.88	4.6×10^{10}	9×10^{10}	383	13.1			
d. W. Can.	27.5	23.4	0.45	2.67	6192	74.2	22.26	5.06	9.38	10.5	1.82	1.20	6.37	2.5×10^{10}	5×10^{10}	392	13.1			
e. W. Can.	27.5	23.4	0.45	2.67	6192	56.5	20.33	14.43	14.03	15.3	2.49	0.74	9.65	1.08×10^{10}	2.1×10^{10}	374	13.1			
2. a. S. Am.	6.93	6.54	1.0	4.85	13000	74.1	15	10.51	3.88	7.2	0.84	1.10	4.29	2×10^{11}	2.5×10^{11}	340	10.8	4.5×10^{10}	1.7×10^{11}	360
b. S. Am.	6.93	11.0	0.6	4.85	11700	81	20	7.0	3.80	7.1	0.40	0.80	2.60	1.1×10^{12}	1.4×10^{12}	340	10.8	1.2×10^{11}	7.4×10^{11}	380
3. Spain	10.0	13.0	0.6	4.50	11160	76.0	30.4	6.28	8.61	12.0	0.41	0.71	3.65	1.5×10^{12}	2×10^{12}	340	8.1	1.5×10^{11}	10^{12}	400
4.* E.Bit.	≈4	≈10	≈0.8	≈5.0	≈12.5	83	28	5	0.7	1.4	0.30	1.60	0.6	2×10^{12}	2×10^{12}	300+	≈7.0			
5.** E.Bit.	4.3	5.64	1.1	5.0	12600	80.4	28.76	8.85	2.32	3.84	0.35	2.47	2.59	1.7×10^{12}	1.7×10^{12}	300	7.8	4×10^{11}	1.3×10^{12}	350
																			Hot Case	
6. a. E.Bit.	5.0	12.5	0.6	4.5	12500	88.2	35.2	4.66	1.02	1.37	0.69	0.77	1.57	3.9×10^{11}			7.8	3.2×10^{11}	1.5×10^{9} @	600
b. E.Bit.	5.0	12.5	0.6	4.5	12500	88.47	35.34	4.66	1.02	1.37	0.40	0.77	1.57	1.1×10^{12}			7.8	6.5×10^{11}	4.2×10^{9}	600
c. E.Bit.	5.0	12.5	0.6	4.5	12500	88.67	35.42	4.66	1.02	1.37	0.20	0.77	1.57	4.9×10^{12}			7.8	1.1×10^{12}	1.5×10^{10}	600
7. a. S. Afr.	8	16	0.5	3.5	≈10000	75.9	34.5	6.0	9.0	11.0	0.15	0.3	4.0	1.5×10^{13}			≈7.0			
b. S. Afr.	8	11	0.4	4.2	≈10000	93.4	24	2.7	1.0	1.6	0.5	1.1	0.3	9×10^{11}			≈7.5			
c. S. Afr.	8	14	0.3	4.0	≈10000	96.7	34.7	1.1	0.1	0.2	0.04	0.2	0.2	1.0×10^{14}			≈7.5			

*ESP after mechanical collector.

**Washed coal.

Note: Ash chemistry analyses based upon laboratory coal samples.

Bickelhaupt (2) model. In this group, we gratefully acknowledge permission by F. L. Smidth and Co., Inc., to use data for items 1-3, 5.

For Table 1 an attempt was made to select cases as close as possible to ≈300F gas temperature, not only for practical ESP operations, but also for reasonable comparisons with the calculated resistivity data on Table 2. For the in situ data, we have a range of 260-350F, overall average 304F, and standard deviation ≈8%. For the 18 closest cases, the average is 304F and the standard deviation is 4.3%. The range of data in Tables 1 and 2 traverse important practical applications for modern fly ash precipitators with reasonably good diversity of coal sources and ash properties.

RESULTS AND DISCUSSION

For low S coals, our silicate index HSiO is fairly generally applicable. Figure 1 shows the in situ fly ash resistivity data (Table 1) and the resistivities calculated on Bickelhaupt's model (300F, no SO_3) as a function of this index. Curve A can be represented by the equation, $\ln \rho = 25.85-2.9 \ln (HSiO)$. The bulk of the standard computer calculated data from Table 2 agrees quite well with the in situ data, most of which are for low sulfur coals. Curve B, having essentially the same slope, might indicate nominal minimum expected resistivity for medium to high S eastern type coals. It would appear from our results, however, that some caution should be exercised in using the Bickelhaupt method with SO_3 correction for low S coals, particularly those having lignitic type ash. Note that using the standard SO_3 correction in Table 2 would drop indicated Bickelhaupt resistivities by about one-half to one order of magnitude below the in situ data curve. With the high CaO ashes the beneficial effects of SO_3 may indeed be largely lost in affecting the resistivity of the bulk ash.

The importance of alkali content in controlling the bulk resistivity of low S coal ashes seems to be well established. Figure 2 illustrates the strong effect of sodium from our data. Another variation of such effects resides in the alkali silicate index, ASi, which is plotted against resistivity in Figure 3. This shows generally pretty good correlation for both bituminous and lignitic ashes, in situ and Bickelhaupt derived resistivities. The alkali-silicate index was derived from long experience with our other silicate type index x/y, where it was noted that some spread among points occurred between eastern and western in situ data. Deviations also tended to occur in bituminous ashes for very low and very high iron content. The x/y index is overly sensitive to wide variations in Fe content, most consistent results being obtained for typically ≈4-10% as Fe_2O_3. Fe content apparently has some effect on resistivity, but to a much lesser extent than sodium. According to Bickelhaupt, the iron may in some way have a catalytic effect on the usefulness of the potassium ion. Eliminating the Fe from the x/y index pulls the diverse data much closer together as represented in Figure 3. There are, however, a few points still to the right of the average curve in the region $3x10^{11}$-$4x10^{12}$ohm-cm. The reasons at this time are obscure.

Long standing in resistivity prediction is the Alkali Sulfate Index (ASI) used by Flakt (10). Considering the temperature variations and diversity of

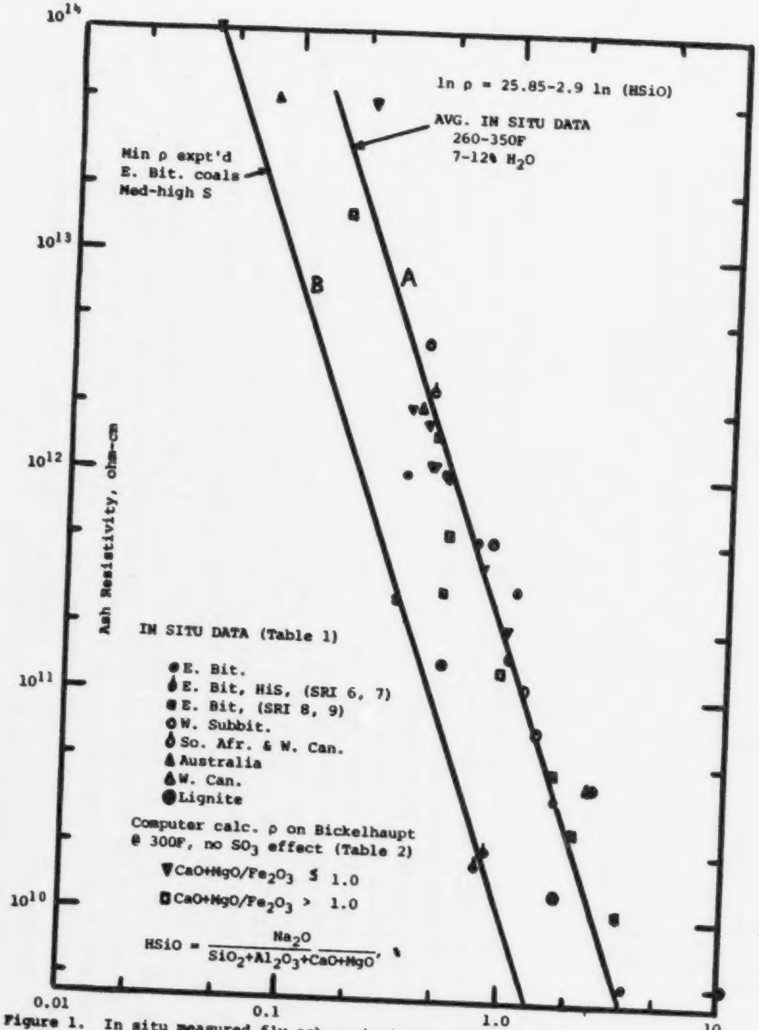

Figure 1. In situ measured fly ash resistivity and resistivity calculated by computer on Bickelhaupt model (300F, no SO_3 effect) as a function of ash silicate index. Chemical constituents % wgt. in ash and HSiO expressed as per cent.

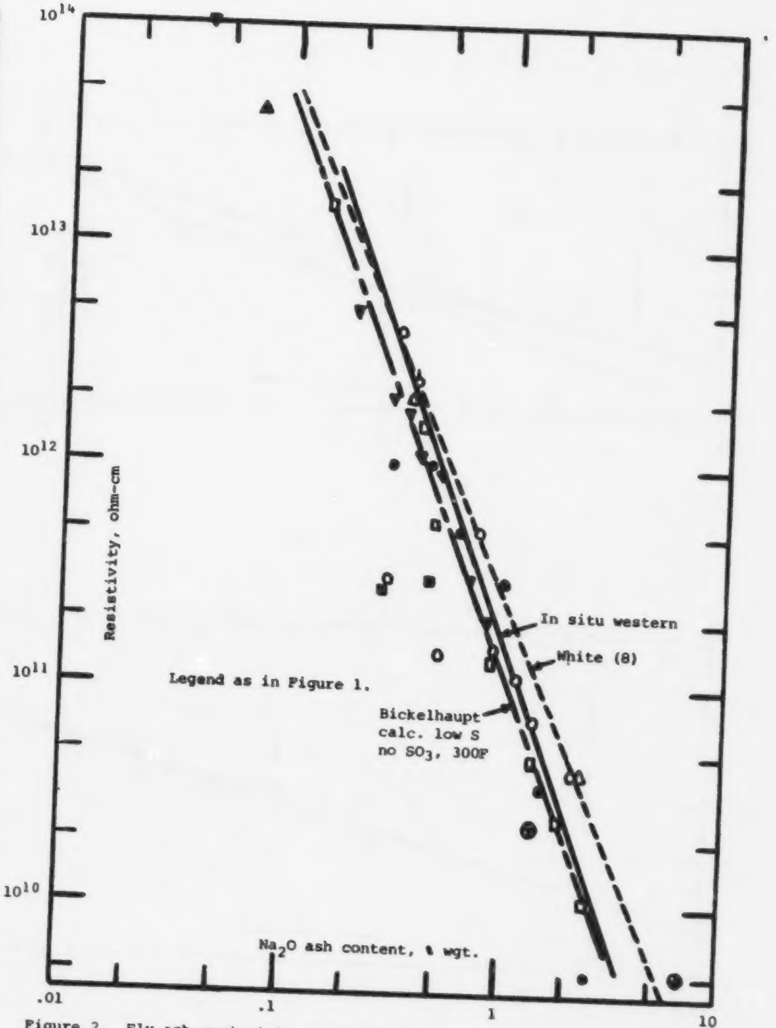

Figure 2. Fly ash resistivity vs Na_2O ash content for low S coals, ≈300F.

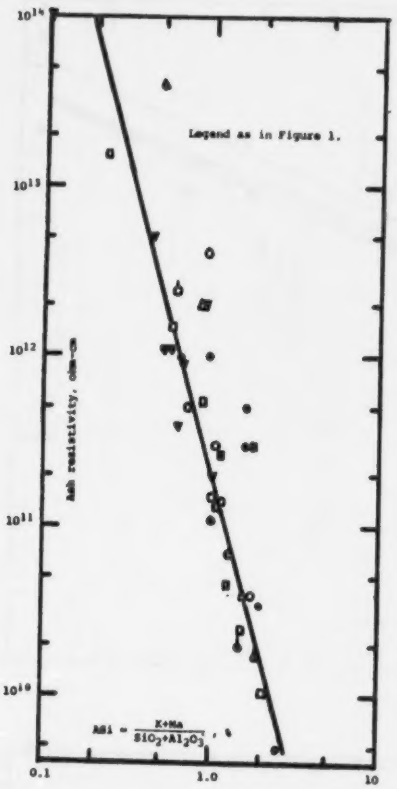

Figure 3. Fly ash resistivity vs alkali silicate index. K, Na are monoatomic wgt. % in ash.

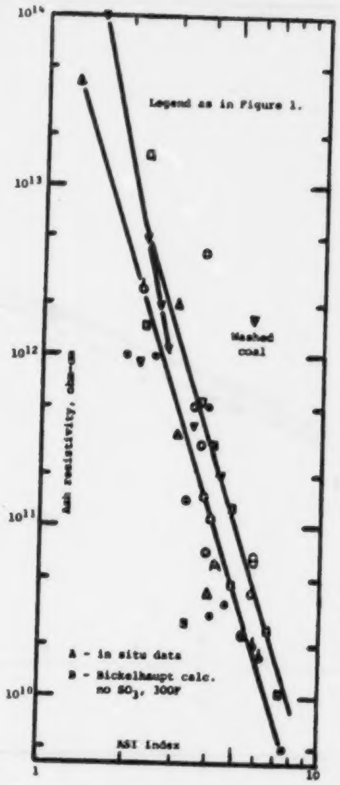

Figure 4. Fly ash resistivity vs alkali sulfate index.

our data, it can be considered a useful index as shown in Figure 4. In this case, the in situ data show up more or less about 0.2-0.5 order of magnitude below the Bickelhaupt model calculated data at 300F, no SO_3. Examination of alkali index alone (K_2O+Na_2O+P_2O_5), without any SO_3 effect as in the ASI, correlates quite well with in situ resistivity data on low S western coals, albeit the negative slope of the curve is quite high (≈10.4) in a log-log plot. This again points up our conclusion that the SO_3 effect in low S, lignitic ash appears not very significant in controlling effective ash resistivity in precipitators. This is not to say that some SO_3 does not sulfate the sodium and potassium oxides, but rather it is the alkali metal ions, per se, that seem to have the greatest influence on ultimate ash resistivity.

A plot of ρ vs silica-sodium index SiO_2/Na_2O shows the same general results indicated by Frisch (9) for low S western coals (250-300F gas). Our data extend his curve to about 10^{14}ohm-cm including low S bituminous type ashes, both in situ and Bickelhaupt calculated resistivities (300F, no SO_3). Maximum spread of a few points above and below the average curve is typically about 0.5 order magnitude on resistivity.

Data plotted for indices K_s, K_H, BMO and DOF show less effective general correlations with resistivity under the diverse conditions in our data bank. However, within limits and possibly for certain specialized applications as previously indicated, they can be useful. High values of K_s, for example, definitely would be associated with low moisture, low S, high ash coals having bituminous type ash exhibiting high resistivity properties. Our plot of in situ eastern bituminous data shows a reasonable correlation with ρ - e.g., $K_s \approx 10$ at 10^{10}, 18-20 at 10^{11}, 35-45 at 10^{12}, and 150 at $4\text{-}5\times10^{13}$ ohm-cm, respectively. With few exceptions our in situ data for DOF < 0.4 shows high resistivity expectations for low S eastern bituminous coals as suggested by Dunston. Our data for the BMO index fall into widely separated groups with different slopes.

SUMMARY OF USEFUL INDICES

Table 3 summarizes useful indices with equations for typical average resistivity predictions.

TABLE 3. SUMMARY MOST USEFUL ASH CHEMISTRY INDICES FOR RESISTIVITY

Index	Average Resistivity Formula (≈300F)	Application
1. $HSiO = \frac{Na_2O}{y+CaO+MgO}$, %	$\ln \rho = 25.85 - 2.9 \ln (HSiO)$	Low S general
2. Na_2O	$\ln \rho = 25.777 - 2.67 \ln (Na_2O)$	In situ western
	$\ln \rho = 26.487 - 2.572 \ln (Na_2O)$	In situ western White (8)
	$\ln \rho = 25.45 - 2.53 \ln (Na_2O)$	Low S coals Bickelhaupt model calc., no SO_3
3. $ASi = \frac{K+Na}{SiO_2+Al_2O_3}$, %	$\ln \rho = 26.00 - 3.56 \ln (ASi)$	General, some anomolies in bituminous ash
4. ASI = alkali sulfate	$\ln \rho = 32.49 - 5.06 \ln (ASI)$	In situ data
	$\ln \rho = 33.50 - 5.16 \ln (ASI)$	Bickelhaupt model calc., no SO_3
5. $AI = K_2O+Na_2O+P_2O_5$	$\ln \rho = 33.71 - 10.4 \ln (AI)$	In situ western
6. SiO_2/Na_2O	$\ln \rho = 18.22 + 1.652 \ln \frac{(SiO_2)}{(Na_2O)}$	Low S western and eastern
7. $x/y = \frac{Na+K+Fe}{SiO_2+Al_2O_3}$, %	$\ln \rho = 34.64 - 5.19 \ln x/y$	In situ E. bit.
	$\ln \rho = 34.55 - 5.89 \ln x/y$	In situ western

COMPARISONS AMONG RESISTIVITY INDICES AND OTHER FACTORS

An example illustrated for the Bickelhaupt method (3) has the following properties used for comparative analyses: coal as received % wgts, C = 57.2, $H_2 = 3.74$, $O_2 = 3.03$, $N_2 = 1.02$, S = 0.79, M = 8.41, ash = 25.8, ≈10,300 BTU/lb; ash analyses % wgts, $Li_2O = 0.04$, $Na_2O = 0.45$, $K_2O = 3.7$, MgO = 1.4,

$CaO = 0.7$, $Fe_2O_3 = 6.7$, $Al_2O_3 = 27.6$, $SiO = 58.2$, $TiO_2 = 1.7$, $P_2O_5 = 0.1$, $SO_3 = 0.2$; gas analyses, $SO_2 = 680$ ppm vol, $H_2O = 8.228\%$ vol, $SO_3 = 2.72$ ppm vol.

The ash is bituminous with very low slagging, fouling potential and high silica + alumina = 85.8%. Most of the chemical indices predict resistivity $\approx 10^{12}$ohm-cm in situ at ≈300F, which corresponds with the base Bickelhaupt model with no SO_3 effect - the net ρ with all corrections, including SO_3, being $4.4\text{-}7.7\times10^{11}$ohm-cm. This figure compares best with predictions using the x/y, ASi and ASI indices. Conservative estimates would place nominal expected ash resistivity in the range 7×10^{11} to 10^{12}ohm-cm.

SOME PRECIPITATOR DESIGN AND PERFORMANCE EFFECTS

Important factors affecting bulk ash resistivity and precipitator performance capability include ash chemistry, gas temperature, pressure and moisture content, ash specific surface, and degree of H_2SO_4 adsorption. In addition, other major factors include SCA, electric field strength as limited by sparking or other effects, allowable average current density and quality of its distribution, duct width, degree of TR match to load, and effectiveness of automatic voltage controls and rapping systems. One must also be concerned with boiler operations, excess air slagging and fouling conditions - particularly loss of valuable sodium in critical cases hydrophobic ash properties, and the amount and particle size distribution of any carbon present in the ash. Further, it is important to remember that the dynamic ash resistivity as seen by the operating precipitator may vary significantly due to temperature variations, or due to changes in ash composition, field to field, as well as between coal samples and ash actually reaching the ESP. Subtle matters of experience and judgment are often necessary in assessing overall effects of any predicted resistivity condition from coal samples, per se. We have often investigated correlations of dynamic ash resistivity as calculated from ESP electrical data with various ash chemistry indices.

Precipitator performance factors, e.g., power density, current density, effective migration velocities, etc., can be correlated with coal-ash chemistry indices and resistivity (4) under various operating conditions. Figure 5 illustrates some typical effects in three small boilers for average ESP current density as a function of the coal S-ash index α, on eastern and midwest bituminous coals. Figure 6 shows ESP collection effeciency as a function of ash chemistry index x/y for three different plants firing various eastern bituminous coals. Ash chemistry index correlations at any given plant are expected to

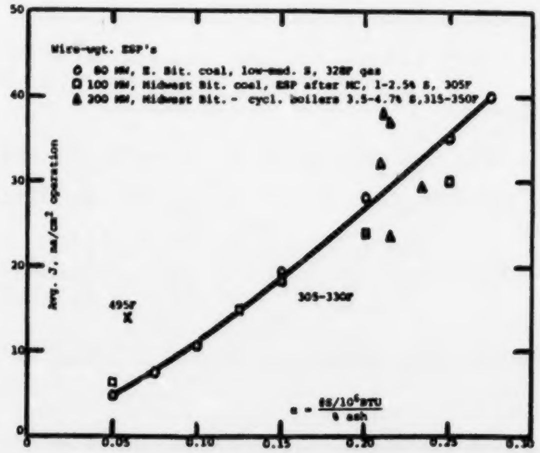

Figure 5. Average precipitator current density vs coal S-ash index, α.

produce reasonably consistent results for known conditions. Experience shows that well designed ESP's with good, uniform, current density distribution can deal with ash resistivities as much as an order of magnitude higher than that possible in poorer designs.

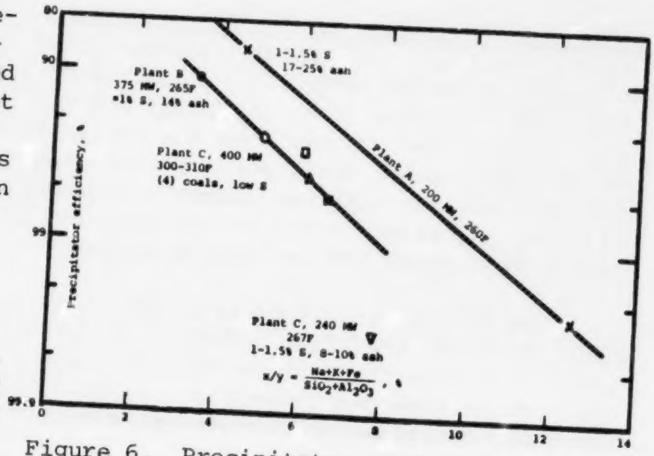

Figure 6. Precipitator performance as a function of x/y ash chemistry index for three plants, eastern bit. coals. Na, K, Fe are monoatomic % wgts. in ash.

Our experience with high silica + alumina ashes $\gtrsim$ ≈80% of total ash content shows that hydrophobic properties may be present to inhibit full usefulness of moisture and often SO_3 conditioning. These fly ashes are generally susceptible to effective NH_3 conditioning, including high temperature (700-750F) cases. We have also used NH_3 conditioning successfully on cat cracker, aluminum silicate dust at similar high gas temperatures; optimum mixtures of NH_3 and water vapor content exist. Many western coal ashes can be treated with SO_3 conditioning, albeit at levels often requiring two or three times that required for typical high resistivity bituminous ashes. In troublesome hot precipitators at relatively low gas densities, we have found the critical bulk ash resistivity to be as much as an order of magnitude lower (≈10^9ohm-cm) than the customary figure experienced with low temperature ESP's. Precipitators with difficult ashes have also been treated successfully with sodium additives to achieve ≈1.5 to 2.5% Na_2O in the ESP ash.

CONCLUSIONS

Several coal-ash factors and/or ash chemistry indices related to assessing resistivity conditions and operations in cold side fly ash precipitators (≈300F) have been investigated for a wide variety of coal-ash properties using in situ resistivity measurements in comparison with resistivities calculated from Bickelhaupt's computer model (2). Ash chemistry indices can be useful not only for precipitator design and performance analyses, but also for selecting preferred coal sources to achieve optimum results.

The strong influence of alkali content, principally sodium, in controlling the bulk resistivity of low sulfur coal ashes from diverse sources is confirmed and well established. For both low S lignitic and bituminous type ashes, the most generally applicable indices seem to be those based upon sodium, per se, and on a silicate type index HSiO = $Na_2O/SiO_2+Al_2O_3+CaO+MgO$, where items are % wgt in ash and HSiO expressed as per cent. Fairly good correlation between these indices and resistivities, both measured in situ and calculated on the Bickelhaupt model (300F, no SO_3) has been found. For high CaO lignitic ashes, and indeed for many bituminous low S coal ashes at gas temperatures 300+F, the potential benefits of SO_3 may be largely lost or greatly reduced. Our results suggest that caution be exercised in using the Bickelhaupt method with SO_3 correction in such cases. Our investigations on the Alkali Sulfate Index (ASI) and its variations for lignitic western ash also suggest that, while some SO_3 may sulfate the potassium and sodium oxides, it is alkali metal ions, per se, that seem to have the greatest influence on ultimate ash resistivity. Other indices can also be useful under special conditions. Equations based on our data for average resistivity predictions at ≈300+F from seven indices are presented.

Low sulfur bituminous type ashes having very high silica + alumina content (80-90+%) are often deficient in alkali and exhibit very high resistivities. Our experience shows that such ashes are susceptible to NH_3 conditioning even at high gas temperature (≈700-750F). These are also good candidates for pulse energization, as are the difficult lignitic ashes too.

Many factors are involved in the net dynamic ash resistivity conditions as seen by a precipitator and some discussion is included. Subtle applications of experience and judgment are often necessary in assessing overall effects of any predicted resistivity condition from coal samples, per se. Uniform corona current density distribution delivers a premium in precipitator performance; such well designed systems can handle ash resistivities up to an order of magnitude above those possible in poorly designed equipment.

Accurate and careful chemical analyses of dusts are necessary for reliable resistivity prediction. We look forward to future progress in analyses of actual chemical species present in fly ash, and to developments for coping with persistent ash resistivity problems.

REFERENCES

1. Selle, S. J., Tufte, P. H. & Gronhovd, G. H. A study of the electrical resistivity of fly ashes from low-sulfur western coals using various methods. Paper 72-107, 65th Annual Meeting of the Air Pollution Control Ass'n, Miami Beach, Fla., June 1972.

2. Bickelhaupt, R. E. A technique for predicting fly ash resistivity. EPA-600/7-79-204. Symposium on the Transfer and Utilization of Particulate Control Technology, U.S. EPA, Research Triangle Park, N.C., Aug.1979.

3. A Manual for the Use of Electrostatic Precipitators to Collect Fly Ash Particles. EPA 600/8-80-025. U.S. EPA IERL, Research Triangle Park, N.C., May 1980. pp. 340-361.

4. Hall, H. J. High voltage power supplies and microprocessor controls for electrostatic precipitators. Paper presented at the International Conference on Electrostatic Precipitation, Monterey, Calif., 14-16 Oct. 1981. Proceedings published by Air Pollution Control Ass'n, 1982.

5. Farthing, W.E. Particle sampling and measurement. Envir. Sci. & Technology, Vol. 16, No. 4, 1982. Review of Third Symposium on Advances in Particle Sampling and Measurement, Datona Beach, Fla., Oct. 1981.

6. IEEE Standard criteria and guidelines for the laboratory measurement and reporting of fly ash resistivity. #548-1981. Institute of Electrical Engineers, Inc. New York, N. Y., 24 April 1981.

7. Bosio, M. and Durie, R. A. The control of boiler fouling during the combustion of Leigh Creek coal (Elect. Trust of S. Australia). Paper 8, Austr. Inst. of Fuel Conference on the Changing Technology of Fuel, Adelaide, 5-7 Nov. 1974.

8. White, H. J. Resistivity problems in electrostatic precipitation. JAPCA, vol. 24, No. 4, April 1974. p. 334.

9. Frisch, N. W. and Dorchak, T. P. Impact of fuel on precipitator performance. Pollution Engineering, May 1978.

10. Matts, Sigvard. Coal-ash compositon and its effects on precipitator performance. Flakt, Inc. Technical Bulletin, Vol. No. 1, No. 3, Oct. 1977.

11. Kropp, L. I., Shmigol, I. N., Chekanov, G. S., et al. Joint US/USSR test program for reducing fly ash resistivity, JAPCA, Vol. 29, No. 6, June 1979.

12. Dunston, James B., Jr. Effects of ash chemistry on precipitator performance. Paper 81-17.3, 74th Annual Meeting of the Air Pollution Control Ass'n, Phila., PA., 21-16 June, 1981.

13. Gooch, John P. Electrostatic precipitator performance. EPA report 600/7-79-044a, Feb. 1979.

14. Bickelhaupt, Roy E. and Sparks, L. E. Predicting fly ash resistivity - an evaluation. EPA report 600/9-80-039a, Sept. 1980.

15. Carr, Robert C. and Ensor, D. S. Evaluation of the George Neal electrostatic precipitator. EPA report 600/9-80-039a, Sept. 1980.

16. Gronhovd, G. H., et al. Some studies on stack emissions from lignite fired power plants. Lignite Symposium, Grand Forks Energy Res. Lab., BuMines. 9-10 May 1973.

The work described in this paper was not funded by the U.S. Environmental Protection Agency and therefore the contents do not necessarily reflect the views of the Agency and no official endorsement should be inferred.

A NEW ENERGIZATION METHOD FOR ELECTROSTATIC PRECIPITATORS

MITSUBISHI INTERMITTENT ENERGIZATION SYSTEM

by: Takashi Ando
Mitsubishi Heavy Industries, Ltd.
Kobe Shipyard & Engine Works
Kobe, Japan

Naoji Tachibana
Mitsubishi Heavy Industries, Ltd.
Kobe Shipyard & Engine Works
Kobe, Japan

Dr. Yōichi Matsumoto
Mitsubishi Heavy Industries, Ltd.
Takasago Technical Institute
Takasago, Hyoogo, Japan

ABSTRACT

Mitsubishi Heavy Industries, Ltd. developed a new energization system for ESPs and has proved its favorable performance on many operating full-scale ESPs with high resistivity ash. This paper is to introduce the new equipment named Mitsubishi Intermittent Energization System (abbreviated to MIE) which supplies high voltage to ESP intermittently with adjustable supplying and suppressing times by means of power control thyristors with electronic circuit. MIE mitigates the degradation of collecting efficiency due to back corona and its effect can be estimated by voltage-current characteristics at gas load operation. The best improvement is expected for the case of low voltage and large current. A long term actual operation on an iron ore sintering machine has shown that the modified migration velocity w_k of 100% at conventional energization is improved to 147% by MIE and at the same time the power consumption of 100% is reduced to 20%.

The advantages of MIE can be summarized as follows:
(1) improvement in collecting efficiency for high resistivity ash
(2) energy saving
(3) small additional cost

This paper includes explanation of equipment, result of laboratory test and measurement of full-scale ESPs.

INTRODUCTION

In Japan, the change in the energy situation which started from the energy crisis in 1973 gave impetus to a review of fuels. As a result, coal has been again highlighted as a fuel for thermal power plants, and the planning and construction of coal-fired thermal power plants are positively progressing. However, coal has many environmental problems in contrast to oil. In particular, amount of dust (fly-ash) in the flue gas produced by pulverized coal combustion is more than 100 times that of oil combustion. Therefore, coal-fired thermal power plants require high performance of ESP.

However, the electric resistivity of fly-ash varies widely according to the kind of coals and has a significant effect on the performance of ESP. The value of resistivity has a peak in the temperature range (130°C to 150°C) of the flue gas at the outlet of the air preheater where a cold-side ESP is installed, and such conditions are unfavorable for stable and efficient dust collection. This trend increases as the sulfur content of coal decreases. Japan with few coal resources is necessarily dependent on overseas imports. However, most of overseas coals are low sulfur content less than 1% and the fly-ash produced from such coal has extremely high resistivity and significantly impairs ESP performance.

Under the circumstances, our current task for ESP was to develope a new technology to meet the following requirements;

(1) to mitigate degradation of ESP performance due to high resistivity dust
(2) energy saving
(3) low initial cost

Our studies have resulted in the development and commercialization of a new technology of an "Intermittent Energization System" (marketed under the trade name of the Mitsubishi Intermittent Energization System: MIE). A new high voltage power supply equipment has been developed for MIE incorporating modern electronic technology.

CONCEPT AND EQUIPMENT

The fundamental concept of MIE was found during a study of the relationship between the voltage-current waveforms and the collecting efficiency . At that time, a momentary high ESP voltage was encountered just after switching on the power supply to an ESP with a heavy back corona.

PRINCIPLE

When high resistivity dust deposits on the collecting electrode, it acts as an insulation layer and, therefore, can be expressed by the equivalent circuit consisting of a resistor R and a capacitor C as shown in Fig. 1a. The transient change of the voltage across the dust layer V_d is expressed by the following Eq. (1) when a constant corona current ($i=I_o$) has been applied to the dust layer from time t=0:

$$V_d=R\cdot I_o\cdot(1-e^{-t/t_o}) \tag{1}$$

where t_o is the time constant ($t_o=C \times R$) and is caluculated (1) by Eq. (2).

$$t_o=8.85\cdot E_r\cdot P_d\cdot 10^{-14} \text{ (sec)} \tag{2}$$

where

E_r : specific dielectric constant of the dust layer
P_d : specific resistivity of the dust layer

For instance, t_o = 0.27sec when $E_r=3$ and $P_d=10^{12}$ohm·cm. Fig. 1b shows a graphical representation of the Eq. (1). The voltage V_d rises gradually and a back corona occurs when the electric field strength $E_d = V_d/d$ (d: thickness of the dust layer) exceeds its break-down electric field strength E_{db}. That is;

$$E_d(=V_d/d)\geqq E_{db} \tag{3}$$

It takes time t_1 from the start of current I_o to the occurrence of a back corona as shown in Fig. 1b . The back corona starting time t_1 is calculated by Eq. (4) which is obtained from Eqs. (1) and (3).

$$t_1=t_o\cdot\ln(1/(1-E_{db}/(P_d\cdot i_o))) \tag{4}$$

where i_o is the current density. For instance, t_o=0.27 sec and t_1= 0.109 sec when E_{db}=10kV/cm, i_o=0.3mA/m^2, E_r=3 and P_d=10^{12} ohm·cm.

Therefore, by deenergizing before the back corona starting time t_1 and re-energizing when the voltage V_d returns to the original low level, ESP can be operated suppressing back corona. The method of repeating energization and deenergization at given intervals is the basis of the MIE.

Theoretically, the dust migration velocity w is expressed by:

$$w=k\cdot E_o\cdot Ep \tag{5}$$

where

k : constant

E_o : charging field strength

Ep : precipitating field strength

As E_o and Ep are roughly proportional to the peak value Vp and the mean value V_m of the ESP voltage respectively, the value of w is expressed by:

$$w\propto Vp\cdot Vm \tag{6}$$

Once a back corona occurs, positive ions are discharged from the dust layer into the gas space to increase the ESP current and reduce Vp. However, Vp does not decrease by use of MIE because it tries to interrupt the ESP current before a back corona starts. Furthermore, even if there are periodical interruptions of the ESP current, Vm does not decrease so much because of the equivalent capacitance across the electrodes. In consequence, w in Eq.(6) will increase by MIE.

The effect of MIE was experimentally demonstrated by a "visual model ESP" which was made with one set of collecting plates and discharge electrodes housed in a transparent plastic case. The photographes in Fig. 2 show the flying trajectories of the dust. In each photo, the collecting electrode is located at the left hand side and the discharge electrode at the right hand side. The collecting electrode was coated by a mica sheet to produce a simulated back corona discharge. Pearlite particles were used as dust and, being fed from the top, were left to drift downward by gravity.

Fig. 2a is for a conventional energization and indicates that the dust particles come near to the collecting plate but are repelled, and, finally, go down through the ESP without capture. Fig. 2b is for MIE and clearly shows that most of the particles migrate toward the collecting plate without repulsion. These two photographs simply illustrate the increased efficiency of MIE over the conventional energization.

POWER SUPPLY EQUIPMENT

As mentioned above, the method of repeating energization and deenergization at given intervals is the basis of the MIE. This is graphically represented regarding the ESP current by Fig. 3. Since the current flow time T_1 ranges from several to tens of milisecond and the current pause time T_2 ranges from several to hundreds of milisecond , a conventional thyristor controlled power supply equipment fortunately can be utilized with modification of the control circuit.

Fig. 4 shows a block diagram of a power supply equipment for the MIE. The main power lines consisting of thyristors, a high voltage transformer and high voltage rectifiers are the same as for conventional energization system. The only difference is the control circuit: it should be modified. A periodical blocking unit is added on the signal line from the conventional control circuit to the thyristors . This unit blocks the signal to the thyristors, periodically, so that the current to ESP may be shaped as shown in Fig. 3. T_1 and T_2 are adjusted by manual operating knobs or automatic control circuit. The current flow level I_1 is automatically adjusted. For example, by using a spark rate control or a current limiting control. This addition, however, necessitates the comlete rearrangement of the printed board.

Typical waveforms of the output voltage and current photographed on an operating MIE power supply equipment are shown in Fig. 5. Fig. 5a is for conventional and Fig. 5b for MIE when the duty ratio Rc is 1/3 . The duty ratio Rc is introduced as ratio of $T_1/(T_1+T_2)$ assuming T_1 and T_2 are expressed by numbers of half-cycle. For instance, the duty ratio Rc is 1/3 when T_1=two half-cycles and T_2= four half-cycles.

TEST PLAN

Laboratory tests and gathering the operating data from full-scale ESPs were made so as to confirm the effectiveness and obtain concrete design guides for MIE with respect to its two primary aims, i.e., performance improvement and energy saving.

The tests were carried out under the following conditions for MIE :-

a) Current-flow time T_1	: one to four half-cycles
b) Duty ratio Rc	: 1 to 1/20
c) Peak current value	: nearly rated current level

TEST RIG WITH PILOT ESP

Since adjustable ranges of test conditions are limited in the actual operating plants, a coal firing test rig with a pilot ESP was used. Fig. 6 shows the schematic diagram of the test rig. Primarily, the rig consists of a pulverizier, a furnace, coolers and an ESP. The test rig is designed to fire pulverized coal, reproducing the equivalent exhaust gas and ash that are generated from commercial boilers. The associated pilot ESP consists of two fields and employs the same discharge and collecting electrodes as those of full-scale ESPs.

Fourteen (14) sets of tests were carried out firing each of seven Australian coals and three Canadian coals.

FULL-SCALE ESPS

Eight (8) ESPs are now in commercial operation with MIE: five coal-fired thermal power plants , two iron ore sintering plants and one oil-fired thermal power plant. 23 sets of the operating data were gathered in total. The kinds of coal fired in the coal-fired thermal power plants were two American coals, two Australian coals, two Japanese coals, one Canadian coal, one Chinese coal, one South African coal.

TEST RESULT AND DISCUSSION

IMPROVEMENT OF COLLECTING EFFICIENCY

The improvement of collecting efficiency was evaluated by the enhancement factor H that was introduced by Feldman (2). The H value is defined as thc ratio of the modified migration velocity w_k for MIE to conventional and the w_k is calculated by the following equation:-

$$\eta = 1 - e^{-(w_k \cdot A/V)^m} \qquad (7)$$

where

η : collecting efficiency
A : collecting area
V : volumetric gas flow rate
m : exponent depending on inlet particle size distribution
m=0.5 in this paper

According to observation of variation of the H values and V/I characteristics, it was found that test results were roughly classified into three types as follows:-

Type I : V/I characteristics show a steep increase; no voltage rising with increasing current due to heavy back corona. The maximum efficiency stands at Rc of nearly 1/3 to 1/5.

Type II : V/I characteristics situate between types I and III. Back corona takes place to some extent. The maximum efficiency stands at Rc of nearly 1/2 to 1/3.

Type III: V/I characteristics look normal ; no back corona is suggested from V/I characteristics. No improvement of efficiency is expected by MIE.

Regarding the pilot ESP, one representative result of each type is listed in Table. 1. Regarding full-scale ESPs, one representative result of each type is listed in Table. 2 for the coal-fired thermal power plants. One test result each of an oil-fired thermal power plant as well as an iron ore sintering machine are listed in Table. 3. Their V/I characteristics are shown in Fig. 7. The enhancement factors are graphically shown in Fig. 10.

The remarkable facts derived from the test results were as follows:-

(1) The largest H value of Type I was 1.47 for case H on a full-scale ESP and the same was 1.72 for case A in laboratory tests. The largest H value of Type II was 1.09 for case F on a full-scale ESP and 1.31 for case C in laboratory tests. The H values of full-scale ESP seem to be nearly 20% less than those of laboratory test.

(2) The Type classification can be made primarily by the dust resistivity, but not always. It rather corresponds to the steepness of V/I characteristics.

(3) The lower the voltage of V/I characteristics is, the larger the enhancement factor is. For instance, referring to Tables 2 and 3 and Fig. 7, case H with a voltage of 24 kv had the H value of 1.47 whereas case E with 30 kv had 1.16.

(4) The classification is interconnected with the properties of coal as stated below:-
Type I : Low sulfur, low alkali overseas coals
Type II : General overseas coals except Type I
Type III: High sulfur, high alkali domestic coals
Therefore, performance for MIE can also be estimated more or less by the kind of coal and its properties.

(5) Type III is anticipated in case of the hot side ESP because the resistivity decreases by increasing the operating temperature. Certain data, however, also indicate the Type II performance and suggest occurrence of a back corona even in hot-side ESP.

ENERGY SAVING

It is shown by Fig. 8 that the power consumption is nearly proportional to the duty ratio. Therefore, energy saving is easily estimated by the duty ratio with which MIE is operated. Type I has the most effective energy saving. The saving amount is 70 to 90% . Type II is 50 to 70%.

It is natural that the power consumption can also be reduced by decreasing current in conventional energization. Comparison of power consumption between conventional energization and MIE are shown in Fig. 9. Fig. 9a is for Type I and Fig. 9b is for Type III. It should be noted that regarding energy saving, MIE in some cases is effective even for Type III. As is seen in Fig. 9b, very small degradation of w_k takes place. That is, energy saving of 50 % is achieved with a little degradation of the efficiency for Type III.

VOLTAGE AND CURRENT WAVEFORMS

Fig. 5 shows the voltage and current waveforms obtained from a full-scale ESP of type I. The value of $V_p \times V_m$ referred by Eq. (6) was calculated from the waveforms and are shown in Table 5 as well as the corresponding migration velocity w, which was calculated from the measured collecting efficiency. It is noted that the value of $V_p \times V_m$ was remarkably increased by MIE with a corresponding increase of the w value.

The effect of MIE is summarized in Table 5 as classified by Types.

CONCLUSION

It can be said that the MIE is recommendable for ESPs where a back corona takes place more or less. The modified migration velocity w_k is improved to 110-150% with the power consumption reduced to 10-30% in the favourable cases. The power consumption can be reduced by 50% with a small degree of degradation in the collecting efficiency even in cases where no improvement in efficiency is expected. Moreover, the initial cost for MIE is rather small since the main power lines of the conventional energization systems need no modification ; only the control circuit must be modified .

The MIE was commercialized due to the social needs for mitigating the degradation of ESPs in the coal-fired thermal power plants and also for the power saving . It should be mentioned additionally that this was also made possible by the recent advanced electronic techniques utilizing power control thyristors and electronic circuits, which are capable of turning on and off a large amount of current at a high speed with sophisticated control.

At present, the developement of Mitsubishi Intermittent Energization System is still in the progress of refinement. The main target of our current research for MIE is development of full automatic control system utilizing microcomputor.

REFERENCES

1. Harry J. White, Industrial electrostatic precipitation, Addison-Werley Publishing Co., inc. (1963)

2. Paul L. Feldman and Helmut I. Milde, Pulsed Energization for Enhanced Electrostatic Precipitation in High-Resistivity Applications, Symposium on Transfer and Utilization of Particulate Control Technology, July 1978

TABLE 1. TEST RESULT OF PILOT ESP*

Cases		A	B	C
Kind of coal		Canadian I	Australian I	Australian II
Coal characteristics				
Ash	wt%	13.8	11.2	11.6
Combustible sulfur	wt%	0.3	0.8	0.6
Gas temp.	°C	150	150	150
Resistivity of dust	ohm·cm	7×10^{12}	4.5×10^{11}	1.1×10^{12}
Collecting efficiency				
Conventional		88.45	99.76	96.10
MIE at Rc=1/2		88.75	99.65	97.43
MIE at Rc=1/3		92.01	99.54	97.55
MIE at Rc=1/5		94.13	99.27	96.70
MIE at Rc=1/10		89.55	-	95.10
Enhancement factor				
Conventional		1.00	1.00	1.00
MIE at Rc=1/2		1.02	0.88	1.27
MIE at Rc=1/3		1.37	0.80	1.31
MIE at Rc=1/5		1.72	0.66	1.11
MIE at Rc=1/10		1.09	-	0.86
Type for MIE		I	III	II

* Gas flow rate (designed) : 500 Nm^3/H

TABLE 2. MEASUREMENT OF FULL-SCALE ESP FOR COAL-FIRED BOILERS

Cases		D	E	F*
Unit capacity		185 T/H	185 T/H	75 MW
Designed conditions				
Gas flow rate	m^3N/H	190,000	190,000	280,000
Inlet dust content	g/m^3N	20.0	20.0	0.44
Outlet dust content	g/m^3N	0.08	0.08	0.2
Kind of coal		Domestic	Canadian II	Australian III
Coal characteristics				
Ash	wt%	22.6	10.2	18.4
Combustible sulfur	wt%	0.3	0.2	0.4
Gas temp.		110	113	198
Resistivity of dust	ohm·cm	1.4×10^{10}	4.5×10^{12}	7.0×10^{11}
Dust grain (50 % dia.)	micron	14.0	17.0	3.4
Collecting efficiency (%)				
Conventional		99.97	99.59	86.02
MIE at Rc=1/2		99.95	99.66	87.16
MIE at Rc=1/3		99.90	99.72	84.21
MIE at Rc=1/5		-	99.73	83.97
MIE at Rc=1/10		-	-	-
Enhancement factor				
Conventional		1.00	1.00	1.00
MIE at Rc=1/2		0.83	1.07	1.09
MIE at Rc=1/3		0.72	1.14	0.88
MIE at Rc=1/5		-	1.16	0.87
MIE at Rc=1/10		-	-	-
Type for MIE		III	I	II

* having other MC and ESP ahead

TABLE 3. MEASUREMENT OF FULL-SCALE ESP FOR OTHER PLANTS

Cases		G	H
Unit capacity		150 T/H	$262 m^2$
Designed conditions			
Gas flow rate	m^3N/H	165,000	512,000
Inlet dust content	g/m^3N	0.25	1.00
Outlet dust content	g/m^3N	0.05	0.03
Plants		Oil-fired thermal power plant	Iron ore sintering plant
Gas temp.	°C	154	95 to 112
Resistivity of dust	ohm·cm	10^4	10^{12} to 10^{13}
Dust grain (50 % dia.)	micron	0.25	20.0
Collecting efficiency (%)			
Conventional		97.45	88.28
MIE at Rc=1/2		96.97	89.24
MIE at Rc=1/3		96.55	91.78
MIE at Rc=1/5		94.14	92.58
MIE at Rc=1/10		-	-
Enhancement factor			
Conventional		1.00	1.00
MIE at Rc=1/2		0.91	1.08
MIE at Rc=1/3		0.84	1.36
MIE at Rc=1/5		0.60	1.47
MIE at Rc=1/10		-	-
Type for MIE		III	I

TABLE 4. SUMMARY: EFFECT OF MIE

Types	Type I	Type II	Type III
Dust resistivity (ohm·cm)	High resistivity (10^{11} to 10^{13})	Medium resistivity (10^{10} to 10^{12})	Medium-Low (less than 10^{11})
V/I characteristics	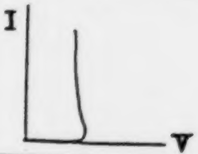	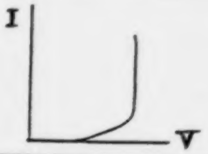	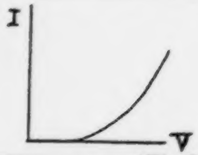
Optimum duty ratio R_C	1/5 to 1/3	1/3 to 1/2	1/2 to 1
Enhancement factor (at optimum duty)	1.1 to 1.5	1.1 to 1.3	0.8 to 1.0
Power consumption %	10 to 30	30 to 50	50 to 100
Coal characteristics	overseas low sulfur low alkali	general overseas	domestic high sulfur high alkali
Plants	·Coal-fired thermal power plant ·Iron ore sintering plant	·Coal-fired thermal power plant	·Coal-fired thermal power plant ·Oil-fired thermal power plant ·Cement plant ·Refuse incinerator

TABLE 5. COMPARISON* OF VOLTAGE WAVEFORMS AND PERFORMANCE

Items		Conventional energization	MIE	MIE/Conventional
Rc		1	1/3	
V_p	kV	30	46	
V_m	kV	24	21	
$V_p x V_m$		720	966	1.34
w	%	100	117	1.17

* referring to Fig. 5

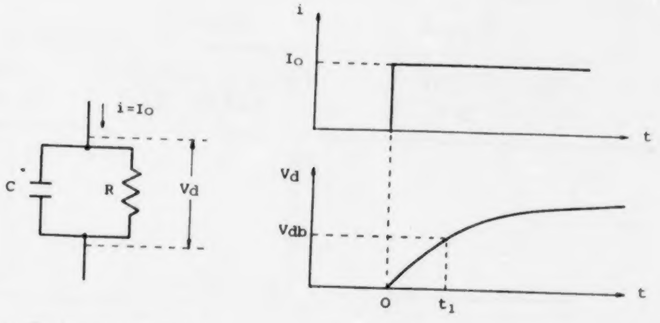
i=Io
C
R
Vd
i
Io
t
Vd
Vdb
0
t_1
t

a. Equivalent circuit

b. Step response

Figure 1. Electrical characteristics of dust layer

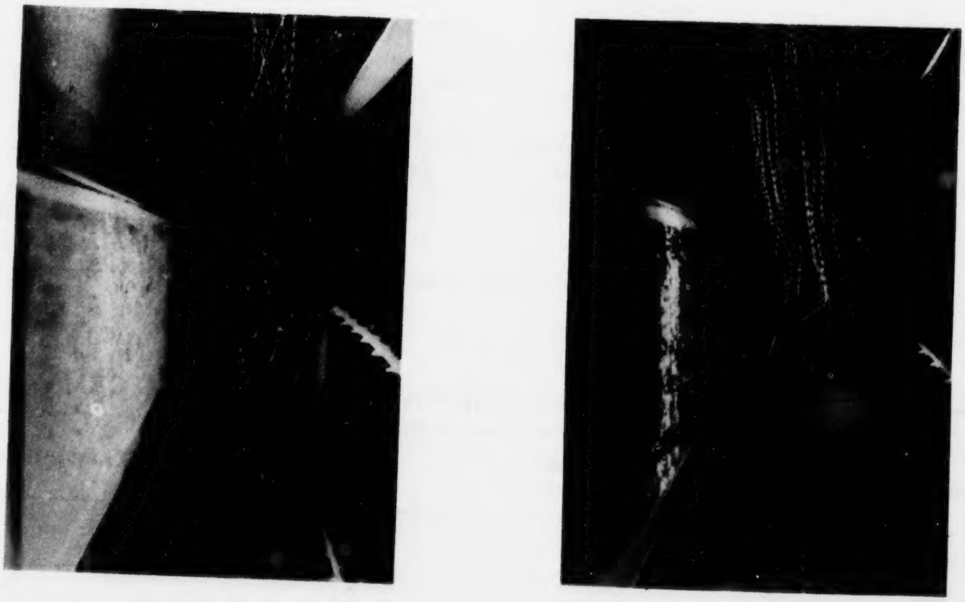

a. Conventional

b. MIE

Figure 2. Flying dust trajectories

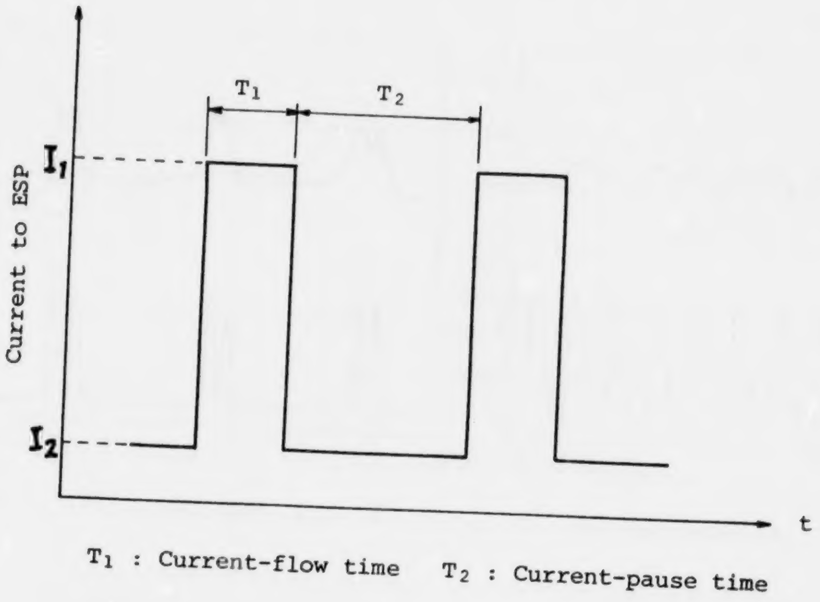

Figure 3. Current to ESP

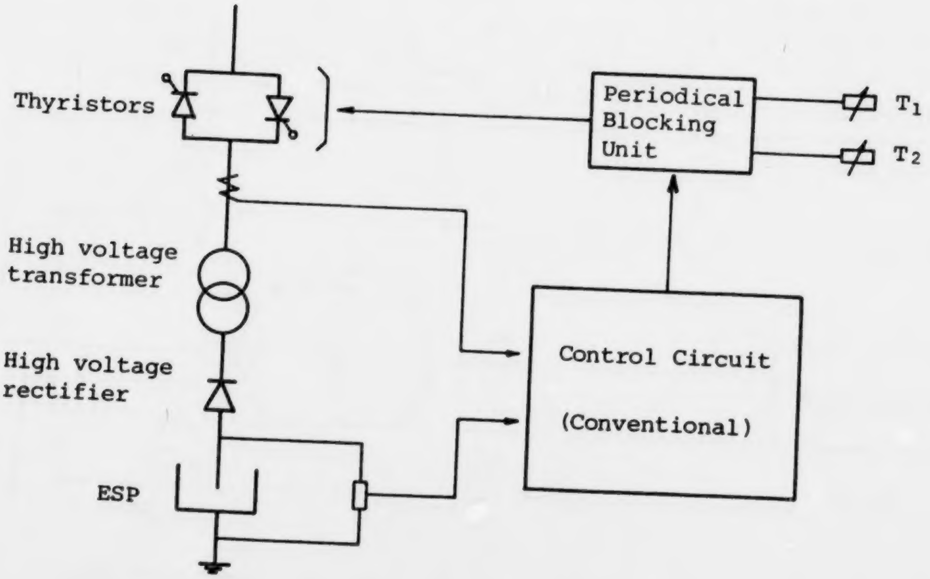
Thyristors
Periodical Blocking Unit
T1
T2
High voltage transformer
High voltage rectifier
Control Circuit
(Conventional)
ESP

Figure 4. Block diagram of MIE power supply equipment

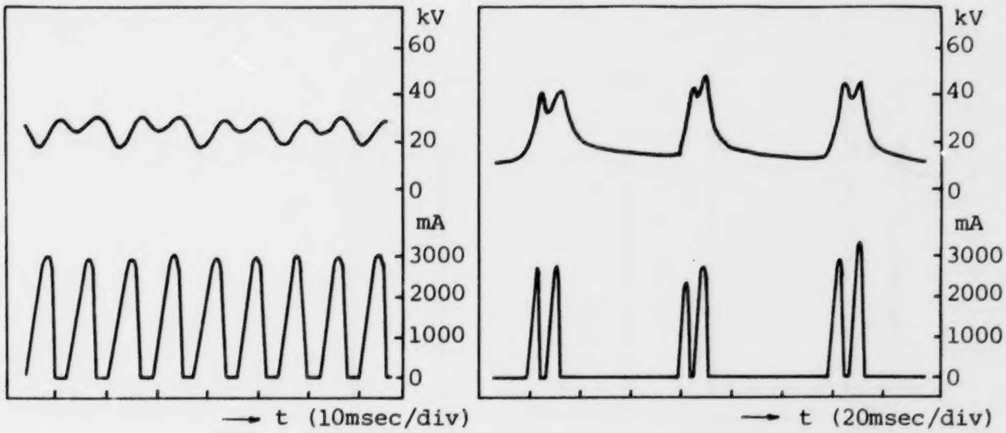

a. Conventional

b. MIE (Rc = 1/3)

Figure 5. Voltage and current waveforms

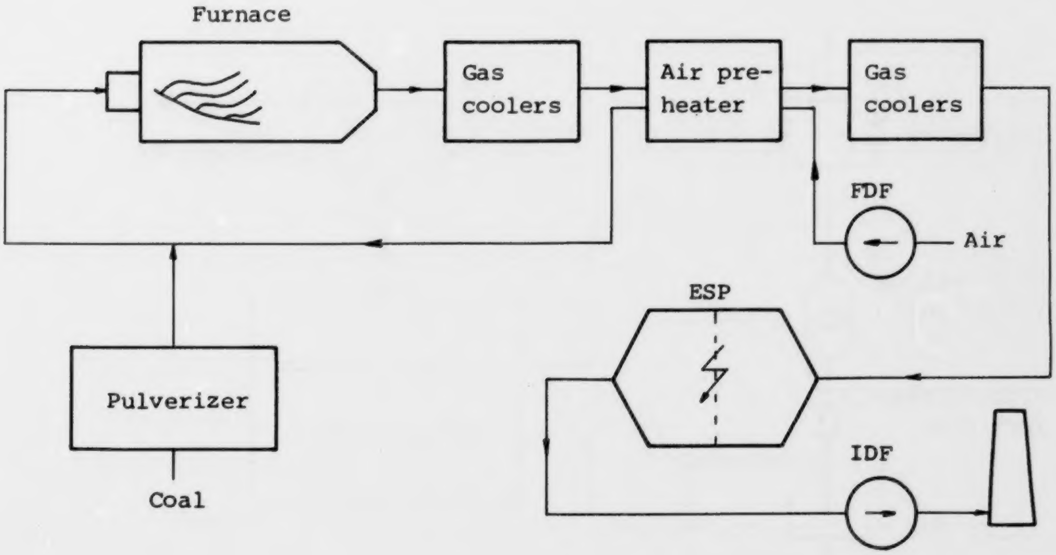
Furnace
Gas coolers
Air pre-heater
Gas coolers
FDF
Air
ESP
Pulverizer
Coal
IDF

Figure 6. Schematic diagram of coal firing test rig

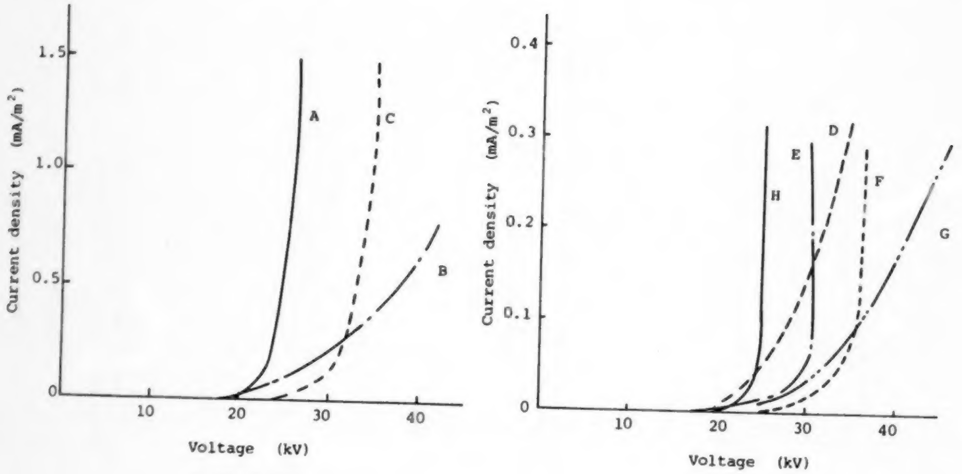

a. Pilot ESP

b. Full-scale ESP

Figure 7. Gas load V/I characteristics

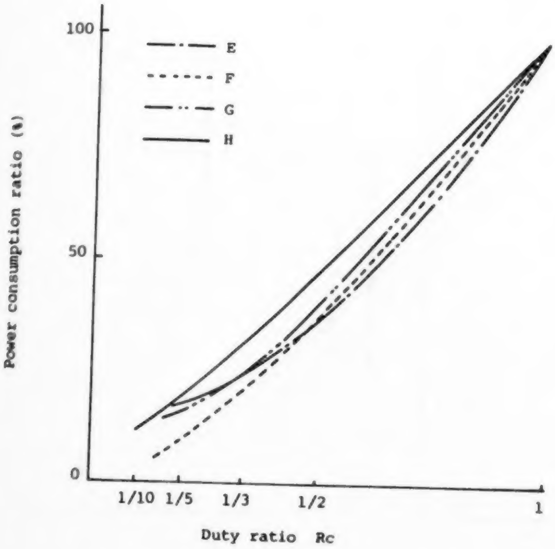

Figure 8. Power consumption

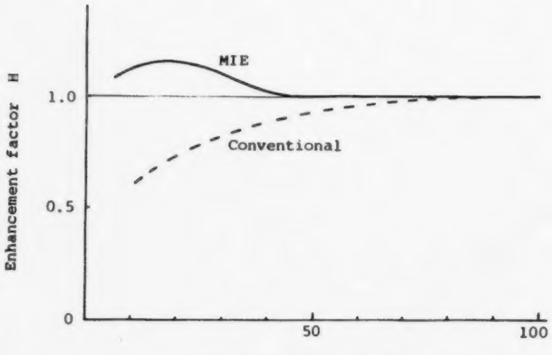

a. Type I (case E)

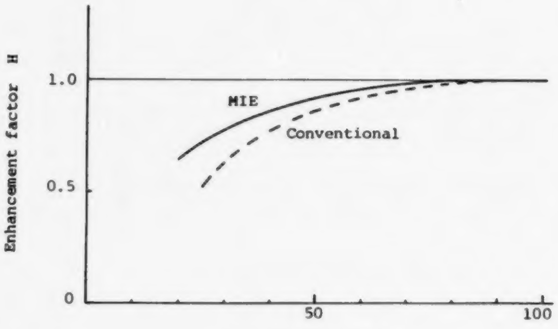

b. Type III (case D)

Figure 9. Comparison of energy saving

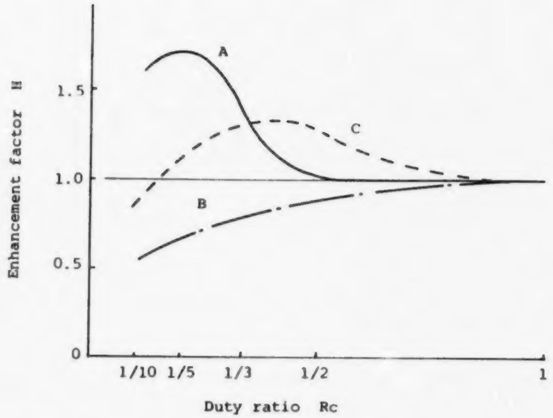

a. Pilot ESP

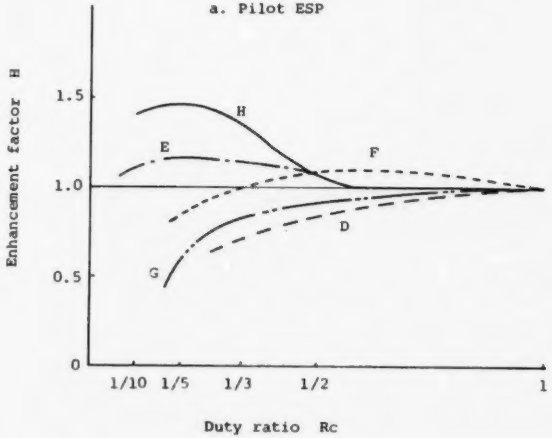

b. Full-scale ESP

Figure 10. Performance improvement of MIE

SOME MEASURED CHARACTERISTICS OF AN ELECTROSTATIC PRECIPITATOR OBTAINED USING A MICROCOMPUTER CONTROLLER

by: M.J. Duffy, T.S. Ng, Z. Herceg and K.J. McLean
University of Wollongong
Wollongong, N.S.W. Australia. 2519.

ABSTRACT

This paper presents a new microcomputer control system for electrostatic precipitators. The system, currently in its second stage of development, is capable of actively controlling, monitoring and recording the characteristics of an electrostatic precipitator.

The results of tests carried out on the precipitator along with the output of a dust monitor mounted on the precipitator output are also presented in an attempt to determine the optimum operating conditions.

The work described in this paper was not funded by the U.S. Environmental Protection Agency and therefore the contents do not necessarily reflect the view of the Agency and no official endorsement should be inferred.

INTRODUCTION

Electrostatic precipitators are one of the most efficient and economical means of removing particulates from effluent gasses in large coal-fired power stations. The basic principles of operation, design and application of electrostatic precipitators have been well documented (1, 2 and 3) and so will not be discussed here.

Since Australian coals are low in sulphur content the resultant fly ash has a high resistivity. It is this high resistivity which adversely affects the performance of the precipitator. In particular the 'back corona' formed on the collecting plates has the effect of reducing the spark-over voltage, increasing re-entrainment and reverse charging the suspended particles by positive ions injected into the gas stream. The consequence of these effects is to reduce the precipitator's performance.

The most efficient operating conditions within the precipitator have in the past been largely a matter of 'ballpark' approximation relying upon occasional adjustment of the automatic analogue control system. This method of operation is adequate provided that the conditions within the precipitator remain static. However as internal conditions vary with unit load, the degree of contamination and the type of coal used, this method becomes inefficient.

With the development of relatively cheap C.P.U.[1] and memory chips the use of microcomputers is becoming more pronounced in precipitator control as pointed out by Hall (4) for a variety of control and diagnostic purposes. The computer is able to react to changing operating conditions as they occur resulting in the theoretical maximum possible efficiency being obtained (5).

PROJECT DEVELOPMENT

The development of the Computer Controlled Electrostatic Precipitator System (C.C.E.P.) was proposed in three phases. The initial phase required that the computer replace the existing automatic analogue control system (6). By discretely sampling the precipitator zone voltage, current and spark rate the computer is able to supply an appropriate control input to the zone based upon a simple algorithm.

In the next phase the precipitator conditions are recorded and incorporated with the output of a dust monitor, mounted in the precipitator output, and stored on cassette tape. This information is later used to evaluate the relative performance of the computer and analogue control systems, to quantify the voltage-current characteristics of the precipitator in normal operation and in static tests as well as in comparing the results obtained using different control algorithms. It is the purpose of this paper to report some of the results achieved to date, explain the capabilities of the system and detail the projected development.

---

1. C.P.U. Central Processing Unit, e.g., 6502.

Having characterised the effects of different control strategies on precipitator performance the final phase will be to incorporate the input from the dust monitor as well as the past history of the precipitator in an adaptive control algorithm using a high level language like BASIC for the manipulation of the information and primitive ASSEMBLY routines for input-output purposes.

The system to be described in this paper is currently installed in one pass of a four pass electrostatic precipitator at the Electricity Commission of New South Wales Munmorah Power Station, New South Wales, Australia. Subject to satisfactory performance it will be extended to include the remaining passes in a complete computer network system which will be capable of informing an operator of the performance of his precipitator using pictorial and numerical displays.

DESCRIPTION OF THE SYSTEM

Figure 1 shows the block diagram of the power supply and existing control hardware in one zone of the electrostatic precipitator. The saturable reactor is used as a control element to vary the primary voltage to the high voltage transformer. The reactance of the reactor is controlled by the d.c. current in its control winding. It is this d.c. control current that is indirectly varied by the existing analogue control board using feedback supplied from the precipitator voltage, current and spark rate.

The control system (C.C.E.P.), shown within the dashed box of Figure 1, replaces the existing analogue inputs on the control boards of the five zones by changing over the contacts of a relay. These contacts are controlled by a count down timer which is refreshed periodically, while the computer is in control of the precipitator, so that it never times out. In the event of a power failure, the hardware ensures that control is automatically passed back to the analogue control system.

The microcomputer itself uses a 6502 C.P.U. chip together with twenty kilobytes of memory and six, eight bit input output ports which are connected to interfacing hardware as shown in Figure 2. The hardware comprises buffer amplifiers for each zone voltage and current together with an analogue multiplexer and a high speed analogue to digital converter (A/D). The spark rate is buffered and recorded separately using digital counters which are read periodically by the computer.

Control of the precipitator is achieved by using eight bit latches and digital to analogue converters (D/A) for each zone. The D/A's are connected to the zone through buffer amplifiers which scale the input so as to vary the precipitator secondary voltage in two hundred volt steps.

CONTROL ALGORITHM

Until now, all of the control on the precipitator has relied upon emulating the present analogue control system. That is, to control the

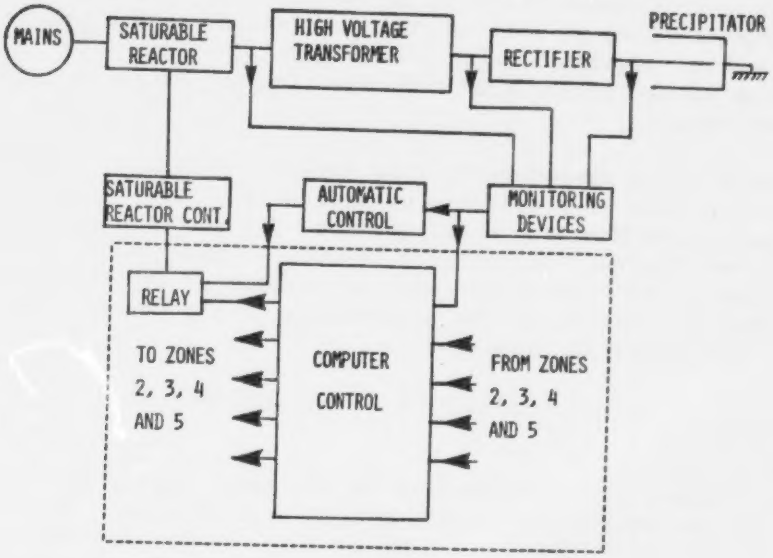
MAINS
SATURABLE REACTOR
HIGH VOLTAGE TRANSFORMER
RECTIFIER
PRECIPITATOR
SATURABLE REACTOR CONT.
AUTOMATIC CONTROL
MONITORING DEVICES
RELAY
TO ZONES 2, 3, 4 AND 5
COMPUTER CONTROL
FROM ZONES 2, 3, 4 AND 5

Figure 1: Power Supply and Existing Control Hardware with Microcomputer System Attached.

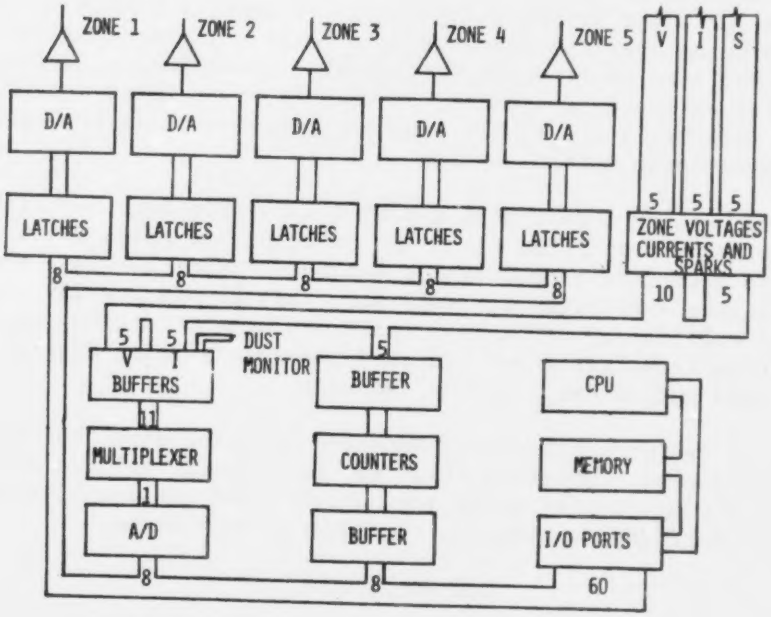
ZONE 1
ZONE 2
ZONE 3
ZONE 4
ZONE 5
V
I
S
D/A
D/A
D/A
D/A
D/A
LATCHES
LATCHES
LATCHES
LATCHES
LATCHES
5
5
5
ZONE VOLTAGES CURRENTS AND SPARKS
8
8
8
8
8
10
5
5
5
V
I
DUST MONITOR
5
BUFFERS
BUFFER
CPU
11
MULTIPLEXER
COUNTERS
MEMORY
1
A/D
BUFFER
I/O PORTS
8
8
60

Figure 2: Microcomputer with Interface Circuitry.

precipitator using the spark rate as the reference variable with specific limits being imposed upon voltage and current.

The current control algorithm, shown in Figure 3, requires the computer to increase its control voltage by one step until the precipitator spark rate reaches a reference value. If the reference is exceeded the computer will back off the voltage. If, however, the reference is exceeded by a fixed amount, the computer will assume that the zone is sparking heavily and so will back off the voltage more vigorously and then set a flag. On the next pass through the zone, approximately one minute later, the computer will examine the flag. If it is set and the excess sparking has ceased the computer will restore the control voltage to a few steps below its former value.

It was hoped that this strategy would maintain zone voltages close to their maximum vlaues for more efficient dust collection while, at the same time, avoiding long time delays while the computer recovered from excessive sparking. Field test results tend to support the validity of this argument.

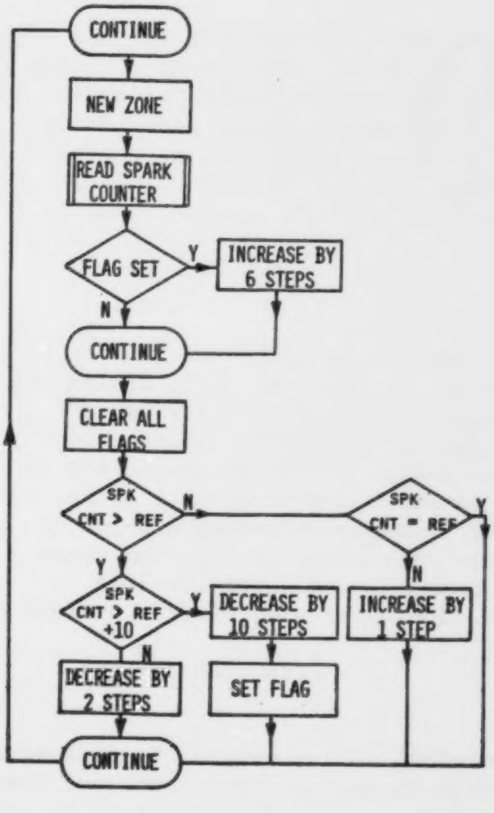
CONTINUE
NEW ZONE
READ SPARK COUNTER
FLAG SET
Y
N
INCREASE BY 6 STEPS
CONTINUE
CLEAR ALL FLAGS
SPK CNT > REF
N
Y
SPK CNT = REF
Y
N
SPK CNT > REF +10
Y
N
DECREASE BY 10 STEPS
INCREASE BY 1 STEP
DECREASE BY 2 STEPS
SET FLAG
CONTINUE

Figure 3: Flow Chart for Control Algorithm (1 Zone)

RESULTS OF TESTS

A typical plot of one zone's performance is shown in Figure 4 with the spark rate plot shown in Figure 5. From these results it is easy to see that the computer is indeed capable of regulating zone spark rates although this is not the case for spark rates in excess of twenty sparks per minute. This appears to be due to the instability caused within the zone due to the excess spark rates.

Having plotted the performance of a control algorithm the next step is to determine the optimum spark rate. To enable this the computer can be programmed to dynamically increase the reference spark rate by a fixed amount at fixed intervals of time. Again the performance is evaluated by using the output of the dust monitor connected into the output of the pass.

This test was carried out again by taking the precipitator voltage, on all zones, below the spark-over voltage and manually increasing the voltage to a point of heavy sparking. The computer printout for this case is shown in Figures 6 and 7 for one zone.

In both cases the results, although at this stage preliminary, showed that the dust output is fairly independent of spark rate over a wide range of values. This may, however, be due to excessive dust contamination as earlier tests indicated a much greater sensitivity. Peaks in dust output occur for voltages below the spark-over potential and at spark rates in excess of one hundred sparks per minute. This may be observed in the dust monitor output plot for the above case as shown in Figure 8.

CONCLUSIONS

While at this stage no definite conclusions regarding precipitator optimum performance may be inferred it is reasonable to say that the microcomputer control system has demonstrated its versatility in a wide range of operating environments and proved superior to the existing analogue control system in several instances. That is not to say that the system has proved to be the ultimate in precipitator control either, but over the test period, it has provided much valuable information which was previously unobtainable. This information must ultimately benefit the research and development of electrostatic precipitators and hopefully lead to a better understanding of their internal operation under many diverse operating environments.

ACKNOWLEDGEMENTS

The author gratefully acknowledges the financial assistance provided by the National Energy Research, Development and Demonstration Programme administered by the Commonwealth Department of National Development and Energy as well as the assistance, both financial and material, provided by the Electricity Commission of New South Wales and its officers.

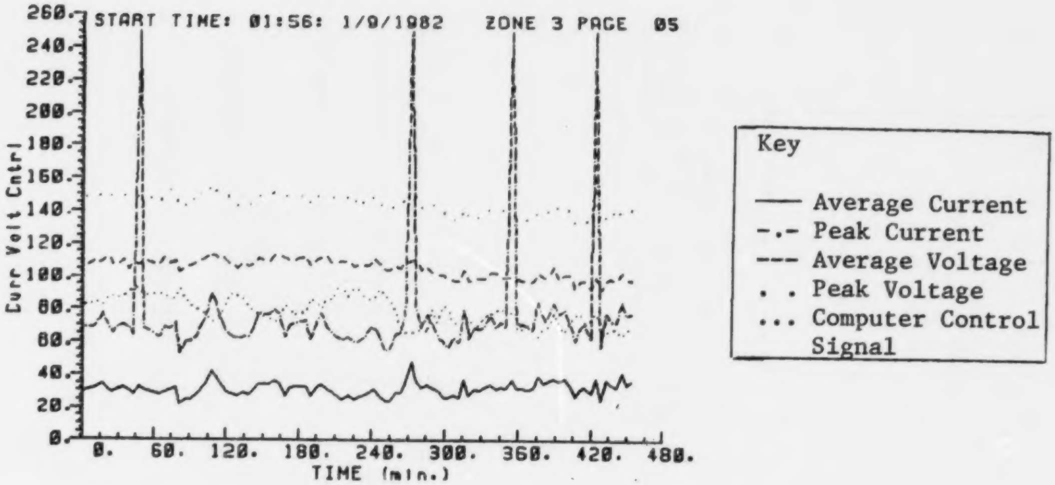

Figure 4: Voltage, Current and Control Signal of Precipitator with Microcomputer in Normal Operation (1 Zone).

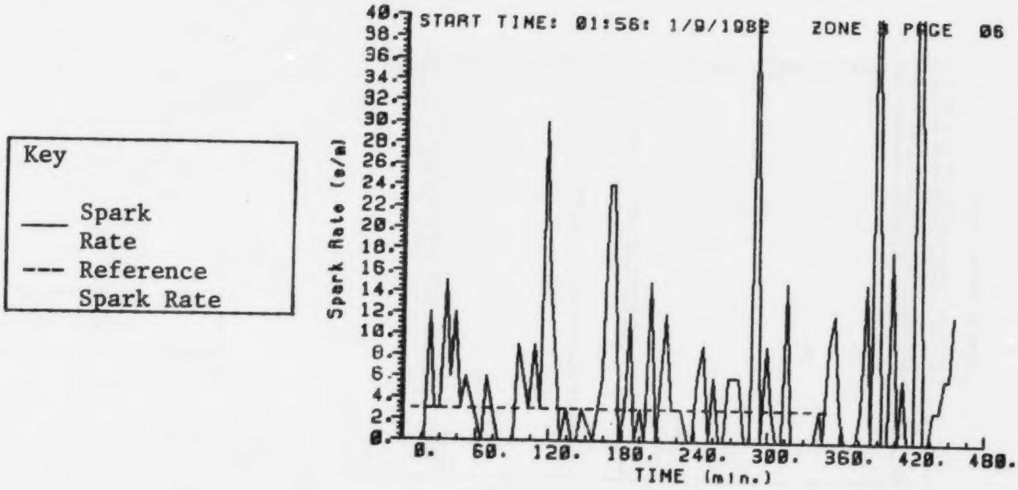

Figure 5: Spark Rate (sparks/minute) During the Same Period.

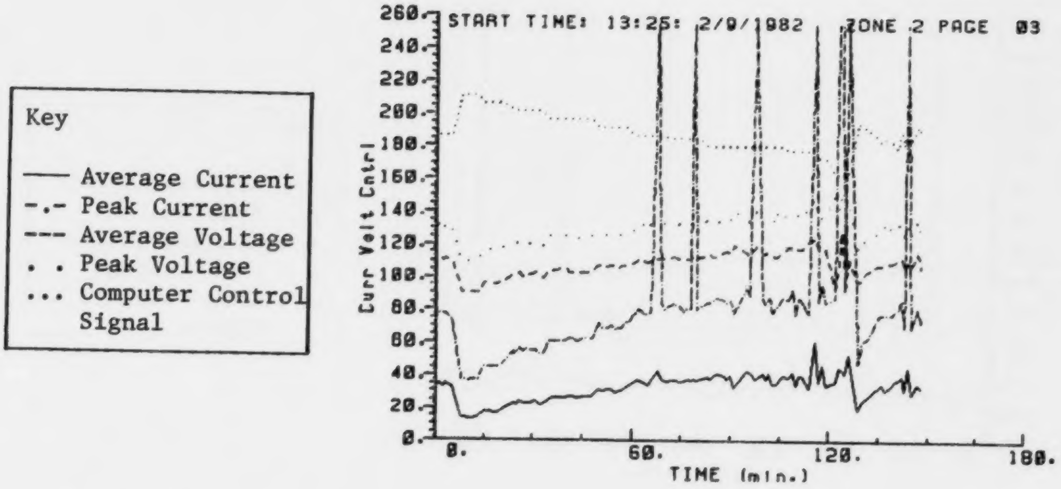

Figure 6: Voltage, Current and Control Signal of Precipitator with Microcomputer in Manual Operation (1 Zone).

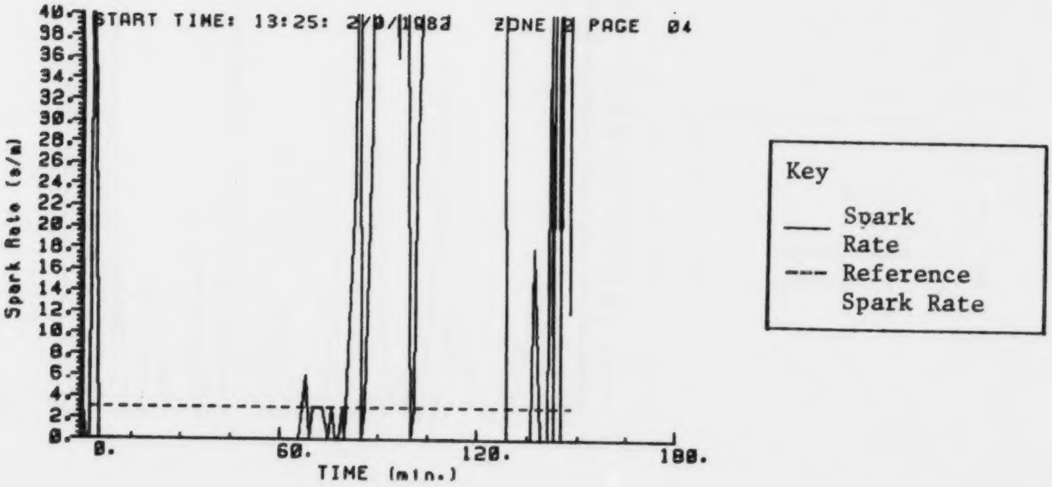

Figure 7: Spark Rate (sparks/minute) During the Same Period.

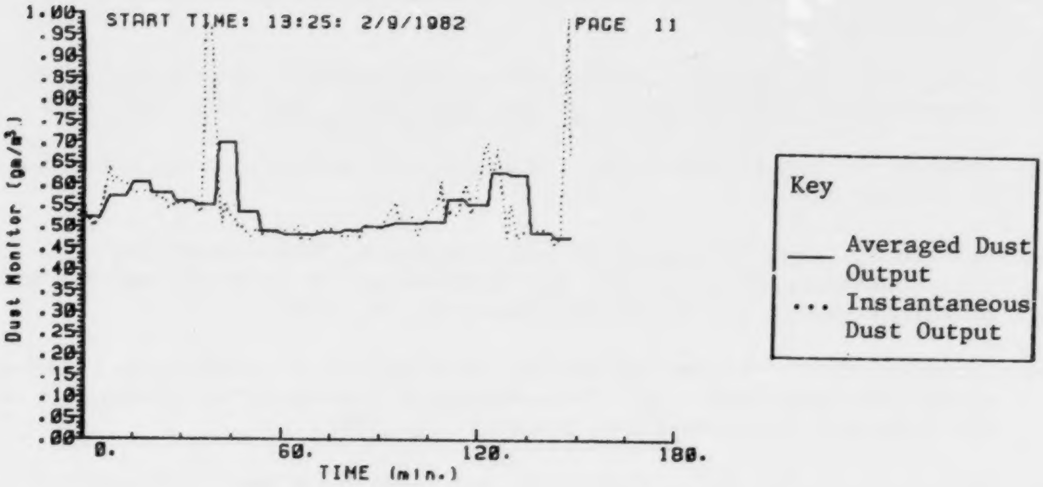

Figure 8: Dust Monitor Output (grams/m^3) During the Same Period.

REFERENCES

1. White, H.J. Industrial electrostatic precipitation, Reading, Mass., Addison-Wesley, 1963.

2. Hall, H.J. Design and application of high voltage power supplies in electrostatic precipitation, J. Air Poll. Cont. Ass., 25: 132, 1975.

3. Oglesby, S. and Nichols, G.B. Electrostatic precipitation, New York, M. Dekker, 1978.

4. Hall, H.J. High voltage power supplies and microprocessor controls for electrostatic precipitation. In: Proceedings of International Conference on Electrostatic Precipitation, Monterey, CA, 1981.

5. Schummer, H.W. Process and energy optimization of precipitator plants using microcomputers. In: Proceedings of International Conference on Electrostatic Precipitation, Monterey, CA, 1981.

6. McLean, K.J., Ng, T.S., Herceg, Z. and Rana, Z A new microcomputer system and strategy for the control of electrostatic precipitators. Paper presented at 3rd EPA Symposium on Transfer and Utilisation of Particulate Control Technology, March 9-13, 1981.

ELECTROSTATIC PRECIPITATOR ENERGIZATION AND CONTROL SYSTEMS

by: K. M. Bradburn and K. Darby
Lodge-Cottrell Dresser
Houston, Texas 77002

ABSTRACT

This paper reviews the development of systems for the energization and control of electrostatic precipitators, ranging from heavy duty thyristors used to control the input to the T/R set to the use of microprocessor technology which gives the facility for a precipitator total energy management system (TEMS). The impact of these changes is described first on the T/R set, then on the automatic voltage control system to maximize precipitator efficiency.

Reference is made to the electrical demands of a precipitator, under varying operating conditions, to justify the advantages of the TEMS concept.

The system comprises a local control and power unit for each T/R set, a supervisory control unit and a control room monitor which allow visual (CRT) display and print out of operating data and parameters remote from the precipitator.

In addition to improved automatic voltage control, TEMS offers the facility for integrating additional operations and parameters such as stack opacity, rapping, hopper heating, hopper ash level alarm, precipitator start-up and shutdown. This results in complete system control and improved operation with lower power consumption and operating costs.

Using a telephone modem, precipitator engineers remote from the plant can accurately and instantaneously monitor and adjust precipitator operation and give technical support to plant engineers for prompt correction of any operating problems.

INTRODUCTION

Nearly one hundred years ago, Sir Oliver Lodge in England made the first attempt to apply electrostatic precipitation to an industrial application. Inadequacies in the power supply equipment, however, severely limited the success of this first installation. To commemorate this significant occasion, the Commonwealth Scientific and Industrial Research Organization of Australia 2nd Electrostatic Precipitator Conference will be held in 1983, the centenary year of electrostatic precipitation.

It was not until 1907 that Frederick Cottrell used the then newly developed synchronous mechanical rectifier as the power source for the first commercial precipitator.

Throughout the years both mechanical and high vacuum tube rectifiers were commercially used in precipitators, but the associated system was limited to one of manual operation. It was not until the late 1940's that the first automatic transformer/rectifier control became a reality.

Another decade passed before high voltage silicon rectifiers and saturable reactors came into common use. These components remained the basic power equipment until the emergence, in the mid 1960's, of modern SCR (thyristor), linear reactor and solid state automatic voltage control.

Today's precipitator control systems have now entered the computer age with the use of microprocessors. Such technology has provided the opportunity for the establishment of a fully integrated precipitator control system.

One particular area of interest which the microprocessor system includes is the ability to use an opacity feedback signal to adjust the power consumed by the precipitator, thereby providing a basis for some power economy when precipitator operating conditions are more favorable than the design conditions.

This Paper gives an illustration of the power/opacity relationship for a full scale precipitator and indicates the level of power savings which may be possible. In addition, a description of a microprocessor system is given which incorporates the facility to realize such saving as one of its many features.

PRECIPITATOR PERFORMANCE - POWER CHARACTERISTICS

Until microprocessors became available for control purposes, electrostatic precipitators were designed with a T/R set for each electrical bus section and usually incorporated an automatic control, either in the form of a flash or spark counter or, in the case of Lodge-Cottrell, a device which set the mean discharge electrode voltage at the highest possible level. The aim of such controls was to ensure that at all times and under varying conditions, the precipitator was giving the maximum possible efficiency.

The Lodge-Cottrell system operated on the principle illustrated in Figure 1. This shows that if the electrical input is set at a condition where the mean discharge electrode voltage, including the effect of the loss of field voltage during flashover, is at the maximum level possible, then the effective migration velocity, hence, the particulate removal efficiency will be at the highest level. In the original patent for this type of control, recognizing that opacity would also be at a minimum for maximum particulate removal efficiency, an alternative to the use of the maximum value of discharge electrode voltage was included, whereby the control was achieved by using a signal from an opacity meter; in this case the system aimed at minimum opacity. The minimum opacity and the maximum mean value of discharge electrode voltage were shown to correspond to the same condition of precipitator efficiency. Both systems had the advantage that the absolute accuracy of the control signal input was not critical, since the control system would seek maximum voltage, or minimum opacity, regardless of the absolute value.

The overriding design requirement of an electrostatic precipitator is that it shall meet the environmental particulate emission standards under the most onerous of its design conditions. These may be summed up as represented by the maximum gas flow rate which the precipitator is required to treat, the maximum inlet particulate concentration and the properties of ash and gas as determined by the properties of the fuel. The automatic voltage control system will for any of these conditions seek to give the best possible particulate removal efficiency under the conditions existing in the precipitator at any particular time. For the different conditions of gas volume, particulate properties, etc., the voltage and current corresponding to the optimum efficiency vary considerably, and in many cases, the removal efficiency and the power applied will be considerably greater than that needed to satisfy particulate emission requirements.

Figure 2 illustrates the characteristics of a typical precipitator system attached to a 120 MW power station boiler. Each precipitator had two chambers in parallel and three electrical fields in series. The graphs show a number of important characteristics of the plant under a wide variation of load conditions. Note first the central Graph B, which shows the D.C. power input to one precipitator chamber. It will be seen that for a gas flow from below 300,000 to one in excess of 400,000 cfm actual, there is actually a slight decrease in total power absorbed for optimum precipitator efficiency obtainable at those flow rates.

Refer next to Graph A. This shows the power input per unit of gas treated. It will be seen that from the full load to the lowest illustrated, there is approximately a 50% increase in specific power usage. Graph C shows the mass emission of particulate. This reduces by 75% due to the longer exposure of the gas to the electric field. While this reduction in mass emission may seem a very desirable situation, it should be noted that the actual power absorbed has increased, if only by a small percentage, and the specific power input, the power per unit volume treated, has increased by more than 50%. Bearing in mind that the particulate emission at the full load condition was, in the case of this particular plant, already well within the limit set by the environmental laws, then it could be argued that there was little point in reducing the mass emission at the expense of very substantial increases in specific power. The mass emission could have been maintained at a constant value as the load diminished with a substantial saving in electric power by reducing the power input to the precipitator.

The implication of the magnitude of possible saving is illustrated by the table below. This shows the electrical supply system for a 600 MW boiler designed to fire U.S. midwestern sub-bituminous coal to give particulate removal of 99.85% efficiency. Each of two precipitators has 6 fields in series and 36 isolatable bus sections. The important numbers here are the power rating of the T/R sets, the total installed capacity is 4220 kVA A.C. or 2970 KW D.C. While in practice the absorbed power of the precipitator system may only be 70% of the installed capacity, this represents a significant portion of the output generated by the boiler and turbine.

TABLE

Boiler Output	600 MW
Coal Fired	Midwestern Sub-bituminous
Precipitator Installation	
Design Efficiency	99.85%
Number of Precipitators	2
Number of Fields	6
Number of Isolatable Bus Sections	72 Total
T/R Sets	
Number of Sets	72
Design Rating	36 at 55 kV, 600 mA 36 at 55 kV, 900 mA
Total Rectifier Installed Capacity	2970 KW D.C. - 4220 kVA A.C.

To demonstrate the possibility of power saving, a program of tests was carried out on a 120 MW boiler at Agecroft Power Station in the U. K.

Each precipitator had two chambers in parallel and three electrical fields in series, and the tests were carried out at full boiler rating. The coal fired was a hard bituminous coal of a relatively high sulphur content (1.8%) and was such that it gave very favorable precipitation conditions, in fact a typical condition which is normally associated with a high absorbed corona power. The precipitation characteristics of the ash were much better than that on which the design was based. With rectifiers on all three fields operating at optimum, power consumption was approximately 23 kVA and opacity, that is base or mean opacity, was about 5% corresponding to a particulate emission of 15 mg/Nm^3. Apart from the mean opacity there are periodic short duration spikes on the opacity meter trace due to reentrainment when the plates are rapped. The maximum height of spike results from the rapping of the outlet field. The effect of reentrainment is included in the emission concentration quoted.

Two series of tests were performed. In the first series of tests illustrated in Figure 3, each of the three fields in turn was reduced in power input until it approached the minimum possible with the other two fields maintained at optimum. This resulted in the opacity increasing only to 10%, equivalent to 35 mg/Nm^3, with a reduction in power input of over 60%. The significant difference was that the spikes due to rapping reentrainment were minimum when power reduction was carried out only on the inlet, and greatest when on the outlet field.

In Figure 4 the same series of tests were repeated, but in this case one out of three fields was maintained at optimum power input, while the other two fields were gradually reduced by the same amount. Under these conditions the opacity increased to a maximum average value of 20%, for a reduction in power input of 80%. Thus the guarantee for this plant, which required an opacity of 20%, would still have been met with only 20% of the power input which the automatic voltage control systems would normally feed to the system. Of particular interest here is the greater amplitude of the rapping spikes. These approached almost total opacity when either the center and outlet or the inlet and outlet fields were reduced. The maximum height of spike again resulted from rapping of the plates of the outlet field. While of considerable amplitude, in a large system, since they are only a few seconds in duration, spaced a considerable time apart and occur in only one section at a time, when mixed with the gases from other units, the effect of even the large rapping spikes did not result in any visible plume at the stack. Even so the evidence that these large spikes occur could be a reason for limiting the power reduction.

It can be seen from Figure 4 that it would be better, if such an operating approach were adopted, to limit the reduction of voltage to the first two fields since this reduces the rapping spikes to roughly half of the amplitude of the other two conditions.

This particular operating condition with an extremely favorable fuel for the precipitator, which in practice gave migration velocities in excess of 13 cm/sec., probably represents close to the upper limit of power that can be saved by reducing the performance such that the precipitator maintains the guaranteed opacity or mass emission at full boiler rating.

The reason this extreme power change takes place is illustrated in Figure 5(A). This shows the variation of corona current with increasing discharge electrode voltage, and it will be noted that the upper half of the curve shows a doubling of corona current for relatively small increases in discharge electrode voltage. In an electrostatic precipitator, very little of the current actually flowing is used to charge the particulate, but is transported across the interelectrode space in the form of ionized gas. According to precipitator theory, once the particles have acquired their limiting charge, then the rate of removal from the gas stream should be roughly proportional to the square of the voltage applied to the discharge electrodes. This is illustrated in Figure 5(B) for the conditions recorded in Figure 5(A). It will be seen that there is an approximate linear relationship between the square of the electrode voltage and the opacity. The opacity increased from 5% to 15% for a 60% decrease in the square of the applied voltage. The rapidly increasing corona current, as the applied voltage is increased, contributes little to the efficiency of the precipitator.

It is stressed that this particular example is for a type of fuel where the maximum economy and power input is possible due to the very good precipitation conditions which would be encountered. There would be some power economies for most fuels. If particulate mass emission rather than opacity is regarded as the regulating condition, since for the same opacity at reduced boiler loads the mass emission reduces proportionally to the gas flow, then further power reductions are possible. Illustrated here, however, is a way in which the use of microprocessor control can substantially reduce the power consumed. If the control system includes the input of a signal from the opacity meter, then this can be used to override the tendency for the automatic voltage control systems to strive for maximum power and maximum efficiency while still maintaining a constant stack opacity sufficient to meet environmental regulations with the advantage of very substantial economies in operating costs.

The tests described above were, of necessity, of short duration, and conditions could change if the plant were operated for a substantial period at reduced power input; that is, more than a few hours, at any one of the conditions shown. For example, with the precipitator operating at the optimum value, there is a considerable rate of spark-over within the precipitator; and it has been observed by the Authors that if the rate of flashover is maintained at a sufficiently high level, then the efficiency of the precipitator can also be maintained for a considerable period even without rapping. On one installation this was demonstrated over a period of seven days with the rapping switched off. This results from the fact that each flashover, which is the discharge of the electrode formed condenser, is the equivalent of a mechanical blow on the collector and discharge system. In another paper presented at this Symposium, this will be discussed in some detail, but in practice rapping forces of the order of 20 to 30 'g' were measured in the region of the plate corresponding to the flashover. The implications of this are important since with a precipitator field being subjected to random flashover as would be normal with a well aligned precipitator, each of the plates is being subjected at some point or other, due to the flashover, to blows sufficient to remove at least the freshly deposited ash. This means that in contrast to the idea that the thickness of the ash layer on the plates builds up progressively between the mechanical rapping blows, there is a continual cleaning process of the collector system, with the result that though the mechanical rapping is cyclic, the variation in cleanliness of the plate between rapping blows does not vary as much as might be expected.

Figure 6 shows photographs of a laboratory rig built to demonstrate the effect of flashover on a layer of electrostatically deposited ash about 5 mm. thick. The area over which ash is removed is, as expected, quite large relative to the spark point contact.

It would appear, therefore, that the method of power economy whereby the input to the fields is reduced so that flashover is virtually eliminated, could have undesirable side effects from the point of view of plate build-up and the effect of this build-up on the electrical field and hence, precipitator efficiency. This would of course be dependent on the rapping efficiency of the mechanical system also, but this could not completely eliminate the gradual build-up effect between rapping blows which would be reduced by the flashover effect. An alternative to gradual reduction of power input would be to switch off sections or fields in sequence so that the resulting opacity still achieved the required level. This was the basis of the second series of tests in which different numbers and combinations of fields were switched off. This is obviously a much coarser control than the first series and with the three fields of the unit tested, there was very little flexibility possible in the system.

On this three field system, switching off the inlet field showed an opacity increase of from 5 to 10%, while switching off of the inlet and center fields increased the opacity to 35%. Any combination of deenergizing fields which included the outlet field, had a much greater effect on the increase in opacity; and it would seem logical, therefore, that with such a system, deenergization should begin with the first field. On the six field precipitator, for example, it could be possible to switch off two or more fields and still meet the required opacity at low loads and favorable conditions. This could halve the power absorbed by the precipitator if environmentally acceptable.

In the various tests described above, although all of short duration, a period of weeks was needed to collect the information given. It is preferable to repeat these tests on a variety of other types of coal ashes, including the midwestern sub-bituminous widely used here in the United States, and the very highly resistive ashes which result from the firing of hard bituminous coals in New South Wales, Australia. The facility exists for extending the role of the microprocessor to control precipitator corona power such that the opacity or mass emission is maintained at a constant value with substantial reduction in operating costs. The correlation of mass emission and opacity can be obtained from performance testing. In the tests described above, the rapping frequency was not varied as fields upstream were turned off or reduced in efficiency. The microprocessor is capable of making changes to the rapping cycle to compensate for the variation of particulate concentration entering the field.

ENERGY MANAGEMENT SYSTEM

The advent of microprocessor technology has afforded the opportunity to not only give improved transformer/rectifier control and monitoring but also the facility to integrate many additional operations, parameters and features, giving a total energy management system.

Some of the features of such a system are:

a) Improved transformer/rectifier control and precipitator performance

b) High level system reliability

c) Convenient remote control, monitoring and data logging

d) Closed loop control of stack opacity

e) Integrated rapping frequency control

f) Hopper ash level monitoring

g) Hopper heating monitoring and control

h) Maintenance scheduling and system fault diagnosis

i) Modem communications

The Lodge-Cottrell energy management system which has the facility to incorporate such features comprises:

1) Local automatic voltage controller and power units for each transformer/rectifier set

2) Supervisory controller

3) Boiler control room monitor.

The overall system is designed to be tolerant of individual component failures. There is no critical component in the system. Failure of an individual Local AVC Unit or Power Unit will result in the loss of one T/R set. Upon the failure of a Supervisor Unit, the associated Local Units automatically revert to local operation.

LOCAL AVC UNIT

The primary component of the system is the Local Automatic Voltage Control Unit, which processes all precipitator signals from an electrical section, provides local display and annunciation capability, provides switch inputs for the user, communicates with the Supervisor Unit, receives ALL "ON" and ALL "OFF" commands from a remote source and provides the control signal required by the Power Unit.

The Local Unit employs two independent microcomputers. One is used to perform all control functions, the other is used to derive the signals for front panel display. The software for these two computers has been designed to be self-starting.

The automatic voltage control strategy employed by the microprocessor AVC is more advanced than earlier designs, while maintaining the same fundamental control strategy. This is to maintain the highest possible average T/R unit output voltage, under all operating conditions, except when functioning with an opacity signal override.

In the automatic operating mode, the AVC has a quick run up feature which operates when the unit is brought into service. The T/R unit output voltage increases at approximately four times the normal rate until the first drop in the average voltage is sensed. Thereafter, the normal control strategy takes over.

Automatic current limiting is provided to protect the T/R set and precipitator components and predominates over both automatic and manual control. Unlike earlier designs that sense the average value of the T/R unit primary current, this AVC Unit senses the rms value.

The rms value of the T/R primary current is digitally filtered to provide optimum closed-loop stability while the system is current limiting.

The T/R voltage divider signal is digitally filtered to provide optimum performance. The parameter RESPONSE is used to control the filtering process, matching control performance to the characteristics of a specific application. In addition, the parameter STEP is used to set the sensitivity of control.

The manual control mode is functionally identical to that provided by earlier AVC's. When the system is in the MANUAL mode, the T/R voltage can be manually raised or lowered by the operator.

Each Local AVC Unit (Figure 7) continuously displays five basic operating values: secondary bushing voltage (kV), secondary bushing current (mA), line voltage (volts), line current (Amps), power consumption (KW). Parameter settings can also be selected and displayed as required and standard alarm conditions are indicated.

In addition to its basic function, the Local AVC also performs rapper control functions and implements an additional important new performance feature: the ability to regulate the frequency of rapping associated with the electrical section the AVC regulates.

The rapper control system is automatically adjusted to accommodate Local Units that are out of service, i.e., the Local Control Unit will continue to operate even though its associated Power Unit or T/R set may not be capable of operation. Should a Local Unit fail completely, the adjacent AVC in that field would automatically control the rapping. In addition, the frequency of rapping of the downstream field would be adjusted accordingly for the increase in particulate loading.

LOCAL POWER UNIT

The respective Power Unit for each automatic voltage control unit modulates the line voltage supplied to the T/R set in accordance with commands supplied from that Local AVC Unit. The Power Unit can be located up to 1500 meters away from its associated Local AVC Unit. The SCR power control elements in the Power Unit are conservatively rated and adequately cooled for plant operating conditions.

Phase modulation, as opposed to integral cycle switching, is employed to provide the fine control required for optimizing secondary voltage. A single phase configuration is employed.

The SCR's are of disc package construction and in order to provide reliable operation in the rigorous precipitator application, exceptionally high I^2T ratings are used. To protect the SCR, an R-C snubber network is provided along with a high-power metal oxide varistor; in addition, a high-speed fuse is provided to give ultimate overcurrent protection.

SUPERVISOR

Broadly conceived, the Supervisor is a loop in the precipitator control system (Figure 8) that is closed by operator response to concisely presented information. As a complete system, it is a computer in communication with up to 128 local Automatic Voltage Controllers which control the individual sections of the precipitator.

Local AVC units are "intelligent" in the sense that once they are programmed with a set of initial parameters, they will independently control their bus sections. The addition of the supervisor computer brings to a central location the configuration of local unit parameters and operational data. Hence, information on the whole precipitator plant can be concisely displayed. Full control of all Local Units is available at this central location, abnormal operation which the Supervisor Unit is programmed to recognize is instantly displayed allowing correction or remedial action to be taken immediately.

As with any complex system, various parts of the system have distinct boundaries and specific communication requirements. Choosing the boundaries and the communication wisely means:

a. The functional requirements can be met.

b. Failure of any components will be known and have minimal effect. Repair can be made without a total system shutdown.

c. The system is structured to permit progressive expansion.

The following basic specifications satisfy these requirements (Figure 9):

a. The Supervisor is a microcomputer board system, which has a well defined structure of communication among core parts of a computer.

b. The Supervisor communicates with Local Unit controllers through RS-422 communications protocol. This allows high speed communication on a simple coax cable connecting all Local Units and the Supervisor. Each unit has its own address on this bus. Additional Local Units and other peripherals can be added.

c. The Local Units can control the bus sections independently of the Supervisor. Failure of the Supervisor will not affect the Local Control Units, and failure of a Local Control Unit only affects that respective energized section.

The Supervisor Console consists of a color CRT, keyboard, printer, telephone modem, two disc drives, and microcomputer. The Supervisor computer communicates with the local AVC's and Control Room Monitor via RS-422 buses. Also included in the hardware structure is the ability to accommodate 16 single ended A/D channels (4-20 mA in, minimum 10 bit resolution), and facility to address 16 parallel lines of I/O - 8 in, 8 out. This parallel interface is through 110 VAC lines.

The Supervisor CRT will display any of the following parameters at one time for the precipitator system: secondary bushing voltages, secondary bushing currents, line voltages, line currents, unit power consumption, and the status of each transformer/rectifier:

a. Unit "TRIPPED" - designated by flashing background.

b. Unit "OFF" - designated by red background.

c. Unit "OUT OF SERVICE" - designated by blue background.

The Supervisor CRT will display all of the following for each Local AVC Unit: secondary voltage, secondary current, line voltage, line current, unit power consumption, voltage drop counter, operation status.

In the system display mode, the total system can be placed in service, taken out of service, placed in system start-up or shutdown mode.

In the individual local AVC display mode, all functions of the Local Unit are available at the supervisor control.

The Supervisor has complete facility for data acquisition; system or local unit history, voltage/current relationships for local units, historical trends for all basic parameters can be tabulated, plotted, printed on the data logger or transferred to the portable storage media.

In addition to the data acquisition facility, reference information can be stored. Operating and maintenance instructions can be stored and displayed on the CRT as required. Trouble diagnostic guides can be stored in the form of logic diagrams to assist in maintenance and trouble shooting of the equipment. Maintenance schedules, records and replacement parts lists can be stored to provide a permanent record.

SUPERVISOR TELEPHONE MODEM

The Supervisor Telephone Modem gives the system the ability to communicate with a remote supervisor console located in a utility's main office or the precipitator supplier's home office such as here in Houston (Figure 8).

At this location, which may be several thousands of miles from the plant, the precipitator can be monitored and adjusted if required. The availability of accurate and instantaneous operating data to precipitation engineers located in the home office allows technical support to be given to plant engineers for speedy correction of any operational problems which may develop.

CONTROL ROOM MONITOR

The Control Room Monitor is a color CRT and keyboard, and is the boiler shift operator interface to the system. The information displayed allows the operator to see the status of all the precipitator controllers at a glance. The control functions at this station are limited. The system can be turned on or off, tripped sections can be reset, and placed in or out of the start-up/shutdown mode.

Switches are provided for system and Local Unit control. Four of these are control, namely: "system on", "system off", "start-up/shutdown" and "opacity control", as provided on the supervisor.

The remaining five control the information displayed on the CRT. The standard mode of display is the kV of each section, but any one of the five parameters: kilovolts, millamperes, line voltage, line amperes and kilowatts, can be displayed in the same format.

In addition, when the operator moves the cursor arrow to a section on which he wants more detailed information and activates the cursor switch, the CRT will display all parameter readings specific to that section, together with a listing of additional control functions, such as automatic, manual, raise, lower, manual rapping, which are also cursor activated.

If a Local Unit is off line for any reason, this will be noted on the CRT and the duration of failure will also be displayed. The last set of meter readings, prior to the trip, will be retained until the unit is returned to operation.

SUMMARY

A microprocessor based precipitator control system, such as outlined above, has many features not formerly available. One of these is the ability to control transformer/rectifier power through the use of an opacity feedback signal.

While maintaining constant opacity economies in power consumption can result when:

a) Particulate properties are more favorable to precipitation than those on which the precipitator design was based.

b) Reduction in the gas flow rate to the precipitator occurs.

While power economy is functionally available, the ramifications of such a control philosophy must be thoroughy investigated by the owner to ensure that it is environmentally acceptable.

The work described in this paper was not funded by the U. S. Environmental Protection Agency and, therefore, the contents do not necessarily reflect the views of the Agency and no official endorsement should be inferred.

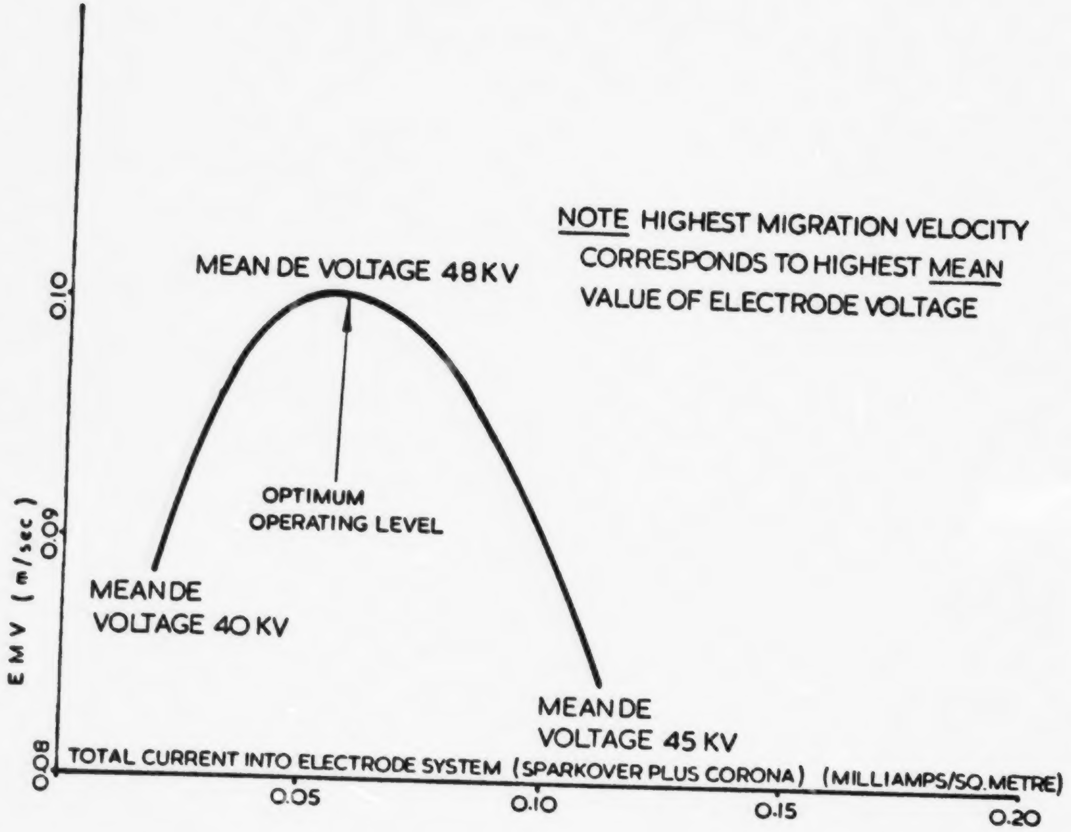

Figure 1. Effect of Power Input to Electrode System on Effective Migration Velocity

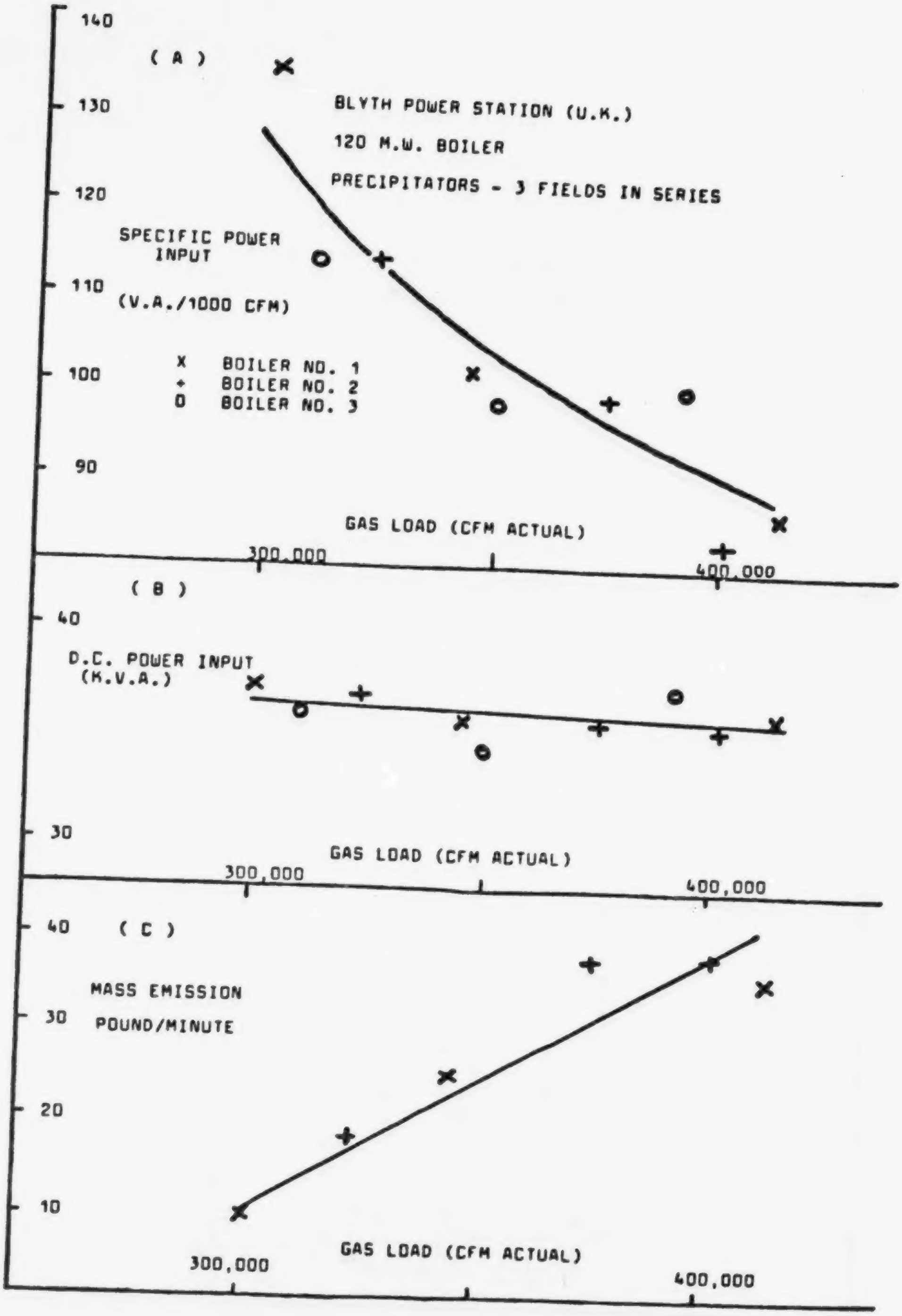

Figure 2. Effect of Varying Gas Load on Ash Emission and Precipitator Power

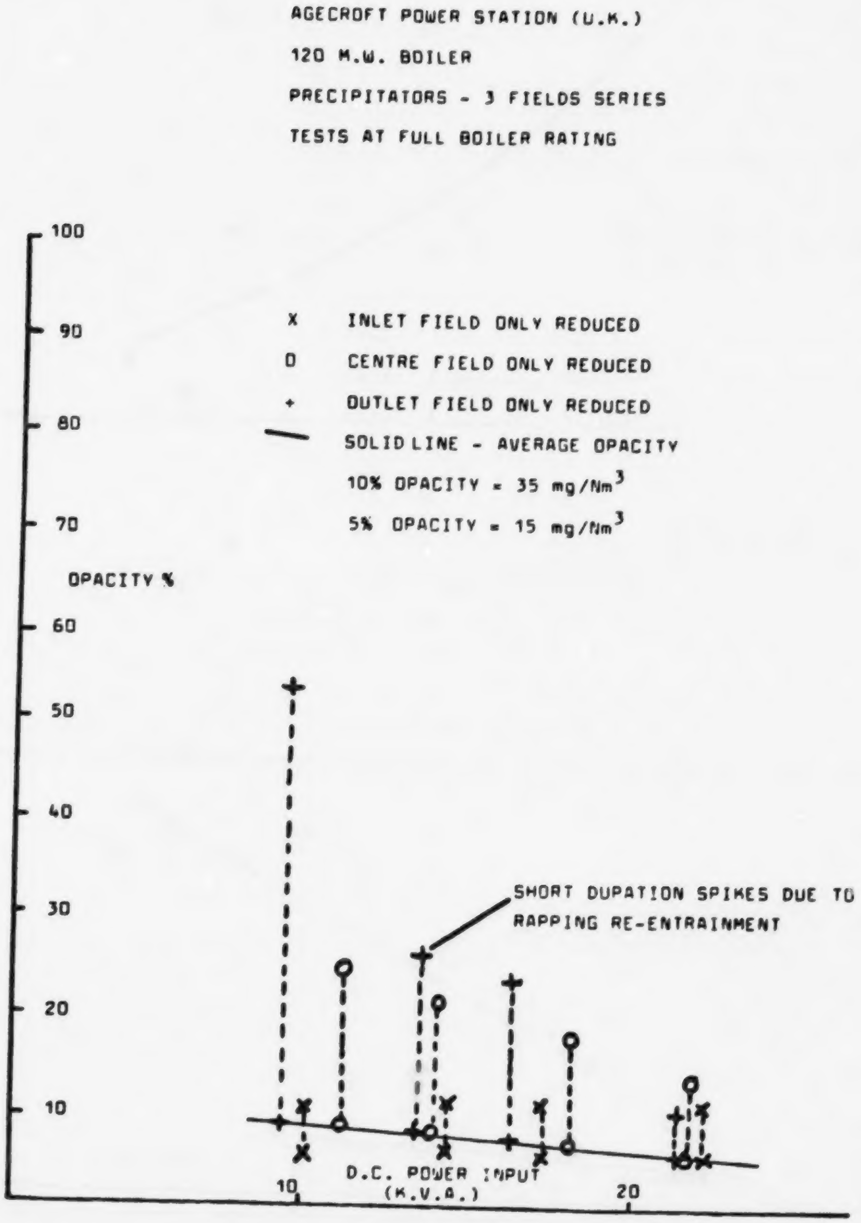

Figure 3. Effect on Stack Opacity of Reducing Power Input to Fields

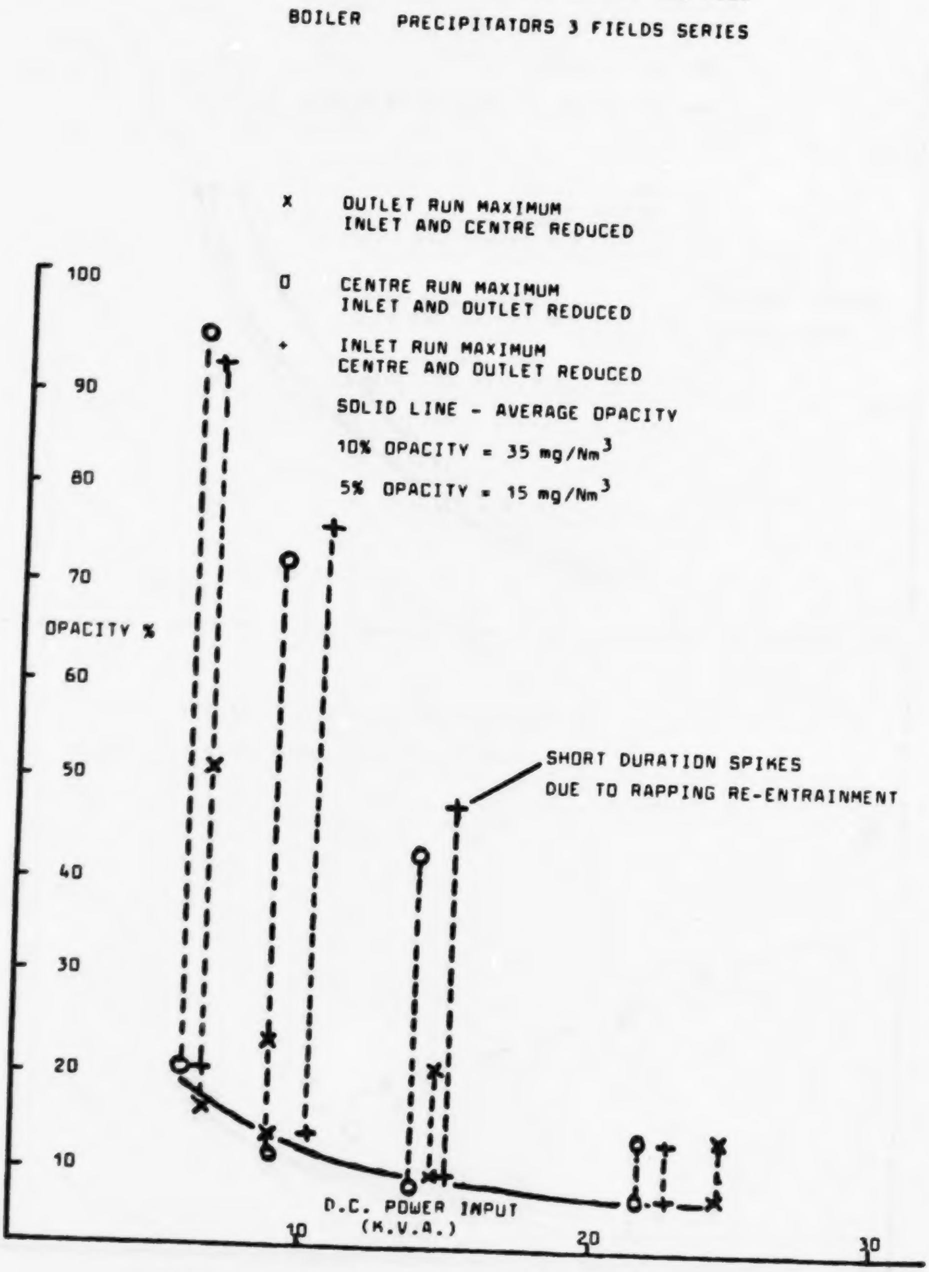

Figure 4. Effect on Opacity of Reducing Power Input to Fields

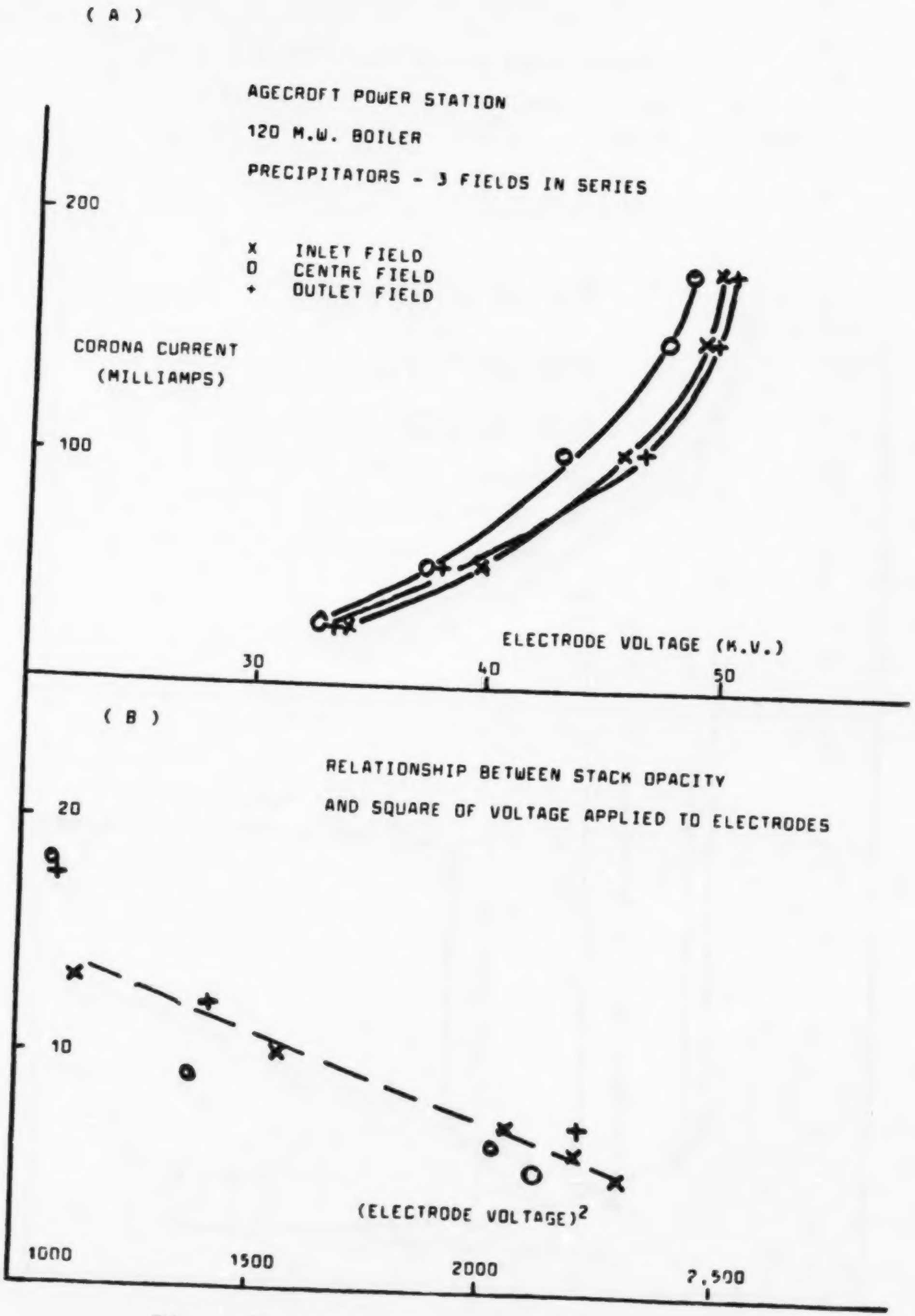

Figure 5. Voltage - Current Relationship

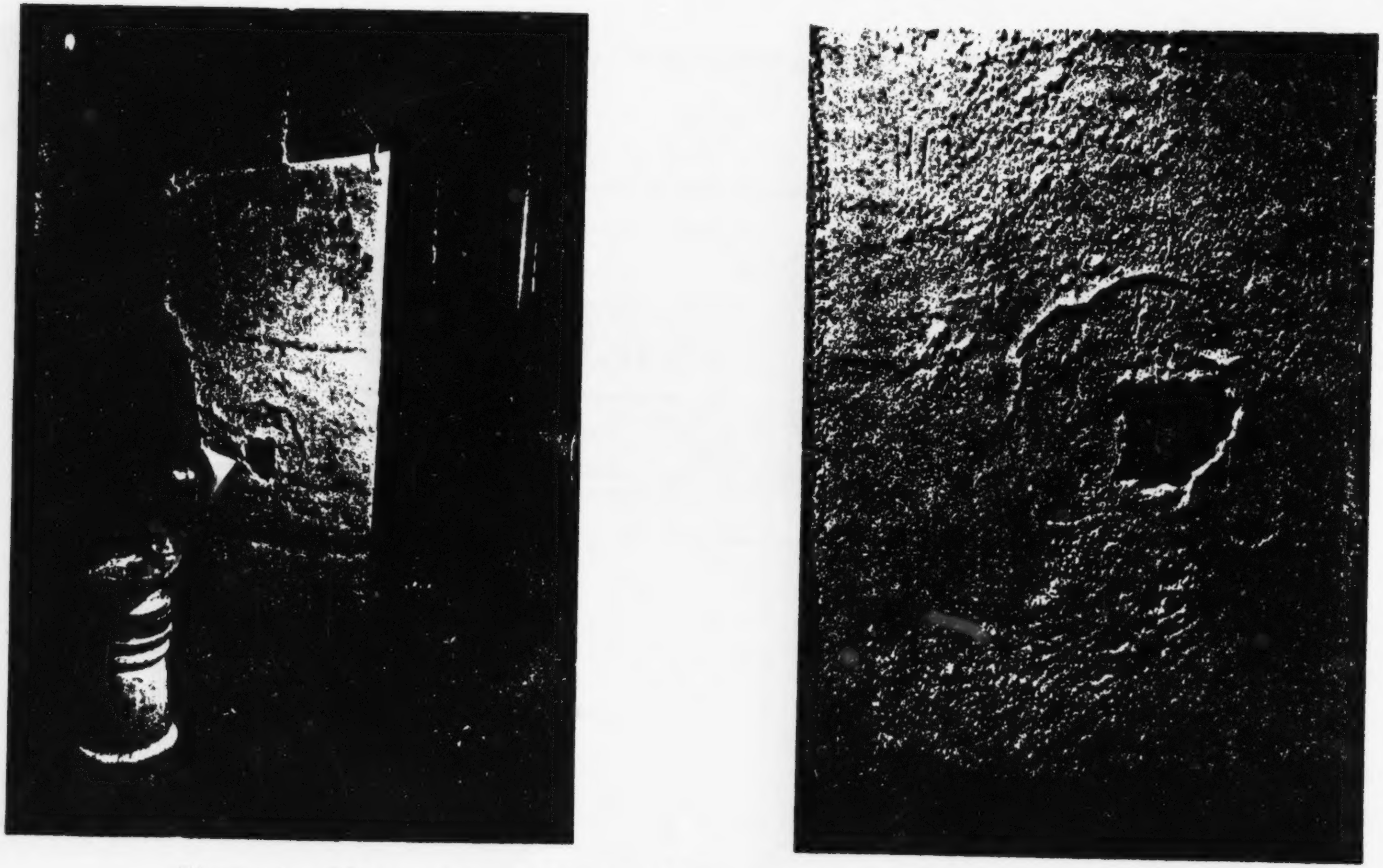

Figure 6. Effect of Spark Over on Electrostatically Deposited Ash Layer

Reproduced from best available copy.

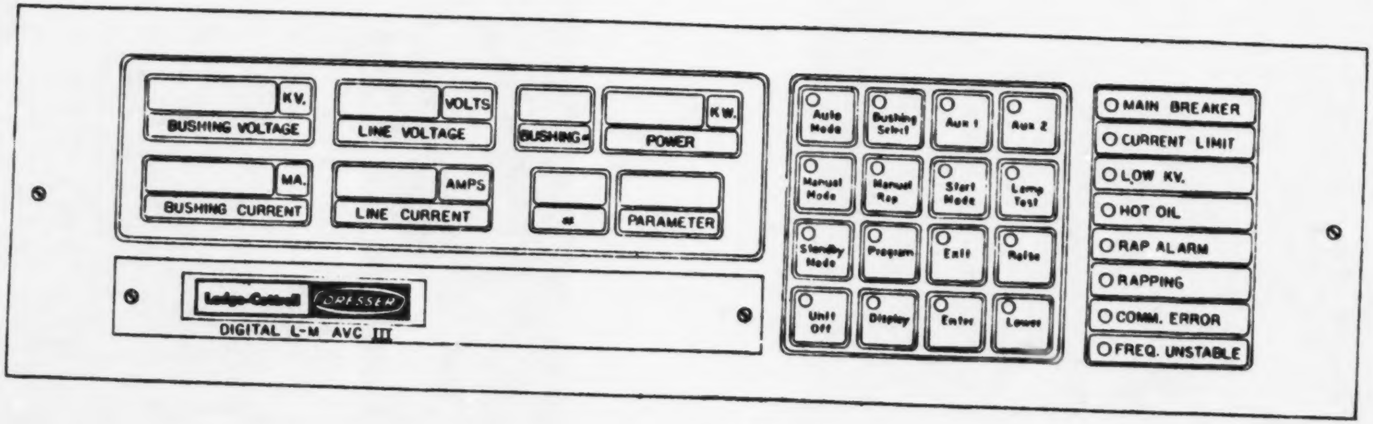
KV.
BUSHING VOLTAGE
MA.
BUSHING CURRENT
VOLTS
LINE VOLTAGE
AMPS
LINE CURRENT
BUSHING
KW.
POWER
#
PARAMETER
Lodge-Cottrell
DRESSER
DIGITAL L-M AVC III
Auto Mode
Bushing Select
Aux 1
Aux 2
Manual Mode
Manual Rap
Start Mode
Lamp Test
Standby Mode
Program
Exit
Raise
Unit Off
Display
Enter
Lower
MAIN BREAKER
CURRENT LIMIT
LOW KV.
HOT OIL
RAP ALARM
RAPPING
COMM. ERROR
FREQ. UNSTABLE

Figure 7. Local Panel Display

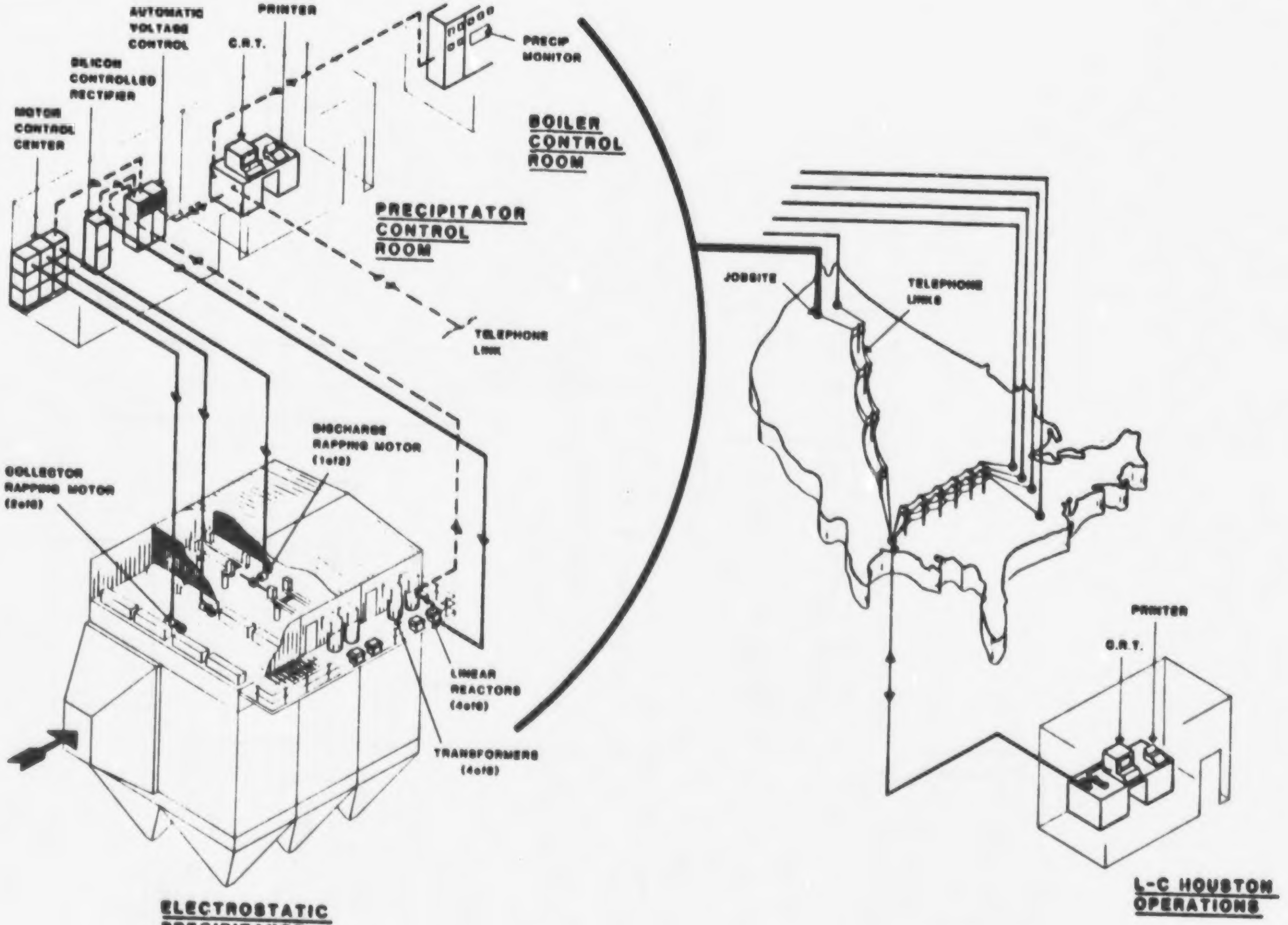
AUTOMATIC VOLTAGE CONTROL
PRINTER
C.R.T.
PRECIP MONITOR
SILICON CONTROLLED RECTIFIER
MOTOR CONTROL CENTER
BOILER CONTROL ROOM
PRECIPITATOR CONTROL ROOM
TELEPHONE LINK
JOBSITE
TELEPHONE LINKS
DISCHARGE RAPPING MOTOR (1of2)
COLLECTOR RAPPING MOTOR (2of8)
LINEAR REACTORS (4of8)
TRANSFORMERS (4of8)
PRINTER
C.R.T.
ELECTROSTATIC PRECIPITATOR
L-C HOUSTON OPERATIONS

Figure 8. AVC System Loop Diagram

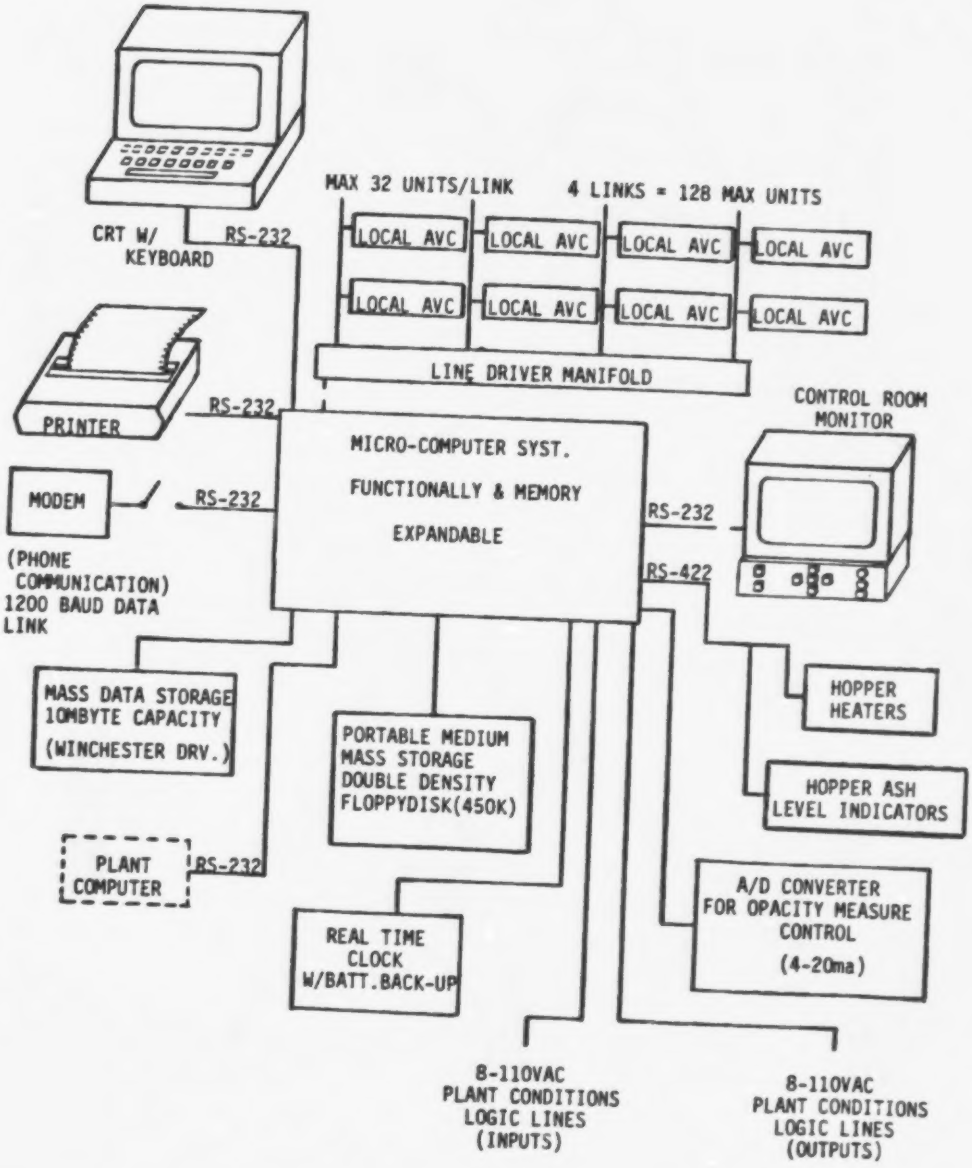
CRT W/ KEYBOARD
RS-232
MAX 32 UNITS/LINK
4 LINKS = 128 MAX UNITS
LOCAL AVC
LOCAL AVC
LOCAL AVC
LOCAL AVC
LOCAL AVC
LOCAL AVC
LOCAL AVC
LOCAL AVC
LINE DRIVER MANIFOLD
PRINTER
RS-232
MICRO-COMPUTER SYST.
FUNCTIONALLY & MEMORY
EXPANDABLE
CONTROL ROOM MONITOR
RS-232
RS-422
MODEM
RS-232
(PHONE COMMUNICATION) 1200 BAUD DATA LINK
MASS DATA STORAGE 10MBYTE CAPACITY (WINCHESTER DRV.)
PORTABLE MEDIUM MASS STORAGE DOUBLE DENSITY FLOPPYDISK(450K)
HOPPER HEATERS
HOPPER ASH LEVEL INDICATORS
PLANT COMPUTER
RS-232
A/D CONVERTER FOR OPACITY MEASURE CONTROL (4-20ma)
REAL TIME CLOCK W/BATT.BACK-UP
8-110VAC PLANT CONDITIONS LOGIC LINES (INPUTS)
8-110VAC PLANT CONDITIONS LOGIC LINES (OUTPUTS)

Figure 9. Supervisor System Hardware

APPLYING MODULAR MICROCOMPUTER CONTROL ELEMENTS IN A PRECIPITATOR CONTROL SYSTEM

by: Ira M. Wexler
Environmental Elements Corporation
Baltimore, Maryland 21203

ABSTRACT

The declining cost of microcomputers allows the control designer to implement microcomputers into individual components of a precipitator control system. This distributed processing technique allows the integration of the individual controls with a master computer, and also provides the controls with intelligence required to operate independently, should the need arise. The individual microcomputer elements used to control transformer/rectifiers, rapping systems and alarm systems are described. Techniques used to integrate these elements with a master precipitator controller providing data acquisition, energy management, and control optimization are also defined. In addition, a fail-safe operating philosophy which takes advantage of the intelligence designed into the individual controls is presented. Finally, the impact of this technology on the end user is discussed, using an actual installation at a utility boiler.

INTRODUCTION

In a precipitator control environment, where reliability is a paramount consideration, the application of digital microcomputer hardware and software must be carefully thought out. In addition, a well designed control system should supply the plant operator with confidence in its operation and maintainability.

This paper presents the implementation of such a system by describing the individual control elements involved and the techniques and philosophies used to integrate the elements into an intelligent, user-friendly, reliable system.

These techniques and philosophies have been proven to be successful by five years of field experience with several hundred microcomputer based controls in operation.

HISTORICAL BACKGROUND

Prior to 1976, only analog type precipitator controls were in service. The emergence of the microcomputer spurred a development effort to incorporate the microcomputer intelligence into a precipitator control. The result of this first effort was the DIGICON Automatic Power Controller, used to control the power to an individual Transformer-Rectifier set. The next logical step in the development was the OPTI-CON II Data Management System, to be used as a Master precipitator control. Concurrently, the Intelligent Rapper Control and the Intelligent Peripheral Controller were developed.

INTELLIGENT CONTROL ELEMENT DESIGN PHILOSOPHIES

The design of microcomputer based equipment for precipitator controls requires special consideration. The equipment which will be subsequently discussed utilizes the following criteria:

1. The equipment is designed specifically for use in precipitator control applications, rather than an adaptation or modification of off-the-shelf programmable controllers or minicomputers.

2. All operating programs in the intelligent control elements are stored in non-volatile EPROM (erasable programmable read only memory). This means that the operating program is resident on a semiconductor "chip" in each element. The data is always available and is retained on power loss. The advantages of this method are legion. First, no programming knowledge is required by plant personnel, since the programs have already been qualified and developed. Secondly, program loading from cassettes, floppy diskettes or other media and the unreliability associated with them are completely eliminated. Lastly, the operating programs can still be process adaptive by using temporary volatile (read-write) memory for the storage of certain data. A sustained power loss will erase this information, but the program in the EPROM will replace it with default values on power-up, permitting continued operation without plant operator intervention.

3. All hardware is designed specifically to operate in an industrial environment, freeing the control designer from the restrictions of air conditioned atmospheres and conditioned power lines.

4. Incoming power and data lines are hardware protected from voltage transients typically encountered in an industrial location.

5. Linear (as opposed to switching) power supplies are used, which have been designed to permit a power loss of up to 100 milliseconds with no discontinuity in operation. Operation after longer power losses is self-recovering, as described above.

6. Error detecting and correcting software is used to protect against system control loss as a result of garbled or erroneous data.

7. During power-up, each microcomputer element will run thru a self check program. If a problem is found, an indication is given to the operator.

EQUIPMENT DESCRIPTION

INTELLIGENT T/R CONTROL ELEMENT

The intelligent T/R (Transformer Rectifier) control element consists of the following equipment housed in a NEMA 12 control cabinet (Figure 1):

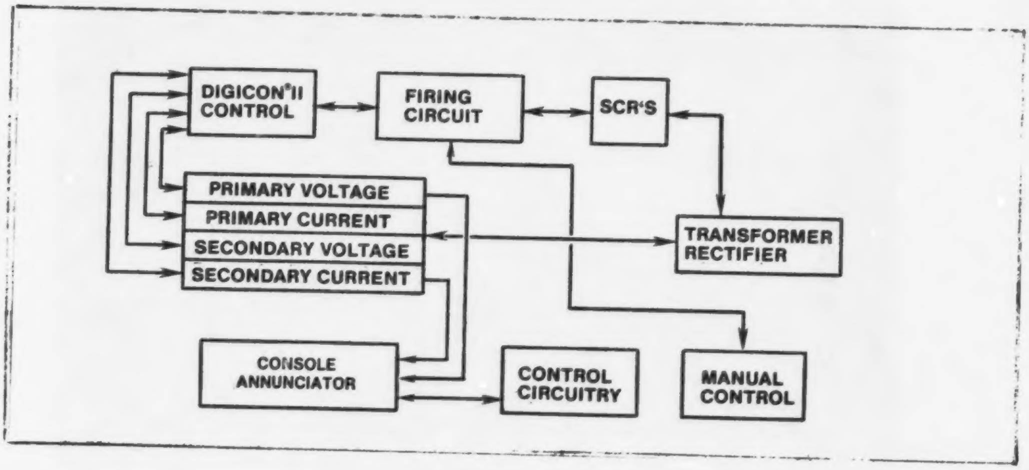
DIGICON®II CONTROL
FIRING CIRCUIT
SCR'S
PRIMARY VOLTAGE
PRIMARY CURRENT
SECONDARY VOLTAGE
SECONDARY CURRENT
TRANSFORMER RECTIFIER
CONSOLE ANNUNCIATOR
CONTROL CIRCUITRY
MANUAL CONTROL

FIGURE 1
CONTROL CONSOLE BLOCK DIAGRAM

1. An SCR (Silicon Controller Rectifier) package used to regulate the power supplied to the T/R.

2. T/R analog metering circuitry and low voltage control, switching, and alarm circuitry.

3. The DIGICON^{R} II Automatic Power Controller (Figure 2). This unit, housed in a NEMA 12 type enclosure, monitors the primary and secondary voltage and current associated with the T/R and controls the power applied to the T/R as a function of its operating software (program). In addition, a serial communications link is provided to the OPTI-CON^{TM}-II Data Management System Controller, which is used to provide the exchange of information between both units. Indicator lights and thumbwheel switches on the Automatic Power Controller provide the necessary interaction with the plant operator.

4. The Control Console Annunciator. This microcomputer based device, which operates independently of the Automatic Power Controller, actually performs several functions. First, the spark rate is counted and displayed on a three digit display. Secondly, the annunciator monitors the control operation for overspark and undervoltage conditions, and finally the unit annunciates the various control console trip mechanisms (overcurrent, T/R high temperature) on the three digit display. In addition, this device also contains a serial communications link to the Data Management System Controller.

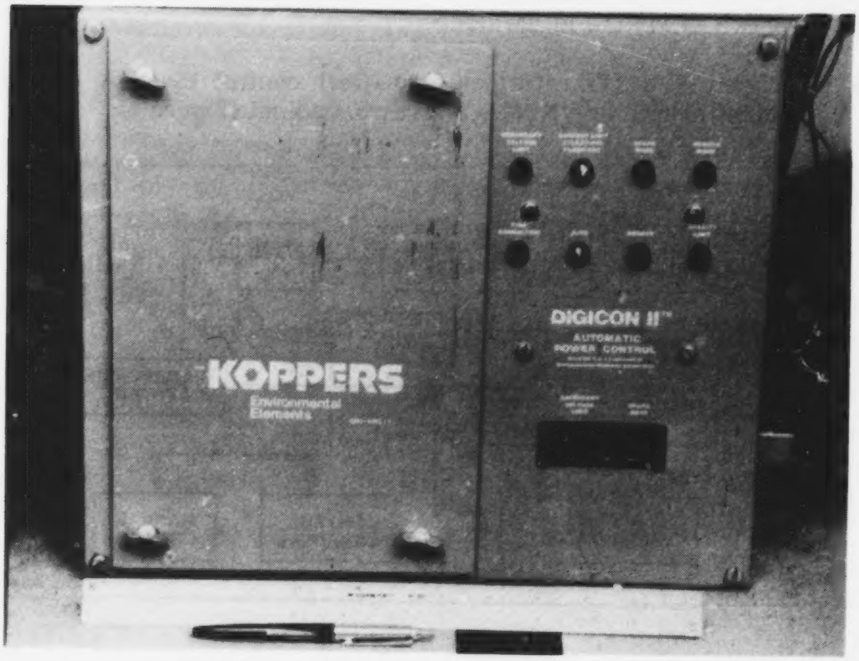

FIGURE 2
AUTOMATIC POWER CONTROLLER

INTELLIGENT RAPPER CONTROL ELEMENT

The Rapper Control Element consists of the following equipment housed in a NEMA 12 control cabinet, mounted on or near the precipitator roof:

1. Power conversion circuitry to supply the proper voltages and currents to fire the rappers. The circuitry is configured such that various types of rapping devices (such as pneumatic, electric, and motor drives for mechanical rapping) can be intermixed in the same control cabinet.

2. Digital switches and indicators used to select the rapping intervals and intensities and display the status of the system.

3. A microcomputer element to control the timing sequences and single out faulted rappers on an individual basis.

4. A serial communications link to the Data Management System Controller used to report the status of the rapper controller and accept changes to timing and intensity parameters.

INTELLIGENT PERIPHERAL CONTROL ELEMENT

In a precipitator control environment, it may be desirable to monitor or integrate related control parameters (such as temperature, contact closures, pressures, or other analog data) into the system.

For example, hopper level indicators, flue gas temperatures or any number of parameters may be monitored and displayed on the CRT and line printer. Another example would be the use of a hopper temperature differential measurement to control a screw conveyor motor.

If the number of peripheral points is small (less than 16), this function is carried out in the Data Management System Controller. However, if a large number of points are to be monitored, or if one or more complex control loops are involved, control is delegated to an intelligent peripheral control element.

This element consists of its own microcomputer, an operating program in EPROM, signal conditioning circuitry, and a serial communications link to the Data Management System Controller.

DATA MANAGEMENT SYSTEM CONTROLLER

All of the previously discussed control elements are connected by their serial communication links to the Data Management System Controller. Figure 7 presents a block diagram of the entire system. This device, also housed in a NEMA 12 type enclosure, consists of the following: (Figures 3 thru 6)

1. A serial communications link to a CRT (Cathode Ray Terminal) and a printer. The latter devices are used to display, record, and change data relating to precipitator control thru simple commands.

2. A serial communications link to a modem, which, at the plant operator's discretion can transfer control to a remote location thru the telephone lines. A monitoring facility in Baltimore is presently in use to assist customers with precipitator troubleshooting by using telephone access to the Data Management System at the customer's location.

3. An optional communications link to the customer's plant computer. When this link is used, the Data Management System becomes an intelligent "front end" for the precipitator, allowing the plant computer access to the commands and information used in the Data Management System.

4. Operating programs in EPROM which perform the following functions:

    a. Processes and formats the data gathered from the intelligent control elements and displays it on the CRT.

    b. Allows the plant operator to alter various parameters (such as rapping cycle times, T/R control, etc.) using the CRT.

    c. Periodically instructs the printer to record selected data. (Figure 8)

    d. Integrates stack transmissometer data with the precipitator control elements to define an energy management control algorithm.

    e. Supervises the operation of peripherals connected to the intelligent peripheral control element.

Although it may appear that this Data Management System Controller is the heart of the control system, it is important to remember that the rest of the control elements can operate independently due to their inherent intelligence. The next section describes the philosophies used to integrate the individual control elements into an intelligent system.

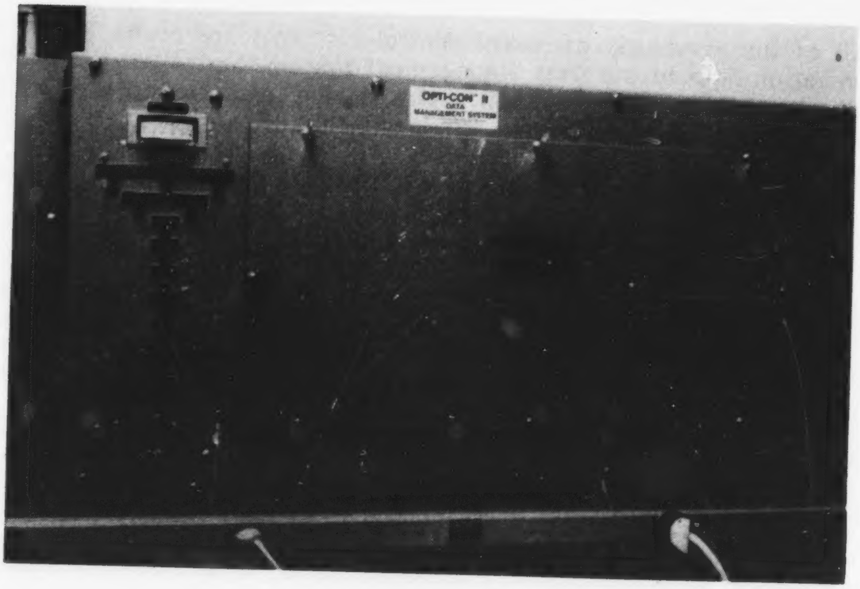

FIGURE 3
DATA MANAGEMENT SYSTEM CONTROLLER

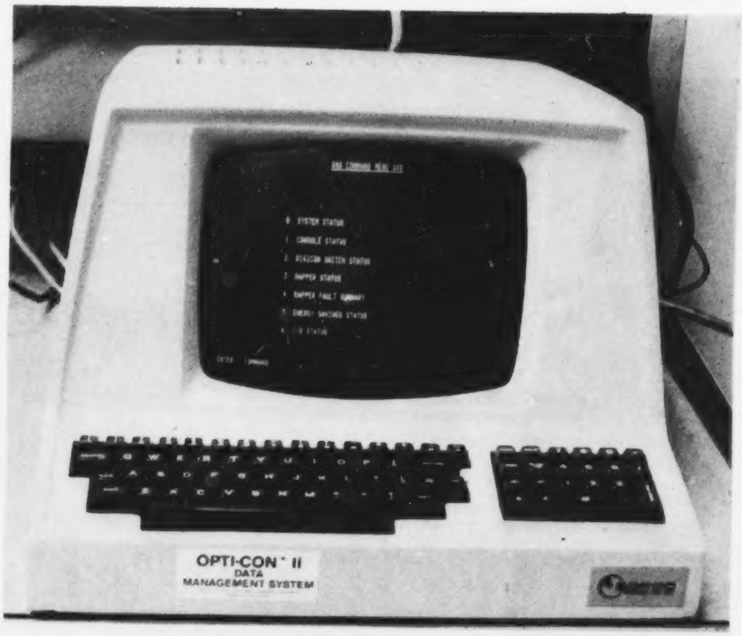
OPTI-CON™ II
DATA
MANAGEMENT SYSTEM

FIGURE 4
OPERATOR CRT TERMINAL

OPTI-CON™ II
DATA
MANAGEMENT SYSTEM

FIGURE 5
DATA MANAGEMENT SYSTEM PRINTER

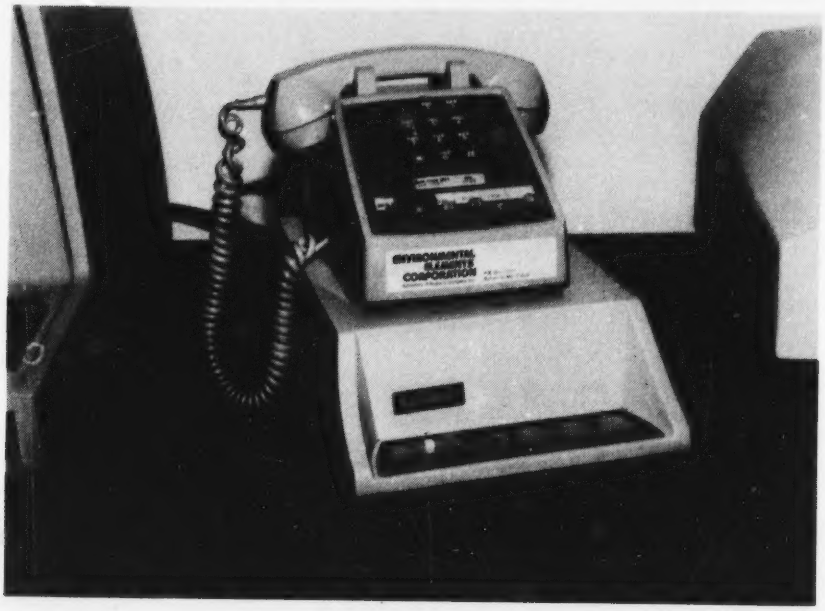
ENVIRONMENTAL ELEMENTS CORPORATION

FIGURE 6
TELEPHONE MODEM

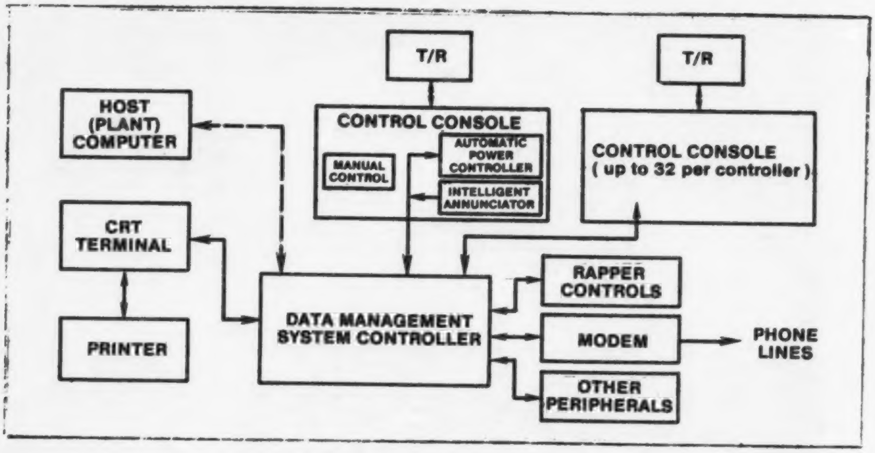
T/R
T/R
HOST (PLANT) COMPUTER
CONTROL CONSOLE
MANUAL CONTROL
AUTOMATIC POWER CONTROLLER
INTELLIGENT ANNUNCIATOR
CONTROL CONSOLE (up to 32 per controller)
CRT TERMINAL
PRINTER
DATA MANAGEMENT SYSTEM CONTROLLER
RAPPER CONTROLS
MODEM
OTHER PERIPHERALS
PHONE LINES

FIGURE 7
PRECIPITATOR BLOCK DIAGRAM

INTELLIGENT SYSTEM DESIGN PHILOSOPHIES

Integrating the intelligent control elements into a reliable system again requires careful consideration. When reliability is important, it is imperative that the malfunction of a control element will not cause either a snowball or domino effect or a gross system failure. The following techniques have been employed in the OPTI-CON II Data Management System to carry out these requirements:

1. Each control element in the system can operate independently, as a result of its inherent individual microcomputer intelligence.

2. Fail-safe mechanisms are incorporated in system software. No hardware handshaking lines are employed, since such lines could fail in a manner to indicate normal operation. The use of software watch-dog timers, and periodic enquiry-response exchanges provide a true fail-safe mode of operation.

   An analogy to this philosophy can be illustrated by two people using a telephone. The absence of a dial tone (handshaking line) would normally indicate that someone is on the line. If this were the only indication of a connection and if the telephone hardware should fail, both people would wait forever for communication. However, each party would realize (due to their inherent intelligence) that the absence of a voice response indicates a malfunction. The people would hang up and go about their normal business.

3. System data is checked for parity, framing and overrun errors to insure integrity.

4. The system is configured in a star pattern; data highways are not used. The failure or degradation of no single cable can cause system failure. Refer to Figure 7.

5. System data is transferred serially in an RS422 format. This format provides high speed, long distance transmission and possesses high noise immunity. Data cables require no special conduit runs and may be placed in cable trays with 480V power wiring.

USER FRIENDLINESS AND MAINTAINABILITY

To gain acceptance, an intelligent system must provide ease of understanding, operation, and maintainability. The following techniques are used to implement these objectives:

1. Since all programming is intact in EPROM, the plant operator is relieved from this task. Flexibility is still maintained, however, by allowing the operator simple commands to alter system operation. For example, the energy-savings mode may be enabled or disabled by a single keystroke command. As another example, rapping cycle times may be changed by a simple sequence of keystrokes.

2. The CRT-operator interaction is menu driven. The operator selects desired information from a menu of available displays and commands. Refer to Figure 9 and 10.

3. Operator generated commands into the system are checked and error trapped, thus preventing the entry of unrealistic or false parameters into the system.

4. Printouts of data on a periodic or demand basis are provided to aid in record keeping. Figure 8 is a typical display from an operating salt cake recovery precipitator.

5. Equipment is designed to be repaired by the substitution of modular circuit boards. No special diagnostic equipment or skills are needed.

6. To insure added reliability, all major system elements are burned in for a minimum of 100 hours.

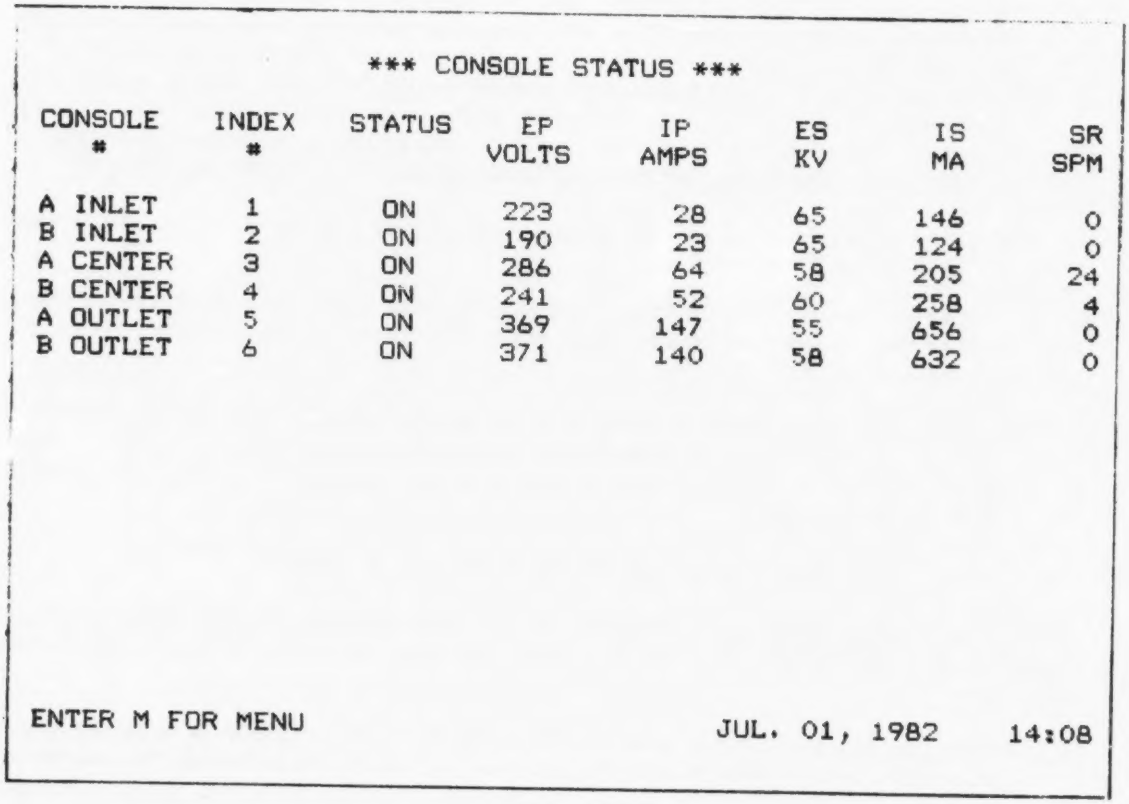

```
                         *** CONSOLE STATUS ***

CONSOLE     INDEX    STATUS     EP        IP       ES       IS      SR
   #          #               VOLTS      AMPS      KV       MA      SPM

A INLET       1        ON       223        28      65      146       0
B INLET       2        ON       190        23      65      124       0
A CENTER      3        ON       286        64      58      205      24
B CENTER      4        ON       241        52      60      258       4
A OUTLET      5        ON       369       147      55      656       0
B OUTLET      6        ON       371       140      58      632       0









ENTER M FOR MENU                             JUL. 01, 1982    14:08
```

FIGURE 8
PRINTOUT OF CONTROL CONSOLE DATA
FROM A SALT CAKE PRECIPITATOR

```
                    *** COMMAND MENU ***


       0. SYSTEM STATUS

       1. CONSOLE STATUS

       2. DIGICON SWITCH STATUS

       3. RAPPER STATUS

       4. RAPPER FAULT SUMMARY

       5. ENERGY SAVINGS STATUS

       6. I/O STATUS


       ENTER COMMAND ?
```

FIGURE 9
DATA MANAGEMENT SYSTEM COMMAND MENU

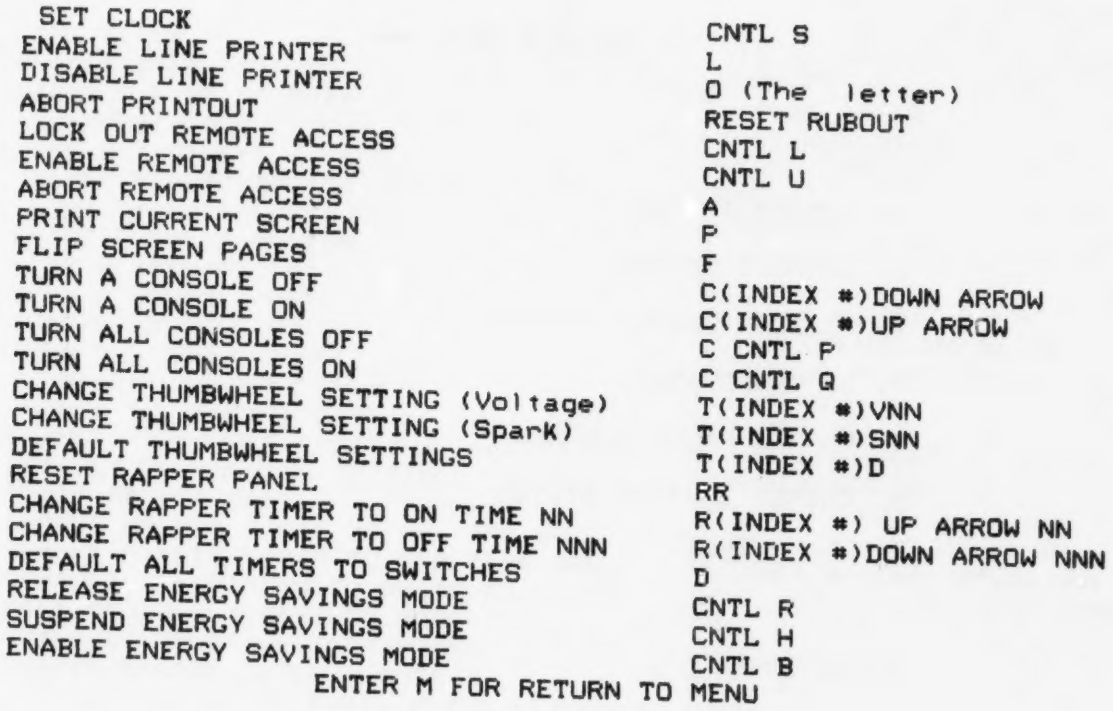

```
 SET CLOCK                                      CNTL S
ENABLE LINE PRINTER                             L
DISABLE LINE PRINTER                            O (The  letter)
ABORT PRINTOUT                                  RESET RUBOUT
LOCK OUT REMOTE ACCESS                          CNTL L
ENABLE REMOTE ACCESS                            CNTL U
ABORT REMOTE ACCESS                             A
PRINT CURRENT SCREEN                            P
FLIP SCREEN PAGES                               F
TURN A CONSOLE OFF                              C(INDEX #)DOWN ARROW
TURN A CONSOLE ON                               C(INDEX #)UP ARROW
TURN ALL CONSOLES OFF                           C CNTL P
TURN ALL CONSOLES ON                            C CNTL Q
CHANGE THUMBWHEEL SETTING (Voltage)             T(INDEX #)VNN
CHANGE THUMBWHEEL SETTING (Spark)               T(INDEX #)SNN
DEFAULT THUMBWHEEL SETTINGS                     T(INDEX #)D
RESET RAPPER PANEL                              RR
CHANGE RAPPER TIMER TO ON TIME NN               R(INDEX #) UP ARROW NN
CHANGE RAPPER TIMER TO OFF TIME NNN             R(INDEX #)DOWN ARROW NNN
DEFAULT ALL TIMERS TO SWITCHES                  D
RELEASE ENERGY SAVINGS MODE                     CNTL R
SUSPEND ENERGY SAVINGS MODE                     CNTL H
ENABLE ENERGY SAVINGS MODE                      CNTL B
                 ENTER M FOR RETURN TO MENU
```

FIGURE 10
COMMAND REFERENCE DISPLAY

RESULTS

The first OPTI-CON system was installed on a flyash precipitator in a power plant application 2 1/2 years ago. (Microcomputer based Automatic Power Controllers have been in the field for 5 1/2 years). In this application, the boiler experienced varying loads, due to seasonal and usage demands. The customer conducted an evaluation program of energy savings during several months of OPTI-CON system operation. The following results were obtained:

1. The average daily power savings were 125HP/hour or 93 KWH.
2. The yearly savings amounted to $30,720, based on a power cost of $.04/KWH
3. The present worth of a 125 HP savings amounted to $125,000 based on escalating fuel costs of 7% per year.

Other systems are presently in operation at several other locations, and feedback has been positive both in operation and reliability aspects.

SUMMARY AND CONCLUSIONS

From the previous discussions, it can be seen that the use of individual modular intelligent control elements constitutes a reliable and versatile method of precipitator control. Proper hardware and software design philosophies also reinforce system integrity and produce reliable, intelligent and cost effective solutions in precipitator control.

The work described in this paper was not funded by the U.S. Environmental Protection Agency and therefore the contents do not necessarily reflect the views of the Agency and no official endorsement should be inferred.

This work was funded by Environmental Elements Corporation which accepts total responsibility for its contents. No official endorsement by any govermental organization is either sought or desired.

THE CURRENT STATUS, FUTURE DIRECTIONS, AND ECONOMIC CONDITIONS IN THE APPLICATIONS OF ESP's

Sabert Oglesby
Southern Research Institute
Birmingham, Alabama 35255

The subject I have been asked to address today is the current status, future directions, and economic considerations in the application of electrostatic precipitators. By current status, I assume is meant the type of equipment that would be offered in response to a bid invitation today for various dust control applications. In the U. S., the majority of electrostatic precipitators offered today are of the conventional design with standard weighted-wire or rigid-frame electrodes, conventional 10-12 inch plate spacing and power supplies of conventional design. There is a decided trend in this country toward greater use of rigid-frame discharge electrodes and flail-hammer rappers of the type commonly used in European installations. Power supplies are conventional, but there are a variety of types of control systems currently offered. The trend in recent years has been toward faster response and greater reliability in the control circuitry.

There are a number of exceptions to the more or less conventional installations. In Europe and Japan there have been a number of precipitators installed with wider than normal plate spacing. The practice in Europe began in the cement industry, where aluminum plates were installed to minimize corrosion from the alkali-laden gases from a cement kiln. Inlet sections were made with normal spacing and downstream sections were wider than normal to reduce the cost of collection electrodes. There are also some wide-plate precipitators installed in Japan.

The greatest advancement that has been made in electrostatic precipitator technology in the past 10-12 years has been in better applications. For the most part, the practice of using catalogs of migration velocity values to arrive at the size precipitator required to meet a given level of emission has largely been overcome. Both manufacturers and users have become much more sophisticated in the sizing process, and considerable effort goes into characterizing the effluents to insure that emission limits will be met. I don't have any figures to back up the contention, but based on our observations, one can be reasonably well assured that present-day ESP installations will perform within their guarantee and operate reliably.

Precipitators can also more than meet the new source performance standards. Emissions of as low as .001 lbs/million BTU have been measured on an installation with an SCA of about 500 ft^2/1000 cfm.

Many new concepts for overcoming some limitations of electrostatic precipitator problems or enhancing precipitator performance are in either the research or advanced development stage, and many of these will be the subject of papers at this symposium.

The subjects being most widely discussed for advancements in electrostatic precipitators are conditioning to modify dust resistivity, pulsed power supplies, precharging, wide-plate spacing, microcomputer controls, alternative rapping schedules, and different electrode geometries. To these must be added advancements in fundamental knowledge of the precipitation process. Much progress has been made in recent years in developing equations to predict particle charging, electric field, and collection, and these have led to mathematical models which have been extremely useful in sizing and troubleshooting. Progress is continuing in this area as methods are developed for including electron charging, gas turbulence, and better information on reentrainment in the various models.

Conditioning to modify electrical resistivity is certainly not new. The first such installation reported in the literature was made by Cottrell to reduce the resistivity of smelter dust. However, there are some relatively new concepts in conditioning, such as addition of sodium compounds to coal to reduce resistivity of fly ash for hot-side precipitators, and the use of ammonia compounds to achieve better performance in some precipitators by reducing both resistivity and reentrainment or increasing the collection electric field by space charge enhancement.

For the most part, conditioning is resorted to for increasing the performance of an existing precipitator that was sized too small to collect a high resistivity dust or to accommodate a change in fuel supply or other factors that change the dust resistivity. Conditioning, however, is becoming much better accepted as systems become simpler and more reliable, and has reached a stage of development where it represents one option that can be more cost effective for new installations.

Pulsed power supplies have also been used primarily for upgrading an existing system, as opposed to being supplied as a part of a new installation. One of the major advantages cited for a pulsed power supply is that the number and uniformity of emitting points along the discharge electrode is increased, thereby resulting in a more uniform current density at the collection electrode. Also, it is suggested that back corona can be minimized because the pulses are short compared to the relaxation time of the dust layer. Both of these factors permit operation at higher electrical conditions, especially if the dust resistivity is high. It has been reported that improved electrical conditions achieved with pulsing can result in an increase in precipitation rate parameter by a factor of 2 for a high resistivity dust, but only a 10% or so improvement for lower resistivity dusts. Pulsed power supplies appear to have a definite possibility for some retrofit applications where the improved precipitation rate parameter can bring the system in compliance.

There is still some uncertainty as to how pulsed power supplies function to give increased performance. Measurements of particle charge show some increase with pulsed power, but not enough to account for the decreases in emissions. Further studies are planned to more precisely define the system parameters. Hopefully, pulsed systems can be designed to be cost effective and find their way into new precipitator installations.

Precharging represents another area of potential precipitator improvement. The concept of precharging is not new, but there are some new approaches. The potential advantage seems to be in the use of a combination precharger and modified downstream collector which has a low current, high field electrode system. The advantage of precharging is that a short precharging section can be used which permits some techniques to be utilized to overcome high dust resistivities that would be impractical for a full-sized precipitator. Precharging has also been suggested as a means of achieving a higher than normal charge on dust whether or not there is a resistivity problem. Examples of precharging systems include the tri-electrode charger being studied by Southern Research Institute under contract with EPA, a cooled electrode system being studied by Denver Research Institute, and the high-intensity ionizer system that was investigated by EPRI .

I suppose the jury is still out on the practicality of prechargers. There is no doubt of the correctness of the theory, but there may be some practical problems in their application. The tri-electrode precharger and the high-intensity ionizer have both proven that particles can be charged rapidly in a precharger. In the case of the HII, a discharge of the dust due to electrical breakdown seems to be a limiting factor in obtaining a higher than normal particle charge. The tri-electrode precharger does not attempt to put a higher charge than could be achieved when collecting a low-resistivity dust, and the system is not plagued with discharge problems. The concept of enhanced downstream collection by providing a low-current, high-field electrode system does give good results on a reasonably large (30,000 cfm) pilot-scale system.

There is considerable interest in wide-plate spacing for a number of applications, especially in other than inlet sections. From a theoretical standpoint, wide-plate spacing would enhance the space charge contribution to the field at the plate. This should increase collection efficiency about proportional to the increase in field. Another consideration is the more uniform current density that should be achievable with wider-spaced plates and the higher voltage that can be attained due to the diminished influence of electrode spacing variations. Additional studies are currently being planned to attempt to quantify the beneficial effects of wide-plate spacing and the conditions under which these benefits can be realized.

Use of microcomputers for many precipitator control functions is another new development that offers many possibilities for increased reliability and performance. Present day microcomputers are programmable to control voltage input to maintain optimum electrification. Because of the memory and adaptive capabilities, microcomputers can be programmed to maintain voltage and current at optimal values, thus improving performance over conventional analog control circuits. They can also be programmed to prevent development of power arcs and other disruptions that reduce reliability.

In addition to control of the TR sets, microcomputers can also be arranged to control rapping sequence, ash discharge schedules, and addition of flue gas additives for conditioning. Microcomputers can also be used to reduce energy consumption by optimizing the power input to meet opacity requirements.

Many of the advancements that have been made in precipitator technology in recent years have been in improved understanding of the fundamentals of the precipitation process. Particle-charging equations have been developed to a point that charge can be predicted with reasonable accuracy, except for higher temperature operation where electron charging is significant. Results of tests to determine charge on dusts exiting from full-scale precipitators agree quite well with calculated values using more recently developed charging equations. Similarly, electric field measurements show good agreement with calculated values for wire-plate electrode structures, and data are being accumulated to account for various other types of discharge electrodes. Considerable attention is also being given to collection mechanisms to account for turbulent diffusion and other factors that influence collection. All of these have been combined into precipitator mathematical models that have helped to define the operating conditions and assisted greatly in both sizing and analysis of precipitator performance.

One of the most significant advancements that has been made in recent years is in development of better methods for measuring and predicting dust resistivity, and in defining the conduction mechanisms. Of the problems associated with precipitators in the past, a very large percentage of them are associated with failure to recognize or account for high-resistivity dust. This problem has been greatly reduced with the development of better methods of predicting dust resistivity based on dust and flue gas composition.

The future of electrostatic precipitators for many applications is related to cost and reliability. Precipitator cost is a direct function of the plate area involved, and attempts to reduce costs must address the problems of reducing the collecting surface area. For low-resistivity dusts, the plate area requirements are minimal and precipitators constitute the most cost-effective means of particulate emissions control. However, for very high resistivities, large plate areas are required and alternative particulate control systems are likely to be more cost effective.

Economic factors are important considerations in the selection of the type of dust control equipment for a given application. Unfortunately, costs are highly variable, depending upon resistivity of the dust, extent of ductwork, size of hoppers, and other factors. Perhaps because of these variations, there have been relatively few definitive cost studies. A 1978 analysis by Stearns-Roger for EPRI showed costs ranging from about $19 to $32 per square foot of collecting area, the higher cost being associated with a small precipitator. These costs are for a complete system including ductwork, ash-handling equipment erection, and engineering. Costs, according to the Stearns-Roger study, are broken down into categories, with the precipitator and supports representing about 35-40% of the total, ductwork about 10-20%, and erection costs 35-40%. All other costs represent about 10% of the total. Since precipitator and erection costs represent 75-80% of the total, it is apparent that major cost reductions must come from reduced precipitator size.

As a general rule, electrostatic precipitators are competitive with fabric filters at specific collecting surface areas of up to around 600 ft^2/1000 cfm.

The competitive position of precipitators is influenced by a number of factors, including interest rates, energy costs, and labor costs. Precipitators have the advantage of lower energy consumption and lower maintenance costs. From a cost standpoint, the major disadvantage is the higher first cost. This has to be offset by reduced operating costs in order to remain competitive.

I have alluded to several developments that are currently being studied and to some extent applied to full-scale precipitators. These represent reasonably near-term developments that should become state-of-the-art for many applications, assuming they are successful.

In the longer term, there are a number of areas for precipitator improvement. These constitute those areas where precipitators are constrained to operate at less than theoretical limits. One example is the electrical operating conditions. Theoretically, breakdown of the dust layer would occur at much higher currents than present limits. One of the reasons for this limit is the non-uniformity of current density. In negative corona, maximum current occurs opposite a corona tuft. If a more uniform corona can be developed, much higher electrical operating conditions can be maintained. Pulsed power supplies reportedly achieve a greater uniformity, but there may be possibilities for achieving this uniformity at less cost through shaping of conventional waveforms or through electrode design.

Another area of potential development is in tailoring charging and collection sections to achieve optimum collection. Most present-day precipitators have the same electrode structure throughout. By tailoring a section to maintain a high field at low current just beyond a charging region, much better collection rates might be achieved.

Finally, more attention should be given to reducing rapping losses. In a typical precipitator, reentrained dust, primarily from the last field, amounts to something around 30 to 70% of the emission. A substantial reduction in reentrainment would markedly improve precipitator performance.

It is improvements such as these that may substantially reduce precipitator sizes required, and in turn affect precipitator costs and their competitive position for particulate control.

AUTHOR INDEX

AUTHOR NAME PAGE

ADAIR, L. I-460
ADAMS, R.L. II-35
ANDO, T. II-474
ARMSTRONG, J. III-241
ARSTIKAITIS, A.A. II-194
BALL, C.E. III-370
BANKS, R.R. I-37, I-62
BARRANGER, C.B. I-132
BAYLIS, A.P. II-384
BELTRAN, M.R. II-51
BENSON, S.A. III-97
BERGMAN, F. III-154
BIESE, R.J. I-446
BOSCAK, V. III-66
BRADBURN, K.M. II-499
BRADLEY, L.H. II-369
BRINKMANN, A. III-211
BUCK, V. III-335
BUMP, R.L. II-17
CAPPS, D.D. I-121
CARR, R.C. I-148
CHAMBERS, R. I-226, I-239
CHANG, R. III-271
CHEN, F.L. III-347
CHEN, Y.J. I-506
CHIANG, T. II-184
CHRISTENSEN, E.M. II-243
CHRISTIANSEN, J.V. II-243
CILIBERTI, D.F. III-282, III-318
CLEMENTS, J.S. II-96
COE,JR, E.L. II-416
COLE, W.H. III-1

COOK, D.R. II-349
COWHERD,JR, C. III-183
COY, D.W. III-370
CRYNACK, R.R. II-1
CUSCINO, T. III-154
CUSHING, K.M. I-148
DAHLIN, R.S. I-192
DARBY, K. II-499
DAVIS, R.H. II-96
DAVIS, W.T. I-521
DAVISON, J.W. III-166
DELANEY, S. I-357
DEMIAN, A. III-66
DENNIS, R. I-22, III-81
DIRGO, J.A. III-26, III-81
DISMUKES, E.B. II-444
DONOVAN, R.P. I-77, I-107, I-316, I-327, I-342
DORCHAK, T.P. III-114
DRENKER, S. III-271, III-282
DRIGGERS, G.W. II-194
DUBARD, J.L. II-337
DUFFY, M.J. II-489
DURHAM, M. II-84, III-241
EBREY, J.M. II-349
ENGLEHART, P.J. III-183
ENSOR, D.S. III-347
FAULKNER, M.B. II-204, II-337
FINNEY, W.C. II-96
FORTUNE, O.F. I-482, I-494
FOSTER, J.T. I-37, I-91
FREDERICK, E.R. I-536
FRISCH, N.W. III-114
FURLONG, D.A. I-287, I-342
GARDNER, R.P. I-77, I-107
GAWRELUK, G.R. II-17
GELFAND, P. II-35

GIBBS, J.L. II-430
GILES, W.B. III-41, III-53
GOLAN, L.P. III-226
GOLDBRUNNER, P.R. II-401
GOLIGHTLEY, R.M. I-164
GOOCH, J.P. II-444
GOODWIN, J.L. III-226
GRANT, M.A. III-81
GREEN, G.P. I-192
GREINER, G.P. I-287, I-357
GRONBERG, S. III-141
GRUBB, W.T. I-62, I-91, I-179
HALL, H.J. II-459
HALOW, J.S. II-96
HANSON , P. I-460
HARMON, D. I-226, I-239, III-131
HAWKINS, L.A. II-194
HERCEG, Z. II-489
HOVIS, L.S. I-22, I-77, I-107, I-287, I-316, I-327, I-342, I-357, III-81, III-347
HOWARD, J.R. I-164
INGRAM, T.J. I-446
ISAHAYA, F. II-154
ITAGAKI, T. II-322
JACOB, R.O. I-446
JENSEN, R.M. I-431
JONES, R. I-303
KASIK, L.A. II-430
KETCHUCK, M. I-482
KINSEY, J. III-154
KOHL, A.L. III-300
KUBY, W. III-271
KUNKA, S. I-239
KUTEMEYER, P.M. III-211
LAMB, G.E.R. I-303
LARSEN, P.S. II-243

LAWLESS, P.A. II-271
LEE, W. I-303
LEITH, D. III-26
LEONARD, G.L. II-230
LEWIS, M. I-179
LIPPERT, T.E. III-280, III-318
LUGAR, T.W. II-184
MARCHANT,JR, G.H. II-444
MASON, D.M. III-256
MASUDA, S. II-139, II-169, II-322, III-386
MATSUMOTO, Y. II-474
MATULEVICIUS, E.S. III-226
MCCAIN, J.D. III-198
MCCOLLOR, D.P. III-97
MCDONALD, J.R. II-204
MCKENNA, J.D. I-210
MCLEAN, K.L. II-489
MENARD, A. I-255
MILLER, M.L. I-482
MILLER, R.L. I-494
MILLER, S.J. III-97
MITCHNER, M. II-230
MOSLEHI, G.B. II-288, II-306
MOSLEY, R.B. II-204
MOYER, R.B. I-460
MUSGROVE, J. I-382
MYCOCK, J.C. I-210
NAKATANI, H. II-169
NG, T.S. II-489
NOVOGORATZ, D. II-349
OGLESBY, S. II-534
O'ROURKE, R. III-318
PEARSON, G. I-121
PETERS, H.J. I-179
PIULLE, W. II-401
PONTIUS, D.H. II-65

PUDELEK, R.E. I-521
PUTTICK, D.G. II-126
QUACH, M.T. I-506
RAMSEY, G.H. I-316, I-327
RANADE, M.A. III-347
REED, G.D. I-521
REHMAT, A. III-256
REIDER, J.P. III-183
REISINGER, A.A. I-179
RICHARDS, R.M. I-255
RICHARDSON, J.W. I-210
RINARD, G. II-84, III-241
ROOP, R.N. I-460
ROSS, D.R. I-164
RUGENSTEIN, W.A. II-430
RUGG, D. II-84, III-241
RUSSELL-JONES, A. II-384
SAIBINI, J. I-132
SAMUEL, E.A. I-1, II-218
SANDELL, M.A. II-1
SAWYER, J. III-271
SEARS, D.R. I-192, III-97
SELF, S.A. II-230, II-228, II-306
SHACKLETON, M. III-271
SHISHIKUI, Y. II-139
SMITH, W.B. I-148
SORENSON, P.H. III-362
SPARKS, L.E. II-204, II-271, II-337
SPENCE, N. I-132
SPENCER,III, H.W. I-506
STELMAN, D. III-300
STOCK, D.E. II-261
SUHRE, D. III-335
SUNTER, T.C. I-48
SURATI, H. II-51
TACHIBANA, N. II-474

TASSICKER, O.J. III-271, III-282
THOMPSON, C.S. III-12
THOMSEN, H.P. II-243
TOKUNAGA, O. II-96
TREXLER, E.C. II-96
TRILLING, C.A. III-300
TSAO, K.C. III-256
VANN BUSH, P. II-65
VANOSDELL, D.W. I-287, I-342
WALSH, M.A. I-482
WEBER, E. II-111
WELLAN, W.G. I-420
WEXLER, I.M. II-521
WHITTLESEY, M. I-482
WILCOX, K. III-154
WILLIAMSON, A.D. III-198
YAMAMOTO, T. III-241
YEAGER, K.E. . . . . III-xv

☆ U.S. GOVERNMENT PRINTING OFFICE 1985 - 559-111/10738